CELL COMMUNICATION IN VASCULAR BIOLOGY

EDITED BY: Xavier F. Figueroa, Walter N. Durán and Mauricio P. Boric
PUBLISHED IN: Frontiers in Physiology, Frontiers in Cell and Developmental Biology and Frontiers in Cardiovascular Medicine

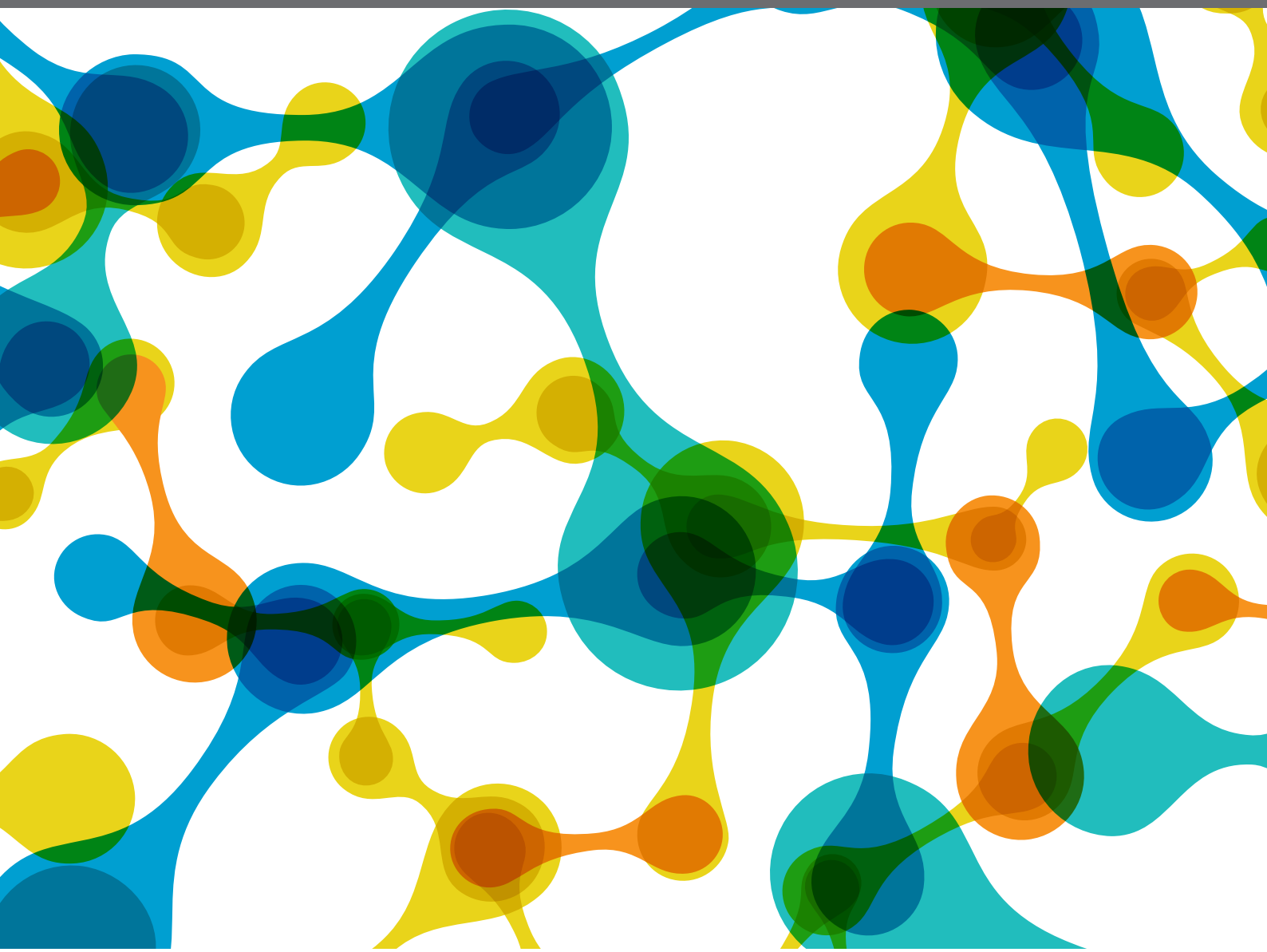

frontiers Research Topics

frontiers

ISSN 1664-8714
ISBN 978-2-88966-676-8
DOI 10.3389/978-2-88966-676-8

About Frontiers

Frontiers is more than just an open-access publisher of scholarly articles: it is a pioneering approach to the world of academia, radically improving the way scholarly research is managed. The grand vision of Frontiers is a world where all people have an equal opportunity to seek, share and generate knowledge. Frontiers provides immediate and permanent online open access to all its publications, but this alone is not enough to realize our grand goals.

Frontiers Journal Series

The Frontiers Journal Series is a multi-tier and interdisciplinary set of open-access, online journals, promising a paradigm shift from the current review, selection and dissemination processes in academic publishing. All Frontiers journals are driven by researchers for researchers; therefore, they constitute a service to the scholarly community. At the same time, the Frontiers Journal Series operates on a revolutionary invention, the tiered publishing system, initially addressing specific communities of scholars, and gradually climbing up to broader public understanding, thus serving the interests of the lay society, too.

Dedication to Quality

Each Frontiers article is a landmark of the highest quality, thanks to genuinely collaborative interactions between authors and review editors, who include some of the world's best academicians. Research must be certified by peers before entering a stream of knowledge that may eventually reach the public - and shape society; therefore, Frontiers only applies the most rigorous and unbiased reviews.
Frontiers revolutionizes research publishing by freely delivering the most outstanding research, evaluated with no bias from both the academic and social point of view. By applying the most advanced information technologies, Frontiers is catapulting scholarly publishing into a new generation.

What are Frontiers Research Topics?

Frontiers Research Topics are very popular trademarks of the Frontiers Journals Series: they are collections of at least ten articles, all centered on a particular subject. With their unique mix of varied contributions from Original Research to Review Articles, Frontiers Research Topics unify the most influential researchers, the latest key findings and historical advances in a hot research area! Find out more on how to host your own Frontiers Research Topic or contribute to one as an author by contacting the Frontiers Editorial Office: frontiersin.org/about/contact

CELL COMMUNICATION IN VASCULAR BIOLOGY

Topic Editors:
Xavier F. Figueroa, Pontificia Universidad Católica de Chile, Chile
Walter N. Durán, The State University of New Jersey, United States
Mauricio P. Boric, Pontificia Universidad Católica de Chile, Chile

Citation: Figueroa, X. F., Durán, W. N., Boric, M. P., eds. (2021). Cell Communication in Vascular Biology. Lausanne: Frontiers Media SA. doi: 10.3389/978-2-88966-676-8

Table of Contents

frontiers in Physiology

EDITORIAL
published: 03 March 2021
doi: 10.3389/fphys.2021.656959

Editorial: Cell Communication in Vascular Biology

Mauricio P. Boric[1], *Walter N. Durán*[2] *and Xavier F. Figueroa*[1]*

[1] *Departamento de Fisiología, Facultad de Ciencias Biológicas, Pontificia Universidad Católica de Chile, Santiago, Chile,*
[2] *Department of Pharmacology, Physiology and Neuroscience, New Jersey Medical School, Rutgers, The State University of New Jersey, Newark, NJ, United States*

Keywords: vascular function, blood flow distribution, cell communication, endothelial cell, vascular smooth muscle cell, vascular diseases, cerebral circulation

Editorial on the Research Topic

Cell Communication in Vascular Biology

This Research Topic comprises 5 review articles and 10 original contributions in the field of cell communication in Vascular Biology. Contributors used a variety of experimental approaches and models, or exercised keen analysis of published reports, to assess intercellular signaling between different pairs of cell types, such as the endothelium with vascular smooth muscle (VSM), platelets, leukocytes, tumor cells, and trophoblasts; but also, VSM and macrophages or among complex systems like intact vessels, the neurovascular unit and placenta. Communication includes direct cell-cell contact by adhesion molecules or gap junctions; classic receptor-mediated paracrine signaling and intercellular genetic modification by non-coding RNAs (NcRNA) or microvesicles transfer; all of this in the context of physiological regulation and different pathologies.

Control of blood flow supply by the vascular system is essential to keep the homeostasis of each cell of the organism, and then, blood flow distribution must be dynamically regulated to match the changing metabolic demand of surrounding tissue. Although the amount of blood flow depends on the total cross-sectional area of arteries (i.e., total number and caliber) irrigating a particular territory, blood vessels are not inert conduits aimed to passively transport blood into the tissues, but they actually are complex, multicellular structures that must work as a unit to rapidly adjust the distribution of blood flow according to the minute-to minute cellular requirements (Segal et al., 2000; Segal, 2005). The vessel wall is mainly constituted by smooth muscle cells and endothelial cells; thus, cell-to-cell communication is fundamental for the fine synchronization of function between these two cell types along the length of the vessels (Segal, 2015). It should be noted that synchronization and coordination are accomplished by an intricate system of complementary signaling pathways, which involves the interaction of direct cell-to-cell communication via gap junctions and the release of autocrine/paracrine signals (Figueroa and Duling, 2009; Moncada and Higgs, 2018). The relevance of this interaction is highlighted by the fine coordination of endothelial and smooth muscle cell function observed in the control of vasomotor tone through gap junctions located at the myoendothelial junctions (i.e., myoendothelial gap junctions) and endothelium-derived relaxing signals, such as nitric oxide (NO), prostaglandins and an unidentified signal known as endothelium-derived hyperpolarizing factor (EDHF) (Busse et al., 2002). The regulation of these signaling pathways is elegantly depicted in this Research Topic by Schmidt and de Wit.

Gap junctions are made up by the association of two hemichannels provided by each adjacent cell and, in turn, hemichannels are formed by connexin proteins (Sáez et al., 2003; Molica et al., 2018). However, individual hemichannels can be functional and work as a complementary signaling pathway to pannexins, which form channels with similar characteristics to hemichannels. Both connexin hemichannels and pannexin channels can contribute to the intercellular vascular

OPEN ACCESS

Edited and reviewed by:
Cor de Wit,
University of Lübeck, Germany

Correspondence:
Xavier F. Figueroa
xfigueroa@bio.puc.cl

Specialty section:
This article was submitted to Vascular Physiology, a section of the journal Frontiers in Physiology

Received: *21 January 2021*
Accepted: *09 February 2021*
Published: *03 March 2021*

Citation:
Boric MP, Durán WN and Figueroa XF (2021) Editorial: Cell Communication in Vascular Biology. Front. Physiol. 12:656959. doi: 10.3389/fphys.2021.656959

signaling by the release of autocrine/paracrine signals, such as ATP, NO, and PG (Begandt et al., 2017), as noted in the article of Kameritsch and Pogoda.

Coordination of endothelial and smooth muscle cell function does not only rely on the intercellular signaling generated in a particular vessel segment (i.e., radial communication), but also on the longitudinal communication along the whole vessel length. In addition, small arteries and arterioles form a complex network in the microcirculation, where different vessel segments must work in concert to regulate blood flow distribution by precise, well-integrated changes in the luminal diameter (Segal, 2005; Figueroa and Duling, 2009), as demonstrated by the conduction of vasomotor responses along the longitudinal axis of microvessels (Møller et al.).

In addition to the complex signaling interaction between the cells of the vascular wall, regulation of blood flow distribution in peripheral tissues depends on both local signals from the surrounding tissues and the autonomic nervous system, basically the sympathetic nervous system (Thomas and Segal, 2004; Westcott and Segal, 2013; Gaete et al., 2014). However, paradoxically, cerebral blood flow is mainly controlled by local signaling across the neurovascular unit (neurons, astrocytes and cell types of the vascular wall) through a communication mechanism known as neurovascular coupling or vasculo-neuronal coupling, depending on the direction of the signaling, from neurons to vessels or from vascular cells to neurons, respectively (Moore and Cao, 2008; Muñoz et al., 2015; Kim et al., 2016; Iadecola, 2017). Importantly, the article of Presa et al. illustrates that pathological conditions, such as hypertension, may lead to alterations in these communication mechanisms with a subsequent cognitive decline.

Not only the amount of blood flow through different territories must be regulated according to demand, but the vascular wall constitutes a regulated barrier for transport or exclusion of small metabolites, proteins and circulating blood cells. In this context, brain function also relies on the control of neuronal environment by endothelial cells in the blood brain barrier (BBB) (Obermeier et al., 2013) and the functional integrity of the barrier can be stressed in inflammatory conditions, as shown by Ittner et al. It should be noted that endothelial cells are not only important for the correct BBB function, but also for the blood-labyrinth-barrier (BLB) integrity of the stria vascularis in the cochlea (Shi, 2016). Interestingly, connexin-mediated communication plays a central role in the BBB signaling (Gaete et al., 2014) and now the study of Zhang J. et al. extends these data, demonstrating the relevance of Cx43 in the BLB functional integrity and, consequently, in the hearing function. In addition to the regulation of endothelial barrier integrity and exchange functions, cell adhesion and transmigration are important features that may be altered in pathological conditions (Durán et al., 2010; Filippi, 2019). The mechanisms involved in the communication of the vascular wall with blood circulating cells are complex; and in this article collection, endothelial interaction with and transmigration of leucocytes and tumor cells in the peripheral circulation, and the role of NO in these processes is clearly detailed by Aguilar et al..

Two complementary compartments can be recognized in the vascular system, the arterial and venous circulations. Both compartments, in turn, are divided into two functionally different vascular territories: the macrocirculation and microcirculation, which are structurally designed to perform different functions in response to distinct stimuli. In this context, it is noteworthy that fine control of gene expression is essential to maintain the functional integrity of the different segments of the vascular system and, consistent with this notion, the progress of diverse vascular-related pathologies is associated with variations in the transcriptional profile (Lamont and Childs, 2006; Man et al., 2016). Therefore, a thorough analysis of the changes in the gene expression pattern is required to understand the morphological and functional modifications observed in diverse pathological and clinical conditions, which highlights the contribution of the studies reported in this article collection regarding vessel remodeling induced by drastic hemodynamic changes, by Zhang X. et al. in an aortic constriction model and Jie et al. in an arteriovenous fistula model. Likewise, in agreement with the relevance of the fine control of gene expression in vascular homeostasis, regulatory NcRNA, such as long non-coding RNAs (lncRNA) and microRNAs (miRNA), have been recognized to be key players in the control of endothelial and smooth muscle cell function (Balamurali and Stoll, 2020; Ono et al., 2020). Accordingly, NcRNAs have been found to be involved in the pathogenesis of several cardiovascular diseases, but also, they have been proposed as therapeutic target molecules, in line with the results presented in the articles of Cheng et al. in spine cord injury repair and Su et al. in diabetic neointimal hyperplasia. Interestingly, miRNAs can be transmitted through microvesicles (Van Niel et al., 2018), which is addressed in this article collection by Zheng et al., showing that miRNA release via endothelial microvesicles can be involved in the pulmonary vascular leakage and lung injury observed in sepsis.

Cardiovascular diseases are the leading cause of morbidity and mortality worldwide and endothelial cells play a fundamental role in the control of cardiovascular homeostasis by the synthesis and release of a wide spectrum of signals that modulate angiogenesis, inflammation, hemostasis, vasomotor tone, and vascular permeability (Sturtzel, 2017). Then, in agreement with the importance of the endothelium, disturbance, impairment, or loss of normal function of endothelial cells (i.e., endothelial dysfunction) has been recognized as one of the most prominent risk factors for the development of cardiovascular diseases (Endemann and Schiffrin, 2004; Hirase and Node, 2012). Endothelial dysfunction has been directly linked with the initiation and evolution of hypertension and atherosclerosis (Gimbrone and García-Cardeña, 2016; Konukoglu and Uzun, 2016), but it has also been associated with physiological as well as pathophysiological processes, including aging, heart failure, coronary syndrome, thrombosis, intravascular coagulation, type I and II diabetes, obesity, inflammation, sepsis, and sleep apnea syndrome (Endemann and Schiffrin, 2004). In this article collection, the role of endothelial dysfunction in pre-eclampsia is highlighted and strengthened by the work of Liu et al.. However, it should be

noted that vascular homeostasis and integrity also depend on the smooth muscle layer of the vessel wall (Majesky, 2016); in this context, Beck et al. address the impact of endothelial dysfunction in arterial remodeling in diabetes. Similarly, Ackers et al. show that alterations in smooth muscle cell signaling pathways can lead to the development of vascular diseases, such as atherosclerosis.

Overall, this Research Topic provides a comprehensive review and original contributions for the continued investigation of regulation of cell communications in vascular biology.

AUTHOR CONTRIBUTIONS

XF: manuscript writing and edition. MB and WD: contribution in manuscript writing and edition. All authors contributed to the article and approved the submitted version.

FUNDING

This work was supported by Grant #1150530 (to XF) from Fondo Nacional de Desarrollo Científico y Tecnológico (FONDECYT) and by NIH-NHLBI grant 1R01HL146539 (to WD).

REFERENCES

Balamurali, D., and Stoll, M. (2020). Non-coding RNA databases in cardiovascular research. *Non-coding RNA* 6, 1–13. doi: 10.3390/ncrna6030035

Begandt, D., Good, M. E., Keller, A. S., DeLalio, L. J., Rowley, C., Isakson, B. E., et al. (2017). Pannexin channel and connexin hemichannel expression in vascular function and inflammation. *BMC Cell Biol.* 18, 1–16. doi: 10.1186/s12860-016-0119-3

Busse, R., Edwards, G., Félétou, M., Fleming, I., Vanhoutte, P. M., and Weston, A. H. (2002). EDHF: Bringing the concepts together. *Trends Pharmacol. Sci.* 23, 374–380. doi: 10.1016/S0165-6147(02)02050-3

Durán, W. N., Breslin, J. W., and Sánchez, F. A. (2010). The NO cascade, eNOS location, and microvascular permeability. *Cardiovasc. Res.* 87, 254–261. doi: 10.1093/cvr/cvq139

Endemann, D. H., and Schiffrin, E. L. (2004). Endothelial dysfunction. *J. Am. Soc. Nephrol.* 15, 1983–1992. doi: 10.1097/01.ASN.0000132474.50966.DA

Figueroa, X. F., and Duling, B. R. (2009). Gap Junctions in the control of vascular function. *Antioxid. Redox Signal.* 11, 251–266. doi: 10.1089/ars.2008.2117

Filippi, M. D. (2019). Neutrophil transendothelial migration: updates and new perspectives. *Blood* 133, 2149–2158. doi: 10.1182/blood-2018-12-844605

Gaete, P. S., Lillo, M. A., and Figueroa, X. F. (2014). Functional role of connexins and pannexins in the interaction between vascular and nervous system. *J. Cell. Physiol.* 229, 1336–1345. doi: 10.1002/jcp.24563

Gimbrone, M. A., and García-Cardeña, G. (2016). Endothelial cell dysfunction and the pathobiology of atherosclerosis. *Circ. Res.* 118, 620–636. doi: 10.1161/CIRCRESAHA.115.306301

Hirase, T., and Node, K. (2012). Endothelial dysfunction as a cellular mechanism for vascular failure. *Am. J. Physiol. Hear. Circ. Physiol.* 302, H499–H505. doi: 10.1152/ajpheart.00325.2011

Iadecola, C. (2017). The neurovascular unit coming of age: a journey through neurovascular coupling in health and disease. *Neuron* 96, 17–42. doi: 10.1016/j.neuron.2017.07.030

Kim, K. J., Diaz, J. R., Iddings, J. A., and Filosa, J. A. (2016). Vasculo-neuronal coupling: retrograde vascular communication to brain neurons. *J. Neurosci.* 36, 12624–12639. doi: 10.1523/JNEUROSCI.1300-16.2016

Konukoglu, D., and Uzun, H. (2016). "Endothelial dysfunction and hypertension," in *Hypertension: From Basic Research to Clinical Practice. Advances in Experimental Medicine and Biology,* Vol. 956, ed M. S. Islam (Cham: Springer), 511–540. doi: 10.1007/5584_2016_90

Lamont, R. E., and Childs, S. (2006). MAPping out arteries and veins. *Sci. STKE* 2006:e39. doi: 10.1126/stke.3552006pe39

Majesky, M. W. (2016). Vascular smooth muscle cells. *Arterioscler. Thromb. Vasc. Biol.* 36, e82–e86. doi: 10.1161/ATVBAHA.116.308261

Man, H. S. J., Yan, M. S., Lee, J. J. Y., and Marsden, P. A. (2016). Epigenetic determinants of cardiovascular gene expression: vascular endothelium. *Epigenomics* 8, 959–979. doi: 10.2217/epi-2016-0012

Molica, F., Figueroa, X. F., Kwak, B. R., Isakson, B. E., and Gibbins, J. M. (2018). Connexins and pannexins in vascular function and disease. *Int. J. Mol. Sci.* 19:1663. doi: 10.3390/ijms19061663

Moncada, S., and Higgs, E. A. (2018). Molecular mechanisms and therapeutic strategies related to nitric oxide. *FASEB J.* 9, 1319–1330. doi: 10.1096/fasebj.9.13.7557022

Moore, C. I., and Cao, R. (2008). The hemo-neural hypothesis: on the role of blood flow in information processing. *J. Neurophysiol.* 99, 2035–2047. doi: 10.1152/jn.01366.2006

Muñoz, M. F., Puebla, M., and Figueroa, X. F. (2015). Control of the neurovascular coupling by nitric oxide-dependent regulation of astrocytic Ca^{2+} signaling. *Front. Cell. Neurosci.* 9:59. doi: 10.3389/fncel.2015.00059

Obermeier, B., Daneman, R., and Ransohoff, R. M. (2013). Development, maintenance and disruption of the blood-brain barrier. *Nat. Med.* 19, 1584–1596. doi: 10.1038/nm.3407

Ono, K., Horie, T., Baba, O., Kimura, M., Tsuji, S., Rodriguez, R. R., et al. (2020). Functional non-coding RNAs in vascular diseases. *FEBS J.* doi: 10.1111/febs.15678. [Epub ahead of print].

Sáez, J. C., Berthoud, V. M., Brañes, M. C., Martínez, A. D., and Beyer, E. C. (2003). Plasma membrane channels formed by connexins: their regulation and functions. *Physiol. Rev.* 83, 1359–1400. doi: 10.1152/physrev.00007.2003

Segal, S. S. (2005). Regulation of blood flow in the microcirculation. *Microcirculation* 12, 33–45. doi: 10.1080/10739680590895028

Segal, S. S. (2015). Integration and modulation of intercellular signaling underlying blood flow control. *J. Vasc. Res.* 52, 136–157. doi: 10.1159/000439112

Segal, S. S., John, T., and Haven, N. (2000). Integration of blood flow control to skeletal muscle: key role of feed arteries. *Acta Physiol. Scand.* 168, 511–518. doi: 10.1046/j.1365-201x.2000.00703.x

Shi, X. (2016). Pathophysiology of the cochlear intrastrial fluid-blood barrier (review). *Hear. Res.* 338, 52–63. doi: 10.1016/j.heares.2016.01.010

Sturtzel, C. (2017). "Endothelial cells," in *The Immunology of Cardiovascular Homeostasis and Pathology. Advances in Experimental Medicine and Biology*, Vol 1003, eds S. Sattler and T. Kennedy-Lydon (Cham: Springer), 71–91. doi: 10.1007/978-3-319-57613-8_4

Thomas, G. D., and Segal, S. S. (2004). Neural control of muscle blood flow during exercise. *J. Appl. Physiol.* 97, 731–738. doi: 10.1152/japplphysiol.00076.2004

Van Niel, G., D'Angelo, G., and Raposo, G. (2018). Shedding light on the cell biology of extracellular vesicles. *Nat. Rev. Mol. Cell Biol.* 19, 213–228. doi: 10.1038/nrm.2017.125

Westcott, E. B., and Segal, S. S. (2013). Perivascular innervation: a multiplicity of roles in vasomotor control and myoendothelial signaling. *Microcirculation* 20, 217–238. doi: 10.1111/micc.12035

Conflict of Interest: The authors declare that the research was conducted in the absence of any commercial or financial relationships that could be construed as a potential conflict of interest.

frontiers in Cardiovascular Medicine

ORIGINAL RESEARCH
published: 05 May 2020
doi: 10.3389/fcvm.2020.00073

Increased Catecholamine Levels and Inflammatory Mediators Alter Barrier Properties of Brain Microvascular Endothelial Cells *in vitro*

*Cora Ittner[1], Malgorzata Burek[1], Stefan Störk[2], Michiaki Nagai[3] and Carola Y. Förster[1]**

[1] Department of Anaesthesia and Critical Care, University of Würzburg, Würzburg, Germany, [2] Comprehensive Heart Failure Center, University of Würzburg, Würzburg, Germany, [3] Department of Internal Medicine, General Medicine and Cardiology, Hiroshima City Asa Hospital, Hiroshima, Japan

OPEN ACCESS

Edited by:
Mauricio Boric P., Pontifical Catholic University of Chile, Chile

Reviewed by:
Christoph Eugen Hagemeyer, Monash University, Australia
Adriana Georgescu, Institute of Cellular Biology and Pathology (ICBP), Romania

***Correspondence:**
Carola Y. Förster
Foerster_C@ukw.de

Specialty section:
This article was submitted to Atherosclerosis and Vascular Medicine, a section of the journal Frontiers in Cardiovascular Medicine

Received: *03 February 2020*
Accepted: *14 April 2020*
Published: *05 May 2020*

Citation:
Ittner C, Burek M, Störk S, Nagai M and Förster CY (2020) Increased Catecholamine Levels and Inflammatory Mediators Alter Barrier Properties of Brain Microvascular Endothelial Cells in vitro. Front. Cardiovasc. Med. 7:73. doi: 10.3389/fcvm.2020.00073

Recent studies have suggested a pathogenetic link between ischemic stroke and Takotsubo cardiomyopathy (TCM) with poor outcome, when occurring simultaneously. Increased catecholamine (CAT) levels as well as elevated inflammatory mediators (INF) are found in the blood of patients with ischemic stroke concomitant with Takotsubo syndrome (TTS). On molecular level, the impact of these stressors combined with hypoxemia could compromise the integrity of the blood brain barrier (BBB) resulting in poor outcomes. As a first step in the direction of investigating possible molecular mechanisms, an *in vitro* model of the described pathological constellation was designed. An immortalized murine microvascular endothelial cell line from the cerebral cortex (cEND) was used as an established *in vitro* model of the BBB. cEND cells were treated with supraphysiological concentrations of CAT (dopamine, norepinephrine, epinephrine) and INF (TNF-α and Interleukin-6). Simultaneously, cells were exposed to oxygen glucose deprivation (OGD) as an established *in vitro* model of ischemic stroke with/without subsequent reoxygenation. We investigated the impact on cell morphology and cell number by immunofluorescence staining. Furthermore, alterations of selected tight and adherens junction proteins forming paracellular barrier as well as integrins mediating cell-matrix adhesion were determined by RT-PCR and/or Western Blot technique. Especially by choosing this wide range of targets, we give a detailed overview of molecular changes leading to compromised barrier properties. Our data show that the proteins forming the BBB and the cell count are clearly influenced by CAT and INF applied under OGD conditions. Most of the investigated proteins are downregulated, so a negative impact on barrier integrity can be assumed. The structures affected by treatment with CAT and INF are potential targets for future therapies in ischemic stroke and TTS.

Keywords: blood-brain barrier, microvascular endothelium, cEND cell line, takotsubo syndrome, catecholamines, inflammation, *in vitro*

INTRODUCTION

Recent clinical publications and literature reviews point out that takotsubo syndrome (TTS) occurring in combination with ischemic stroke is a notable clinical constellation (1). The link between these two pathologies is not well-understood yet, especially not on molecular level.

Takotsubo cardiomyopathy (TCM) is a cardiac pathology at first glance mimicking acute coronary syndrome (ACS). The most important clinical feature is the absence of coronary occlusion which differentiates TCM from ACS (2). Characteristic wall motion abnormalities predominantly affecting the left ventricle are observed. This phenomenon is described as apical ballooning. Patients are mostly postmenopausal women, who present dyspnea, chest pain as well as new ECG alterations and/or elevated cardiac enzymes (2). Precursory cerebrovascular disease no longer interdicts to diagnose TCM. In one to two thirds of patients suffering from TCM, a previous psychically or physically stressful trigger can be identified (3, 4).

Interestingly, there is no strict sequence, whether ischemic stroke or TCM develop first. Ischemic stroke is described as a neurological precipitant of TTS. In contrast, thrombus formation caused by left ventricular dysfunction within TCM can also lead to ischemic stroke. Hereby, ischemic strokes in patients with TTS are usually severe and classified by an initially higher NIHSS score in comparison with patients without TTS. Poor outcomes are frequent in the patients of ischemic stroke with TTS (1, 5).

Patients presenting the described pathological pattern, show characteristically altered laboratory findings: Supraphysiological CAT blood levels can be determined (6). This reflects the plausible theory of TTS pathogenesis consisting in raised CAT, which are assumed to mediate myocardial wall motion abnormalities (3). Furthermore, elevated inflammatory markers are found (1). This correlates with the known fact of raised INF in ischemic areas after stroke. Resident cerebral immune cells as well as migrated immune cells synthesize, inter alia, pro-inflammatory cytokines like TNF-α and IL-6 (7). Especially cardioembolic strokes are associated with increased CRP, TNF-α, and IL-6 levels compared to other subtypes of ischemic insults (8). Although, the role of the two mentioned cytokines is still diversely discussed, clinical and experimental data suggest an aggravation of ischemic brain damage by inflammatory spillover. Furthermore, dysfunction of the cerebral microvascular endothelium in the frame of ischemic stroke is promoted by systemic inflammation (7).

The depicted clinical situation presents a pathological process within the brain-heart axis. In general, the brain-heart axis is a dual system, which works up and down stream: cardiac dysfunction may trigger neurovascular deterioration and vice versa (9). Ischemic stroke and TCM seem to interact due to the influence of the insular cortex on the modulation of the autonomic nervous system. *In vivo* animal models as well as human studies have shown ischemic lesions affecting the insular cortex cause autonomic dysregulation (10), especially when concerning the left hemisphere, the impairment of the insular cortex produces a sympathetic overdrive reflected by elevated CAT levels (11). Clinical findings correspondingly suggest a predominance of ischemic strokes affecting the insular cortex and/or adjacent brain regions preceding TTS (12).

As part of the brain-heart axis, the BBB reacts to hypoxic events caused by cardiac impairment and vice versa (9). Therefore, when investigating pathologies of the brain-heart axis the BBB has to be included in speculation on possible pathogenetic mechanisms.

Sustained integrity of the BBB is mandatory for maintaining the homeostasis of the central nervous system (CNS). Thus, the CNS gets its unique position by not being exposed unselectively to systemic alterations such as inflammation (13). Restricted permeability is provided by microvascular endothelial cells forming dense cell-cell contacts: a dynamic interface is ensured by tight junctions (TJ) and adherens junctions (AJ) building a restrictive barrier (14, 15). If circulating noxious agents affect vascular endothelium itself, TJ as well as AJ could not be maintained properly leading to a breakdown of the BBB (16). Cerebral vascular endothelium forming the BBB, on its blood facing side, is constantly exposed to systemically circulating INF, and elevated CAT blood levels. The proinflammatory cytokines TNF-α and IL-6, as elevated in acute TTS (1) are proven to be harmful factors for the integrity of the BBB by compromising TJ protein as well as AJ protein expression *in vitro* (17, 18). Systemical administration of epinephrine lead to a disruption of the BBB *in vivo* (19). Furthermore, focal ischemia results in a breakdown of the BBB, which produces increased permeability. Aggravation of brain damage by secondary effects such as brain edema is provoked (13). TJ proteins claudin-5, occludin as well as AJ protein VE-cadherin were shown to be targets of hypoxic conditons *in vitro* (20).

Based on these assumptions, we suggest that the severity of ischemic stroke in patients with TTS is caused by aggravated dysfunction of the BBB. An intensified impairment of the vascular endothelial cells generated by elevated CAT levels and INF combined with hypoxia is hypothesized. As a first step of investigating this pathologic constellation, an *in vitro* experiment was designed. Supraphysiological CAT levels combined with INF were applied under OGD (20). An immortalized murine cerebral endothelial cell line (cEND) was chosen as a well-established *in vitro* model of the BBB (21). The present study provides a comprehensive overview of molecular changes of cerebral microvascular endothelium, exposed to an *in vitro* simulation of characteristic laboratory findings in patients suffering from TTS and ischemic stroke simultaneously.

MATERIALS AND METHODS

Chemicals

TNF-α, Dopamine, Epinephrine as well as Norepinephrine were purchased from Sigma-Aldrich. Interleukin-6 was purchased from Thermo Fisher. Epinephrine and Norepinephrine were dissolved in 0.5 M hydrochloric acid, Interleukin-6 in 100 nM acetic acid. TNF-α and Dopamine are readily soluble in water, so cell culture medium was used for dissolving. Final dilution of every agent was made shortly before the experiment in cell culture medium.

Cell Culture

As an *in vitro* model of the Blood Brain Barrier (BBB) we used the murine microvascular cerebral endothelial cell line cEND. Cells were isolated, immortalized, and cultivated as described previously (21–23).

Cell Treatment

Cells were grown to confluence within 5 days in Dulbeccos's modified eagles medium (DMEM) growth medium on 6-well-plates coated with gelatin. Growth medium consisted of DMEM (Sigma-Aldrich, D5796) containing 10% heat-inactivated fetal calf serum (FCS), 50 U/ml penicillin-streptomycin, 2% L-glutamine, 2% MEM vitamins, 2% non-essential amino acid solution (NEAA), and 2% sodium pyruvate. Subsequently, cells were differentiated for 48 h with DMEM differentiation medium containing 1% FCS as well as 50 U/ml penicillin-streptomycin. Stress factors were applied under different incubation conditions. Stress factors were defined as a combination of CAT [150 μM dopamine (24), 1 μM epinephrine (25), 1 μM norepinephrine (25)], and INF [100 nM TNF-α (18) and 5 pg/ml Interleukin-6 (26)]. For application on cells, stress factors were diluted to final concentration in DMEM differentiation medium or DMEM medium without glucose. Solvent of each agent was added in same concentration to control.

Oxygen Glucose Deprivation (OGD) and Reoxygenation

After differentiation cells were washed twice with PBS. Subsequently, 1.5 ml DMEM without glucose per well were added, followed by incubation under OGD condition for 4 h. OGD condition was defined as 1% O_2, 5% CO_2, 37°C and saturated humidity atmosphere as previously described (20). Control was incubated simultaneously under normoxia condition in 1.5 ml DMEM medium containing glucose per well. After OGD, samples were analyzed directly or reoxygenated for 20 h. Reoxygenation was conducted by washing cells twice with PBS, adding 3 ml DMEM medium containing glucose per well and incubation under normoxia condition (5% CO_2, 37°C, saturated humidity atmosphere) (20, 27).

Immunofluorescence Staining

Cells were cultivated on collagen IV-coated coverslips (diameter of 12 mm). Cultivation was conducted as described above. After finished treatment, cells were washed twice with PBS. Fixation for 10 min, with ice-cold methanol, followed by washing (twice; PBS), and 15 min, of PBS containing 1% BSA. Before incubation with primary antibodies overnight at 4°C, samples were blocked for 1 h at RT with PBS containing 1% BSA and 5% normal swine serum. As primary antibodies were chosen: Claudin-5 (1:500; Thermo Fisher (Alexa fluor), #352588) and ZO-1 (1:500; Thermo Fisher, #402300) diluted in PBS with 1% BSA/ 5% normal swine serum. After washing (3 times for 5 min. with PBS), secondary antibodies diluted in PBS with 1% BSA/ 5% normal swine serum were applied: DAPI (1:3000; Sigma-Aldrich, #D9542) and Alexa fluor 594 donkey anti rabbit IgG (1:2000; Thermo Fisher, #A21207). Coverslips were fixed onto slides by using Mountant permaflour (Thermo Fisher, #TA-030-FM) and dried overnight at RT. Subsequently, analysis was performed with a Keyence fluorescence microscope (BIOREVO BZ-9000). The number of cells with intact DAPI-stained nuclei was estimated by counting the nuclei in a defined area of interest for each treatment.

Western Blot Analysis

Western Blot analysis were performed as previously described (28). Briefly, cells were washed twice with ice cold PBS before being lysed in RIPA buffer containing protease inhibitors cocktail (Roche) and harvested. After sonication (10 times for 0.5 sec on ice), samples were centrifuged (11,000 rcf for 1 min) and supernatant was saved for quantification of protein content. Protein content was determined by BCA protein Assay Kit (Thermo Fisher). Protein separation was conducted using NuPAGE Kit (Thermo Fisher). Previously, samples were mixed with Laemmli buffer and reducing agent as indicated, followed by denaturation of 10 min. at 70°C. A NuPage 4–12% Bis-Tris-Gel (Thermo Fisher) was used for separation. The blot to a PVDF membrane was accomplished by electrophoretically wet transfer overnight (4°C) using a Electrophoretic Transfer Cell (BioRad). Subsequently, membrane was washed in PBS-T (3 times for 10 min.), blocked with 5% non-fat dry milk in PBS (1 h) and incubated overnight (4°C) with the primary antibody diluted in PBS containing 1% BSA. As primary antibodies we used: mouse anti-claudin-5 (1:500; Thermo Fisher, #35-2500), guinea pig anti-occludin (1:200; Acris, #358-504), rabbit anti-ZO-1 [1:500; Thermo Fisher, #40-2300), rat anti-VE-cadherin [pure; generated with hybridoma technique (29)] and anti-ß-aktin-HRP (1:25.000; Sigma-Aldrich, #A3854). Before applying secondary antibodies, membrane was washed with PBS-T (PBS with addition of 0.1% Tween) (3 times for 10 min) and blocked with 5% non-fat dry milk in PBS (20 min). Secondary antibodies were: anti-mouse IgG (1:3000; Roche, #12015218001), anti-guinea pig IgG (1:5000; Santa Cruz Biotechnology, #sc2438), anti-rabbit IgG (1:3000; Cell Signaling Technology, #7074S), and anti-rat IgG (1:5000; Thermo Fisher, Cat#61-9520). After washing the membrane with PBS-T (3 times for 10 min), incubation in ECL solution (2 min) followed. For imaging, Fluorchem FC2 MultiImager II (AlphaInnotech) was used. Density of protein bands was determined by ImageJ software (version 1.52a).

Real-Time PCR

Real-time PCR analysis were performed as previously described (30). Briefly, cells were washed twice with sterile PBS. Subsequently, samples were harvested and RNA was isolated as well as purified from lysed cells following manufacterer's instructions of Nucleospin RNA (Macherey-Nagel, #740955). Reverse transcription for generating cDNA was performed by using High Capacity cDNA Reverse Transcription Kit (Applied Biosystems, #4368814). TaqMan Fast Advanced Master Mix (Applied Biosystems, #4444557) with 1 μg cDNA for RT-PCR. For determining gene expression, the following TagMan Gene Expression Assay primers were chosen: Claudin-5 (Mm00727012_s1), occludin (Mm00500912_m1), ZO-1 (Mm00493699_m1), VE-cadherin (Mm00486938_m1), Itgα1 (Mm01306375_m1), Itgαv (Mm00434486_m1). All purchased from Thermo Fisher. Calnexin RNA was used as the

housekeeping gene (Canx; Mm00500330_m1). Subsequently, reverse transcription and amplification was conducted by using 7300 Real Time PCR System (Applied Biosystems) and under the following conditions: 95°C for 10 min, 50 cycles for each target, 60°C for 1 min.

Analysis and Statistics

Data are presented as mean ± standard error of the mean (SEM). Number of independent experiments is indicated under figures. Statistical significance was evaluated by One-way ANOVA with Tukey's correction for multiple comparison using GraphPad Prism. Statistical significance was assumed for $P < 0.05$.

RESULTS

We wanted to examine, whether supraphysiological CAT concentrations and INF, as found in TTS patients (1), change AJ and TJ structure under normoxic and ischemic conditions. We chose VE-cadherin as a representative of AJ proteins and claudin-5, ZO-1 as well as occludin as representative of TJ proteins. In addition, integrin-α-1, and integrin-α-v were selected as targets reflecting the possible interaction with extracellular matrix (ECM) components. Integrin-α-1, a subunit of the collagen receptor integrin $\alpha1\beta1$, binds collagen type IV (31), whereas integrin-α-v forms part of the vitronectin receptor $\alpha v\beta3$ (32). We used cEND cells, an immortalized murine microvascular endothelial cell line from the cerebral cortex, which is a well-established *in vitro* model of the BBB (21).

Barrier Compromising Effects of Catecholamines and Inflammatory Mediators on cEND Cells Under Normoxic Conditions

To investigate how CAT or INF affect cEND cells, we treated cEND cells for 24 h under standard culturing conditions, called normoxia conditions (24 h NORMOX). We used a mixture of 150 μM dopamine (24), 1 μM epinephrine (25), and 1 μM norepinephrine (25) for CAT samples. Treatment with INF consisted of 100 nM TNF-α (18) and 5 pg/ml Interleukin-6 (26). All stressors were diluted in differentiation medium (1% FCS) to final concentration. Potential effects on cell morphology were determined by staining of cell-cell junctions using anti-claudin-5 and ZO-1 antibodies (**Figure 1**). As observed in control samples, the expressed claudin-5 and ZO-1 were located at the cell-cell contacts (**Figures 1A,B**) (21). After treatment with CAT or INF, the cell morphology was altered and the localization of junctional proteins at cell-cell junction sites was reduced. Treatment with CAT resulted in a disruption of the homogenous cell monolayer, while the cellular morphology was still spindle-shaped (**Figure 1A**). The percentage of cells with intact nuclei was significantly lower in samples treated with CAT compared to the control (**Figure 1C**). cEND cells lost their elongated spindle-shaped morphology (21) due to treatment with INF and showed more cobble-stone-like phenotype (**Figure 1B**). The number of cells with intact nuclei was also significantly lower than in the untreated control (**Figure 1C**). As demonstrated in **Figure 1C**, CAT alone caused a stronger breakdown of the homogenous cell monolayer compared to INF. A lower number of cells with intact nuclei indicates that CAT and INF treatment induces cell death in cEND cells.

To investigate whether the barrier properties of cEND cells are also affected at the protein and mRNA, cells were treated as described above. Subsequently, RT-PCR and Western Blot were performed (**Figure 1**, **Table 1**). Protein level of ZO-1 was reduced by 0.57 ± 0.04-fold while claudin-5, occludin and VE-cadherin were not altered by the administration of CAT (**Figure 1D**). CAT caused a decreased gene expression of claudin-5 to 0.47 ± 0.02-fold, ZO-1 to 0.38 ± 0.05-fold, and VE-cadherin to 0.55 ± 0.02-fold of control. A change in the mRNA level of occludin could not be detected. Integrin-α-1 mRNA was decreased by 0.19 ± 0.02-fold while integrin-α-v expression increased up to 1.82 ± 0.24-fold of control. Protein expression of selected targets was not significantly altered by INF (results not shown). INF led to impaired gene expression of occludin (0.39 ± 0.05-fold), ZO-1 (0.51 ± 0.05-fold), and VE-cadherin (0.85 ± 0.02-fold), but did not alter claudin-5 mRNA level. Integrin-α-v gene expression increased up to 3.31 ± 0.54-fold after INF treatment, while no differences were detected in integrin-α-1 mRNA level (**Table 1**).

Barrier Compromising Effects of Catecholamine Levels and Inflammatory Mediators on cEND Cells in Hypoxic Condition *In vitro*

We combined elevated levels of CAT and INF with hypoxic and hypoglycemic conditions called oxygen glucose deprivation (OGD) with or without subsequent reoxygenation. OGD was previously established in cEND as an *in vitro* model of ischemic stroke (20). From that point on, CAT and INF were combined and labeled as stress factors. Stress factors were diluted to final concentration in differentiation or glucose-free medium to be used under selected incubation conditions. Four different incubation conditions were defined: 4 h of normoxia (4 h NORMOX), 24 h of normoxia (24 h NORMOX), 4 h of OGD, and 4 h of OGD with subsequent reoxygenation under normoxia condition (REOX).

First, we analyzed the cell morphology after these treatments. The cells were grown on coverslips, differentiated, and incubated as described above (**Figure 2**). Possible effects on cell morphology were determined by staining of TJs with anti-claudin-5 and -ZO-1 antibodies. Cells grown without stress factors under normoxia conditions (4 h NORMOX and 24 h NORMOX) as well as OGD condition showed no changes in the cell morphology (**Figures 2A–C**) nor in cell number (**Figure 2E**). cEND cells showed a homogenous endothelial monolayer and the typical elongated spindle-shaped morphology as described before (21, 22) Both stained TJ proteins, claudin-5, and ZO-1, were located at the TJs (**Figures 2A–C**). The reoxygenation sample without stress factors showed a disrupted cell monolayer with irregular cellular morphology and delocalized TJ-proteins (**Figure 2D**) but no reduced cell number (**Figure 2E**). The effects of stress factors applied under normoxia conditions depended on time. After 4 h of treatment, endothelial cell

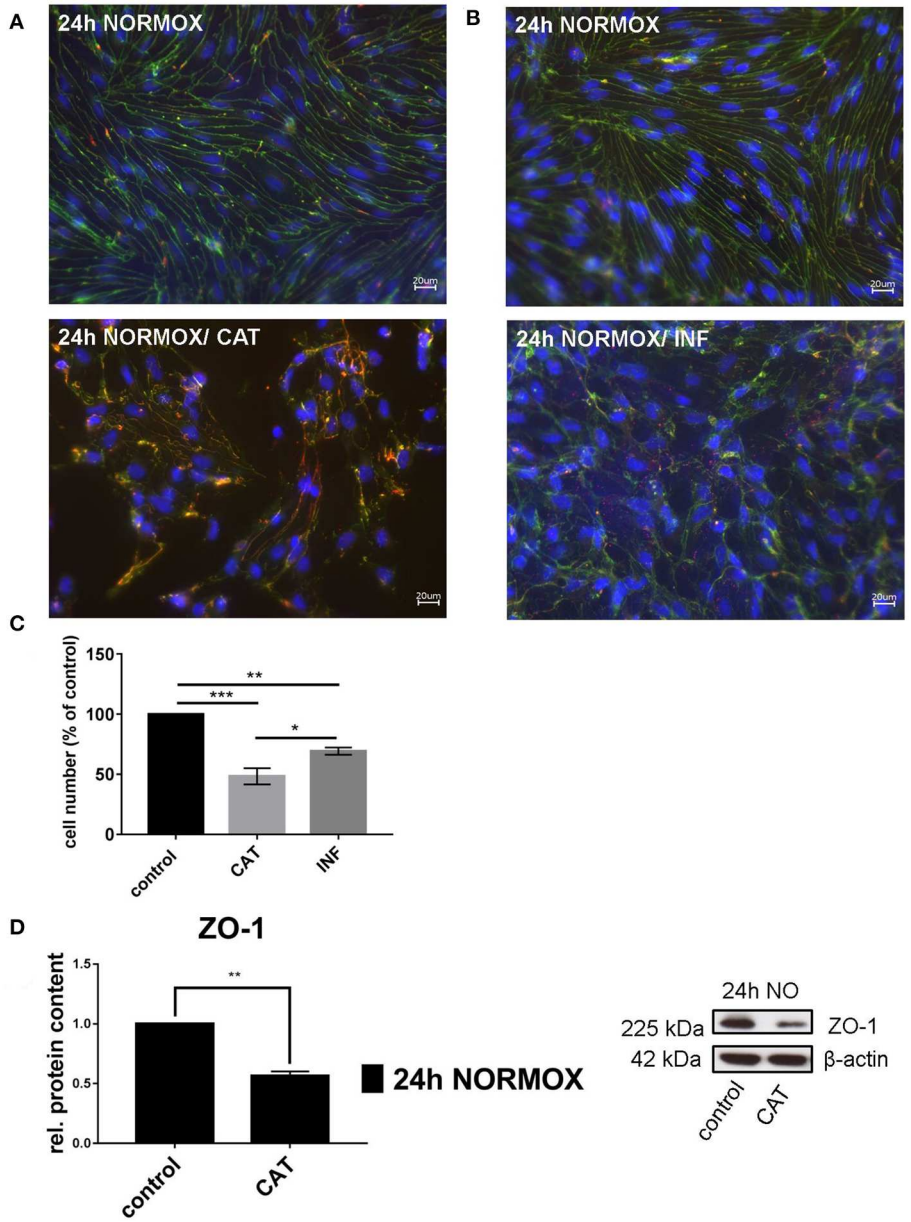

FIGURE 1 | Effects of catecholamines and inflammatory mediators under normoxia conditions on cEND cells. Cells were grown to confluence with subsequent differentiation. Catecholamines (CAT) or inflammatory mediators (INF) were applied for 24 h under normoxia conditions (24 h NORMOX). **(A,B)** Immunofluorescence staining of tight junction proteins claudin-5 (green) and ZO-1 (red) as markers of morphological changes of the endothelial cell monolayer. DAPI (blue) was used for staining of nuclei. Magnification 400 times, scale bar 20 μm. **(C)** Cell number after CAT and INF treatment normalized to control. **(D)** CAT induced changes of ZO-1 protein expression in cEND cells investigated by Western blot. Data is presented as the means (± SEM) of $n = 5$ independent experiments. Altered protein expression was normalized to β-actin. ZO-1 protein level changes are expressed as fold over untreated control, which was set 1. $^{*}P < 0.05$, $^{**}P < 0.01$, $^{***}P < 0.001$.

monolayer changed slightly, while after 24 h of treatment, stress factors led to complete destruction of the cell monolayer (**Figures 2A,B**/stress factors) and a significant reduction of cell number (**Figure 2E**). Combination of OGD with stress factors potentiated these effects (**Figures 2C**/stress factors and **Figure 2E**). Morphologically, the most severe effect was caused by the administration of stress factors under reoxygenation conditions (**Figure 2D**/stress factors and **Figure 2E**). A typical morphological phenotype of cEND cells was no longer observed. The cells completely lost their spindle-shaped appearance and showed an irregular morphology without monolayer formation and significantly reduced cell numbers. Stained TJ proteins were visible as small aggregates outside the cell-cell contacts (**Figure 2D**/stress factors).

TABLE 1 | Modulated target gene expression in cEND cells by elevated catecholamine levels or inflammatory mediators under normoxia conditions for 24 h.

	Claudin-5	ZO-1	Occludin	VE-cadherin	Itg α 1	Itg α v
CAT	0.47 ± 0.02***	0.38 ± 0.05***	1.05 ± 0.11n.s.	0.55 ± 0.02***	0.19 ± 0.02***	1.82 ± 0.24*
INF	1.18 ± 0.21n.s.	0.51 ± 0.05***	0.39 ± 0.05***	0.85 ± 0.02**	0.68 ± 0.15n.s.	3.31 ± 0.54**

*Catecholamines (CAT) or inflammatory mediators (INF) were applied for 24 h under normoxia conditions. After total RNA-extraction from lysed cells, mRNA was quantified by real-time PCR. Fold expression vs. untreated control, which was set 1. Values are the means (± SEM) of n = 5 (INF) or n = 6 (CAT) independent experiments, followed by statistical significance *P < 0.05, **P < 0.01, ***P < 0.001. n.s, not significant.*

Elevated Catecholamine Levels and Inflammatory Mediators Combined With Oxygen Glucose Deprivation Cause a Change in Gene Expression

We performed a real-time PCR, in order to investigate how the treatment with stress factors under different incubation conditions influences the gene expression of selected targets in cEND cells. First, we compared effects of stress factors under 4 h NORMOX, OGD, and REOX conditions, respectively (**Table 2**). Claudin-5 (0.49 ± 0.07-fold) and ZO-1 (0.7 ± 0.08-fold) gene expression was downregulated by OGD alone but upregulated again after REOX (claudin-5 0.88 ± 0.07-fold; ZO-1 1.26 ± 0.06-fold). This upregulation was not observed in combination with stress factor treatment. Similar changes were observed for occludin mRNA. VE-cadherin mRNA was significantly increased by OGD alone up to 1.56 ± 0.11-fold, followed by a decrease after REOX to 1.02 ± 0.03-fold. REOX in combination with stress factors caused a downregulation to 0.41 ± 0.06-fold of control. Integrin-α-1 was induced by REOX alone up to 1.43 ± 0.12-fold, but reduced to 0.05 ± 0.06-fold after REOX in combination with stress factors. Integrin-α-v mRNA was upregulated by OGD (4.08 ± 0.72-fold), while REOX caused downregulation (1.0 ± 0.04-fold). Within the same incubation conditions, stress factors did not have significant effects on every target (**Table 2**). Under 4 h NORMOX conditions, gene expression of ZO-1, occludin and integrin-α-1 was reduced by stress factors, whereas integrin-α-v was upregulated in comparison with untreated controls. OGD combined with stress factors affected mRNA levels of ZO-1, occluding, and VE-cadherin compared to OGD alone. After reoxygenation combined with stress factors gene expression of claudin-5, ZO-1, VE-cadherin, and integrin-α-1 was decreased in comparison with REOX alone. Subsequently, the data shown in **Table 2** under REOX and REOX/stress factors were then used again in **Table 3**, but in this case the mRNA expression of selected targets was normalized to 24 h NORMOX (**Table 3**). The comparison in **Table 2** enables an assessment of the gene expression over time, while **Table 3** shows the mRNA levels only at 24 h point under various conditions. Claudin-5 gene expression did not change significantly after REOX with and without stress factor treatment. ZO-1 and VE-Cadherin consistently showed the same tendencies as claudin-5. The mRNA levels of occludin (1.35 ± 0.07-fold) and integrin-α-1 (1.32 ± 0.07-fold), however, were upregulated by REOX, but only without stress factors. As already mentioned above, in this experiment stress factor administration did not have significant effects on every target as well (**Table 3**). Integrin-α-v gene expression was induced by 24 h NORMOX in combination with stress factors (1.82 ± 0.3-fold) compared to 24 h NORMOX alone. No significant change of integrin-α-v mRNA level by stress factor administration under REOX conditions was observed in comparison with REOX alone. However, REOX conditions combined with stress factor administration led to a significant decrease of the expression of all other target genes compared to REOX alone. Within 24 h NORMOX conditions stress factors caused reduced gene expression of claudin-5, ZO-1, occludin, VE-cadherin, and integrin-α-1 as well. Interestingly, effects of stress factor administration under REOX conditions did not differ from those under 24 h NORMOX conditions. As already observed in immunofluorescence staining, the effects of stress factors under normoxia conditions evolved over time, especially in the case of claudin-5 (**Tables 2**,**3**). After 4 h, mRNA levels of claudin-5 and VE-cadherin were not changed, whereas after 24 h of stress factor administration gene expression of all targets was significantly decreased.

Protein Expression in cEND Cells Is Changed by Elevated Catecholamine Levels and Inflammatory Mediators Under Oxygen Glucose Deprivation Conditions

As described above, differentiated cells were treated with stress factors under selected incubation conditions. To study changes in protein levels, cEND cells were lysed, and analyzed by Western Blot. Initially, protein levels were determined after administration of stress factors under OGD as well as REOX conditions in comparison with 4 h NORMOX conditions (**Figure 3A**). VE-cadherin expression was compromised by OGD to 0.57 ± 0.07-fold of control, followed by an increase up to 0.98 ± 0.07-fold after reoxygenation. This was not observed in combination with stress factors. Compared to the untreated control under the same incubation conditions, stress factors significantly influenced the protein content only in REOX samples. Claudin-5, occluding, and ZO-1 protein levels (all not shown) showed the same tendencies as VE-cadherin, but without statistical significance. Finally, changed protein levels after REOX were compared to 24 h NORMOX conditions (**Figure 3B**). Treatment with stress factors in combination with REOX led to an increase in occludin up to 0.81 ± 0.03-fold of control compared to stress factor administration under 24 h NORMOX conditions (0.49 ± 0.07-fold). Expression

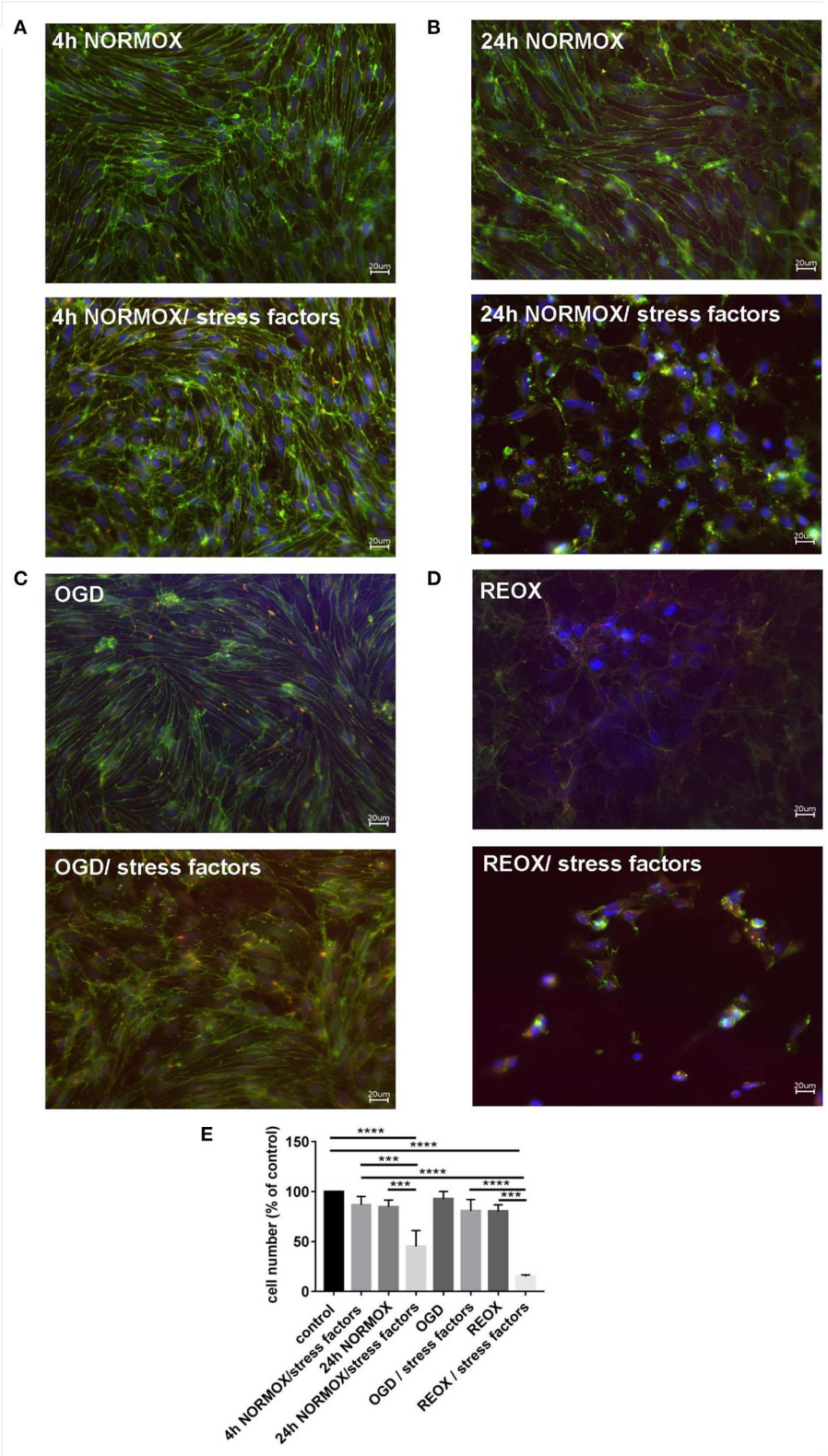

FIGURE 2 | Loss of morphological integrity of cEND cells exposed to elevated catecholamine levels and inflammatory mediators. Immunofluorescence staining of tight junction proteins claudin-5 (green) and ZO-1 (red) as markers of morphological changes of the endothelial cell monolayer. DAPI (blue) was used for staining

(Continued)

FIGURE 2 | nuclei. Cells were grown on cover slips to confluence. After differentiation cEND cells were treated with combination of catecholamines and inflammatory mediators (stress factors). Stress factors were administered under different incubation conditions. Magnification 400 times, scale bar 20 μm. **(A)** Stress factor application for 4h under normoxia conditions (4 h NORMOX). **(B)** Stress factor application for 24 h under normoxia conditions (24h NORMOX). **(C)**. Stress factor application for 4 h under oxygen glucose deprivation conditions (OGD). **(D)** Stress factor application for 4 h under OGD conditions with 20 h of subsequent reoxygenation under normoxia conditions (REOX). **(E)** Cell number in treatments shown in **(A–D)** normalized to control. ***$P < 0.001$, ****$P < 0.0001$.

TABLE 2 | Modulated target gene expression in cEND cells by stress factors under oxygen glucose deprivation (OGD) conditions and after subsequent reoxygenation (REOX) in comparison with 4 h of normoxia (4 h NORMOX).

	Claudin-5	ZO-1	Occludin	VE-cadherin	Itg α 1	Itg α v
4 h NORMOX	1	1	1	1	1	1
4 h NORMOX/stress factors	0.92 ± 0.05 n.s.	0.3 ± 0.02 ***	0.21 ± 0.02 ***	0.73 ± 0.07 n.s.	0.54 ± 0.02 ***	3.8 ± 0.6 *
OGD	0.49 ± 0.07 ***§	0.7 ± 0.08 *§	0.34 ± 0.06 ***§	1.56 ± 0.11 ***§	0.69 ± 0.05 n.s.§	4.08 ± 0.72 *§
OGD/stress factors	0.56 ± 0.11 **&	0.33 ± 0.03 ***$	0.08 ± 0.02 ***$	1.06 ± 0.07 n.s.$&	0.47 ± 0.07 ***	6.5 ± 1.08 ***
REOX	0.88 ± 0.07 n.s.	1.26 ± 0.06 n.s.	1.12 ± 0.07 n.s.	1.03 ± 0.03 n.s.	1.43 ± 0.12 **	± 0.04 n.s.
REOX/ stress factors	0.29 ± 0.06 ***#%	0.28 ± 0.1 ***#	0.26 ± 0.05 ***#	0.41 ± 0.06 ***#%μ	0.05 ± 0.06 ***#%μ	1.47 ± 0.05 n.s.μ

After total RNA-extraction from lysed cells, mRNA was quantified by real-time PCR. Fold expression vs. untreated control (4 h NORMOX), which was set 1. All values are the means (± SEM) of n = 10 independent experiments,: statistically significant vs. 4 h or normoxia (4 h NORMOX) (*P < 0.05, **P < 0.01, ***P < 0.001. n.s, not significant), §, REOX statistically significant vs. OGD; $, OGD/stress factors vs. OGD; #, REOX/stress factors vs. REOX; &, OGD/stress factors vs. 4 h NORMOX/stress factors; %, REOX/ stress factors statistically significant vs. 4 h NORMOX/ stress factors; μ, REOX/stress factors statistically significant vs. OGD/stress factors.*

of ZO-1 protein stayed unaffected by REOX conditions in comparison with 24 h NORMOX. Stress factors impaired significantly ZO-1 protein expression in both 24 NORMOX and REOX samples compared to untreated controls. Claudin-5 and VE-cadherin (both not shown) showed the same tendencies. Similar to gene expression, the effects of stress factors under NORMOX conditions were apparently time-dependent. All protein levels were significantly decreased after 24 h of stress factor administration, but not after 4 h exposure (**Figures 3A,B**).

DISCUSSION

The cardiovascular system is regulated by a central autonomic network consisting among others of the insular cortex, which is exposed to higher risk of cerebrovascular disease (10, 33). Damage in insular cortex has been associated with myocardial injury and TTS (10, 34). Based on clinical data, the simultaneous incidence of ischemic stroke and TTS has a poor outcome (1, 5, 11). Increased CAT and INF levels are one of the TTS characteristics (6). To date, the molecular mechanisms underlying these events are not fully elucidated. We hypothesized that the characteristic clinical constellation of elevated CAT and INF levels combined with OGD leads to an aggravated breakdown of the BBB, which subsequently contributes to severe ischemic stroke and poor clinical outcomes. In this study, we used an *in vitro* BBB model to study the effects of CAT/INF/OGD treatment. To our best knowledge, this is the first report examining BBB properties under such conditions.

Breakdown of the BBB is a key feature of neuroinflammatory conditions as encountered in multiple sclerosis (MS), meningitis, brain tumors, encephalitis, and cerebral ischemia, which inevitably leads to weakening of the vessels and predisposing them to leakage and rupture (35–37). BBB breakdown in frame of TTS could potentially be mediated by the effects of pro-inflammatory cytokines and CAT forming the basis for increased vulnerability to cerebrovascular dysfunction and stroke. In serum of acute phase TTS patients elevated levels of CAT such as dopamine, epinephrine, and norepinephrine and the pro-inflammatory cytokines TNFα, IL6, and IL10 have been reported (6, 38). In the pathology of ischemic stroke, TNFα and IL6 appear to be associated with BBB damage as seen on enhanced magnetic resonance imaging (MRI) scans (39). Using a rat model of experimental ischemia, it has been postulated that CAT are released in response to stress and ameliorate the ischemic brain damage (40). To address these observations at the molecular level, we decided to develop an *in vitro* pathology model of TTS based on our well-characterized murine brain endothelial cell line cEND (21). We previously validated this BBB model as suitable to study the barrier-compromising effects of pro-inflammatory stimuli and OGD, demonstrating that incubation of cEND monolayers with TNFα or OGD led to a down-regulation of TJ proteins and changes in pro-inflammatory cytokine expression (18, 20, 27, 41–43). Moreover, cEND express high levels of TJ, AJ, and ECM proteins and were used for permeability studies (41, 44, 45). In this study, we expand our characterization to the combined barrier-compromising effects of INF, CAT, and OGD conditions as partially encountered in acute phase TTS. We demonstrate

TABLE 3 | Modulated target gene expression in cEND cells by stress factors under oxygen glucose deprivation with subsequent reoxygenation (REOX) in comparison with 24 h of normoxia (24 h NORMOX).

	Claudin-5	ZO-1	Occludin	VE-cadherin	Itg α 1	Itg α v
24 h NORMOX	1	1	1	1	1	1
24 h NORMOX/stress factors	0.25 ± 0.05 ***	0.15 ± 0.05 ***	0.08 ± 0.01 ***	0.46 ± 0.05 ***	0.19 ± 0.05 ***	1.82 ± 0.3 **
REOX	0.87 ± 0.03 n.s.	1.12 ± 0.04 n.s.	1.35 ± 0.07 ***	1.05 ± 0.03 n.s.	1.32 ± 0.07 **	± 0.04 n.s.
REOX/stress factors	0.33 ± 0.06 ***§	0.24 ± 0.08 ***§	0.32 ± 0.06 ***§	0.32 ± 0.01 ***§	0.05 ± 0.01 ***§	1.51 ± 0.12 n.s.

*After total RNA-extraction from lysed cells, mRNA was quantified by real-time PCR. Fold expression vs. untreated control (24 h NORMOX), which was set 1. Target gene expression was normalized to calnexin mRNA and shown as fold over untreated control, which was constantly set 1. All values are the means (± SEM) of n = 10 independent experiments, followed by statistical significance **P < 0.01, ***P < 0.001. n.s, not significant vs. 24 h NORMOX, § REOX/stress factors statistically significant vs. REOX, REOX/stress factors is not statistically significant vs. 24 h NORMOX/stress factors.*

compromised endothelial barrier function and reduced or altered junctional protein expression, resulting from incubation of cEND with (i) INF of TTS, (ii) with CAT elevated in TTS or, (iii) the combination of INF and CAT. As markers of BBB disruption we chose a barrier-integrity representing targets such the TJ and AJ components Cldn5, occludin, ZO-1, and VE-cadherin. As markers for interaction with ECM we chose Itg α1 and Itg αv, which were previously demonstrated to be altered in inflammatory processes (32). We observed an alteration in cellular morphology and cell number following incubation of cEND monolayers with TTS acute phase CAT/INF administered separately and simultaneously. Under normoxic conditions, morphology, monolayer integrity, cell number as well as TJ forming protein levels were more affected by incubation with CAT than INF. This was significantly mirrored at the expression level of analyzed marker proteins. Messenger RNA levels of ZO-1 and VE-cadherin were reduced by both treatments, while occludin was downregulated by INF, and claudin-5 by CAT. Expression levels of Itg α1 was reduced in response to INF/CAT treatment. Concomitantly, an upregulation of the αv of vitronectin was observed. Matching data supporting the important role of functional integrin-ECM binding have been demonstrated *in vivo*, while breakdown of the BBB has been observed in mice lacking selected integrins (46). In addition, altered expression patterns of specifically Itg α1 and Itg αv have been observed in MS lesions (47). The influence of altered integrin expression pattern on cellular differentiation has been described in integrin knock out mice and for epithelial and endothelial cells *in vitro* (32, 48, 49). Moreover, a role of integrins in epithelial barrier formation has been described in mammary epithelial cells (50). This supports the notion that a reduction of Itg α1 levels with concomitant increase in Itg αv levels can be considered a reliable marker of endothelial inflammation in TTS as well.

Increasing the permeability of the endothelial barrier caused by impaired cell-cell adhesion is believed to be an early event in ischemic stroke (51). Accordingly, increased barrier breakdown was observed under OGD with common TTS stressors, most notably under OGD/REOX conditions corresponding to ischemia-reperfusion injury. Monolayer morphology, monolayer integrity, and cell count were significantly affected in response to INF/CAT in OGD. CAT is known to induce apoptosis. CAT treatment of oligodendrocytes cultures induced apoptosis mediated by oxidative stress (52). TNFα induces apoptosis in human endothelial cells of various vascular beds (53, 54). A combination of all these factors escalated the effects on cEND and resulted in significant cell loss. Morphological changes were accompanied by decreased protein and mRNA levels of marker proteins. Interestingly, occludin, ZO-1, and Itg α1 were more affected by INF/CAT than claudin-5. These results indicate a susceptibility of ZO-1 and Itg α1 to INF/CAT/OGD, which are both key components of TJ complexes and cell matrix, respectively. The effect of the administered stress factors is time-dependent and does not have the same dimension for each target chosen. In addition, stress factors only partially amplify OGD effects. Possible intracellular pathways that may mediate the effects of supra-physiological CAT concentrations on cEND monolayers will have to be investigated in future studies. However, available literature information points toward a role for β-adrenergic stimulation (and cAMP mobilization) as an important barrier enhancing mechanism: (i) Chi et al. showed that a direct application of a beta-adrenergic receptor agonist to the brain parenchyma increased the permeability of the BBB, and that this effect could be prevented with a beta-adrenoceptor antagonist (55). (ii) Murphy and Johanson had proven the adrenergic-induced enhancement of brain barrier system permeability to small nonelectrolytes (56). (iii) A possible molecular pathway that could be involved is highlighted by the work of Ohara et al. (57). The beta 2-adrenergic receptor/cAMP pathway was shown to be involved in TNFα-stimulated ICAM-1 expression, which indicates the possible involvement of adrenergic mediation of BBB integrity, given (iiii) that the physiological role of ICAM-1 is to mediate neutrophil BBB transmigration (58). (iiiii) Neutrophils in turn mediate immune cell mediated communication between the immune system and the brain, which is specifically enhanced in systemic inflammatory insults that can exacerbate ongoing brain pathologies via immune cell trafficking (59).

An important limitation of the present study is that we only analyzed selected stress factors present in TTS *in vitro*.

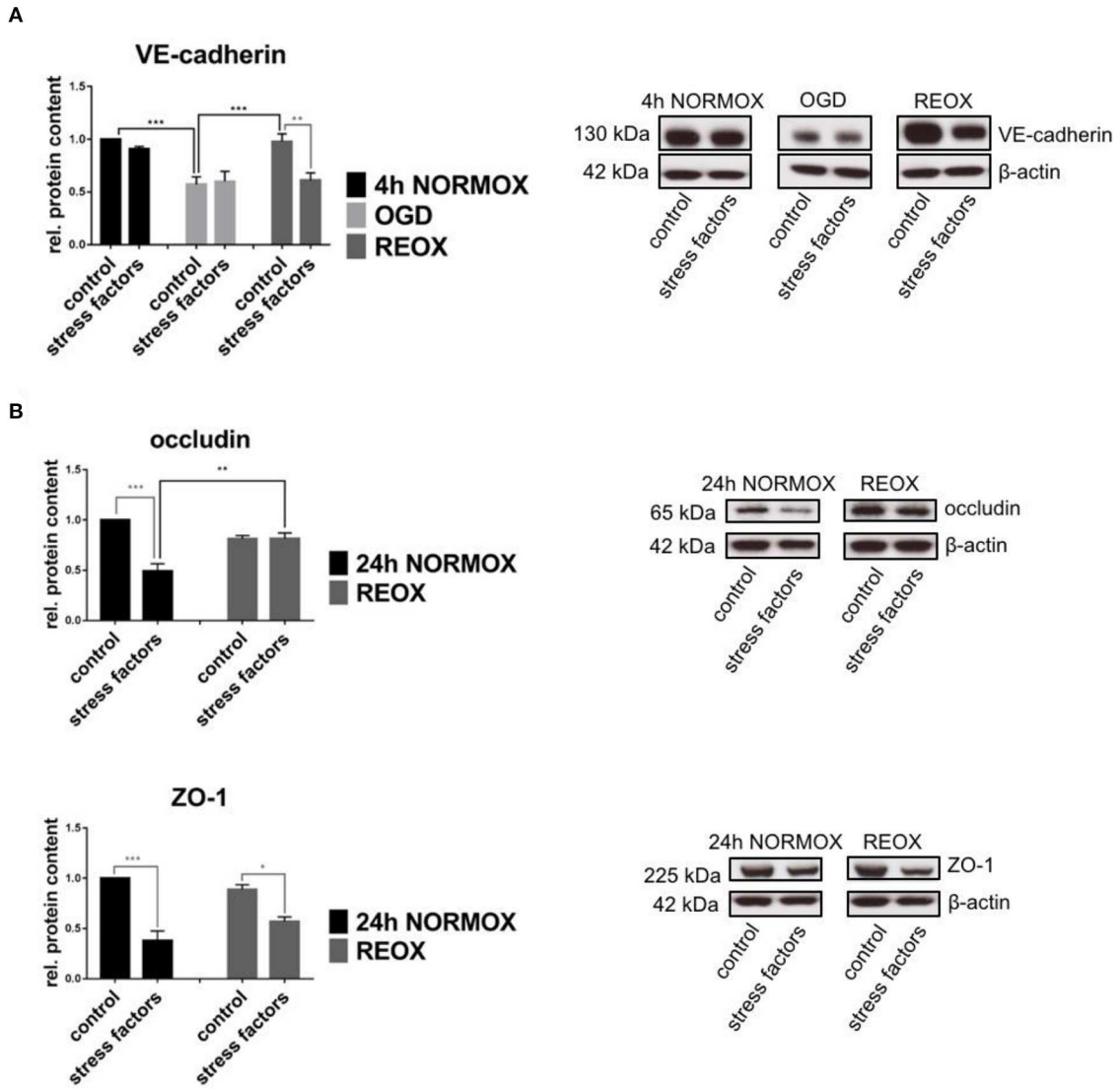

FIGURE 3 | Protein expression in cEND cells is changed by elevated catecholamine levels and inflammatory mediators under oxygen glucose deprivation conditions. Cells were grown to confluence with subsequent differentiation. Stress factors were applied under different incubation conditions. Protein levels were examined by Western blot. Changed protein expression was normalized to β-actin. Changes of protein levels determined by densitometric analysis are expressed as fold over untreated control, which was set as 1. **(A)** VE-cadherin protein expression after stress factor administration under oxygen glucose deprivation conditions (OGD) and subsequent reoxygenation (REOX) in comparison with 4 h of normoxia (4 h NORMOX). Values are the means (± SEM) of $n = 8$ independent experiments. **(B)** Occludin and ZO-1 protein levels changed by stress factors after reoxygenation conditions (REOX) compared to 24 h of normoxia conditions (24 h NORMOX). Values are the means (± SEM) of $n = 10$ independent experiments. $^{*}P < 0.05$, $^{**}P < 0.01$, $^{***}P < 0.001$.

It is not clear, how the observed effects develop *in vivo* over time. *In vitro*, a stable concentration of stressors without preconditioning was used. In this model, we cannot determine whether increasing stress factors will affect the BBB in other ways over time. In addition, we used a simplified BBB *in vitro* model based on only one cell type, the brain microvascular endothelial cells, derived from mice. Other neurovascular unit cells such as pericytes and astrocytes are known to play an important role in maintaining the barrier *in vivo* and *in vitro* (60, 61). Differences in species could also play a role in our system (62). Therefore, studies with TTS stress factors will be carried out in future using a human *in vitro* BBB model in co-culture with astrocytes and pericytes.

CONCLUSION

In summary, the present study provides the first evidence for the impairment of BBB by TTS stressors, CAT, and INF. In

addition, the barrier-compromising effects of CAT and INF were highest during the reoxygenation phase, suggesting that TTS stressors along with other pathophysiological mechanisms, could contribute to secondary brain damage after stroke.

DATA AVAILABILITY STATEMENT

All datasets generated for this study are included in the article/supplementary material.

AUTHOR CONTRIBUTIONS

CI performed experiments and wrote the manuscript. CI, MB, SS, MN, and CF designed the experiments, analyzed, and interpreted the data. All authors critically revised the manuscript.

ACKNOWLEDGMENTS

We thank Elisabeth Wilken and Anja Neuhoff for their excellent technical assistance.

REFERENCES

1. Jung JM, Kim JG, Kim JB, Cho KH, Yu S, Oh K, et al. Takotsubo-like myocardial dysfunction in ischemic stroke: a hospital-based registry and systematic literature review. *Stroke*. (2016) 47:2729–36. doi: 10.1161/STROKEAHA.116.014304
2. Said SM, Saygili E, Rana OR, Genz C, Hahn J, Bali R, et al. Takotsubo cardiomyopathy: what we have learned in the last 25 years? a comparative literature review. *Curr Cardiol Rev*. (2016) 12:297–303. doi: 10.2174/1573403X12666160211125601
3. Prasad A, Lerman A, Rihal CS. Apical ballooning syndrome (tako-tsubo or stress cardiomyopathy): a mimic of acute myocardial infarction. *Am Heart J*. (2008) 155:408–17. doi: 10.1016/j.ahj.2007.11.008
4. Eitel I, Von Knobelsdorff-Brenkenhoff F, Bernhardt P, Carbone I, Muellerleile K, Aldrovandi A, et al. Clinical characteristics and cardiovascular magnetic resonance findings in stress (takotsubo) cardiomyopathy. *JAMA*. (2011) 306:277–86. doi: 10.1001/jama.2011.992
5. Dande AS, Pandit AS, Galin ID. Takotsubo cardiomyopathy followed by neurogenic stunned myocardium in the same patient: gradations of the same disease? *Cardiology*. (2011) 118:175–8. doi: 10.1159/000328464
6. Pelliccia F, Kaski JC, Crea F, Camici PG. Pathophysiology of takotsubo syndrome. *Circulation*. (2017) 135:2426–41. doi: 10.1161/CIRCULATIONAHA.116.027121
7. Jin R, Liu L, Zhang S, Nanda A, Li G. Role of inflammation and its mediators in acute ischemic stroke. *J Cardiovasc Transl Res*. (2013) 6:834–51. doi: 10.1007/s12265-013-9508-6
8. Piccardi B, Giralt D, Bustamante A, Llombart V, Garcia-Berrocoso T, Inzitari D, et al. Blood markers of inflammation and endothelial dysfunction in cardioembolic stroke: systematic review and meta-analysis. *Biomarkers*. (2017) 22:200–9. doi: 10.1080/1354750X.2017.1286689
9. Chen Z, Venkat P, Seyfried D, Chopp M, Yan T, Chen J. Brain-heart interaction: cardiac complications after stroke. *Circ Res*. (2017) 121:451–68. doi: 10.1161/CIRCRESAHA.117.311170
10. Nagai M, Dote K, Kato M, Sasaki S, Oda N, Kagawa E, et al. The insular cortex and takotsubo cardiomyopathy. *Curr Pharm Des*. (2017) 23:879–88. doi: 10.2174/1381612822666161006123530
11. Nagai M, Hoshide S, Kario K. The insular cortex and cardiovascular system: a new insight into the brain-heart axis. *J Am Soc Hypertens*. (2010) 4:174–82. doi: 10.1016/j.jash.2010.05.001
12. Yoshimura S, Toyoda K, Ohara T, Nagasawa H, Ohtani N, Kuwashiro T, et al. Takotsubo cardiomyopathy in acute ischemic stroke. *Ann Neurol*. (2008) 64:547–54. doi: 10.1002/ana.21459
13. Daneman R, Prat A. The blood-brain barrier. *Cold Spring Harb Perspect Biol*. (2015) 7:a020412. doi: 10.1101/cshperspect.a020412
14. Chow BW, Gu C. The molecular constituents of the blood-brain barrier. *Trends Neurosci*. (2015) 38:598–608. doi: 10.1016/j.tins.2015.08.003
15. Serlin Y, Shelef I, Knyazer B, Friedman A. Anatomy and physiology of the blood-brain barrier. *Semin Cell Dev Biol*. (2015) 38:2–6. doi: 10.1016/j.semcdb.2015.01.002
16. Forster C. Tight junctions and the modulation of barrier function in disease. *Histochem Cell Biol*. (2008) 130:55–70. doi: 10.1007/s00418-008-0424-9
17. Blecharz-Lang KG, Wagner J, Fries A, Nieminen-Kelha M, Rosner J, Schneider UC, et al. Interleukin 6-mediated endothelial barrier disturbances can be attenuated by blockade of the IL6 receptor expressed in brain microvascular endothelial cells. *Transl Stroke Res*. (2018) 9:631–42. doi: 10.1007/s12975-018-0614-2
18. Silwedel C, Forster C. Differential susceptibility of cerebral and cerebellar murine brain microvascular endothelial cells to loss of barrier properties in response to inflammatory stimuli. *J Neuroimmunol*. (2006) 179:37–45. doi: 10.1016/j.jneuroim.2006.06.019
19. Semenas E, Sharma HS, Wiklund L. Adrenaline increases blood-brain-barrier permeability after haemorrhagic cardiac arrest in immature pigs. *Acta Anaesthesiol Scand*. (2014) 58:620–9. doi: 10.1111/aas.12293
20. Kleinschnitz C, Blecharz K, Kahles T, Schwarz T, Kraft P, Gobel K, et al. Glucocorticoid insensitivity at the hypoxic blood-brain barrier can be reversed by inhibition of the proteasome. *Stroke*. (2011) 42:1081–9. doi: 10.1161/STROKEAHA.110.592238
21. Forster C, Silwedel C, Golenhofen N, Burek M, Kietz S, Mankertz J, et al. Occludin as direct target for glucocorticoid-induced improvement of blood-brain barrier properties in a murine *in vitro* system. *J Physiol*. (2005) 565:475–86. doi: 10.1113/jphysiol.2005.084038
22. Burek M, Salvador E, Forster CY. Generation of an immortalized murine brain microvascular endothelial cell line as an *in vitro* blood brain barrier model. *J Vis Exp*. (2012) 29:e4022. doi: 10.3791/4022
23. Helms HC, Abbott NJ, Burek M, Cecchelli R, Couraud PO, Deli MA, et al. *In vitro* models of the blood-brain barrier: an overview of commonly used brain endothelial cell culture models and guidelines for their use. *J Cereb Blood Flow Metab*. (2016) 36:862–90. doi: 10.1177/0271678X16630991
24. Dukes AA, Van Laar VS, Cascio M, Hastings TG. Changes in endoplasmic reticulum stress proteins and aldolase A in cells exposed to dopamine. *J Neurochem*. (2008) 106:333–46. doi: 10.1111/j.1471-4159.2008.05392.x
25. Ali A, Diebel L, Liberati D. Stress hormone epinephrine increases IgA transport across respiratory epithelial surfaces. *J Am Coll Surg*. (2014) 218:450–8. doi: 10.1016/j.jamcollsurg.2013.11.011
26. Shao YY, Lin H, Li YS, Lee YH, Chen HM, Cheng AL, et al. High plasma interleukin-6 levels associated with poor prognosis of patients with advanced hepatocellular carcinoma. *Jpn J Clin Oncol*. (2017) 47:949–53. doi: 10.1093/jjco/hyx103
27. Salvador E, Burek M, Forster CY. Stretch and/or oxygen glucose deprivation (OGD) in an *in vitro* traumatic brain injury (TBI) model induces calcium alteration and inflammatory cascade. *Front Cell Neurosci*. (2015) 9:323. doi: 10.3389/fncel.2015.00323
28. Blecharz KG, Burek M, Bauersachs J, Thum T, Tsikas D, Widder J, et al. Inhibition of proteasome-mediated glucocorticoid receptor degradation restores nitric oxide bioavailability in myocardial endothelial cells *in vitro*. *Biol Cell*. (2014) 106:219–35. doi: 10.1111/boc.201300083
29. Gotsch U, Borges E, Bosse R, Boggemeyer E, Simon M, Mossmann H, et al. VE-cadherin antibody accelerates neutrophil recruitment *in vivo*. *J Cell Sci*. (1997) 110:583–8.
30. Dilling C, Roewer N, Forster CY, Burek M. Multiple protocadherins are expressed in brain microvascular endothelial cells and might play a role in tight junction protein regulation. *J Cereb Blood Flow Metab*. (2017) 37:3391–400. doi: 10.1177/0271678X16688706
31. Defilippi P, Van Hinsbergh V, Bertolotto A, Rossino P, Silengo L, Tarone G. Differential distribution and modulation of expression of alpha 1/beta

1 integrin on human endothelial cells. *J Cell Biol*. (1991) 114:855–63. doi: 10.1083/jcb.114.4.855
32. Forster C, Kahles T, Kietz S, Drenckhahn D. Dexamethasone induces the expression of metalloproteinase inhibitor TIMP-1 in the murine cerebral vascular endothelial cell line cEND. *J Physiol*. (2007) 580:937–49. doi: 10.1113/jphysiol.2007.129007
33. Marins FR, Iddings JA, Fontes MA, Filosa JA. Evidence that remodeling of insular cortex neurovascular unit contributes to hypertension-related sympathoexcitation. *Physiol Rep*. (2017) 5:e13156. doi: 10.14814/phy2.13156
34. Nagai M, Dote K, Kato M. Central autonomic network and takotsubo cardiomyopathy: how left insular cortex interact? *Eur Heart J*. (2019) 40:3061. doi: 10.1093/eurheartj/ehz476
35. Hamann GF, Okada Y, Fitridge R, Del Zoppo GJ. Microvascular basal lamina antigens disappear during cerebral ischemia and reperfusion. *Stroke*. (1995) 26:2120–6. doi: 10.1161/01.STR.26.11.2120
36. Rosenberg GA. Matrix metalloproteinases and neuroinflammation in multiple sclerosis. *Neuroscientist*. (2002) 8:586–95. doi: 10.1177/1073858402238517
37. Sellner J, Leib SL. In bacterial meningitis cortical brain damage is associated with changes in parenchymal MMP-9/TIMP-1 ratio and increased collagen type IV degradation. *Neurobiol Dis*. (2006) 21:647–56. doi: 10.1016/j.nbd.2005.09.007
38. Wilson HM, Cheyne L, Brown PAJ, Kerr K, Hannah A, Srinivasan J, et al. (2018). Characterization of the myocardial inflammatory response in acute stress-induced (takotsubo) cardiomyopathy. *JACC Basic Transl Sci*. 3:766–78. doi: 10.1016/j.jacbts.2018.08.006
39. Hotter B, Hoffmann S, Ulm L, Meisel C, Fiebach JB, Meisel A. IL-6 plasma levels correlate with cerebral perfusion deficits and infarct sizes in stroke patients without associated infections. *Front Neurol*. (2019) 10:83. doi: 10.3389/fneur.2019.00083
40. Koide T, Wieloch TW, Siesjo BK. Circulating catecholamines modulate ischemic brain damage. *J Cereb Blood Flow Metab*. (1986) 6:559–65. doi: 10.1038/jcbfm.1986.102
41. Burek M, Konig A, Lang M, Fiedler J, Oerter S, Roewer N, et al. Hypoxia-induced MicroRNA-212/132 alter blood-brain barrier integrity through inhibition of tight junction-associated proteins in human and mouse brain microvascular endothelial cells. *Transl Stroke Res*. (2019) 10:672–83. doi: 10.1007/s12975-018-0683-2
42. Blecharz KG, Haghikia A, Stasiolek M, Kruse N, Drenckhahn D, Gold R, et al. Glucocorticoid effects on endothelial barrier function in the murine brain endothelial cell line cEND incubated with sera from patients with multiple sclerosis. *Mult Scler*. (2010) 16:293–302. doi: 10.1177/1352458509358189
43. Burek M, Haghikia A, Gold R, Roewer N, Chan A, Förster CY. Differential cytokine release from brain microvascular endothelial cells treated with dexamethasone and multiple sclerosis patient sera. *J Steroids Hormonal Sci*. (2014) 5:128. doi: 10.4172/2157-7536.1000128
44. Blecharz-Lang KG, Prinz V, Burek M, Frey D, Schenkel T, Krug SM, et al. Gelatinolytic activity of autocrine matrix metalloproteinase-9 leads to endothelial de-arrangement in moyamoya disease. *J Cereb Blood Flow Metab*. (2018) 38:1940–53. doi: 10.1177/0271678X18768443
45. Kaiser M, Burek M, Britz S, Lankamp F, Ketelhut S, Kemper B, et al. The influence of capsaicin on the integrity of microvascular endothelial cell monolayers. *Int J Mol Sci*. (2018) 20:122. doi: 10.3390/ijms20010122
46. Del Zoppo GJ, Milner R. Integrin-matrix interactions in the cerebral microvasculature. *Arterioscler Thromb Vasc Biol*. (2006) 26:1966–75. doi: 10.1161/01.ATV.0000232525.65682.a2
47. Sobel RA, Hinojoza JR, Maeda A, Chen M. Endothelial cell integrin laminin receptor expression in multiple sclerosis lesions. *Am J Pathol*. (1998) 153:405–15. doi: 10.1016/S0002-9440(10)65584-8
48. Sheppard D. *In vivo* functions of integrins: lessons from null mutations in mice. *Matrix Biol*. (2000) 19:203–9. doi: 10.1016/S0945-053X(00)00065-2
49. Gumbiner BM. Cell adhesion: the molecular basis of tissue architecture and morphogenesis. *Cell*. (1996) 84:345–57. doi: 10.1016/S0092-8674(00)81279-9
50. Forster C, Makela S, Warri A, Kietz S, Becker D, Hultenby K, et al. Involvement of estrogen receptor beta in terminal differentiation of mammary gland epithelium. *Proc Natl Acad Sci USA*. (2002) 99:15578–83. doi: 10.1073/pnas.192561299
51. Griemert EV, Recarte Pelz K, Engelhard K, Schafer MK, Thal SC. PAI-1 but Not PAI-2 gene deficiency attenuates ischemic brain injury after experimental stroke. *Transl Stroke Res*. (2019) 10:372–80. doi: 10.1007/s12975-018-0644-9
52. Khorchid A, Fragoso G, Shore G, Almazan G. Catecholamine-induced oligodendrocyte cell death in culture is developmentally regulated and involves free radical generation and differential activation of caspase-3. *Glia*. (2002) 40:283–99. doi: 10.1002/glia.10123
53. Deshpande SS, Angkeow P, Huang J, Ozaki M, Irani K. Rac1 inhibits TNF-alpha-induced endothelial cell apoptosis: dual regulation by reactive oxygen species. *FASEB J*. (2000) 14:1705–14. doi: 10.1096/fj.99-0910com
54. Lopez-Ramirez MA, Fischer R, Torres-Badillo CC, Davies HA, Logan K, Pfizenmaier K, et al. Role of caspases in cytokine-induced barrier breakdown in human brain endothelial cells. *J Immunol*. (2012) 189:3130–9. doi: 10.4049/jimmunol.1103460
55. Chi OZ, Wang G, Chang Q, Weiss HR. Effects of isoproterenol on blood-brain barrier permeability in rats. *Neurol Res*. (1998) 20:259–64. doi: 10.1080/01616412.1998.11740516
56. Murphy VA, Johanson CE. Adrenergic-induced enhancement of brain barrier system permeability to small nonelectrolytes: choroid plexus versus cerebral capillaries. *J Cereb Blood Flow Metab*. (1985) 5:401–12. doi: 10.1038/jcbfm.1985.55
57. Ohara Y, Mccarron RM, Hoffman TT, Sugano H, Bembry J, Lenz FA, et al. Adrenergic mediation of TNF alpha-stimulated ICAM-1 expression on human brain microvascular endothelial cells. *Acta Neurochir Suppl*. (2000) 76:117–20. doi: 10.1007/978-3-7091-6346-7_24
58. Lyck R, Enzmann G. The physiological roles of ICAM-1 and ICAM-2 in neutrophil migration into tissues. *Curr Opin Hematol*. (2015) 22:53–9. doi: 10.1097/MOH.0000000000000103
59. Pflieger FJ, Hernandez J, Schweighofer H, Herden C, Rosengarten B, Rummel C. The role of neutrophil granulocytes in immune-to-brain communication. *Temperature*. (2018) 5:296–307. doi: 10.1080/23328940.2018.1538598
60. Armulik A, Genove G, Mae M, Nisancioglu MH, Wallgard E, Niaudet C, et al. Pericytes regulate the blood-brain barrier. *Nature*. (2010) 468:557–61. doi: 10.1038/nature09522
61. Neuhaus W, Gaiser F, Mahringer A, Franz J, Riethmuller C, Forster C. The pivotal role of astrocytes in an *in vitro* stroke model of the blood-brain barrier. *Front Cell Neurosci*. (2014) 8:352. doi: 10.3389/fncel.2014.00352
62. Urich E, Lazic SE, Molnos J, Wells I, Freskgard PO. Transcriptional profiling of human brain endothelial cells reveals key properties crucial for predictive *in vitro* blood-brain barrier models. *PLoS ONE*. (2012) 7:e38149. doi: 10.1371/journal.pone.0038149

Conflict of Interest: The authors declare that the research was conducted in the absence of any commercial or financial relationships that could be construed as a potential conflict of interest.

frontiers in Physiology

ORIGINAL RESEARCH
published: 23 June 2020
doi: 10.3389/fphys.2020.00667

Endothelial Dysfunction and Passive Changes in the Aorta and Coronary Arteries of Diabetic db/db Mice

*Lilliana Beck[1], Junjing Su[1], Simon Comerma-Steffensen[1,2], Estéfano Pinilla[1], Rune Carlsson[1], Raquel Hernanz[1,3], Majid Sheykhzade[4], Carl Christian Danielsen[1] and Ulf Simonsen[1]**

[1] Department of Biomedicine, Pulmonary and Cardiovascular Pharmacology, Faculty of Health Aarhus University, Aarhus, Denmark, [2] Department of Biomedical Sciences/Animal Physiology, Veterinary Faculty, Central University of Venezuela, Maracay, Venezuela, [3] Departamento de Ciencias Básicas de la Salud, Universidad Rey Juan Carlos, Alcorcón, Spain, [4] Department of Drug Design and Pharmacology, Faculty of Health and Medical Sciences, University of Copenhagen, Copenhagen, Denmark

OPEN ACCESS

Edited by:
Michael A. Hill,
University of Missouri, United States

Reviewed by:
Chris R. Triggle,
Weill Cornell Medicine – Qatar, Qatar
Tim Murphy,
University of New South Wales, Australia

***Correspondence:**
Ulf Simonsen
us@biomed.au.dk;
us@farm.au.dk

Specialty section:
This article was submitted to Vascular Physiology, a section of the journal Frontiers in Physiology

Received: *03 November 2019*
Accepted: *25 May 2020*
Published: *23 June 2020*

Citation:
Beck L, Su J, Comerma-Steffensen S, Pinilla E, Carlsson R, Hernanz R, Sheykhzade M, Danielsen CC and Simonsen U (2020) Endothelial Dysfunction and Passive Changes in the Aorta and Coronary Arteries of Diabetic db/db Mice. Front. Physiol. 11:667. doi: 10.3389/fphys.2020.00667

Endothelial cell dysfunction and vessel stiffening are associated with a worsened prognosis in diabetic patients with cardiovascular diseases. The present study hypothesized that sex impacts endothelial dysfunction and structural changes in arteries from diabetic mice. In diabetic (db/db) and normoglycaemic (db/db+) mice, the mechanical properties were investigated in pressurized isolated left anterior descending coronary arteries and aorta segments that were subjected to tensile testing. Functional studies were performed on wire-mounted vascular segments. The male and female db/db mice were hyperglycaemic and had markedly increased body weight. In isolated aorta segments without the contribution of smooth muscle cells, load to rupture, viscoelasticity, and collagen content were decreased suggesting larger distensibility of the arterial wall in both male and female db/db mice. In male db/db aorta segments with smooth muscle cell contribution, lumen diameter was smaller and the passive stretch-tension curve was leftward-shifted, while they were unaltered in female db/db aorta segments versus control db/db+ mice. In contrast to female db/db mice, coronary arteries from male db/db mice had altered stress-strain relationships and increased distensibility. Transthoracic echocardiography revealed a dilated left ventricle with unaltered cardiac output, while aortic flow velocity was decreased in male db/db mice. Impairment of acetylcholine relaxation was aggravated in aorta from female db/db compared to control and male db/db mice, while impairment of sodium nitroprusside relaxations was only observed in aorta from male db/db mice. The remodeling in the coronary arteries and aorta suggests an adaptation of the arterial wall to the reduced flow velocity with sex-specific differences in the passive properties of aorta and coronary arteries. The findings of less distensible arteries and more pronounced endothelial dysfunction in female compared to male diabetic mice may have implications for the observed higher incidence of macrovascular complications in diabetic women.

Keywords: acetylcholine, endothelium, aorta, coronary arteries, stiffness, viscoelasticity

INTRODUCTION

Patients with diabetes have a greater risk of atherosclerosis and cardiovascular complications than non-diabetics (Rydén et al., 2013). Genetic disposition, hyperglycaemia, production of advanced glycation end products (AGEs), hyperlipidemia, insulin resistance, and hypertension have been reported to explain the accelerated diabetic macroangiopathy and progression to cardiovascular disease. Diabetic macroangiopathy is characterized by increased vessel stiffness, thickness, and endothelial dysfunction (Sasaki et al., 2008; Prenner and Chirinos, 2015).

Nitric oxide (NO) derived from the endothelium has a variety of functions including regulation of vascular tone, inhibition of platelet aggregation and adhesion of inflammatory leukocytes to the endothelial cells, and therefore endothelial dysfunction is thought to be of importance for the development of atherosclerosis and nephropathy in diabetes (Paneni et al., 2013). In animal models and humans with types 1 and 2 diabetes mellitus, endothelium-dependent vasodilatation is impaired in both large and small arteries (Caballero et al., 1999; Pannirselvam et al., 2002; Gao et al., 2007, 2008; Zhang et al., 2008; Bagi et al., 2015; Chen et al., 2015; Lee et al., 2017; Katare et al., 2018). Acute hyperglycaemia is also associated with impaired endothelium-dependent vasodilatation and decreased NO bioavailability (Brodsky et al., 2017), and inactivation of NO by oxygen-derived free radical species is thought to be an important mechanism in this condition (Pannirselvam et al., 2002; Gao et al., 2007; Paneni et al., 2013). Hyperglycaemia and oxidative stress lead to increased production of AGEs and a further reduction in NO production (Gao et al., 2008; Farmer and Kennedy, 2009), but the consequences of the endothelial dysfunction on the altered structure and vascular stiffening are unclear.

In addition to endothelial dysfunction, diabetic macroangiopathy is characterized by increased extracellular matrix deposition around the smooth muscle cells and vessel stiffing which by itself is predictive of cardiovascular disease progression (Hansen et al., 2006; Vlachopoulos et al., 2010). In type 2 diabetic db/db mice, aorta, mesenteric arteries, and septal coronary arteries seem to respond in a tissue-specific manner (Katz et al., 2011), as vessel stiffness seems to be increased in aorta and mesenteric arteries, while septal coronary arteries respond with decreased intraluminal diameter and decreased stiffness (Katz et al., 2011; Husarek et al., 2015). Comparing intact and decellularized aorta and coronary microvessels from db/db mice which allow investigation of the extracellular matrix also suggested that the microvessels are more influenced by the adverse consequences of type 2 diabetes at earlier stages of disease progression than conduit arteries (Anghelescu et al., 2015).

Changes in endothelial function and stiffness have been reported independently for different vascular beds (Bagi et al., 2005, 2015; Zhang et al., 2008; Katz et al., 2011; Anghelescu et al., 2015; Husarek et al., 2015). Although the physiological relevance of local aldosterone production remains unclear, recent studies have suggested that vascular smooth muscle, as well as perivascular adipocyte production of aldosterone, may contribute to vascular dysfunction in obese and diabetic mice (Briones et al., 2012; Matsuzawa et al., 2013). These studies provide support to the assumption that the development of endothelial dysfunction followed by altered stiffness and vascular structure is not necessarily global, but it may be specific for each vascular bed in diabetes.

Sex and obesity also impact the development of cardiovascular complications in diabetes. Obesity is a major risk factor of type 2 diabetes in both sexes, and while men are more obese at young age, women above 45 years are often overweight or tend to be more obese than men (Kautzky-Willer et al., 2016). Moreover, diabetic men appear at a higher risk for diabetic microvascular complications, while the consequences of macrovascular complications may be greater in women (Maric-Bilkan, 2017). Compared to diabetic men, diabetes in women is associated with greater increases of cardiovascular risk, myocardial infarction, and stroke mortality. This is not the case with non-diabetic subjects (Peters et al., 2014). However, with few exceptions, most of the studies in animal models have been conducted in males (Docherty et al., 2019).

The present study hypothesized that sex impacts endothelial dysfunction and structural changes in arteries from diabetic mice. Diabetic (db/db) mice develop obesity, insulin resistance, hyperglycaemia, and hyperlipidemia similar to that seen in human type 2 diabetes due to a spontaneous mutation in the leptin receptor gene (Hummel et al., 1966). To address the hypothesis, we investigated the structural changes as well as stiffness and endothelial function in aorta from female and male control and diabetic mice. Given that most studies in coronary arteries from db/db mice studied septal arteries (Katz et al., 2011; Husarek et al., 2015; McCallinhart et al., 2018) or coronary microvessels (Zhang et al., 2008; Lee et al., 2017), we investigated whether the same structural changes take place in the left anterior descending (LAD) coronary arteries from male and female diabetic mice. Previous studies have found impaired left ventricle function in diabetic db/db mice (Plante et al., 2014; Baumgardt et al., 2016; Moon et al., 2016; Xu et al., 2016) and even suggested that cardiac dysfunction may precede vascular dysfunction in diabetic mice (Katare et al., 2018). Therefore, we asked also whether vascular changes can be explained by changes in cardiac function and aortic flow, and therefore transthoracic echocardiography and blood pressure measurements was performed in a subset of male control and diabetic mice.

MATERIALS AND METHODS

Animals and Preparation of Samples

Male and female 8-week-old db/db mice (C57BLKS/J-lepr^{db}/lepr^{db}) and age- and sex-matched db/db+ littermate controls (C57BLKS/J-lepr^{db}/lepr^{db+}) were purchased from Taconic Europe (Ry, Denmark). The mice were housed in the animal facility in 365 × 207 × 140 mm cages with standard wood bedding and space for three to four mice, and they had free access to water and laboratory diet (Brogaarden, Middelfart, Denmark). The mice had a 12-hour light/dark cycle, and to avoid influence of torpor (Swoap and Gutilla, 2009; Ayala et al., 2010), the mice were allocated to experimentation early in the light

period. Glucose was monitored weekly in non-fasting animals by use of arterial tail blood. Blood glucose was measured twice each time with a Contour Blood Glucose Monitoring System (Bayer, Copenhagen, Denmark). The mice were killed by decapitation followed by exsanguination for the mechanical and the functional studies. All animal care and experimental protocols in this study were conducted under the supervision of a veterinarian and in accordance with the Danish legislation of animal use for scientific procedures as described in the "Animal Testing Act" (Consolidation Act No. 726 of 9 September 1993 as amended by Act No. 1081 of 20 December 1995) and approved by the Danish Animal Experiments Inspectorate (permission 2014-15-2934-01059). The Danish Animal Testing Act fully and extensively covers the requirements included in the Guide for the Care and Use of Laboratory Animals as adopted and promulgated by the United States National Health Institute, and the animal studies are reported in compliance with the ARRIVE guidelines (Kilkenny et al., 2010; McGrath and Lilley, 2015). The mice were examined at 16 weeks of age.

Passive Mechanical Studies in Aorta Segments

Mechanical testing was performed on aorta segments from 10 db/db and 8 db/db+ male mice to 12 db/db and 14 db/db + female mice. Three to five ring specimens with a height of 1 mm were cut from the frozen descending thoracic aorta and placed in a 50 mM Tris/HCl buffer (pH 7.4) at room temperature. Side branches were avoided in the cutting process. The cross-sectional area of the specimens was measured (**Supplementary Figure S1**), and afterward, the specimens were frozen at −20°C until analysis at which time specimens were thawed at room temperature.

The in-house built setup for mechanical testing has previously been described (Van Soldt et al., 2015; Filogonio et al., 2018). Briefly, the specimen was mounted around two parallel, orthogonally bent spring steel hooks with a diameter of 0.35 mm and submerged in the Tris/HCl buffer at room temperature. One hook was connected to a load cell of 3 N capacity (Kistler-Morse DSC-6 transducer, DMT, Aarhus, Denmark) and the other hook was moved by a step motor (DM224i API Motion, Amherst, NY, United States) at 0.1667 mm/s. Deformation was obtained from the step motor drive and load cell readings were acquired by a data acquisition unit [Model 34970A, Hewlett Packard (Keysight), Palo Alto, CA, United States]. Each specimen was first subjected to five loading cycles to 35 mN and then to a rupture test. The ruptured specimens were collected for collagen analysis.

From the fifth hysteresis cycle, the area between the loading and de-loading load-deformation curves (the energy of the hysteresis loop) was calculated in percent of the loading area. This percentage expresses the relative importance of viscosity, whereas the energy recovered to the total energy input indicates a higher elastic efficiency (Shadwick, 1992). The initial luminal perimeter, l_0, was obtained from the rupture load-deformation curve where the load increased to above a minimal value (0.1 mN) during deformation. Maximal stiffness was calculated as the maximal slope of the load-strain curve. Stiffness and strain corresponding to pressures, P, of 100 and 120 mm Hg were estimated from the load-strain curve by finding the combination of load (F) and strain fulfilling the Laplace equation (see Van Soldt et al., 2015) for P ($P = F/(r \times h)$, where $r = l/2\pi$ and $h = 1$ mm and l is height and luminal perimeter, respectively, of ring specimen). Maximal stress and maximal modulus and maximal mechanical quality of collagen were estimated by normalization of maximal load and maximal stiffness by cross-sectional area and unit collagen [UC, mg collagen/mm initial luminal perimeter (l_0)], respectively.

Functional Studies of Aorta Segments

Freezing and thawing of the samples do not allow to take into account the endothelial function and vessel tone determined by the vascular smooth muscle. Therefore, in a different set of mice (11 male db/db+ and 11 db/db, and 12 female db/db+ and 10 db/db mice) the descending thoracic aorta was placed in physiological salt solution (PSS) immediately after euthanasia and ring segments of 2 mm were dissected and mounted on two 100 μm steel wires in microvascular myographs (Danish Myo Technology, Aarhus, Denmark) for isometric tension recordings. PSS was of the following composition (mmol/L): NaCl 119, KCl 4.7, KH_2PO_4 1.18, $MgSO_4$ 1.17, $NaHCO_3$ 25, $CaCl_2$ 1.6, EDTA 0.026 and glucose 5.5. To avoid acute hyperglycaemic effects on endothelial function (Bangshaab et al., 2019), which may confound the relation of endothelial to structural function, experiments on arteries from both control db/db+ and diabetic db/db male and female mice were conducted with the same glucose concentration. The organ baths were heated to 37°C and equilibrated with 5% CO_2 to maintain the desired pH of 7.4. The segments were allowed to equilibrate for 10 min. To determine the optimal passive to an active relationship in the aorta, the segments were incrementally stretched by increasing the internal circumference (IC) successively with 100 μm and then stimulated with potassium-rich PSS (KPSS, 60 mM) each time.

For the initial viability test, we tested the endothelial cell function; aorta segments were contracted with phenylephrine (10^{-7} M), and after reaching a stable plateau, concentration-response curves were constructed for acetylcholine (10^{-9} to 10^{-5} M) and the NO donor sodium nitroprusside (SNP, 10^{-10} to 10^{-5} M).

Determination of Collagen and Elastin Content in Aorta

Collagen content was determined for each of the aorta ring segments from male and female mice that were subjected to passive mechanical testing. Besides, the fractional aorta collagen and elastin content were determined relative to dry defatted weight. Thus, four pooled samples of aorta pieces from 10 db/db to 9 db/db+ male mice were defatted with acetone and freeze-dried. Elastin content (dry weight) was determined after extraction of all other tissue components (Lansing et al., 1952) and collagen content was determined from hydroxyproline in the extract. Hydroxyproline content was determined by colorimetric determination after a modified Woessner method (Danielsen and Andreassen, 1988). Collagen was calculated as 7.46 × hydroxyproline content (Neuman and Logan, 1950).

Passive Properties of Coronary Arteries

To determine the passive properties of the left anterior descending coronary artery (LAD) from 6 male db/db+ and 6 db/db mice and from female 6 db/db+ and 6 db/db mice, arterial segments (lengths of 1.7 ± 0.5 mm) were mounted in a 110P pressure myograph system (Danish Myo Technology, Aarhus, Denmark) in a calcium-free PSS. During the dissection of the LAD, as much myocardium as possible was carefully removed to enable optimal measurements of the internal and external diameters. Furthermore, any visible side-branches were ligated. Once mounted on the myograph, the vessels were unbuckled by the adjustment of the cannulas at 100 mmHg intraluminal pressure and the inner and outer diameters were recorded. It was possible to calculate the structural and mechanical parameters from the internal (Di) and external (De) vessel diameters measured under passive conditions at intraluminal pressures ranging from 10 to 140 mmHg. The passive properties of the coronary arteries mounted in the pressure myograph were calculated as previously described (**Supplementary Table S1**; Hernanz et al., 2012; Schjørring et al., 2015).

Functional Studies in Coronary Arteries

Functional studies in coronary arteries were performed on segments from 6 db/db+ and 6 db/db male mice. Due to technical difficulties, the groups were not of equal size and did not include coronary arteries from female mice. Coronary small arteries with a length of approximately 2 mm were mounted on two 25 μm wires in microvascular myographs (Danish Myo Technology, Aarhus, Denmark) for isometric tension recordings as described above for the aorta segments. The segments were stretched to their optimal diameter, which corresponded to an internal circumference of 90% of that achieved when the vessels were exposed to a passive tension yielding a transmural pressure of 100 mmHg in coronary arteries (Simonsen et al., 1999). The viability of the segments was confirmed by their ability to contract to first potassium-rich PSS (KPSS, 60 mM) and subsequently to the thromboxane analog U46619 (10^{-7} M). In U46619-contracted segments, after reaching a stable plateau, concentration-response curves were constructed for acetylcholine (10^{9}–10^{-5} M) and SNP (10^{-10}–10^{-5} M).

The following drugs were used: Acetylcholine, phenylephrine hydrochloride (PE), SNP (sodium nitroprusside), and U46619 (9α-epoxymethanoprostaglandin $F_{2\alpha}$) were from Sigma (St Louis, MO, United States). Unless otherwise stated, the substances were dissolved in distilled water. The vehicle concentration in the bath was low, and parallel control curves were run to examine whether the vehicle affected vascular contractility.

Transthoracic Echocardiography

Transthoracic echocardiography was performed on 7 db/db and 7 db/db+ male mice. Anesthesia was induced with 7% sevoflurane mixed in 100% oxygen with the mouse placed in a clear Perspex induction chamber and maintained with 3–4% sevoflurane through a nose mask. Echocardiography (Vevo2100, Visual Sonics, Toronto, Canada) was performed using a linear array probe (MS 550D, 22–55 MHz) on the spontaneously breathing mouse that was placed in the left lateral decubitus position on a heating pad adjusted to 37°C. The animal's electrocardiography (ECG) signal was captured through copper electrodes on the heating pad. Images of the left ventricle (LV, B-mode, and M-mode) were acquired from the left parasternal short-axis view at mid-papillary level and images of the aorta and pulmonary artery (B-mode and pulse wave Doppler mode) were acquired from the right and left parasternal long-axis views, respectively, (Pistner et al., 2010). Following echocardiography, the mice underwent invasive mean arterial measurement as described below.

Image analysis was performed using the in-built software. All measurements were taken as an average of three consecutive cardiac cycles. The duration of P-wave, the duration of the PR segment (defined as the segment between the end of the P-wave and the beginning of R-wave) and QT-interval were measured (**Supplementary Figure S4**). PR-interval was calculated as the sum of the durations of P-wave and PR-segment, and the QT interval was corrected for heart rate yielding QT_C. LV dimensions were measured, and LV function was evaluated (Gao et al., 2011) using the equations in **Table 1**. Stiffness of the ascending aorta was assessed by its circumferential strain (Trachet et al., 2015), and cardiac output was estimated as the average of the aortic and pulmonary flow (Tournoux et al., 2011; Slama et al., 2015).

Mean Arterial Pressure Measurement

For *in vivo* arterial pressure measurements, male mice were anesthetized with intraperitoneal administration of pentobarbital (50 mg/kg). The pain was assessed regularly during surgery and pressure measurements by pressing a needle against the paw. In the case of a reaction, additional anesthesia (30 mg/kg pentobarbital) was administered. The carotid artery was isolated following a mid-neck-incision, and a water-filled disposable catheter (MLT0699, ADInstruments, United Kingdom) was inserted. The catheter was fixed afterward by a couple of sutures of 6-0 silk (Johnson & Johnson, Belgium) connected to a four channels PowerLab system (ML485, ADInstruments,

TABLE 1 | Calculation of ventricular function and aortic circumferential strain.

LV FS	$\frac{LVID_d - LVID_s}{LVID_d} \cdot 100\%$
LV EF	$\frac{LVID_d^3 - LVID_s^3}{LVID_d^3} \cdot 100\%$
LV FAC	$\frac{Area_d - Area_s}{Area_d} \cdot 100\%$
LVPW thickening	$\frac{LVPW_s - LVPW_d}{LVPW_d} \cdot 100\%$
Aorta circumferential strain	$\frac{1}{2} \cdot \left(\left(\frac{ID_{AO,s}}{ID_{AO,d}} \right)^2 - 1 \right) \cdot 100\%$
Aortic flow	$\pi \cdot (ID_{AO}/2)^2 \cdot VTI_{AO} \cdot HR$
Pulmonary flow	$\pi \cdot (ID_{PA}/2)^2 \cdot VTI_{PA} \cdot HR$

AO: aorta, d: diastole, EF: ejection fraction, FAC: fractional area change, FS: fractional shortening, HR: heart rate, ID: inner diameter, LV: left ventricle, LVID: left ventricular inner diameter, LVPW: left ventricular posterior wall, PA: pulmonary artery s: systole, VTI: velocity time integral.

United Kingdom), which was connected to a computer that runs LabChart v7 (ADInstruments, United Kingdom). Mean arterial blood pressure (MAP) was measured within a 5 min of stable pulsatile wave pulse. The mice were euthanized by injecting a high dose of pentobarbital (100 mg/kg), and tissue was isolated for *in vitro* protocols.

Data Evaluation and Statistical Analysis

Data are presented as means ± standard error of the mean (SEM) or median (interquartile range). Statistical analyses were performed using Stata 13 (StataCorp, College Station, TX, United States) or GraphPad Prism 7.02 (GraphPad Software Inc., California, United States). Differences between the db/db+ and db/db mice were compared by the unpaired Student's *t*-test, Welch's *t*-test for unequal variances, or Mann–Whitney test (non-parametric test), where appropriate. Concentration-response curves were constructed using a non-linear curve-fit model, and the half-maximal relaxation (EC_{50}) was determined:

$$y = bottom + \frac{(top - bottom)}{1 + 10^{((logEC50 - x)^{*} slope)}}$$

Two-way ANOVA, followed by a *post hoc* Bonferroni test, was used to test for differences in concentration-response curves in isolated vessel segments. The significance level was $^{*}P < 0.05$ for all tests.

RESULTS

Characteristics of the Animals

The experimental weight in male and female db/db mice was significantly higher than in db/db+ mice (**Table 2**), and blood glucose was markedly higher in male and female db/db mice compared to db/db+ control mice (**Table 2**). The blood glucose levels were not different in db/db+ male versus female mice but was higher in male versus female db/db mice. The tibia length of the normoglycaemic db/db+ male mice (1.78 ± 0.01 cm, $n = 15$) was significantly longer than in diabetic male db/db mice (1.66 ± 0.02 cm, $P < 0.001$, $n = 11$). Heart weight indexed to tibia length was unaltered and was, respectively, 94 ± 4 mg/cm ($n = 15$) and 97 ± 6 mg/cm ($n = 11$) in male db/db+ and db/db mice.

Passive Properties and Collagen Content in Aorta Segments

The passive internal diameters of the frozen and thawed aorta segments from db/db mice were, respectively, 767 ± 27 and 752 ± 26 μm in aorta segments from male db/db+ and db/db mice. Wall thickness was significantly reduced in aorta from male db/db mice (**Figure 1A**). Consistent with the lower wall thickness, the maximal load (**Figure 1B**) and stiffness (not shown) were significantly reduced. The collagen content per mm luminal circumference was reduced (**Table 3**), but the maximal load and stiffness normalized to collagen per mm luminal circumference (N × mm/mg, not shown) were not found to be different. This indicates that the mechanical quality of the collagen is similar in male db/db and db/db+ mice. Reduction in wall thickness only partially explains the reduction in maximal mechanical strength since maximal load and stiffness normalized to vessel wall area i.e., maximal stress (not shown) and maximal elastic modulus (**Figure 1C**), respectively, were not different. Cyclic testing to a low load value gave higher energy recovery for db/db mice (energy loss is less in db/db mice, **Figure 1D**). The distensibility of the aortic specimens at a load corresponding to 100 and 120 mm Hg (i.e., physiological pressures) was unaltered in these mice (**Table 4**). Thus, the aorta in male db/db mice appears to be able to accommodate more blood during systole and to recoil with less energy loss, i.e., has a better efficiency as an elastic reservoir (Windkessel). Since both the collagen and elastin percentages as well as the collagen: elastin ratio were unaltered in male db/db mice (**Table 3**), a reduction in the absolute collagen content (μg) also implies a reduction in absolute elastin content (μg) in db/db mice.

Passive mechanical studies were also performed in aorta segments from female db/db and db/db+ mice. The passive internal diameters of the frozen and thawed aorta segments were, respectively, 650 ± 15 and 688 ± 20 μm, in aorta segments from female db/db+ and db/db mice. In contrast to male db/db mice, the wall thickness of the aorta segments from female db/db mice was unaltered (**Figure 1A**). In the aorta, the maximal load was significantly reduced in female db/db mice (**Figure 1B**) as was the maximal stiffness (not shown). This can be explained by the reduced collagen content per mm luminal circumference from 5.67 ± 0.23 ($n = 14$) in female db/db+ to 4.48 ± 0.14 mg × 10^{-3}/mm ($P < 0.05$, $n = 12$) in db/db mice. Similar to the aorta from male db/db mice maximal load and stiffness normalized to collagen per mm luminal circumference (N × mm/mg, not shown) was not found to be different. Also in contrast to male mice, the aortic segments with inactivated smooth muscle cells from female db/db mice showed increased ($p < 0.05$) distensibility (strain) at 100 and 120 mm Hg (**Table 4**).

In addition to the extracellular matrix, the vascular smooth muscle layer also contributes to the properties of vascular

TABLE 2 | Body weight and blood glucose levels.

	Male			Female		
	n	Body weight (g)	Blood glucose (mmol/L)	n	Body weight (g)	Blood glucose (mmol/L)
db/db+	33	29[18–36]	7.9[5.6–12.4]	33	21[10–27]#	7.4[4.3–13.8]
db/db	33	51[42–60]*	28.5[17.0–33.3]*	35	49[39–53]*	18[9.8–31.8]*

*The results are represented as medians [IQR], where n indicates the number of animals examined. *P < 0.05 versus db/db+ . #P < 0.05 versus the same parameter in male mice in the same condition.*

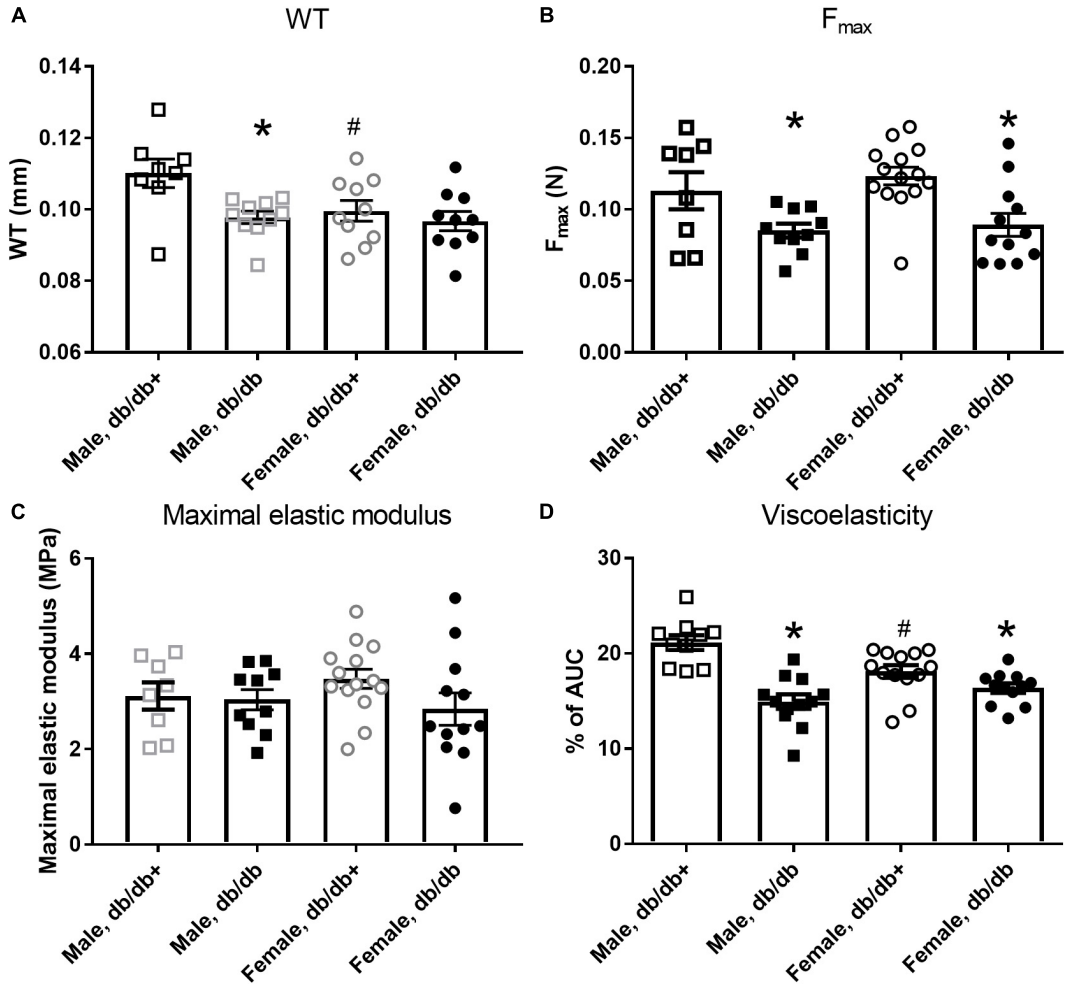

FIGURE 1 | Mechanical properties of aorta segments from male and female diabetic db/db and normoglycaemic db/db+ mice. Aorta segments from diabetic db/db mice show **(A)** reduced wall thickness (WT) in segments from male db/db (n = 10) versus db/db+ (n = 8) mice, but not in female db/db (n = 12) and db/db+ (n = 14) mice and **(B)** reduced maximal load (Fmax), **(C)** unaltered maximal elastic modulus, and **(D)** reduced viscoelasticity. The results are means ± SEM. *$P < 0.05$, db/db versus db/db+ controls. $^{\#}P < 0.05$, female versus male mice in same condition.

segments. Tension-stretch test was therefore performed on freshly dissected specimen in physiological saline. Successively stretching revealed increased passive tension development in wire-mounted aorta segments from diabetic db/db male mice (**Figure 2A**). At the optimal active tension, the aorta segments from male db/db mice had a mean internal diameter of 823 ± 53 μm (n = 8) which was significantly decreased compared to the diameter of segments [1144 ± 43 μm (n = 8)] isolated from db/db+ mice. These findings show that in the presence of active vascular smooth muscle cells, the response to passive stretch was markedly increased in aorta from male db/db mice.

In contrast, wire-mounted aorta segments from female db/db mice that were successively stretched revealed no change in passive tension development (**Figure 2B**). The aorta segments from diabetic female db/db mice had lumen diameters of 762 ± 91 μm (n = 8) at optimal tension, which was significantly decreased compared to segments isolated from db/db+ mice with lumen diameters of 1088 ± 45 μm ($P < 0.05$, n = 8).

Passive Properties in Coronary Arteries From Diabetic Mice

External diameters were slightly increased in coronary arteries form female db/db compared to db/db+ mice, but otherwise

TABLE 3 | Collagen per mm luminal circumference and percentage collagen and elastin of dry defatted weight.

	Male db/db+	Male db/db
Collagen (mg × 10^{-3}/mm)	6.00 ± 0.49 (8)	4.42 ± 0.08* (10)
Collagen (%)	14.6 ± 0.5 (9)	13.8 ± 1.1 (10)
Elastin (%)	32.1 ± 0.9 (9)	30.8 ± 2.1 (10)
Collagen/elastin ratio	0.450 ± 0.020	0.454 ± 0.012

*Means ± SEM (No. of mice). Percentages of collagen and elastin were determined for 4 pools of aortas from 2 to 3 mice. *P < 0.05 db/db versus db/db+ . Collagen content for aorta from female mice is listed in the result section, while elastin content was not determined in female mice.*

TABLE 4 | Distensibility (strain) of the aortic wall at two loading pressures.

	Male db/db+ (n = 8)	Male db/db (n = 10)	Female db/db+ (n = 14)	Female db/db (n = 12)
100 mmHg	0.747 ± 0.013	0.767 ± 0.015	0.759 ± 0.021	0.862 ± 0.036*
120 mmHg	0.837 ± 0.014	0.855 ± 0.013	0.856 ± 0.019	0.955 ± 0.036*

*The values are means ± SEM. *P < 0.05 db/db versus db/db+.*

diameters of the coronary arteries from male and female db/db mice were unaltered compared to segments from db/db+ mice (**Figures 3A,B**). The wall thickness was significantly decreased in segments from male db/db mice (**Figure 3C**), while it was unaltered in coronary arteries from female db/db mice (**Figure 3D**). The wall to lumen ratio was unaltered (**Figures 3E,F**). In agreement with the decreased wall thickness, the incremental distensibility was markedly increased at low pressures in coronary arteries from male db/db mice (**Figure 3G**). In contrast, incremental distensibility was decreased in coronary arteries from female db/db arteries compared to age-matched db/db+ mice (**Figure 3H**).

The stress-strain curve was rightward shifted indicating decreased stiffness in coronary arteries from male db/db mice (**Figure 4A**), while the stress-strain curve of coronary arteries from female db/db mice was unaltered (**Figure 4B**).

Functional Studies in the Aorta and Coronary Arteries

At the optimal passive tension, the active tension responses to 60 mM KPSS were not significantly altered in aorta segments from female db/db+ and db/db mice were, respectively, 5.5 ± 1.1 Nm^{-1} (n = 12) and 4.4 ± 0.4 Nm^{-1} (n = 10), and in aorta segments from male db/db+ and db/db mice, respectively, 7.5 ± 0.5 Nm^{-1} (n = 11) and 6.6 ± 0.8 Nm^{-1} (n = 11).

The arteries were contracted with 10^{-7} M phenylephrine, which induced comparable contractions in the aorta segments (**Table 5**). Phenylephrine-contracted segments relaxed to acetylcholine, but the acetylcholine relaxation curves were significantly reduced in aorta segments from male and female db/db mice (**Figures 5A,B** and **Table 5**). Comparing acetylcholine relaxations in aorta segments from male versus female control db/db+ mice showed the concentration-relaxation curves were not different, while acetylcholine relaxations were significantly reduced in aorta segments from female versus male db/db mice (**Figure 5C** and **Table 5**). These findings suggest the impairment of relaxations to the endothelium-dependent vasodilator, acetylcholine, is more pronounced in aorta segments from female db/db mice.

The NO donor SNP induced concentration-dependent relaxations, which were significantly reduced in aorta segments from male db/db mice (**Figure 5D**). These findings suggest endothelial dysfunction and reduced smooth muscle response to a NO donor in aorta from male db/db mice. Relaxations induced by the NO donor SNP were unchanged in aorta segments from female db/db mice (**Figure 5E**). Comparing SNP relaxations in aorta segments from male versus female db/db + showed maximum relaxations were less in segments from female mice (**Table 5**) while comparing male and female db/db mice showed that the concentrations-response curves were not different.

In addition to a sex-specific difference in vascular function, the age and most likely glucose exposure time appears to play a role. Another series of mice, showed that in 11-week-old male db/db mice there was only a small rightward shift in the concentration-response curves for acetylcholine and no changes in the SNP relaxations comparing aorta from db/db versus control db/db+ mice (**Supplementary Figure S2**); and while there were no difference in responses to acetylcholine and SNP in the aorta from 11-week versus 16-week old db/db+ mice, both acetylcholine and SNP relaxations were diminished in the aorta from 16-week-old db/db mice (**Supplementary Figure S2**).

In wire-mounted coronary arteries, the internal diameters were, respectively, 211 ± 12 μm (n = 6) and 210 ± 12 μm (n = 7) from male diabetic db/db and db/db+ mice. In the coronary arteries of db/db mice contracted with U46619, acetylcholine relaxation was impaired in arteries from male diabetic mice compared to db/db+ control mice (**Supplementary Figure S3A**). The relaxations induced by the NO donor, SNP, were significantly reduced in coronary arteries from db/db mice (**Supplementary Figure S3B**).

Blood Pressure and Transthoracic Echocardiography

Mean arterial blood pressure measured in anesthetized male mice was not different in male diabetic db/db compared to db/db + control animals (**Table 6**), but the heart rate was lower. The duration of the PR-interval, QT-interval and the corrected QT-interval on the ECG were significantly prolonged in diabetic animals (**Table 6** and **Supplementary Figure S4**). The duration of P-wave was not significantly different from the controls, however, therefore the prolonged PR-interval was due to prolonged duration of the PR-segment (43.2 ms vs. 37.3 ms, p = 0.035).

Left ventricle dimensions were measured (**Figure 6**), and LV cavity size, both the absolute size and per centimeter tibia length, of the db/db mice was significantly greater than the heterozygote mice (**Table 6**). LV posterior wall thickening, fractional foreshortening, ejection fraction and fractional area change were lower in the db/db mice. However, only the difference in the posterior wall thickening was statistically significant. The stroke volume was similar in the two groups of mice and the cardiac output was mildly reduced (no statistical significance) as a result of lower heart rate. Echocardiography of aorta showed decreased mean flow and maximal flow velocity in diabetic db/db mice (**Table 6** and **Supplementary Figure S5**). The circumferential strain of the ascending aorta

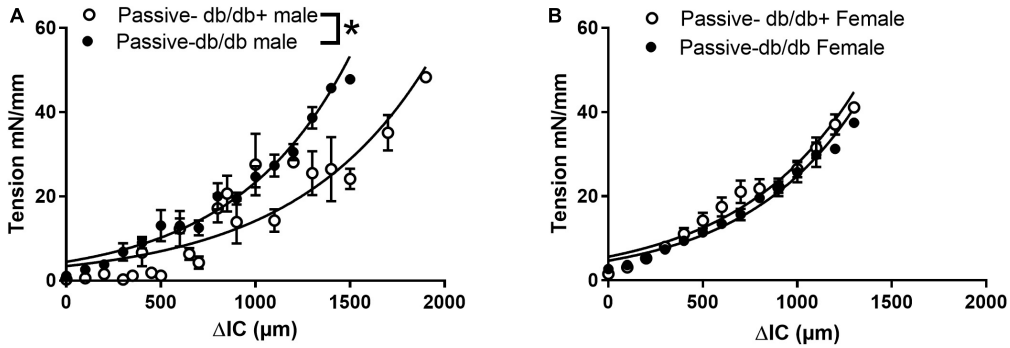

FIGURE 2 | Passive and active properties of aorta segments from male and female diabetic db/db and normoglycaemic db/db+ mice. Aorta segments were mounted in myographs for isometric tension measurements allowing us to also evaluate the active vascular smooth muscle component. **(A)** Passive stretch of aorta segments measured as increase in internal circumference (ΔIC) against increase in force (ΔF) from male db/db (n = 6) and db/db+ mice (n = 6). **(B)** The passive stretch of aorta segments measured as an increase in internal circumference (ΔIC) against an increase in force (ΔF) from female diabetic db/db (n = 6) and control db/db+ mice (n = 6). The results are means ± SEM, $^*P < 0.05$, db/db versus db/db+ controls.

was lower in the db/db mice, but the difference did not reach statistical significance.

DISCUSSION

In this comprehensive study we have examined in detail the passive and active changes in the mechanical and functional properties of the large arteries as well as the alterations in cardiac function and hemodynamics in diabetic mice. In addition, we investigated the impact of sex and age on the mechanical and functional properties of the arteries in diabetic mice.

We observed a structural adaptation of the heart and vasculature to increased body weight, increased blood glucose and decreased locomotion in the diabetic animals. Consistent with a reduced vessel wall thickness and collagen content in the aorta of male db/db mice, we observed a reduced maximal load and decreased viscoelasticity indicative of a more efficient Windkessel function. Similar findings were observed in the coronary artery. However, testing the arterial segments with preserved vascular smooth muscle function revealed increased vasomotor tone and endothelial dysfunction in diabetic male mice. This was evidenced by increased tension development to stretching and impaired relaxation to acetylcholine and sodium nitroprusside and the impairment was more pronounced in older diabetic male mice. Sex-specific vascular changes were also observed. While the decrease in maximum load and viscoelasticity of the aorta in female diabetic mice was comparable to that of the male mice, the impairment to acetylcholine relaxation was more pronounced in female mice. Moreover, in contrast to diabetic male mice, the incremental distensibility of the coronary artery decreased in diabetic female mice.

Vascular Remodeling

Macroangiopathy associated with the development of accelerated atherosclerosis plays an important role in the development of vascular complications in type 2 diabetic patients (Di Marzio et al., 2006). The findings regarding aortic remodeling in diabetic mouse models are more controversial. In aorta from diabetic ob/ob mice, the media thickness is increased and this is ascribed to an increased amount of proteoglycans in the vessel wall (Okon et al., 2003), while in db/db mice, wall thickness of the aorta was reported to be similar to that of the control mice (Guo et al., 2005). *In vitro* studies reported larger diameters of stretched aorta segments from db/db mice (Piercy and Taylor, 1998), but recent *in vivo* studies suggested similar aortic diameters measured with echocardiography (Faita et al., 2018). In the present study, the diameters of the aorta in db/db versus control mice were similar using echocardiography, and in segments without active contribution from smooth muscle cells. In segments with active smooth muscle cells, the diameter of aorta segments from db/db male mice was smaller suggesting a larger smooth muscle response to stretch. Moreover, wall thickness was decreased in aorta from male db/db mice. These findings suggest that mean arterial diameters are similar in aorta from db/db and control mice, but that an adaptation to a lower flow velocity with thinning of the vessel wall and change in the passive properties have taken place in the aorta from db/db mice (**Figure 1**). Apart from the hyperglycemia, the db/db mice due to the leptin receptor defect have pronounced obesity which may also contribute to these alterations.

In patients with type 2 diabetes, a hypertrophic remodeling with larger media-to-lumen ratio take place in small subcutaneous arteries (Rizzoni et al., 2001; Schofield et al., 2002). Mesenteric small arteries, septal coronary arteries, and coronary microvessels from db/db mice also have increased media-to-lumen ratio and smaller lumen diameters consistent with changes observed when hypertrophic inward remodeling takes place (Katz et al., 2011; Anghelescu et al., 2015; Husarek et al., 2015; Nguyen Dinh Cat et al., 2018). Hypertrophic outward remodeling has also been suggested to occur in even smaller (internal lumen diameters∼50 μm) mesenteric arteries from db/db mice (Souza-Smith et al., 2011). In the present study, similar experimental setups did not reveal any differences

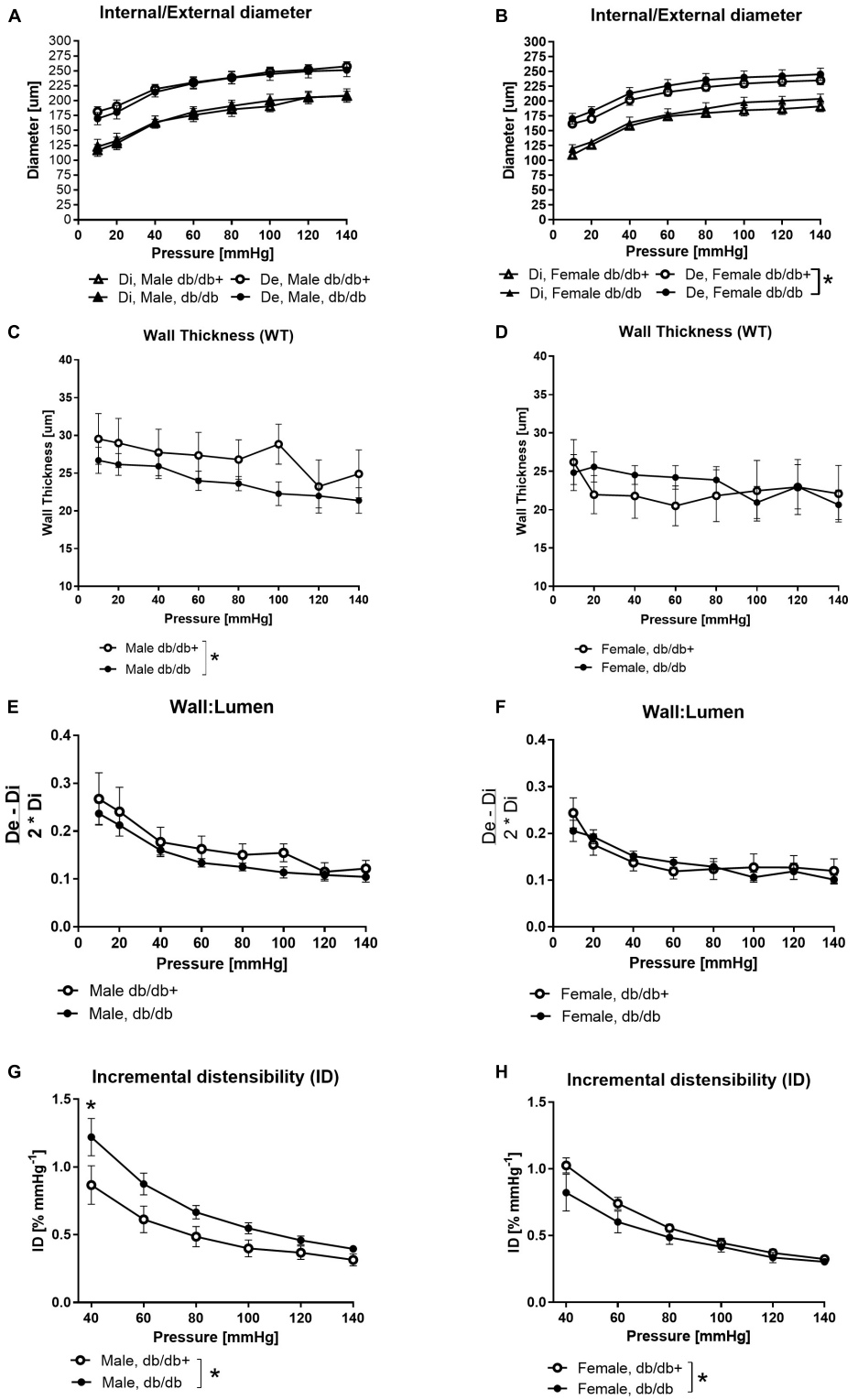

FIGURE 3 | Structural and mechanical changes in left anterior descending (LAD) coronary artery from male diabetic mice. **(A,B)** Increasing pressure (10–140 mmHg) changes in external (De) and internal (Di) diameters, **(C,D)** wall thickness, **(E,F)** wall:lumen ratio, and **(G,H)** incremental distensibility. The vessel wall thickness is significantly lower in male mice, while distensibility is significantly higher in arteries from male db/db mice and significantly lower in arteries from female db/db mice compared to the db/db+ controls. The results are means ± SEM. *$P < 0.05$, db/db ($n = 6$) versus db/db+ controls ($n = 6$).

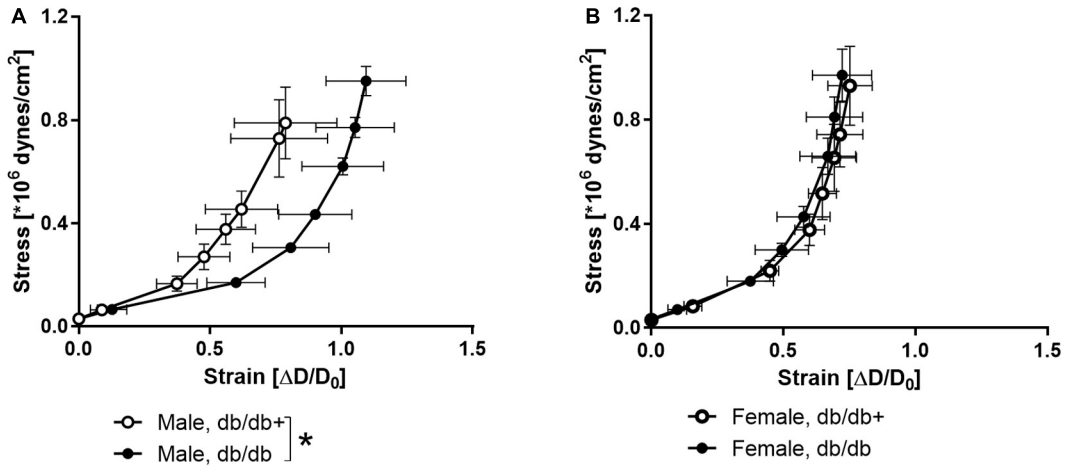

FIGURE 4 | Stress-strain curves in coronary arteries. Strain measured as change in diameter (ΔD) over initial vessel diameter (D_0) plotted against stress in coronary arteries from **(A)** db/db+ and db/db male mice and **(B)** db/db+ and db/db female mice. *$P < 0.05$, db/db ($n = 6$) versus db/db+ controls ($n = 6$).

TABLE 5 | Relaxations induced by acetylcholine (Ach) and sodium nitroprusside (SNP) in aorta segments from male (M) and female (F) normoglycaemic (db/db+) and diabetic (db/db) mice.

	PhE	ACh		PhE	SNP	
	Nm^{-1}	-log(EC_{50})	Max relaxation (%)	Nm^{-1}	-log(EC_{50})	Max relaxation (%)
M db/db+	2.2 ± 0.5	7.47 ± 0.15	72.3 ± 4.3	2.5 ± 0.5	7.93 ± 0.08	96.0 ± 2.2
M db/db	2.3 ± 0.6	6.34 ± 0.07*	57.9 ± 3.1*	3.7 ± 0.9	7.49 ± 0.17	84.3 ± 4.5*
F db/db+	1.7 ± 0.2	7.07 ± 0.12	69.8 ± 4.2	1.7 ± 0.4	7.83 ± 0.12	85.2 ± 3.7#
F db/db	1.8 ± 0.4	6.38 ± 0.45	31.5 ± 9.6*#	2.3 ± 0.2	8.21 ± 0.20	76.9 ± 3.7

*Aorta segments were contracted with phenylephrine (PhE, tension in Nm^{-1}). EC_{50} is the concentration causing half-maximal relaxation. The data are means ± SEM of n = 6–7 animals. *$P < 0.05$, Students t-test versus the same parameter in aorta segments from db/db+ mice. #$P < 0.05$, Students t-test versus same parameter in male mice of same strain.*

between the inner and outer diameters of the left anterior descending coronary artery from male db/db mice compared to control db/db+ mice. The inner diameters of the arterial segments in the present study are similar to previous studies on the mouse septal coronary artery (Katz et al., 2011; Husarek et al., 2015). However, taking the dilation of the left ventricle observed with echocardiography in db/db mice into consideration, it cannot be excluded that the longitudinal stretch of the LAD may contribute to increased resistance and reduced coronary blood flow in the diabetic mouse heart, as previously observed in the male db/db mice (Husarek et al., 2015).

Arterial Stiffness

Arterial stiffening is considered an independent risk factor for both macro-and micro-vascular complications in type 2 diabetes (Schram et al., 2004; Prenner and Chirinos, 2015). Aortic stiffness is markedly increased in the diabetic Zucker rat and is attributed to increased fibronectin and collagen IV (Sista, 2005). In the present study, the maximum stiffness of the aorta was decreased in the male db/db mice consistent with the decreased wall thickness, while the maximal elastic modulus remained the same. The aortic stiffness evaluated *in vivo* also appeared unchanged consistent with a recent study (Faita et al., 2018). The stress-strain relationship was rightward shifted in coronary arteries from male db/db mice. These findings agree with previous findings of decreased stiffness in mouse septal coronary arteries (Katz et al., 2011; Husarek et al., 2015), but contrast markedly with previous studies reporting increased stiffness in mesenteric arteries (Nguyen Dinh Cat et al., 2018). These findings suggest that the changes are related to the vascular bed affected in the db/db mice, and in the mesenteric bed, vascular smooth muscle or perivascular formation of aldosterone may contribute to the development of changes in the arterial function and structure (Briones et al., 2012; Matsuzawa et al., 2013). Although there is an increase in subcutaneous fat accumulation, in the db/db mice, fat accumulation primarily takes place around the viscera and there is less accumulation in the thorax and around the coronary arteries that are embedded in the myocardium, hence allowing less access from fat-derived autacoids than in the mesenteric vascular bed.

Arterial Viscoelasticity

In large arteries from diabetic patients, elasticity was reported to be decreased (Airaksinen et al., 1993). Septal coronary arteries from db/db mice exhibit decreased elastic modulus, while incremental elastic modulus was increased in the femoral arteries

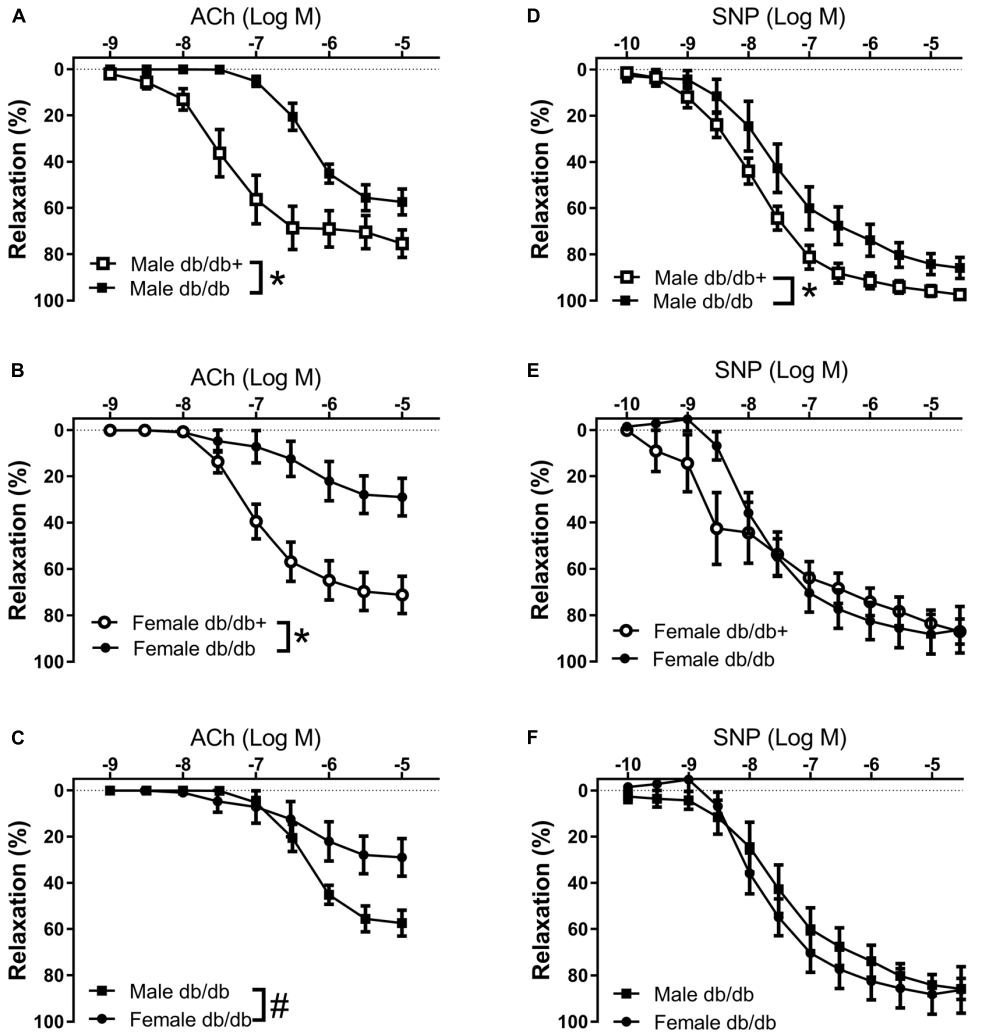

FIGURE 5 | Impaired endothelium-dependent relaxation in aorta from diabetic db/db mice. Average aorta relaxations in segments contracted with phenylephrine. **(A)** Impaired acetylcholine (ACh) relaxation in diabetic db/db male mice (n = 6) compared to normoglycaemic db/db+ male mice (n = 6). **(B)** Impaired acetylcholine relaxation in diabetic db/db female mice (n = 6) compared to normoglycaemic db/db+ (n = 7) female mice. **(C)** The impairment of acetylcholine relaxation was more pronounced in aorta segments from female compared to male diabetic db/db mice. **(D)** Impaired SNP relaxation in aorta from diabetic db/db male mice (n = 6) compared to normoglycaemic db/db+ (n = 7) male mice. **(E)** Unaltered relaxations induced by the NO donor sodium nitroprusside (SNP) in diabetic db/db female mice (n = 6) compared to normoglycaemic db/db+ female mice (n = 6). **(F)** SNP relaxations were similar in aorta segments from male and female db/db mice. The results are means ± SEM. $^{*}P < 0.05$ db/db versus db/db+ control mice. $^{\#}P < 0.05$, female versus male mice in the same condition.

of the same mice (Katz et al., 2011). In the present study, the viscoelastic behavior was decreased in aorta from both female and male db/db mice as well as in coronary arterioles from male mice (**Figure 2**). This can be explained by compositional changes in the content of collagen, elastin, glycosaminoglycans (GAG), and/or smooth muscle cells. We found a decreased collagen content and unaltered fractional elastin content in the aorta from male db/db mice. In the aorta, engagement of elastic fibers plateau around a strain of 0.2 (Chow et al., 2014), while at physiological pressures, aorta operates at a higher strain (>0.5), and therefore requires substantial recruitment of collagen fibers. Therefore, the reduced collagen content will lead to decreased viscoelasticity, i.e., less energy dissipation to pressure waves. It may also contribute to the decrease in maximal load at a breaking point in the aorta segments from both female and male diabetic db/db mice.

Vascular Contractility

Several studies have found increased contractility both to high extracellular K^+ and to alpha-adrenoceptor agonists in the aorta and small arteries from diabetic rats and mice (Piercy and Taylor, 1998; Pannirselvam et al., 2002, 2005; Xie et al., 2006; Sallam et al., 2011). In several of these studies of aorta from db/db mice, the passive tension in segments from db/db and db/db+ mice were set to a fixed passive tension load, e.g., 5.5 mN, corresponding to 30 mmHg, or 1.5 g (Piercy and Taylor, 1998; Miike et al., 2008; Sallam et al., 2011). In the present

TABLE 6 | Mean arterial pressure (MAP) and echocardiographic results in a subset of male control db/db + and diabetic db/db mice.

	db/db+ (*N* = 7)	db/db (*N* = 7)	*p*
MAP (mmHg)	73 ± 5	68 ± 2	0.38
Heart rate (min^{-1})	400 ± 17	340 ± 11	0.01*
Ejection time (ms)	54.8 ± 2.8	65.2 ± 2.8	0.02*
Duration of diastole (ms)	96.6 ± 4.6	112.4 ± 5.8	0.05
p-wave duration (ms)	13.5 ± 0.7	14.7 ± 0.8	0.26
PR-interval (ms)	50.7 ± 1.5	58.0 ± 1.5	0.01*
QT interval (ms)	50.5 ± 1.5	64.0 ± 3.0	0.001*
QTc (ms)	41.2 ± 1.3	48.0 ± 1.4	0.004*
$LVPW_d$ (mm)	1.01 ± 0.07	1.11 ± 0.08	0.39
$LVPW_d$/TL (mm/cm)	0.57 ± 0.04	0.67 ± 0.05	0.14
LVPW thickening (%)	61.4 ± 8.1	37.8 ± 2.2	0.03*
$LVID_d$ (mm)	3.59 ± 0.09	3.92 ± 0.09	0.03*
$LVID_d$/TL (mm/cm)	2.02 ± 0.05	2.36 ± 0.05	< 0.001
$LVarea_d$ (mm^2)	8.89 ± 0.37	11.2 ± 0.45	0.002*
LV $area_d$/TL (mm^2/cm)	5.00 ± 0.21	6.72 ± 0.27	< 0.001*
Fractional foreshortening (%)	42.3 ± 3.0	37.5 ± 1.9	0.20
Ejection fraction (%)	79.8 ± 3.1	75.1 ± 2.1	0.23
Fractional area change (%)	65.7 ± 2.5	58.8 ± 2.9	0.10
Aorta ID_d (mm)	1.28 ± 0.05	1.27 ± 0.03	0.90
Aorta ID_d/TL (mm/cm)	0.72 ± 0.03	0.72 ± 0.02	0.90
Circumferential strain (%)	23.1 ± 2.4	17.8 ± 4.3	0.30
Aortic V_{max} (mm/s)	1008 ± 110	655 ± 76	0.02*
Aortic V_{mean} (mm/s)	581 ± 63	379 ± 43	0.02*
Stroke volume (mm^3)	29.2 ± 2.5	29.7 ± 3.4	0.91
Stroke volume/TL (mm^3/cm)	16.4 ± 1.43	16.7 ± 1.92	0.91
Cardiac output (ml/min)	11.5 ± 0.7	10.0 ± 1.1	0.28
Cardiac output/TL (ml/min/cm)	6.46 ± 0.39	5.63 ± 0.62	0.28

*BM: body mass, d: end-diastole, ID: inner diameter, LV: left ventricle, PW: posterior wall, TL: tibia length, V: velocity. The values are means ± SEM. *P < 0.05, versus db/db+ (Student's t-test).*

study, the arterial segments were stretched for optimal tension development, and at this level the active responses were similar. However, the myogenic response to stretch was increased in aorta from male db/db mice, which is in agreement with previous studies demonstrating increased contractility in aorta from male db/db mice. In contrast, we found that the active responses to stretch were similar in aorta segments from db/db and control female mice. These findings suggest that sex play a role for the augmentation of smooth muscle contractility in the aorta from male db/db mice.

Reduced relaxations to the NO donor, SNP also suggest alterations of smooth muscle function diabetes. Thus, endothelium-independent concentration-dependent relaxations to the NO donor SNP were unaltered in the aorta of 6–8-week-old mice, rightward shifted in the aorta of 11 weeks old male db/db mice (Miike et al., 2008), and markedly reduced in the aorta from 14 to 20 weeks old male db/db mice (Sallam et al., 2011). We also observed that SNP-induced endothelium-independent vasodilatations were markedly impaired in the aorta and coronary arteries from 16-week old male diabetic db/db mice, while there was no change in SNP relaxations of aorta from 11-week old male db/db mice. These observations suggest that long-term exposure to high glucose levels lead to impairment of SNP relaxations in aorta from male db/db mice. In contrast to the male db/db mice, SNP relaxations in aorta from female db/db mice were unaltered suggesting that the smooth muscle dysfunction is most pronounced in aorta from male db/db mice. The diabetic female mice had smaller body weight and less increase in plasma glucose compared to male mice, and this may contribute to the observations that structural and aorta contractility alterations appear to be less pronounced in aorta from diabetic female mice compared to diabetic male mice.

Endothelial Dysfunction

Numerous studies have shown endothelial dysfunction in patients with type 2 diabetes (Shi and Vanhoutte, 2017) and in mouse coronary arterioles (Gao et al., 2007; Zhang et al., 2008; Choi et al., 2012; Kassan et al., 2014) and aorta segments from db/db mice (Piercy and Taylor, 1998; Miike et al., 2008; Sallam et al., 2011). Acetylcholine relaxation is unaltered in aorta of 6-week old male db/db mice (Miike et al., 2008), but impaired endothelium-dependent acetylcholine relaxation is present in 6–8-week old male db/db mice which have higher glucose levels and subsequently progresses with further reduction of acetylcholine relaxation in aorta of db/db mice at 11 weeks (Miike et al., 2008) and 14–20 weeks (Sallam et al., 2011). In aorta from male db/db mice, we also observed an age-dependent progression in the impairment of acetylcholine relaxation. In addition, the impairment of acetylcholine relaxation was significantly reduced in the aorta of female db/db mice, not only compared to aorta from control animals, but also compared to the aorta from male db/db mice. The blood glucose level *per se* is unlikely to explain the difference in impaired endothelial function compared to male diabetic db/db mice, as the levels were lower in female versus male db/db mice (**Table 2**). Sex hormones affect the cardiovascular system, but comparing arteries from male and female animals often show that estrogens are protective and improve endothelial function (Wellman et al., 1996), but this is opposite to the present findings of decreased acetylcholine relaxation. Weight and inflammation were suggested as the major determinants of vascular dysfunction in the aorta of male db/db mice (Sallam et al., 2011). Expressed relative to the control animals, the weight gain in female db/db mice is markedly larger than in male db/db mice in the present study, which would agree with weight being important for endothelial dysfunction. Although further investigation will be required to clarify the underlying mechanism, our results may contribute to understand the observation of higher incidence of macrovascular complications in diabetic women compared to diabetic men (Maric-Bilkan, 2017).

Heart Rhythm and Function in Diabetic db/db Mice

The heart rate of the animals, both db/db+ and db/db mice, is low. This is likely attributed to full anesthesia. In contrast to diabetic human subjects (Ewing et al., 2015), there was a fall in heart rate in the diabetic mice, which is consistent with previous observations (Park et al., 2008; Senador et al., 2009). This could be due to reduced locomotor activity and metabolism

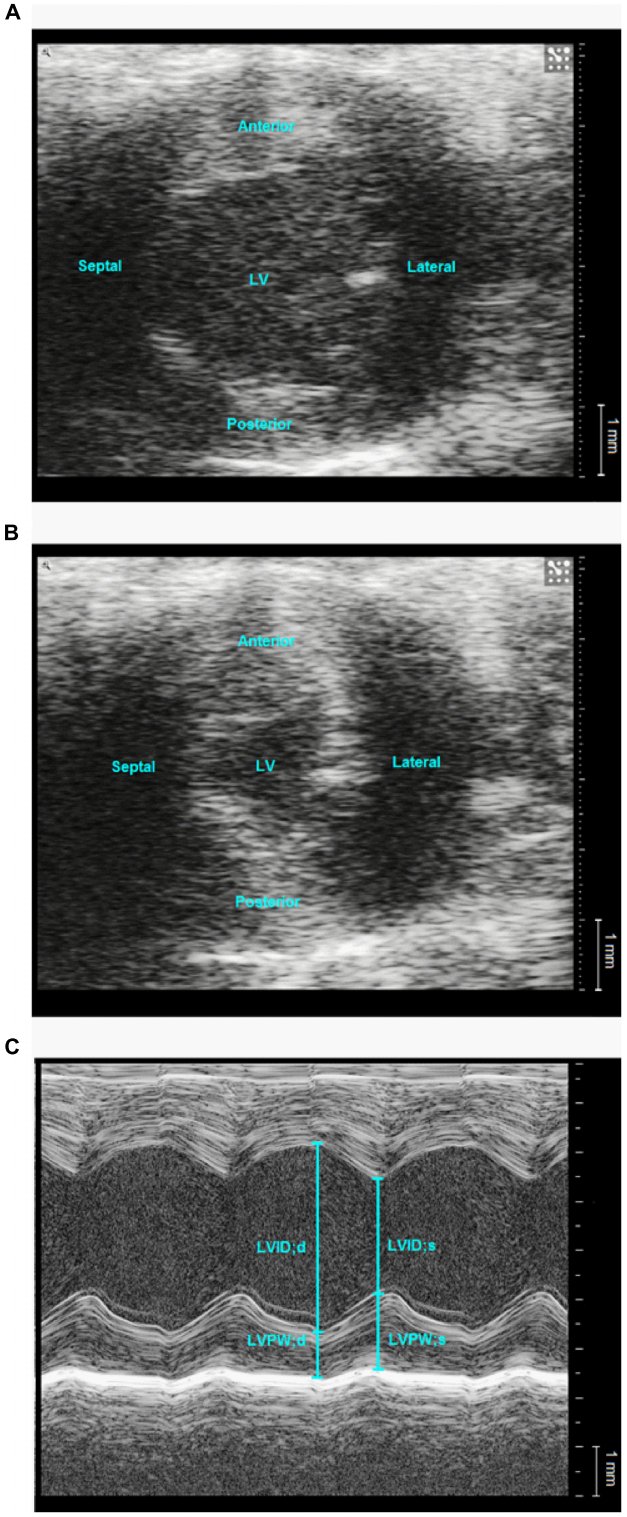

FIGURE 6 | Representative echocardiographic images of left ventricle in a normoglycaemic db/db+ mouse. Representative B-mode **(A,B)** and M-mode **(C)** images of the left ventricle (LV) at mid-papillary level from the parasternal short axis view. LV area was measured at end-diastole **(A)** and end-systole **(B)**. d: diastole, LVID: left ventricular inner diameter, LVPW: left ventricular posterior wall, s: systole.

(Park et al., 2008) and/or altered autonomic balance in the diabetic mouse hearts (Senador et al., 2009). Mice can increase their heart rate by only 30–40%, while humans can increase the heart rate by ∼300% (Kaese and Verheule, 2012). Therefore, increasing the heart rate will only lead to a small increase in stroke volume and cardiac output in mice. In contrast, decreased heart rate, i.e., longer cardiac duration with a longer diastolic filling time, will lead to an increase in ventricular preload resulting in increased ventricular contractility and stroke volume as dictated by Starling's law. This may partially explain the observed decrease in heart rate in diabetic mice. Diabetes is associated with an increased risk of impaired electrical conduction in the heart, due to autonomic neuropathy in diabetic patients. Defects such as atrioventricular block, bundle branch block, and prolonged QT/QTc, will correlate to incremented cardiovascular risk factors, leading to increased mortality rates (Movahed, 2007). In diabetic mice, the prolonged PR-interval indicates impaired atrioventricular conduction. We also observed a wide M-shaped QRS-complex, and the QRS complex is composed of not only depolarization but also early repolarization in mice (Boukens et al., 2014). A prolonged QRS could be due to prolonged depolarization or early repolarization of the ventricles resulting in a longer ejection time in the diabetic mice, which seems like a further functional compensatory effect of the diabetic autonomic neuropathy.

Left ventricle systolic function in db/db mice has previously been reported to be impaired (Plante et al., 2014; Baumgardt et al., 2016; Moon et al., 2016; Xu et al., 2016). Although different types of control animals (C57BL6 or db/db+) have been included, and db/db mice were investigated at different ages, reduced stroke volume, foreshortening fraction, ejection fraction, and cardiac output values have been reported and seem to develop with increasing age of the animals (Plante et al., 2014; Baumgardt et al., 2016; Moon et al., 2016; Xu et al., 2016). In the present study, the LV systolic function of the db/db mice was reduced as evidenced by the decreased posterior wall thickening, fractional foreshortening, ejection fraction and fractional area change, although the reduction in the three latter parameters did not reach statistical significance. Due to the prolonged diastolic filling time and ejection time, the stroke volume was maintained and the cardiac output was only mildly reduced (statistically insignificant) as a consequence of lower heart rate.

Diabetic cardiomyopathy can occur in the hypertrophic and/or the dilated form or as restrictive cardiomyopathy in diabetic patients with preserved ejection fraction (Seferoviæ and Paulus, 2015). In db/db mice, a recent study observed low LV mass and systolic dysfunction suggesting restrictive cardiomyopathy rather than hypertrophic remodeling of the heart in db/db animals (Faita et al., 2018). In the present study, heart weight was unaltered expressed as raw weight and as a ratio to tibia length. Moreover, we did not observe any significant increase in the posterior wall thickness, while the LV cavity was significantly larger in the diabetic db/db mice suggestive of LV dilatation. The presence of hypertension was suggested to play a role in the cardiac volumes in db/db mice (Van Bilsen et al., 2014), but in a subset of animals, we did not find differences in mean arterial pressures measured with an invasive catheter.

Although tail blood pressure measurements suggested that db/db mice are hypertensive (Bagi et al., 2005; Van Bilsen et al., 2014), our findings are in agreement with other studies reporting no difference in telemetric blood pressure values (Su et al., 2008; Katz et al., 2011; Souza-Smith et al., 2011; Husarek et al., 2015; Faita et al., 2018). The increased end-diastolic LV cavity dimensions may also be related to a longer diastolic filling time, and hence adaptation of the heart to larger body weight and reduced locomotor activity.

Limitations

The experiments on arteries from both control db/db+ and diabetic db/db male and female mice were conducted with the same glucose concentration of 5.5 mM. This was to avoid acute hyperglycaemic effects on endothelial function (Bangshaab et al., 2019), which may confound the relation of endothelial to structural function. However, both the male and female db/db mice were exposed to high plasma glucose concentrations for several weeks. We cannot exclude the impairment of endothelial function would be more pronounced in the presence of high glucose levels in the bath solution when arteries from db/db mice were examined, and this may also influence the observed sex differences.

There are several echocardiographic studies in male db/db mice (Plante et al., 2014; Baumgardt et al., 2016; Moon et al., 2016; Katare et al., 2018), and in the present study, we also chose to focus on the male db/db mice to clarify whether the pronounced vascular changes can be explained by changes in cardiac function and aortic flow. Despite measurements of a series of parameters, our results only reflect one-time point in the development of alterations in db/db mice, and due to low animal availability, there is a lack of some of the parameters in female db/db mice in the present study.

CONCLUSION AND PERSPECTIVES

The vessel thickness and viscoelasticity were decreased in aorta from diabetic male db/db mice, and the aortic Windkessel function seems more efficient. Together with the observed left ventricular dilatation and reduction in aortic flow velocity, these findings suggest a structural adaptation of the heart and vasculature to the increased body weight and decreased locomotion in these animals. Sex-specific differences are apparent in vessel segments with smooth muscle contribution as the passive stretch-tension curve was leftward-shifted in the aorta from male db/db mice, while it was unaltered in female db/db aorta segments versus control db/db+ mice. The reduced relaxations to the NO donor, SNP also suggest alterations of smooth muscle function in the aorta from male diabetic db/db mice. In the aorta from female diabetic db/db mice, acetylcholine relaxation was significantly impaired compared to the aorta from both the control and male diabetic db/db mice. The findings that impairment of vascular endothelial function was most pronounced in the aorta from female diabetic mice may have implications for the observed higher incidence of macrovascular complications in diabetic women.

DATA AVAILABILITY STATEMENT

The datasets generated for this study are available on request to the corresponding author.

ETHICS STATEMENT

The animal study was reviewed and approved by Danish Animal Experiments Inspectorate (permission 2014-15-2934-01059).

AUTHOR CONTRIBUTIONS

LB, EP, RC, and RH performed the functional examination of vessel segments *in vitro*. LB, RC, and CD examined the passive properties of the vessel segments. JS performed the transthoracic echocardiographic examination. SC-S performed the blood pressure measurements. All authors contributed to the design of the study and in the analysis of the data. LB, JS, and US wrote the first draft of the manuscript. All authors revised and approved the final version of the manuscript.

FUNDING

US was supported by the Danish Heart Foundation (12-04-R90-A4012-22702 and 16-R107-A6681-22967), the Novo Nordisk Foundation (NNF130C0007739), and the Danish Research Council (DFF-6110-00622B). RH was supported by the Young researchers mobility grant "Jose Castillejo" 2012 from the Ministry of education, Spain. SC-S was supported by CDCH-UCV (Consejo de Desarrollo Científico y Humanístico de la Universidad Central de Venezuela), Venezuela.

ACKNOWLEDGMENTS

We thank Susie Mogensen and Heidi Knudsen for their technical support.

SUPPLEMENTARY MATERIAL

The Supplementary Material for this article can be found online at: https://www.frontiersin.org/articles/10.3389/fphys.2020.00667/full#supplementary-material

FIGURE S1 | Representative image of an aorta ring segment.

FIGURE S2 | Acetylcholine and sodium nitroprusside relaxations in the aorta from 11- and 16-week old control (db/db+) and diabetic male mice.

FIGURE S3 | Impaired acetylcholine and sodium nitroprusside relaxations in coronary arteries contracted by the thromboxane analog, U46619.

FIGURE S4 | Representative electrocardiogram from a diabetic db/db mouse and a control db/db+ mouse.

FIGURE S5 | Representative echocardiographic images of aorta in a db/db mouse.

TABLE S1 | Calculation of passive properties of coronary arteries.

REFERENCES

Airaksinen, K. E. J., Salmela, P. I., Linnaluoto, M. K., Ikäheimo, M. J., Ahola, K., and Ryhänen, L. J. (1993). Diminished arterial elasticity in diabetes: association with fluorescent advanced glycosylation end products in collagen. *Cardiovasc. Res.* 27, 942–945. doi: 10.1093/cvr/27.6.942

Anghelescu, M., Tonniges, J. R., Calomeni, E., Shamhart, P. E., Agarwal, G., Gooch, K. J., et al. (2015). Vascular mechanics in decellularized aortas and coronary resistance microvessels in type 2 diabetic *db/db* mice. *Ann. Biomed. Eng.* 43, 2760–2770. doi: 10.1007/s10439-015-1333-4

Ayala, J. E., Samuel, V. T., Morton, G. J., Obici, S., Croniger, C. M., Shulman, G. I., et al. (2010). Standard operating procedures for describing and performing metabolic tests of glucose homeostasis in mice. *DMM Dis. Model. Mech.* 3, 525–534. doi: 10.1242/dmm.006239

Bagi, Z., Erdei, N., Toth, A., Li, W., Hintze, T. H., Koller, A., et al. (2005). Type 2 diabetic mice have increased arteriolar tone and blood pressure: enhanced release of COX-2-derived constrictor prostaglandins. *Arterioscler. Thromb. Vasc. Biol.* 25, 1610–1616. doi: 10.1161/01.ATV.0000172688.26838.9f

Bagi, Z., Koller, A., and Kaley, G. (2015). Superoxide-NO interaction decreases flow- and agonist-induced dilations of coronary arterioles in Type 2 diabetes mellitus. *Am. J. Physiol. Circ. Physiol.* 285, H1404–H1410. doi: 10.1152/ajpheart.00235.2003

Bangshaab, M., Gutierrez, A., Huynh, K. D., Knudsen, J. S., Arcanjo, D. D. R., Petersen, A. G., et al. (2019). Different mechanisms involved in liraglutide and glucagon-like peptide-1 vasodilatation in rat mesenteric small arteries. *Br. J. Pharmacol.* 17, 386–399. doi: 10.1111/bph.14534

Baumgardt, S. L., Paterson, M., Leucker, T. M., Fang, J., Zhang, D. X., Bosnjak, Z. J., et al. (2016). Chronic co-administration of sepiapterin and l-citrulline ameliorates diabetic cardiomyopathy and myocardial ischemia/reperfusion injury in obese type 2 diabetic mice. *Circ. Heart Fail.* 9:e002424. doi: 10.1161/CIRCHEARTFAILURE.115.002424

Boukens, B. J., Rivaud, M. R., Rentschler, S., Coronel, R., and Boukens, B. J. D. (2014). The journal of physiology misinterpretation of the mouse ECG: "musing the waves of *Mus musculus*." *J. Physiol.* 592, 4613–4626. doi: 10.1113/jphysiol.2014.279380

Briones, A. M., Cat, A. N. D., Callera, G. E., Yogi, A., Burger, D., He, Y., et al. (2012). Adipocytes produce aldosterone through calcineurin-dependent signaling pathways: implications in diabetes mellitus-associated obesity and vascular dysfunction. *Hypertension* 59, 1069–1078. doi: 10.1161/HYPERTENSIONAHA.111.190223

Brodsky, S. V., Morrishow, A. M., Dharia, N., Gross, S. S., and Goligorsky, M. S. (2017). Glucose scavenging of nitric oxide. *Am. J. Physiol. Physiol.* 280, F480–F486. doi: 10.1152/ajprenal.2001.280.3.f480

Caballero, A. E., Arora, S., Saouaf, R., Lim, S. C., Smakowski, P., Park, J. Y., et al. (1999). Microvascular and macrovascular reactivity is reduced in subjects at risk for type 2 diabetes. *Diabetes* 48, 1856–1862. doi: 10.2337/diabetes.48.9.1856

Chen, H., Kold-Petersen, H., Laher, I., Simonsen, U., and Aalkjaer, C. (2015). Impaired endothelial calcium signaling is responsible for the defective dilation of mesenteric resistance arteries from *db/db* mice to acetylcholine. *Eur. J. Pharmacol.* 767, 17–23. doi: 10.1016/j.ejphar.2015.09.043

Choi, S. K., Galán, M., Kassan, M., Partyka, M., Trebak, M., and Matrougui, K. (2012). Poly(ADP-Ribose) polymerase 1 inhibition improves coronary arteriole function in type 2 diabetes mellitus. *Hypertension* 59, 1060–1068. doi: 10.1161/HYPERTENSIONAHA.111.190140

Chow, M. J., Turcotte, R., Lin, C. P., and Zhang, Y. (2014). Arterial extracellular matrix: a mechanobiological study of the contributions and interactions of elastin and collagen. *Biophys. J.* 106, 2684–2692. doi: 10.1016/j.bpj.2014.05.014

Danielsen, C. C., and Andreassen, T. T. (1988). Mechanical properties of rat tail tendon in relation to proximal-distal sampling position and age. *J. Biomech.* 21, 207–212. doi: 10.1016/0021-9290(88)90171-6

Di Marzio, D., Mohn, A., Mokini, Z., Giannini, C., and Chiarelli, F. (2006). Macroangiopathy in adults and children with diabetes: from molecular mechanisms to vascular damage (Part 1). *Horm. Metab. Res.* 38, 691–705. doi: 10.1055/s-2006-955081

Docherty, J. R., Stanford, S. C., Panattieri, R. A., Alexander, S. P. H., Cirino, G., George, C. H., et al. (2019). Sex: a change in our guidelines to authors to ensure that this is no longer an ignored experimental variable. *Br. J. Pharmacol.* 176, 4081–4086. doi: 10.1111/bph.14761

Ewing, D. J., Irving, J. B., Kerr, F., Wildsmith, J. A. W., and Clarke, B. F. (2015). Cardiovascular responses to sustained handgrip in normal subjects and in patients with diabetes mellitus: a test of autonomic function. *Clin. Sci.* 46, 295–306. doi: 10.1042/cs0460295

Faita, F., Di Lascio, N., Rossi, C., Kusmic, C., and Solini, A. (2018). Ultrasonographic characterization of the *db/db* mouse: an animal model of metabolic abnormalities. *J. Diabetes Res.* 2018:4561309. doi: 10.1155/2018/4561309

Farmer, D. G. S., and Kennedy, S. (2009). RAGE, vascular tone and vascular disease. *Pharmacol. Ther.* 124, 185–194. doi: 10.1016/j.pharmthera.2009.06.013

Filogonio, R., Wang, T., and Danielsen, C. C. (2018). Analysis of vascular mechanical properties of the yellow anaconda reveals increased elasticity and distensibility of the pulmonary artery during digestion. *J. Exp. Biol.* 221:jeb177766. doi: 10.1242/jeb.177766

Gao, X., Belmadani, S., Picchi, A., Xu, X., Potter, B. J., Tewari-Singh, N., et al. (2007). Tumor necrosis factor-α induces endothelial dysfunction in Lepr db mice. *Circulation* 115, 245–254. doi: 10.1161/CIRCULATIONAHA.106.650671

Gao, X., Zhang, H., Schmidt, A. M., and Zhang, C. (2008). AGE/RAGE produces endothelial dysfunction in coronary arterioles in Type 2 diabetic mice. *Am. J. Physiol. Hear. Circ. Physiol.* 295, H491–H498. doi: 10.1152/ajpheart.00464.2008

Gao, S., Ho, D., Vatner, D. E., and Vatner, S. F. (2011). "Echocardiography in mice," in *Curr. Protoc. Mouse Biol.* (John Wiley & Sons, Inc). 1, 71–83. doi: 10.1002/9780470942390.mo100130

Guo, Z., Su, W., Allen, S., Pang, H., Daugherty, A., Smart, E., et al. (2005). COX-2 Up-regulation and vascular smooth muscle contractile hyperreactivity in spontaneous diabetic *db/db* mice. *Cardiovasc. Res.* 67, 723–735. doi: 10.1016/j.cardiores.2005.04.008

Hansen, T. W., Staessen, J. A., Torp-Pedersen, C., Rasmussen, S., Thijs, L., Ibsen, H., et al. (2006). Prognostic value of aortic pulse wave velocity as index of arterial stiffness in the general population. *Circulation* 113, 664–670. doi: 10.1161/CIRCULATIONAHA.105.579342

Hernanz, R., Martín, Á., Pérez-Girõn, J. V., Palacios, R., Briones, A. M., Miguel, M., et al. (2012). Pioglitazone treatment increases COX-2-derived prostacyclin production and reduces oxidative stress in hypertensive rats: role in vascular function. *Br. J. Pharmacol.* 166, 1303–1319. doi: 10.1111/j.1476-5381.2012.01825.x

Hummel, K. P., Dickie, M. M., and Coleman, D. L. (1966). Diabetes, a new mutation in the mouse. *Science* 153, 1127–1128. doi: 10.1126/science.153.3740.1127

Husarek, K. E., Katz, P. S., Trask, A. J., Galantowicz, M. L., Cismowski, M. J., and Lucchesi, P. A. (2015). The angiotensin receptor blocker losartan reduces coronary arteriole remodeling in type 2 diabetic mice. *Vascul. Pharmacol.* 76, 28–36. doi: 10.1016/j.vph.2015.06.013

Kaese, S., and Verheule, S. (2012). Cardiac electrophysiology in mice: a matter of size. *Front. Physiol.* 3:345. doi: 10.3389/fphys.2012.00345

Kassan, M., Choi, S.-K., Galán, M., Lee, Y.-H., Trebak, M., and Matrougui, K. (2014). Enhanced p22 PHOX expression impairs vascular function through p38 and ERK1/2 MAP kinase-dependent mechanisms in type 2 diabetic mice. *Am. J. Physiol. Circ. Physiol.* 306, H972–H980. doi: 10.1152/ajpheart.00872.2013

Katare, R., Pearson, J. T., Lew, J. K. S., Wei, M., Tsuchimouchi, H., Du, C. K., et al. (2018). Progressive decrease in coronary vascular function associated with Type 2 diabetic heart disease. *Front. Physiol.* 9:696. doi: 10.3389/fphys.2018.00696

Katz, P. S., Trask, A. J., Souza-Smith, F. M., Hutchinson, K. R., Galantowicz, M. L., Lord, K. C., et al. (2011). Coronary arterioles in type 2 diabetic (*db/db*) mice undergo a distinct pattern of remodeling associated with decreased vessel stiffness. *Basic Res. Cardiol.* 106, 1123–1134. doi: 10.1007/s00395-011-0201-0

Kautzky-Willer, A., Harreiter, J., and Pacini, G. (2016). Sex and gender differences in risk, pathophysiology and complications of type 2 diabetes mellitus. *Endocr. Rev.* 37, 278–316. doi: 10.1210/er.2015-1137

Kilkenny, C., Browne, W. J., Cuthill, I. C., Emerson, M., and Altman, D. G. (2010). The ARRIVE guidelines checklist animal research: reporting in vivo experiments. *Br. J. Pharmacol.* 8, 8–9. doi: 10.1371/journal.pbio.1000412

Lansing, A. I., Rosenthal, T. B., Alex, M., and Dempsey, E. W. (1952). The structure and chemical characterization of elastic fibers as revealed by elastase and by electron microscopy. *Anat. Rec.* 114, 555–575. doi: 10.1002/ar.1091140404

Lee, J., Lee, S., Zhang, H., Hill, M. A., Zhang, C., and Park, Y. (2017). Interaction of IL-6 and TNF-α contributes to endothelial dysfunction in type 2 diabetic mouse hearts. *PLoS One* 12:e0187189. doi: 10.1371/journal.pone.0187189

Maric-Bilkan, C. (2017). Sex differences in micro- and macro-vascular complications of diabetes mellitus. *Clin. Sci.* 131, 833–846. doi: 10.1042/CS20160998

Matsuzawa, Y., Suematsu, S., Saito, J., Omura, M., and Nishikawa, T. (2013). Vascular aldosterone production at the pre-diabetic stage of young otsuka long-evans tokushima fatty (OLETF) rats, compared with long-evans tokushima otsuka (LETO) rats. *Molecules* 18, 15636–15647. doi: 10.3390/molecules181215636

McCallinhart, P. E., Sunyecz, I. L., and Trask, A. J. (2018). Coronary microvascular remodeling in type 2 diabetes: synonymous with early aging? *Front. Physiol.* 9:1463. doi: 10.3389/fphys.2018.01463

McGrath, J. C., and Lilley, E. (2015). Implementing guidelines on reporting research using animals (ARRIVE etc.): new requirements for publication in BJP. *Br. J. Pharmacol.* 172, 3189–3193. doi: 10.1111/bph.12955

Miike, T., Kunishiro, K., Kanda, M., Azukizawa, S., Kurahashi, K., and Shirahase, H. (2008). Impairment of endothelium-dependent ACh-induced relaxation in aorta of diabetic *db/db* mice-possible dysfunction of receptor and/or receptor-G protein coupling. *Naunyn Schmiedebergs Arch. Pharmacol.* 377, 401–410. doi: 10.1007/s00210-008-0261-3

Moon, J. Y., Woo, J. S., Seo, J. W., Lee, A., Kim, D. J., Kim, Y. G., et al. (2016). The dose-dependent organ-specific effects of a dipeptidyl peptidase-4 inhibitor on cardiovascular complications in a model of type 2 diabetes. *PLoS One* 11:e0150745. doi: 10.1371/journal.pone.0150745

Movahed, M. R. (2007). Diabetes as a risk factor for cardiac conduction defects: a review. *Diabetes Obes. Metab.* 9, 276–281. doi: 10.1111/j.1463-1326.2006.00609.x

Neuman, R. E., and Logan, M. A. (1950). The determination of collagen and elastin in tissues. *J. Biol. Chem.* 186, 549–556.

Nguyen Dinh Cat, A., Callera, G. E., Friederich-Persson, M., Sanchez, A., Dulak-Lis, M. G., Tsiropoulou, S., et al. (2018). Vascular dysfunction in obese diabetic *db/db* mice involves the interplay between aldosterone/mineralocorticoid receptor and Rho kinase signaling. *Sci. Rep.* 8:2952.

Okon, E. B., Szado, T., Laher, I., McManus, B., and Van Breemena, C. (2003). Augmented contractile response of vascular smooth muscle in a diabetic mouse model. *J. Vasc. Res.* 40, 520–530. doi: 10.1159/000075238

Paneni, F., Beckman, J. A., Creager, M. A., and Cosentino, F. (2013). Diabetes and vascular disease: pathophysiology, clinical consequences, and medical therapy: part I. *Eur. Heart J.* 34, 2436–2446. doi: 10.1093/eurheartj/eht149

Pannirselvam, M., Verma, S., Anderson, T. J., and Triggle, C. R. (2002). Cellular basis of endothelial dysfunction in small mesenteric arteries from spontaneously diabetic (*db/db* -/-) mice: role of decreased tetrahydrobiopterin bioavailability. *Br. J. Pharmacol.* 136, 255–263. doi: 10.1038/sj.bjp.0704683

Pannirselvam, M., Wiehler, W. B., Anderson, T., and Triggle, C. R. (2005). Enhanced vascular reactivity of small mesenteric arteries from diabetic mice is associated with enhanced oxidative stress and cyclooxygenase products. *Br. J. Pharmacol.* 144, 953–960. doi: 10.1038/sj.bjp.0706121

Park, S., Bivona, B. J., Feng, Y., Lazartigues, E., and Harrison-Bernard, L. M. (2008). Intact renal afferent arteriolar autoregulatory responsiveness in *db/db* mice. *Am. J. Physiol. Physiol.* 295, F1504–F1511. doi: 10.1152/ajprenal.90417.2008

Peters, S. A., Huxley, R. R., and Woodward, M. (2014). Diabetes as risk factor for coronary heart disease in women compared with men. *Diabetologia* 57, 1542–1551. doi: 10.1007/s00125-014-3260-6

Piercy, V., and Taylor, S. G. (1998). A comparison of spasmogenic and relaxant responses in aortae from C57/BL/KsJ diabetic mice with those from their non-diabetic litter mates. *Pharmacology* 56, 267–275. doi: 10.1159/000028208

Pistner, A., Belmonte, S., Coulthard, T., and Blaxall, B. (2010). Murine echocardiography and ultrasound imaging. *J. Vis. Exp.* 42:2100. doi: 10.3791/2100

Plante, E., Menaouar, A., Danalache, B. A., Broderick, T. L., Jankowski, M., and Gutkowska, J. (2014). Treatment with brain natriuretic peptide prevents the development of cardiac dysfunction in obese diabetic *db/db* mice. *Diabetologia* 57, 1257–1267. doi: 10.1007/s00125-014-3201-4

Prenner, S. B., and Chirinos, J. A. (2015). Arterial stiffness in diabetes mellitus. *Atherosclerosis* 238, 370–379. doi: 10.1016/j.atherosclerosis.2014.12.023

Rizzoni, D., Porteri, E., Guelfi, D., Muiesan, M. L., Valentini, U., Cimino, A., et al. (2001). Structural alterations in subcutaneous small arteries of normotensive and hypertensive patients with non-insulin-dependent diabetes mellitus. *Circulation* 103, 1238–1244. doi: 10.1161/01.CIR.103.9.1238

Rydén, L., Grant, P. J., Anker, S. D., Berne, C., Cosentino, F., Danchin, N., et al. (2013). ESC guidelines on diabetes, pre-diabetes, and cardiovascular diseases developed in collaboration with the EASD. *Eur. Heart J.* 34, 3035–3087. doi: 10.1093/eurheartj/eht108

Sallam, N., Fisher, A., Golbidi, S., and Laher, I. (2011). Weight and inflammation are the major determinants of vascular dysfunction in the aortae of *db/db* mice. *Naunyn Schmiedebergs Arch. Pharmacol.* 383, 483–492. doi: 10.1007/s00210-011-0614-1

Sasaki, N., Yamashita, T., Takaya, T., Shinohara, M., Shiraki, R., Takeda, M., et al. (2008). Augmentation of vascular remodeling by uncoupled endothelial nitric oxide synthase in a mouse model of diabetes mellitus. *Arterioscler. Thromb. Vasc. Biol.* 28, 1068–1076. doi: 10.1161/ATVBAHA.107.160754

Schjørring, O. L., Carlsson, R., and Simonsen, U. (2015). Pressure myography to study the function and structure of isolated small arteries. *Methods Mol. Biol.* 1339, 277–295. doi: 10.1007/978-1-4939-2929-0_19

Schofield, I., Malik, R., Izzard, A., Austin, C., and Heagerty, A. (2002). Vascular structural and functional changes in type 2 diabetes mellitus: evidence for the roles of abnormal myogenic responsiveness and dyslipidemia. *Circulation* 106, 3037–3043. doi: 10.1161/01.CIR.0000041432.80615.A5

Schram, M. T., Henry, R. M. A., Van Dijk, R. A. J. M., Kostense, P. J., Dekker, J. M., Nijpels, G., et al. (2004). Increased central artery stiffness in impaired glucose metabolism and type 2 diabetes: the Hoorn study. *Hypertension* 43, 176–181. doi: 10.1161/01.HYP.0000111829.46090.92

Seferoviæ, P. M., and Paulus, W. J. (2015). Clinical diabetic cardiomyopathy: a two-faced disease with restrictive and dilated phenotypes. *Eur. Heart J.* 36, 1718–1727. doi: 10.1093/eurheartj/ehv134

Senador, D., Kanakamedala, K., Irigoyen, M. C., Morris, M., and Elased, K. M. (2009). Cardiovascular and autonomic phenotype of *db/db* diabetic mice. *Exp. Physiol.* 94, 648–658. doi: 10.1113/expphysiol.2008.046474

Shadwick, R. (1992). "Soft composites," in *Biomechanics—Materials: A Practical Approach*, ed. J. Vincent (Oxford: Oxford University Press), 133–164.

Shi, Y., and Vanhoutte, P. M. (2017). Macro- and microvascular endothelial dysfunction in diabetes. *J. Diabetes* 9, 434–449. doi: 10.1111/1753-0407.12521

Simonsen, U., Triguero, D., García-Sacristán, A., and Prieto, D. (1999). Cholinergic modulation of non-adrenergic, non-cholinergic relaxation in isolated, small coronary arteries from lambs. *Pflugers Arch. Eur. J. Physiol.* 438, 177–186. doi: 10.1007/s004240050896

Sista, A. K. (2005). Increased aortic stiffness in the insulin-resistant Zucker *fa/fa* rat. *Am. J. Physiol. Heart Circ. Physiol.* 289, H845–H851. doi: 10.1152/ajpheart.00134.2005

Slama, M., Susic, D., Varagic, J., Ahn, J., and Frohlich, E. D. (2015). Echocardiographic measurement of cardiac output in rats. *Am. J. Physiol. Circ. Physiol.* 284, H691–H697. doi: 10.1152/ajpheart.00653.2002

Souza-Smith, F. M., Katz, P. S., Trask, A. J., Stewart, J. A., Lord, K. C., Varner, K. J., et al. (2011). Mesenteric resistance arteries in type 2 diabetic *db/db* mice undergo outward remodeling. *PLoS One* 6:e23337. doi: 10.1371/journal.pone.0023337

Su, W., Guo, Z., Randall, D. C., Cassis, L., Brown, D. R., and Gong, M. C. (2008). Hypertension and disrupted blood pressure circadian rhythm in Type 2 diabetic *db/db* mice. *Am. J. Physiol. Circ. Physiol.* 295, H1634–H1641. doi: 10.1152/ajpheart.00257.2008

Swoap, S. J., and Gutilla, M. J. (2009). Cardiovascular changes during daily torpor in the laboratory mouse. *Am. J. Physiol. Regul. Integr. Comp. Physiol.* 297, R769–R774. doi: 10.1152/ajpregu.00131.2009

Tournoux, F., Petersen, B., Thibault, H., Zou, L., Raher, M. J., Kurtz, B., et al. (2011). Validation of noninvasive measurements of cardiac output in mice using echocardiography. *J. Am. Soc. Echocardiogr.* 24, 465–470. doi: 10.1016/j.echo.2010.12.019

Trachet, B., Fraga-Silva, R. A., Londono, F. J., Swillens, A., Stergiopulos, N., and Segers, P. (2015). Performance comparison of ultrasound-based methods to assess aortic diameter and stiffness in normal and aneurysmal mice. *PLoS One*, 10:e0129007. doi: 10.1371/journal.pone.0129007

Van Bilsen, M., Daniels, A., Brouwers, O., Janssen, B. J. A., Derks, W. J. A., Brouns, A. E., et al. (2014). Hypertension is a conditional factor for the development of cardiac hypertrophy in type 2 diabetic mice. *PLoS One* 9:e85078. doi: 10.1371/journal.pone.0085078

Van Soldt, B. J., Danielsen, C. C., and Wang, T. (2015). The mechanical properties of the systemic and pulmonary arteries of python regius correlate with blood pressures. *J. Morphol.* 276, 1412–1421. doi: 10.1002/jmor.20429

Vlachopoulos, C., Aznaouridis, K., and Stefanadis, C. (2010). Prediction of cardiovascular events and all-cause mortality with arterial stiffness. A systematic review and meta-analysis. *J. Am. Coll. Cardiol.* 55, 1318–1327. doi: 10.1016/j.jacc.2009.10.061

Wellman, G. C., Bonev, A. D., Nelson, M. T., and Brayden, J. E. (1996). Gender differences in coronary artery diameter involve estrogen, nitric oxide, and Ca2+-dependent K+ channels. *Circ. Res.* 79, 1024–1030. doi: 10.1161/01.RES.79.5.1024

Xie, Z., Su, W., Guo, Z., Pang, H., Post, S. R., and Gong, M. C. (2006). Up-regulation of CPI-17 phosphorylation in diabetic vasculature and high glucose cultured vascular smooth muscle cells. *Cardiovasc. Res.* 69, 491–501. doi: 10.1016/j.cardiores.2005.11.002

Xu, Z., Wang, S., Ji, H., Zhang, Z., Chen, J., Tan, Y., et al. (2016). Broccoli sprout extract prevents diabetic cardiomyopathy via Nrf2 activation in *db/db* T2DM mice. *Sci. Rep*. 6:30252. doi: 10.1038/srep30252

Zhang, C., Park, Y., Picchi, A., and Potter, B. J. (2008). Maturation-induces endothelial dysfunction via vascular inflammation in diabetic mice. *Basic Res. Cardiol.* 295, 407–416. doi: 10.1007/s00395-008-0725-0

Conflict of Interest: The authors declare that the research was conducted in the absence of any commercial or financial relationships that could be construed as a potential conflict of interest.

frontiers in Physiology

ORIGINAL RESEARCH
published: 07 July 2020
doi: 10.3389/fphys.2020.00742

Restoring the Platelet miR-223 by Calpain Inhibition Alleviates the Neointimal Hyperplasia in Diabetes

Meiling Su[1,2†], Shunyang Fan[3†], Zhenwei Ling[1,2†], Xuejiao Fan[1,2], Luoxing Xia[1,2], Yingying Liu[1,2], Shaoying Li[1,2], Yuan Zhang[1,2], Zhi Zeng[1,2] and Wai Ho Tang[1,2*]*

[1] *Joint Program in Cardiovascular Medicine, Affiliated Guangzhou Women and Children's Medical Centre, Zhongshan School of Medicine, Sun Yat-sen University, Guangzhou, China,* [2] *Institute of Pediatrics, Guangzhou Women and Children's Medical Centre, Guangzhou Medical University, Guangzhou, China,* [3] *Heart Center, The Third Affiliated Hospital of Zhengzhou University, Zhengzhou, China*

Platelet hyperactivity is the hallmark of diabetes, and platelet activation plays a crucial role in diabetic vascular complications. Recent studies have shown that upon activation, platelet-derived miRNAs are incorporated into vascular smooth muscle cells (VSMCs), regulating the phenotypic switch of VSMC. Under diabetes, miRNA deficiency in platelets fails to regulate the VSMC phenotypic switch. Therefore, manipulation of platelet-derived miRNAs expression may provide therapeutic option for diabetic vascular complications. We seek to investigate the effect of calpeptin (calpain inhibitor) on the expression of miRNAs in diabetic platelets, and elucidate the downstream signaling pathway involved in protecting from neointimal formation in diabetic mice with femoral wire injury model. Using human cell and platelet coculture, we demonstrate that diabetic platelet deficient of miR-223 fails to suppress VSMC proliferation, while overexpression of miR-223 in diabetic platelets suppressed the proliferation of VSMC to protect intimal hyperplasia. Mechanistically, miR-223 directly targets the insulin-like growth factor-1 receptor (IGF-1R), which inhibits the phosphorylation of GSK3β and activates the phosphorylation of AMPK, resulting in reduced VSMC dedifferentiation and proliferation. Using a murine model of vascular injury, we show that calpeptin restores the platelet expression of miR-223 in diabetes, and the horizontal transfer of platelet miR-223 into VSMCs inhibits VSMC proliferation in the injured artery by targeting the expression of IGF-1R. Our data present that the platelet-derived miR-223 suppressed VSMC proliferation via the regulation miR-223/IGF-1R/AMPK signaling pathways, and inhibition of calpain alleviates neointimal formation by restoring the expression of miR-223 in diabetic platelet.

Keywords: diabetes mellitus, platelet, vascular smooth muscle cells, miR-223, calpain, neointimal hyperplasia

OPEN ACCESS

Edited by:
Xavier Figueroa, Pontificia Universidad Católica de Chile, Chile

Reviewed by:
Ling-Qing Yuan, Second Xiangya Hospital, Central South University, China
Sarah Jane George, University of Bristol, United Kingdom

***Correspondence:**
Zhi Zeng
zengzhi@gwcmc.org
Wai Ho Tang
waiho.tang@yahoo.com

[†] *These authors have contributed equally to this work*

Specialty section:
This article was submitted to Vascular Physiology, a section of the journal Frontiers in Physiology

Received: *28 February 2020*
Accepted: *08 June 2020*
Published: *07 July 2020*

Citation:
Su M, Fan S, Ling Z, Fan X, Xia L, Liu Y, Li S, Zhang Y, Zeng Z and Tang WH (2020) Restoring the Platelet miR-223 by Calpain Inhibition Alleviates the Neointimal Hyperplasia in Diabetes. Front. Physiol. 11:742. doi: 10.3389/fphys.2020.00742

INTRODUCTION

Diabetes mellitus (DM) is an important risk factor of intima hyperplasia and vascular restenosis, resulting in diabetic vascular complications (Kornowski et al., 1997; Davi and Patrono, 2007). It is known that platelet hyperreactivity is the hallmark of DM, and the activated platelets (APs) release thromboxane and PDGF, which induce vascular smooth muscle cells (VSMCs) switching

from a quiescent contractile phenotype to a highly synthetic and proliferating phenotype upon vascular injury and repair (Millette et al., 2005). Excessive proliferation of VSMCs leads to intimal hyperplasia in DM (Faries et al., 2001). Therefore, the regulation of VSMC phenotypic switch plays a crucial role in maintaining the vascular stability.

Although platelets are anucleate cells, they contain enriched and diverse miRNAs and mRNAs (Landry et al., 2009; Nagalla et al., 2011). We and others have demonstrated that the platelet-derived miRNAs can be transferred and incorporated into recipient cells such as VSMCs, endothelial cells, and macrophages (Risitano et al., 2012; Kirschbaum et al., 2015; Zeng et al., 2019). Our study has also shown that the horizontal transfer of platelet miRNA (miR-143/145 and miR-223) inhibits VSMC dedifferentiation and proliferation, but the altered miRNA expression of diabetic platelets fails to inhibit VSMC dedifferentiation, consequently leading to increased neointimal formation (Zeng et al., 2019). Recent report has shown that Dicer is a calpain substrate, and calpain-dependent cleavage of Dicer reduced the expression of miRNAs in diabetic platelets (Elgheznawy et al., 2015). The altered expression of platelet miRNAs such as miR-223 can be restored by treatment of a calpain inhibitor in diabetic mice (Elgheznawy et al., 2015), suggesting that calpain inhibitor may provide therapeutic adjunct for platelet-associated vascular disease in diabetes.

In the present study, we seek to elucidate the mechanism by which inhibition of calpain regulated VSMC phenotypic switch via upregulating the expression of platelet-derived miRNAs, and the potential application of calpeptin on platelet-associated vascular disease in diabetes. Here we demonstrate that diabetic platelet deficient of miR-223 fails to suppress VSMC proliferation, while overexpression of miR-223 in diabetic platelets suppressed the proliferation of VSMC to protect intimal hyperplasia. Mechanistically, miR-223 directly targets the insulin-like growth factor-1 receptor (IGF-1R), which inhibits the phosphorylation of GSK3β and activates the phosphorylation of AMPK, resulting in reduced VSMC dedifferentiation and proliferation. Using a murine model of vascular injury, we show that calpeptin restores the platelet expression of miR-223 in diabetes, and the horizontal transfer of platelet miR-223 into VSMCs inhibits VSMC proliferation in the injured artery by targeting the expression of IGF-1R. Collectively, our results demonstrate that the platelet-derived miR-223 inhibits VSMC proliferation via miR-223/IGF-1R/AMPK signaling axis, and inhibition of calpain alleviates neointimal formation by restoring the expression of miR-223 in diabetic platelet.

MATERIALS AND METHODS

Platelet Isolation and Purification

Human peripheral blood was obtained from Guangzhou Women and Children's Medical Center. Informed consent of underage subjects was obtained from their parents. Our study was compiled and approved by the Institutional Review Board of Guangzhou Women and Children's Medical Center (Human Investigation Committee No. 201944101). Venous blood samples (approximately 4 ml) were drawn from Non-DM and DM subjects from Guangzhou Women and Children's Medical Center. Venous blood samples (approximately 4 ml) were drawn into blood collection tubes containing 3.8% trisodium citrate (w/v). Platelet-rich plasma (PRP) was centrifuged at 1200 rpm at 25°C for 15 min. PRP were then treated with 100 nM Prostaglandin E1 (PGE1, Sigma) and centrifuged at 2500 rpm for another 5 min. After discarding the supernatant, the platelet pellet was resuspended with 3 ml Hank's Balanced Salt Solution (HBSS, NaCl 135 mM, $MgCl_2$ 1 mM, $NaHCO_3$ 12 mM, $CaCl_2$ 1 mM, KCl 2.9 mM, Glucose 5 mM, BSA 0.35%, HEPES 10 mM).

For murine platelets, blood was drawn from the left ventricle after anesthesia. Platelet-rich plasma (PRP) was prepared by centrifuging at 1200 rpm for 15 min, and blood coagulation was inhibited by adding the anticoagulant citrate dextrose solution. By centrifuging at 2600 rpm for 5 min, washed platelets were prepared from PRP and were resuspended in HBSS. Platelet concentration was adjusted at 2×10^8 cells/mL using a platelet counter. To prevent platelet activation, the centrifuge temperature was kept at room temperature during the washing step.

Animals

The male C57BL/6 mice (8 weeks old) were purchased from Guangzhou Medical University. Procedures were approved by the Institutional Animal Care and Use Committee of Guangzhou Medical University (No. SYXK2016-0168). Eight week old mice were injected with 50mg/kg streptozotocin (STZ, Sigma) to induce diabetes for 5 consecutive days. The mice were randomly divided into four groups and were intraperitoneally injected PBS or calpeptin (calpain inhibitor) (30 mg/kg/day) diluted in DMSO in PBS every other day. The mice in the AgomiR group were administered with Agomir-223 200 μl at a concentration of 20 mM via tail vein injection. The calpeptin ware purchased from the SelleckChemicals Co, while the AgomiRs and miRNA mimic from Shanghai GenePharma Co.

Femoral Artery Wire Injury Model

The endothelial injury in the right femoral artery was done by guidewire abrasion. After anesthetizing the experimental mice, the right thigh was depilated from hair and disinfected with alcohol. The proximal part of the femoral artery and saphenous artery were dissected under the microscope, followed by a temporary stop of blood flow with a silk thread. Then the 0.25 mm diameter guidewire was inserted into the femoral artery from the saphenous artery, inserted and withdrawn 3 times to sufficiently create endothelial wear. The saphenous artery was ligated and the wound was sutured to allow the mice to enter a recovery phase. The contralateral femoral artery was sham-operated without guidewires injured as control. Four weeks after injury, the mice were anesthetized, sacrificed for harvesting the femoral, and fixed in 4% paraformaldehyde. After 30% sucrose dehydration, the arterial tissue was embedded in the Tissue-Tek O.C.T (SAKURA, United States) agent and performed a frozen section.

Cell Culture

Human coronary artery smooth muscle cells (HCASMC) were purchased from Cell Application at passage 4, cultured in High Glucose DMEM (Gibco, United States) supplemented with 10% fetal bovine serum (Gibco, United States), 100 U/ml penicillin (Gibco, United States), and 100 μg/ml streptomycin (Gibco, United States). The cells were cultured in the incubator with 5% CO_2 and 37°C. HCASMCs were cocultured with or without resting platelets (RPs) or 0.1 U/ml thrombin activated platelets (APs). After isolation and purification, platelets from healthy subject (HS) and DM patients were counted and added directly to the cultured VSMC (1: 100) for 48 h.

Transfection of miRNA

HCASMCs were transfected with miR-223 mimic or miR negative control (miR-NC, GenePharma, China) at 100 nM by using Lipofectamine RNAiMAX reagent (Invitrogen, United States). Cells were seeded to be 60–80% confluent before transfection. Lipofectamine reagent and miRNA mimic were diluted in Opti-MEM Medium (Gibco, United States) and mixed for 5 min before added to HCASMCs. Also, HCASMCs were transfected with miR-223 antagomir and miR-NC (Shanghai GenePharma Co) for 24 h, and then VSMCs were cocultured with the purified platelets from HS. After cultured for 48 h, the cells were harvested for subsequent experiments.

CCK8 Assay

Cell Counting Kit-8 Kits (CCK8; Dojindo, Japan) were used to evaluate cell proliferation. HCASMCs were seeded into a 96-well plate at a concentration of 1.0×10^4 cells/well. Post-transfection 48 h, HCASMCs were incubated with 10 μl CCK8 in 100 μl DMEM for 2 h. The absorbance was detected at 450 nm with a microplate reader (Thermo Fisher Scientific).

BrdU Incorporation Assay

The HCASMCs were starved in the DMEM without serum and then were transfected with miR-223 mimic and miR-NC as described above. Forty-eight hours after transfection, cell proliferation was determined by using the BrdU Cell Proliferation Assay Kit (Millipore, United States) according to the manufacturer's protocol. Before measurement, BrdU was added to the cultured cells and incubated for 12 h. After washing with PBS, the cells were fixed and DNA denatured with 4% paraformaldehyde. After fixation, cells were labeled with peroxidase-conjugated BrdU antibody and then incubated with peroxidase substrate. Finally, a stop solution was added to stop the reaction. The absorbance (A_{450}–$A_{550\ nm}$) representing the cell proliferation was measured on a microplate reader.

EdU Imaging Assay

Cell proliferation rate was measured with Click-iT EdU Alexa Fluor 488 Imaging Kit (Invitrogen, United States). HCASMCs were seeded into glass-bottom culture dishes at a concentration of 1.0×10^4 cells/ml and transfection experiments were performed as described above. Before termination of cell culture, EdU was added at a final transformation concentration 10 μg/L and incubated with cells at 37°C for 1 h. After incubation, cells were washed with PBS, fixed with 3.7% paraformaldehyde for 15 min, and permeabilized with 0.5% Triton®X-100 for 20 min. The Click-iT® reaction cocktail prepared 15 min in advance was added to the notch of each well and incubated at room temperature for 30 min, protected from light. After washing, DNA staining was performed using Hoechst 33342 solution at a concentration of 1: 2000. The EdU positive cells were observed and captured under the inverted fluorescence microscope (Leica), and the cell count was calculated by using Image J.

Luciferase Reporter Assay

IGF-1R 3′-UTR plasmid was obtained from Biolink Technology Co. The HEK-293 cells were plated in a 24-well plate in a concentration of 50%. After 24 h plated, the 1μg plasmid and 50 nM miR-223 mimic and miR-NC were transfected by using Lipofectamine RNAiMAX reagent (Invitrogen, United States). Luciferase reporter analyses were performed according to the manufacturer's instructions after 48 h of transfection by using Dual Luciferase Assay Kit (Promega, United States). The Firefly and Renilla fluorescence values were detected by the microplate infinite M1000 (Tecan) and the firefly fluorescence normalized by Renilla was served as luciferase activity.

HE Staining

The frozen sections of the tissues were dried at room temperature for 30 min and placed in PBS for 10 min. According to the following sequence, the tissues were placed in hematoxylin for 1 min, hydrochloric acid alcohol for 2,3 sec, and then moved to eosin for 8–10 sec. Finally, the tissues were rinsed in running water and then mounted with neutral gum.

Immunofluorescence

Cells and tissues were fixed and permeabilized by 4% paraformaldehyde (Servicebio, China) and 0.2% Triton-100X (Solarbio, China) in PBS, respectively; staining was with antibodies and their corresponding secondary antibodies. Primary antibodies used include IGF-1R (1:100, ab182408, Abcam, United States) and α-smooth muscle actin (Acta2; 1:100, ab119952, Abcam, United States). After 24 h, sections were incubated with the Alexa Fluor 594-conjugated anti-rabbit IgG secondary antibody and Alexa Fluor 488-conjugated anti-goat IgG secondary antibody (Thermo Fisher Scientific) (1:200) for 60 min and stained with the chromatin-specific dye Hoechst for 5 min at RT. The confocal images were taken with a Leica SP8 (Leica) confocal microscope.

Western Blot Analysis

The cells were harvested with RIPA lysate containing protease inhibitors or phosphatase inhibitor cocktail. Extract protein by centrifugation at 4°C at 12,000 rpm and heated at 95°C with loading buffer. The protein samples were resolved in 12% SDS-PAGE gels and transferred to PVDF membranes (Millipore, United States). PVDF membranes were incubated with 5% skim milk powder (Biofroxx, Germany) for 2 h and then incubated with primary antibodies used including:

IGF-1R (1:1000, ab182408, Abcam, United States); ACTA2 (1:2000, ab119952, Abcam, United States); calponin (1:2000, CNN1; ab46794, Abcam, United States); transgelin (TAGLAN; 1:2000, ab14106, Abcam, United States); KLF4 (1:2000, 101508, GenetTex, United States); KLF5 (1:2000, ab137676, Abcam, United States); osteopontin (1:2000, OPN; ab91655, Abcam, United States); Akt (1:1000, 9272S, CST, United States); Phospho-Akt (1:500, Ser473) (4060S, CST, United States); GSK3β (1:1000, 9315S, CST, United States); Phospho-GSK3β (Ser9) (1:500, 9336S, CST, United States); Src (1:1000, MAB3389, R&D, United States); Phospho-Src (Y419) (1:500, AF2685, R&D, United States); JNK (1:1000, 9252S, CST, United States); Phospho-JNK (Thr172) (1:500, 4668S, CST, United States); AMPK (1:1000, 2532S, CST, United States); Phospho-AMPK (Thr183/Tyr185) (1:500, 2535S, CST, United States); Acetyl-CoA Carboxylase (1:1000, ACC; 3662S, CST, United States); Phospho-ACC (Ser79) (1:500, 3661S, CST, United States); p21 (1:1000, 2847, CST, United States); P27 (1:1000, 3688, CST, United States); GAPDH (1:3000, ab125247, Abcam, United States); α-tubulin (1:3000, ab52866, Abcam, United States); α-actinin (1:3000, ab18061, Abcam, United States). The next day, the PVDF membranes were incubated with a secondary antibody (1:2000) dissolved in 5% nonfat milk after three times of washing with TBST. The specific band for the target protein was detected by ChemiDoc XRS+ system, and the band intensities were calculated using the Image Lab software.

Proteomic Phosphokinase Array

The cell lysate was extracted from the cells after the treatment as described above, and the protein was quantified with a bicinchoninic acid kit. According to the manufacturer's instructions, after blocking with Array Buffer 1, the phosphokinase array membrane was incubated with diluted cell lysate overnight. After washing three times with Wash Buffer to remove unbound protein, the array was incubated with a cocktail of biotinylated detection antibodies for 2 h at room temperature. Streptavidin-HRP and chemiluminescent detection reagents were applied, and the signal was detected by ChemiDoc XRS+ system. Refer to the coordinates of analytes and controls provided in the appendix of the kit instructions, the signal at each capture spot corresponding to the amount of phosphorylated protein bound was analyzed.

Extraction and Purification of miRNA and qRT-PCR

Total RNA purification kit (Axygen, United States) was used to extract and purify miRNA including miRNA from cells, and purification of miRNA were reverse transcribed with miRNeasy Serum/Plasma kit (Qiagen, Germany) and U6 snRNA Normalization RT-PCR Quantitation Kit (GenePharma). After normalizing the nucleic acid concentration by quantification, reverse transcription PCR was performed to obtain stable cDNA by using the PrimeScript RT reagent Kit (Takara, Japan). Transcript levels of the target genes were analyzed by qPCR using the $2^{-\Delta\Delta Ct}$ method. The primer sequences were listed in **Supplementary Table 1**.

Statistical Analysis

All data are presented as mean ± SD. All analysis was performed using Graph Pad Prism v.5.0 (GraphPad, La Jolla, CA, United States). Comparisons between two groups were analyzed using unpaired nonparametric Student's *t*-test. Comparisons between more than two groups were analyzed using one-way ANOVA analysis with the Dunnett's multiple correction. $P < 0.05$ was considered statistically significant.

RESULTS

MiR-223 Deficiency in Diabetic Platelet Failed to Suppress VSMC Proliferation

Consistent to our previous (Zeng et al., 2019), VSMCs cocultured with DM-APs showed downregulation of VSMCs differentiation markers α-SMA (ACTA2), Calponin (CNN1), and SM22α (TAGLN) compared to HS-APs group (**Figure 1A**). Also, the expression of VSMCs dedifferentiation markers Osteopontin (OPN), MYH10, KLF4, and KLF5 was significantly increased in VSMCs cocultured with DM-APs (**Figure 1A**). Pretreatment with miR-223 antagomir, we found that the SMCs differentiation markers ACTA2 and CNN1 of VSMCs cocultured with HS-APs treated by miR-223 antagomir was significantly inhibited than VSMCs cocultured with HS-APs. Also, the expression of VSMCs dedifferentiation markers KLF4 was significantly increased in VSMCs cocultured with HS-APs treated by miR-223 antagomir (**Supplementary Figure S1**). Pretreatment with RNase A (degrades the RNA), we found that the proliferation rate of VSMCs cocultured with APs treated by RNase A was significantly higher than VSMCs cocultured with APs (**Figure 1B**). Also, overexpression of miR-223 significantly suppressed VSMC proliferation (**Figures 1C,D**). These results suggested that platelet-derived miR-223 was transferred and incorporated into VSMCs, inhibiting VSMC proliferation. Deficiency in diabetic platelet fails to suppress VSMC proliferation.

MiR-223 Directly Targets the IGF-1R, Which Inhibits the Phosphorylation of Akt and GSK3β

Bioinformatics analysis identified a binding site for miR-223 in the 3′-UTR of IGF-1R. When we cloned IGF-1R 3′ UTR into luciferase report, we found that a miR-223 mimic significantly inhibited the luciferase activity; however, the inhibition of luciferase activity was abrogated by mutated control group (**Figure 2A**). To identify whether miR-223 could bind to IGF-1R and inhibited the expression, we performed that VSMC was treated with a miR-223 mimic. As expected, the expression of IGF-1R in VSMC was significantly decreased by overexpression of miR-223 compared to control group. The data suggest miR-223 can directly target the 3′-UTR of IGF-1R and inhibit its expression in VSMC (**Figures 2A–C**). Also, we performed overexpression of IGF-1R in VSMCs. We found that VSMC proliferation was significantly increased in overexpression of IGF-1R of VSMCs compared with control group using CCK8 (**Figure 2D**). The binding of IGF-1 to its

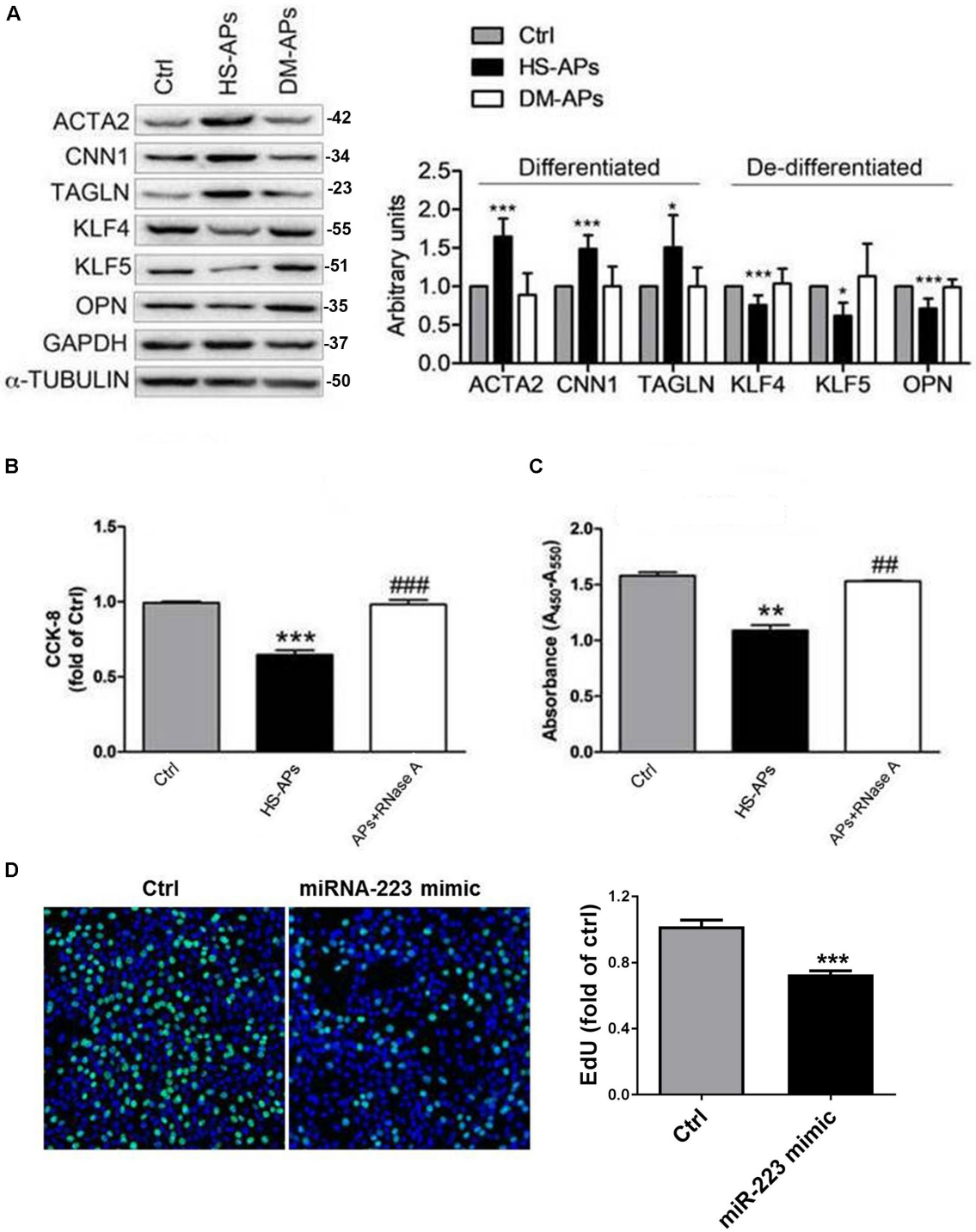

FIGURE 1 | MiR-223 deficiency in diabetic platelet fails to suppress VSMC proliferation. Activated platelets (APs) from healthy subject (HS) and DM patients were cocultured with human VSMCs for 48 h. **(A)** Expression of differentiation markers ACTA2, CNN1, and TAGLN and dedifferentiation markers OPN, MYH10, KLF4, and KLF5 in control (Ctrl) VSMCs and APs cocultured with VSMCs (HS-APs, DM-APs) was detected with western blot analysis. **(B,C)** The rate of proliferation was determined by CCK8 assay and Brdu assay in VSMCs treated with APs pretreated by RNase A (degrades the RNA). Data are presented as mean ± SD ($n = 6$). Comparisons between more than two groups were analyzed using one-way ANOVA analysis with the Dunnett's multiple correction. $^{*}P < 0.05$, $^{**}P < 0.01$, $^{***}P < 0.001$ vs Ctrl (VSMCs without platelets); $^{\#}P < 0.05$, $^{\#\#}P < 0.01$, $^{\#\#\#}P < 0.001$ vs HS-APs. **(D)** The rate of proliferation was determined by EdU incorporation assay in VSMCs transfected with miR-223 mimic. Data are presented as mean ± SD ($n = 6$). Comparisons between two groups were analyzed using unpaired nonparametric Student's *t*-test.$^{*}P < 0.05$ vs Ctrl (miR-NC).

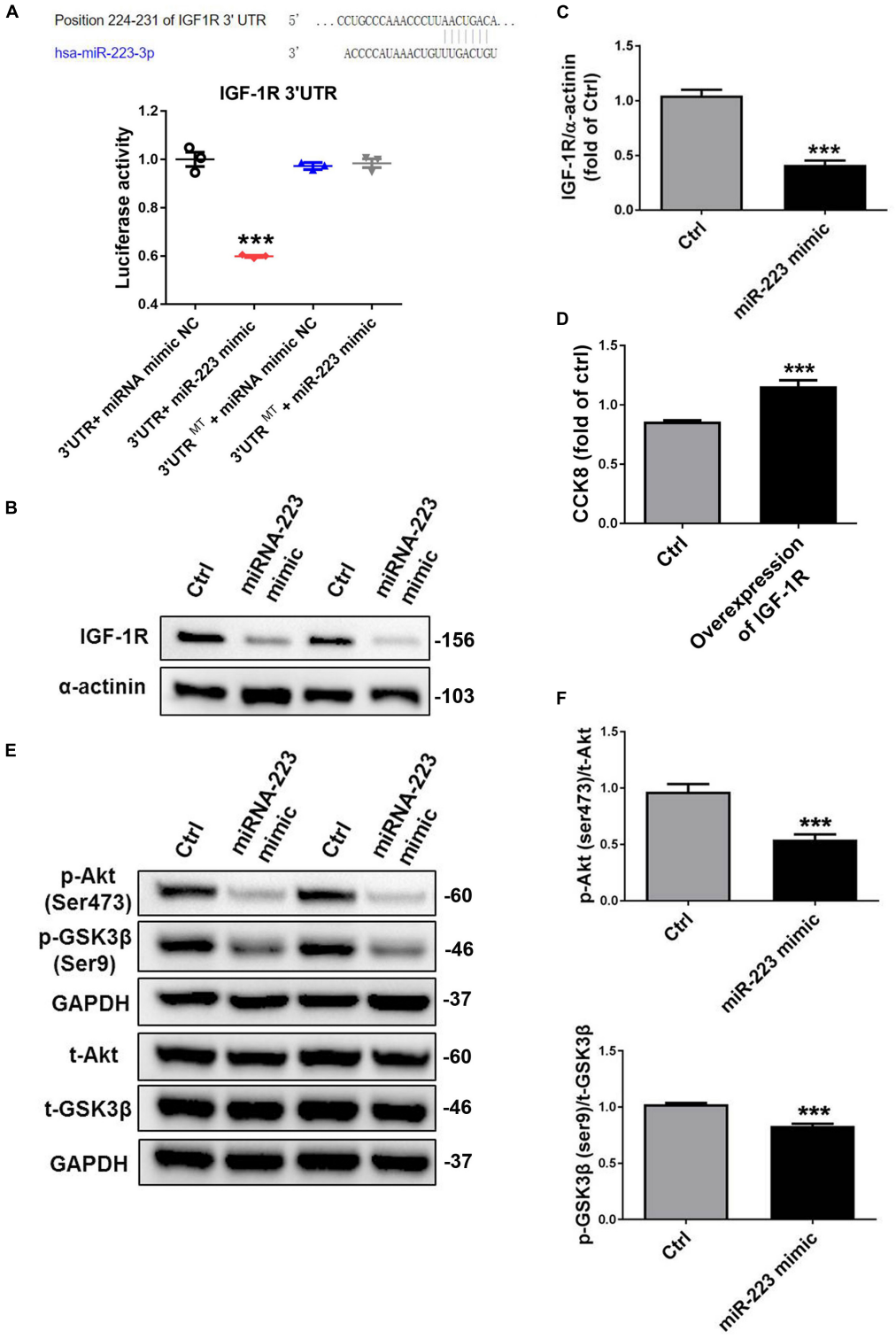

FIGURE 2 | MiR-223 directly targets the IGF-1R, which inhibits the phosphorylation of Akt and GSK3β. **(A)** Bioinformatics analysis identified a binding site for miR-223 in the 3′-UTR of IGF-1R. Luciferase activity assay in VSMCs following introduction of IGF-1R 3′ UTR or mutant 3′ UTR (mut) with or without miR-223 mimic ($n = 3$). VSMCs were transfected with miR-223 mimic for 48 h. **(B,C)** The expression of IGF-1R in VSMC was detected with western blot analysis. **(D)** The rate of proliferation was determined by CCK8 assay in VSMCs transfected with overexpression of IGF-1R. **(E,F)** The phosphorylation of Akt and GSK3β in VSMC was determined with western blot analysis. Data are presented as mean ± SD ($n = 6$). Comparisons between two groups were analyzed using unpaired nonparametric Student's *t*-test. $^{*}P < 0.05$, $^{**}P < 0.01$, $^{***}P < 0.001$ vs Ctrl (miR-NC).

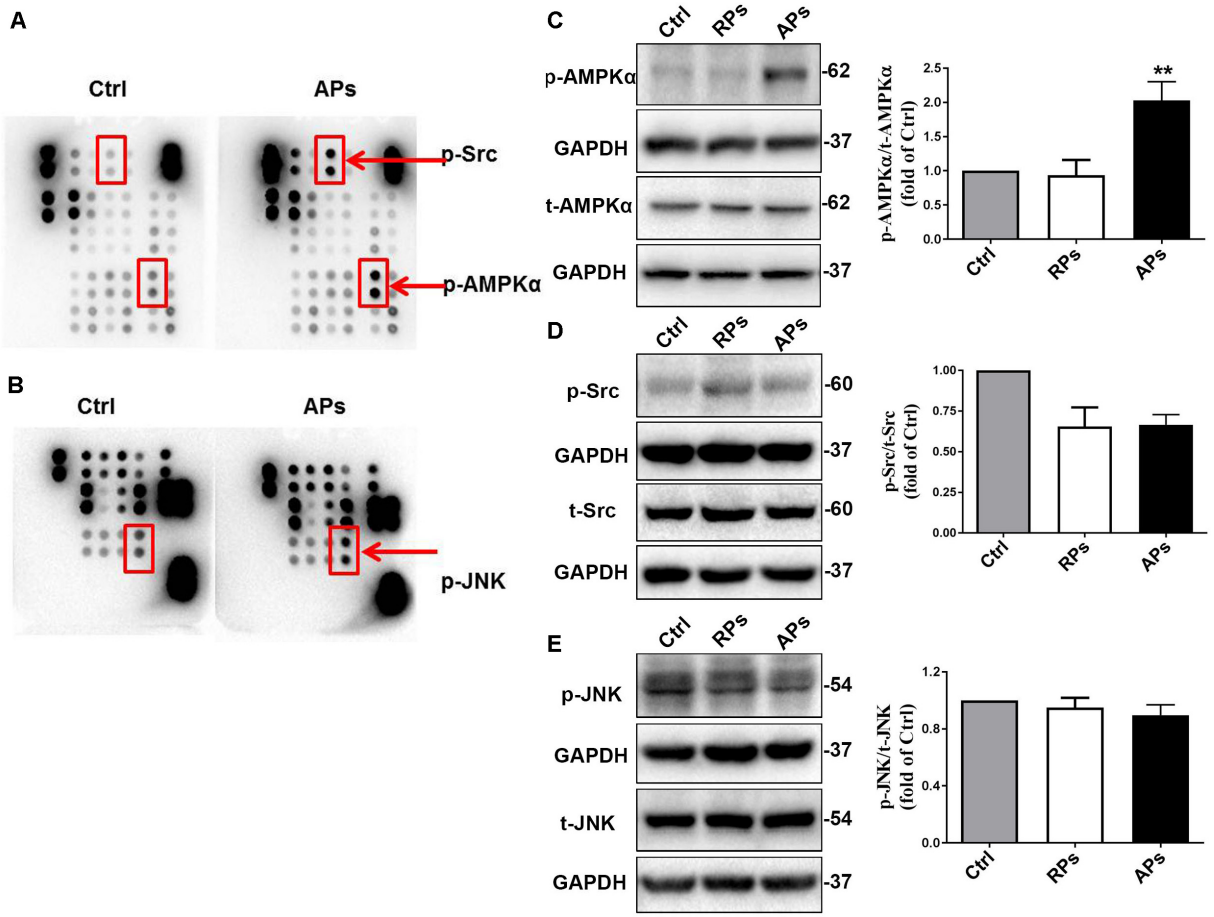

FIGURE 3 | APs activate the AMPKα signal pathway to suppress VSMC proliferation. **(A,B)** The phosphorylation of AMPKα, Src and Jun were assessed by proteomics analysis of phosphokinase arrays in control (Ctrl) VSMCs and APs cocultured with VSMCs. The phosphorylation of **(C)** AMPKα, **(D)** Src, and **(E)** Jnk was determined with western blot analysis in control (Ctrl) VSMCs, RPs, and APs cocultured with VSMCs. Data are presented as mean ± SD ($n = 6$). Comparisons between more than two groups were analyzed using one-way ANOVA analysis with the Dunnett's multiple correction. $^{**}P < 0.01$ vs Ctrl (VSMCs without platelets).

receptor (IGF-1R) can activate the cascade signals including IRS family, thereby activating phosphatidyl inositol 3-kinase (PI3K) and Akt signaling pathway (Delafontaine et al., 2004). Thus we determined the downstream signal pathway involved in inhibiting VSMC proliferation treated with a miR-223 mimic. **Figures 2E,F** showed that the phosphorylation of Akt and GSK3β was inhibited by the miR-223 mimic than that of control group. Our data demonstrate that miR-223 directly targets IGF-1R in VSMC, which inhibits the phosphorylation of Akt and GSK3β, resulting in reduced VSMC dedifferentiation and proliferation.

APs Activate the AMPKα Signal Pathway to Suppress VSMC Proliferation

To further determine the downstream signal pathway of Akt/GSK3β involved in inhibiting VSMC proliferation, we determined that the phosphorylation of AMPKα, Src and Jnk were assessed by proteomics analysis of phosphokinase arrays in control (Ctrl) VSMCs and APs cocultured with VSMCs. As shown in **Figures 3A,B**, the phosphorylation of AMPKα, Src and Jnk in VSMCs treated with APs were significantly increased compared to the control group. Using western blot analysis, we further confirmed that the phosphorylation of AMPKα in VSMCs treated with APs was significantly upregulated compared to the control group (**Figure 3C**). However, we found that the phosphorylation of Src and Jnk did not change in VSMCs cocultured with resting platelets (RPs) or APs (**Figures 3D,E**). These results suggest that APs activate the AMPKα signal pathway to suppress VSMC proliferation.

To further investigate whether platelet-derived miR-223 suppressed VSMC proliferation through AMPKα signal pathway, we treated with a miR-223 mimic or miR negative control (Ctrl) in VSMCs. Similarly, we found that the phosphorylation of AMPKα in VSMCs with treatment of a miR-223 mimic was significantly increased compared to that of the Ctrl group (**Figure 4A**). As expected, we found that the phosphorylation of AMPKα in VSMCs cocultured with DM-APs was significantly inhibited compared to that in VSMCs with treatment of HS-APs (**Supplementary Figure S2**). We found that the phosphorylation of acetyl-CoA Carboxylase (ACC), the substrate of AMPKα, was

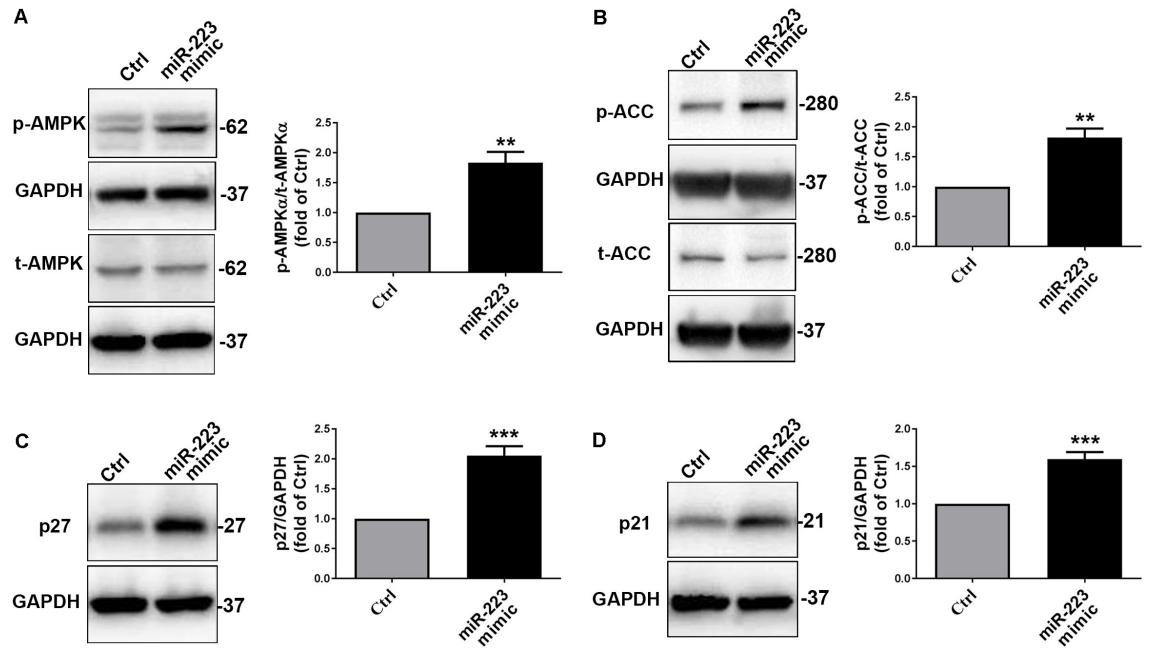

FIGURE 4 | The platelet-derived miR-223 suppressed VSMC proliferation via the regulation AMPK signaling pathways. VSMCs were transfected with miR-223 mimic for 48 h. **(A,B)** The phosphorylation of AMPKα and ACC were assessed by western blot analysis in VSMCs transfected with miR-223 mimic. **(C,D)** The expression of cell cycle marks including p27 and p21 was determined with western blot analysis in VSMCs transfected with miR-223 mimic. Data are presented as mean ± SD (n = 6). Comparisons between two groups were analyzed using unpaired nonparametric Student's t-test. $^{*}P < 0.05$, $^{**}P < 0.01$, $^{***}P < 0.001$ vs Ctrl (miR-NC).

significantly higher in VSMCs treated with a miR-223 mimic than Ctrl group (**Figure 4B**). We also found that treatment with miR-223 mimic significantly increased the expression of p27 and p21 (**Figures 4C,D**), suggesting that VSMC proliferation was suppressed by miR-223. Taken together, these results indicated that the platelet-derived miR-223 suppressed VSMC proliferation via the regulation of miR-223/IGF-1R/AMPK signaling pathways.

Inhibition of Calpain Restored the Expression of miR-223 in Diabetic Platelets

Our previous study has demonstrated a significant upregulation of miRNAs including miR-223, miR-143, and miR-145 in VSMCs cocultured with APs compared to VSMCs group. As shown in **Figures 5A,B**, the expression of miR-223 was downregulated in mouse and human diabetic platelets compared with non-DM group. We found that miR-223 level was significantly higher in diabetic platelets treated with a calpeptin (calpain inhibitor) than that of diabetic platelets (**Figures 5C,D**), suggesting that inhibition of calpain restores the expression of miR-223 in diabetic platelets. After restoring the expression of miR-223 in diabetic platelets and then coculturing with HCASMCs, we found the inhibition of Calpain restored the expression of miR-223 in diabetic platelets suppressed the proliferation of HCASMCs (**Figures 5E,F**). These data demonstrate that calpeptin restores the expression of miR-223 in diabetic platelets and transferred more platelet-derived miR-223 into VSMC, thereby suppressing VSMC proliferation in vitro.

Inhibition of Calpain Alleviates Neointimal Formation by Restoring the Expression of miR-223 in Diabetic Platelet

Calpeptin is a specific pharmacological inhibitor for calpain activation, and administration of calpeptin restored the expression of miR-223 in diabetic murine platelet (Elgheznawy et al., 2015). To restore the downregulated miR-223 in diabetic platelet, we used streptozotocin induced (STZ-DM) mice and rescued the condition with a calpeptin and AgomiR-223 by femoral wire injury. Four weeks after injury, we found the expression of IGF-1R in uninjured vessels was reduced, while the expression of IGF-1R was upregulated in injured vessels of STZ-DM mice treated with miR-NC (miR negative control) (**Figures 6A,C**). Treatment with AgomiR-223 and calpeptin significantly suppressed the expression of IGF-1R in STZ-DM mice (**Figure 6A**). The results suggest that calpeptin and AgomiR-223 restored the expression of miR-223 in diabetic platelets to suppress VSMC proliferation via targeting IGF-1R in vivo. To verify the effect of calpeptin and AgomiR-223 on neointimal formation, the intimal to media (I/M ration) was detected in STZ-DM and Non-DM mice. As shown in **Figures 6B,D**, the neointimal hyperplasia and intimal size were increased in STZ-DM mice after 4 weeks of femoral arterial injury; however, the effect was rescued by treatment with

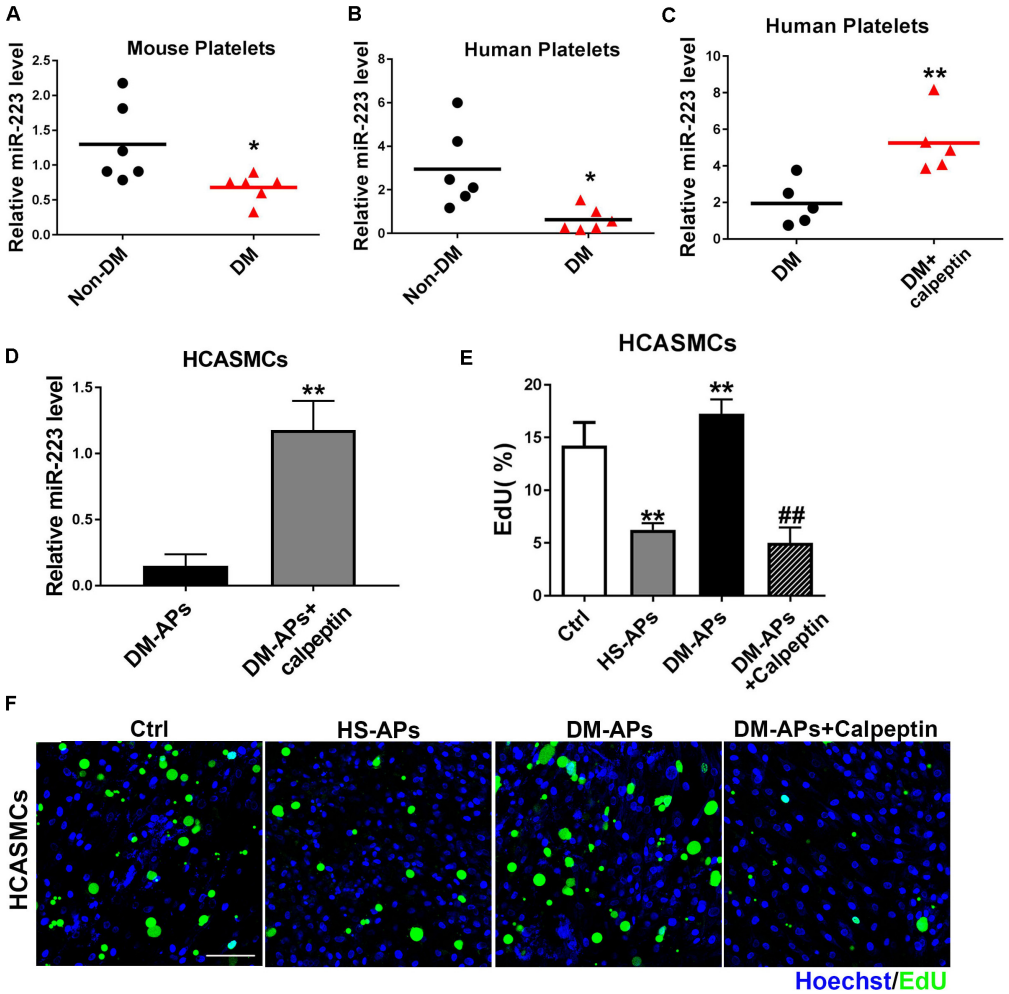

FIGURE 5 | Treatment of a calpeptin restored the expression of miR-223 in diabetic platelets. **(A,B)** The miR-223 level in mouse and human platelets was detected by qRT-PCR assays. Data are presented as mean ± SD (n = 6). Comparisons between two groups were analyzed using unpaired nonparametric Student's t-test. $^{*}P < 0.05$ vs Non-DM. **(C,D)** Diabetic platelets were treated with a calpeptin for 24 h in vitro. The expression of miR-223 in human platelets and HCASMCs was detected by qRT-PCR assays. Data are presented as mean ± SD (n = 6). Comparisons between two groups were analyzed using unpaired nonparametric Student's t-test. $^{**}P < 0.01$ vs DM. **(E,F)** The rate of proliferation was determined by EdU incorporation assay in VSMCs treated with calpeptin. Data are presented as mean ± SD (n = 6). Comparisons between more than two groups were analyzed using one-way ANOVA analysis with the Dunnett's multiple correction. $^{**}P < 0.01$ vs Ctrl (VSMCs without platelets); $^{\#\#}P < 0.01$ vs DM-APs.

calpeptin and AgomiR-223. We found that the expression of miR-223 was significantly downregulated in diabetic platelets of injured mice compared with non-DM injured group. However, the expression of miR-223 was restored by treatment with calpeptin and AgomiR-223, suggesting that inhibition of calpain restores the expression of miR-223 in injured DM mice (**Figure 6E**).Collectively, these data demonstrate that calpeptin restores the downregulated miR-223 in diabetic platelets and transferred more platelet-derived miR-223 into VSMC, thereby suppressing VSMC proliferation through targeting IGF-1R in the injured vessel, resulting in alleviation of neointimal formation in diabetes.

In summary, our data manifested that the platelet-derived miR-223 suppressed VSMC proliferation via the regulation IGF-1R/AMPK signaling pathway. However, treatment with calpeptin (calpain inhibitor) restored the expression of miR-223 in diabetic platelets, which was then transferred into VSMCs and inhibited VSMC proliferation at the site of vascular injury. Thus calpeptin may serve as therapeutic adjunct for playing a protective role in diabetic neointimal hyperplasia (**Figure 7**).

DISCUSSION

In the present study, we demonstrate that diabetic platelet deficient of miR-223 fails to suppress VSMC phenotypic switch. The incorporated platelet miR-223 directly targets the insulin-like growth factor-1 receptor (IGF-1R) in VSMCs, which inhibits the phosphorylation of GSK3β and AMPK, resulting in reduced VSMC dedifferentiation and proliferation. In murine model of

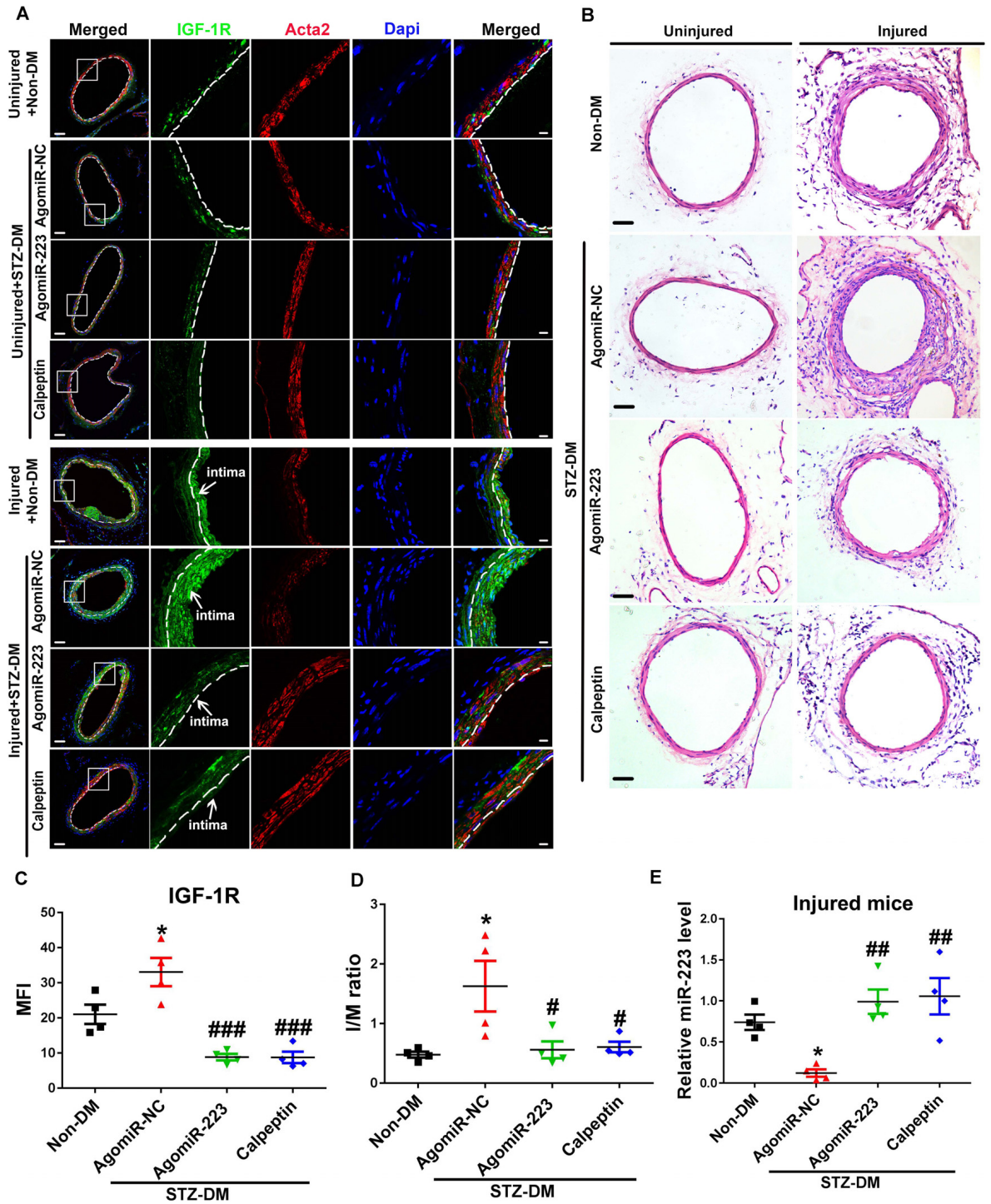

FIGURE 6 | Inhibition of calpain alleviates neointima formation by restoring the expression of miR-223 in diabetic platelet. **(A)** Immunofluorescence analysis of IGF-1R in uninjured or injured femoral arteries from Non-DM mice, and STZ-DM mice treated with AgomiR-NC or AgomiR-223 or calpeptin at 4 weeks after wire injury (n = 4). Green, IGF-1R; red, Acta2 blue; Dapi nuclear staining in VSMCs. Scale bars: 20 μm. **(B)** H&E staining of serial cross sections of femoral arteries from Non-DM mice, and STZ-DM mice treated with AgomiR-NC or AgomiR-223 or calpeptin at 4 weeks after wire injury (n = 4). Scale bars: 50 μm. **(C)** Quantification of IGF-1R expression in VSMCs in injured DM mice. **(D)** The intima size (I/M ration) in the injured femoral arterial sections has been quantified. **(E)** The miR-223 level in injured DM mice was detected by qRT-PCR assays. Data are presented as mean ± SD (n = 4). Comparisons between more than two groups were analyzed using one-way ANOVA analysis with the Dunnett's multiple correction. $^{*}P < 0.05$ vs non-DM; $^{\#}P < 0.05$, $^{\#\#}P < 0.01$, $^{\#\#\#}P < 0.001$ vs STZ-DM mice treated with AgomiR-NC.

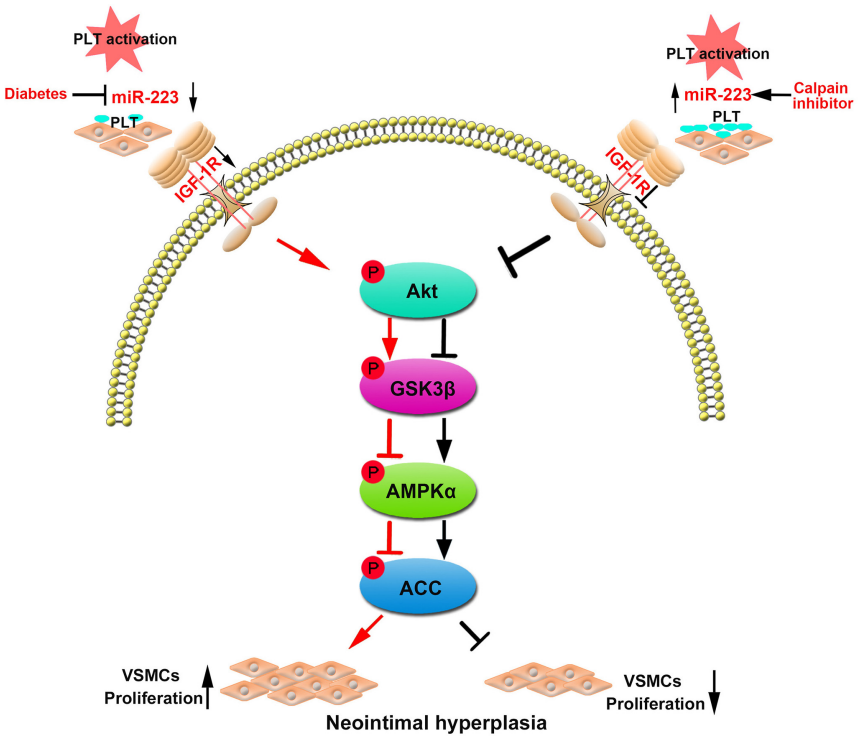

FIGURE 7 | Restoring the platelet miR-223 by calpeptin alleviates the neointimal hyperplasia in diabetes through miR-223/IGF-1R/AMPK signaling pathway. MiR-223 deficiency in diabetic platelet failed to suppress VSMC proliferation during vascular injury. The platelet-derived miR-223 suppressed VSMC proliferation via the regulation IGF-1R/AMPK signaling pathways. Interestingly, treating with a calpeptin restores the downregulated expression of miR-223 in diabetic platelets to suppress VSMC proliferation via targeting IGF-1R and plays a protective role in diabetic neointimal hyperplasia.

vascular injury, we show that calpeptin restores the platelet expression of miR-223 in diabetes, and the horizontal transfer of platelet miR-223 into VSMCs inhibits VSMC proliferation in the injured artery by targeting the expression of IGF-1R. Collectively, our results demonstrate that inhibition of calpain regulated VSMC phenotypic switch via miR-223/IGF-1R/AMPK signaling axis, supporting the potential application of calpeptin on platelet-associated vascular disease in diabetes.

Diabetes mellitus is an important risk factor of intimal hyperplasia and restenosis (Davi and Patrono, 2007). The phenotypic switch of VSMCs plays a crucial role in the onset of intimal hyperplasia in DM. The process of VSMC phenotypic switch (dedifferentiation and proliferation) was regulated by cytokines including insulin-like growth factor-1 (IGF-1), platelet-derived growth factor (PDGF), and epidermal growth factor (EGF) (Delafontaine and Lou, 1993). Previous studies have reported miR-223 inhibited VSMC proliferation via target ITGB3 or RhoB/MLC2 in VSMCs (Zeng et al., 2016; Liu et al., 2019). Recently, our previous studies have demonstrated PDGFRβ is a key target of platelet-derived miR-223, which is incorporated into VSMCs and suppressed VSMC proliferation (Zeng et al., 2019). Previous studies have demonstrated treating with IGF-1 antibody inhibited VSMC proliferation, which was induced by angiotensin and thrombin (Delafontaine et al., 2004; Ma et al., 2006), suggesting that IGF-1 also plays a crucial role in VSMC proliferation (Jones and Kazlauskas, 2001). The binding of IGF-1 to its receptor (IGF-1R) can activate the cascade signals including IRS family, thereby activating phosphatidyl inositol 3-kinase (PI3K) and Akt signaling pathway (Saltiel and Kahn, 2001; Delafontaine et al., 2004). In the present study, we identified that IGF-1R was the direct target of miR-223, and platelet-derived miR-223 was incorporated into VSMCs thereby inhibiting IGF-1R, leading to the phosphorylation of Akt and GSK3β. Report showed PI3K-Akt signaling pathway could suppress glycogen synthase kinase 3 (GSK3) activity, leading to inhibit the function of AMPK via interactions with AMPKβ (Fukushima et al., 2012; Suzuki et al., 2013). It has been reported that activated phosphorylation of AMPKα to inhibit cells proliferation (Igata et al., 2005; Lee et al., 2015). Our phosphoproteomics array results showed that the incorporated platelet miR-223 significantly increased the phosphorylation of AMPKα and its substrate ACC in VSMCs cocultured with activated platelets. Therefore, platelet-derived miR-223 after incorporated into VSMCs at least in part suppress VSMC proliferation via targeting IGF-1R and activating AMPK to reduce neointimal hyperplasia in DM.

In diabetic platelets, the reduction of miRNAs leads to the upregulation of protein expression such as β1 integrin, resulting in increased platelet aggregation (Elgheznawy et al., 2015). Calpain family is intracellular Ca^{2+}-activated cysteine proteases, which involved in cellular signaling, cell growth (Salimi et al., 2018), apoptosis (Storr et al., 2011), and platelet activation in DM (Elgheznawy et al., 2015). Increasing evidence

has demonstrated calpain activation involved in cardiovascular complication of DM such as increased vascular permeability (Scalia et al., 2007), atherosclerosis (Miyazaki et al., 2011), and heart failure (Letavernier et al., 2012). The activation of calpain in DM is closely associated with the loss of platelet dicer, resulting in the significant dysregulation of platelet miRNA levels. Calpeptin is a specific pharmacological inhibitor for calpain activation, and administration of calpeptin restored the expression of miR-223 in diabetic murine platelet (Elgheznawy et al., 2015). Moreover, calpeptin was found to be an effective therapeutic drug for preventing endothelial dysfunction of mesenteric arteries in DM (Randriamboavonjy et al., 2017). Consistent with these studies, our results showed that the expression of miR-223 in diabetic platelets was restored by treatment of calpeptin. Thus, we employed calpeptin to treat STZ-DM murine model of vascular injury. We also found that calpeptin has inhibited the activative effect calpain on neointima hyperplasia in STZ-DM murine model of vascular injury. Both treatment with AgomiR-223 and calpeptin reduced neointimal hyperplasia and intimal size. At the site of injury, the increased IGF-1R expression in VSMCs was attenuated by treatment with AgomiR-223 and calpeptin. These results suggest that calpeptin may serve as therapeutic adjunct for intimal hyperplasia via the upregulation of platelet miR-223 in diabetes.

In summary, we provide evidence that the horizontal transfer of platelet miR-223 suppresses VSMC proliferation via targeting IGF-1R and activating AMPK. However, in diabetes, calpain activation contributes to the reduced expression of dicer, resulting in the deficiency of platelet miR-223. Treatment with calpeptin restored the expression of miR-223 in diabetic platelets, which was then transferred into VSMCs and inhibited VSMC proliferation at the site of vascular injury. Therefore, calpeptin may serve as therapeutic adjunct for platelet and VSMC associated vascular diseases in DM.

DATA AVAILABILITY STATEMENT

The datasets generated for this study are available on request to the corresponding author.

ETHICS STATEMENT

The studies involving human participants were reviewed and approved by Institutional Review Board of Guangzhou Women and Children's Medical Center (Human Investigation Committee No. 2018022605). Written informed consent to participate in this study was provided by the participants' legal guardian/next of kin. The animal study was reviewed and approved by Institutional Animal Care and Use Committee of Guangzhou Medical University (No. SYXK2016-0168).

AUTHOR CONTRIBUTIONS

MS and SF performed the experimental design, the majority of experiments, analyzed majority of the data, and drafted manuscript. ZL and LX performed part of experiments and the data analyses. XF, YL, YZ, and SL performed animal experiments and image analyses. ZZ and WT directed all aspects of the experiments, the data analyses, manuscript editing and review. All authors contributed to the article and approved the submitted version.

FUNDING

This work was supported by the National Natural Science Foundation of China (Grant Nos. 81670117, 81970437, 81903605, and 81902144), the Guangdong Province Science and Technology Project (Grant No. 2017A050506008), the Guangdong Outstanding Young Scientist Funding (Grant No. 2016A030306049), and the fund from Guangzhou Women and Children's Medical Center/Guangzhou Institute of Pediatrics (Grant No. IP-2018-022).

SUPPLEMENTARY MATERIAL

The Supplementary Material for this article can be found online at: https://www.frontiersin.org/articles/10.3389/fphys.2020.00742/full#supplementary-material

REFERENCES

Davi, G., and Patrono, C. (2007). Platelet activation and atherothrombosis. *N. Engl. J. Med.* 357, 2482–2494. doi: 10.1056/NEJMra071014

Delafontaine, P., and Lou, H. (1993). Angiotensin II regulates insulin-like growth factor I gene expression in vascular smooth muscle cells. *J. Biol. Chem.* 268, 16866–16870.

Delafontaine, P., Song, Y. H., and Li, Y. (2004). Expression, regulation, and function of IGF-1, IGF-1R, and IGF-1 binding proteins in blood vessels. *Arterioscler. Thromb. Vasc. Biol.* 24, 435–444. doi: 10.1161/01.ATV.0000105902.89459.09

Elgheznawy, A., Shi, L., Hu, J., Wittig, I., and Laban, H. (2015). Dicer cleavage by calpain determines platelet microRNA levels and function in diabetes. *Circ. Res.* 117, 157–165. doi: 10.1161/CIRCRESAHA.117.305784

Faries, P. L., Rohan, D. I., Takahara, H., Wyers, M. C., and Contreras, M. A. (2001). Human vascular smooth muscle cells of diabetic origin exhibit increased proliferation, adhesion, and migration. *J. Vasc. Surg.* 33, 601–607. doi: 10.1067/mva.2001.111806

Fukushima, T., Nakamura, Y., Yamanaka, D., Shibano, T., and Chida, K. (2012). Phosphatidylinositol 3-kinase (PI3K) activity bound to insulin-like growth factor-I (IGF-I) receptor, which is continuously sustained by IGF-I stimulation, is required for IGF-I-induced cell proliferation. *J. Biol. Chem.* 287, 29713–29721. doi: 10.1074/jbc.M112.393074

Igata, M., Motoshima, H., Tsuruzoe, K., Kojima, K., and Matsumura, T. (2005). Adenosine monophosphate-activated protein kinase suppresses vascular smooth muscle cell proliferation through the inhibition of cell cycle progression. *Circ. Res.* 97, 837–844. doi: 10.1161/01.RES.0000185823.73556.06

Jones, S. M., and Kazlauskas, A. (2001). Growth-factor-dependent mitogenesis requires two distinct phases of signalling. *Nat. Cell Biol.* 3, 165–172. doi: 10.1038/35055073

Kirschbaum, M., Karimian, G., Adelmeijer, J., Giepmans, B. N., Porte, R. J., and Lisman, T. (2015). Horizontal RNA transfer mediates platelet-induced

hepatocyte proliferation. *Blood* 126, 798–806. doi: 10.1182/blood-2014-09-600312

Kornowski, R., Mintz, G. S., Kent, K. M., Pichard, A. D., and Satler, L. F. (1997). Increased restenosis in diabetes mellitus after coronary interventions is due to exaggerated intimal hyperplasia. A serial intravascular ultrasound study. *Circulation* 95, 1366–1369. doi: 10.1161/01.cir.95.6.1366

Landry, P., Plante, I., Ouellet, D. L., Perron, M. P., Rousseau, G., and Provost, P. (2009). Existence of a microRNA pathway in anucleate platelets. *Nat. Struct. Mol. Biol.* 16, 961–966. doi: 10.1038/nsmb.1651

Lee, K. Y., Lee, D. H., and Choi, H. C. (2015). Mesoglycan attenuates VSMC proliferation through activation of AMP-activated protein kinase and mTOR. *Clin. Hypertens.* 22:2. doi: 10.1186/s40885-016-0037-x

Letavernier, E., Zafrani, L., Perez, J., Letavernier, B., Haymann, J. P., and Baud, L. (2012). The role of calpains in myocardial remodelling and heart failure. *Cardiovasc. Res.* 96, 38–45. doi: 10.1093/cvr/cvs099

Liu, A., Liu, Y., Li, B., Yang, M., Liu, Y., and Su, J. (2019). Role of miR-223-3p in pulmonary arterial hypertension via targeting ITGB3 in the ECM pathway. *Cell Prolif.* 52:e12550. doi: 10.1111/cpr.12550

Ma, Y., Zhang, L., Peng, T., Cheng, J., and Taneja, S. (2006). Angiotensin II stimulates transcription of insulin-like growth factor I receptor in vascular smooth muscle cells: role of nuclear factor-kappaB. *Endocrinology* 147, 1256–1263. doi: 10.1210/en.2005-0888

Millette, E., Rauch, B. H., Defawe, O., Kenagy, R. D., Daum, G., and Clowes, A. W. (2005). Platelet-derived growth factor-BB-induced human smooth muscle cell proliferation depends on basic FGF release and FGFR-1 activation. *Circ. Res.* 96, 172–179. doi: 10.1161/01.RES.0000154595.87608.db

Miyazaki, T., Taketomi, Y., Takimoto, M., Lei, X. F., and Arita, S. (2011). m-Calpain induction in vascular endothelial cells on human and mouse atheromas and its roles in VE-cadherin disorganization and atherosclerosis. *Circulation* 124, 2522–2532. doi: 10.1161/CIRCULATIONAHA.111.021675

Nagalla, S., Shaw, C., Kong, X., Kondkar, A. A., and Edelstein, L. C. (2011). Platelet microRNA-mRNA coexpression profiles correlate with platelet reactivity. *Blood* 117, 5189–5197. doi: 10.1182/blood-2010-09-299719

Randriamboavonjy, V., Kyselova, A., Elgheznawy, A., Zukunft, S., Wittig, I., and Fleming, I. (2017). Calpain 1 cleaves and inactivates prostacyclin synthase in mesenteric arteries from diabetic mice. *Basic Res. Cardiol.* 112:10. doi: 10.1007/s00395-016-0596-8

Risitano, A., Beaulieu, L. M., Vitseva, O., and Freedman, J. E. (2012). Platelets and platelet-like particles mediate intercellular RNA transfer. *Blood* 119, 6288–6295. doi: 10.1182/blood-2011-12-396440

Salimi, R., Bandaru, S., Devarakonda, S., Gokalp, S., and Ala, C. (2018). Blocking the cleavage of filamin A by calpain inhibitor decreases tumor cell growth. *Anticancer. Res.* 38, 2079–2085. doi: 10.21873/anticanres.12447

Saltiel, A. R., and Kahn, C. R. (2001). Insulin signalling and the regulation of glucose and lipid metabolism. *Nature* 414, 799–806. doi: 10.1038/414799a

Scalia, R., Gong, Y., Berzins, B., Zhao, L. J., and Sharma, K. (2007). Hyperglycemia is a major determinant of albumin permeability in diabetic microcirculation: the role of mu-calpain. *Diabetes Metab. Res. Rev.* 56, 1842–1849. doi: 10.2337/db06-1198

Storr, S. J., Carragher, N. O., Frame, M. C., Parr, T., and Martin, S. G. (2011). The calpain system and cancer. *Nat. Rev. Cancer* 11, 364–374. doi: 10.1038/nrc3050

Suzuki, T., Bridges, D., Nakada, D., Skiniotis, G., and Morrison, S. J. (2013). Inhibition of AMPK catabolic action by GSK3. *Mol. Cell.* 50, 407–419. doi: 10.1016/j.molcel.2013.03.022

Zeng, Y., Zhang, X., Kang, K., Chen, J., and Wu, Z. (2016). MicroRNA-223 attenuates hypoxia-induced vascular remodeling by targeting RhoB/MLC2 in pulmonary arterial smooth muscle cells. *Sci. Rep.* 6:24900. doi: 10.1038/srep24900

Zeng, Z., Xia, L., Fan, X., Ostriker, A. C., Yarovinsky, T., Su, M., et al. (2019). Platelet-derived miR-223 promotes a phenotypic switch in arterial injury repair. *J. Clin. Invest.* 129, 1372–1386. doi: 10.1172/JCI124508

Conflict of Interest: The authors declare that the research was conducted in the absence of any commercial or financial relationships that could be construed as a potential conflict of interest.

frontiers in Cell and Developmental Biology

ORIGINAL RESEARCH
published: 16 July 2020
doi: 10.3389/fcell.2020.00643

Endothelial Microvesicles Induce Pulmonary Vascular Leakage and Lung Injury During Sepsis

Danyang Zheng, Jie Zhang, Zisen Zhang, Lei Kuang, Yu Zhu, Yue Wu, Mingying Xue, Hongliang Zhao, Chenyang Duan, Liangming Liu† and Tao Li*†*

State Key Laboratory of Trauma, Burns and Combined Injury, Shock and Transfusion Department, Research Institute of Surgery, Daping Hospital, Army Medical University, Chongqing, China

OPEN ACCESS

Edited by:
Xavier Figueroa, Pontificia Universidad Católica de Chile, Chile

Reviewed by:
Ming-Lin Liu, University of Pennsylvania, United States
P. Mauricio Boric, Pontificia Universidad Católica de Chile, Chile

***Correspondence:**
Liangming Liu
liangmingliu@yahoo.com
Tao Li
lt200132@163.com

†*These authors have contributed equally to this work*

Specialty section:
This article was submitted to Signaling, a section of the journal Frontiers in Cell and Developmental Biology

Received: *13 April 2020*
Accepted: *26 June 2020*
Published: *16 July 2020*

Citation:
Zheng D, Zhang J, Zhang Z, Kuang L, Zhu Y, Wu Y, Xue M, Zhao H, Duan C, Liu L and Li T (2020) Endothelial Microvesicles Induce Pulmonary Vascular Leakage and Lung Injury During Sepsis. Front. Cell Dev. Biol. 8:643. doi: 10.3389/fcell.2020.00643

Sepsis is a prevalent severe syndrome in clinic. Vascular leakage and lung injury are important pathophysiological processes during sepsis, but the mechanism remains obscure. Microvesicles (MVs) play an essential role in many diseases, while whether MVs participate in vascular leakage and lung injury during sepsis is unknown. Using cecal ligation and puncture induced sepsis rats and lipopolysaccharide stimulated vascular endothelial cells (VECs), the role and the underlying mechanism of endothelial microvesicles (EMVs) in pulmonary vascular leakage and lung injury were observed. The role of MVs from sepsis patients was verified. The results showed that the concentration of MVs in blood was significantly increased after sepsis. MVs from sepsis rats and patients induced apparent pulmonary vascular leakage and lung injury, among which EMVs played the dominant role, in which miR-23b was the key inducing factor in vascular leakage. Furthermore, downregulation and upregulation of miR-23b in EMVs showed that miR-23b mainly targeted on ZO-1 to induce vascular leakage. MVs from sepsis patients induced pulmonary vascular leakage and lung injury in normal rats. Application of classic antidepressants amitriptyline reduced the secretion of EMVs, and alleviated vascular leakage and lung injury. The study suggests that EMVs play an important role in pulmonary vascular leakage and lung injury during sepsis by transferring functional miR-23b. Antagonizing the secretion of EMVs and the miR-23b might be a potential target for the treatment of severe sepsis.

Keywords: endothelial microvesicles, vascular leakage, microRNA-23b, lung injury, sepsis

INTRODUCTION

Sepsis is a life-threatening organ dysfunction caused by a dysregulated host response to infection, which leads to tissue damage and organ dysfunction even multiple organ dysfunction syndrome (MODS) with high mortality (Rhodes et al., 2017). Recent epidemiologic studies showed that sepsis incidence rate has been up to 535 cases per 100,000 person-years and still rising in the United States, meanwhile the in-hospital mortality was up to 25−30%, which indicated that sepsis remains a huge task to be overcome all around the world (Fleischmann et al., 2016). The lung is usually one of the first failure organs during the development of multiple dysfunction after sepsis (Wu et al., 2007), and vascular leakage plays a fundamental role in lung injury, which is characterized by the endothelial

barrier dysfunction and vascular endothelial permeability increment, meanwhile it is the crucial reason for the organ dysfunction in sepsis (Hou et al., 2017). Although the mechanism of vascular leakage has been studied for years, there is no effective treatment clinically, and it needs to be further investigated.

Plenty of cells in circulation are stimulated during sepsis, such as platelets, vascular endothelial cells and leukocytes, and may secrete microvesicles (MVs) subsequently (Becker et al., 2016; Karpman et al., 2017; Todorova et al., 2017). MVs are defined as membrane derived vesicles which are secreted into the extracellular environment by almost all types of cells under both normal and stress conditions such as diabetes and atherosclerosis (Tkach and Thery, 2016). The concentration of MVs, especially for platelet MVs (PMVs) and endothelial MVs (EMVs) in circulation, is positively correlated to the severity of diseases (Mastronardi et al., 2011; Hoefer et al., 2015; Martinez and Andriantsitohaina, 2017). Cheow et al. (2016) found that leukocyte MVs (LMVs) and EMVs could promote the generation of thrombin during myocardial infarction, and led to the disorder of coagulation and fibrinolysis system. Laher (2011) found that MVs could regulate the relaxation of blood vessel after sepsis by inducing the generation of superoxide anion and inducible Nitric Oxide Synthase (iNOS) (Lovren and Verma, 2013). Whether MVs play an important role in vascular leakage after sepsis remains unknown.

It is considered that MVs participate in the pathological processes of tissue and organ dysfunction either by directly interacting with cells or by transferring bioactive molecules as proteins, DNA, miRNA, lipids into target cells. Recent studies identified that miRNAs in MVs played important roles in some diseases (Zhang et al., 2010; Zhou et al., 2014; Xu et al., 2017; Zheng et al., 2017). For example, the MV-carrying miR-105 could reduce the expression of tight junction proteins such as ZO-1, which was related to the destruction of vascular barrier (Zhou et al., 2014). Hence, we hypothesized that MVs might carry and transfer some miRs to participate in vascular leakage and lung injury after sepsis (Zhou et al., 2014).

To test this hypothesis, we used the cecal ligation and puncture (CLP) induced sepsis rats and lipopolysaccharide (LPS) stimulated vascular endothelial cells (VEC), and the role and the underlying mechanisms of MVs in vascular leakage and lung injury after sepsis were investigated in the present study.

MATERIALS AND METHODS

Ethical Approval of the Study Protocol

All animal experiments were performed in accordance with the principles of the Guide for the Care and Use of Laboratory Animals published by the United States National Institutes of Health (NIH Publications, eighth edition, 2011) and was approved by the Research Council and Animal Care and Use Committee of the Research Institute of Surgery (Daping Hospital, Army Medical University, Chongqing, China, No. DHEC-2012-069).

Patients Information

The current study included 14 sepsis patients and 15 healthy subjects. Between January and December 2016, 14 sepsis patients were recruited from ICU of Daping Hospital, Army Medical University by reference of the criteria of Surviving Sepsis Campaign (2016 Version), and 4 patients were excluded because of age (out of range of 20−60). 15 healthy volunteers were recruited from the State Key Laboratory of Trauma, Burns and Combined Injury. Demographic characteristics of 10 sepsis patients and 15 healthy volunteers are shown in **Supplementary Table S1**. The study protocol was approved by the Ethics Committee of the Research Institute of Surgery, and the study was registered in Clinical Trial Registry (ChiCTR-OOC-16008352). Peripheral venous blood samples (30 mL) were collected from every patient and healthy volunteer, and microvesicles were subsequently isolated and then stored in −80°C.

Animals Preparation and Sepsis Model

Adult male and female Sprague-Dawley (SD) rats (200−220 g) which were obtained from the Animal Center of Army Medical Center, Army Medical University (Third Military Medical University) were used in the current study. The sepsis model of rats was induced by cecal ligation and puncture (CLP) procedure with aseptic methods as described previously (Liu et al., 2016a). Briefly, rats were anesthetized by pentobarbital sodium (30 mg/kg IP), then the cecum was fully exposed and ligated 0.7 cm from the end. Afterward the ligated cecum was punctured by a triangular pyramid, and the puncture incision was about 0.1 cm × 0.1 cm. Then the cecum was put back into the enterocoelia, and the abdomen was closed by interrupted suture, and subsequently 5 mL of normal saline was injected intraperitoneally. After the operation the rats were returned to the cages and allowed for food and water *ad libitum*.

Cell Preparation

Vascular endothelial cells were obtained from the pulmonary vein of SD rats as described previously (Liu et al., 2016a,b). Briefly, rats were anesthetized and sterilized with iodine, then rats received thoracotomy by sterile instruments. The pulmonary veins were separated from hilus pulmonis after the heart was cut off. After washed with sterile PBS for 5 times, the veins were sheared to 1 mm × 1 mm pieces, and the inner surface of the veins wad attached on the bottom of the culture flask with 5 mL ECM (Scicell, America; 5% fetal bovine serum, 1% antibiotics) medium. 3 days later, the pieces were removed from the flask, and the cells crawling on at the bottom of the culture flask were VECs, and the 3−5 passage of VECs were used in the present study. Platelets were obtained from the blood of SD rats as follows: abdominal aorta blood was collected in EDTA blood tubes (BD, America). Afterward the blood was centrifuged at 200 × *g* for 15 min (room temperature) to remove blood cells, and the supernatant was platelet rich plasma. Then platelet rich plasma was centrifuged at 1,200 × *g* for 15 min (room temperature),

and the sediment was purified platelets. After washed twice by D-hanks solution, the sediment was suspended in 5 mL Dulbecco-modified Eagle medium-F12 (Hyclone, Logan, UT, United States) supplemented with 20% fetal bovine serum and 1% antibiotics (Mairhofer et al., 2002). Leukocytes were obtained according to the instruction of Leucocyte separation kit (TBD, China) and were then cultured in 5 mL DMEM-F12 medium.

MV Harvest and Characterization

Microvesicles were harvested from blood and cultured cell supernatant according to the experiments. Blood samples were collected in BD-EDTA tubes, and cell media supernatant samples were collected (after stimulated by 1 μg/mL LPS (Sigma, America) for 24 h in basal medium without serum) in sterile centrifuge tubes. The samples were centrifuged at 500 × *g*, 15 min at 4°C to remove the residual cells. Then the supernatant was carefully collected and centrifuged at 2000 × *g*, 20 min at 4°C to remove cell debris. And the supernatant was centrifuged at 20,000 × *g*, 70 min at 4°C to pellet MVs. After washed by sterile PBS, the MVs were finally centrifuged at 20,000 × *g*, 70 min at 4°C, the pellet was suspended in PBS and stored in −80°C until use (Mastronardi et al., 2011; Matthay, 2017).

Microvesicles were analyzed by transmission electron microscopy, dynamic light scattering and flow cytometry, respectively. For transmission electron microscopy (TEM) analysis, the MV pellet was fixed with 2.5% glutaraldehyde in PBS at 4°C for 24 h. After rinsing twice with 0.1 M PBS, samples were then postfixed in 1% OsO_4 at room temperature for 70 min. After rinsing 3 times with 0.1 M PBS, samples were dehydrated by a series of graded ethanol. Finally, the samples were embedded in TAAB 812 and 100 nm sections were prepared on grids. MV was analyzed by JEM 1400 (JEOL Instruments) transmission electron microscopy.

Dynamic light scattering analysis was performed by Zetasizer Nano ZS (Malvern Instruments) at room temperature with 633 nm He-Ne laser, automatic attenuator. Each sample was measured 3 times at least.

For flow cytometry (FCM) analysis, MVs were applied on high sensitivity imaging flow cytometry Amnis ImageStream MK II (IS^X) (Amnis/Millipore, Seattle, United States), detected by X40 magnification, high sensitivity using INSPIRE software. After washed and suspended by 100 μl PBS, MVs were subsequently stained with CD31 (FITC, 1:100), CD61 (PE, 1:100), CD45 (V450, 1:100), and Annexin V (APC, 1:50) for 25 min at room temperature in the dark according to the experiment design, and all antibodies for FCM were purchased from BD, America. Annexin V-binding buffer (BD, America) was used when MVs were stained with Annexin V. Different sizes of standard beads (0.2, 0.5, and 0.8 μm, Bangs laboratories, America) were used to set gate for MVs. Isotype of matched antibodies were used as controls.

Preparation of PKH-26 Labeled EMVs

Microvesicles were labeled by red fluorescent dye PKH-26 (Sigma, America) according to the instruction. Briefly, after washed by PBS, MVs were incubated with PKH-26 by 1:1000 at 37°C for 30 min, then MVs were centrifuged at 20,000 × *g*, 70 min to remove the remaining dye. After washed by PBS, PKH-26 labeled MVs were added into rats or VECs according to the experiment.

Measurement of Vascular Leakage of Lung, Kidney, and Intestine

Rats were anesthetized, then FITC-BSA (9 mg/kg) was injected to rats from jugular vein. 2 h later, 20 ml PBS was used to flush vessels in each tissue (lung, kidney or intestine). In detail, 20 ml PBS was slowly injected from the jugular vein to flush the vessels in lung; and 20 ml PBS was slowly injected from the renal artery to flush the vessels in kidney after laparotomy; and an equal volume of PBS was slowly injected from the superior mesenteric artery to flush the vessels in intestine after laparotomy. Afterward rats were sacrificed by euthanasia, then left lung, left kidney and jejunum (about 6 cm) were separated. After washed by PBS, tissues were weighed up and cut into pieces, followed by complete homogenate in 5 mL PBS, then the fluorescence intensity of FITC-BSA was measured by F-4500 fluorescence spectrophotometer (Hitachi Corporation, Japan). We used the term "BSA leakage" to represent the extent of vascular leakage, and BSA leakage of each tissue was calculated by fluorescence intensity (A.U.) / tissue weight (g) (Zhang et al., 2015).

Bronchoalveolar Lavage (BAL) Collection and the Measurement of Protein and Cell Counts in BAL

Bronchoalveolar Lavage was performed by instilling 2 mL of cold PBS into the trachea. The BAL fluid was obtained by centrifugation at 500 × *g* for 20 min (4°C), and the supernatant was used to measure protein concentration with Pierce BCA protein assay kit (Thermo Fisher Scientific, America). Then the sediment was suspended by 1 mL PBS, and the BAL cell counts were performed by cell counting chamber (Gotzfried et al., 2018; Izzotti et al., 2018).

Transmembrane Electrical Resistance (TER) and BSA Leakage of VECs

Transmembrane Electrical Resistance and BSA leakage of VECs were measured as previously described (Zhang et al., 2015; Liu et al., 2016a,b). Briefly, VECs were seeded on upper inserts (100,000 cells per well) of a 6 cell Transwell cultureplate, (polycarbonate, 0.4 μm, Corning). Different stimuli (LPS or MVs) were treated with VECs according to the experiment design after VECs were full confluence, and TER of VECs was assessed by Voltohmmetre (World Precision Inc, America) every 30 min. BSA leakage of VECs was measured after TER analysis, FITC-BSA (10 μg/ml) was added into upper inserts of the Transwell, and 200 μl of the medium of the lower chamber at 10, 20, 30, 40, 50, and 60 min was collected for the measurement of fluorescence intensity, and an equal volume of fresh medium was added into the lower chamber after medium collection. The formula of the BSA leakage was as follows: BSA leakage

(%) = (A10+A20+A30+A40+A50+A60) / total fluorescence intensity, and Ax represented the fluorescence intensity at x min.

HE Staining and Immunofluorescence (FITC-BSA Leakage) of Lung

Rats were anesthetized and the lung was flushed with PBS. Then left lung was formaldehyde-fixed followed by paraffin-embedded for hematoxylin and eosin (HE) staining. The slides were observed by Leica microscope (Germany). For immunofluorescence of lung, rats were anesthetized and injected with FITC-BSA (9 mg/kg) for 2 h. After flushed with PBS, the left lung was formaldehyde-fixed followed embedded in Tissue-Tek O.C.T. Compound (Sakura, America). Afterward frozen sections were performed and the slides were stained with DAPI (Thermo, America), then the leakage of FITC-BSA in lung was observed by Laser confocal microscope (Zhou et al., 2014).

FITC-BSA Leakage of Mesenteric Microvessels

Rats were anesthetized and received laparotomy, then the ileocecal portion of the mesentery was exposed and placed in a transparent plastic stage. The surface of mesentery was moisturized with 37°C saline throughout the whole procedure to keep it warm and moist. Then rats were injected with FITC-BSA (20 mg/kg) intravenously. 10 min after basal observation, fluorescence intensity of FITC-BSA in mesenteric microvessels was measured at 0, 5, and 10 min by virtue of inverted intravital microscopy (HAMAMATSU, Japan) using Image-Pro Plus 5.0 software (Li et al., 2014).

Immunofluorescence (IF) of VECs

Immunofluorescence staining of VECs were measured as previously described with some adjustment (Zhang et al., 2015). Briefly, VECs were seeded on Confocal Petri dishes (Corning, America) and subjected with appropriate treatment at 70% confluence. Then VECs were fixed in 4% formaldehyde for 15 min (room temperature), and permeabilized with 0.1% Triton-100 for 3 min (room temperature), blocked with 5% BSA (Sigma, America), then probed with ZO-1 antibody (Thermo, America) and FITC conjugated secondary antibody (Thermo Fisher Scientific, America). The dishes were analyzed by confocal scanning microscope (Leica, Germany).

RNA Extraction, RT-qPCR

MiRNA was extracted from microvesicles or VECs using the miRCute RNA isolation kit (TIANGEN) following the manufacturer's instructions. The isolated RNA was reverse transcribed using the All-in-One^{TM} miRNA RT Detection kit (Genecopoeia, America). RT-PCR was performed using the All-in-One^{TM} miRNA qPCR detection kit (Genecopoeia, America) on a C1000^{TM} Thermal Cycler Real-Time PCR system from Applied Biosystems (Bio-Rad, United States). Fold induction was calculated using the Ct method as follows: $\Delta\Delta$Ct = (Ct target miRNA - Ct U6), and the final values were determined using $2^{-\Delta\Delta Ct}$ (Zhang et al., 2010).

Transfection of VECs and Harvest of Modified EMVs

To generate modified EMVs, VECs were transfected with 2 nM miR-23b inhibitor, miR-23b mimic or miR-23b vehicle (synthesized by Genecopoeia) with lipofectamine 2000 (Invitrogen) when VECs were 70% confluence, respectively. 12 h after transfection, the medium was changed to serum-free medium, and transfected VECs were stimulated with or without LPS for another 24 h, then modified EMVs were harvested. MiR-23b mimic labeled with FAM (green) at the 3' end was synthesized by Genecopoeia, and the sequence of miR-23b mimic and inhibitor were as follows:

miR-23b mimic;
5′-AUCACAUUGCCAGGGAUUACC-3′ Sense strand;
5′-GGUAAUCCCUGGCAAUGUGAU-3′ Antisense strand;
miR-23b inhibitor;
5′-GGUAAUCCCUGGCAAUGUGAU-3′.

Dual Luciferase Reporter Assay for the Binding of ZO-1

Luciferase assay was performed to determine the effect of miR-23b on mRNA expression of ZO-1 and the 3' untranslated region (UTR) of ZO-1 (Liu et al., 2016b). Briefly, VECs were seeded in 6-well plates and transfected with miR-23b overexpressed plasmid. After 24 h, luciferase reporter vector of ZO-1 (psiCHECK vector), mutant luciferase vector and control vector were transfected by Lipofectamine 2000. VECs were lysed after 24 h, and lysates were measured by dual luciferase reporter system (Promega, San Luis Obispo, CA, United States) on a 20/20-nl luminometer (Promega). Firefly luciferase activity of every sample was normalized to that of Renilla luciferase activity to correct the variations in transfection efficiency between samples.

Western Blot

Vascular endothelial cells were lysed, and cell-protein extracts were separated by SDS—PAGE and transferred to PVDF membrane, then probed with appropriate antibodies and analyzed by Odyssey Clx (LI-COR, America). ZO-1, VE-cadherin were purchased from Thermo, and Occludin and β-actin were purchased from CST (America) (Zhang et al., 2015).

Statistical Analysis

Data of animal studies were repeated at least 8 independent experiments. Data of cell studies were repeated at least 6 independent experiments (data of western blot was repeated for 3 times), and data from one representative experiment were shown. Data from miRNA expression were presented as mean ± SEM, and other data were presented as mean ± SD. Statistical analysis was performed by SPSS 19.0. Differences among or between groups with $n \geq 6$ were analyzed by one-way ANOVA or independent T-test. The significance of data from western blot was determined by one-way Kruskal-Wallis of variance. Values of $p < 0.05$ were considered significant.

RESULTS

Different Types of MV Were All Increased After Sepsis, and Led to Vascular Leakage of Vital Organ and Lung Injury

In order to investigate the role of MVs in pulmonary vascular leakage and lung injury after sepsis, MVs were purified from the blood of normal (ctl-MV) and CLP rats (CLP-MV) by ultracentrifugation, and the concentration of MVs, pulmonary vascular leakage and lung injury were observed. MVs from CLP rats were injected into rats intravenously, and the effect of MVs on pulmonary vascular leakage and lung injury were studied.

For flow cytometry results showed that MVs carried externalized phosphatidylserine (**Figure 1A**), which was considered to be the marker of MVs in most cases, and the majority of MVs was 200−1000 nm. Furthermore, imaging flow cytometry showed the exact image of MVs, which exhibited spherical structure (**Figure 1C**). The concentration of MVs from the normal rats (ctl-MV) was 1.19×10^6/mL, and they were increased to 1.26, 1.53, 1.82, 2.11×10^6/mL at 2, 8, 12, and 16 h after sepsis, respectively (**Figure 1B**), and the increment rate was 6, 29, 53, and 77%. MVs exhibited spherical morphology with typical bimolecular membrane structure and the size was from 100 to 1000 nm in electron microscopy (**Figure 1D**). Verification by dynamic light scattering, the size of MVs was from 82.09 to 859.2 nm with a mean size of 352.98 nm (**Figure 1E**). The size and morphology of MVs obtained were accordant with the existing literatures (Mastronardi et al., 2011; Tkach and Thery, 2016; Martinez and Andriantsitohaina, 2017).

The vascular leakage of lung was significantly aggravated after sepsis (**Figure 1F**), along with the change of vascular leakage of kidney (**Figure 1G**) and intestine (**Figure 1H**). Immunofluorescence of lung showed that a small amount of FITC-BSA could be found in pulmonary interstitium at 2 h, while the leakage of FITC-BSA was significantly enhanced at 8 h after sepsis, which appeared a time dependent manner after sepsis (**Figure 1I**). Meanwhile, lung injury was also aggravated in a time dependent manner, which was characterized by tissue edema, leukocyte and erythrocyte infiltration (**Figure 1J**). The cell counts and protein in bronchoalveolar lavage fluid (BAL) were also significantly increased after sepsis (**Figures 1K,L**). Considering that the vascular leakage had the highest increase rate at 16 h after sepsis, we chose the 16 h time point as the observation time point for CLP model in the following experiments.

To further identify the role of MVs in pulmonary vascular leakage and lung injury after sepsis, MVs from normal and sepsis rats were injected into normal rats (1×10^7 MVs, 2 times, every 8 h), the pulmonary vascular leakage and lung injury were measured at 16 h after the first injection. The results showed that pulmonary vascular leakage was significantly increased after injection of MVs from CLP rats, along with the vascular leakage in kidney and intestine (**Figures 2A–C**), while MVs from normal rats had no effect on vascular leakage. Meanwhile, MVs from CLP rats led to obvious leakage of FITC-BSA in lung and mesenteric microvessels (**Figures 2F,G**), induced tissue edema, leukocyte and erythrocyte infiltration in lung (**Figure 2H**), and increased the cell counts and protein in BAL (**Figures 2D,E**). These results indicate that MVs play an important role in vascular leakage of vital organ and lung injury after sepsis.

There are several types of MV in blood, including endothelial MVs (EMV), platelet MVs (PMV), leukocyte MVs (LMV), etc. To further investigate which type of MV plays the leading role in the regulation of vascular leakage, MVs from CLP rats were applied on FCM to measure the exact profile of different MVs. The concentration of EMVs, PMVs and LMVs (**Figures 3D,E**) were 1.07×10^5/mL, 9.05×10^5/mL, 9.66×10^4/mL in control group, respectively (**Figures 3A,B**). In sepsis rats, the concentration of EMVs, PMVs and LMVs increased to 4.27×10^5/mL, 1.32×10^6/mL, and 2.17×10^5/mL, respectively (**Figure 3C**). The increment rates were 3.99, 1.46, and 2.25 fold at 16 h after sepsis, and the concentration of EMVs was increased most after sepsis.

Furthermore, different types of MVs were harvested from LPS stimulated VECs, platelets and leukocytes, which were also injected into normal rats (1×10^7 MVs, 2 times, every 8 h), the same results were obtained as in MVs harvested from CLP rats, which showed pulmonary vascular leakage was significantly aggravated in EMV group after injection, while pulmonary vascular leakage was slightly increased in PMV and LMV group (**Figure 3F**). EMVs and LMVs induced apparent increment in cell counts and protein infiltration in BAL (**Figures 3G,H**), while PMVs injection led to minor increment on cell counts and protein infiltration.

Subsequently, EMVs, PMVs and LMVs were applied to stimulate VECs with a dose of 1×10^6. The results showed that EMVs reduced the transmembrane electrical resistance (TER) of VEC significantly, while LMV and PMV only slightly reduced the TER of VEC (**Figure 3I**). Meanwhile, the BSA leakage of VECs was significantly increased after incubation of EMVs, while LMVs and PMVs had little effect on the BSA leakage of VECs (**Figure 3J**). These results indicate that EMVs are the most pivotal type of MVs which play the leading role in pulmonary vascular leakage and lung injury after sepsis.

EMVs Induced Pulmonary Vascular Leakage and Lung Injury by Transferring miR-23b

To investigate how EMVs interact with VECs, red fluorescent dye PKH-26 labeled EMVs were injected into normal rats via femoral vein with a dose of 1×10^7, 8 h after injection the pulmonary vein was isolated and observed by the confocal fluorescence microscopy. Immunofluorescence showed that PKH-26-labeled EMVs were taken up by the vascular endothelium (green fluorescence showed CD31+) (**Figure 3K**). Interestingly, PKH-26 labeled EMVs could be also found in the sub-endothelial and media of the pulmonary vein, which indicated that EMVs could penetrate the endothelial barrier to the depth of blood vessels, and played an important role in sepsis. Furthermore, PKH-26-labeled EMVs were incubated with VECs, and results showed that EMVs were incorporated into VECs in a time dependent manner (**Figure 3L**), confirming both vascular endothelium and VEC can uptake EMVs.

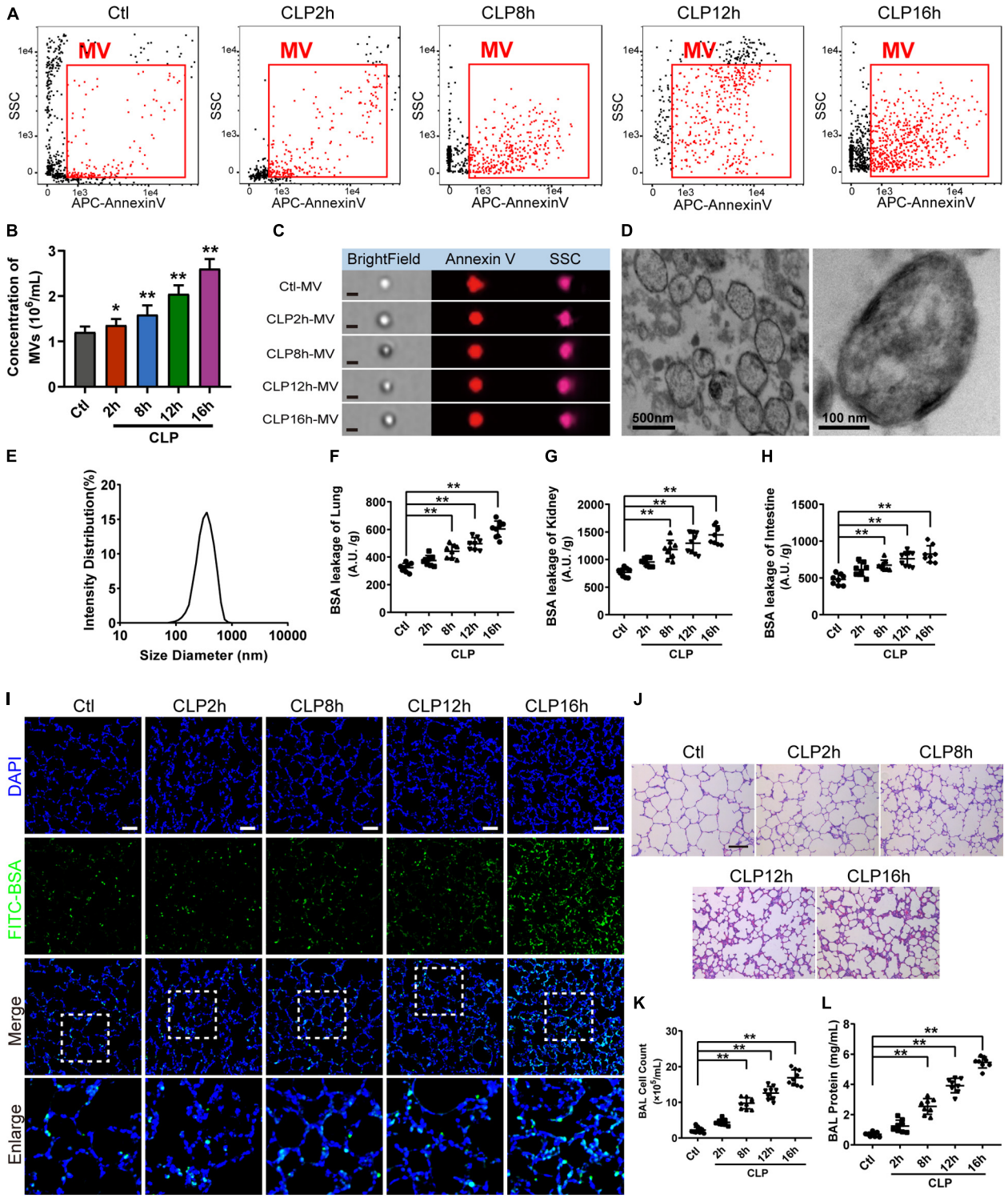

FIGURE 1 | MV concentration, vascular leakage and lung injury increased in sepsis rats. **(A)** Flowcytometry analysis of MVs. The detection gate (0.1–1 μm) was set on SSC and APC channel by standard beads. **(B)** MV concentration measured by flowcytometry. **(C)** Representative flowcytometry microphotographs of MVs from different groups. The scale bar represents 1 μm. **(D)** Representative transmission electron microscope microphotographs of MVs harvested from CLP (cecal ligation and puncture) rats. **(E)** Dynamic light scattering analysis of the diameter of MVs. **(F–H)** Vascular BSA leakage of lung, kidney and intestine in CLP rats (n = 8), measured by the detection of the fluorescence intensity of FITC-BSA accumulation in 2 h in tissue homogenate. **(I)** BSA leakage of lung in CLP rats, determined by the appearance of intravenously injected FITC-BSA *in vivo*, representative photograph was shown. The scale bar represents 50 μm. **(J)** Lung injury in CLP rats accessed by HE staining, representative photograph was shown. The scale bar represents 100 μm. **(K)** Counts of total cells in BAL from CLP rats (n = 8). **(L)** Protein concentration in BAL from CLP rats (n = 8). Ctl, normal control; clt-MV, MVs from normal rats; CLP-MV, MVs from sepsis rats; $^*P < 0.05$ and $^{**}P < 0.01$.

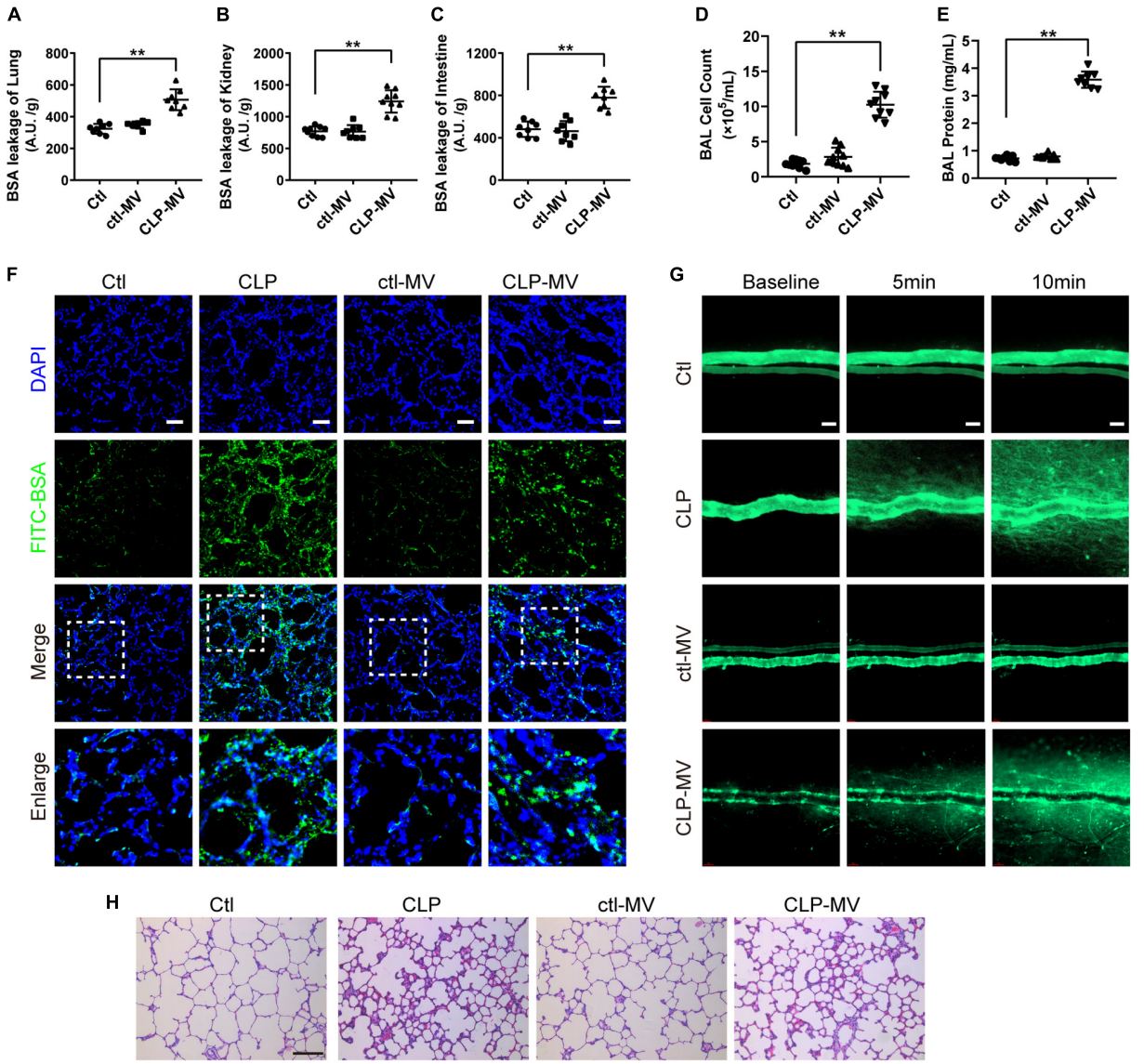

FIGURE 2 | MVs obtained from sepsis rats induced pulmonary vascular leakage and lung injury. **(A–C)** Vascular BSA leakage of lung, kidney and intestine in rats injected with MVs (n = 8), measured by the detection of the fluorescence intensity of FITC-BSA accumulation in 2 h in tissue homogenate. **(D,E)** Cell counts and protein concentration in BAL from rats injected with MVs (n = 8). **(F)** BSA leakage of lung in rats injected with MVs, determined by the appearance of intravenously injected FITC-BSA *in vivo*, representative photograph was shown. The scale bar represents 50 μm. **(G)** BSA leakage of mesentery microvessel in rats injected with of MVs, dynamically measured by inverted intravital microscopy *in vivo*. The scale bar represents 50 μm. **(H)** Lung injury in rats injected with MVs accessed by HE staining, representative photograph was shown. The scale bar represents 100 μm. Ctl, normal control; clt-MV, MVs from normal rats; CLP-MV, MVs from sepsis rats; $^{**}P < 0.01$.

To investigate whether EMVs induce pulmonary vascular leakage after sepsis by carrying miR, we observed the miR expression profile in EMVs harvested from LPS treated VECs (LPS-EMV) and untreated VECs (ctl-EMV) at first. 24 miRNAs which were highly related to vascular leakage and lung injury were measured. The results showed that the expression of miR-23b, miR-105, miR-126, miR-133, miR-218, and miR-302 in LPS-EMVs were significantly higher than ctl-EMVs (**Figure 4A**), during which the most enriched miRNA in LPS-EMVs was miR-23b, with a 13.58-fold increment rate.

To verify whether EMVs transfer miR-23b into VECs, we measured the expression of miR-23b in VECs after incubation by LPS-EMVs and ctl-EMVs. The results showed that LPS-EMVs stimulation effectively increased the expression of miR-23b in VECs while ctl-EMVs had no effect (**Figure 4B**). Furthermore, we transfected FAM-labeled (green fluorescence) miR-23b into VECs to generate containing green fluorescence EMVs, which were then incubated with target VECs. Microscopically, FAM-labeled miR-23b could be found in the cytoplasm of target VECs, which provided a visual proof that miR-23b was transferred into

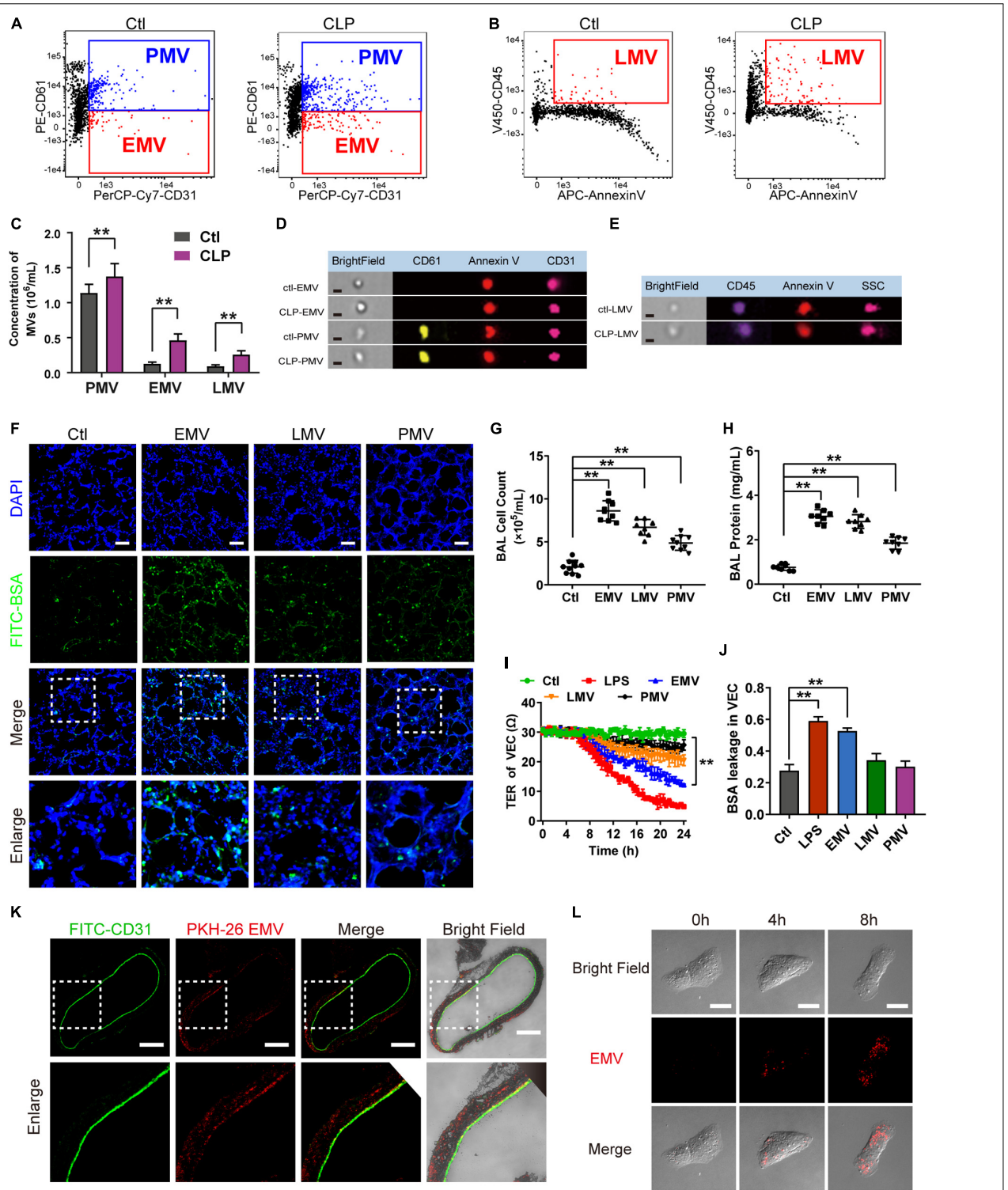

FIGURE 3 | EMVs led to pulmonary vascular leakage and lung injury after sepsis. **(A–C)** Flowcytometry analysis of PMVs, EMVs, and LMVs from CLP rats. CD61+/CD31+ represents PMVs, and CD61-/CD31+ represents EMVs, and CD45+/Annexin V+ represents LMVs. **(D,E)** Representative flowcytometry microphotographs of different MVs. The scale bar represents 1 μm. **(F)** BSA leakage of lung in rats injected with different MVs, determined by the appearance of intravenously injected FITC-BSA *in vivo*, representative photograph was shown. The scale bar represents 50 μm. **(G,H)** Cell counts and protein concentration in BAL from rats injected with different MVs ($n = 8$). **(I)** TER (transmembrane electrical resistance) of VEC monolayers incubated with different MVs. **(J)** BSA leakage of VECs incubated with different MVs ($n = 6$). **(K)** Endocytosis of PKH-26 labeled EMV (red) in pulmonary vein, representative photograph was shown. The scale bar represents 200 μm. **(L)** Endocytosis of PKH-26 labeled EMV (red) in VECs, representative photograph was shown. Ctl, normal control. The scale bar represents 20 μm. $^{**}P < 0.01$.

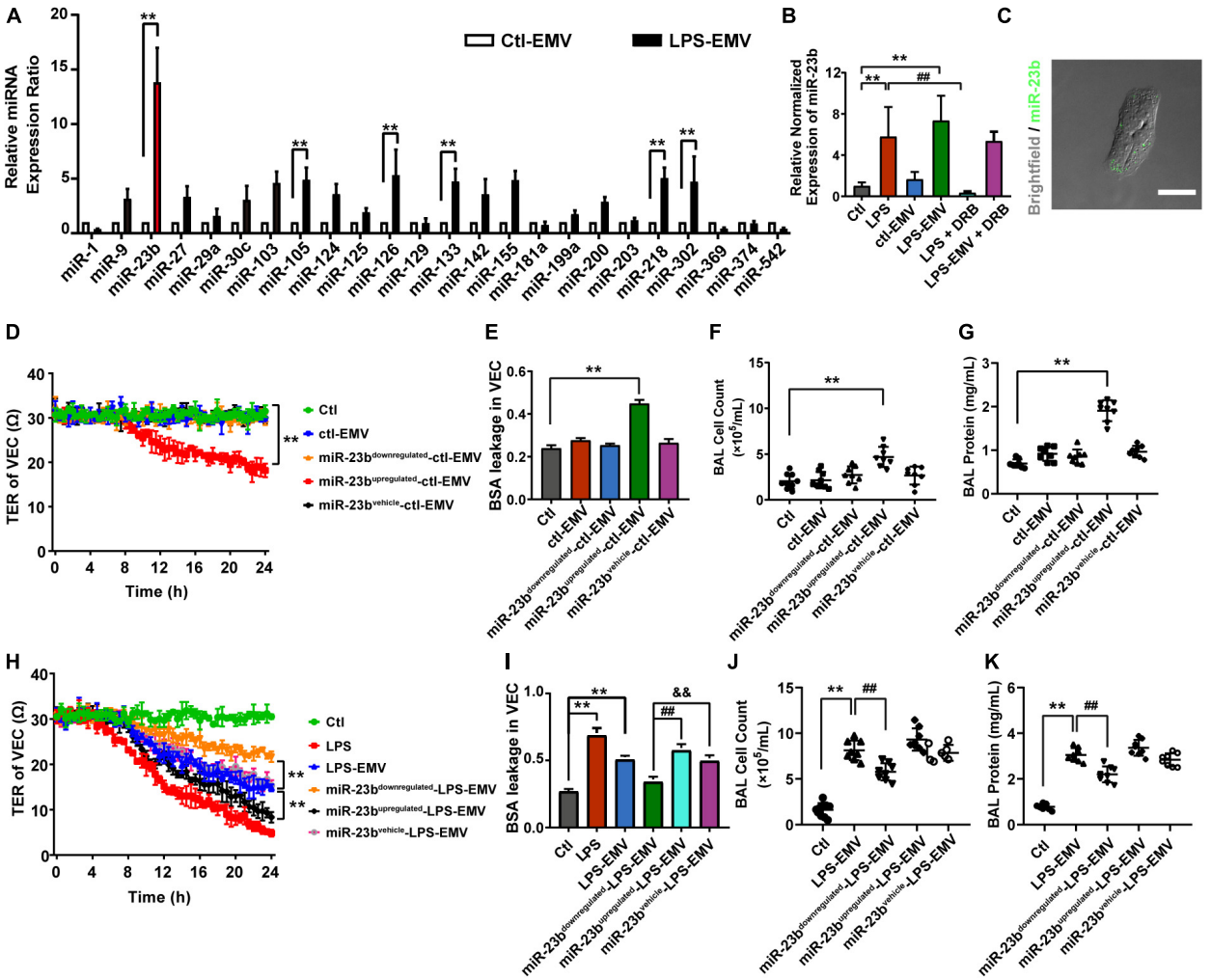

FIGURE 4 | The expression profile of miRNA in EMVs and the effects of EMVs with miR-23b inhibition and overexpression on vascular leakage. **(A)** Comparison of miRNA expression profile in EMVs obtained from VECs treated with (LPS-EMVs) or without (ctl-EMVs) LPS (100 ng/mL), measured by quantitative RT-PCR. **(B)** Quantitative RT-PCR analysis of miR-23b in VECs incubated with LPS-EMVs in the presence of DRB (5,6-Dichlorobenzimidazole1-β-D-ribofuranoside). DRB is RNA polymerase II inhibitor, which can interfere the endogenous synthesis of RNA. **(C)** Representative microphotograph of the internalization of EMVs carrying FAM-miR-23b into VECs. The scale bar represents 20 μm. **(D)** TER of VEC monolayers incubated with different types of ctl-EMVs. **(E)** BSA leakage of VECs incubated with different types of ctl-EMVs ($n = 6$). **(F,G)** Cell counts and protein concentration in BAL from rats injected with different types of ctl-EMVs ($n = 8$). **(H)** TER of VEC monolayers incubated with different types of LPS-EMVs, LPS group was the positive control (the same below). **(I)** BSA leakage of VECs incubated with different types of LPS-EMVs ($n = 6$). **(J,K)** Cell counts and protein concentration in BAL from rats injected with different types of LPS-EMVs ($n = 8$). Ctl, normal control; ctl-EMV, EMVs from normal VECs; LPS-EMV, EMVs from VECs treated with LPS; $^{**}P < 0.01$, $^{\&\&}P < 0.01$ and $^{\#\#}P < 0.01$.

VECs by EMVs (**Figure 4C**). To further investigate whether the increase of miR-23b in VECs was from the EMV-carried miR, RNA polymerase II inhibitor DRB was used to interfere the endogenous synthesis of RNA in target VECs. DRB showed no influence on the increase of miR-23b after EMV stimulation, which indicated that the increase of miR-23b in target VECs was resulted from the EMV contained miR-23b transfer rather than endogenous miR-23b in target VECs (**Figure 4B**).

In order to investigate whether EMVs induce pulmonary vascular leakage and lung injury by transferring miR-23b, the miR-23b inhibitor and miR-23b mimic were used to prepare modified EMVs. In the present study, VECs were firstly transfected as described, and then treated with or without LPS, thus we defined the modified EMVs according to the sequence of treatment as: miR-23b^{upregulated}-LPS-EMV, miR-23b^{downregulated}-LPS-EMV, miR-23b^{vehicle}-LPS-EMV, miR-23b^{upregulated}-ctl-EMV, miR-23b^{downregulated}-ctl-EMV and miR-23b^{vehicle}-ctl-EMV, respectively.

Then modified EMVs treated without LPS were incubated with VECs, and miR-23b^{downregulated}-ctl-EMVs and miR-23b^{vehicle}-ctl-EMVs showed no effect on TER and BSA leakage of VECs, while incubation of miR-23b^{upregulated}-ctl-EMVs led to the decrease of TER of VECs, and the increase of BSA leakage of VECs (**Figures 4D,E**). Meanwhile, incubation of

miR-23b^{upregulated}-ctl-EMVs induced apparent increase of cell count and protein in BAL (**Figures 4F,G**).

To further confirm the role of miR-23b in vascular leakage and lung injury, modified EMVs treated with LPS were applied to stimulate VECs. Compared with control group, LPS-EMVs induced significant leakage in VECs, while miR-23b^{downregulated}-LPS-EMVs abolished the LPS-EMV induced leakage of VECs, and miR-23b^{upregulated}-LPS-EMVs further aggravated the leakage (**Figures 4H,I**). Furthermore, miR-23b^{upregulated}-LPS-EMVs aggravated the increment of cell count and protein effusion in BAL caused by LPS-EMVs (**Figures 4J,K**). These results indicated that the EMV transferring miR-23b induced pulmonary vascular leakage and lung injury.

EMVs Induced Vascular Leakage and Lung Injury by Inhibiting ZO-1 Expression

In general, there are several key proteins in the regulation of vascular leakage: tight junction protein ZO-1, Occludin and adherent junction protein VE-cadherin. To investigate which protein may take part in vascular leakage and lung injury by miR-23b containing EMV, at first we predicted the potential target of miR-23b by Targetscan, and found ZO-1 mRNA might be the most feasible target of miR-23b among those targets (Data not shown).

Further experiment found that ctl-EMVs and miR-23b^{downregulated}-ctl-EMVs showed no influence on the expression of ZO-1, and miR-23b^{upregulated}-ctl-EMVs significantly inhibited the expression of ZO-1 (**Figure 5A**) and impaired the integrity of ZO-1 barrier (**Figure 5B**). Meanwhile, miR-23b^{upregulated}-ctl-EMVs had no effect on the expression of Occludin and VE-cadherin (**Figure 5B**), which indicated that the effect of miR-23b containing EMVs was related to ZO-1 inhibition.

Furthermore, LPS-EMVs decreased the ZO-1 expression, and miR-23b^{upregulated}-LPS-EMVs aggravated the decrease of ZO-1 expression induced by LPS-EMVs, while miR-23b^{downregulated}-LPS-EMVs attenuated the LPS-EMVs induced increase of ZO-1 expression (**Figure 5C**). Identically, miR-23b^{upregulated}-LPS-EMVs caused more harm to ZO-1 barrier, and miR-23b^{downregulated}-LPS-EMVs could attenuate the LPS-EMVs induced endothelial barrier damage (**Figure 5D**). Dual luciferase reporter assay verified that miR-23b could act on the 3'-UTR of ZO-1 mRNA (**Figures 5E,F**). Interestingly, LPS-EMVs had little effect on the expression of ZO-1 mRNA (**Figure 5G**), which suggested that miR-23b in EMVs regulated the expression by affecting the 3'-UTR of ZO-1 without degradation of the ZO-1 mRNA.

MVs From Sepsis Patients Induced Pulmonary Vascular Leakage and Lung Injury in Rats

To further verify the role of MVs on pulmonary vascular leakage and lung injury after sepsis, we collected MVs from sepsis patients to stimulate normal rats. In this experiment, 10 patients and 15 healthy adults were recruited for MV collecting (**Supplementary Table S1**). The concentration of circulating MVs in sepsis patients (sepsis-MV) was significantly higher than that in healthy adults (healthy-MVs) (**Figures 6A–C**).

Then MVs from sepsis patients were applied to normal rats, and data showed that MVs from sepsis patients induced apparent pulmonary vascular leakage in rats while MVs from healthy adults had no effect (**Figure 6D**). Meanwhile, MVs from sepsis patients led to apparent lung injury and protein effusion in BAL (**Figures 6E–G**). Furthermore, MVs from sepsis patients led to apparent leakage in VECs (**Figures 6H,I**). As compared with MVs from healthy adults, MVs from sepsis patients reduced the expression of ZO-1 and impaired the integrity of ZO-1 (**Figures 6J,K**). Meanwhile, the expression of miR-23b in MVs from sepsis patients was significantly higher than that in MVs from healthy adults (**Figure 6L**). These results further confirmed that miR-23b-containing MVs in sepsis patients played an essential role in pulmonary vascular leakage and lung injury.

Inhibition of EMV Generation Ameliorates Pulmonary Vascular Leakage and Lung Injury After Sepsis

As the accumulation of EMVs in blood after sepsis led to subsequent damage on vessels, we aimed to attenuate the effect of EMVs by inhibiting the generation of EMVs. 10 μM of acid SMase inhibitor amitriptyline was used to treat VEC for 24 h, and data showed that amitriptyline effectively reduced the release of EMVs (**Figures 7A–C**). EMVs obtained from amitriptyline and LPS treated VECs (Ami-LPS-EMV) and amitriptyline could attenuate the LPS-EMVs induced pulmonary vascular leakage (**Figure 7D**) and attenuate the cell count and protein infiltration in BAL (**Figures 7F,G**), and the lung injury (**Figure 7E**). *In vivo* study showed that amitriptyline could reduce EMVs production in sepsis rats in a dose-dependent manner at 50 and 100 μM (**Figures 7H–J**).

DISCUSSION

The present study showed that EMVs played an important role in pulmonary vascular leakage and lung injury after sepsis, in this process, miR-23b played a critical role. Inhibition of the release of MV including EMV with amitriptyline could significantly alleviate sepsis induced vascular leakage and lung injury. This study provides a new sight for exploration of the treatment of sepsis.

Lung injury is the leading cause of death during sepsis and the main failure organ in the development of multiple organ dysfunction after sepsis (Wu et al., 2007). Vascular leakage is one of the most important pathophysiological processes in lung injury, which is considered to be related to abundant cytokines in blood after sepsis (Hou et al., 2017). It has been proved that cytokines such as Angiopoietin2, VEGF, TGF-β and HMGB1 are important in the occurrence of vascular leakage (Hotchkiss et al., 2016; Hattori et al., 2017). For example, circulating TGF-β induced protein (TGFBIp) level was increased after sepsis, and the subsequent interaction with integrin αvβ5 could result in the increased proinflammatory responses, and promote the adhesion and migration of leukocytes across the endothelium,

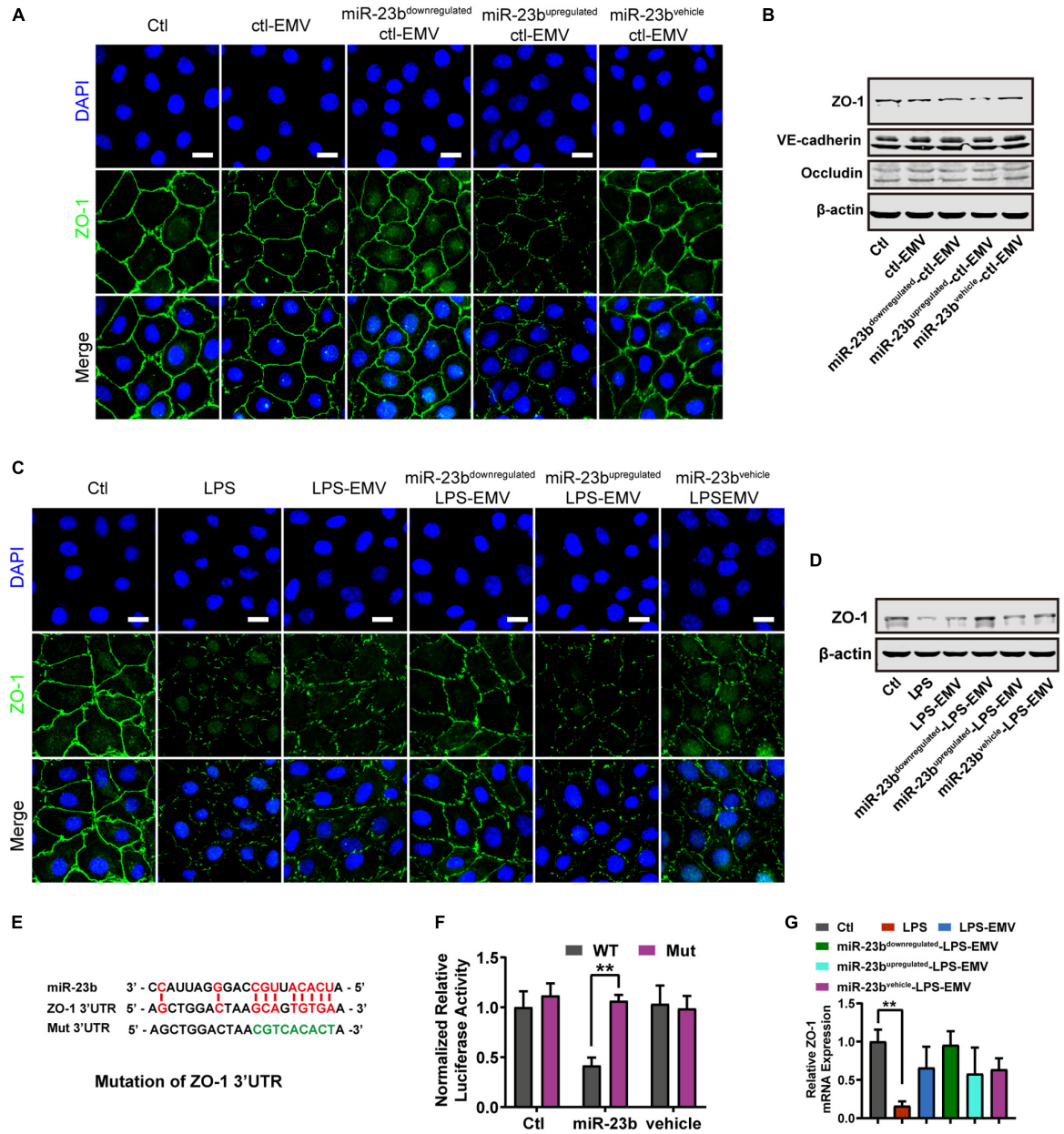

FIGURE 5 | The effect of EMVs with miR-23b inhibition and overexpression on ZO-1 expression. **(A)** Immunofluorescence for ZO-1 in VECs incubated with different types of ctl-EMVs. The scale bar represents 20 μm. **(B)** Western blot analysis of ZO-1 in VECs incubated with different types of ctl-EMVs (n = 3). **(C)** Immunofluorescence for ZO-1 in VECs incubated with different types of LPS-EMVs. LPS group was the positive control (The same below). The scale bar represents 20 μm. **(D)** Western blot analysis of ZO-1 in VECs incubated with different types of LPS-EMVs (n = 3). **(E)** Schematic showing miR-23b predicted binding sites in ZO-1 3'-UTR and mutant ZO-1 3'-UTR sequence (Mut). Mut sequence of ZO-1 3'-UTR was introduced by replacing the wild type binding sequence (GCAGTGTGA) with a mutant sequence (CCTTTACAT, in green). **(F)** Effects of miR-23b on the 3'-UTR of ZO-1 and the mutant of ZO-1, measured by Dual-Luciferase System. **(G)** Quantitative RT-PCR analysis of ZO-1 mRNA in VECs incubated with different types of LPS-EMVs. Ctl, normal control; ctl-EMV, EMVs from normal VECs; LPS-EMV, EMVs from VECs treated with LPS; $^{**}P < 0.01$, $^{\#\#}P < 0.01$, and $\&\&P < 0.01$.

which eventually aggravated vascular leakage and the progress of sepsis (Bae et al., 2014). Several therapies were designed to inhibit the impact of cytokines, but the results were not satisfactory, which indicated that there were many other factors involved in the process. Recent studies showed that MVs played important roles in the occurrence and development of sepsis, including coagulation, inflammation and immunodeficiency, etc. The present study revealed that MV, especially EMVs played an important role in vascular leakage and lung injury after sepsis.

The concentration of MV in circulation is low in healthy rats, which is mainly composed of PMVs, with a proportion of up to 76.1%, while the proportion of EMVs, LMVs is

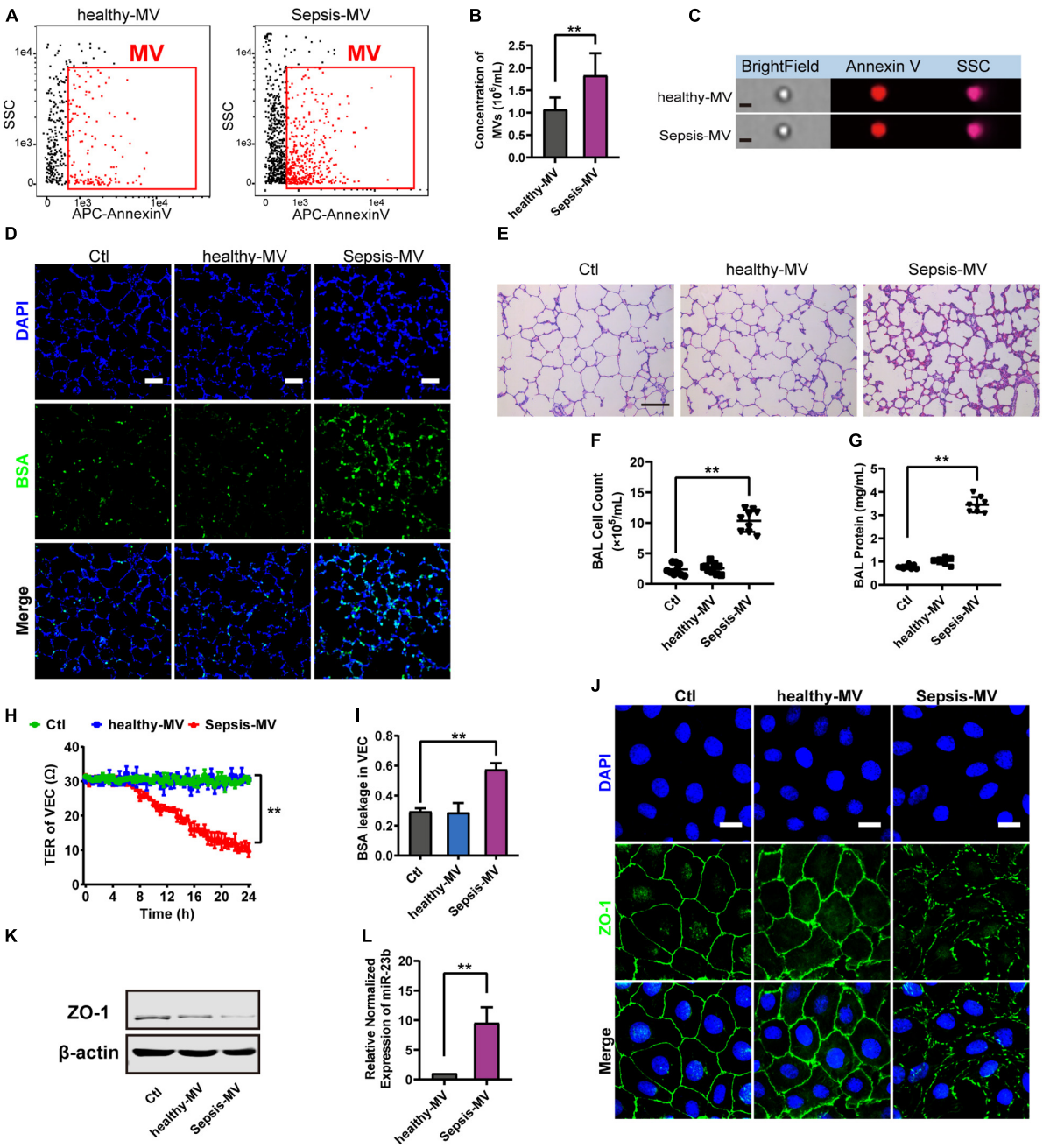

FIGURE 6 | MVs harvested from sepsis patients induced pulmonary vascular leakage and lung injury. **(A,B)** Flowcytometry analysis of MVs from heathy people (healthy-MVs) and sepsis patients (sepsis-MVs). **(C)** Representative flowcytometry microphotographs of healthy-MVs and sepsis-MVs. The scale bar represents 1 μm. **(D)** BSA leakage of lung in rats injected with healthy-MVs or sepsis-MVs, determined by the appearance of intravenously injected FITC-BSA *in vivo*, representative photograph was shown. The scale bar represents 50 μm. **(E)** Lung injury in rats injected with healthy-MVs or sepsis-MVs, accessed by HE staining, representative photograph was shown. The scale bar represents 100 μm. **(F,G)** Cell counts and protein concentration in BAL from rats injected with different MVs (n = 8). **(H)** TER (transmembrane electrical resistance) of VEC monolayers incubated with different MVs. **(I)** BSA leakage of VECs incubated with different MVs (n = 6). **(J)** Immunofluorescence for ZO-1 in VECs incubated with different MVs. The scale bar represents 20 μm. **(K)** Western blot analysis of ZO-1 in VECs incubated with different MVs (n = 3). **(L)** Quantitative RT-PCR analysis of miR-23b in VECs incubated with different MVs. Ctl, normal control; ** $P < 0.01$.

low (Mastronardi et al., 2011). Previous studies have found that PMV can participate in the activation of exogenous coagulation reaction after sepsis (Delabranche et al., 2016). By expressing high-affinity binding sites for coagulation factors Va, VIII, and IXa on its surface, and carrying platelet activating factor (PAF), PMVs can react with platelets and monocyte, which can continuously activate thrombin generation thus promote coagulation process. LMVs can carry a variety

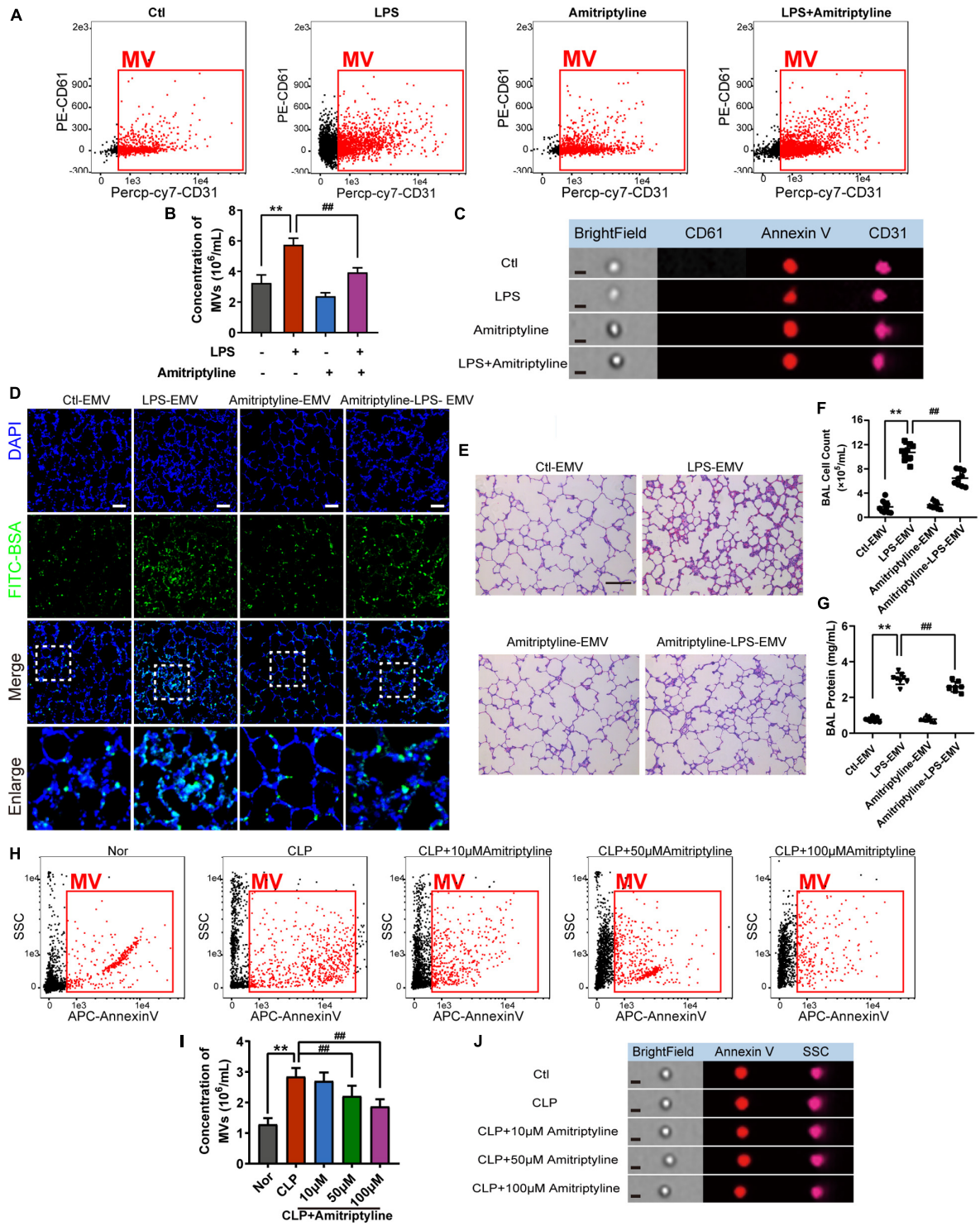

FIGURE 7 | Amitriptyline inhibited the generation of EMVS and attenuated the effect of EMVs on pulmonary vascular leakage. **(A,B)** Flowcytometry analysis of EMVs from VECs treated with/without LPS or amitriptyline. **(C)** Representative flowcytometry microphotographs of different EMVs. The scale bar represents 1 μm. **(D)** BSA leakage of lung in rats injected with different EMVs, determined by the appearance of intravenously injected FITC-BSA *in vivo*, representative photograph was shown. The scale bar represents 50 μm. **(E)** Lung injury in rats injected with different EMVs, accessed by HE staining, representative photograph was shown. The scale bar represents 100 μm. **(F,G)** Cell counts and protein concentration in BAL from rats injected with different EMVs ($n = 8$). **(H,I)** Flowcytometry analysis of MVs from CLP rats treated with different doses of amitriptyline. **(J)** Representative flowcytometry microphotographs of different MVs. The scale bar represents 1 μm. Ctl, normal control; $^{**}P < 0.01$ and $^{\#\#}P < 0.01$.

of inflammatory factors from leukocytes, for example, they can transfer myeloperoxidase into endothelial cells, which will interfere with the myeloperoxidase-hydrogen peroxide-chloride system, leading to the damage of endothelial cells and inflammation aggravation (Bae et al., 2014). EMVs are mainly secreted from the damaged endothelial cells, which are related to endothelial injury, remodeling and angiogenesis (Paone et al., 2019). However, the present study revealed that the proportion of EMVs was significantly increased, from 9.0 to 20.2% in sepsis rats, which may be related to the extensive activation of vascular endothelium during sepsis. Because VECs are the first barrier for pathogenic factors when sepsis occurred (Aird, 2003). Stimulated VECs secret a large number of EMVs subsequently, which reach all parts of the body along with the circulation, leading to the extensive activation of vascular endothelium throughout the body, and inducing the aggravation of sepsis. Except for EMVs, the present study found the concentration of PMVs and LMVs were also significantly increased during sepsis. Among the three types of MVs, the present study showed that EMVs played the leading role in pulmonary vascular leakage and lung injury.

MVs could provide shelter for miRNAs to keep them from being degraded by RNase in the blood, which has been proved that miRNAs could be selectively packaged into MVs to participate in multiple diseases (Zhang et al., 2010; Zhou et al., 2014; Xu et al., 2017; Zheng et al., 2017). MiR-23b was firstly identified to be an oncogene which is related to breast cancer, glioma and kidney cancer, and it participates in the regulation of cytoskeletal reconstruction, cell invasion, metastasis and inflammatory reactions (Donadelli et al., 2014; Grossi et al., 2018). Our present study found that miR-23b was abundant in EMV after sepsis. By predicting potential target of miR-23b using Targetscan, tight junction ZO-1 was found to be the most feasible target of miR-23b, rather than tight junction Occludin nor adherent junction VE-cadherin. Tight junction ZO-1 plays an important role in maintaining the stability of the barrier of VECs, and the destruction of ZO-1 results in the leakage of vessels. Besides, there are many other miR as miR-105, miR-132 could also participate in the regulation of vascular leakage in other diseases (Zhou et al., 2014; Gu et al., 2019), but these miRs showed little change in EMVs after sepsis, which suggests that the miR-23b is selectively packaged into EMVs during the progress of sepsis, and the mechanism of selective package needs to be further studied. In addition, MVs separated from sepsis patients could also lead to pulmonary vascular leakage and lung injury in rats, and aggravate the leakage of pulmonary vascular endothelial cells, suggesting that MVs as a vehicle for intercellular information exchange can transmit biological information between species.

Amitriptyline was known to be effective for antidepressant effect in mental illness, which was found to be able to reduce acid SMase activity and the synthesis of phospholipid. Acid SMase plays a role in the synthesis of membrane lipids (Awojoodu et al., 2014; Depciuch et al., 2017), thus amitriptyline is thought able to be a non-specific drug to inhibit the secretion of MVs, and it was proved to be effective at the dose of 100 μM (Awojoodu et al., 2014). Our present study found that 50 and 100 μM amitriptyline significantly inhibited the release of EMVs during sepsis and alleviated the pulmonary vascular leakage and lung injury. This result suggests that amitriptyline may be a therapeutic candidate for the treatment of pulmonary vascular leakage induced by MVs. However, the mechanism of MV generation is complicated, which is relevant to phosphatidylserine, sphingomyelin, flippase, floppase and Ca^{2+}, etc (Buzas et al., 2018; Malloci et al., 2018; Meldolesi, 2018), amitriptyline could reduce the formation of MVs to some extent, while how to effectively use amitriptyline to inhibit the secretion of MVs needs further investigation.

Nevertheless, there are some limitations in the present study. Firstly, the number of patients we recruited was a small population, whether EMVs play an important role in vascular leakage in sepsis patients needs further verification. Secondly, there are many factors such as tissue factor, MMPs etc (Krizanac-Bengez et al., 2006; Yeh et al., 2013; Lee et al., 2014), which may affect vascular barrier in addition to ZO-1, whether EMVs-induced vascular leakage is related to MMPs or TF needs to be further investigated. Thirdly, the present study was focused on the role of MVs, while exosomes may also participate in the vascular leakage because of the similar origins (Caivano et al., 2017), whether exosomes from VECs also play an important role needs further investigation.

In conclusion, our study showed that EMVs play an important role in pulmonary vascular leakage and lung injury during sepsis by transferring functional miR-23b. Antagonizing the secretion of EMVs and its miR-23b may alleviate the vascular leakage and lung injury. EMVs and miR-23b might be a potential therapeutic target for vascular leakage and organ injury in sepsis.

DATA AVAILABILITY STATEMENT

All datasets presented in this study are included in the article/ **Supplementary Material**.

ETHICS STATEMENT

The studies involving human participants were reviewed and approved by the Ethics Committee of the Research Institute of Surgery (Daping Hospital, Army Medical University). The patients/participants provided their written informed consent to participate in this study. The animal study was reviewed and approved by Research Council and Animal Care and Use Committee of the Research Institute of Surgery (Daping Hospital, Army Medical University, Chongqing, China, Number DHEC-2012-069).

AUTHOR CONTRIBUTIONS

DZ, JZ, ZZ, and HZ performed the experiments and analyzed the data. DZ, LK, YZ, YW, and CD collected the clinical samples and approved the manuscript. LL and TL participated in the study design. All authors have read and approved the manuscript, and ensured that it is the case.

FUNDING

This work was supported by a grant from the General Program of National Natural Science Foundation of China (Grant No. 81570441), the Key Project of National Natural Science Foundation of China (Grant No. 81730059), and the Key Projects and Innovation Group of National Natural Science Foundation of China (Grant No. 81721001). The sponsor had been no involvement in study design; in the collection, analysis, and interpretation of data; in the writing of the report; and in the decision to submit the article for publication.

SUPPLEMENTARY MATERIAL

The Supplementary Material for this article can be found online at: https://www.frontiersin.org/articles/10.3389/fcell.2020.00643/full#supplementary-material

REFERENCES

Aird, W. C. (2003). The role of the endothelium in severe sepsis and multiple organ dysfunction syndrome. *Blood* 101, 3765–3777. doi: 10.1182/blood-2002-06-1887

Awojoodu, A. O., Keegan, P. M., Lane, A. R., Zhang, Y., Lynch, K. R., Platt, M. O., et al. (2014). Acid sphingomyelinase is activated in sickle cell erythrocytes and contributes to inflammatory microparticle generation in SCD. *Blood* 124, 1941–1950. doi: 10.1182/blood-2014-01-543652

Bae, J. S., Lee, W., Nam, J. O., Kim, J. E., Kim, S. W., Kim, S., et al. (2014). Transforming growth factor beta-induced protein promotes severe vascular inflammatory responses. *Am. J. Respir. Crit. Care Med.* 189, 779–786. doi: 10.1164/rccm.201311-2033OC

Becker, A., Thakur, B. K., Weiss, J. M., Kim, H. S., Peinado, H., and David, L. (2016). Extracellular vesicles in cancer: cell-to-Cell mediators of metastasis. *Cancer Cell* 30, 836–848. doi: 10.1016/j.ccell.2016.10.009

Buzas, E. I., Toth, E. A., Sodar, B. W., and Szabo-Taylor, K. E. (2018). Molecular interactions at the surface of extracellular vesicles. *Semin. Immunopathol.* 40, 453–464. doi: 10.1007/s00281-018-0682-0

Caivano, A., Del, V. L., and Musto, P. (2017). Do we need to distinguish exosomes from microvesicles in hematological malignancies? *Leukemia* 31, 2009–2010. doi: 10.1038/leu.2017.205

Cheow, E. S., Cheng, W. C., Lee, C. N., de Kleijn, D., Sorokin, V., and Siu, K. S. (2016). Plasma-derived extracellular vesicles contain predictive biomarkers and potential therapeutic targets for myocardial ischemic (MI) injury. *Mol. Cell Proteomics* 5, 2628–2640. doi: 10.1074/mcp.m115.055731

Delabranche, X., Quenot, J. P., Lavigne, T., Mercier, E., Francois, B., Francois, S., et al. (2016). Early detection of disseminated intravascular coagulation during septic shock: a multicenter prospective study. *Crit. Care Med.* 44, e930–e939. doi: 10.1097/CCM.0000000000001836

Depciuch, J., Sowa-Kucma, M., Nowak, G., Szewczyk, B., Doboszewska, U., and Parlinska, M. W. (2017). The role of zinc deficiency-induced changes in the phospholipid-protein balance of blood serum in animal depression model by Raman, FTIR and UV-vis spectroscopy. *Biomed. Pharmacother.* 89, 549–558. doi: 10.1016/j.biopha.2017.01.180

Donadelli, M., Dando, I., Fiorini, C., and Palmieri, M. (2014). Regulation of miR-23b expression and its dual role on ROS production and tumour development. *Cancer Lett.* 349, 107–113. doi: 10.1016/j.canlet.2014.04.012

Fleischmann, C., Scherag, A., Adhikari, N. K. J., Hartog, C. S., Tsaganos, T., Peter, S., et al. (2016). Assessment of global incidence and mortality of hospital-treated sepsis. Current estimates and limitations. *Am. J. Respir. Crit. Care Med.* 193, 259–272. doi: 10.1164/rccm.201504-0781OC

Gotzfried, J., Smirnova, N. F., Morrone, C., Korkmaz, B., Yildirim, A. O., Jenne, D. E., et al. (2018). Preservation with alpha1-antitrypsin improves primary graft function of murine lung transplants. *J. Heart Lung. Transplant* 37, 1021–1028. doi: 10.1016/j.healun.2018.03.015

Grossi, I., Salvi, A., Baiocchi, G., Portolani, N., and De Petro, G. (2018). Functional role of microRNA-23b-3p in cancer biology. *Microrna* 7, 156–166. doi: 10.2174/2211536607666180629155025

Gu, Y., Cai, R., Zhang, C., Xue, Y., Pan, Y., Zhou, Z., et al. (2019). MiR-132-3p boosts caveolae-mediated transcellular transport in glioma endothelial cells by targeting PTEN/PI3K/PKB/Src/Cav-1 signaling pathway. *Faseb J.* 33, 441–454. doi: 10.1096/fj.201800095RR

Hattori, Y., Hattori, K., Suzuki, T., and Matsuda, N. (2017). Recent advances in the pathophysiology and molecular basis of sepsis-associated organ dysfunction: novel therapeutic implications and challenges. *Pharmacol. Ther.* 177, 56–66. doi: 10.1016/j.pharmthera.2017.02.040

Hoefer, I. E., Steffens, S., Ala-Korpela, M., Back, M., Badimon, L., Paul, C. E., et al. (2015). Novel methodologies for biomarker discovery in atherosclerosis. *Eur. Heart J.* 36, 2635–2642. doi: 10.1093/eurheartj/ehv236

Hotchkiss, R. S., Moldawer, L. L., Opal, S. M., Reinhart, K., and Turnbull, I. R. (2016). Sepsis and septic shock. *Nat. Rev. Dis. Primers* 2:16045. doi: 10.1038/nrdp.2016.45

Hou, P. C., Filbin, M. R., Wang, H., Ngo, L., Huang, D. T., John, A. K., et al. (2017). Endothelial permeability and hemostasis in septic shock: results from the ProCESS trial. *Chest* 152, 22–31. doi: 10.1016/j.chest.2017.01.010

Izzotti, A., Longobardi, M., La Maestra, S., Micale, R. T., Pulliero, A., Flora, S. D., et al. (2018). Release of MicroRNAs into body fluids from ten organs of mice exposed to cigarette smoke. *Theranostics* 8, 2147–2160. doi: 10.7150/thno.22726

Karpman, D., Stahl, A. L., and Arvidsson, I. (2017). Extracellular vesicles in renal disease. *Nat. Rev. Nephrol.* 13, 545–562. doi: 10.1038/nrneph.2017.98

Krizanac-Bengez, L., Hossain, M., Fazio, V., Mayberg, M., and Janigro, D. (2006). Loss of flow induces leukocyte-mediated MMP/TIMP imbalance in dynamic in vitro blood-brain barrier model: role of pro-inflammatory cytokines. *Am. J. Physiol. Cell Physiol.* 291, C740–C749. doi: 10.1152/ajpcell.00516.2005

Laher, I. (2011). Microparticles have macro effects in sepsis. *Crit. Care Med.* 39, 1842–1843. doi: 10.1097/CCM.0b013e31821cb06d

Lee, H., Jun, J., Jung, E., Koo, B., and Kim, Y. (2014). Epigalloccatechin-3-gallate inhibits ocular neovascularization and vascular permeability in human retinal pigment epithelial and human retinal microvascular endothelial cells via suppression of MMP-9 and VEGF activation. *Molecules* 19, 12150–12172. doi: 10.3390/molecules190812150

Li, C., Li, Q., Liu, Y. Y., Wang, M. X., Pan, C. S., Li, Y., et al. (2014). Protective effects of Notoginsenoside R1 on intestinal ischemia-reperfusion injury in rats. *Am. J. Physiol. Gastrointest. Liver Physiol./* 306, G111–G122. doi: 10.1152/ajpgi.00123.2013

Liu, L., Wu, H., Zang, J., Yang, G., and Zhu, Y. (2016a). 4-phenylbutyric acid reveals good beneficial effects on vital organ function via anti–endoplasmic reticulum stress in septic rats*. *Crit. Care Med.* 44, e689–e701. doi: 10.1097/CCM.0000000000001662

Liu, L., Zang, J., Chen, X., Yang, G., Zhu, Y., Wu, Y., et al. (2016b). Role of miR-124 and miR-141 in the regulation of vascular reactivity and the relationship to RhoA and Rac1 after hemorrhage and hypoxia. *Am. J. Physiol. Heart Circ. Physiol.* 310, H206–H216. doi: 10.1152/ajpheart.00651.2014

Lovren, F., and Verma, S. (2013). Evolving role of microparticles in the pathophysiology of endothelial dysfunction. *Clin. Chem.* 59, 1166–1174. doi: 10.1373/clinchem.2012.199711

Mairhofer, M., Steiner, M., Mosgoeller, W., Prohaska, R., and Salzer, U. (2002). Stomatin is a major lipid-raft component of platelet alpha granules. *Blood* 100, 897–904. doi: 10.1182/blood.V100.3.897

Malloci, M., Perdomo, L., Veerasamy, M., Andriantsitohaina, R., Simard, G., Carmen, M. M., et al. (2018). Extracellular vesicles: mechanisms in human health and disease. *Antioxid Redox Signal.* 30, 813–856. doi: 10.1089/ars.2017.7265

Martinez, M. C., and Andriantsitohaina, R. (2017). Extracellular vesicles in metabolic syndrome. *Circ. Res.* 120, 1674–1686. doi: 10.1161/CIRCRESAHA.117.309419

Mastronardi, M. L., Mostefai, H. A., Meziani, F., Martinez, M. C., Asfar, P., Andriantsitohaina, R., et al. (2011). Circulating microparticles from septic

shock patients exert differential tissue expression of enzymes related to inflammation and oxidative stress. *Crit. Care Med.* 39, 1739–1748. doi: 10.1097/CCM.0b013e3182190b4b

Matthay, M. A. (2017). Extracellular vesicle transfer from mesenchymal stromal cells modulates macrophage function in acute lung injury. Basic science and clinical implications. *Am. J. Respir. Crit. Care Med.* 196, 1234–1236. doi: 10.1164/rccm.201706-1122ED

Meldolesi, J. (2018). Exosomes and ectosomes in intercellular communication. *Curr. Biol.* 28, R435–R444. doi: 10.1016/j.cub.2018.01.059

Paone, S., Baxter, A. A., Hulett, M. D., and Poon, I. (2019). Endothelial cell apoptosis and the role of endothelial cell-derived extracellular vesicles in the progression of atherosclerosis. *Cell Mol. Life Sci.* 76, 1093–1106. doi: 10.1007/s00018-018-2983-9

Rhodes, A., Evans, L. E., Alhazzani, W., Levy, M. M., Antonelli, M., Gordon, B. R., et al. (2017). Surviving sepsis campaign. *Crit. Care Med.* 45, 486–552. doi: 10.1097/CCM.0000000000002255

Tkach, M., and Thery, C. (2016). Communication by extracellular vesicles: where we are and where we need to go. *Cell* 164, 1226–1232. doi: 10.1016/j.cell.2016.01.043

Todorova, D., Simoncini, S., Lacroix, R., Sabatier, F., and Dignat-George, F. (2017). Extracellular vesicles in angiogenesis. *Circ. Res.* 120, 1658–1673. doi: 10.1161/CIRCRESAHA.117.309681

Wu, R., Dong, W., Zhou, M., Zhang, F., Marini, C. P., Ping, W., et al. (2007). Ghrelin attenuates sepsis-induced acute lung injury and mortality in rats. *Am. J. Respir. Crit. Care Med.* 176, 805–813. doi: 10.1164/rccm.200604-511OC

Xu, B., Zhang, Y., Du, X. F., Li, J., Zi, H. X., Bu, J., et al. (2017). Neurons secrete miR-132-containing exosomes to regulate brain vascular integrity. *Cell Res.* 27, 882–897. doi: 10.1038/cr.2017.62

Yeh, H. H., Chang, W. T., Lu, K. C., Lai, W. W., Liu, H. S., and Wu, C. S. (2013). Upregulation of tissue factor by activated Stat3 contributes to malignant pleural effusion generation via enhancing tumor metastasis and vascular permeability in lung adenocarcinoma. *PLoS One* 8:e75287. doi: 10.1371/journal.pone.0075287

Zhang, J., Yang, G., Zhu, Y., Peng, X., Li, T., Liu, L. M., et al. (2015). Role of connexin 43 in vascular hyperpermeability and relationship to Rock1-MLC20 pathway in septic rats. *Am. J. Physiol. Lung Cell. Mol. Physiol.* 309, L1323–L1332. doi: 10.1152/ajplung.00016.2015

Zhang, Y., Liu, D., Chen, X., Li, J., Li, L., Wang, D., et al. (2010). Secreted monocytic miR-150 enhances targeted endothelial cell migration. *Mol. Cell* 39, 133–144. doi: 10.1016/j.molcel.2010.06.010

Zheng, B., Yin, W. N., Suzuki, T., Zhang, X. H., Zhang, Y., Hong, Z., et al. (2017). Exosome-Mediated miR-155 transfer from smooth muscle cells to endothelial cells induces endothelial injury and promotes atherosclerosis. *Mol. Ther.* 25, 1279–1294. doi: 10.1016/j.ymthe.2017.03.031

Zhou, W., Fong, M. Y., Min, Y., Somlo, G., Liu, L., Yang, Y., et al. (2014). Cancer-Secreted miR-105 destroys vascular endothelial barriers to promote metastasis. *Cancer Cell* 25, 501–515. doi: 10.1016/j.ccr.2014.03.007

Conflict of Interest: The authors declare that the research was conducted in the absence of any commercial or financial relationships that could be construed as a potential conflict of interest.

frontiers in Cell and Developmental Biology

ORIGINAL RESEARCH
published: 06 August 2020
doi: 10.3389/fcell.2020.00744

LncRNA Xist Contributes to Endogenous Neurological Repair After Chronic Compressive Spinal Cord Injury by Promoting Angiogenesis Through the miR-32-5p/Notch-1 Axis

*Xing Cheng[1], Jin Xu[2], Zhengran Yu[1], Jinghui Xu[1] and Houqing Long[1]**

[1] Department of Spine Surgery, The First Affiliated Hospital, Sun Yat-sen University, Guangzhou, China, [2] State Key Laboratory of Biocontrol, School of Life Sciences, Sun Yat-sen University, Guangzhou, China

OPEN ACCESS

Edited by:
Xavier Figueroa, Pontificia Universidad Católica de Chile, Chile

Reviewed by:
Kangsheng Tu, The First Affiliated Hospital of Xi'an Jiaotong University, China
Xiaojian Cao, Nanjing Medical University, China
Mohsen Nategh, The University of Melbourne, Australia

***Correspondence:**
Houqing Long
houqinglong@163.com

Specialty section:
This article was submitted to Signaling, a section of the journal Frontiers in Cell and Developmental Biology

Received: *04 June 2020*
Accepted: *16 July 2020*
Published: *06 August 2020*

Citation:
Cheng X, Xu J, Yu Z, Xu J and Long H (2020) LncRNA Xist Contributes to Endogenous Neurological Repair After Chronic Compressive Spinal Cord Injury by Promoting Angiogenesis Through the miR-32-5p/Notch-1 Axis. Front. Cell Dev. Biol. 8:744. doi: 10.3389/fcell.2020.00744

Endogenous repair after chronic compressive spinal cord injury (CCSCI) is of great clinical interest. Ischemia-hypoxia-induced angiogenesis has been proposed to play an important role during this repair process. Emerging evidence indicates that long non-coding RNAs (lncRNAs) are involved in the pathophysiological processes of various diseases. Here, we identified a lncRNA (Xist; X-inactive specific transcript) with upregulated expression in cervical spine lesions during endogenous neurological repair in CCSCI rats. Therapeutically, the introduction of Xist to rats increased neurological function *in vivo* as assayed using the Basso, Beattie, and Bresnahan (BBB) score and inclined plane test (IPT). We found that the introduction of Xist enhanced endogenous neurological repair by promoting angiogenesis and microvessel density after CCSCI, while depletion of Xist inhibited angiogenesis and cell sprouting and migration. Mechanistically, Xist promoted angiogenesis by sponging miR-32-5p and modulating Notch-1 expression both *in vitro* and *in vivo*. These findings suggest a role of the Xist/miR-32-5p/Notch-1 axis in endogenous repair and provide a potential molecular target for the treatment of ischemia-related central nervous system (CNS) diseases.

Keywords: endogenous neurological repair, chronic compressive spinal cord injury, angiogenesis, Xist, miR-32-5p, Notch-1

INTRODUCTION

Chronic compressive spinal cord injury (CCSCI) is one of the most common causes of non-traumatic incomplete spinal cord injury (SCI) in middle-aged and elderly patients (Tetreault et al., 2015). Compression-induced ischemia-hypoxia is an important pathophysiological change after CCSCI (Fehlings and Skaf, 1998; Moghaddamjou et al., 2020). In the clinic, some patients with serious CCSCI show no neurological symptoms, while those with mild CCSCI may suffer different levels of neurological impairment. It is known that endogenous neurological repair after incomplete SCI plays an important role in the variation of neurological symptoms among patients (Raineteau and Schwab, 2001; Rasmussen and Carlsen, 2016). Understanding the molecular mechanisms underlying endogenous neurological repair will facilitate the clinical treatment of CCSCI.

It has been reported that vascular events after SCI not only affect the progress of secondary tissue damage but also establish a new environment that may promote neural plasticity in the chronically injured spinal cord (Mautes et al., 2000; Wang et al., 2018). We have previously revealed that the extent of angiogenesis is related to neurological function recovery following chronic compressive SCI (Long et al., 2014; Cheng et al., 2015). Zoe et al., reported that loss of proliferating NG2 + pericytes prevents intra-lesion angiogenesis and influences scar-forming processes, impairing endogenous repair after SCI in mice (Hesp et al., 2018). A therapy that uses intrathecal anti-Nogo-A antibodies is currently in clinical trials for SCI since it may improve vascular sprouting and repair and reduce neurological deficits (Zörner and Schwab, 2010; Rust et al., 2019). This evidence confirms that angiogenesis plays a key role in the progress of neurological repair after SCI, especially during the chronic injury phase. Many factors and pathways have been shown to be important in the regulation of angiogenesis (Casella et al., 2002; Kitamura et al., 2007; Acar et al., 2012; Yang et al., 2017; Ni et al., 2019). Notch-1 is a well-known factor that can alter the level of angiogenesis in various diseases including rheumatoid arthritis (Gao et al., 2012), cancer (Dos Santos et al., 2017; Jin et al., 2017), and psoriasis (Rooney et al., 2014) by regulating downstream genes.

Long non-coding RNAs (lncRNAs) have emerged as an important factor in multiple pathophysiological processes of central nervous system (CNS) diseases, such as angiogenesis, neurogenesis, and apoptosis (Chandran et al., 2017). For instance, the lncRNA CCAT2 promotes angiogenesis in glioma through the activation of VEGFA signaling by sponging miR-424 (Sun et al., 2020). The lncRNA MALAT-1 has been shown to have neuroprotective effects on spinal cord ischemic/reperfusion injury by regulating miR-204 (Qiao et al., 2018). LncRNAs have also been reported to participate in the regulation of stem cell self-renewal and differentiation in stroke-induced neurogenesis (Fan et al., 2020). Recent studies suggest that lncRNAs are important regulators of the pathophysiological processes of CNS diseases, especially those associated with ischemia; therefore, we are interested in the contribution of lncRNAs to endogenous neurological repair after CCSCI. Some research have proposed that the neurological functional recovery of female is often better than that of male after SCI in human and rodent studies (Sipski et al., 2004; Xiao et al., 2017). Interestingly, we identified a female specific lncRNA, X-inactive specific transcript (Xist), which showed differential expression during endogenous neurological repair in CCSCI rats. Bioinformatics analysis showed that Xist and Notch-1 (a well-known factor for angiogeneiss) are direct targets of miR-32-5p. We found that Xist improved neurological function *in vivo* by promoting angiogenesis through the miR-32-5p/Notch-1 axis. We further investigated the function of the Xist/miR-32-5p/Notch-1 axis in angiogenesis during endogenous neurological repair and confirmed its role in tube formation and cell sprouting and migration *in vitro*. Our findings indicate that the Xist/miR-32-5p/Notch-1 axis may be a novel molecular target for endogenous repair in ischemia-associated CNS diseases.

MATERIALS AND METHODS

Animal Studies

All experimental procedures were approved by the Research Ethics Committee of Sun Yat-sen University, Guangzhou, China and conformed to all relevant regulatory standards. In total, 192 adult female Sprague–Dawley rats (weighing 250–300 g; aged 28–30 weeks) were randomly allocated to the Sham (n = 25) and chronic compressive spinal cord injury (CCSCI) (n = 167) groups. According to the study duration and treatments, CCSCI rats were randomly divided into the following groups: the 4-week CCSCI group (4W SCI; n = 25); the 8-week CCSCI group (8W SCI; n = 43); the 8-week CCSCI with Xist small interfering RNA group (8W SCI + siXist; n = 31); the 8-week CCSCI with NC Xist siRNA group (8W SCI + NC siXist; n = 31); the 8-week with DAPT (8W SCI + DAPT; n = 8); the 8-week with NC DAPT (8W SCI + NC; n = 9); the 8-week with agomiR-32-5p group (8W SCI + agomiR-32-5p; n = 9); and the 8-week with agomiR-32-5p and Xist group (8W SCI + agomiR-32-5p + Xist; n = 11). The rats were housed in groups of 4-5 per cage on a 12/12-h light/dark cycle with free access to food and water.

Intraperitoneal/Intravenous Injection and Gene Delivery

DAPT solution (1 μg/μL) was prepared by dissolving DAPT powder (MCE, United States) in 0.01 M phosphate-buffered saline (PBS) containing 5% dimethyl sulfoxide. For gene delivery, 10 μL recombinant lentivirus (GeneCopoeia, Guangzhou, China) was delivered to the rats using a microinjection syringe via intraperitoneal or intravenous injection 4 wpi. Solutions at 5×10^7 titer units (TU)/mL containing 50 μL negative control, siXist, or Xist lentivirus (3 μL/g per rat), DAPT (1 mg/kg per rat) solution, and agomiR-32-5p (3.5 μL/g per rat) were used. AgomiR-32-5p was synthesized by BGI (Shenzhen, China). MiR-32-5p mimics and inhibitors were purchased from Guangzhou Yeshan Biological Technology Co., Ltd. The sequences are shown in **Supplementary Table S1**. HUVECs were transfected with miR-32-5p mimics, inhibitors, or their parental negative controls using Lipofectamine® 2000 reagent according to the manufacturer's instructions (Invitrogen).

Chronic Compressive Spinal Cord Injury

Each rat in the sham and CCSCI groups was anesthetized with 10% chloral hydrate (300 mg/kg) (Guangzhou FISCLAB Environ. Sci-Tech. Co., Ltd., Guangzhou, China).

Following exposure of the spinal process and laminas of C4-C6 from the posterior, the ligamentum flavum and C5 lamina were removed to access the epidural space. In the SCI group, the polymer (1→4)-3,6-anhydro-a-l-galactopyranosyl-(1→3)-β-D-galactopyranan) sheet (1 mm × 3 mm × 1 mm) was implanted into the C6 epidural space on the dorsal part of the spinal cord. Spinal cord compression was achieved by expansion of the polymer caused by liquid absorption (Long et al., 2014; Cheng et al., 2015). This sheet can absorb liquid in the spinal canal to expand its volume sevenfold (around 2.3 mm × 4.2 mm × 2.2 mm) at the end (Kim et al., 2004;

Long et al., 2013). In the sham group, the C5 lamina was removed without insertion of the polymer. Following surgery, the incision was closed in layers with complete hemostasis. To prevent dehydration, animals received a subcutaneous (s.c.) injection of lactated Ringer's solution (200 μL) immediately after surgery. All rats were administered an intramuscular injection of penicillin G (80 U/g) during surgery to prevent infection, and carprofen (4–5 mg/kg, Rimadyl, Pfizer) was injected subcutaneously 2 days post-surgery for further pain relief as needed. All surgeries were performed by the same experienced investigator.

Neurological Function Evaluation

To evaluate the recovery of neurological function after CCSCI, motor function was assessed using the Basso, Beattie, and Bresnahan (BBB) locomotor scale (Basso et al., 1995) and inclined plane test (IPT) (Chang et al., 2008) on day 1 post-injury (dpi) and 1, 2, 3, 4, 5, 6, 7, and 8 weeks post-injury (wpi). The range of BBB scores was between 0 and 21. A score of 0 reflects complete paralysis, whereas a score of 21 indicates normal locomotion. Lower scores (0–7) express isolated joint movements with little or no hindlimb movement; intermediate scores (8–13) express intervals of uncoordinated stepping; and higher scores (14–21) express forelimb and hindlimb coordination. For the IPT, rats were placed horizontally on a smooth tilt board. The angle of the board started from a horizontal position (0°) and increased by 5–10° after every attempt. The maximum angle at which the rats remained on the board for 10 s was recorded. BBB score raw data in the 8W SCI group were used to evaluate the recovery of animals at 8 wpi as compared with at 4 wpi [Recovery BBB score (SCI): BBB score (8 wpi) – BBB score (4 wpi); Recovery BBB score $\geq$ SD of recovery BBB score (SCI) was defined as significantly recovered, and no recovery was defined as a recovery BBB score $<$ SD of the recovery BBB score (SCI)]. The evaluation was conducted by two investigators blinded to the group assignments.

Micro-Computed Tomography

To assess the alteration in microvessel density in the lesion side of the cervical spinal cord, the cervical spinal cord of rats in different groups was subjected to micro-computed tomography (Micro-CT) (ZKKS-MCT-Sharp-II, Guangzhou Zhongkekaisheng Medical Technology Co., Ltd., Guangzhou, China) scanning after gelatin-lead oxide intracardiac injection. Animals were anesthetized with an overdose of 80–120 mg/kg intravenous sodium pentobarbital (Guangzhou Fischer Chemical Co., Ltd) and transcardially perfused using heparinized saline by adjusting the perfusion height (110 cm H_2O) and rate (20 mL/min). Subsequently, gelatin-lead oxide mixed liquor (medical gelatin 5 g, lead oxide 100 g, distilled water 100 mL) was continually infused into the aortic cannula by syringe (6–8 mL/min) for 5 min, until the viscera was completely red, to ensure full diffusion of the contrast medium. The cervical spinal cords were then carefully harvested and fixed overnight with 4% formaldehyde in phosphate-buffered solution. Prior to micro-CT scanning, the tissues surrounding the spine were carefully removed under a microscope. Three-dimensional reconstruction of each specimen was performed using the 3D-Med 4.3 software (Guangzhou ZhongkeKaisheng Medical Technology Co., Ltd., Guangzhou, China) and the relative microvessel density of all specimens in each group was calculated.

Immunohistochemistry

In brief, rats in different groups were euthanized with an overdose of intravenous sodium pentobarbital and transcardially perfused with 0.9% saline followed by 4% paraformaldehyde in 0.1 M phosphate buffer (PFA). The C5-C7 spinal cord was harvested, fixed overnight with 4% formaldehyde in phosphate-buffered solution at 4°C, and embedded in paraffin. A series of 25-μm thick spinal cord sections were used for immunohistochemical staining. Slides were placed in a plastic rack and vessel for microwave epitope retrieval. Sections were incubated overnight at 4°C with a rabbit polyclonal antibody against Notch-1 (1:200; ab8925, Abcam, Cambridge, United Kingdom), a mouse monoclonal antibody against HES-1 (1:50; sc-166410, Santa Cruz Biotechnology, Inc., United States), and a mouse monoclonal antibody against VEGFA (1:200; ab1316, Abcam, Cambridge, United Kingdom). Subsequently, the sections were sequentially incubated with a ready-to-use DAKO ChemMate EnVisionTM kit (cat. no. K500711; Dako; Agilent Technologies, Inc., Santa Clara, CA, United States) for 30 min at room temperature. Images of each section of the perilesional spinal cord were taken at 20×, 200×, and 400× magnification using an XC30 camera mounted on an Olympus microscope (Olympus Corporation, Tokyo, Japan). Three random images at 200 × magnification were captured for semi-quantitative analysis. The brown area in the sham spinal cord was analyzed and background density was excluded to create the standard. Subsequently, the integrated optical density (IOD) was calculated using the Image-Pro Plus 6.0 software (Media Cybernetics, Inc., Rockville, MD, United States).

In situ Hybridization

In situ hybridization (ISH) of HIF-1α was performed using a commercial kit (Wuhan Boster Bio., Co., Ltd) to evaluate the level of hypoxia at 4 wpi and 8 wpi. Briefly, spinal cord sections (4-μm) were dewaxed, dehydrated, and washed. Subsequently, endogenous peroxidase was blocked with 3% H_2O_2 and sections were pretreated with antigen retrieval using proteinase K (1 μg/mL) in citromalic acid (1 mol/L) at 37°C for 2 h. After prehybridization, the sections were hybridized using HIF-1α oligonucleotide probes (Wuhan Boster Bio., Co., Ltd) at 42°C overnight. The hybridization solution was removed by 2 × saline sodium citrate (SSC) at 37°C for 10 min, 1 × SSC twice at 37°C for 5 min, and 0.5 × SSC for 10 min at room temperature. Sections were then incubated with blocking solution (5% BSA in 1% PBST) at room temperature for 1 h. Subsequently, sections were incubated for 1 h at 37°C with biotinylated mouse anti-digoxin (Wuhan Boster Bio., Co., Ltd) followed by the addition of SABC solution (Wuhan Boster Bio., Co., Ltd) at 37°C for 20 min. A DAB chromogenic substrate kit was used and color development was controlled under a microscope within 30 minutes. Section were counterstained with Mayor's hematoxylin and dehydrated. Images of each section of the spinal cord were taken at 100× and 400× magnification using an XC30 camera mounted on an Olympus microscope (Olympus

Corporation, Tokyo, Japan). The cytoplasm staining of positive cells is brownish yellow.

Cell Culture

For *in vitro* experiments, human umbilical vein endothelial cells (HUVECs) and human embryonic kidney (HEK) 293T cells were purchased from the American Type Culture Collection (Manassas, VA, United States). Cells were cultured in Endothelial Cell Growth Medium (Merck, Darmstadt, Germany) supplemented with 10% heat-inactivated fetal bovine serum (FBS; Thermo Fisher Scientific, 10500-064) and 1% penicillin/streptomycin (Sigma, St. Louis, MO, United States). HEK-293T cells were cultured in Dulbecco's Modified Eagle Medium (DMEM; Gibco, Grand Island, NY, United States) supplemented with 10% FBS. HUVECs were seeded at an appropriate number on an appropriate size of culture flask (Sarstedt AG & Co., Nümbrecht, Germany). Cells were maintained in an incubator filled with 95% air and 5% CO_2 at 37°C. To simulate the hypoxic-ischemic conditions caused by CCSCI, HUVECs were incubated in a hypoxic incubator filled with 94% N_2, 5% CO_2, and 1% O_2 at 37°C, as previously described (Hu et al., 2019). There were 9 groups for *in vitro* experiments as follows: Control; Hypoxia; Hypoxia transfected with NC Xist siRNA (H + NC siXist); Hypoxia transfected with Xist siRNA (H + siXist); Hypoxia transfected with NC miR-32-5p (H + NC miR-32-5p); Hypoxia transfected with miR-32-5p mimics (H + miR-32-5p mimics); Hypoxia transfected with miR-32-5p mimics and Xist (H + miR-32-5p mimics + Xist); Hypoxia with DAPT treatment (H + DAPT); and Hypoxia with DAPT treatment and transfected with miR-32-5p inhibitors (H + DAPT + miR-32-5p inhibitors).

Tube Formation Assay

To evaluate the angiogenic capacity *in vitro*, HUVECs were harvested and seeded on Matrigel-coated 48-well plates (BD Biosciences) at a density of 2×10^4/well and incubated under different conditions (normal and hypoxia). Following different treatments for 48 h, tube formation was visualized and photographed using a phase contrast inverted microscope at 100 × magnification. Quantitation of the number of tubules was performed using the Image J software with the Angiogenesis Analyzer plugin16.

Sprouting Assay

To evaluate the sprouting capacity, a modified assay was performed as described previously (Hu et al., 2019). HUVEC monolayers were digested with 0.25% trypsin and seeded on a prepared 6-well plate in M199 medium containing 10% FBS. HUVECs were grown in clumps as observed under a microscope, following which the cell clusters were incubated with VEGF gel on a 24-well plate under different conditions. After 48 h, the total number of sprouts on the 5 cell clusters per well in each group was recorded and averaged.

Wound Healing Assay

To evaluate the migration capacity, the bottom of plates containing HUVECs at 90% confluence was scratched with a 1000-μL pipette tip to create a linear region void of cells. The media was then removed and the cells were washed with PBS, subjected to the appropriate treatment, and incubated under different conditions. Images of the denuded zone were recorded using an inverted microscope (Olympus, Japan) at 0 and 48 h. Data are representative of three individual experiments.

Real-Time Quantitative Polymerase Chain Reaction

Total RNA was extracted from the cervical spinal cord and HUVECs using TRIzol® regent (Invitrogen, Carlsbad, CA, United States) according to the manufacturer's protocol. The purity of the RNA was determined and reverse transcription (PrimeScriptTM RT reagent Kit) and real-time quantitative PCR (SYBR Premix Ex Taq II) were performed following the kit instructions (Takara Biotechnology Co., Ltd., China). The detailed primer sequences used in RT-qPCR are exhibited in **Supplementary Table S2**. Threshold cycle (CT) values were recorded and the relative expression of target genes was calculated using the equation $2^{-\Delta\Delta Ct}$ (Hu et al., 2019).

Luciferase Reporter Assay

The Xist fragment containing the putative miR-32-5p binding site was cloned into the pmirGlo vector (Promega, United States) and named WT Xist. Mutation of the putative miR-32-5p target sequence in the 3-UTR of Xist was generated using a site-directed gene mutagenesis kit (Takara) and named MUT Xist. HEK-293T cells were co-transfected separately with the two constructs or empty vector and miR-32-5p mimics or inhibitors. For miR-32-5p and Notch-1 interaction, the putative and mutated miR-32-5p target binding sequences in Notch-1 were synthesized and cells were co-transfected with the WT or MUT Notch-1 reporter gene plasmid or pmirGlo plasmids using Lipofectamine® 2000 (Invitrogen). At 48 h post-transfection, cells were harvested and the firefly luciferase activity was measured using a dual-luciferase reporter assay system (Promega) and normalized to Renilla luciferase activity (Jin et al., 2018; Hu et al., 2019).

Statistical Analysis

All data are expressed as the mean ± standard error of the mean (SEM). Statistical tests were carried out using the GraphPad Prism 7.0 software (San Diego, CA, United States). Motor function recovery results were analyzed by repeated measures analysis of variance (ANOVA) to reveal overall group differences and significant changes over time. A Student's *t*-test was performed for comparisons between two groups, and one-way analysis of variance followed by Tukey's *post hoc* test was used for comparisons among multiple groups. Statistical significance was set at $p < 0.05$.

RESULTS

Xist Promotes Endogenous Neurological Repair After CCSCI

Following incomplete chronic compressive spinal cord injury (CCSCI), endogenous neurological repair occurs in a sizable

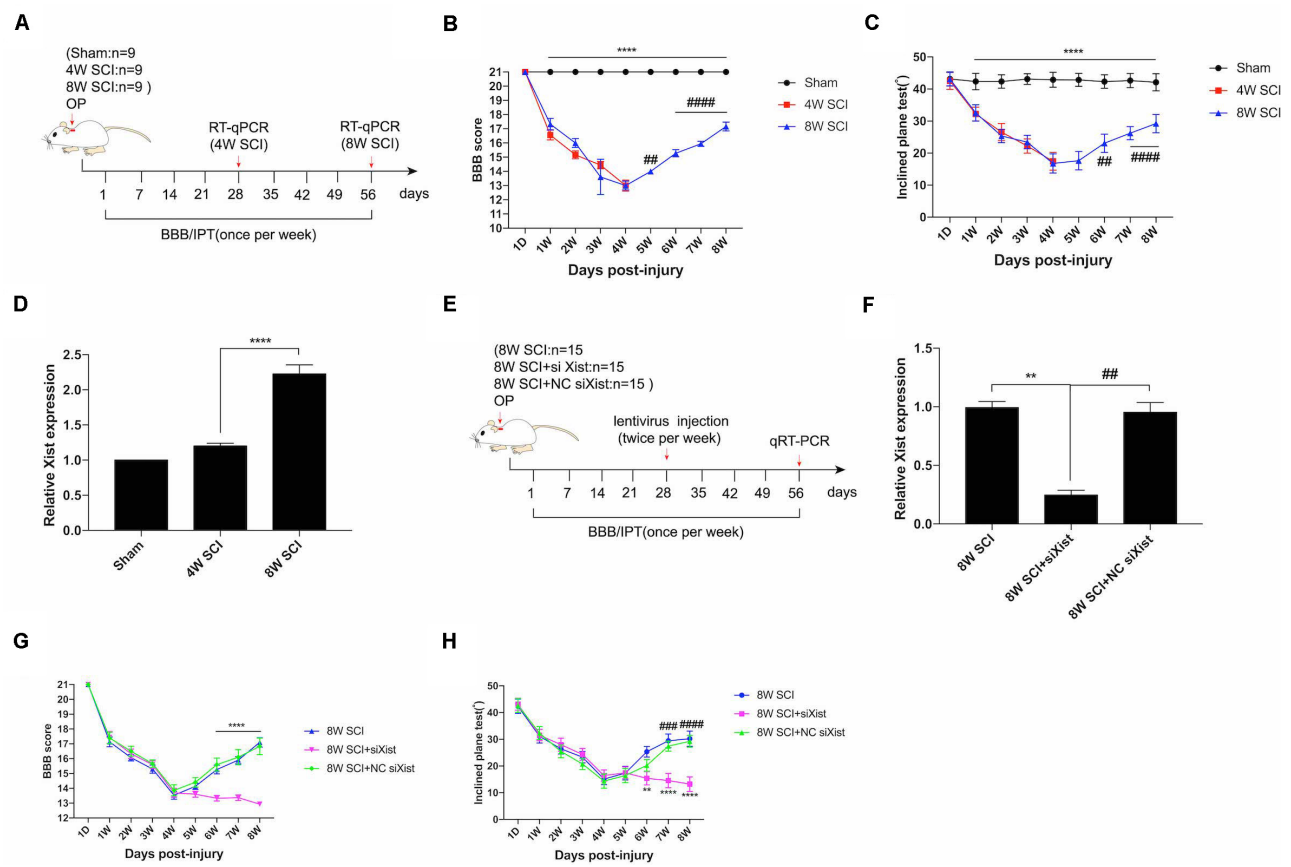

FIGURE 1 | Xist is upregulated during endogenous neurological repair after CCSCI. **(A)** Experimental design. **(B)** Animals were tested weekly starting from 1 dpi in an open field, and the endogenous neurological repair was evaluated according to the Basso, Beattie, and Bresnahan (BBB) score. $^{****}p < 0.0001$: the 8W SCI group vs. the sham group; $^{\#\#}p < 0.01$, $^{\#\#\#\#}p < 0.0001$: the 8W SCI group vs. the 4W SCI group. **(C)** Animals were tested weekly starting from 1 dpi using the inclined plane test (IPT), and the angle (°) was recorded to reveal endogenous neurological repair. $^{****}p < 0.0001$: the 8W SCI group vs. the sham group; $^{\#\#}p < 0.01$, $^{\#\#\#\#}p < 0.0001$: the 8W SCI group vs. the 4W SCI group. **(D)** Relative Xist expression in the cervical spinal cord was determined by RT-qPCR in the sham, 4W SCI, and 8W SCI groups. $^{****}p < 0.0001$: the 8W SCI group vs. the 4W SCI group. **(E)** Experimental design to explore the role of Xist in endogenous neurological repair. **(F)** Relative Xist expression in the cervical spinal cord was determined by RT-qPCR in the 8W SCI, 8W SCI + siXist, and 8W SCI + NC siXist groups. $^{**}p < 0.01$: the 8W SCI group vs. the 8W SCI + siXist group; $^{\#\#}p < 0.01$: the 8W SCI + siXist group vs. the 8W SCI + NC siXist group. **(G)** The endogenous neurological repair was evaluated using the BBB score. $^{****}p < 0.0001$: the 8W SCI + siXist group vs. the 8W SCI + NC siXist group. **(H)** The endogenous neurological repair was scored using the IPT. $^{**}p < 0.01$, $^{****}p < 0.0001$: the 8W SCI + siXist group vs. the 8W SCI group; $^{\#\#\#}p < 0.001$, $^{\#\#\#\#}p < 0.0001$: the 8W SCI + siXist group vs. the 8W SCI + NC siXist group. Data are expressed as the mean ± SEM.

number of patients; similar results have also been observed in animal models (Rosenzweig et al., 2010; Hilton et al., 2016; Rasmussen and Carlsen, 2016). Here, we used the Basso, Beattie, and Bresnahan (BBB) score and inclined plane test (IPT) to evaluate the changes in neurological function in a rat model of CCSCI. In our model, over 80% of rats significantly recovered from 4 wpi to 8 wpi (**Supplementary Figure S1**). Functional assays showed that the motor function gradually decreased from 1 wpi to 4 wpi and recovered from 4 wpi to 8 wpi (**Figures 1A–C**). The improvement in BBB and IPT scores at 8 wpi revealed that endogenous neurological repair was achieved. Interestingly, we found that the lncRNA Xist was markedly upregulated at 8 wpi (**Figure 1D**). To understand the role of Xist in endogenous neurological repair, we introduced siXist or its NC into CCSCI rats (**Figure 1E**) and examined the depletion effect using RT-qPCR (**Figure 1F**). As shown in **Figures 1G,H**, silencing Xist inhibited endogenous neurological repair. The neurological function, as indicated by the BBB and IPT scores, was not recovered from 4 wpi to 8 wpi following Xist depletion, indicating that Xist contributes to endogenous neurological repair.

Xist Promotes Angiogenesis After CCSCI *in vivo*

It has been reported that angiogenesis is an important process for endogenous spinal cord repair (Casella et al., 2002). To explore the biological changes after CCSCI and the effects of Xist on endogenous neurological repair, we measured angiogenesis after CCSCI using micro-CT (**Figure 2A**) and vascular endothelial growth factor (VEGF) staining (**Supplementary Figure S4A**) for different interventions. The compression material was clearly shown on CT, verifying spinal cord compression (**Figure 2C**).

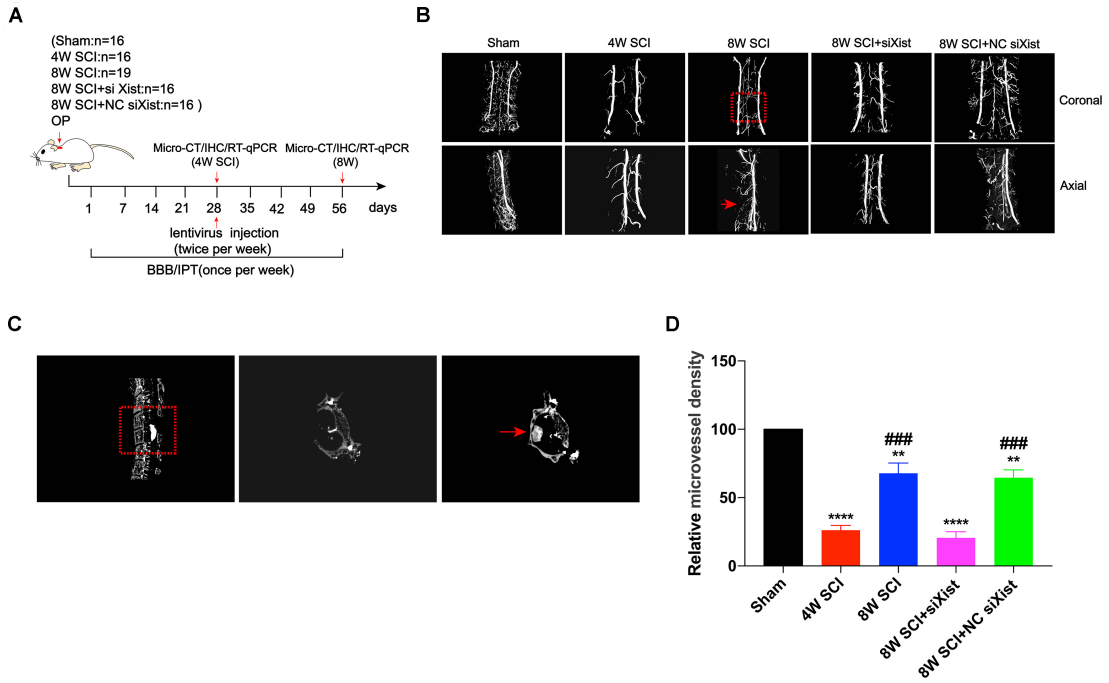

FIGURE 2 | Xist knockdown inhibits angiogenesis after CCSCI. **(A)** Experimental design. **(B)** Three-dimensional reconstruction and representative micro-CT images of microvessels of the cervical spinal cord in the sham and SCI groups. The red arrow indicates the compression site of the cervical spinal cord. **(C)** Representative sagittal and transverse CT images of the resected lamina of C5 and the compression material, respectively (red arrow). **(D)** Angiogenesis was evaluated by quantitation of the relative microvessel density. $^{**}p < 0.01$, $^{****}p < 0.0001$ as compared with the sham group; $^{###}p < 0.001$ as compared with the 4W SCI group. Data are expressed as the mean ± SEM.

After three-dimensional reconstruction of cervical spinal cord vessels, we found that the relative microvessel density was significantly decreased at 4 wpi (**Figure 2D**). The poor microvessel density of the cervical spinal cord indicated that a severe ischemia-hypoxia phase may occur at 4 wpi, as detected by assessing the expression level of HIF-1α (**Supplementary Figure S2**). These results are consistent with those reported in our previous study (Cheng et al., 2019). However, the relative microvessel density of the spinal cord was ameliorated at 8 wpi, accompanied by an improvement in motor function (**Supplementary Figure S3**). Knocking down the expression of Xist significantly decreased the microvessel density of the spinal cord as compared with the control or NC siXist at 8 wpi. No difference was seen at 4 wpi (**Figures 2B,D**). In addition, using VEGF as a marker of angiogenesis (Leung et al., 1989; Zeng et al., 2005), we found that depletion of Xist also significantly decreased VEGF expression (**Supplementary Figure S4B**). Taken together, these data indicate that the upregulation of Xist can promote angiogenesis and further improve endogenous neurological repair and motor function.

Notch-1 and Hes-1 Expression Are Downregulated After Xist Knockdown in CCSCI

It has been reported that Notch-1 is an important regulatory factor of angiogenesis (Gao et al., 2012). We confirmed that Notch-1 promoted angiogenesis and endogenous neurological repair after CCSCI by applying DAPT, a γ-secretase inhibitor, to deactivate the Notch-1/Hes-1 signaling pathway (**Figure 3A**). **Figures 3B,C** clearly show that neurological function was inhibited following injection of DAPT since endogenous neurological repair was not achieved at 8 wpi as compared with the control group. Further, we evaluated the alteration in microvessel density by micro-CT and found an increase in the control group at 8 wpi as expected (**Figure 3D**). On the contrary, following DAPT treatment, the relative microvessel density was significantly reduced as compared with the control group (**Figure 3E**). Moreover, VEGF immunostaining revealed that DAPT treatment decreased angiogenesis at 8 wpi following CCSCI (**Supplementary Figure S5**). These results confirm that Notch-1 plays a positive role in angiogenesis and endogenous neurological repair following CCSCI.

To elucidate whether Xist promotes angiogenesis through the Notch-1 pathway, we further detected the expression of Notch-1 and its downstream gene Hes-1 during CCSCI by immunohistochemistry following depletion of Xist (**Figure 3F**). We found that Notch-1 and Hes-1 expression in the cervical spinal cord were increased at 8 wpi in the 8W SCI group but significantly decreased following Xist depletion (**Figures 3G–J**). In addition, both Notch-1 and Hes-1 were mainly expressed in the compressive lesion site of the cervical spinal cord (**Figure 3F**). Similarly, RT-qPCR showed that the expression levels of Notch-1 and Hes-1 mRNA were significantly decreased

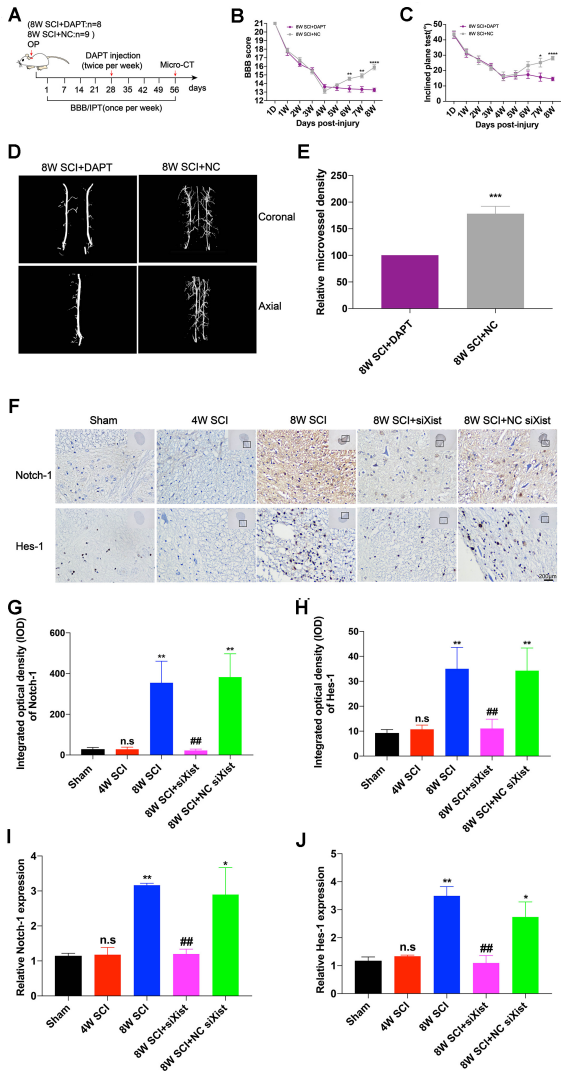

FIGURE 3 | Notch-1 promotes angiogenesis and endogenous neurological repair and causes downregulation of Notch-1 and Hes-1 after Xist depletion in CCSCI rats. **(A)** Experimental design. **(B)** Neurological function was evaluated using the BBB score. **(C)** Neurological function was evaluated using the IPT. **(D)** Three-dimensional reconstruction and representative micro-CT images of the microvessels of the cervical spinal cord. **(E)** Quantitation of the relative microvessel density. Data are expressed as the mean ± SEM. $^{*}p < 0.05$, $^{**}p < 0.01$, $^{****}p < 0.0001$. **(F)** Notch-1 and Hes-1 expression was assessed by immunohistochemistry (20 × and 400 × magnification; scale bar, 200 μm). Notch-1 and Hes-1 are mainly expressed in the lesion site of the cervical spinal cord. **(G)** Notch-1 immunohistochemical staining was quantitated by analyzing the integrated optical density (IOD). **(H)** Hes-1 immunohistochemical staining was quantitated by analyzing the integrated optical density (IOD). **(I)** The relative Notch-1 expression was assessed by RT-qPCR. **(J)** The relative Hes-1 expression was assessed by RT-qPCR. **(G–J)** ns (non-significant) as compared with the sham group; $^{*}p < 0.05$, $^{**}p < 0.01$ as compared with the 4W SCI group; $^{\#\#}p < 0.01$ as compared with the 8W SCI group. All data are expressed as the mean ± SEM. $^{*}p < 0.05$, $^{**}p < 0.01$, $^{***}p < 0.001$, $^{****}p < 0.0001$ as compared with 8W SCI + DAPT group.

after Xist depletion as compared with the 8W SCI and 8W SCI + NC siXist groups. The mRNA expression levels of Notch-1 and Hes-1 were no different between the 4W SCI and 8W SCI + siXist groups. These results indicate that Xist may promote angiogenesis and endogenous neurological repair by moderating Notch-1.

Xist and Notch-1 Are Direct Targets of miR-32-5p

To further explore the relationship between Xist and Notch-1, we identified both Xist and Notch-1 as target genes of miR-32-5p by bioinformatics analysis (**Figures 4A,B**). MiR-32-5p has been reported to play a role in various biological processes such as mediating neuroinflammation and neuropathic pain and promoting cell proliferation. In addition, we observed that miR-32-5p overexpression was increased at 4 wpi and significantly decreased at 8 wpi following CCSCI (**Figure 4C**). Depletion of Xist upregulated the expression of miR-32-5p as compared with the control group (**Figure 4D**), suggesting a possible interaction between Xist and miR-32-5p. To further validate the regulatory relationship between Xist, Notch-1, and miR-32-5p, we created wild-type and mutant dual-luciferase Xist and Notch-1 constructs and expressed them in HEK-293T cells (**Figures 4E,F**). The dual-luciferase reporter assay showed that miR-32-5p mimics suppressed the luciferase activity of wild-type Xist but had no effect on the luciferase activity of mutant Xist (**Figure 4G**). Similarly, miR-32-5p inhibitors increased the luciferase activity of wild-type Xist but had no effect on the luciferase activity of mutant Xist (**Figure 4H**). Moreover, co-transfection of miR-32-5p mimics and the luciferase vector containing wild-type Notch-1 downregulated the relative luciferase activity in HEK-293T cells (**Figure 4I**), while co-transfection of miR-32-5p inhibitors and the luciferase vector containing wild-type Notch-1 increased the relative luciferase activity in HEK-293T cells (**Figure 4J**). These results show that Xist and Notch-1 are direct targets of miR-32-5p *in vitro*.

Overexpression of miR-32-5p Inhibits Endogenous Neurological Repair and Angiogenesis After CCSCI

To explore the function of miR-32-5p and its interaction with Xist *in vivo*, we introduced agomiR-32-5p or agomiR-32-5p and Xist into rats at 4 wpi following CCSCI (**Figure 5A**). We found that rats exposed to agomiR-32-5p showed almost no endogenous neurological repair, while those exposed to agomiR-32-5p and Xist showed an improvement in neurological function (**Figures 5B,C**). The difference in miR-32-5p expression at 8 wpi was confirmed by RT-qPCR (**Figure 5D**).

We further investigated angiogenesis at 8 wpi after CCSCI by micro-CT (**Figures 5E,F**) and VEFG immunostaining (**Supplementary Figure S6A**). **Figure 5E** show that the overexpression of miR-32-5p significantly decreased angiogenesis in CCSCI rats; however, the overexpression of miR-32-5p and Xist had no effect on angiogenesis. Furthermore, the overexpression of miR-32-5p inhibited VEGF expression, while the overexpression of miR-32-5p and Xist significantly promoted VEGF expression at 8

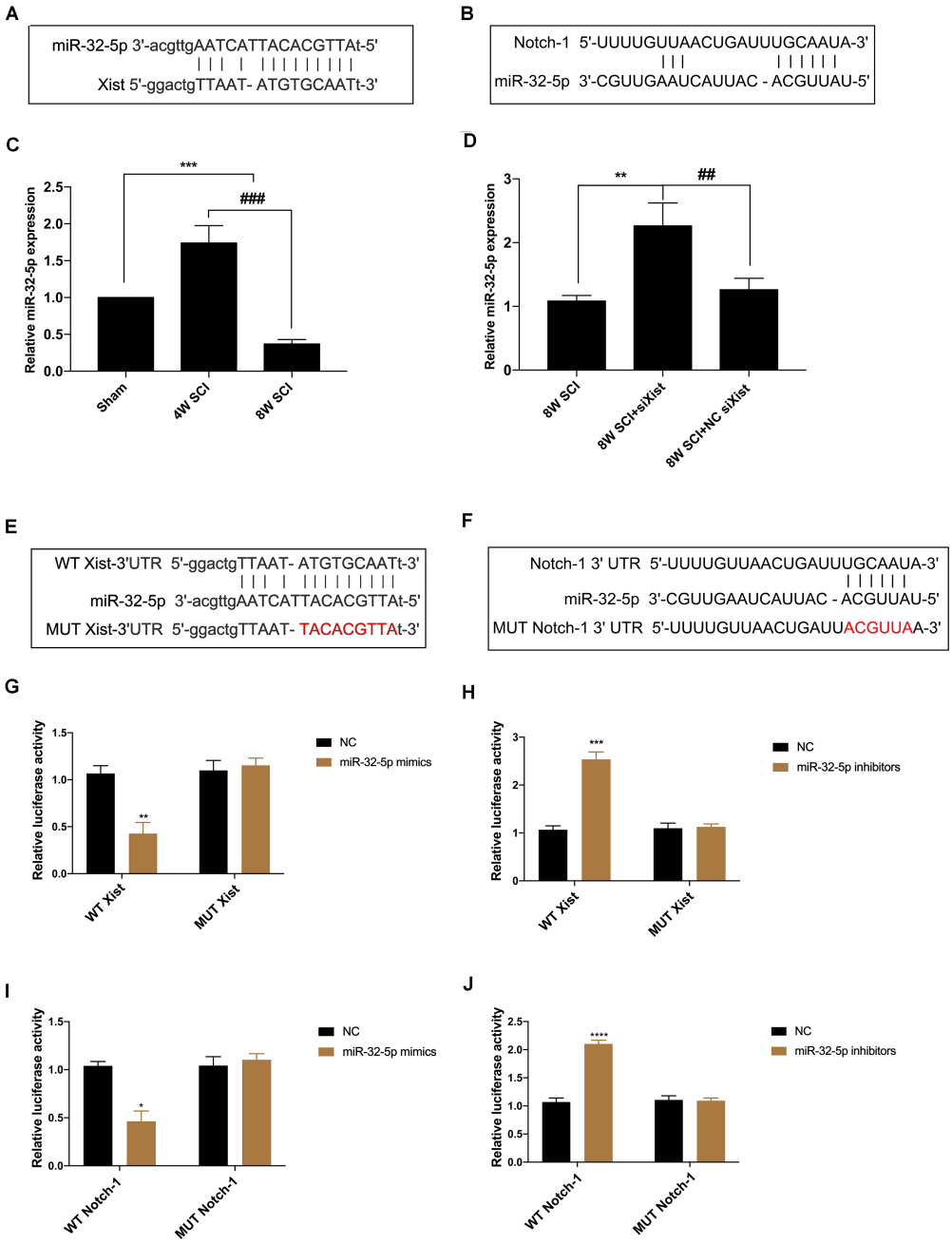

FIGURE 4 | Xist and Notch-1 are direct targets of miR-32-5p. **(A)** Binding regions between miR-32-5p and Xist. Bioinformatics analysis (ChipBase, LncRNAdb, and StarBase) was used to predict the target microRNA regulated by Xist. **(B)** Binding regions between Notch-1 and miR-32-5p. Bioinformatics analysis (TargetScan, Starbase, miRanda, and miRDB) was used to predict the putative target of miR-32-5p. **(C)** Quantitation of the relative miR-32-5p expression in the sham, 4W SCI, and 8W SCI groups by RT-qPCR. **(D)** Quantitation of the relative miR-32-5p expression in the 8W SCI, 8W SCI + siXist, and 8W SCI + NC siXist groups by RT-qPCR. **(E)** Dual-luciferase reporter constructs containing the wild-type (WT Xist) or mutant (MUT Xist) Xist sequence. **(F)** Dual-luciferase reporter constructs containing the wild-type (WT Notch-1) or mutant (MUT Notch-1) Notch-1 sequence. **(G)** Dual-luciferase reporter assay of miR-32-5p and Xist following transfection of miR-32-5p mimics. HEK-293T cells were co-transfected with the miR-32-5p mimics or corresponding NC and the dual-luciferase vector containing WT Xist or MUT Xist and incubated for 48 h. **(H)** Dual-luciferase reporter assay of miR-32-5p and Xist following transfection with miR-32-5p inhibitors. HEK-293T cells were co-transfected with the miR-32-5p inhibitors or the corresponding NC and the dual-luciferase vector containing WT Xist or MUT Xist. **(I)** Dual-luciferase reporter assay of Notch-1 and miR-32-5p following transfection of miR-32-5p mimics. HEK-293T cells were co-transfected with the miR-32-5p mimics or the corresponding NC and the dual-luciferase vector containing WT Notch-1 or MUT Notch-1 and incubated for 48 h. **(J)** Dual-luciferase reporter assay of miR-32-5p and Xist following transfection with miR-32-5p inhibitors. HEK-293T cells were co-transfected with miR-32-5p inhibitors or the corresponding NC and the dual-luciferase vector containing WT Xist or MUT Xist. Three independent experiments were carried out. $^{*}p < 0.05$, $^{**}p < 0.01$, $^{***}p < 0.001$. $^{****}p < 0.0001$; $^{\#\#}p < 0.01$, $^{\#\#\#}p < 0.001$. Data are expressed as the mean ± SEM.

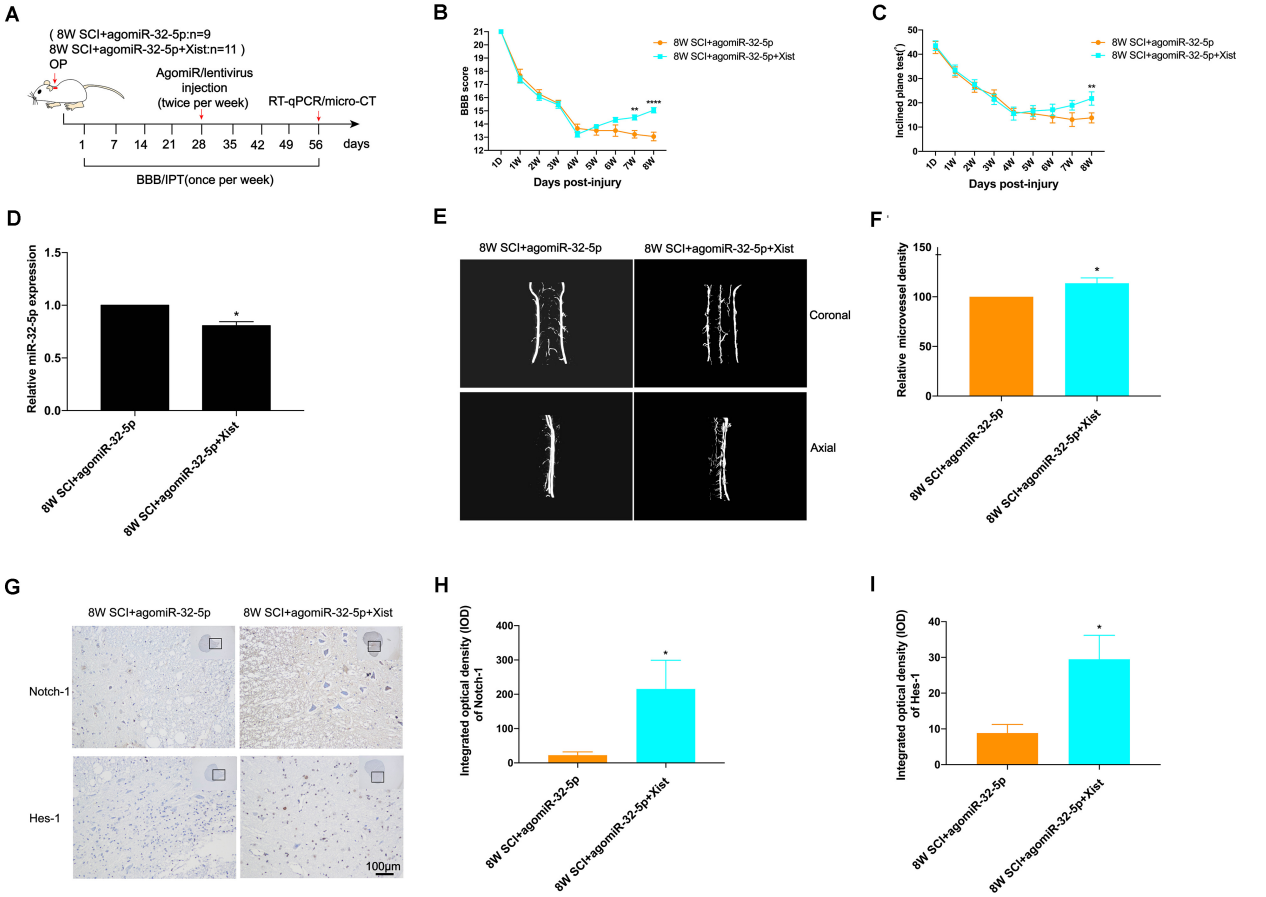

FIGURE 5 | Overexpression of miR-32-5p inhibits endogenous neurological repair and angiogenesis after CCSCI by decreasing Notch-1. **(A)** Experimental design. **(B)** Neurological function was evaluated by the BBB score. **(C)** Neurological function was evaluated by the IPT. **(D)** Quantitation of the relative miR-32-5p expression. **(E)** Three-dimensional reconstruction and representative micro-CT images of the microvessels of the cervical spinal cord. **(F)** Quantitation of the relative microvessel density. **(G)** Notch-1 and Hes-1 expression was assessed by immunohistochemistry (20 × and 200 × magnification; scale bar, 100 μm). **(H)** Notch-1 immunohistochemical staining was quantitated by analyzing the integrated optical density (IOD). **(I)** Hes-1 immunohistochemical staining was quantitated by analyzing the integrated optical density (IOD). $^{*}p < 0.05$, $^{**}p < 0.01$, $^{****}p < 0.0001$. Data are expressed as the mean ± SEM.

wpi (**Supplementary Figure S6B**). These data suggest that the overexpression of miR-32-5p can inhibit endogenous neurological repair and angiogenesis after CCSCI. Furthermore, we detected the expression levels of Notch-1 and Hes-1 by immunohistochemical staining and observed downregulation in the miR-32-5p group as compared with the miR-32-5p + Xist group (**Figures 5G–I**). These results demonstrate that miR-32-5p plays a role in endogenous neurological repair and angiogenesis through repression of the Notch-1 pathway by interacting with Xist.

Xist Promotes Angiogenesis by Regulating the miR-32-5p/Notch-1 Axis *in vitro*

To further understand the regulatory mechanism of the Xist/miR-32-5p/Notch-1 axis, we designed further experiments in cultured HUVECs under normal and hypoxic conditions to simulate the ischemic-hypoxic phase and evaluate tube formation, sprouting, and wound healing (**Figures 6A,C,E**). Similar to the *in vivo* experiments, we transfected HUVECs with siXist to downregulate the expression level of Xist, and with miR-32-5p mimics or inhibitors to alter the expression level of miR-32-5p. Moreover, we also used DAPT to inhibit the Notch-1 signal pathway *in vitro*. **Figure 6** clearly shows that tube formation, sprouting number, and migration rate were increased after 48 h under hypoxic conditions, which is consistent with the results that angiogenesis started at 4 wpi in CCSCI rats. In addition, in comparison with the other groups under hypoxic conditions, HUVECs transfected with siXist or miR-32-5p or treated with DAPT displayed significantly less tube formation and sprouting and a lower migration rate. However, not only did we find that co-transfection with miR-32-5p and Xist significantly promoted angiogenesis in HUVECs but also treatment with DAPT and downregulation of miR-32-5p increased angiogenesis under hypoxic conditions. These results indicate that overexpression of miR-32-5p negatively regulates HUVEC angiogenesis, and inversely, upregulation of Xist and Notch-1 promotes angiogenesis under hypoxic conditions (**Figures 6B,D,F**).

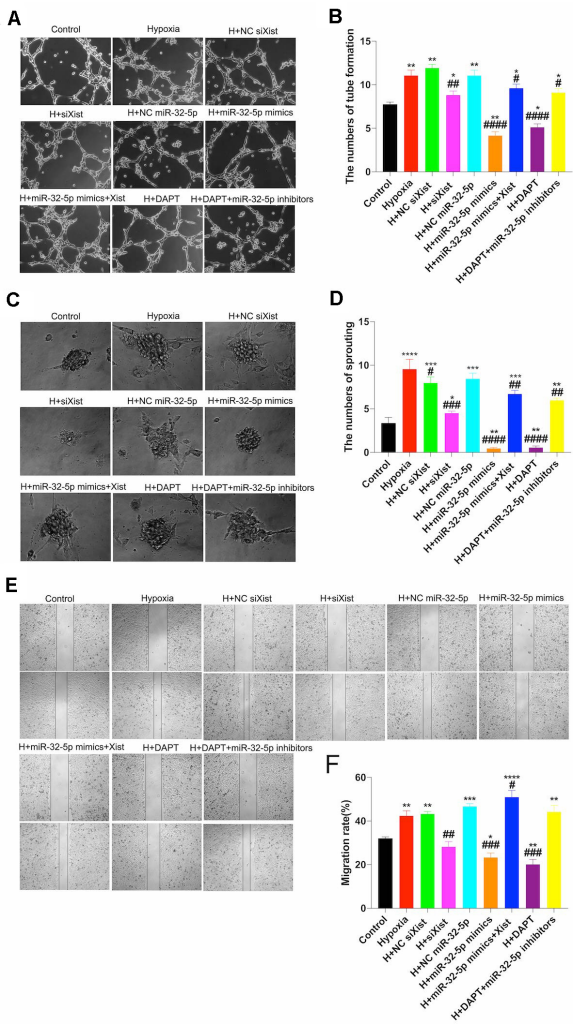

FIGURE 6 | Effect of the Xist/miR-32-5p axis on angiogenesis in HUVECs. **(A)** Representative images of the tube formation assay. HUVECs were exposed to different treatments for 48 h and subsequently subjected to hypoxia for a further 48 h. Tube formation was measured using a CCK8 kit, and sprouting and wound healing assays were performed. **(B)** Quantitation of tube formation was performed by RT-qPCR. **(C)** Representative images of the sprouting assay. **(D)** Quantitation of sprouting was performed by RT-qPCR. **(E)** Representative images of wound healing. **(F)** Quantitation of the migration rate was performed by RT-qPCR. Three independent experiments were carried out. $^{*}p < 0.05$, $^{**}p < 0.01$, $^{***}p < 0.001$, $^{****}p < 0.0001$ compared with the control group; $^{\#}p < 0.05$, $^{\#\#}p < 0.01$, $^{\#\#\#}p < 0.001$, $^{\#\#\#\#}p < 0.0001$ compared with the hypoxia group. Data are expressed as the mean ± SEM.

In addition, we confirmed that Xist expression was upregulated under hypoxic conditions (**Figure 7A**). Further, we detected Notch-1 and Hes-1 expression by RT-qPCR to explore whether alteration in the Xist/miR-32-5p axis regulates HUVEC angiogenesis via the Notch-1 pathway. In accordance with the Notch-1 expression pattern in CCSCI rats, Notch-1 (**Figure 7B**) and Hes-1 (**Figure 7C**) expression levels were higher in the hypoxia groups (Hypoxia; H + NC siXist; H + NC miR-32-5p; H + miR-32-5p mimics + Xist, and H + DAPT + miR-32-5p inhibitors) as compared with the normoxia groups. However, cells transfected with siXist or miR-32-5p mimics or treated with DAPT showed lower Notch-1 and Hes-1 expression levels than the hypoxia group (**Figures 7B,C**). These results further confirm that miR-32-5p can repress Notch-1 expression *in vitro*. Collectively, our data imply that lncRNA Xist is involved in endogenous neurological repair and angiogenesis by sponging miR-32-5p, which negatively regulates the expression of Notch-1 (**Figures 7D,E**).

DISCUSSION

The present study clearly demonstrates that Xist promoted endogenous neurological repair and angiogenesis after CCSCI. The functional impact of Xist may be through Notch-1, which plays a positive role in enhancing angiogenesis during endogenous neurological repair. Notch-1 and its downstream gene Hes-1 were decreased after depletion of Xist both *in vivo* and *in vitro*. Mechanistically, we found that Xist may act as a competing endogenous RNA (ceRNA) to repress the expression of miR-32-5p. We show that miR-32-5p directly targets Notch-1 to suppress its expression, leading to a reduction in angiogenesis and recessed endogenous neurological repair *in vivo*. In addition, overexpression of Xist sponged miR-32-5p and decreased its expression, improving endogenous neurological repair. Finally, we demonstrate that Xist promoted angiogenesis by regulating the miR-32-5p/Notch-1 axis.

For half a century, Xist has been known as a regulator that transcriptionally silences one of the X chromosomes in mammalian females to achieve dosage compensation. It is surprising to find that Xist can also promote endogenous neurological repair and angiogenesis after CCSCI. However, a significant difference in neuronal recovery between genders has been observed in both patients and animal models. In the last decade, the potential clinical relevance of gender to clinical and neurological outcomes after SCI has attracted much attention (Furlan et al., 2005, 2019a,b; Kay et al., 2010; Chan et al., 2013). With respect to the effects of different genders on locomotor recovery, Datto et al. (2015) reported significant differences in female rats as early as 4 weeks post-SCI, which remained significant at 13 weeks post-SCI. Similarly, others have proposed that the recovery of neurological function in females is often better than in males after SCI in both human and rodent studies (Sipski et al., 2004; Xiao et al., 2017). However, the underlying molecular mechanism for the gender difference in neurological function recovery has not yet been elucidated. In combination with previous observations from clinical and rodent studies, our findings provide new insight to explain the gender differences regarding endogenous neurological repair after CCSCI.

We propose that Xist contributes to endogenous spinal cord repair through the regulation of Notch-1 by competing for miR-32-5p. We identified that Xist and Notch-1 are targets of miR-32-5p by bioinformatics prediction and validated the regression effect of miR-32-5p using *in vitro* experiments. We found that miR-32-5p overexpression can decrease Notch-1, and co-transfection with Xist can offset the negative

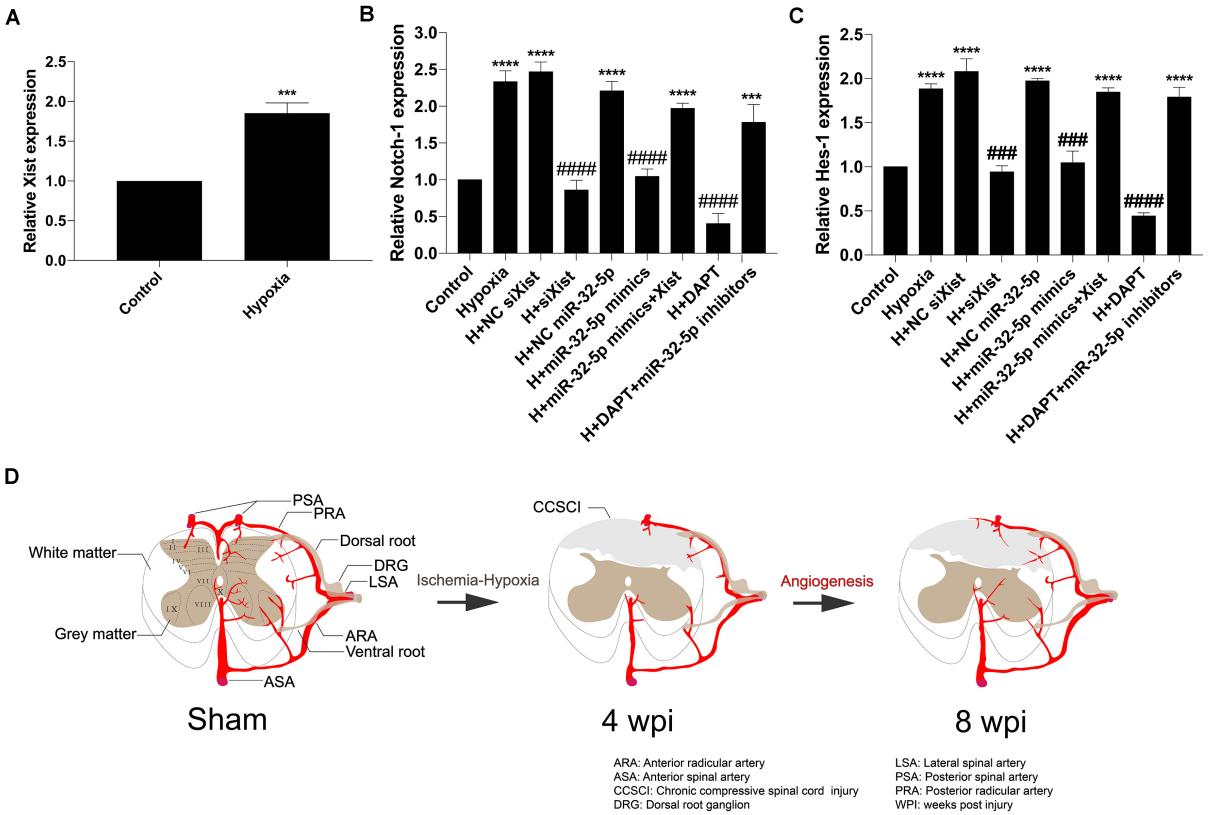

FIGURE 7 | The Xist/miR-32-5p axis exerts its role in angiogenesis by regulating Notch-1 expression. **(A)** The expression of Xist in HUVECs under hypoxic condition was quantitated by RT-qPCR. **(B)** HUVECs were exposed to different treatments. The expression of Notch-1 in HUVECs following transfection was quantitated by RT-qPCR. **(C)** The expression of Hes-1 following transfection was quantitated by RT-qPCR. Three independent experiments were carried out. $^{***}p < 0.001$, $^{****}p < 0.0001$ compared with the control group; $^{\#\#\#}p < 0.001$, $^{\#\#\#\#}p < 0.0001$ compared with the hypoxia group. Data are expressed as the mean ± SEM. **(D)** Diagram of the angiogenesis process after CCSCI. **(E)** The hypothetical function of Xist in hypoxia-induced angiogenesis in the current study.

biological effects resulting from overexpression of miR-32-5p. Canonically, Xist is localized in the nucleus, while miRNAs are typically found in the cytoplasm. One mystery remains: the location at which Xist sponges miR-32-5p. Many studies have shown that Xist can act as an miRNA sponge in other diseases: Wei et al. (2018) suggested that Xist contributes to neuropathic pain development by sponging miR-154-5p in rats with chronic constriction injury; Cheng et al. (2017) reported that Xist can promote glioma angiogenesis by acting as a molecular sponge of miR-429; Yu et al. (2017) showed that depletion of Xist is able to inhibit glioma angiogenesis and increase blood-tumor barrier permeability by targeting miR-137; and Hu et al. (2019) suggested that Xist participates in hypoxia-induced angiogenesis in human brain microvascular endothelial cells by regulating the miR-485/SOX7 axis. According to this evidence, we hypothesized that Xist may

be released from the nucleus and act as a sponge for miR-32-5p in our scenario. Xist has indeed been shown to be present throughout the cytoplasm by RNA-FISH and other techniques (Cabili et al., 2015; Carlevaro-Fita et al., 2016). Taken together, these data indicate that Xist plays an important role in the pathophysiology of ischemia-related diseases with respect to its basic molecular regulatory function.

In our previous studies, we have reported that angiogenesis is related to the recovery of neurological function (Long et al., 2014; Cheng et al., 2015). Here, we confirm that angiogenesis serves as a beneficial factor to improve neurological function after CCSCI, which is supported by many other published studies. For instance, the ubiquitously transcribed tetratricopeptide repeat on chromosome X (UTX)/lysine demethylase 6A (KDM6A) deletion in a mouse SCI model has been shown to promote neurological function by epigenetically regulating vascular regeneration (Ni et al., 2019). Moreover, hepatocyte growth factor was demonstrated to enhance endogenous repair and functional recovery in a rat SCI model by promoting neuron and oligodendrocyte survival, angiogenesis, and axonal regrowth (Kitamura et al., 2007). In the present study, we further found that Xist overexpression can improve neurological endogenous repair by promoting endogenous angiogenesis after CCSCI. Activation of the Notch-1 pathway, an important regulator of angiogenesis, is necessary for the process of endogenous neurological repair.

The current study also has several limitations. First, intraperitoneal/intravenous injection has been applied in nervous system studies as a systemic delivery method (Machida et al., 2013; Njoo et al., 2014). We also revealed that Xist expression was inhibited after Xist knockdown via systemic delivery methods. Intrathecal injection has shown benefits over other systemic delivery routes. These benefits include more specific spinal modulation, which permits reduced dosages and limits side effects. Technically, whether an intraperitoneal/intravenous delivery method can also result in side effects in other systems remains unclear. The second limitation is that ischemia-hypoxia changes were observed after CCSCI. However, more experiments are needed to further illuminate how hypoxia induces the upregulation of Xist after CCSCI. Thirdly, it remains unclear whether a different direction of the implant in the spinal cord may lead to compressive injury in a different spinal cord area or tract, thus resulting in different motor performance.

CONCLUSION

The present study indicates a positive role for the lncRNA Xist in endogenous spinal cord repair following CCSCI. We show that Xist can promote endogenous repair and facilitate angiogenesis by acting as an miR-32-5p/Notch-1 axis regulator. Our findings suggest that Xist may act as a novel molecular therapeutic target for CCSCI and provide new insight into the gender differences in CCSCI.

DATA AVAILABILITY STATEMENT

The original contributions presented in the study are included in the supplementary material, further inquiries can be directed to the corresponding author.

ETHICS STATEMENT

The animal study was reviewed and approved by The Research Ethics Committee of Sun Yat-sen University, Guangzhou, China.

AUTHOR CONTRIBUTIONS

XC performed the experiments, analyzed the data, and wrote the manuscript. JX conceived the study and revised the manuscript. ZY and JHX performed the experiments and analyzed the data. HL conceived, designed, and supervised the research. All authors read and approved the final manuscript.

FUNDING

This study was supported by the National Natural Science Foundation of China (81450020 to HL).

ACKNOWLEDGMENTS

We thank Prof. Yong Hu (Hong Kong University) for providing compressive materials.

SUPPLEMENTARY MATERIAL

The Supplementary Material for this article can be found online at: https://www.frontiersin.org/articles/10.3389/fcell.2020.00744/full#supplementary-material

REFERENCES

Acar, G., Tanrıöver, G., and Demir, R. (2012). Angiogenesis in neurological disorders: a review. *Neurol. Res.* 34, 627–635. doi: 10.1179/1743132812Y.0000000068

Basso, D. M., Beattie, M. S., and Bresnahan, J. C. (1995). A sensitive and reliable locomotor rating scale for open field testing in rats. *J. Neurotrauma* 12, 1–21. doi: 10.1089/neu.1995.12.1

Cabili, M. N., Dunagin, M. C., McClanahan, P. D., Biaesch, A., Padovan-Merhar, O., Regev, A., et al. (2015). Localization and abundance analysis of human lncRNAs at single-cell and single-molecule resolution. *Genome Biol.* 16:20. doi: 10.1186/s13059-015-0586-4

Carlevaro-Fita, J., Rahim, A., Guigó, R., Vardy, L. A., and Johnson, R. (2016). Cytoplasmic long noncoding RNAs are frequently bound to and degraded at ribosomes in human cells. *RNA* 22, 867–882. doi: 10.1261/rna.053561.115

Casella, G. T. B., Marcillo, A., Bunge, M. B., and Wood, P. M. (2002). New vascular tissue rapidly replaces neural parenchyma and vessels destroyed by a contusion injury to the rat spinal cord. *Exp. Neurol.* 173, 63–76. doi: 10.1006/exnr.2001.7827

Chan, W.-M., Mohammed, Y., Lee, I., and Pearse, D. D. (2013). Effect of gender on recovery after spinal cord injury. *Transl. Stroke Res.* 4, 447–461. doi: 10.1007/s12975-012-0249-7

Chandran, R., Mehta, S. L., and Vemuganti, R. (2017). Non-coding RNAs and neuroprotection after acute CNS injuries. *Neurochem. Int.* 111, 12–22. doi: 10.1016/j.neuint.2017.01.015

Chang, M.-W., Young, M.-S., and Lin, M.-T. (2008). An inclined plane system with microcontroller to determine limb motor function of laboratory animals. *J. Neurosci. Methods* 168, 186–194. doi: 10.1016/j.jneumeth.2007.09.013

Cheng, X., Long, H., Chen, W., Xu, J., Huang, Y., and Li, F. (2015). Three-dimensional alteration of cervical anterior spinal artery and anterior radicular artery in rat model of chronic spinal cord compression by micro-CT. *Neurosci. Lett.* 606, 106–112. doi: 10.1016/j.neulet.2015.08.050

Cheng, X., Long, H., Chen, W., Xu, J., Wang, X., and Li, F. (2019). The correlation between hypoxia-inducible factor-1α, matrix metalloproteinase-9 and functional recovery following chronic spinal cord compression. *Brain Res.* 1718, 75–82. doi: 10.1016/j.brainres.2019.04.034

Cheng, Z., Li, Z., Ma, K., Li, X., Tian, N., Duan, J., et al. (2017). Long Non-coding RNA XIST promotes glioma tumorigenicity and angiogenesis by acting as a molecular sponge of miR-429. *J Cancer* 8, 4106–4116. doi: 10.7150/jca.21024

Datto, J. P., Bastidas, J. C., Miller, N. L., Shah, A. K., Arheart, K. L., Marcillo, A. E., et al. (2015). Female rats demonstrate improved locomotor recovery and greater preservation of white and gray matter after traumatic spinal cord injury compared to males. *J. Neurotrauma* 32, 1146–1157. doi: 10.1089/neu.2014.3702

Dos Santos, S. N., Sheldon, H., Pereira, J. X., Paluch, C., Bridges, E. M., El-Cheikh, M. C., et al. (2017). Galectin-3 acts as an angiogenic switch to induce tumor angiogenesis via Jagged-1/Notch activation. *Oncotarget* 8, 49484–49501. doi: 10.18632/oncotarget.17718

Fan, B., Pan, W., Wang, X., Wei, M., He, A., Zhao, A., et al. (2020). Long non-coding RNA mediates stroke-induced neurogenesis. *Stem Cells* 38, 973–985. doi: 10.1002/stem.3189

Fehlings, M. G., and Skaf, G. (1998). A review of the pathophysiology of cervical spondylotic myelopathy with insights for potential novel mechanisms drawn from traumatic spinal cord injury. *Spine* 23, 2730–2737. doi: 10.1097/00007632-199812150-00012

Furlan, J. C., Craven, B. C., and Fehlings, M. G. (2019a). Is there any gender or age-related discrepancy in the waiting time for each step in the surgical management of acute traumatic cervical spinal cord injury? *J. Spinal Cord Med.* 42, 233–241. doi: 10.1080/10790268.2019.1614291

Furlan, J. C., Craven, B. C., and Fehlings, M. G. (2019b). Sex-related discrepancies in the epidemiology, injury characteristics and outcomes after acute spine trauma: a retrospective cohort study. *J. Spinal Cord Med.* 42, 10–20. doi: 10.1080/10790268.2019.1607055

Furlan, J. C., Krassioukov, A. V., and Fehlings, M. G. (2005). The effects of gender on clinical and neurological outcomes after acute cervical spinal cord injury. *J. Neurotrauma* 22, 368–381. doi: 10.1089/neu.2005.22.368

Gao, W., Sweeney, C., Connolly, M., Kennedy, A., Ng, C. T., McCormick, J., et al. (2012). Notch-1 mediates hypoxia-induced angiogenesis in rheumatoid arthritis. *Arthritis Rheum.* 64, 2104–2113. doi: 10.1002/art.34397

Hesp, Z. C., Yoseph, R. Y., Suzuki, R., Jukkola, P., Wilson, C., Nishiyama, A., et al. (2018). Proliferating NG2-cell-dependent angiogenesis and scar formation alter axon growth and functional recovery after spinal cord injury in mice. *J. Neurosci.* 38, 1366–1382. doi: 10.1523/JNEUROSCI.3953-16.2017

Hilton, B. J., Anenberg, E., Harrison, T. C., Boyd, J. D., Murphy, T. H., and Tetzlaff, W. (2016). Re-Establishment of cortical motor output maps and spontaneous functional recovery via spared dorsolaterally projecting corticospinal neurons after dorsal column spinal cord injury in adult mice. *J. Neurosci.* 36, 4080–4092. doi: 10.1523/JNEUROSCI.3386-15.2016

Hu, C., Bai, X., Liu, C., and Hu, Z. (2019). Long noncoding RNA XIST participates hypoxia-induced angiogenesis in human brain microvascular endothelial cells through regulating miR-485/SOX7 axis. *Am. J. Transl. Res.* 11, 6487–6497.

Jin, H., Du, X.-J., Zhao, Y., and Xia, D.-L. (2018). XIST/miR-544 axis induces neuropathic pain by activating STAT3 in a rat model. *J. Cell. Physiol.* 233, 5847–5855. doi: 10.1002/jcp.26376

Jin, Z., Zhan, T., Tao, J., Xu, B., Zheng, H., Cheng, Y., et al. (2017). MicroRNA-34a induces transdifferentiation of glioma stem cells into vascular endothelial cells by targeting Notch pathway. *Biosci. Biotechnol. Biochem.* 81, 1899–1907. doi: 10.1080/09168451.2017.1364965

Kay, E., Deutsch, A., Chen, D., Semik, P., and Rowles, D. (2010). Effects of gender on inpatient rehabilitation outcomes in the elderly with incomplete paraplegia from nontraumatic spinal cord injury. *J. Spinal Cord Med.* 33, 379–386. doi: 10.1080/10790268.2010.11689716

Kim, P., Haisa, T., Kawamoto, T., Kirino, T., and Wakai, S. (2004). Delayed myelopathy induced by chronic compression in the rat spinal cord. *Ann. Neurol.* 55, 503–511. doi: 10.1002/ana.20018

Kitamura, K., Iwanami, A., Nakamura, M., Yamane, J., Watanabe, K., Suzuki, Y., et al. (2007). Hepatocyte growth factor promotes endogenous repair and functional recovery after spinal cord injury. *J. Neurosci. Res.* 85, 2332–2342. doi: 10.1002/jnr.21372

Leung, D. W., Cachianes, G., Kuang, W. J., Goeddel, D. V., and Ferrara, N. (1989). Vascular endothelial growth factor is a secreted angiogenic mitogen. *Science* 246, 1306–1309. doi: 10.1126/science.2479986

Long, H.-Q., Li, G.-S., Lin, E.-J., Xie, W.-H., Chen, W.-L., Luk, K. D.-K., et al. (2013). Is the speed of chronic compression an important factor for chronic spinal cord injury rat model? *Neurosci. Lett.* 545, 75–80. doi: 10.1016/j.neulet.2013.04.024

Long, H.-Q., Xie, W.-H., Chen, W.-L., Xie, W.-L., Xu, J.-H., and Hu, Y. (2014). Value of micro-CT for monitoring spinal microvascular changes after chronic spinal cord compression. *Int. J. Mol. Sci.* 15, 12061–12073. doi: 10.3390/ijms150712061

Machida, A., Kuwahara, H., Mayra, A., Kubodera, T., Hirai, T., Sunaga, F., et al. (2013). Intraperitoneal administration of AAV9-shRNA inhibits target gene expression in the dorsal root ganglia of neonatal mice. *Mol. Pain* 9:36. doi: 10.1186/1744-8069-9-36

Mautes, A. E., Weinzierl, M. R., Donovan, F., and Noble, L. J. (2000). Vascular events after spinal cord injury: contribution to secondary pathogenesis. *Phys. Ther.* 80, 673–687. doi: 10.1093/ptj/80.7.673

Moghaddamjou, A., Badhiwala, J. H., and Fehlings, M. G. (2020). Degenerative cervical myelopathy: changing frontiers. *World Neurosurg.* 135, 377–378. doi: 10.1016/j.wneu.2019.12.138

Ni, S., Luo, Z., Jiang, L., Guo, Z., Li, P., Xu, X., et al. (2019). UTX/KDM6A deletion promotes recovery of spinal cord injury by epigenetically regulating vascular regeneration. *Mol. Ther.* 27, 2134–2146. doi: 10.1016/j.ymthe.2019.08.009

Njoo, C., Heinl, C., and Kuner, R. (2014). In vivo SiRNA transfection and gene knockdown in spinal cord via rapid noninvasive lumbar intrathecal injections in mice. *J. Vis. Exp.* 22:51229. doi: 10.3791/51229

Qiao, Y., Peng, C., Li, J., Wu, D., and Wang, X. (2018). LncRNA MALAT1 is neuroprotective in a rat model of spinal cord ischemia-reperfusion injury through miR-204 regulation. *Curr. Neurovasc. Res.* 15, 211–219. doi: 10.2174/1567202615666180712153150

Raineteau, O., and Schwab, M. E. (2001). Plasticity of motor systems after incomplete spinal cord injury. *Nat. Rev. Neurosci.* 2, 263–273. doi: 10.1038/35067570

Rasmussen, R., and Carlsen, E. M. (2016). Spontaneous functional recovery from incomplete spinal cord injury. *J. Neurosci.* 36, 8535–8537. doi: 10.1523/JNEUROSCI.1684-16.2016

Rooney, P., Connolly, M., Gao, W., McCormick, J., Biniecka, M., Sullivan, O., et al. (2014). Notch-1 mediates endothelial cell activation and invasion in psoriasis. *Exp. Dermatol.* 23, 113–118. doi: 10.1111/exd.12306

Rosenzweig, E. S., Courtine, G., Jindrich, D. L., Brock, J. H., Ferguson, A. R., Strand, S. C., et al. (2010). Extensive spontaneous plasticity of corticospinal projections after primate spinal cord injury. *Nat. Neurosci.* 13, 1505–1510. doi: 10.1038/nn.2691

Rust, R., Grönnert, L., Gantner, C., Enzler, A., Mulders, G., Weber, R. Z., et al. (2019). Nogo-A targeted therapy promotes vascular repair and functional recovery following stroke. *Proc. Natl. Acad. Sci. U.S.A.* 116, 14270–14279. doi: 10.1073/pnas.1905309116

Sipski, M. L., Jackson, A. B., Gómez-Marín, O., Estores, I., and Stein, A. (2004). Effects of gender on neurologic and functional recovery after spinal cord injury. *Arch. Phys. Med. Rehabil.* 85, 1826–1836. doi: 10.1016/j.apmr.2004.04.031

Sun, S.-L., Shu, Y.-G., and Tao, M.-Y. (2020). LncRNA CCAT2 promotes angiogenesis in glioma through activation of VEGFA signalling by sponging miR-424. *Mol. Cell. Biochem* 468, 69–82. doi: 10.1007/s11010-020-03712-y

Tetreault, L., Goldstein, C. L., Arnold, P., Harrop, J., Hilibrand, A., Nouri, A., et al. (2015). Degenerative cervical myelopathy: a spectrum of related disorders affecting the aging spine. *Neurosurgery* 77(Suppl. 4), S51–S67. doi: 10.1227/NEU.0000000000000951

Wang, T., Fang, X., and Yin, Z.-S. (2018). Endothelial progenitor cell-conditioned medium promotes angiogenesis and is neuroprotective after spinal cord injury. *Neural. Regen. Res.* 13, 887–895. doi: 10.4103/1673-5374.232484

Wei, M., Li, L., Zhang, Y., Zhang, Z.-J., Liu, H.-L., and Bao, H.-G. (2018). LncRNAX inactive specific transcript contributes to neuropathic pain development by sponging miR-154-5p via inducing toll-like receptor 5 in CCI rat models. *J. Cell. Biochem*. 120, 1271–1281. doi: 10.1002/jcb.27088

Xiao, J., Zhang, J., Zhao, Y., Huang, W., Guo, Z., Su, B., et al. (2017). Sex differences of steroid receptor coactivator-1 expression after spinal cord injury in mice. *Neurol. Res.* 39, 1022–1027. doi: 10.1080/01616412.2017.1367077

Yang, M., Li, C.-J., Sun, X., Guo, Q., Xiao, Y., Su, T., et al. (2017). MiR-497 195 cluster regulates angiogenesis during coupling with osteogenesis by maintaining endothelial Notch and HIF-1α activity. *Nat. Commun.* 8:16003. doi: 10.1038/ncomms16003

Yu, H., Xue, Y., Wang, P., Liu, X., Ma, J., Zheng, J., et al. (2017). Knockdown of long non-coding RNA XIST increases blood-tumor barrier permeability and inhibits glioma angiogenesis by targeting miR-137. *Oncogenesis* 6:e303. doi: 10.1038/oncsis.2017.7

Zeng, Q., Li, S., Chepeha, D. B., Giordano, T. J., Li, J., Zhang, H., et al. (2005). Crosstalk between tumor and endothelial cells promotes tumor angiogenesis by MAPK activation of Notch signaling. *Cancer Cell* 8, 13–23. doi: 10.1016/j.ccr.2005.06.004

Zörner, B., and Schwab, M. E. (2010). Anti-Nogo on the go: from animal models to a clinical trial. *Ann. N. Y. Acad. Sci.* 1198(Suppl. 1), E22–E34. doi: 10.1111/j.1749-6632.2010.05566.x

Conflict of Interest: The authors declare that the research was conducted in the absence of any commercial or financial relationships that could be construed as a potential conflict of interest.

frontiers in Cell and Developmental Biology

MINI REVIEW
published: 07 August 2020
doi: 10.3389/fcell.2020.00754

Laminins Regulate Placentation and Pre-eclampsia: Focus on Trophoblasts and Endothelial Cells

*Min Liu, Yangxue Yin, Hongbiao Yu and Rong Zhou**

Department of Obstetrics and Gynecology, West China Second University Hospital, Sichuan University; Key Laboratory of Birth Defects and Related Diseases of Women and Children, Sichuan University, Ministry of Education, Chengdu, China

Pre-eclampsia is a systemic vascular disease characterized by new-onset hypertension and/or proteinuria at ≥20 weeks of gestation and leads to high rates of maternal and perinatal morbidity and mortality. Despite the incomplete understanding of pre-eclampsia pathophysiology, it is accepted that insufficient spiral artery remodeling and endothelial dysfunction are major contributors. Laminins (LNs) are a vital family of extracellular matrix (ECM) molecules present in basement membranes that provide unique spatial and molecular information to regulate implantation and placentation. LNs interact with cell surface receptors to trigger intracellular signals that affect cellular behavior. This mini-review summarizes the role of LNs in placental development during normal pregnancy. Moreover, it describes how LN deficiency can lead to the pre-eclampsia, which is associated with trophoblast and vascular endothelial dysfunction. New research directions and the prospect of clinical diagnosis of LN deficiency are discussed, and the gaps in basic and clinical research in this field are highlighted.

Keywords: pre-eclampsia, laminin, trophoblast, endothelial dysfunction, placenta

OPEN ACCESS

Edited by:
Xavier Figueroa, Pontificia Universidad Católica de Chile, Chile

Reviewed by:
Luis Sobrevia, Pontificia Universidad Católica de Chile, Chile
Caroline Dunk, Lunenfeld-Tanenbaum Research Institute, Canada

***Correspondence:**
Rong Zhou
zhourong_hx@scu.edu.cn

Specialty section:
This article was submitted to Cellular Biochemistry, a section of the journal Frontiers in Cell and Developmental Biology

Received: *11 April 2020*
Accepted: *20 July 2020*
Published: *07 August 2020*

Citation:
Liu M, Yin Y, Yu H and Zhou R (2020) Laminins Regulate Placentation and Pre-eclampsia: Focus on Trophoblasts and Endothelial Cells. Front. Cell Dev. Biol. 8:754. doi: 10.3389/fcell.2020.00754

INTRODUCTION

Pre-eclampsia, is a pregnancy disease mainly characterized by gestational hypertension (≥140/90 mmHg) at gestation ≥20 weeks (Homer et al., 2008); it affects 3–5% of pregnancies and is more common in low- and middle-income countries (Ananth et al., 2013; Mol et al., 2016). Once diagnosed, the only effective treatment is cesarean delivery. Even if other appropriate treatment is administered for in pregnancy hypertensive diseases, there are still long-term effect on the children and mothers (Mate et al., 2019). Pre-eclampsia is a placental disease with two stages. The first is placental structure abnormality characterized by insufficient spiral artery remodeling and reduced placental perfusion. During a normal pregnancy, placentation begins with the recognition and adhesion of the trophectoderm to the uterine epithelium; trophoblast stem cells originate from the embryonic trophectoderm and differentiate into various trophoblast lineages [as reviewed in Silva and Serakides (2016)]. A recent review (Aplin et al., 2020) clearly summarized the steps in normal and failed uterine spiral arterial conversion. Cytotrophoblast cells invade into the decidua (interstitial trophoblast), and then the wall of maternal uterine spiral artery is destroyed, including the endothelium and smooth muscle cell. Extracellular matrix (ECM) components of the vessel wall are replaced with a fibro-fibrinoid structure, within which residual endovascular trophoblast often remains embedded. The remodeled uterine spiral arteries are characterized by lower resistance and higher flow, and they perfuse the placental villi to support

placental and fetal development (Brosens et al., 2019). However, conversion failure results in poor blood supply to the intervillous spaces (Brosens et al., 2011). The second stage is manifestation of maternal hypertension and proteinuria with systemic endothelial dysfunction. An imbalance between pro- and anti-angiogenic proteins can lead to increased blood pressure and pre-eclampsia in pregnancy. Some vascular endothelial protective factors [e.g., nitric oxide/nitric oxide synthase, vascular endothelial growth factor (VEGF)] are key factors in maintaining blood pressure, vascular endothelial environmental stability, and angiogenesis (Cudmore et al., 2006). Conversely, vascular endothelial damage factors [e.g., soluble fms-like tyrosine kinase 1 (sFlt-1), soluble endoglin (sEng)] exert anti-angiogenetic effects (De Falco, 2012; Graupner et al., 2019). The transition between the two stages is thought to be due to the release of such factors from the abnormally developed placenta into maternal circulation.

Normal placentation depends on cell-to-cell and cell-to-ECM interactions. The ECM consists of several unmodified and conjugated proteins such as collagen, fibronectin, laminins (LNs) and others that provide a microenvironment for placental cells and regulate cell functions including proliferation, migration, invasion, and signaling (Kim et al., 2014; Graubner et al., 2018). LNs are ECM molecules that comprise a family of glycoproteins found predominantly in basement membranes; they interact with cell surface receptors that transmit intracellular signals that regulate cellular behavior (Lala et al., 2012). Some studies have shown that LN deficiency is associated with many human diseases (McGowan and Marinkovich, 2000). Animal and human studies have shown that LNs are involved in placental development and affect the function of cytotrophoblastic cells (Kuo et al., 2018). This review outlines the critical role of LNs in placental development and molecular mechanisms involved in pre-eclampsia development.

STRUCTURE AND FUNCTION OF LAMININ

As shown in **Figure 1**, the basement membrane is the thin sheet of ECM that underlies epithelial and endothelial cells and surrounds muscle cells, Schwann cells, and connective tissue. LNs are ECM molecules that comprise a family of glycoproteins found predominantly in basement membranes, as a trimeric protein containing five α, three β, and three γ chains that are genetically distinct (Domogatskaya et al., 2012). The trimers are named according to their composition of α, β, and γ chains. For example, LN-523 is made of α5, β2, and γ3 chains (Tzu and Marinkovich, 2008).

Laminins influence cell adhesion, migration, phenotype maintenance, survival, and differentiation (Durbeej, 2010). The LNβ3 chain mediates apoptosis, proliferation, invasion, and metastasis of pancreatic cancer cells *via* the phosphoinositide 3-kinase (PI3K)/Akt signaling pathway (Zhang et al., 2019). Difficulties in isolating LN isoforms from tissues have hampered studies of their biological roles, and most information has come from research on diseases caused by gene mutations or using knockout mice. For instance, LNα5 gene mutation leads to defects in neural tube closure, finger separation, placentation, kidney formation, pulmonary lobe separation, hair morphogenesis, and intestinal smooth muscle differentiation (Miner and Li, 2000; Nguyen et al., 2002; Bolcato-Bellemin et al., 2003). Integrins, dystroglycan, syndecans, and Lutheran/basal cell adhesion molecule (BCAM) are cellular receptors for LNs (Desgrosellier and Cheresh, 2010; Aumailley, 2018; Jin et al., 2019). The biological effects of LNs are presumably largely mediated by surface receptors that link LN matrices to intracellular signaling pathways [as reviewed in Durbeej (2010)]. One group suggested that LNs promote the differentiation and proliferation of rat embryonic stem cells into cardiomyocytes by interacting with the integrin pathway (Wang et al., 2019). Lutheran/BCAM is oncogenic in human urothelial cancers in the presence of its ligands LN-511, LN-521 (Chang et al., 2017).

LAMININS AND PLACENTATION

Laminin is the basement membrane component that initially promotes cell adhesion and angiogenesis in early embryonic development (Givant-Horwitz et al., 2004). LN-111 affects cell-cell adhesion by changing the localization of vascular endothelial cadherin (Miner et al., 2004). LN activity is closely correlated with the blastocyst implantation window. LN levels in the basement membrane of the placental villi are decreased in late pregnancy compared to early pregnancy, due to the completion of the adhesion and infiltration process of placental trophoblasts (Turpeenniemi-Hujanen et al., 1992). Trophectoderm defects can lead to improper embryo implantation, and abnormal placental formation has deleterious effects on later stages of pregnancy, potentially causing conditions such as pre-eclampsia and intrauterine growth restriction (Red-Horse et al., 2004). Thus, LN is essential for proper embryo implantation and subsequent placental formation. One study showed that cytotrophoblast invasion was evident in some $LN\beta1^{-/-}$ mouse embryos, but the extent of invasion was greatly reduced compared with normal embryos (Miner et al., 2004). Moreover, cytotrophoblast behavior and differentiation may be affected by interactions with LN-specific isoforms, thereby regulating the structural formation of the placenta, and attachment of invasive trophoblasts to the basement membrane can trigger the expression of matrix metalloproteinases (MMPs) necessary for their separation from the basement membrane, degradation, and migration (Ramos et al., 1990). LN knockout (LNα1, LNβ1, LNβ5) is embryonic lethal in mice. During placental development, LNα5 knockout mice exhibit malformed placental labyrinths and abnormal trophoblast differentiation (Miner et al., 1998; Sekiguchi and Yamada, 2018). In addition, Pijnenborg et al. (1996) described a contribution of LNs to fibrinoid deposition within physiologically remodeled spiral arteries in baboons. Collectively, these findings indicate that LN is particularly important for the subsequent differentiation of cytotrophoblast cells and spiral artery remodeling.

Laminin activates cellular surface receptors to assist in its biological functions, and most recent studies have focused on integrins and LN-111 receptor (LR1). LNs and integrins differ

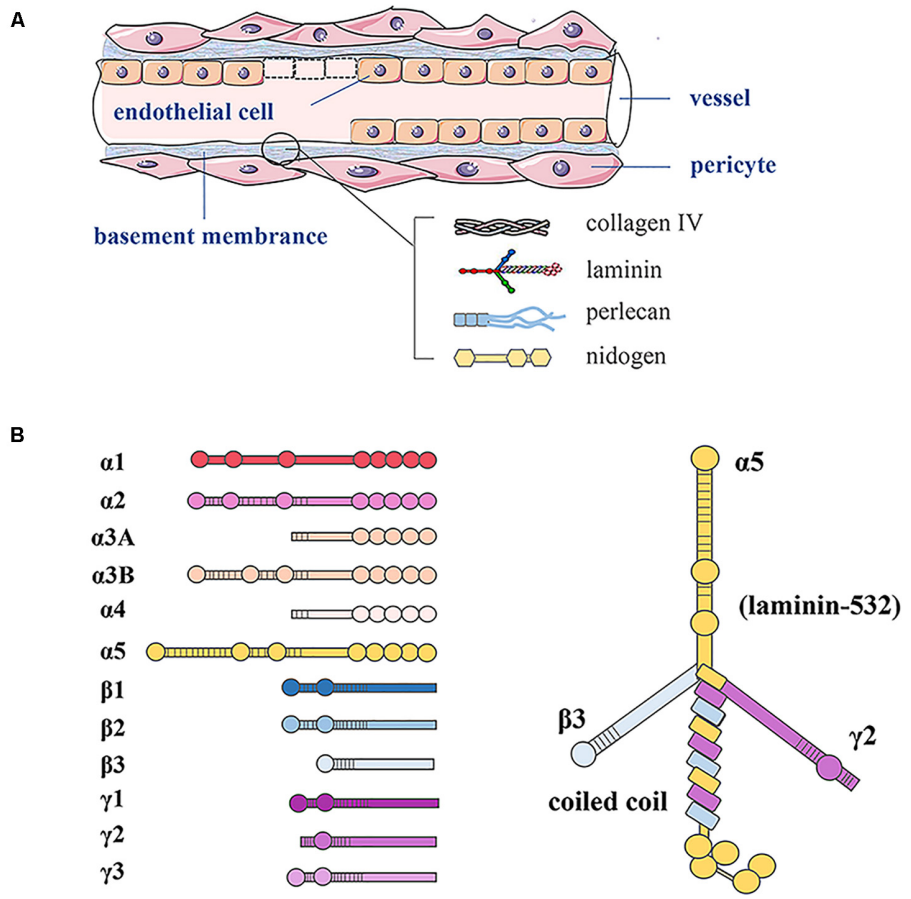

FIGURE 1 | Basement membrane constituents in vessels and LN structure. **(A)** In blood vessels, the basement membrane separates endothelial cells from supporting cells such as pericytes and connective tissue. The basement membrane consists of LN, type IV collagen, perlecan, and nidogen. **(B)** LN as a trimeric protein containing five α, three β, and three γ chains; all laminin chains share a common domain structure with a number of globular and rod-like domains.

in their binding specificities and affinities (typically including integrins α3β1, α6β1, α7β1, and α6β4), and integrin expression patterns are strictly regulated during placental development (Maltepe and Fisher, 2015). For example, integrins α6β1 and α7β1 bind to LNs and are abundant in the basement membrane of the endometrial epithelium during the implantation window (Merviel et al., 2001). Integrin serves as a master switch for cytotrophoblast transition from a proliferative (α6β4 and α5β1) to an invasive (α1β1) phenotype; this provides a foundation for studying pathological conditions characterized by insufficient trophoblast invasion (Kilburn et al., 2000). Increased LR1 expression in decidual cells of partial and complete moles may enable trophoblasts or other cells (e.g., endothelial cells and lymphocytes) to control invasion by modifying the structure of its primary ligand, LN-111 (Nelson et al., 2008; Kurdoglu et al., 2009).

LAMININS AND PRE-ECLAMPSIA

Trophoblast invasion of the uterine decidua and maternal vascular system is the key to successful embryo implantation and pregnancy, and LNs play a critical role in this multistep process. Despite an incomplete understanding of pre-eclampsia pathophysiology, it is generally though that the primary mechanisms are insufficient spiral artery remodeling and endothelial dysfunction (Gauster et al., 2009). Thus, we mainly analyze the relationship between LNs and pre-eclampsia from the perspective of improper regulation of LNs on biological behaviors of trophoblasts and vascular endothelial function.

Abnormal Biological Functions of Trophoblasts

In recent years, abnormal trophoblast function has been proposed to play a major role in pre-eclampsia pathogenesis. Potential cause of trophoblast invasion defect in pre-eclampsia including abnormal levels of cytokines, growth factors, placental factors, and interleukins (Moser et al., 2018). The ratio of type IV collagen to LNs is significantly higher in pre-eclamptic placentas compared to controls, most likely reflecting a lower level of LNs in the villi (Risteli et al., 1984). A study of microarray datasets reported that decreased expression of the LNα2 chain in the basal plate may be involved in the development of pre-eclampsia

(Winn et al., 2011). Proteomic analysis also showed that significantly lower LN levels in placental trophoblastic cells from pre-eclampsia pregnant women compared to controls, including LNβ2 (12.5-fold), LNα5 (9.1-fold), and LNγ1 chain (5.6-fold) (Ma et al., 2014). Pre-eclampsia placentas exhibit lower LNα5 chain levels, and this deficiency inhibits proliferation and invasion but promotes cell apoptosis in HTR-8/SVneo cells, possibly through inhibition of the PI3K/AKT/mammalian target of rapamycin (mTOR) signaling (Zhang et al., 2018). Downregulation of LNα4 also inhibited the proliferation, migration, and invasion of trophoblasts to suppress the expression of vascular factors in HTR-8/SVneo cells (Ji et al., 2019). Moreover, Shan et al. reported significantly lower expression of LNα4 in human pre-eclampsia placentas compared to control, and LNα4 plays a crucial role in trophoblast differentiation and invasion (Shan et al., 2015). Such changes in placental LN levels could weaken trophoblast attachment to the underlying basement membrane and also modify villi permeability and exchange properties.

Signal transduction *via* LRs in normal and malignant trophoblasts influence their adhesion to the basement membrane (Burrows et al., 1995). LR1 is a non-integrin-type receptor for LN-111 that exerts many effects on cell migration, adhesion, differentiation, invasion, signaling, and tumor metastasis. Decreased immunohistochemical staining for LR1 protein in cytotrophoblasts and syncytiotrophoblasts was observed in pre-eclamptic placentas, and decreased LR1 in cytotrophoblasts might lead to shallow trophoblastic invasion (Kurdoglu et al., 2011). LR1 knockdown remarkably suppressed the migration and invasion potential of JEG3 cells by reducing MMP-2 and MMP-9 activities, suggesting a possible pathogenetic mechanism of pre-eclampsia (Wang et al., 2013, 2015). Zhou et al. (1997) reported that trophoblastic invasion of the uterine spiral artery is limited because there is no decrease in integrin α6β4 and no increase in integrin α1β1 in pre-eclampsia pregnancies. Another group observed that integrin β1 mRNA was decreased in placental tissue from pre-eclampsia subjects, and then verified its involvement in dysregulating trophoblast cell invasion, survival, and angiogenesis in HTR8/Svneo cells (Li et al., 2013). The slightly decreased integrins αv and β1 subunits in the cytotrophoblasts may be a structural basis for poor placental perfusion in pre-eclampsia (Vatansever et al., 2003). Collectively, these findings demonstrate that integrin expression pattern are highly regulated during cytotrophoblast differentiation, and alterations in this process are the pathological basis of endovascular trophoblast invasion into the uterine spiral arteries.

Vascular Endothelial Dysfunction

Maternal endothelial dysfunction caused by placental factors (pro- and anti-angiogenic proteins) has long been considered one of the pathophysiological factors underlying severe pre-eclampsia (Roberts and Hubel, 2009). However, whether angiomodulatory imbalance is a consequence of an underlying pathology that is common to several different types of placental dysfunction is still unclear, as is whether it reflects a specific abnormality of earlier placental development (Aplin et al., 2020). There is now sufficient evidence to suggest that tissue-specific of LNs and their associated signaling regulates cell behavior and angiogenesis [as reviewed in Simon-Assmann et al. (2011)]. Native LN-111 from the human placenta can promote the formation of interconnected vascular networks among human umbilical vein endothelial cells (HUVECs) (Hackethal et al., 2018). LNα4 chain was strongly expressed in endothelial cells in placental villi and decidua, and its expression was decreased in third-trimester pre-eclamptic placentas (Thyboll et al., 2002). Moreover, LNα4 small-interfering RNA transfection and hypoxia-reoxygenation intervention reduced HUVEC migration and tube formation abilities by activating mitogen-activated kinase signaling (Shan et al., 2015). Down-regulated LNα5 is observed in pre-eclampsia placentas and inhibits HUVECs proliferation, migration, and angiogenesis through PI3K/AKT/mTOR pathways (Zhang et al., 2020). However, there are no data to indicate that the endothelial-derived LNα5 chain is involved in initiating the process as its expression occurs in the later stages of angiogenesis (Langen et al., 2017) when it plays critical roles in vascular stability, maturation, and barrier function (Sorokin et al., 1997; Liu et al., 2018). The above findings indicate that LNs are critical factors for endothelial cells to undergo angiogenesis and differentiate into interconnected tubules. LN deficiency may directly lead to abnormal angiogenesis and pathologic placental development. LNs also regulate angiogenesis through different vascular factors. Glomerular endothelial lesions associated with pre-eclampsia are caused by the blocking VEGF/VEGF receptor (VEGFR) and transforming growth factor-β/endoglin signaling pathways by sFlt-1 and sEng, respectively, leading to glomerular endothelial pore loss, cell swelling, and proteinuria (Abrass et al., 2006). A lack of LNα3 in mice or LNβ3 in humans leads to similar defects (Hata et al., 2005). Downregulation of αvβ3 integrin reduces the priming of endothelial cells and tubulogenesis by inhibiting VEGFR activation (Helal-Neto et al., 2016). LN-111 induces expression of pro-angiogenic molecules, such as VEGF and Cxc chemokine receptor 4, thus leading to increased angiogenesis and tumor growth (Mammadova-Bach et al., 2018). These lines of evidence suggest that LNs can directly and indirectly cause vascular endothelial dysfunction and induce severe pre-eclampsia.

The effect of LR signaling on endothelial cell functions is also important. Interaction between α6β1 integrin and LN-411 might promote endothelial cell migration *in vivo*, since their expression patterns overlap with those of newly formed capillaries, where endothelial cells are actively migrating (Sixt et al., 2001). Hypoxia transcriptionally upregulates angiogenic integrins (αv, β1, β3, and β5) in microvascular endothelial cells along with promoting migration and tube formation in human microvascular endothelial cells (Befani and Liakos, 2017). However, the relationship between LR-induced endothelial dysfunction and pre-eclampsia has not been investigated in detail.

FUTURE PERSPECTIVES

To date, most LN signaling studies in pre-eclampsia have focused on trophoblast function, but a few have investigated other aspects. One found that miR-126-3p promoted matrix-dependent

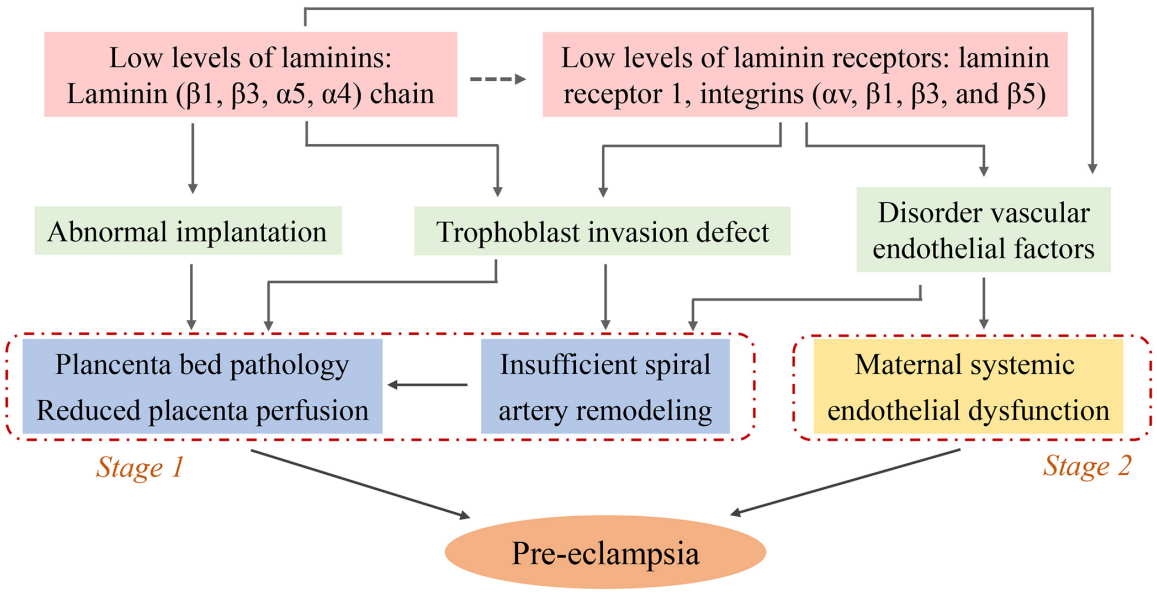

FIGURE 2 | Schematic diagram illustrating the potential causes for the low level of laminins induced- pre-eclampsia: focus on trophoblasts and endothelial cells. The decreased levels of serum LN and placental LN expression (pale pink) contribute to abnormal implantation, trophoblast invasion defect, and disorder vascular endothelial factors (pale green). These pathophysiological states lead to placenta bed pathology, insufficient uterine spiral artery remodeling (blue, known as stage 1 of pre-eclampsia) and maternal systemic endothelial dysfunction (yellow, known as stage 2 of pre-eclampsia). The figure leaves open the possibility that some LNs might play the role by binding to their receptors (dotted arrow, pale pink), while the role of these receptors is clearly known (solid arrow).

perivascular cell attachment, migration, and intercellular interaction (Pitzler et al., 2016). LN-111 is capable of inducing epigenetic changes by inhibiting Dnmt1 expression and preventing methylation of the E-cadherin promoter, ultimately promoting metastatic colonization during breast cancer (Benton et al., 2009). However, there is no clear epigenetic mechanism by which LNs regulate occurrence of pre-eclampsia pathogenesis. It is also noteworthy that vascular endothelial cells express only two LN isoforms: LN-411 and LN-511. LN-411 is expressed by all endothelial cells regardless of their developmental stage, and its expression is strongly upregulated by cytokines and growth factors involved in inflammatory events. LN-511 is primarily detectable in endothelial cell basement membranes of capillaries and venules beginning 3–4 weeks postnatal, and its expression is only upregulated by strong proinflammatory signals (Hallmann et al., 2005). Moreover, the ECM can regulate chemokine production in damaged endothelial cells (Zimmerlin et al., 2013). Thus, we hypothesized that LNs expressed by endothelial cells might be involved in the inflammatory response during pre-eclampsia pathogenesis.

Mortality from pre-eclampsia has decreased significantly in the United States due to increased prenatal monitoring and early intervention (Ghossein-Doha et al., 2018). Therefore, it is of considerable significance to explore and identify biomarkers for the detection or control of pre-eclampsia and to develop targeted strategies. Serum or plasma angiogenic factors and cytokines appear to be a reliable risk-stratification approach among women with suspected pre-eclampsia, such as sFlt-1, sEng, placental growth factor (PlGF), interleukin-6, and the sFlt-1/PlGF ratio (Chaiworapongsa et al., 2014). Serum LN level is an important index to assess the degree of liver fibrosis in chronic hepatitis (Lebensztejn et al., 2004). So, could LN be a promising biomarker for diagnosing pre-eclampsia? There is a paucity of prospective studies in this filed with both large sample sizes and well-defined, strict inclusion and exclusion criteria. Furthermore, it is necessary to develop specific and sensitive assays for clinical measurement of LNs.

CONCLUSION

Laminins play a critical role in pre-eclampsia as demonstrated by a series of clinical and basic studies. Serum LN levels and placental LN expression are decreased in pre-eclamptic pregnancies. Low LN levels are able to induce abnormal biological functions of placental trophoblast cells and vascular endothelial dysfunction, which lead to implantation failure, inappropriate placental spiral artery remodeling and placental vascular injury, these are the main pathological bases for pre-eclampsia. Moreover LRs, especially integrin-type receptor-mediated signaling pathways may be important contributors (summarized in **Figure 2**). However, the specific molecular mechanisms are complex and unclear, and a more detailed understanding of the signaling mechanisms is needed. This review proposed a possible mechanism of altered LN-induced pre-eclampsia, including epigenetic modifications, cytokines, and inflammatory events. Finally, LNs are promising diagnostic and prognostic biomarkers for this disease. Additional studies can help guide the use of LN clinical diagnosis and identify prevention and treatment targets for pre-eclampsia.

AUTHOR CONTRIBUTIONS

ML and RZ designed the outline of the review and wrote the initial manuscript. All authors edited and approved the final manuscript.

FUNDING

This work was supported by the National Natural Science Foundation of China (Nos. 81571465 and 81871175).

REFERENCES

Abrass, C. K., Berfield, A. K., Ryan, M. C., Carter, W. G., and Hansen, K. M. (2006). Abnormal development of glomerular endothelial and mesangial cells in mice with targeted disruption of the lama3 gene. *Kidney Int.* 70, 1062–1071. doi: 10.1038/sj.ki.5001706

Ananth, C. V., Keyes, K. M., and Wapner, R. J. (2013). Pre-eclampsia rates in the United States, 1980-2010: age-period-cohort analysis. *BMJ* 347:f6564. doi: 10.1136/bmj.f6564

Aplin, J. D., Myers, J. E., Timms, K., and Westwood, M. (2020). Tracking placental development in health and disease. *Nat. Rev. Endocrinol.* 1–16. doi: 10.1038/s41574-020-0372-6

Aumailley, M. (2018). Isolation and analysis of laminins. *Methods Cell Biol.* 143, 187–205. doi: 10.1016/bs.mcb.2017.08.011

Befani, C., and Liakos, P. (2017). Hypoxia upregulates integrin gene expression in microvascular endothelial cells and promotes their migration and capillary-like tube formation. *Cell Biol. Int.* 41, 769–778. doi: 10.1002/cbin.10777

Benton, G., Crooke, E., and George, J. (2009). Laminin-1 induces E-cadherin expression in 3-dimensional cultured breast cancer cells by inhibiting DNA methyltransferase 1 and reversing promoter methylation status. *FASEB J.* 23, 3884–3895. doi: 10.1096/fj.08-128702

Bolcato-Bellemin, A. L., Lefebvre, O., Arnold, C., Sorokin, L., Miner, J. H., Kedinger, M., et al. (2003). Laminin alpha5 chain is required for intestinal smooth muscle development. *Dev. Biol.* 260, 376–390. doi: 10.1016/s0012-1606(03)00254-9

Brosens, I., Pijnenborg, R., Vercruysse, L., and Romero, R. (2011). The "great obstetrical syndromes" are associated with disorders of deep placentation. *Am. J. Obstet. Gynecol.* 204, 193–201. doi: 10.1016/j.ajog.2010.08.009

Brosens, I., Puttemans, P., and Benagiano, G. (2019). Placental bed research: I. The placental bed: from spiral arteries remodeling to the great obstetrical syndromes. *Am. J. Obstet. Gynecol.* 221, 437–456. doi: 10.1016/j.ajog.2019.05.044

Burrows, T. D., King, A., Smith, S. K., and Loke, Y. W. (1995). Human trophoblast adhesion to matrix proteins: inhibition and signal transduction. *Hum. Reprod.* 10, 2489–2500. doi: 10.1093/oxfordjournals.humrep.a136329

Chaiworapongsa, T., Chaemsaithong, P., Yeo, L., and Romero, R. (2014). Pre-eclampsia part 1: current understanding of its pathophysiology. *Nat. Rev. Nephrol.* 10, 466–480. doi: 10.1038/nrneph.2014.102

Chang, H. Y., Chang, H. M., Wu, T. J., Chaing, C. Y., Tzai, T. S., Cheng, H. L., et al. (2017). The role of Lutheran/basal cell adhesion molecule in human bladder carcinogenesis. *J. Biomed. Sci.* 24:61. doi: 10.1186/s12929-017-0360-x

Cudmore, M., Ahmad, S., Al-Ani, B., Hewett, P., Ahmed, S., and Ahmed, A. (2006). VEGF-E activates endothelial nitric oxide synthase to induce angiogenesis via cGMP and PKG-independent pathways. *Biochem. Biophys. Res. Commun.* 345, 1275–1282. doi: 10.1016/j.bbrc.2006.04.031

De Falco, S. (2012). The discovery of placenta growth factor and its biological activity. *Exp. Mol. Med.* 44, 1–9. doi: 10.3858/emm.2012.44.1.025

Desgrosellier, J. S., and Cheresh, D. A. (2010). Integrins in cancer: biological implications and therapeutic opportunities. *Nat. Rev. Cancer* 10, 9–22. doi: 10.1038/nrc2748

Domogatskaya, A., Rodin, S., and Tryggvason, K. (2012). Functional diversity of laminins. *Annu. Rev. Cell Dev. Biol.* 28, 523–553. doi: 10.1146/annurev-cellbio-101011-155750

Durbeej, M. (2010). Laminins. *Cell Tissue Res.* 339, 259–268. doi: 10.1007/s00441-009-0838-2

Gauster, M., Moser, G., Orendi, K., and Huppertz, B. (2009). Factors involved in regulating trophoblast fusion: potential role in the development of preeclampsia. *Placenta* 30(Suppl. A), S49–S54. doi: 10.1016/j.placenta.2008.10.011

Ghossein-Doha, C., Hooijschuur, M. C. E., and Spaanderman, M. E. A. (2018). Pre-Eclampsia: a twilight zone between health and cardiovascular Disease? *J. Am. Coll. Cardiol.* 72, 12–16. doi: 10.1016/j.jacc.2018.04.049

Givant-Horwitz, V., Davidson, B., and Reich, R. (2004). Laminin-induced signaling in tumor cells: the role of the M(r) 67,000 laminin receptor. *Cancer Res.* 64, 3572–3579. doi: 10.1158/0008-5472.CAN-03-3424

Graubner, F. R., Boos, A., Aslan, S., Kucukaslan, I., and Kowalewski, M. P. (2018). Uterine and placental distribution of selected extracellular matrix (ECM) components in the dog. *Reproduction* 155, 403–421. doi: 10.1530/REP-17-0761

Graupner, O., Karge, A., Flechsenhar, S., Seiler, A., Haller, B., Ortiz, J. U., et al. (2019). Role of sFlt-1/PlGF ratio and feto-maternal Doppler for the prediction of adverse perinatal outcome in late-onset pre-eclampsia. *Arch. Gynecol. Obstet.* 301, 375–385. doi: 10.1007/s00404-019-05365-9

Hackethal, J., Schuh, C., Hofer, A., Meixner, B., Hennerbichler, S., Redl, H., et al. (2018). Human placenta Laminin-111 as a multifunctional protein for tissue engineering and regenerative medicine. *Adv. Exp. Med. Biol.* 1077, 3–17. doi: 10.1007/978-981-13-0947-2_1

Hallmann, R., Horn, N., Selg, M., Wendler, O., Pausch, F., and Sorokin, L. M. (2005). Expression and function of laminins in the embryonic and mature vasculature. *Physiol. Rev.* 85, 979–1000. doi: 10.1152/physrev.00014.2004

Hata, D., Miyazaki, M., Seto, S., Kadota, E., Muso, E., Takasu, K., et al. (2005). Nephrotic syndrome and aberrant expression of laminin isoforms in glomerular basement membranes for an infant with Herlitz junctional epidermolysis bullosa. *Pediatrics* 116, e601–e607. doi: 10.1542/peds.2005-0160

Helal-Neto, E., Brandao-Costa, R. M., Saldanha-Gama, R., Ribeiro-Pereira, C., Midlej, V., Benchimol, M., et al. (2016). Priming endothelial cells with a melanoma-derived extracellular matrix triggers the activation of alphavbeta3/VEGFR2 axis. *J. Cell Physiol.* 231, 2464–2473. doi: 10.1002/jcp.25358

Homer, C. S., Brown, M. A., Mangos, G., and Davis, G. K. (2008). Non-proteinuric pre-eclampsia: a novel risk indicator in women with gestational hypertension. *J. Hypertens.* 26, 295–302. doi: 10.1097/HJH.0b013e3282f1a953

Ji, Y., Zhou, L., Wang, G., Qiao, Y., Tian, Y., and Feng, Y. (2019). Role of LAMA4 gene in regulating extravillous trophoblasts in pathogenesis of preeclampsia. *Med. Sci. Monit.* 25, 9630–9636. doi: 10.12659/MSM.917402

Jin, S. H., Kim, S. K., and Lee, S. B. (2019). M. leprae interacts with the human epidermal keratinocytes, neonatal (HEKn) via the binding of laminin-5 with alpha-dystroglycan, integrin-beta1, or -beta4. *PLoS Negl. Trop. Dis.* 13:e0007339. doi: 10.1371/journal.pntd.0007339

Kilburn, B. A., Wang, J., Duniec-Dmuchowski, Z. M., Leach, R. E., Romero, R., and Armant, D. R. (2000). Extracellular matrix composition and hypoxia regulate the expression of HLA-G and integrins in a human trophoblast cell line. *Biol. Reprod.* 62, 739–747. doi: 10.1095/biolreprod62.3.739

Kim, J. H., Jekarl, D. W., Kim, M., Oh, E. J., Kim, Y., Park, I. Y., et al. (2014). Effects of ECM protein mimetics on adhesion and proliferation of chorion derived mesenchymal stem cells. *Int. J. Med. Sci.* 11, 298–308. doi: 10.7150/ijms.6672

Kuo, C. Y., Guo, T., Cabrera-Luque, J., Arumugasaamy, N., Bracaglia, L., Garcia-Vivas, A., et al. (2018). Placental basement membrane proteins are required for effective cytotrophoblast invasion in a three-dimensional bioprinted placenta model. *J. Biomed. Mater. Res. A* 106, 1476–1487. doi: 10.1002/jbm.a.36350

Kurdoglu, M., Bayram, I., Kolusari, A., Erten, R., Adali, E., Bulut, G., et al. (2009). Expression of laminin receptor 1 in gestational trophoblastic diseases and normal placenta and its relationship with the development of postmolar tumors. *Gynecol. Oncol.* 114, 306–309. doi: 10.1016/j.ygyno.2009.05.010

Kurdoglu, M., Kurdoglu, Z., Ozen, S., Kucukaydin, Z., Bulut, G., Erten, R., et al. (2011). Expression of laminin receptor 1 in human placentas from normal and preeclamptic pregnancies and its relationship with the severity of preeclampsia. *J. Perinat. Med.* 39, 411–416. doi: 10.1515/JPM.2011.024

Lala, N., Girish, G. V., Cloutier-Bosworth, A., and Lala, P. K. (2012). Mechanisms in decorin regulation of vascular endothelial growth factor-induced human

trophoblast migration and acquisition of endothelial phenotype. *Biol. Reprod.* 87:59. doi: 10.1095/biolreprod.111.097881

Langen, U. H., Pitulescu, M. E., Kim, J. M., Enriquez-Gasca, R., Sivaraj, K. K., Kusumbe, A. P., et al. (2017). Cell-matrix signals specify bone endothelial cells during developmental osteogenesis. *Nat. Cell Biol.* 19, 189–201. doi: 10.1038/ncb3476

Lebensztejn, D. M., Kaczmarski, M., Sobaniec-Lotowska, M., Bauer, M., Voelker, M., and Schuppan, D. (2004). Serum laminin-2 and hyaluronan predict severe liver fibrosis in children with chronic hepatitis B. *Hepatology* 39, 868–869. doi: 10.1002/hep.20147

Li, P., Guo, W., Du, L., Zhao, J., Wang, Y., Liu, L., et al. (2013). microRNA-29b contributes to pre-eclampsia through its effects on apoptosis, invasion and angiogenesis of trophoblast cells. *Clin. Sci.* 124, 27–40. doi: 10.1042/CS20120121

Liu, G., Wu, R., Yang, B., Deng, C., Lu, X., Walker, S. J., et al. (2018). Human Urine-derived stem cell differentiation to endothelial cells with barrier function and nitric oxide production. *Stem Cells Transl. Med.* 7, 686–698. doi: 10.1002/sctm.18-0040

Ma, K., Jin, H., Hu, R., Xiong, Y., Zhou, S., Ting, P., et al. (2014). A proteomic analysis of placental trophoblastic cells in preeclampsia-eclampsia. *Cell Biochem. Biophys.* 69, 247–258. doi: 10.1007/s12013-013-9792-4

Maltepe, E., and Fisher, S. J. (2015). Placenta: the forgotten organ. *Annu. Rev. Cell Dev. Biol.* 31, 523–552. doi: 10.1146/annurev-cellbio-100814-125620

Mammadova-Bach, E., Rupp, T., Spenle, C., Jivkov, I., Shankaranarayanan, P., Klein, A., et al. (2018). Laminin alpha1 orchestrates VEGFA functions in the ecosystem of colorectal carcinoma. *Biol. Cell.* 110, 178–195. doi: 10.1111/boc.201800007

Mate, A., Blanca, A. J., Salsoso, R., Toledo, F., Stiefel, P., Sobrevia, L., et al. (2019). Insulin therapy in pregnancy hypertensive diseases and its effect on the offspring and mother later in life. *Curr. Vasc. Pharmacol.* 17, 455–464. doi: 10.2174/1570161117666181114125109

McGowan, K. A., and Marinkovich, M. P. (2000). Laminins and human disease. *Microsc. Res. Tech.* 51, 262–279. doi: 10.1002/1097-0029(20001101)51:3<262::aid-jemt6>3.0.co;2-v

Merviel, P., Challier, J. C., Carbillon, L., Foidart, J. M., and Uzan, S. (2001). The role of integrins in human embryo implantation. *Fetal Diagn. Ther.* 16, 364–371. doi: 10.1159/000053942

Miner, J. H., Cunningham, J., and Sanes, J. R. (1998). Roles for laminin in embryogenesis: exencephaly, syndactyly, and placentopathy in mice lacking the laminin alpha5 chain. *J. Cell Biol.* 143, 1713–1723. doi: 10.1083/jcb.143.6.1713

Miner, J. H., and Li, C. (2000). Defective glomerulogenesis in the absence of laminin alpha5 demonstrates a developmental role for the kidney glomerular basement membrane. *Dev. Biol.* 217, 278–289. doi: 10.1006/dbio.1999.9546

Miner, J. H., Li, C., Mudd, J. L., Go, G., and Sutherland, A. E. (2004). Compositional and structural requirements for laminin and basement membranes during mouse embryo implantation and gastrulation. *Development* 131, 2247–2256. doi: 10.1242/dev.01112

Mol, B. W. J., Roberts, C. T., Thangaratinam, S., Magee, L. A., de Groot, C. J. M., and Hofmeyr, G. J. (2016). Pre-eclampsia. *Lancet* 387, 999–1011. doi: 10.1016/S0140-6736(15)00070-77

Moser, G., Windsperger, K., Pollheimer, J., de Sousa Lopes, S. C., and Huppertz, B. (2018). Human trophoblast invasion: new and unexpected routes and functions. *Histochem. Cell Biol.* 150, 361–370. doi: 10.1007/s00418-018-1699-0

Nelson, J., McFerran, N. V., Pivato, G., Chambers, E., Doherty, C., Steele, D., et al. (2008). The 67 kDa laminin receptor: structure, function and role in disease. *Biosci. Rep.* 28, 33–48. doi: 10.1042/BSR20070004

Nguyen, N. M., Miner, J. H., Pierce, R. A., and Senior, R. M. (2002). Laminin alpha 5 is required for lobar septation and visceral pleural basement membrane formation in the developing mouse lung. *Dev. Biol.* 246, 231–244. doi: 10.1006/dbio.2002.0658

Pijnenborg, R., D'Hooghe, T., Vercruysse, L., and Bambra, C. (1996). Evaluation of trophoblast invasion in placental bed biopsies of the baboon, with immunohistochemical localisation of cytokeratin, fibronectin, and laminin. *J. Med. Primatol.* 25, 272–281. doi: 10.1111/j.1600-0684.1996.tb00210.x

Pitzler, L., Auler, M., Probst, K., Frie, C., Bergmeier, V., Holzer, T., et al. (2016). miR-126-3p promotes matrix-dependent perivascular cell attachment, migration and intercellular interaction. *Stem Cells* 34, 1297–1309. doi: 10.1002/stem.2308

Ramos, D. M., Berston, E. D., and Kramer, R. H. (1990). Analysis of integrin receptors for laminin and type IV collagen on metastatic B16 melanoma cells. *Cancer Res.* 50, 728–734.

Red-Horse, K., Zhou, Y., Genbacev, O., Prakobphol, A., Foulk, R., McMaster, M., et al. (2004). Trophoblast differentiation during embryo implantation and formation of the maternal-fetal interface. *J. Clin. Invest.* 114, 744–754. doi: 10.1172/JCI22991

Risteli, J., Foidart, J. M., Risteli, L., Boniver, J., and Goffinet, G. (1984). The basement membrane proteins laminin and type IV collagen in isolated villi in pre-eclampsia. *Placenta* 5, 541–550. doi: 10.1016/s0143-4004(84)80008-9

Roberts, J. M., and Hubel, C. A. (2009). The two stage model of preeclampsia: variations on the theme. *Placenta* 30(Suppl. A), S32–S37. doi: 10.1016/j.placenta.2008.11.009

Sekiguchi, R., and Yamada, K. M. (2018). Basement membranes in development and disease. *Curr. Top. Dev. Biol.* 130, 143–191. doi: 10.1016/bs.ctdb.2018.02.005

Shan, N., Zhang, X., Xiao, X., Zhang, H., Chen, Y., Luo, X., et al. (2015). The role of laminin alpha4 in human umbilical vein endothelial cells and pathological mechanism of preeclampsia. *Reprod. Sci.* 22, 969–979. doi: 10.1177/1933719115570913

Silva, J. F., and Serakides, R. (2016). Intrauterine trophoblast migration: a comparative view of humans and rodents. *Cell Adh. Migr.* 10, 88–110. doi: 10.1080/19336918.2015.1120397

Simon-Assmann, P., Orend, G., Mammadova-Bach, E., Spenle, C., and Lefebvre, O. (2011). Role of laminins in physiological and pathological angiogenesis. *Int. J. Dev. Biol.* 55, 455–465. doi: 10.1387/ijdb.103223ps

Sixt, M., Engelhardt, B., Pausch, F., Hallmann, R., Wendler, O., and Sorokin, L. M. (2001). Endothelial cell laminin isoforms, laminins 8 and 10, play decisive roles in T cell recruitment across the blood-brain barrier in experimental autoimmune encephalomyelitis. *J. Cell Biol.* 153, 933–946. doi: 10.1083/jcb.153.5.933

Sorokin, L. M., Pausch, F., Frieser, M., Kroger, S., Ohage, E., and Deutzmann, R. (1997). Developmental regulation of the laminin alpha5 chain suggests a role in epithelial and endothelial cell maturation. *Dev. Biol.* 189, 285–300. doi: 10.1006/dbio.1997.8668

Thyboll, J., Kortesmaa, J., Cao, R., Soininen, R., Wang, L., Iivanainen, A., et al. (2002). Deletion of the laminin alpha4 chain leads to impaired microvessel maturation. *Mol. Cell Biol.* 22, 1194–1202. doi: 10.1128/mcb.22.4.1194-1202.2002

Turpeenniemi-Hujanen, T., Ronnberg, L., Kauppila, A., and Puistola, U. (1992). Laminin in the human embryo implantation: analogy to the invasion by malignant cells. *Fertil. Steril.* 58, 105–113. doi: 10.1016/s0015-0282(16)55145-0

Tzu, J., and Marinkovich, M. P. (2008). Bridging structure with function: structural, regulatory, and developmental role of laminins. *Int. J. Biochem. Cell Biol.* 40, 199–214. doi: 10.1016/j.biocel.2007.07.015

Vatansever, H. S., Inan, V. S., Lacin, S., and Koyuncu, F. (2003). Immunolocalization of alphaV, alpha3 and beta1 integrins in the human placenta with pre-eclampsia. *Acta Histochem.* 105, 253–260. doi: 10.1078/0065-1281-00708

Wang, D., Wang, Y., Liu, H., Tong, C., Ying, Q., Sachinidis, A., et al. (2019). Laminin promotes differentiation of rat embryonic stem cells into cardiomyocytes by activating the integrin/FAK/PI3K p85 pathway. *J. Cell Mol. Med.* 23, 3629–3640. doi: 10.1111/jcmm.14264

Wang, L., Yu, Y., Guan, H., Liu, T., and Qiao, C. (2015). 67-kDa Laminin receptor contributes to hypoxia-induced migration and invasion of trophoblast-like cells by mediating matrix metalloproteinase-9. *Clin. Exp. Pharmacol. Physiol.* 42, 549–558. doi: 10.1111/1440-1681.12389

Wang, L., Zhang, D., Yu, Y., Guan, H., Qiao, C., and Shang, T. (2013). RNA interference-mediated silencing of laminin receptor 1 (LR1) suppresses migration and invasion and down-regulates matrix metalloproteinase (MMP)-2 and MMP-9 in trophoblast cells: implication in the pathogenesis of preeclampsia. *J. Mol. Histol.* 44, 661–668. doi: 10.1007/s10735-013-9515-6

Winn, V. D., Gormley, M., and Fisher, S. J. (2011). The impact of preeclampsia on gene expression at the maternal-fetal interface. *Pregnancy Hypertens.* 1, 100–108. doi: 10.1016/j.preghy.2010.12.001

Zhang, H., Pan, Y. Z., Cheung, M., Cao, M., Yu, C., Chen, L., et al. (2019). LAMB3 mediates apoptotic, proliferative, invasive, and metastatic behaviors in

pancreatic cancer by regulating the PI3K/Akt signaling pathway. *Cell Death Dis.* 10:230. doi: 10.1038/s41419-019-1320-z

Zhang, X., Li, Q., Jiang, W., Xiong, X., Li, H., Zhao, J., et al. (2020). LAMA5 promotes human umbilical vein endothelial cells migration, proliferation, and angiogenesis and is decreased in preeclampsia. *J. Matern. Fetal Neonatal Med.* 33, 1114–1124. doi: 10.1080/14767058.2018.1514597

Zhang, X. M., Xiong, X., Tong, C., Li, Q., Huang, S., Li, Q. S., et al. (2018). Down-regulation of laminin (LN)- alpha5 is associated with preeclampsia and impairs trophoblast cell viability and invasiveness through PI3K signaling pathway. *Cell Physiol. Biochem.* 51, 2030–2040. doi: 10.1159/000495822

Zhou, Y., Damsky, C. H., and Fisher, S. J. (1997). Preeclampsia is associated with failure of human cytotrophoblasts to mimic a vascular adhesion phenotype. One cause of defective endovascular invasion in this syndrome? *J. Clin. Invest.* 99, 2152–2164. doi: 10.1172/JCI119388

Zimmerlin, L., Park, T. S., Zambidis, E. T., Donnenberg, V. S., and Donnenberg, A. D. (2013). Mesenchymal stem cell secretome and regenerative therapy after cancer. *Biochimie* 95, 2235–2245. doi: 10.1016/j.biochi.2013.05.010

Conflict of Interest: The authors declare that the research was conducted in the absence of any commercial or financial relationships that could be construed as a potential conflict of interest.

frontiers in Physiology

ORIGINAL RESEARCH
published: 07 August 2020
doi: 10.3389/fphys.2020.00961

Lack of Connexins 40 and 45 Reduces Local and Conducted Vasoconstrictor Responses in the Murine Afferent Arterioles

Sophie Møller, Jens Christian Brings Jacobsen, Niels-Henrik Holstein-Rathlou and Charlotte M. Sorensen*

Department of Biomedical Sciences, Faculty of Health and Medical Sciences, University of Copenhagen, Copenhagen, Denmark

OPEN ACCESS

Edited by:
Mauricio P. Boric, Pontificia Universidad Católica de Chile, Chile

Reviewed by:
William F. Jackson, Michigan State University, United States
Armin Kurtz, University of Regensburg, Germany

***Correspondence:**
Sophie Møller
sophie.moller@gmail.com; sopm@nexs.ku.dk

Specialty section:
This article was submitted to Vascular Physiology, a section of the journal Frontiers in Physiology

Received: *14 February 2020*
Accepted: *15 July 2020*
Published: *07 August 2020*

Citation:
Møller S, Jacobsen JCB, Holstein-Rathlou N-H and Sorensen CM (2020) Lack of Connexins 40 and 45 Reduces Local and Conducted Vasoconstrictor Responses in the Murine Afferent Arterioles. Front. Physiol. 11:961. doi: 10.3389/fphys.2020.00961

The juxtaglomerular apparatus (JGA) is an essential structure in the regulation of renal function. The JGA embodies two major functions: tubuloglomerular feedback (TGF) and renin secretion. TGF is one of the mechanisms mediating renal autoregulation. It is initiated by an increase in tubular NaCl concentration at the macula densa cells. This induces a local afferent arteriolar vasoconstriction and a conducted response that can be measured several 100 μm upstream from the juxtaglomerular segment. This spread of the vasomotor response into the surrounding vasculature likely plays a key role in renal autoregulation, and it requires the presence of gap junctions, intercellular pores based on connexin (Cx) proteins. Several Cx isoforms are expressed in the JGA and in the arteriolar wall. Disruption of this communication pathway is associated with reduced TGF, dysregulation of renin secretion, and hypertension. We examine if the absence of Cx40 or Cx45, expressed in the endothelial and vascular smooth muscle cells respectively, attenuates afferent arteriolar local and conducted vasoconstriction. Afferent arterioles from wildtype and Cx-deficient mice (Cx40 and Cx45) were studied using the isolated perfused juxtamedullary nephron preparation. Vasoconstriction was induced *via* electrical pulse stimulation at the glomerular entrance. Inner afferent arteriolar diameter was measured locally and upstream to evaluate conducted vasoconstriction. Electrical stimulation induced local vasoconstriction in all groups. The local vasoconstriction was significantly smaller when Cx40 was absent. The vasoconstriction decreased in magnitude with increasing distance from the stimulation site. In both Cx40 and Cx45 deficient mice, the vasoconstriction conducted a shorter distance along the vessel compared to wild-type mice. In Cx40 deficient arterioles, this may be caused by a smaller local vasoconstriction. Collectively, these findings imply that Cx40 and Cx45 are central for normal vascular reactivity and, therefore, likely play a key role in TGF-induced regulation of afferent arteriolar resistance.

Keywords: gap junction, vascular conducted response, electrical pulse stimulation, renal, intercellular communication

INTRODUCTION

The juxtaglomerular apparatus (JGA) is a specialized structure, formed by the afferent and efferent arteriole, thick limb of the ascending loop of Henle, and mesangial cells. The JGA embodies two major renal functions: tubuloglomerular feedback (TGF), which is part of the mechanism underlying renal autoregulation, and renin secretion. The JGA consists of different cell types with specialized functions: the macula densa (MD) cells, juxtaglomerular cells, mesangial cells, vascular smooth muscle cells (VSMCs), and endothelial cells (ECs). The MD cell of the thick limb of the ascending loop of Henle functions as a NaCl sensor. An increase in NaCl concentration in the tubular fluid eventually causes the VSMC in the afferent arteriole to contract to reduce glomerular filtration rate (GFR) and the juxtaglomerular cells of the afferent arteriole to reduce renin secretion. Mesangial cells are located between the MD cells (the sensor) and the afferent arteriole (the effector). They are believed to play an important role in the signal transduction from the MD to the afferent arteriole (Goligorsky et al., 1997).

The TGF signal originates in the MD cells and elicits local vasoconstriction in the juxtaglomerular part of the afferent arteriole. The response, however, encompasses the entire afferent arteriole, the distal part of the interlobular artery, and travels into the afferent arterioles of neighboring nephrons (Peti-Peterdi, 2006; Marsh et al., 2009). This indicates that the vasoconstrictor signal is conducted within the vascular wall most likely through gap junctions (GJs) coupling ECs to ECs, VSMCs to VSMCs, and ECs to VSMCs.

GJs are fluid-filled pores that allow the movement of small molecules and current between neighboring cells. GJs are made up of two hemichannels, connexons, built from connexins (Cxs) (Nielsen et al., 2012). Six Cxs of the same or different isoforms can assemble to form a connexon, and the two connexons from neighboring cells can dock to form a functional GJ channel (Moreno, 2004). Several Cx isoforms are expressed in the JGA (Hanner et al., 2010). Similarly, in preglomerular arterioles, expression of Cx37, Cx40, Cx43, and Cx45 (Wagner, 2008; Just et al., 2009; Schweda et al., 2009) is found, enabling the cells of the vessel wall, both smooth muscle and endothelial, to act as a syncytium (Goligorsky et al., 1997; Dora et al., 2003; Haefliger et al., 2004; Peti-Peterdi, 2006; Yao et al., 2009).

In the vasculature, Cx40 is the most widely expressed isoform and is predominantly found in the ECs (de Wit et al., 2003; Schweda et al., 2009), as well as in renin-producing cells (Haefliger et al., 2001). In mice, deletion of Cx40 leads to the development of renin-dependent hypertension (de Wit et al., 2000, 2003; Figueroa et al., 2003; Wagner et al., 2007; Just et al., 2009; Sorensen et al., 2012) and reduced conduction of vasodilation (de Wit et al., 2000). Cx45 is expressed in the VSMCs (Wagner, 2008) and mesangial cells (Kurtz et al., 2009; Hanner et al., 2010), and lack of Cx45 expression causes lethal malformations in the vasculature (Krüger et al., 2000; Hanner et al., 2008; Wagner, 2008). Therefore, only a conditional deletion of Cx45 is possible in mice. Previous studies in these mice show that Cx45 plays a role in the propagation of VSMC calcium waves and in TGF (Hanner et al., 2008; Møller et al., 2020). This calcium signaling may be one mechanism by which Cx45 affects vascular conducted responses.

Once the signal from MD has reached the afferent arteriole, the vascular conduction can spread dilation or constriction along the vessel wall, depending on the blood flow needs (Wagner, 2008). Conducted vasoconstriction occurs when depolarizing current propagates upstream *via* GJs (Gustafsson and Holstein-Rathlou, 1999), from the afferent arterioles to the larger arteries, and changes the vascular resistance, thus reducing renal blood flow (Wagner et al., 1997).

In this study, we aim to test if a lack of two specific Cxs affects vascular conduction in the afferent arteriole. Specifically, we explore the roles of Cx40 and Cx45 in the conduction of vasoconstrictor responses to electrical pulse stimulation.

MATERIALS AND METHODS

Animal Preparation

Procedures were approved by the Danish National Animal Experiments Inspectorate. All animals were kept in the animal facility at University of Copenhagen and received tap water and standard chow *ad libitum*. Genotyping was done on DNA from ear clippings using the DirectPCR kit (Viagen Biotech; Los Angeles, CA).

Cx40 wildtype (Cx40 WT) and Cx40 knockout (Cx40 KO) mice were on a mixed C57Bl/6 × 129S4/SvJae genetic background. Mice were purchased for breeding from the European Mouse Mutant Archive (infrafrontier.eu, Munich, Germany). Kidneys from a total of 15 adult mice were used for the studies (Cx40 WT n = 8, five females and three males and Cx40 KO n = 7, four females and three males). The age of the mice ranged from 4 to 14 months.

Homozygous female mice with floxed Cx45 gene ($Cx45^{fl/fl}$, >87% C57Bl/6 background) were mated with homozygous $Cx45^{fl/fl:Nestin\text{-}Cre}$ males, >87% C57Bl/6 background. Breeding pairs were a generous gift from Dr. Klaus Willecke, University of Bonn, Germany; the mice have been described previously (Maxeiner et al., 2005). In their offspring, the Cx45 coding DNA is replaced with an enhanced green fluorescence protein (eGFP) in cells expressing the intermediate filament Nestin during development. The $Cx45^{fl/fl}$ mice are phenotypically wildtype and are used as such (WT). The $Cx45^{fl/fl:Nestin\text{-}Cre}$ mice are used as our knockout (KO). Kidneys from 20 adult mice were used for the studies (Cx45 WT n = 9, three females and six males and Cx45 KO n = 11, nine females and two males), ranging from 2 to 6 months of age.

Imaging System and Software

The experimental setup is shown in **Figure 1**. The vasculature was viewed and recorded using an Olympus BX50WI microscope with a digital 12-bit CCD camera (Pixelfly, PCO, Kelheim, Germany) mounted on the microscope. Images were recorded using the CamWare software (PCO, Kelheim, Germany). Renal perfusion pressure (RPP) readings were obtained using the PowerLab/8SP data acquisition system (ADInstruments, Colorado Springs, CO) and viewed using LabChart 7 software (ADInstruments, Colorado Springs, CO). Post-experimental evaluations of afferent arteriolar

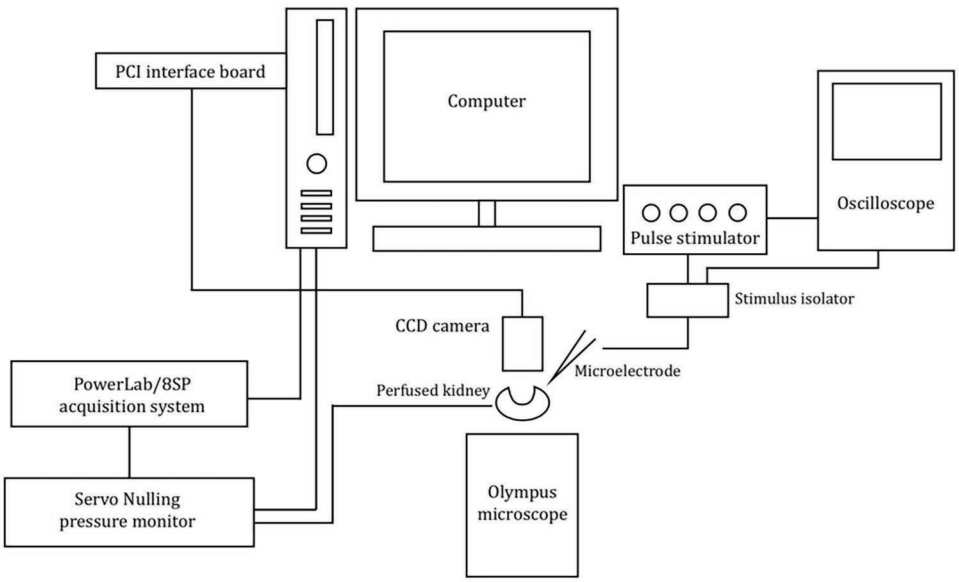

FIGURE 1 | Schematic of the imaging system and experimental setup used. Schematic showing the setup used to measure the afferent arteriolar diameter in response to electrical stimulation.

diameter were performed offline using ImageJ (National Institute of Health, Bethesda, MD).

Surgical Procedure

Experiments were performed using the *in vitro* perfused juxtamedullary nephron preparation, developed by Casellas and Navar (1984), and adapted to mice (Harrison-Bernard et al., 2003; Sorensen et al., 2012). Mice were anesthetized with pentobarbital (50 g/kg *i.p.*, Mebumal, SAD, Denmark). The abdominal aorta was catheterized and immediately perfused with Tyrode's solution (in mmol/L: 136.9 NaCl, 0.42 NaH_2PO_4, 11.9 $NaHCO_3$, 2.7 KCl, 2.2 $MgCl_2$, 5.6 D-glucose, and 1.8 $CaCl_2$) containing 5% BSA (ICPbio International, Auckland, New Zealand) and an amino acid mixture (in mmol/L: 2 alanine, 2 glycine, 5 glutamine, 1 serine, and supplemented with MEM amino acid solution, all from Sigma-Aldrich, Copenhagen, Denmark) at pH 7.4. Kidneys were excised, and the cannula was advanced into the renal artery of the left kidney. The kidney was decapsulated and sectioned longitudinally exposing the intact papilla, which was reflected revealing the inner cortical surface. Venous tissue on the cortical surface was cut, allowing access to the arterial vasculature. Perfusion was isolated to the inner cortical vessels by ligating larger arterial vessels (Dafilon 10/0 sutures, B. Braun Vet Care GmbH, Tuttlingen, Germany).

The cannula system comprised of a 27-gauge blunt needle and a polyethylene (PE-10) line, connected to a servo-nulling pressure system (Instrumentation for Physiology and Medicine, San Diego, CA), allowing for continuous RPP monitoring. RPP was maintained at 95 mmHg throughout the experiment by adjusting the regulator, controlling the flow of 95% O_2-5% CO_2 gas mixture to the perfusion solution reservoir.

Experimental Procedure: Application of Electrical Pulse Stimulation

Borosilicate glass micropipettes (CMA Microdialysis, Kista, Sweden) were pulled on a horizontal Flaming/Brown micropipette puller (Model P-87, Sutter Instrument Co., Novato, CA) and back-filled with a 2 mol/L NaCl solution containing Lissamine green (Sigma-Aldrich, Copenhagen, Denmark). The microelectrode was connected to a stimulus isolator (ISO-flex, A.M.P.I., Jerusalem, Israel) connected to a stimulator (Model S44, Grass Instrument Co., Quincy, MA) and an oscilloscope (1200 A, Hewlett-Packard, Palo Alto, CA). The microelectrode (0.5–0.8 MΩ resistance) was placed at the glomerular entrance of the afferent arteriole, where local afferent vasoconstriction was induced by electrical pulse stimulation (2.5 Hz frequency, 300 ms pulse duration, and 90 V amplitude; Salomonsson et al., 2002; Palanker et al., 2008), as shown in **Figure 2**. A wire was placed in the tissue chamber to serve as the grounding electrode. After a recovery period, an experimental protocol consisting of 30 s recordings of baseline, electrical pulse stimulation, and recovery periods was initiated. The vessels were stimulated for 30 s, a period which was sufficient for it to reach a new steady-state diameter (Steinhausen et al., 1997).

Diameter Measurements

The afferent arteriolar diameter was measured by tracking the vessel edges and the inner diameter was measured every 10 s throughout the experiment. The diameter was measured at the stimulation point at the glomerular entrance (local response) as well as every 50 μm upstream from the glomerulus (conducted response; **Figures 2**, **3**) as far as it was possible to track the vessel (**Table 1**). Each data point represents the average of

three consecutive measurements (after 10, 20, and 30 s of stimulation) in the same position.

Experiments were included if they fulfilled the following: (1) electrical stimulation induced a minimum of 5% constriction in the vessel diameter (local response), (2) post-stimulation, the vessel recovered to at least 50% of its baseline diameter, and (3) diameters were measurable at a minimum of three positions along the vessel (including stimulation site).

Data Handling and Statistical Analyses

Graphical presentation and statistical analyses were performed using SigmaPlot (Systat Software Inc. San Jose, CA, USA), MatLab (MathWorks, Natick, MA, USA), and Rstudio (version 1.3.959; Boston, MA). Vessel diameter during stimulation was normalized to the respective mean resting diameter at the given distance from the stimulation site. Normalized and pooled data for contraction at the stimulation site (0 μm) from each experimental series were evaluated using a one-way ANOVA to test for differences between WT and KO. A one-sample *t*-test testing against 0 was used to evaluate significant constriction at each measurement point.

Length constants of the conducted vasoconstriction were calculated in MATLAB® (The MathWorks Inc., R2017b) for each type of animal by a non-linear least squares fit of the data to the equation $y = ae^{bx}$, where y is the change in diameter at upstream distance x from the stimulation site, a is the y-intercept, and b is the decay rate of the response along the vessel. When conducted vasoconstriction reached 0 or a negative value, constriction was set to 0 for the remaining measurements. The maximum distance from the stimulation point at which the individual vessel could be visualized varied from 100 to 500 μm. Consequently, there were more measurements at the shorter distances. All measurements at a given distance were pooled for each group. Therefore, in each fit, the shorter distances with more measurements weighs in more heavily than longer distances with fewer measurements (**Figure 4**; constants shown in **Table 2**). Each group gives rise to a single fit. To enable statistical comparison of the decay rates between groups, a boot strapping procedure was applied (source code available in **Supplementary Data**). In brief, for each group of animals, a set of data points were obtained by drawing randomly, with replacement, from the original data set. The single exponential decay model was then fitted to this new data set to obtain estimates of a and b. The procedure was repeated 1,000 times, giving new sets of y-interceptions and decay rates. Differences in the latter between WT and KO groups were analyzed using a two-tailed *t*-test.

Previous studies have shown no difference in the measured renal vascular responses between male and female mice, and data were therefore pooled for statistical comparison (Boesen et al., 2012; Brasen et al., 2018; Gohar et al., 2019; Møller et al., 2020). $p \leq 0.05$ was considered statistically significant. All values are reported as means ± SEM unless otherwise stated.

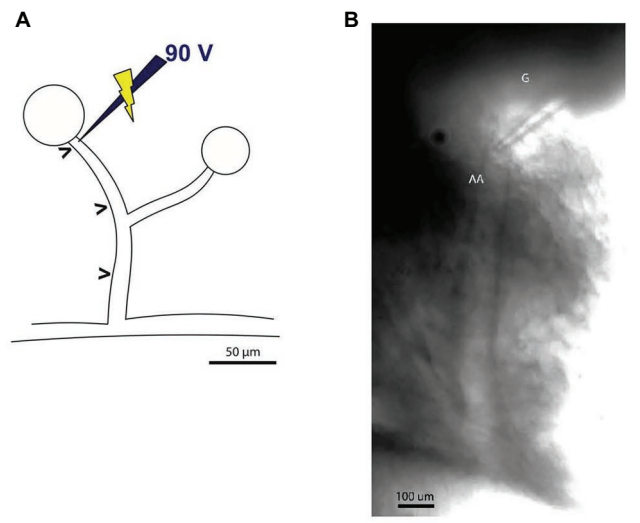

FIGURE 2 | Illustration of the microelectrode positioning for electrical pulse stimulation. **(A)** Stimulation microelectrode was positioned at the glomerular entrance of the afferent arteriole. The diameter was measured at sites labeled (>), corresponding to the stimulation site and sites (50 μm apart) upstream from the microelectrode (maximum distance reached only in some experiments were 450 μm). Schematic representation inspired by Wagner et al. (1997). **(B)** Image of the experimental setup showing the stimulation electrode placed immediately upstream from glomerulus (G) just above the afferent arteriole (AA).

RESULTS

Animals

Mean values of body weight, age, pre-stimulated vessel diameter (measured at 95 mmHg), and traceable vessel length are summarized in **Table 1**. Body weights were significantly higher in Cx40 WT mice (33.1 ± 1.3 g) compared to Cx40 KO mice (27.9 ± 1.7 g, $p = 0.04$) and in Cx45 WT mice (27.4 ± 1.3 g) compared to

TABLE 1 | Mean values of body weight prior to kidney removal, age, pre-stimulated vessel diameter and traceable vessel length starting at the stimulation point on the afferent arteriole.

		N	Body wt. (g)	Age (weeks)	AA diameter (μm)	Measured vessel length (μm)
Cx40	WT	8	33.1 ± 1.3	31.8 ± 5.6	28.7 ± 5.3	259.4 ± 58.2
	KO	7	27.9 ± 1.7	41.9 ± 4.1	15.5 ± 3.4	178.6 ± 26.4
			$p = 0.04$	NS	$p = 0.04$	NS
Cx45	WT	9	27.4 ± 1.3*	16.4 ± 1.1***	30.6 ± 2.7	361.1 ± 28.6
	KO	11	22.5 ± 1.6#	15.9 ± 1.2###	23.6 ± 3.1	295.5 ± 41.8
			$p = 0.007$	NS	NS	NS

*Cx40, connexin 40; Cx45, connexin 45; WT, wildtype; KO, knockout; AA, afferent arteriole; NS, not significant. *p < 0.05; ***p < 0.001 vs. Cx40 WT; #p < 0.05; ###p < 0.001 vs. Cx40 KO.*

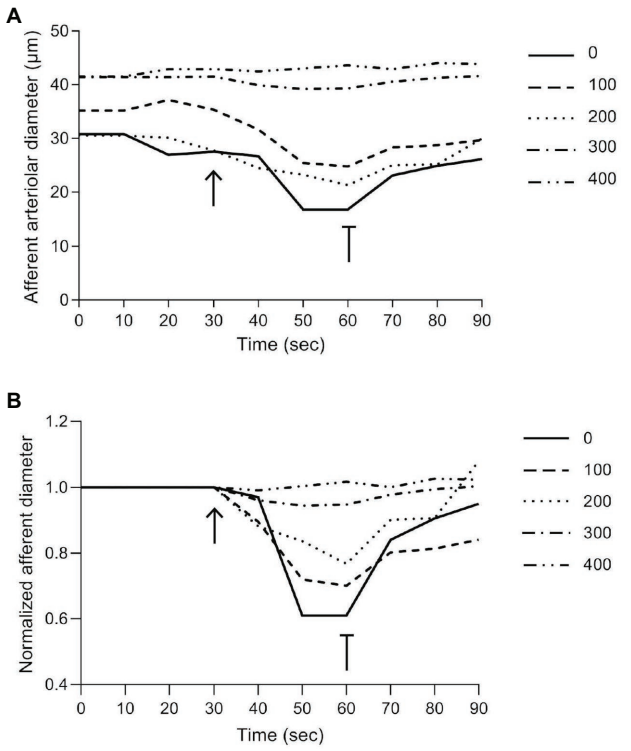

FIGURE 3 | Representative trace of a typical experimental recording from Cx40 WT. **(A)** Absolute changes in afferent arteriolar diameter as a function of time at the stimulation site (0) and at increasing distances from the stimulation site (100–400). **(B)** Changes in normalized afferent arteriolar diameter as a function of time (diameter was normalized by the corresponding local mean diameter prior to the electrical stimulation). The solid line (0) represents the diameter measurements at the stimulation site, while dotted/dashed lines represent upstream measurements. The arrow and T-bar indicate when electrical stimulation was initiated and stopped.

Cx45 KO mice (22.5 ± 1.6 g, $p = 0.007$). Mice from the Cx40 strain were significantly heavier than the Cx45 strain. Age was not different within the groups; however, mice from the Cx40 strain were older than the mice from the Cx45 strain. Resting vessel diameter measured at the glomerular entrance was significantly different between Cx40 WT and Cx40 KO ($p = 0.04$), but not between Cx45 WT and Cx45 KO, or between groups. Maximal traceable vessel length (afferent arteriole and in some cases interlobular arteries) was not significantly different between or within groups.

Afferent Arteriolar Diameter

Figure 2 shows an afferent arteriole branching from an interlobular artery and the micropipette used to deliver the electrical pulse stimulation.

A typical recording of the afferent arteriolar diameter from a Cx40 WT mouse is shown in **Figure 3A** and the normalized diameter is shown in **Figure 3B**. The electrical stimulation (shown by the arrow at 30 s) produces strong vasoconstriction locally (0 µm). Vessel diameter is reduced by approximately 40% of its baseline diameter within the first 20 s of stimulation. Termination of the electrical stimulation (shown by the T-bar at 60 s) results in a quick return to near control diameters. Locally, diameter returned to approximately 85% of its baseline diameter within the first 10 s and by the end of the 30-s recovery, the diameter has returned to near baseline value. The magnitude of the vasoconstriction response is seen to decrease with increasing distances upstream from the stimulation site. At 400 µm, electrical stimulation induced no detectable vasoconstriction in the example shown.

Figure 4 shows the relative reduction in vessel diameter as a function of distance from the stimulation site in Cx40 WT and KO (**Figures 4A,B**). **Figures 4C,D** show data from Cx45 WT and KO, respectively. A data point (◆) in any of the figures represents the average of all the measurements made at that given distance ± SEM. The exponential curve fit is weighted according to the number of observations at a given distance (source code available in **Supplementary Data**). Thus, data points close to the stimulation site with many observations weigh in more heavily than data points further away with fewer observations. Data for the fitted curves are shown in **Table 2**.

Comparing measurements at the stimulation site directly between groups (one-way ANOVA) showed that relative vasoconstriction between Cx40 WT and KO (0.23 ± 0.03 vs. 0.13 ± 0.03; $p < 0.05$) was significantly different. Albeit numerically different, no significant difference was found between Cx45 WT and KO (0.22 ± 0.05 vs. 0.16 ± 0.03; $p = 0.32$). This is in line with the fitted data (**Table 2**), where the y-intersection (a) is equivalent to the local vasoconstriction.

The decay rate (b) of the conducted vasoconstriction evaluated using bootstrapping was significantly smaller in Cx45KO compared to Cx45 WT ($p < 0.05$, **Table 2**) corresponding to a larger length constant in the Cx45WT. There was no significant difference in decay rate between Cx40WT and Cx40KO although it appeared smaller in Cx40 KO.

In all groups, vasoconstriction decreases with increasing distance. Comparing the relative afferent arteriolar constriction in each group against 0, the data showed that in Cx40 WT a significant constriction was measurable up to 200 µm (**Figure 4A**), in Cx40 KO the distance was 50 µm (**Figure 4B**). In the Cx45 group, a significant constriction could be measured at 300 µm in the WT arterioles (**Figure 4C**) and at 250 µm in the KO (**Figure 4D**).

DISCUSSION

The present study investigated the importance of intercellular communication *via* GJs, through Cx40 and Cx45, in the conduction of afferent arteriolar vasoconstriction in response to local electrical stimulation. We have previously shown that lack of Cx40 or Cx45 significantly reduces TGF (Sorensen et al., 2012; Møller et al., 2020). Here, we examine if this reduction is caused by a decrease in the vascular conduction of vasoconstriction. The local and conducted vasoconstrictor responses were measured during stimulation and compared to the diameter measured before stimulation. Decay of constriction was computed for the stimulation period for data pooled from each mouse strain.

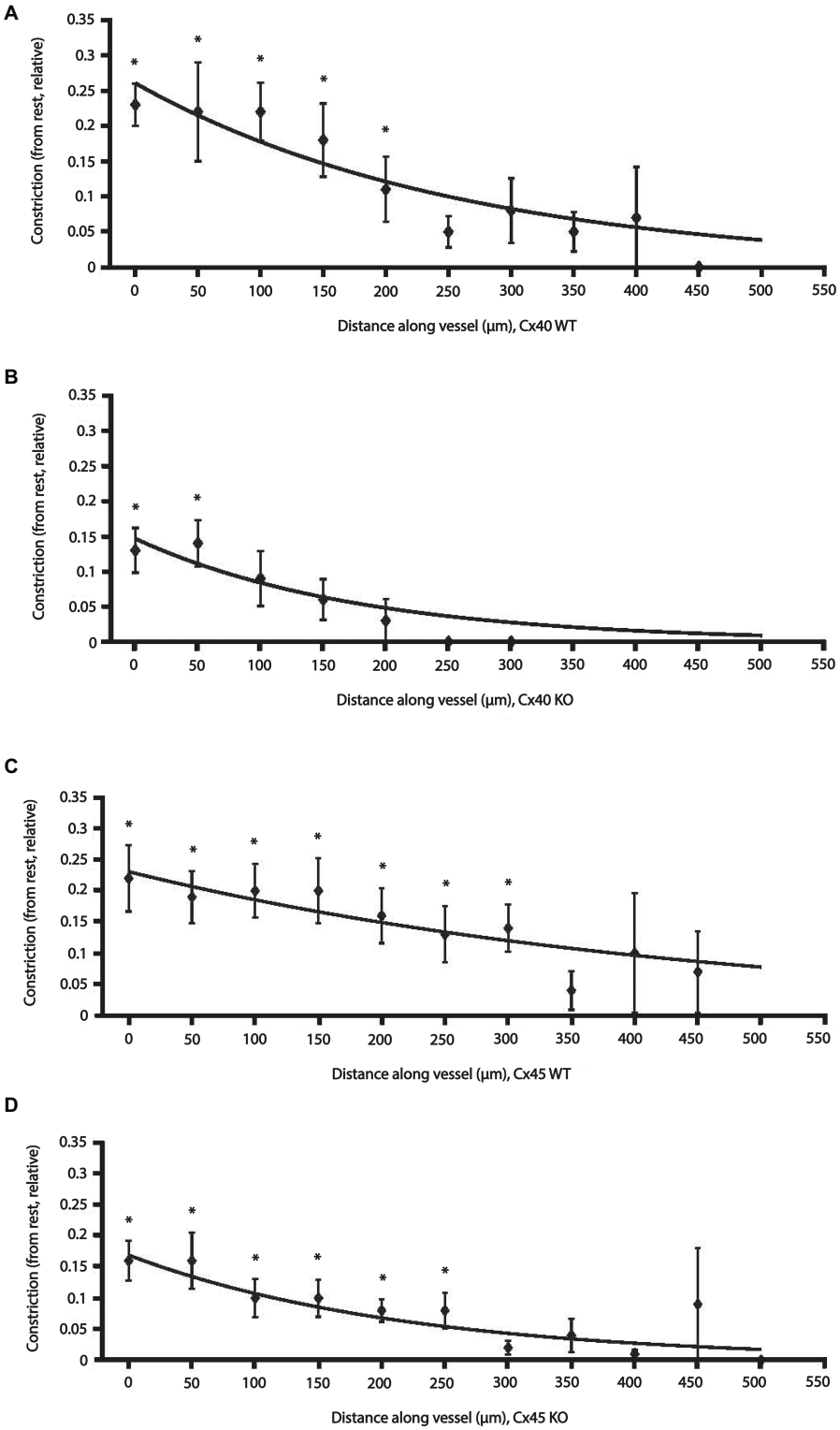

FIGURE 4 | Effect of electrical stimulation on afferent arteriolar diameter in WT and KO of Cx40 and Cx45 mice. Changes in afferent arteriolar diameter as a function of distance from the stimulation point. Data are constriction relative to the local diameter measured at rest. Data are presented as mean ± SEM. The lines are fits to the data points weighted according to the number of observations at each distance and fitted to an exponential model: $y = ae^{bx}$ (please see Methods and Materials section). Data points without error bars: $n = 1$. **(A)** Cx40 WT ($n = 8$) and **(B)** Cx40 KO ($n = 7$). **(C)** Cx45 WT ($n = 9$) and **(D)** Cx45 KO ($n = 11$). $^{*}p < 0.05$ vs. 0.

TABLE 2 | Summary of conducted response characteristics for WT and KO animals of both strains.

Strain	a, 95% CI (μm)	b ($\times10^{-3}$), 95% CI ($\times10^{-3}$) (1/μm)	Length constant (−1/b, μm)
Cx40 WT	0.26, (0.20, 0.33)*	−3.8, (−6.0, −1.7)	363
Cx40 KO	0.15, (0.092, 0.20)	−5.6, (−10.7, −0.47)	179
Cx45 WT	0.23, (0.17, 0.29)	−2.2, (−3.8, −0.53)**	455
Cx45 KO	0.17, (0.12, 0.21)	−4.5, (−7.1, −2.0)	222

Values are calculated by fitting data to a single exponential decaying function: $y=ae^{bx}$ where y is the relative change in diameter at distance x upstream from the stimulation site, a is the y-intercept, and b is the decay rate of the response along the vessel. Significance levels were evaluated using bootstrapping procedure.
$^{*}p < 0.01$ Cx40 WT vs. Cx40 KO; $^{**}p < 0.05$ Cx45 WT vs. Cx45 KO.

VSMCs and ECs work together to coordinate and propagate constriction and dilation along the vessel wall (Li et al., 2015). The conducted vasomotor response is important in the regulation of blood flow and resistance in vascular networks (Gustafsson et al., 2001) and depends on GJs (Segal et al., 1989; Hakim et al., 2008; Braunstein et al., 2009). In afferent arterioles, ECs are primarily coupled through Cx40 (Arensbak et al., 2001) and VSMCs through Cx45 (Møller et al., 2020). GJs also play a role in the signaling between ECs and VSMCs (Emerson and Segal, 2000) through myoendothelial GJs (MEGJs; Haefliger et al., 2004). It is unknown which Cxs are part of MEGJs in the renal vasculature (Wagner, 2008) but Cx45 or Cx40 are likely candidates. In Cx40 KO mice, renal endothelium derived hyperpolarization was significantly reduced compared to WT, suggesting that Cx40 is part of the renal MEGJ (Brasen et al., 2018). Also, Cx40 has been found in junctions between EC and renin secreting cells (transformed VSMC; Haefliger et al., 2001) supporting that Cx40 could be part of the MEGJ.

Both mouse strains used in the present study have been characterized previously. The Cx40 KO was hypertensive (de Wit et al., 2000; Wagner, 2008; Just et al., 2009), but RBF was similar in Cx40 WT and KO (Just et al., 2009). Segmental arterial and afferent arteriolar diameters were not significantly different (Sorensen et al., 2012), but heart weight and afferent wall trans-sectional area were increased in Cx40 KO mice (Sorensen et al., 2012; Jacobsen and Sorensen, 2015), possibly due to the hypertension. The Cx45 KO was reported to be slightly hypertensive (Hanner et al., 2008) or normotensive (Schmidt et al., 2012). Segmental arterial and afferent arteriolar diameters were not significantly different between Cx45 WT and KO, but wall trans-sectional area was decreased in afferent arterioles from Cx45 KO (Møller et al., 2020). In both strains, TGF was found to be reduced in the KO (Sorensen et al., 2012; Møller et al., 2020), whereas the myogenic response was unaffected by the reduction in intercellular communication (Jacobsen and Sorensen, 2015; Møller et al., 2020).

Electrical pulse stimulation induced a local and a conducted vasoconstriction response in afferent arterioles from Cx40 and Cx45 WT and KO mice. The local response measured at the stimulation site was significantly smaller in Cx40 KO compared to Cx40 WT. However, in cremaster arterioles from Cx40 KO mice, local vasoconstriction elicited with electrical stimulation or KCl was similar to that observed in WT mice (Figueroa et al., 2003; Wölfle et al., 2007). As shown before, the afferent arteriolar diameter measured in the juxtaglomerular segment in Cx40 KO was smaller than in WT and smaller than the diameter measured 100 μm upstream (Sorensen et al., 2012). This could suggest an increased baseline afferent arteriolar constriction at the site closest to the glomerulus when Cx40 is not present. Eliminating TGF did not normalize afferent arteriolar diameter, suggesting that TGF is not causing the constriction. Importantly, afferent arteriolar diameter measured upstream from the juxtaglomerular site was not significantly smaller in Cx40 KO (Sorensen et al., 2012). No significant difference in the local vasoconstriction was found between Cx45 WT and KO even though it appeared smaller in Cx45 KO. However, this could be due to the relatively small effects being measured resulting in low statistical power. In mice lacking Cx45 in VSMC, KCl-induced local vasoconstriction was similar to the constriction elicited in WT mice (Schmidt et al., 2012). In isolated segmental arteries from both strains, no difference was found between WT and KO when assessing the vasoconstrictor response to NE (Brasen et al., 2018; Møller et al., 2020). Collectively, these data suggest that the renal vascular reactivity in Cx40 and Cx45 KO is not reduced. Possibly, the decreased juxtaglomerular afferent arteriolar diameter in Cx40 KO affects the local vasoconstriction elicited at this site.

Although the decay rate of vasoconstriction seemed slightly increased in Cx40 KO, no significant difference was found between Cx40 WT and KO. This is in accordance with results obtained in skeletal muscle arterioles, where KCl-induced conducted vasoconstriction was unaffected in Cx40 KO mice (de Wit et al., 2000). It is generally believed that electrical signals travel predominantly in the endothelial layer (Kapela et al., 2018), which is coupled mainly by Cx40. In isolated preglomerular arteries from Cx40 KO, electrical stimulation did not elicit an increase in VSMC intracellular Ca^{2+} measured 500 μm from the stimulation site (Sorensen et al., 2012). However, no measurements were made at shorter distances. In addition, an electrical signal may travel further than what can be measured when using increases in intracellular Ca^{2+} or vasoconstriction as parameters. Comparing the constriction at a given distance against 0 revealed that in Cx40 KO the constriction was only significant at 50 μm. This could be due to the smaller local constriction.

In contract, in Cx45 KO, the decay rate was significantly increased compared to WT. Possibly, Cx45 is part of the MEGJ in the afferent arteriolar wall, and its removal by conditional knockout could reduce communication between the VSMC layer and the endothelium, hence reducing the mechanical response from the VSMC layer. Myoendothelial junctions are unevenly distributed along the wall. The spread of depolarization from VSMCs that are coupled to the endothelium, to VSMCs that are not, could be central for a distant mechanical response to electrical stimulation. In addition, although the endothelium is normally considered the main path for a longitudinal spread of current in the

microcirculation, the presence of VSMC-VSMC coupling by Cx45-containing GJs may also contribute. A possible proposed mechanism is through Ca^{2+} signaling as Cx45 is known to be involved in the propagation of Ca^{2+} waves in VSMC isolated from afferent arterioles (Hanner et al., 2008). Comparing the constriction against 0 showed that in Cx45 KO the constriction was only significant up to 250 μm compared to 300 μm in the WT.

The structure of the vascular wall may affect both the local vasoconstriction and conduction properties. The vascular wall in renal vessels with a diameter <40 μm is thicker compared to vessels from skeletal muscles (Hosoyamada et al., 2015), which would reduce conduction in afferent arterioles. In both KO strains, changes in wall trans-sectional area (WTA) and stress sensitivity in the afferent arteriole have been found (Jacobsen and Sorensen, 2015; Møller et al., 2020). However, WTA and stress sensitivity seemed to be increased in Cx40 KO, whereas it was decreased in Cx45 KO. Whether this can account for the increase in decay rate observed in Cx45 KO remains to be established. Another possibility is that deletion of Cx40 or Cx45 changes the expression of other GJs or ion channels responsible for eliciting the vasoconstriction. Deletion of Cx40 reduced expression of Cx37 in the vasculature (Simon and McWhorter, 2003; de Wit, 2010), which could affect the vascular response. Whether this could also be the case for vascular ion channels is currently not known.

Differences in myogenic activity at the chosen RPP of 95 mmHg may also influence the obtained results. Resting membrane potential of VSMCs in the afferent arteriole in isolated perfused rat kidneys was approximately −40 mV at 80 mmHg RPP (Loutzenhiser et al., 1997). We assume that a comparable resting membrane potential is present in mouse afferent arterioles at an RPP of 95 mmHg. Under these conditions, the afferent arteriole has substantial myogenic tone and addition of nifedipine, an inhibitor of L-type Ca^{2+} channels, significantly increased afferent arteriolar diameter (Sorensen et al., 2012). In Cx40 KO mice, afferent arteriolar diameter remained constant even though RPP was increased from 75 to 95 mmHg (Sorensen et al., 2012) and in Cx45 KO mice the same RPP increase induced a significant reduction in afferent arteriolar diameter (Møller et al., 2020), suggesting that both strains have myogenic tone in the present experimental setup. As no differences have been found in the myogenic response between KO and WT from both strains (Jacobsen and Sorensen, 2015; Møller et al., 2020) it does not seem likely that differences in myogenic tone are affecting the electrically induced vascular responses observed in the present experiments.

A number of limitations are present in our experiments. Due to the experimental setup, it is not possible to position the stimulation pipette next to the vascular wall. A varying layer of tubular tissue will separate the pipette tip and the vascular wall. This limitation has been mitigated by only including arterioles with a minimum local constriction of 5%. In addition, the preparation is not fixed and the arterioles have some vasomotion that could affect the measurements. Consequently, we used an average of the diameter measured over 30 s. Vasoconstriction is not the most sensitive measure to quantify vascular conduction. Changes in membrane potential can be measured using sharp electrodes or patch-clamp (Li et al., 2004). This method is not applicable in our preparation, where the cells of the vascular wall are not freely accessible. Another factor that should be taken into consideration is the age span of the mice (2–14 months). Laboratory mice reach sexual maturity at 8–12 weeks of age (Dutta and Sengupta, 2016); past the age of 18 months, these mice are considered old (Hagan, 2017). We know that age does not affect the myogenic response (Lott et al., 2004), unless subjects are sedentary (Hong and Lee, 2017). In WKY and SHR rats, both cortical and juxtamedullary autoregulatory activity were similar between ages 10 and 70 weeks (Iversen et al., 1998) even though MAP increased significantly in SHR. These findings indicate that vascular function is intact at 14 months of age, and we are not aware of any study that has directly addressed the effect of aging on vascular conduction in the mouse afferent arteriole. Lastly, we have used mixed sexes. Renal autoregulation in the normal physiological state is identical in males and females (Hilliard et al., 2011; Brown et al., 2012) as is renal vascular responses to angiotensin II and PE (Schneider et al., 2010). Thus, the use of mixed sexes would likely not affect the results.

In conclusion, we have shown that knockout of Cx40 reduces local vasoconstriction but does not significantly change the conduction of vasoconstriction. Vascular deletion of Cx45 significantly reduces the vascular conduction induced by electrical stimulation in afferent arterioles. Consequently, vasoconstriction in response to a comparable stimulus is conveyed shorter when intercellular communication between cells in the vascular wall is reduced in the renal microcirculation. This may in turn affect the ability to regulate and autoregulate renal perfusion.

DATA AVAILABILITY STATEMENT

All datasets generated and source code for this study are included in the article/**Supplementary Material**.

ETHICS STATEMENT

The animal study was reviewed and approved by the Danish National Animal Experiments Inspectorate, Ministry of Environment and Food of Denmark, and Danish Veterinary and Food Administration.

AUTHOR CONTRIBUTIONS

SM and CS designed the animal experiments. SM performed animal experiments and drafted manuscript. SM, CS, and JJ analyzed data and prepared figures and tables. SM, JJ, N-HH-R, and CS interpreted results, edited and revised manuscript and approved final version of manuscript.

FUNDING

The study was supported by the Dynamical Systems Interdisciplinary Network, University of Copenhagen and Edith Waagens and Frode Waagens Foundation.

ACKNOWLEDGMENTS

This work is part of the Dynamical Systems Interdisciplinary Network, University of Copenhagen. We thank Max Salomonsson, M.D. Ph.D. for consultation on the electrical stimulation protocol. We also thank Kristoffer Racz for genotyping our connexin 45 mice.

SUPPLEMENTARY MATERIAL

The Supplementary Material for this article can be found online at: https://www.frontiersin.org/articles/10.3389/fphys.2020.00961/full#supplementary-material.

REFERENCES

Arensbak, B., Mikkelsen, H. B., Gustafsson, F., Christensen, T., and Holstein-Rathlou, N. -H. (2001). Expression of connexin 37, 40, and 43 mRNA and protein in renal preglomerular arterioles. *Histochem. Cell Biol.* 115, 479–487. doi: 10.1007/s004180100275

Boesen, E. I., Crislip, G. R., and Sullivan, J. C. (2012). Use of ultrasound to assess renal reperfusion and P-selectin expression following unilateral renal ischemia. *Am. J. Physiol. Ren. Physiol.* 303, F1333–F1340. doi: 10.1152/ajprenal.00406.2012

Brasen, J. C., de Wit, C., and Sorensen, C. M. (2018). Myoendothelial coupling through Cx40 contributes to EDH-induced vasodilation in murine renal arteries: evidence from experiments and modelling. *Acta Physiol.* 222, 1–12. doi: 10.1111/apha.12906

Braunstein, T. H., Sorensen, C. M., and Holstein-Rathlou, N. -H. (2009). Connexin abundance in resistance vessels from the renal microcirculation in normo- and hypertensive rats. *APMIS.* 117, 268–276. doi: 10.1111/j.1600-0463.2009.02432.x

Brown, R. D., Hilliard, L. M., Head, G. A., Jones, E. S., Widdop, R. E., and Denton, K. M. (2012). Sex differences in the pressor and tubuloglomerular feedback response to angiotensin II. *Hypertension* 59, 129–135. doi: 10.1161/HYPERTENSIONAHA.111.178715

Casellas, D., and Navar, L. G. (1984). In vitro perfusion of juxtamedullary nephrons in rats. *Am. J. Physiol. Ren. Physiol.* 246, F349–F358. doi: 10.1152/ajprenal.1984.246.3.F349

de Wit, C. (2010). Different pathways with distinct properties conduct dilations in the microcirculation in vivo. *Cardiovasc. Res.* 85, 604–613. doi: 10.1093/cvr/cvp340

de Wit, C., Bolz, S. -S., Kirchhoff, S., Krüger, O., Willecke, K., and Pohl, U. (2000). Impaired conduction of vasodilation along arterioles in connexin40-deficient mice. *Circ. Res.* 86, 649–655. doi: 10.1161/01.RES.86.6.649

de Wit, C., Roos, F., Bolz, S.-S., and Pohl, U. (2003). Lack of vascular connexin 40 is associated with hypertension and irregular arteriolar vasomotion. *Physiol. Genomics* 13, 169–177. doi: 10.1152/physiolgenomics.00169.2002

Dora, K. A., Xia, J., and Duling, B. R. (2003). Endothelial cell signaling during conducted vasomotor responses. *Am. J. Physiol. Heart Circ. Physiol.* 285, 119–126. doi: 10.1152/ajpheart.00643.2002

Dutta, S., and Sengupta, P. (2016). Men and mice: relating their ages. *Life Sci.* 152, 244–248. doi: 10.1016/j.lfs.2015.10.025

Emerson, G. G., and Segal, S. S. (2000). Electrical coupling between endothelial cells and smooth muscle cells in hamster feed arteries. *Circ. Res.* 87, 474–479. doi: 10.1161/01.RES.87.6.474

Figueroa, X. F., Paul, D. L., Simon, A. M., Goodenough, D. A., Day, K. H., Damon, D. N., et al. (2003). Central role of connexin40 in the propagation of electrically activated vasodilation in mouse cremasteric arterioles in vivo. *Circ. Res.* 92, 793–800. doi: 10.1161/01.RES.0000065918.90271.9A

Gohar, E. Y., Cook, A. K., Pollock, D. M., and Inscho, E. W. (2019). Afferent arteriole responsiveness to endothelin receptor activation: does sex matter? *Biol. Sex Differ.* 10:1. doi: 10.1186/s13293-018-0218-2

Goligorsky, M. S., Iijima, K., Krivenko, Y., Tsukahara, H., Hu, Y., and Moore, L. C. (1997). Role of mesangial cells in macula densa to afferent arteriole information transfer. *Clin. Exp. Pharmacol. Physiol.* 24, 527–531. doi: 10.1111/j.1440-1681.1997.tb01240.x

Gustafsson, F., Andreasen, D., Salomonsson, M., Jensen, B. L., and Holstein-Rathlou, N. -H. (2001). Conducted vasoconstriction in rat mesenteric arterioles: role for dihydropyridine-insensitive Ca^{2+} channels. *Am. J. Physiol. Heart Circ. Physiol.* 280, H582–H590. doi: 10.1152/ajpheart.2001.280.2.H582

Gustafsson, F., and Holstein-Rathlou, N. -H. (1999). Angiotensin II modulates conducted vasoconstriction to norepinephrine and local electrical stimulation in rat mesenteric arterioles. *Cardiovasc. Res.* 44, 176–184. doi: 10.1016/S0008-6363(99)00174-1

Haefliger, J. -A., Demotz, S., Braissant, O., Suter, E., Waeber, B., Nicod, P., et al. (2001). Connexins 40 and 43 are differentially regulated within the kidneys of rats with renovascular hypertension. *Kidney Int.* 60, 190–201. doi: 10.1046/j.1523-1755.2001.00786.x

Haefliger, J. -A., Nicod, P., and Meda, P. (2004). Contribution of connexins to the function of the vascular wall. *Cardiovasc. Res.* 62, 345–356. doi: 10.1016/j.cardiores.2003.11.015

Hagan, C. (2017). When are mice considered old? Available at: https://www.jax.org/news-and-insights/jax-blog/2017/november/when-are-mice-considered-old (Accessed April 9, 2019).

Hakim, C. H., Jackson, W. F., and Segal, S. S. (2008). Connexin isoform expression in smooth muscle cells and endothelial cells of hamster cheek pouch arterioles and retractor feed arteries. *Microcirculation* 15, 503–514. doi: 10.1080/10739680801982808

Hanner, F., Sorensen, C. M., Holstein-Rathlou, N. -H., and Peti-Peterdi, J. (2010). Connexins and the kidney. *Am. J. Phys. Regul. Integr. Comp. Phys.* 298, R1143–R1155. doi: 10.1152/ajpregu.00808.2009

Hanner, F., Maltzahn, J.von, Maxeiner, S., Toma, I., Sipos, A., Krüger, O., et al. (2008). Connexin45 is expressed in the juxtaglomerular apparatus and is involved in the regulation of renin secretion and blood pressure. *Am. J. Phys. Regul. Integr. Comp. Phys.* 295, R371–R380. doi: 10.1152/ajpregu.00468.2007.

Harrison-Bernard, L. M., Cook, A. K., Oliverio, M. I., and Coffman, T. M. (2003). Renal segmental microvascular responses to ANG II in AT1A receptor null mice. *Am. J. Physiol. Ren. Physiol.* 284, F538–F545. doi: 10.1152/ajprenal.00340.2002

Hilliard, L. M., Nematbakhsh, M., Kett, M. M., Teichman, E., Sampson, A. K., Widdop, R. E., et al. (2011). Gender differences in pressure-natriuresis and renal autoregulation: role of the angiotensin type 2 receptor. *Hypertension* 57, 275–282. doi: 10.1161/HYPERTENSIONAHA.110.166827

Hong, K. -S., and Lee, M. -G. (2017). Rescue effect of exercise on impaired arteriolar myogenic response with advancing age. *Exerc. Sci.* 26, 8–16. doi: 10.15857/ksep.2017.26.1.8

Hosoyamada, Y., Ichimura, K., and Sakai, T. (2015). Organ specificity and functional relevance of the arterial structure: a comparative study in the kidney and the skeletal muscle with electron microscopy. *J. Vasc. Res.* 52, 265–272. doi: 10.1159/000442978

Iversen, B. M., Amann, K., Kvam, F. I., Wang, X., and Ofstad, J. (1998). Increased glomerular capillary pressure and size mediate glomerulosclerosis in SHR juxtamedullary cortex. *Am. J. Phys.* 274, F365–F373. doi: 10.1152/ajprenal.1998.274.2.F365

Jacobsen, J. C. B., and Sorensen, C. M. (2015). Influence of connexin40 on the renal myogenic response in murine afferent arterioles. *Phys. Rep.* 3, 1–12. doi: 10.14814/phy2.12416

Just, A., Kurtz, L., de Wit, C., Wagner, C., Kurtz, A., and Arendshorst, W. J. (2009). Connexin 40 mediates the tubuloglomerular feedback contribution to renal blood flow autoregulation. *J. Am. Soc. Nephrol.* 20, 1577–1585. doi: 10.1681/ASN.2008090943

Kapela, A., Behringer, E. J., Segal, S. S., and Tsoukias, N. M. (2018). Biophysical properties of microvascular endothelium: requirements for initiating and conducting electrical signals. *Microcirculation* 25, 1–15. doi: 10.1111/micc.12429

Krüger, O., Plum, A., Kim, J. -S., Winterhager, E., Maxeiner, S., Hallas, G., et al. (2000). Defective vascular development in connexin 45-deficient mice. *Development* 127, 4179–4193.

Kurtz, L., Janssen-Bienhold, U., Kurtz, A., and Wagner, C. (2009). Connexin expression in renin-producing cells. *J. Am. Soc. Nephrol.* 20, 506–512. doi: 10.1681/ASN.2008030252

Li, W. -C., Soffe, S. R., and Roberts, A. (2004). A direct comparison of whole cell patch and sharp electrodes by simultaneous recording from single spinal neurons in frog tadpoles. *J. Neurophysiol.* 92, 380–386. doi: 10.1152/jn.01238.2003

Li, L., Zhang, W., Shi, W. Y., Ma, K. -T., Zhao, L., Wang, Y., et al. (2015). The enhancement of Cx45 expression and function in renal interlobar artery of spontaneously hypertensive rats at different age. *Kidney Blood Press. Res.* 40, 52–65. doi: 10.1159/000368482

Lott, M. E. J., Herr, M. D., and Sinoway, L. I. (2004). Effects of transmural pressure on brachial artery mean blood velocity dynamics in humans. *J. Appl. Physiol.* 93, 2137–2146. doi: 10.1152/japplphysiol.00443.2002

Loutzenhiser, R., Chilton, L., and Trottier, G. (1997). Membrane potential measurements in renal afferent and efferent arterioles: actions of angiotensin II. *Am. J. Physiol.* 273, F307–F314. doi: 10.1152/ajprenal.1997.273.2.F307

Marsh, D. J., Toma, I., Sosnovtseva, O. V., Peti-Peterdi, J., and Holstein-Rathlou, N. -H. (2009). Electrotonic vascular signal conduction and nephron synchronization. *Am. J. Physiol. Ren. Physiol.* 296, F751–F761. doi: 10.1152/ajprenal.90669.2008

Maxeiner, S., Dedek, K., Janssen-Bienhold, U., Ammermüller, J., Brune, H., Kirsch, T., et al. (2005). Deletion of connexin45 in mouse retinal neurons disrupts the rod/cone signaling pathways between AII amacrine and ON cone bipolar cells and leads to impaired visual transmission. *J. Neurosci.* 25, 566–576. doi: 10.1523/JNEUROSCI.3232-04.2005

Møller, S., Jacobsen, J. C. B., Braunstein, T. H., Holstein-Rathlou, N. -H., and Sorensen, C. M. (2020). Influence of connexin45 on renal autoregulation. *Am. J. Physiol. Ren. Physiol.* 318, F732–F740. doi: 10.1152/ajprenal.00185.2019

Moreno, A. P. (2004). Biophysical properties of homomeric and heteromultimeric channels formed by cardiac connexins. *Cardiovasc. Res.* 62, 276–286. doi: 10.1016/j.cardiores.2004.03.003

Nielsen, M. S., Axelsen, L. N., Sorgen, P. L., Verma, V., Delmar, M., and Holstein-Rathlou, N. -H. (2012). Gap junctions. *Compr. Physiol.* 2, 1981–2035. doi: 10.1002/cphy.c110051

Palanker, D., Vankov, A., Freyvert, Y., and Huie, P. (2008). Pulsed electrical stimulation for control of vasculature: temporary vasoconstriction and permanent thrombosis. *Bioelectromagnetics* 29, 100–107. doi: 10.1002/bem.20368

Peti-Peterdi, J. (2006). Calcium wave of tubuloglomerular feedback. *Am. J. Physiol. Ren. Physiol.* 291, F473–F480. doi: 10.1152/ajprenal.00425.2005

Salomonsson, M., Gustafsson, F., Andreasen, D., Jensen, B. L., and Holstein-Rathlou, N. -H. (2002). Local electric stimulation causes conducted calcium response in rat interlobular arteries. *Am. J. Physiol. Ren. Physiol.* 283, F473–F480. doi: 10.1152/ajprenal.00247.2001

Schmidt, V. J., Jobs, A., Maltzahn, J.von, Wörsdörfer, P., Willecke, K., and de Wit, C. (2012). Connexin45 is expressed in vascular smooth muscle but its function remains elusive. *PLoS One* 7:e42287. doi: 10.1371/journal.pone.0042287.

Schneider, M. P., Wach, P. F., Durley, M. K., Pollock, J. S., and Pollock, D. M. (2010). Sex differences in acute ANG II-mediated hemodynamic responses in mice. *Am. J. Phys. Regul. Integr. Comp. Phys.* 299, R899–R906. doi: 10.1152/ajpregu.00638.2009

Schweda, F., Kurtz, L., de Wit, C., Janssen-Bienhold, U., Kurtz, A., and Wagner, C. (2009). Substitution of connexin40 with connexin45 prevents hyperreninemia and attenuates hypertension. *Kidney Int.* 75, 482–489. doi: 10.1038/ki.2008.637

Segal, S. S., Damon, D. N., and Duling, B. R. (1989). Propagation of vasomotor responses coordinates arteriolar resistances. *Am. J. Physiol. Heart Circ. Physiol.* 256, H832–H837. doi: 10.1152/ajpheart.1989.256.3.h832

Simon, A. M., and McWhorter, A. R. (2003). Decreased intercellular dye-transfer and downregulation of non-ablated connexins in aortic endothelium deficient in connexin37 and connexin40. *J. Cell Sci.* 116, 2223–2236. doi: 10.1242/jcs.00429

Sorensen, C. M., Giese, I., Braunstein, T. H., Brasen, J. C., Salomonsson, M., and Holstein-Rathlou, N. -H. (2012). Role of connexin40 in the autoregulatory response of the afferent arteriole. *Am. J. Physiol. Ren. Physiol.* 303, F855–F863. doi: 10.1152/ajprenal.00026.2012

Steinhausen, M., Endlich, K., Nobiling, R., Parekh, N., and Schütt, F. (1997). Electrically induced vasomotor responses and their propagation in rat renal vessels in vivo. *J. Physiol.* 505, 493–501. doi: 10.1111/j.1469-7793.1997.493bb.x

Wagner, C. (2008). Function of connexins in the renal circulation. *Kidney Int.* 73, 547–555. doi: 10.1038/sj.ki.5002720

Wagner, C., de Wit, C., Kurtz, L., Grünberger, C., Kurtz, A., and Schweda, F. (2007). Connexin40 is essential for the pressure control of renin synthesis and secretion. *Circ. Res.* 100, 556–563. doi: 10.1161/01.RES.0000258856.19922.45

Wagner, A. J., Holstein-Rathlou, N. -H., and Marsh, D. J. (1997). Internephron coupling by conducted vasomotor responses in normotensive and spontaneously hypertensive rats. *Am. J. Physiol.* 272, F372–F379. doi: 10.1152/ajprenal.1997.272.3.F372

Wölfle, S. E., Schmidt, V. J., Hoepfl, B., Gebert, A., Alcoléa, S., Gros, D., et al. (2007). Connexin45 cannot replace the function of Connexin40 in along arterioles. *Circ. Res.* 101, 1292–1299. doi: 10.1161/CIRCRESAHA.107.163279

Yao, J., Oite, T., and Kitamura, M. (2009). Gap junctional intercellular communication in the juxtaglomerular apparatus. *Am. J. Physiol. Ren. Physiol.* 296, F939–F946. doi: 10.1152/ajprenal.90612.2008

Conflict of Interest: The authors declare that the research was conducted in the absence of any commercial or financial relationships that could be construed as a potential conflict of interest.

frontiers in Physiology

ORIGINAL RESEARCH
published: 14 August 2020
doi: 10.3389/fphys.2020.00974

Suppression of Connexin 43 Leads to Strial Vascular Hyper-Permeability, Decrease in Endocochlear Potential, and Mild Hearing Loss

*Jinhui Zhang[1†], Xiaohan Wang[1,2†], Zhiqiang Hou[1†], Lingling Neng[1†], Jing Cai[1], Yunpei Zhang[1] and Xiaorui Shi[1]**

[1]Oregon Hearing Research Center, Oregon Health & Science University, Portland, OR, United States, [2]Boston Children's Hospital, Harvard Medical School, Boston, MA, United States

Objective: Connexin 43 (Cx43) is a protein constituent of gap junctions (GJs) in various barrier cells, especially astrocytes and microglia of the blood-brain-barrier (BBB), where it plays an important role in intercellular communication and regulation of the barrier. Despite the importance of Cx43 in other blood barriers, not much attention has been paid to expression and function of Cx43 in the blood-labyrinth-barrier (BLB) of the stria vascularis in the cochlea.

Methods: We used multiple research approaches, including immunocytochemical staining, patch-clamp dye loading technique, real-time quantitative reverse transcription (RT)-PCR, western blot, measurement of endocochlear potential (EP) with an electrode through the scala media, and auditory brainstem response to test hearing function.

Results: We found Cx43 expressed in vascular endothelial cells (ECs) and perivascular resident macrophages (PVMs) in the stria vascularis of adult C57BL/6 mouse cochleae. In particular, we found Cx43 expressed in foot processes of PVMs at points of contact with the endothelium. Consistent with Cx43 expression *in vivo*, we also found Cx43 expressed in EC-EC and EC-PVM interfaces in a co-cultured cell line model. Using a patch-clamp dye loading technique, we demonstrated that Alexa Fluor® 568 dye injected into PVMs diffuses to connected neighboring ECs. The functional coupling between the ECs and PVMs is blocked by 18α-Glycyrrhetinic acid (18α-GA), a GJ blocker. Suppression of Cx43 with small interfering RNA (siRNA) *in vivo* significantly elevated hearing threshold and caused the EP to drop and the blood barrier to become more permeable. In further study, using *in vitro* primary EC cell line models, we demonstrated that suppression of Cx43 disrupts intercellular tight junctions (TJs) in the EC monolayer and increases endothelial monolayer permeability.

Conclusion: Taken together, these findings underscore the importance of Cx43 expression in the normal ear for maintaining BLB integrity, normal EP, and hearing function.

Keywords: mouse, connexin 43, blood-labyrinth-barrier, perivascular macrophage, endocochlear potential, hearing loss

OPEN ACCESS

Edited by:
Mauricio P. Boric, Pontificia Universidad Católica de Chile, Chile

Reviewed by:
Fabio Mammano, University of Padua, Italy
Muhammad Aslam, University of Giessen, Germany

****Correspondence:***
Xiaorui Shi
shix@ohsu.edu

[†]These authors have contributed equally to this work

Specialty section:
This article was submitted to Vascular Physiology, a section of the journal Frontiers in Physiology

Received: *06 April 2020*
Accepted: *16 July 2020*
Published: *14 August 2020*

Citation:
Zhang J, Wang X, Hou Z, Neng L, Cai J, Zhang Y and Shi X (2020) Suppression of Connexin 43 Leads to Strial Vascular Hyper-Permeability, Decrease in Endocochlear Potential, and Mild Hearing Loss. Front. Physiol. 11:974. doi: 10.3389/fphys.2020.00974

INTRODUCTION

Gap junction (GJ) expression in the inner ear is essential for audition (Mammano, 2019). GJ proteins such as connexin 26 (Cx26) and Cx30 are widely distributed in cochlear epithelial cells (Jagger and Forge, 2015; Verselis, 2019). They play critical roles in hearing, including roles in cochlear development and in sustaining auditory function in the mature cochlea (Qu et al., 2012; Verselis, 2019). Mutations in connexins in the cochlear epithelium, in particular mutation of Cx26, is known to be a common cause of congenital hearing loss (Avraham, 2001; Liu et al., 2001; Hoang Dinh et al., 2009; Lee and White, 2009; Martinez et al., 2009; Sun et al., 2009; Hong et al., 2010; Jagger and Forge, 2015; Wingard and Zhao, 2015).

Connexin 43 (Cx43), encoded by the GJ alpha-1 (GJA1) gene, has also been identified in cochlear tissues, including in the stria vascularis, spiral ligament, organ of Corti, and supporting cells of the vestibular sensory epithelia and spiral ganglia (Forge et al., 2003; Suzuki et al., 2003; Nagy et al., 2004; Procacci et al., 2008; Figueroa and Duling, 2009; Liu et al., 2014). Mutation in Cx43 has been reported to be linked to non-syndromic hearing loss (Liu et al., 2001; Martinez et al., 2009; Hong et al., 2010; Wingard and Zhao, 2015). Yet, despite the Cx43 mutation shown involved in congenital hearing loss, the physiological role of Cx43 plays in hearing is largely unknown. This is particularly true regarding its role in the blood-labyrinth barrier (BLB) of the stria vascularis.

The stria vascularis is an ion-transporting tissue in the inner ear that plays an important role in maintaining tissue homeostasis and the endocochlear potential (EP; Wangemann and Schacht, 1996). The stria vascularis lines the scala media and comprises basal cells, intermediate cells, and marginal cells, as well as of the capillary network which perfuses it. Functionally, the stria vascularis produces endolymph and maintains cochlear homeostasis and the EP. The EP is the critical driving force necessary for the depolarization of hair cells (HCs) and is thus central to hearing function (Tasaki and Spyropoulos, 1959; Wangemann, 2002, 2006; Chen and Zhao, 2014). The BLB, a highly specialized capillary network in the stria vascularis, controls exchanges between blood and the intrastitial space in the cochlea (Shi, 2011, 2016). The barrier shields the inner ear from blood-born toxic substances and selectively passes ions, fluids, and nutrients to the cochlea, playing an essential role in maintena nce of the cochlear homeostasis needed for hearing function (Juhn and Rybak, 1981; Juhn, 1988; Shi, 2016). Anatomically, the BLB comprises endothelial cells (ECs) in the strial microvasculature, elaborated tight and adherens junctions, pericytes (PCs), basement membrane (BM), and perivascular resident macrophages (PVMs), which together form a complex "cochlear-vascular unit" (Shi, 2010; Lapenna et al., 2018). Physical interactions between the ECs, PCs, and PVMs, as well as signaling between the cells, are critical for controlling vascular permeability and providing a functionally stable environment (Shi, 2011, 2016).

In the blood-brain-barrier (BBB) of the central nervous system (CNS), Cx43 is predominately expressed in vascular ECs and astrocytes and is especially found in foot process contacts with capillaries (Danesh-Meyer and Green, 2008; Chew et al., 2010; Boulay et al., 2015). The role that Cx43 plays in intercellular communication and regulation of barrier function (other than in the BLB) is widely reported (Naus et al., 1991; Winkler et al., 2011; Boulay et al., 2015). However, the role of Cx43 in the strial BLB has not yet been investigated. In the present study, we report, for the first time, Cx43 immunoreactivity in the strial BLB of adult mouse (C57BL/6) cochleae. We found that downregulation of Cx43 leads to hearing loss. Supression of CX43 also strongly affects BLB integrity, causing strial hyper-permeability and decrease in EP. Further study in primary EC cell line models revealed that the Cx43 has an effect on TJ protein expression in the endothelial barrier. Taken together, the results underscore the importance of Cx43 expression in the strial BLB for maintenance of BLB integrity, normal EP, and hearing function.

Nomenclature: EP, Endocochlear potential; ABR, Auditory brainstem response; PVM, Perivascular resident macrophage.

MATERIALS AND METHODS

Animals

All mice used in this work were purchased from The Jackson Laboratory (Bar Harbor, ME, USA). C57BL/6J mice (stock number: 000664, 6–8 weeks old) were used in all *in vivo* experiments, excepting the B6.129P2(Cg)-Cx3cr1^{tm1Litt}/J transgenic mice (stock number: 005582, 6–8 weeks old) used in the *in vivo* immunofluorescence experiments for the visualization of Cx43 expression in PVMs. All procedures in this study were reviewed and approved by the Institutional Animal Care and Use Committee (IACUC) at Oregon Health & Science University (IP 00000968).

Immunohistochemistry

The procedure for immunohistochemistry was previously reported (Zhang et al., 2012). Briefly, mice were deeply anesthetized by intraperitoneal injection of a cocktail containing ketamine hydrochloride (100 mg/kg, Henry Schein, Melville, NY) and xylazine hydrochloride (40 mg/kg, Par Pharmaceutical Companies, Inc. Spring Valley, NY). After sedation, mice were perfused intravascularly through the left ventricle with phosphate-buffered saline (PBS, pH 7.4) to flush out circulating blood, followed by a 4% paraformaldehyde fixative. The mice were decapitated and the cochleae harvested and fixed in 4% paraformaldehyde overnight. Whole-mounts of stria vascularis were carefully isolated, washed in PBS, permeabilized in 0.5% Triton X-100 (T8787, Sigma-Aldrich, St. Louis, MO) in PBS for 0.5 h, and immuno-blocked with a solution of 1% fish gelatin (G7765, Sigma-Aldrich, St. Louis, MO) in PBS for an additional hour. The specimens were incubated overnight at 4°C with the primary antibody (**Table 1**), a rabbit polyclonal, to detect Cx43 (ab11370, Abcam, Cambridge, MA) in 1% bovine serum albumin (BSA) diluted in PBS. After three washes in PBS, samples were incubated with the secondary antibody, Alexa Fluor 568-conjugated goat anti-rabbit IgG (A-11011, Thermo Fisher Scientific, Waltham, MA), for 1 h at room temperature. Capillaries were labeled with the lectin Griffonia simplicifolia IB4 (GS-IB4)

TABLE 1 | Antibodies used in the study.

Antibodies	Vectors	Cat#	Dilution source (dilution with 1% BSA-PBS)		Application
ZO-1	Invitrogen	61-7300	1:25	Rabbit polyclonal for ZO-1	Labeling TJ associated protein
VE-cadherin	Abcam	Abcam	1:50	Rabbit polyclonal for VE-cadherin	Labeling TJ associated protein
Occludin	Abcam	Ab31721	1:50	Rabbit polyclonal for occludin	Labeling TJ associated protein
Connexin 43	Abcam	Ab11370	1:100	Rabbit polyclonal for connexin 43/ GJA1	Labeling gap junction protein (in tissue)
Connexin 43	Abcam	Ab78055	1:250	Mouse monoclonal for connexin 43/GJA1	Labeling gap junction protein (in cell line)
von Willebrand Factor	Abcam	Ab11713	1:100	Sheep polyclonal for von Willebrand factor	Labeling endothelial cells

conjugated to Alexa Fluor 647 (I32450, Thermo Fisher Scientific, Waltham, MA). The tissues were washed three times and mounted in mounting medium (H-1500, Vector Laboratories, Burlingame, CA).

EC Culture and EC-PVM Co-culture Staining for Cx43

Protocols for generating the cell lines used in these experiments were previously reported (Neng et al., 2013). Briefly, cochleae from 10- to 15-day-old C57BL/6J mice were harvested under sterile conditions. The stria vascularis was gently pulled away from the spiral ligament and placed in ice-cold perilymph solution containing 125 mmol/L NaCl, 3.5 mmol/L KCl, 1.3 mmol/L $CaCl_2$, 1.5 mmol/L $MgCl_2$, 0.51 mmol/L NaH_2PO_4, 10 mmol/L HEPES, and 5 mmol/L glucose at pH7.4 with osmolarity adjusted to 310 mmol/kg. The isolated stria vascularis was washed with gentle shaking in cool perilymph solution for 10 min and transferred to a clean 35-mm collagen I-coated dish with 2 ml of Endothelial Cell Medium (1001, ScienCell™ Research Laboratories, Carlsbad, CA) or Macrophage Medium (1921, ScienCell™ Research Laboratories, Carlsbad, CA). The stria vascularis was cut into small pieces with sterile ophthalmic tweezers under a dissection microscope. Fragmented pieces of the stria vascularis were seeded around the dish to roughly uniform density. The procedure for situating the fragments requires approximately 2 h. The medium is changed every 3 days. The cells are incubated at 37°C in 5% CO_2 for 7–14 days until the cell clones melt. Cell clusters of each phenotype are visible by phase contrast microscopy at 6–7 days, at which time the cells are passaged into a 60-mm collagen I-coated dish. The cultured cells were purified by fluorescence-activated cell sorting. Purified primary PVMs were fluorescence encoded with green fluorescent protein (GFP), as previously described (Neng et al., 2015). Purified primary ECs and fluorescence tagged PVMs were cultured or co-cultured in separate dishes or in mixtures of the two cell types for 3 days. The cells were then fixed in 4% paraformaldehyde in PBS for 15 min at room temperature, permeabilized in 0.5% Triton X-100 in PBS for 5 min, blocked with 1% fish gelatin for 1 h, and incubated overnight at 4°C with the primary antibodies. The primary antibodies for the EC culture included anti-von Willebrand factor (vWF; ab11713, Abcam, Cambridge, MA) for ECs and anti-Cx43 for Cx43 diluted in 1% BSA in PBS. The primary antibody for the EC-PVM co-culture was only anti-Cx43 diluted in 1% BSA in PBS. After three washes in PBS, the samples were incubated with secondary antibodies, either Alexa Fluor 488-conjugated donkey anti-sheep IgG (A-11015, Thermo Fisher Scientific, Waltham, MA) or Alexa Fluor 568-conjugated goat anti-rabbit IgG for 1 h at room temperature. Images were acquired under an FV1000 Olympus laser-scanning confocal microscope (Olympus FV1000, Japan), saved as OIB files, and further processed using Adobe Photoshop CS2 (Adobe Systems, San Jose, CA).

Dye Injection With a Patch-Clamp Pipette

The EC and PVM co-culture was bathed in artificial cerebrospinal fluid (ACSF) at room temperature on day 3. Pipettes for dye delivery were prepared using a micropipette puller (Sutter, P-97). When back-filled with the internal solution, the typical resistance of the pipette is about 15 mΩ in ACSF. The ACSF used to bath the cell line consists of: 137 mM sodium chloride, 0.5 mM sodium bicarbonate, 1 mM sodium phosphate, 3 mM potassium chloride, 2 mM calcium chloride, 1 mM magnesium sulfate, 20 mM HEPES, and 16 mM glucose, with the pH adjusted to 7.4 with sodium hydroxide. The internal solution contains: 125 mM potassium gluconate, 5 mM sodium chloride, 4 mM EGTA, 10 mM HEPES, 4 mM ATP-Mg, 0.5 mM GTP-Na, 10 mM phosphocreatine, and 1 mM magnesium chloride, with the pH adjusted to 7.2 with potassium hydroxide. Alexa 568 Hydrazide 35 μg/ml (A10437, Thermo Fisher Scientific, Waltham, MA) was added to the internal solution and dialyzed for 1 min. Alexa 488 Hydrazide (A10436, Thermo Fisher Scientific, Waltham, MA) was then delivered to the cells (PVMs) in whole-cell mode. Since the Alexa dye is negatively charged, a negative potential (−10 mV) was applied to expedite diffusion of the dye. To block the GJ, 18α-Glycyrrhetinic acid (18α-GA,10 μM, G8503, Sigma-Aldrich, St. Louis, MO) was added to the culture medium for 30 min (Zhu et al., 2016; Jiang et al., 2017).

In vivo siRNA Transfection and Real-Time Quantitative RT-PCR

For the small interfering RNA (siRNA) transfection, mice were anesthetized, a 5 μl solution of Gja1 Silencer® Select Pre-designed siRNA (40 μM, 4390771, Assay ID: s66667, Thermo Fisher Scientific, Waltham, MA) was injected through the posterior-inferior quadrant (Qi et al., 2014) with a Hamilton's microliter syringe (30 G needle), and the middle ear was filled completely with the solution for 3 days. Scrambled siRNA (4390846, Thermo Fisher Scientific, Waltham, MA) of the same concentration was given to the control group. This method was previously used and reported (Zhang et al., 2012).

Three days following the injection, mice were sacrificed, and the cochleae were dissected. Total RNA was extracted from the stria vascularis.

The procedure for quantitative RT-PCR was previously described and reported (Yang et al., 2011). Briefly, a total RNA (300–500 ng) was extracted from control scrambled siRNA treated (n = 6) and Gja1 siRNA treated animals (n = 6) using an RNeasy MinElute Cleanup Kit (74204, Qiagen, Valencia, CA), as per the manufacturer's recommendations. The sample for total RNA was reverse-transcribed with a RETROscript™ Reverse Transcription Kit (AM1710, Thermo Fisher Scientific, Waltham, MA). Complementary DNA (cDNA) synthesized from total RNA was diluted 10-fold with DNase-free water, with each cDNA sample independently measured for three times. Transcripts were quantified by TaqMan® Gene Expression Assays for Gja1 (4331182, Assay ID: Mm00439105_m1, Thermo Fisher Scientific, Waltham, MA) on a model 7300 Real-Time PCR system (Thermo Fisher Scientific, Waltham, MA). The real-time PCR was cycled at 95°C for 20 s, 40 cycles of 95°C for 1 s, and 60°C for 20 s. Mouse glyceraldehyde-3-phosphate dehydrogenase (GAPDH) was used as an endogenous control. Quantitative PCR analysis was performed as per the guidelines provided by Applied Biosystems using the comparative cycle threshold method.

Western Blot Analysis

Total 400 μg protein from strial tissue of control, scrambled siRNA treated, and Gja1 siRNA treated groups was extracted in ice cold ACSF containing Halt™ Protease Inhibitor (1:100; 78425, Thermo Fisher Scientific, Waltham, MA) and transferred to cold RIPA Lysis and Extraction Buffer (89900, Thermo Fisher Scientific, Waltham, MA) with the protease inhibitor. A TissueRuptor (Kimble™ Kontes™ Pellet Pestle™; 11800104, Thermo Fisher Scientific, Waltham, MA) was used to homogenize tissue samples, which were then centrifuged for 15 min at 13,000 rpm. Concentration of proteins in the supernatant was measured using a UV-visible spectrophotometer (NanoDrop 1000, Thermo Fisher Scientific, Waltham, MA). A total of 120 μg protein from each cohort was loaded to lanes of a 10% sodium dodecyl sulfate-polyacrylamide gel to detect Cx43. Proteins were electrophoretically transferred to PVDF membranes and blocked with non-fat milk for 1 h at room temperature. Membranes were then incubated in primary antibody, a rabbit polyclonal anti-Cx43/GJA1 antibody (ab11370, Abcam, Cambridge, MA), or GAPDH (sc-32233, Santa Cruz Biotechnology, Dallas, TX) at a dilution of 1:1000 in skim milk overnight at 4°C. After three washes with TBST, the membranes were incubated for 1 h with the secondary antibody goat anti-rabbit IgG (H + L)-HRP (170-6515, Bio-Rad Laboratories, Hercules, CA) at a dilution of 1:3000 for 1 h at room temperature, and antigens were assessed using ECL Plus Western Blotting Detection Reagents (RPN2132, Amersham Biosciences, Piscataway, NJ). Image J (NIH, 1.52p) was used to quantify samples in the western blot analysis. All image panels presented in the manuscript were constituted from individual images processed and labeled using Adobe Photoshop (version CC 2017) with a resolution of 300 dpi. To enhance visualization, some of the images were equivalently enhanced after composition.

Immunolabeling of Tight Junction-Associated Proteins in Primary Cell Lines and Isolated Strial Capillaries

Around 2 ml of purified ECs at passage 3 (at a density of 3.0×10^5 ml) was seeded and grown on 35-mm collagen I-coated glass-bottom dishes in a growth medium for ~5 days. Cells were then transfected with Gja1 siRNA for 48 h, following the manufacturer's guidelines. For negative control, the cells were transfected with scrambled siRNA. For the transfection, 10 μl TransIT-TKO® Transfection Reagent (MIR 2154, Mirus Bio LLC, Madison, WI) was mixed with 250 μl serum-free medium in a sterile tube, and 25 nM siRNA was added to the mixture. After incubation for 15 min at room temperature, the TransIT-TKO Reagent/siRNA mixture was added to the cell culture dish with 2.25 ml of fresh complete growth medium. The cells were then fixed in 4% PFA (pH 7.2) for 15 min at room temperature and washed in 2 ml of PBS (three times for 10 min). The cells were permeabilized in 0.25% Triton X-100 for 5 min at room temperature, washed with 2 ml PBS (three times for 10 min), and incubated with an immunofluorescence blocking solution at room temperature for 1 h. The cells were incubated overnight at 4°C with primary antibodies, ZO-1 Polyclonal Antibody (61-7100, Thermo Fisher Scientific, Waltham, MA), Anti-VE cadherin antibody (ab33168, Abcam, Cambridge, MA), Anti-Occludin antibody (ab31721, Abcam, Cambridge, MA), and Anti-Connexin 43/GJA1 antibody (ab78055, Abcam, Cambridge, MA; **Table 1**) in 1% BSA in PBS. After three washes in PBS for 10 min, the cells were incubated with the secondary antibody, Alex Fluor 568-conjugated goat anti-rabbit IgG (H + L) and Alex Fluor 488 goat anti-mouse IgG (H + L; A-11001, Thermo Fisher Scientific, Waltham, MA), diluted at 1:100 in 1% BSA in PBS solution for 1 h at room temperature. The cells were washed in 2 ml PBS (three times for 10 min) and imaged under FV1000 Olympus laser-scanning confocal microscope (Olympus FV1000, Japan). For capillary isolation, we used a previously reported "sandwich-dissociation" method for isolation (Yang et al., 2011; Zhang et al., 2012). Specifically, the cochleae from control (scrambled siRNA) and siRNA transfection groups were dissected after cardiovascular perfusion with saline, removed rapidly, and placed in a Petri dish filled with a hysiological solution containing 125 mmol/L NaCl, 3.5 mmol/L KCl, 1.3 mmol/L $CaCl_2$, 1.5 mmol/L $MgCl_2$, 0.51 mmol/L NaH_2PO_4, 10 mmol/L Hepes, and 5 mmol/L glucose at pH 7.4 with osmolarity adjusted to 310 mmol/kg. The stria vascularis was peeled away from the spiral ligament gently with Dumont tweezers (110 mm, 0.1 × 0.06 mm tip) and a Tungsten Dissecting Probe (50 mm, 0.5-mm diameter rod) under an Olympus SZ61 dissecting microscope. The stria vascularis was placed in a glass-bottomed microwell dish (dish diameter: 35 mm; microwell diameter: 10 mm; coverglass: 0.16–0.19 mm; MatTek Corporation) filled with the physiological solution. A glass coverslip (0.16 mm) then was positioned over the stria vascularis, and the tissue was sandwiched gently between the glass surfaces. Gentle pressure was applied to compress the stria vascularis against the two glass surfaces. By repeating this step, the nonvascular tissues were dispersed

into the solution and separated from the capillaries. Nonvascular cells were flushed away gently with a 100-µl micropeptide; the clean microvessels were adhered and "printed" onto the bottom of the dish, analogous to the offset-printing deposit of a pattern of ink onto paper. The isolated capillaries were then immunolabled with ZO-1 Polyclonal Antibody (61-7100, Thermo Fisher Scientific, Waltham, MA), Anti-VE cadherin antibody (ab33168, Abcam, Cambridge, MA), and Anti-Occludin antibody (ab31721, Abcam, Cambridge, MA; Zhang et al., 2012). The samples were imaged under the Olympus laser-scanning confocal microscope.

Assessment of Vascular Permeability *in vivo*

Vascular permeability in the scrambled siRNA treated and Gja1 siRNA treated groups was assessed repeatedly using a albumin-fluorescein isothiocyanate (FITC) conjugate tracer (A9771, FITC-albumin, 66 kDa, Sigma, St. Louis, MO) and a fluorescein isothiocyanate-dextran tracer (FD10S, FITC-dextran, 10 kDa, Sigma, St. Louis, MO). Around 100 µl tracers (40 mg/ml) were intravenously administered to the tail vein of anesthetized control siRNA treated and Gja1 siRNA treated groups for 30 min prior to transcardial perfusion of the mice with PBS. After circulating blood cells were completedly flushed away, the stria vascularis was gently emoved. The tissues were then homogenized in 1% Triton X-100 in PBS, with the lysate centrifuged at 13,000 rpm for 20 min. The fluorescence signal, reflecting concentration of fluorescence tagged tracer trapped in the stria vascularis, was detected with a Tecan GENios Plus microplate reader at an excitation wavelength of 450 nm, with the emission acquired through a 560-nm filter.

Permeability Assay

Purified ECs were seeded on polyethylene terephthalate membranes of Transwell inserts (353095, Corning, New York, NY) in 24-well plates at 10^5 cells per insert and cultured for 3 days to form a complete monolayer, as previous reported (Zhang et al., 2015). The cells were then transfected with Gja1 siRNA or scrambled siRNA for 48 h (at a 25 nM final concentration), as per TransIT-TKO guidelines. Endothelial monolayer permeability was assessed by determining the flux of FITC-dextran in the upper and lower chambers. FITC-dextran (10 kDa, 10 mg/ml) was added to the insert at a final concentration of 1 mg/ml. After 20 min of incubation at room temperature, 100 µl medium was removed from the well of the Receiver Tray and transferred to a 96-well plate for measurements. The permeability of the EC monolayer was measured by detecting FITC-dextran fluorescence using a fluorescence plate reader with filters appropriate for 485 nm excitation and 535 nm emission (Zhang et al., 2012).

Statistics

SPSS (18.0) software was used for the data analysis. For determining sample size, we used power analysis to calculate the minimum sample size for a power of 0.8. We used the "resource equation" method when calculating sample size for ANOVA tested data. Both the Shapiro–Wilk test and Q-Q plot were used to test data distribution. Data were presented as means ± SD. Since we took random samples of each group, the data are independent. Student's *t*-test was used for comparison of two groups and one-way ANOVA was used for comparison of three groups. $p < 0.05$ was considered statistically significant.

RESULTS

Cx43 Immunoreactivity Was Detected in the Cochlear Stria Vascularis, and in a Co-culture of PVM-EC Primary Cell Lines

CX43, a GJ protein, has been identified widely distributed in the cardiac and neural system (Hansen et al., 2014). In this study, using western blot, we detected Cx43 immunoreactivity in adult mouse stria vascularis (**Figure 1A**). With immunofluorescence labeling in combination with confocal microscopy, we found that Cx43 was expressed predominantly in capillary ECs and in the contacts between GFP-tagged PVMs ($PVMs^{GFP}$) and ECs in whole-mounted stria vascularis (**Figure 1B**). Cx43 expression in the EC-PVM contacts is particularly evident in the magnified insert image (*) in **Figure 1B**. Cx43 expression was also seen in the spiral ligment (SL), particularly in fibrocytes (FCs) of the spiral prominence (SP), as shown in a cross-section of the cochlear lateral wall (**Figure 1C**). Consistent with what we see in a whole-mounted surface preparation, Cx43 expression in ECs and PVMs is further demonstrated in the cross-section preparation. The Cx43 expression is better visualized in the zoomed image (#) from an insert (#) in panel C. Consistent with Cx43 expression found in strial ECs and PVMs of whole-mounted tissue, we also detected Cx43 expression in co-culture of primary cell lines of strial ECs and PVMs. Under confocal microscopy, we found Cx43 particularly expressed in EC-EC contacts (**Figure 1D**) of an EC cultured model and in PVM-EC contacts (**Figure 1E**) of an EC + PVM co-culture model. The results indicate that Cx43 is expressed in strial BLB component cells of adult cochlea.

Cx43 Mediation of PVM-EC Communication Tested in an *in vitro* Primary Cell Line Co-culture Model

In this study, we found Cx43 GJs actively involved in intercellular communication between ECs and PVMs in an *in vitro* model. PVMs encoded with GFP were co-cultured with ECs for 2 consecutive days. After the ECs and PVMs established connections (day 3), Alexa Fluor 568 fluorescence dye was delivered to the PVM^{GFP} by a patch-clamp pipette. We identified PVMs by the green fluorescence under an epi-fluorescence microscope. One minute later, we detected that the injected fluorescence dye had propagated to surrounding cells, which included connected ECs and nearby $PVMs^{GFP}$. **Figure 2A** is a representative image showing dye diffusion 1 min after the dye was injected into the $PVMs^{GFP}$ under an epi-fluorescence microscope. **Figure 2B** is the same experiment but recorded under a confocal fluorescence microscope 5 min after the dye was injected to the PVMs. The confocal image enables us to

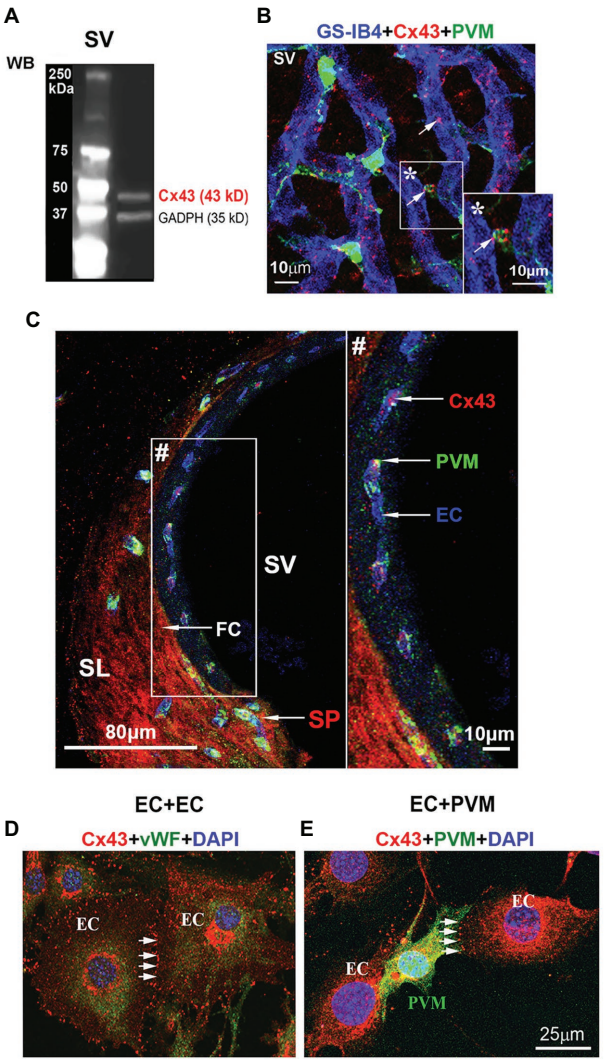

FIGURE 1 | Connexin 43 (Cx43) immunoreactivity detected in the stria vascularis and spiral prominence (SP), and in primary cell lines. **(A)** Western blot analysis shows Cx43 protein tissue expression in the stria vascularis. **(B)** The confocal image of triple immunolabeled cells using antibody for Cx43 to show Cx43-positive spots predominately expressed in blood vessels [labeled with Griffonia simplicifolia IB4 (GS-IB4) conjugated to Alexa Fluor 647] and end-feet of PVMs^{GFP} (green) in a whole-mount surface preparation of the stria vascularis. **(C)** The confocal projection image shows that Cx43 in the SP (SP/arrow) is primarily expressed in endothelial cells (ECs/arrow) and fibrocytes (FCs/arrow) in a cross-section preparation of the cochlear lateral wall. **(D)** The confocal projection image further shows Cx43 expression at the contact border between ECs labeled with antibody for von Willebrand factor (green), an EC marker protein. **(E)** The confocal projection image shows Cx43 expression at the contact border between ECs and PVMs^{GFP} (green). SV, stria vascularis; SL, spiral ligament; SP, spiral prominence; PVM, perivascular resident macrophage; EC, endothelial cell; FC, fibrocyte. * is the magnified insert image of Cx43 expression in the EC-PVM contacts. # is the zoomed image of Cx43 expression from an insert in **panel (C)**.

better display the dye communication between the PVMs and three connected ECs and one neighboring PVM.

To determine whether the dye communication between PVMs^{GFP} and ECs involved Cx43 GJ protein, we employed a GJ blocker, 18α-GA, which has been reported to block Cx43 mediated intercellular communication (Zhu et al., 2016; Jiang et al., 2017). As shown in **Figures 2C,D**, we found that blocking GJ with 18α-GA significantly blocked dye transfer from an injected PVM^{GFP} to the connected ECs. These results suggest that Cx43 mediates intercellular communication between PVMs and ECs.

Downregulation of Cx43 Expression in the Adult Mouse Cochlea Decreases the Endocochlear Potential

The EP is generated by electrogenic secretion of potassium-rich endolymph from the stria vascularis (Patuzzi, 2011). In this study, EP was measured from the scala media by micropipette through it in control siRNA treated and Gja1 siRNA treated mice. Gja1 siRNA (40 μM) at the same concentration of scrambled siRNA (control siRNA) was administered to the cochlea *via* the middle ear cavity for 3 days. Real-time PCR analysis showed that the level of Cx43 messenger RNA (mRNA) in the Gja1 siRNA treated animals was significantly lower than in the control siRNA treated animals (n = 6, $^{**}p < 0.01$, **Figure 3A**). Cx43 protein levels were consistently lower in the Gja1 siRNA treated group (analyzed by WB) than in the control siRNA treated-group [n = 7, $^{*}p$ = 0.013, one-way ANOVA, $^{**}p_{(\text{negative ctrl vs. Gja1 siRNA})}$ = 0.006, **Figures 3B,C**]. We found that the EP was significantly affected by downregulation of Cx43 expression. In the control group, an average EP value is ~ + 107 ± 9.5 mV. In contrast, the EP in Gja1 siRNA treated animals was reduced to ~ + 77 ± 10.4 mV. **Figures 3D,E** demonstrate average EP values and representative EP waveforms in control, siRNA, and scrambled siRNA treated-groups. Our data indicate that normal Cx43 expression is essential for a normal EP.

Downregulation of Cx43 Expression in the Adult Mouse Cochlea Causes Mild Hearing Loss

Hearing sensitivity is also affected by downregulation of Cx43 expression. We found that no significant elevation in hearing threshold was detected in the control siRNA treated-group (**Figures 4A,C**). In contrast, the hearing threshold in the Gja1 siRNA treated-mice was significantly elevated across all tested sound frequencies. **Figures 4B,D** show the respective elevation of hearing threshold at different sound frequencies after Gja1 siRNA treatment at 4 kHz (n = 9, $^{*}p$ = 0.013), 8 kHz (n = 9, $^{*}p$ = 0.039), 12 kHz (n = 9, $^{*}p$ = 0.023), 16 kHz (n = 9, $^{**}p$ = 0.001), 24 kHz (n = 9, $^{***}p < 0.001$), and 32 kHz (n = 9, $^{*}p$ = 0.035). Our data indicate that reduced Cx43 expression in the cochlea causes mild hearing loss across the spectrum from low frequency to high frequency.

Downregulation Cx43 Expression Increases Strial Vascular Leakage *in vivo* and *in vitro*

What mechanisms might explain the drop in EP and hearing loss when Cx43 expression is suppressed? It is known that

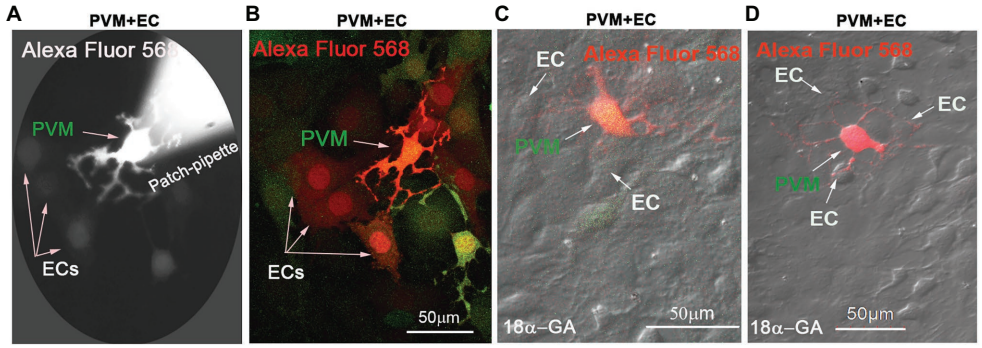

FIGURE 2 | Cx43 mediates intercellular communication between PVMs and ECs in an *in vitro* co-culture model. **(A)** Alexa Fluor 568 dye communication between an injected PVM and nearby ECs 1 min after dye loading under epi-fluorescence microscopy. **(B)** The same experiment was recorded under confocal fluorescence microsopy to better show the injected fluorescent Alexa Fluor 568 dye has spread to surrounding ECs within 5 min of PVM^{GFP} dye injection (green). Arrows indicate dye communication with the cells. **(C,D)** DIC images are overlaid on confocal fluorescence images to show that the injected Alexa Fluor 568 dye was restricted to PVMs (red/green), not transferred to surrounding ECs, when Cx43 was blocked with 18α-Glycyrrhetinic acid (18α-GA).

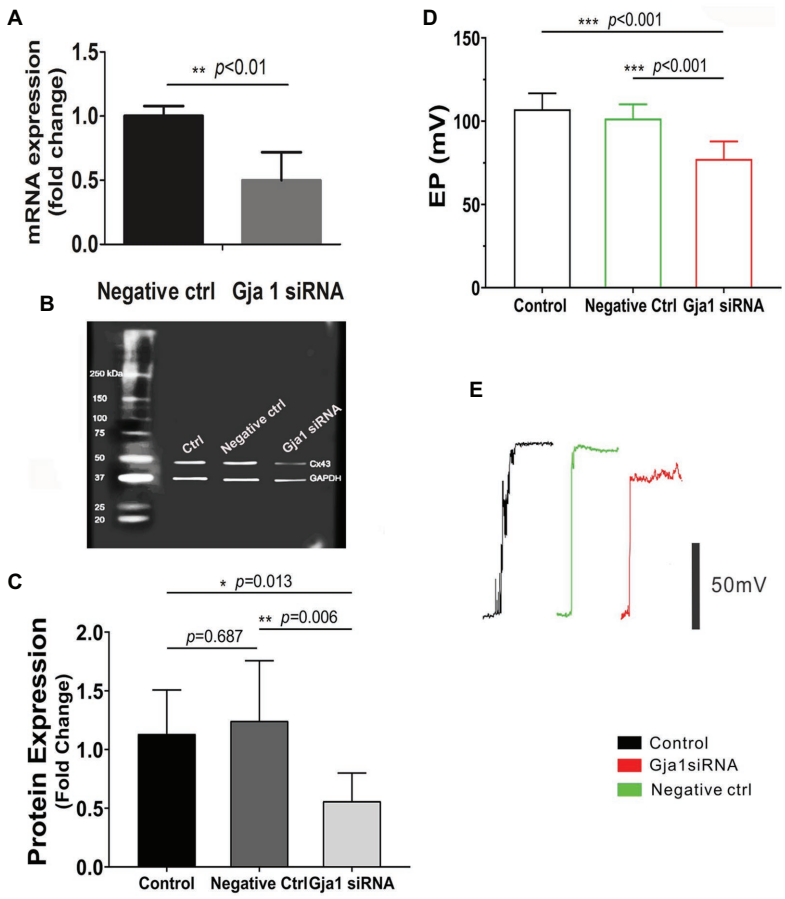

FIGURE 3 | Downregulation of Cx43 reduces endocochlear potential (EP). **(A)** Real-time PCR analysis shows that Cx43 messanger RNA (mRNA) expression is significantly decreased in the stria vascularis of Gja1 small interfering RNA (siRNA) treated groups [$n_{\text{negative ctrl}} = 6$, $n_{\text{Gja1 siRNA}} = 6$, $t(6.186) = 5.327$, $^{**}p_{(\text{negative ctrl vs. Gja1 siRNA})} < 0.01$, Student's *t*-test]. **(B,C)** Western blot analysis shows that Cx43 protein expression is significantly reduced in the Gja1 siRNA treated group [$n = 7$, $F(2,18) = 5.859$, $^{*}p = 0.011$, $p_{(\text{ctrl vs. negative ctrl})} = 0.687$, $^{*}p_{(\text{ctrl vs. Gja1 siRNA})} = 0.013$, $^{**}p_{(\text{negative ctrl vs. Gja1 siRNA})} = 0.006$, one-way ANOVA]. **(D)** Average EP in the control, control scramled siRNA treated, and Gja1 siRNA treated group. A slight but significant decrease in Cx43 protein expression is seen in the Gja1 siRNA treated group, compared to the normal and control groups [$n = 6$, $F(2,21) = 22.045$, $^{***}p < 0.001$, one-way ANOVA, $^{***}p_{(\text{ctrl vs. Gja1 siRNA})} < 0.001$, $^{***}p_{(\text{negative ctrl vs. Gja1 siRNA})} < 0.001$, mean ± SD]. **(E)** Representative EP waveform in the control, control siRNA treated, and Gja1 siRNA treated group.

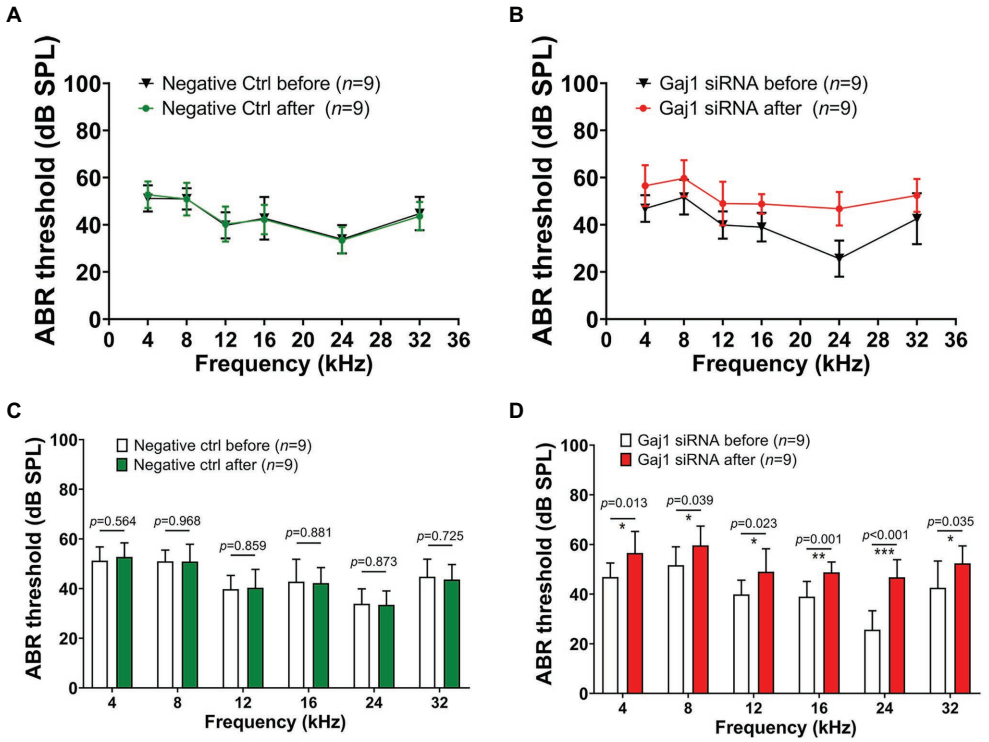

FIGURE 4 | Downregulation of Cx43 expression causes hearing loss. **(A,C)** No elevated hearing threshold was detected at any of the tested frequencies in the control siRNA treated groups (n = 9, $p > 0.05$, Student's t-test, mean ± SD). **(B,D)** Downregulation of Cx43 caused increased hearing threshold at 4 kHz [n = 9, $t(16) = -2.802$, $^{*}p = 0.013$, Student's t-test, mean ± SD], 8 kHz [n = 9, $t(16) = -2.243$, $^{*}p = 0.039$, Student's t-test, mean ± SD], 12 kHz [n = 9, $t(16) = -2.507$, $^{*}p = 0.023$, Student's t-test, mean ± SD], 16 kHz [n = 9, $t(16) = -3.966$, $^{**}p = 0.001$, Student's t-test, mean ± SD], 24 kHz [n = 9, $t(16) = -6.068$, $^{***}p < 0.001$, Student's t-test, mean ± SD], and 32 kHz [n = 9, $t(16) = -2.307$, $^{*}p = 0.035$, Student's t-test, mean ± SD].

direct intercellular communication *via* GJs is critical for control and coordination of blood barrier function (Figueroa and Duling, 2009; Ivanova et al., 2017). In the brain, the absence of Cx43 weakens the BBB (Ezan et al., 2012). Does suppression of Cx43 likewise weaken the BLB? In this study, we investigated the effect of suppressing Cx43 expression on BLB integrity. Vascular permeability was assessed in both *in vitro* in an EC cell line based model and *in vivo*. In the *in vivo* animal model, the vascular permeability in control and Gja1 siRNA treated animals was assessed using an FITC-conjugated dextran tracer. Low molecular weight 10 kDa FITC-dextran or medium molecular weight 66 kDa FITC-albumin was administered intravenously to the mice at a dose of 40 mg/ml in 100 μl physiological solution for 30 min prior to tissue harvest. FITC-dextran leakage was quantified using a leakage index defined in previous publications (Zhang et al., 2015). Our results showed that downregulation of Cx43 increases BLB permeability, as shown in **Figures 5A,B** (n = 3; $^{**}p < 0.001$).

To corroborate our *in vivo* findings, we constructed an *in vitro* endothelial monolayer model (**Figure 5C**), in which a cochlear primary EC cell line was seeded on Transwell filters to form a monolayer (Zhang et al., 2015) and treated with Gja1 siRNA for 48 h. Endothelial monolayer permeability was assessed by determining the flux of FITC-dextran in the lower chambers. The endothelial monolayer barrier was demonstrated to be more permeable in the Gja1 siRNA treated groups, shown in **Figure 5D** than in the control siRNA treated group (n = 12, $^{****}p < 0.0001$).

Downregulation Cx43 Expression Decrease Expression of Tight Junction *in vivo* and *in vitro*

The permeability of the blood barrier is largely a function of the tightness of the intercellular junction. The major TJ-associated proteins in the barrier are occludin, various claudins, ZO-1, and adherens-junction proteins (Jiao et al., 2011; Campbell et al., 2017). Several tight- and adherens-junction proteins, including ZO-1, occludin, and VE-cadherin, have been found in the strial BLB (Zhang et al., 2012, 2015; Shi, 2016). In this study, relative to expression of ZO-1, occludin, and VE-cadherin in the capillaries under normal conditions (**Figures 6A–C**), we found that expression of these proteins in the endothelial tube is clearly changed at day 3 after siRNA treatment *in vivo* (**Figures 6D–F**). Connsistent with the findings seen *in vivo*, TJ protein distribution in the EC monolayer was dramatically altered within 48 h in the siRNA treated groups *in vitro*. In controls, TJs are prominent, outlining the borders of connected ECs throughout the monolayer, as shown in **Figures 6G–I**. In contrast, downregulation of Cx43 leads to randomly scattered, irregular clusters, as shown in **Figures 6J–L**.

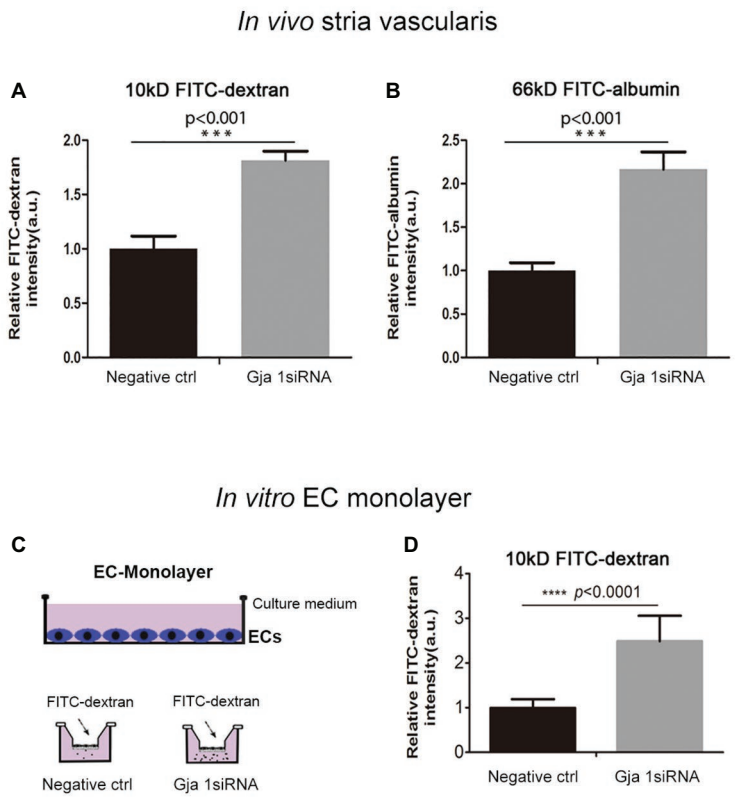

FIGURE 5 | Suppression Cx43 increases vascular leakage *in vivo* and *in vitro*. **(A,B)** More fluorescein isothiocyanate (FITC)-dextran [MW 10 kDa; $n_{ctrl} = 3$, $n_{Gja1\ siRNA} = 3$, $t(4) = -9.797$, $^{***}p_{(ctrl\ vs.\ Gja1\ siRNA)} < 0.001$, Student's *t*-test] and FITC-albumin [MW 66 kDa; $n_{ctrl} = 3$, $n_{Gja1\ siRNA} = 3$, $t(4) = -9.134$, $^{***}p_{(ctrl\ vs.\ Gja1\ siRNA)} < 0.001$, Student's *t*-test] leakage was detected in Gja1 siRNA-treated animals than in control scrambled siRNA treated animals. **(C)** An illustration of the EC monolayer model. **(D)** Significantly increased permeability is found in the EC-monolayer of the Cx43 downregulated group compared to the control EC-monolayer group [$n_{ctrl} = 12$, $n_{Gja1\ siRNA} = 12$, $t(13.404) = -8.626$, $^{****}p_{(ctrl\ vs.\ Gja1\ siRNA)} < 0.0001$, Student's *t*-test, mean ± SD].

DISCUSSION

The GJ protein, Cx43, encoded by the GJA1 gene, is the most abundant connexin in the cardiovascular system. Cx43 is a crucial factor in stabilizing electrical conduction in cardiac muscle and maintaining the integrity of the (BBB; Nagy and Rash, 2000; Boulay et al., 2016). Cx43 is pervasive in the inner ear as well. Mutation of Cx43 was found by Yang, the second most common mutation (27.45%) in the inner ear causing genetic sensorineural hearing loss, after Cx26 mutation causing 45.16% of genetic sensorineural hearing loss (Yang et al., 2007). The mechanism by which Cx43 mutation causes hearing loss is not fully understood. In this study, we used immunocytochemical techniques to examine normal Cx43 expression in the BLB of the stria vascularis. Cx43 expression was found in strial ECs and PVMs in adult C57BL/6 mouse cochlea. In particular, we found extensive Cx43 expression in the contacts between PVMs and ECs. Consistent with Cx43 expression *in situ*, we also found Cx43 expression in co-cultured primary cell lines of strial ECs and PVMs. Using a patch clamp technique, we demonstrated functional communication between PVMs and ECs. When GJs were treated with a GJ blocker, dye communication between the PVMs and ECs was blocked. Suppression of Cx43 with siRNA *in vivo* significantly increased hearing threshold and also caused the EP to drop. Further study showed suppression of Cx43 to markedly affect BLB integrity and increase BLB permeability. Our data indicate that Cx43 is essential for strial BLB integrity, EP, and hearing sensitivity in the adult ear.

Previous studies from different labs have reported detection of Cx43 expression in various cells of the cochlea, including in the organ of Corti, lateral wall, spiral ganglion neurons (SGNs), and their neurite terminals innervating inner and outer HCs (Suzuki et al., 2003; Liu and Yang, 2015). However, reports on the distribution of Cx43 in the cochlea are inconsistent. Most data have shown a broad distribution of Cx43 in different cochlear regions in the early stages of cochlear development, especially for synaptogenesis and establishment of auditory neurotransmission (Liu and Yang, 2015). However, a few groups have shown Cx43 expression in spiral ganglia to persist into adulthood (Liu and Yang, 2015). For example, Kim et al. (2013) reported that Cx43 robustly presents in retro-cochlear centers in adult CBA/J mice. Liu et al. (2014) showed Cx43 expression in satellite glial cells (SGCs) in adult human and guinea pig. These satellite cells play an important role in protecting SGNs. We presume that the inconsistent reports from different

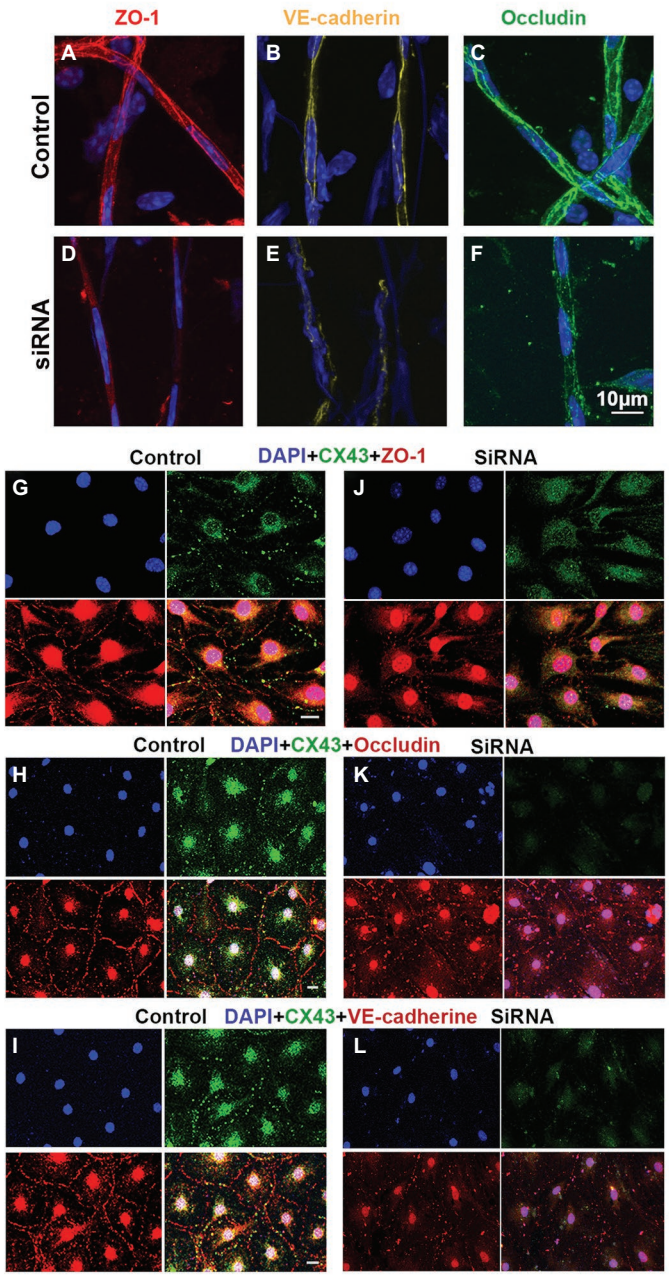

FIGURE 6 | Suppression of Cx43 alters the TJ distribution pattern in EC monolayers. **(A–F)** Tight junction (TJ) protein (ZO-1, VE-cad, and occludin) expression patterns in isolated capillaries of control **(A–C)** and Gja1 siRNA-treated groups **(E–F)**. Gja1 siRNA-treated groups show reduced suppression of ZO-1, VE-cad, and occludin. **(G–I)** TJ protein (ZO-1, VE-cad, and occludin) expression patterns in the control group. **(J–L)** TJ protein (ZO-1, VE-cad, and occludin) expression patterns in the Cx43 suppressed groups. Downregulation of Cx43 had a discernable effect on the distribution pattern of TJ proteins (scale bar: 10 μm).

laboratories might be due to differences in experimental staining procedure and animal species (Nagy et al., 2001).

Cx43 expression in the stria vascularis has only been reported in post-natal mice (P0, P14, or P17; Cohen-Salmon et al., 2004; Liu and Yang, 2015). For example, Suzuki et al. (2003) reported Cx43 expression in the adult stria vascularis of rat cochlea. They demonstrated Cx43-positive areas localized in the stria vascularis and spiral ligament. In the present study, we obtained results consistent with Suzuki, detecting a unique pattern of Cx43 distribution in the strial vascularis of adult mouse cochlea (as shown in **Figure 1**). Cx43 expression was typically expressed in contacts between PVM end-feet and the endothelium of blood vessels. We further verified Cx43 protein in the stria vascularis by western blot. Moreover, we demonstrated that Cx43 mediated intercellular communication occurs between ECs and PVMs in *in vitro* primary cell line models.

These findings provide corroborating evidence in support of an early finding by Takeuchi and Ando (1998), in which they demonstrated that melanocytes, which we later identify as PVMs (Zhang et al., 2012; Neng et al., 2013), communicate and are dye-coupled with ECs through GJs *in vivo*. In this study, we also noticed less Cx43 expression in the vascular network of the spiral ligament (**Figure 1C**), further confirming our earlier conclusion that the two vascular networks are functionally distinct (Shi, 2011). The microvessels in the spiral ligament have roles in regulation of blood flow, as vessels in this region contain a large number of smooth muscle cells and contractile PCs (Shi et al., 2008). In contrast, strial microvessels have endothelium specialized to form a tight BLB, crucial for maintaining the EP, ion transport, and endolymphatic fluid balance, necessary for cochlear sensitivity.

GJs are critical for coordination of cell function, allowing passage of electrical charge between connected cells and exchange of chemical signals and energy substrates (Zhang et al., 2018). It is generally accepted that the stria vascularis in the cochlea produces the K^+-rich endolymph, which is the driving force for sound transduction by sensory HCs (Zdebik et al., 2009). GJs are an important link in the intracellular K^+-recycling pathway to the stria vascularis (Zdebik et al., 2009). The distinctive pattern of Cx43 distribution in strial BLB component cells and the functional communication mediated by Cx43 raises the question: Does Cx43 play a critical role in maintaining BLB integrity and EP generation? To investigate this question, we employed siRNA silencing to downregulate Gja1 in adult mice and suppress Cx43 expression. The downregulation caused the EP to drop, and, correspondingly, hearing loss was seen at some frequencies, particularly high frequencies. The patchy hearing loss could be due to the effective distribution of siRNA in the cochlea. Agents injected into the middle ear can form a concentration gradient from basal regions to the apex (Plontke et al., 2008). Consistent with the notion, we have frequently observed in the lab that delivery of chemicals to the middle ear mostly concentrates at the basal turn, although we have also found the efficacy of some chemicals on cochlear function higher at the apical turn, presumably due to chemical properties.

The strial BLB is normally one of the tightest blood-tissue barriers in mammals and is critical for maintaining cochlear homeostasis, particularly for maintaining the EP. Break in the barrier could result in an intrastrial electric shunt (Cohen-Salmon et al., 2007). In this study, we presume Cx43 expression in endothelium and PVMs together with expression of other GJ proteins, including Cx26 and Cx30, affect K^+ movement and the EP, as shown in **Figure 7**. PVMs are interdigitated between marginal and basal cell processes (Steel and Barkway, 1989) and surrounding blood vessel walls (Shi, 2016). We hypothesize the Cx43 expressed in the PVMs facilitates K^+ transport for maintaining the EP through two pathways: (1) circulating blood ("fresh" K^+ restores K^+ depleted in recycling) and (2) K^+ returned through epithelial-syncytium layers (recycled K^+? as illustrated in **Figure 7**). In the first pathway, K^+ may be taken up into capillary ECs from the blood stream through K^+ channels or $Na^+/K^+/Cl^-$ co-transporters expressed at the apical surface of ECs. The K^+ is subsequently transmitted to PVMs *via* Cx43. In the second pathway, PVMs facilitate K^+ recycling through GJs, including Cx43, expressed in the FCs and basal cells, as we identify in **Figure 1C**. Downregulation of Cx43 would interrupt the K^+ recycling from either source to the intrastrial space and lead to an EP drop. In an earlier paper, we showed that normal PVMs maintain capillary integration by having a role in isolating the intrastrial space from the blood flow (Zhang et al., 2012, 2013). In the present study, we further demonstrate that downregulation of CX43 in ECs weakens BLB integrity (as shown in **Figure 6**) and can cause an intrastrial electric shunt. These would likely contribute to a drop in the EP as well.

In this study, we found that suppressed Cx43 expression causes increased vascular leakage in the strial BLB to low and medium size molecules, as demonstrated in **Figure 5**. Moreover, we found that downregulation of Cx43 had a discernable effect on the distribution pattern of occludins, ZO-1, and adherens-junction proteins such as VE-cadherin. These proteins are essential for the structural and functional integrity of the

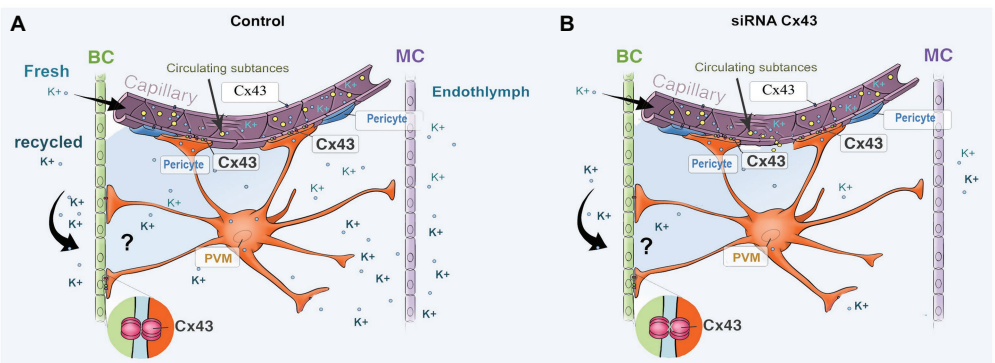

FIGURE 7 | An illustration of the effect of Cx43 expression in endothelium and in PVMs on K^+ movement and EP generation. **(A)** Perivascular resident macrophage (PVM; melanocyte) end-feet contact the capillary wall and also inter-digitally connect with BCs when CX43 is normally expressed. **(B)** siRNA downregulates the expression of CX43, affecting both circulating and recycled K^+, reducing the EP. Downregulation of Cx43 also causes increased BLB permeability, leading to an intrastrial electric shunt which also reduces the EP.

strial BLB (Shi, 2016). In controls, TJs line the borders of contacted ECs, as shown in **Figure 6**. In contrast, with downregulation of Cx43, we see clusters or randomly scatted distributions of TJs along EC-EC contacts. Consistent with our *in vivo* findings that suppression of Cx43 increases strial BLB permeability, downregulation of Cx43 *in vitro* also made the EC monolayers more permeable. Our results are consistent with recent reports on non-auditory systems, in which Cx43 affects TJ formation and loss of Cx43 leads to blood barrier hyper-permeability (Hollenbach et al., 2018; Johnson et al., 2018; Bazzoun et al., 2019). The mechanism by which suppression of Cx43 alters TJ organization was not determined in this study, and, in fact, the mechanism by which suppression of Cx43 alters TJ organization is largely unknown. Some studies have shown that Cx43 hemichannels contribute to the assembly of cell junctions through modulation of the intracellular oxidative status (Chi et al., 2016). Li et al. (2010) has shown that regulation of Cx43 by siRNA can disassemble adhesive assemblies. Other studies have shown that specific domains of Cx43, such as the ser(9) and ser(10) at the C-terminal, serve as binding sites for interaction with various proteins, including ZO-1 (Xiao et al., 2011). A further study from Laing et al. (2005) has shown that the Cx43 has interactions with TJ proteins such as ZO-1 to form lipid rafts in GJ plaques. Taken together, these studies underscore the functional dependence between TJ and GJ proteins. However, further study is needed to fully elucidate the mechanisms by which Cx43 affects expression of TJ protein in the strial BLB. Normal blood flow to the ear is critical for cochlear homeostasis and extremely important for generating the EP on which sound transduction by HCs depends (Ohlemiller et al., 2008). The EP drop could also reflect changes in blood supply due to the downregulation of Cx43.

Taken together, our data confirm Cx43 expression in the strial BLB and spiral ligament of the adult cochlea. Suppression of Cx43 leads to BLB hyper-permeability, decrease in EP, and loss of hearing sensitivity.

DATA AVAILABILITY STATEMENT

All datasets presented in this study are included in the article/ supplementary material.

ETHICS STATEMENT

All procedures in this study were reviewed and approved by the Institutional Animal Care and Use Committee (IACUC) at Oregon Health & Science University (IP 00000968).

AUTHOR CONTRIBUTIONS

JZ, XW, ZH, and LN were involved in all aspects of the experiments. Specifically, JZ, ZH, and LN did the immunohistochemistry, RT-PCR, WB, and ABR test. In addition, ZH and XW performed the EP measurement. JZ and LN performed the *in vitro* cell line study and were involved in data analysis. JZ, ZH, and YZ formatted the references. XS supervised the experiments and wrote the manuscript. All authors contributed to the article and approved the submitted version.

FUNDING

This research was supported by NIH/NIDCD R21 DC016157 (XS), R21 DC016157S1 (XS), R01 DC015781 (XS), R01-DC010844 (XS) and NIH P30-DC005983 (Peter Barr-Gillespie).

ACKNOWLEDGMENTS

The authors thank Mr. Allan Kachelmeier for his editorial assistance.

REFERENCES

Avraham, K. B. (2001). Inherited connexin mutations associated with hearing loss. *Cell Commun. Adhes.* 8, 419–424. doi: 10.3109/15419060109080764

Bazzoun, D., Adissu, H. A., Wang, L., Urazaev, A., Tenvooren, I., Fostok, S. F., et al. (2019). Connexin 43 maintains tissue polarity and regulates mitotic spindle orientation in the breast epithelium. *J. Cell Sci.* 132:jcs223313. doi: 10.1242/jcs.223313

Boulay, A. C., Cisternino, S., and Cohen-Salmon, M. (2016). Immunoregulation at the gliovascular unit in the healthy brain: a focus on connexin 43. *Brain Behav. Immun.* 56, 1–9. doi: 10.1016/j.bbi.2015.11.017

Boulay, A. C., Mazeraud, A., Cisternino, S., Saubamea, B., Mailly, P., Jourdren, L., et al. (2015). Immune quiescence of the brain is set by astroglial connexin 43. *J. Neurosci.* 35, 4427–4439. doi: 10.1523/JNEUROSCI.2575-14.2015

Campbell, H. K., Maiers, J. L., and DeMali, K. A. (2017). Interplay between tight junctions & adherens junctions. *Exp. Cell Res.* 358, 39–44. doi: 10.1016/j.yexcr.2017.03.061

Chen, J., and Zhao, H. B. (2014). The role of an inwardly rectifying K^+ channel (Kir4.1) in the inner ear and hearing loss. *Neuroscience* 265, 137–146. doi: 10.1016/j.neuroscience.2014.01.036

Chew, S. S., Johnson, C. S., Green, C. R., and Danesh-Meyer, H. V. (2010). Role of connexin 43 in central nervous system injury. *Exp. Neurol.* 225, 250–261. doi: 10.1016/j.expneurol.2010.07.014

Chi, Y., Zhang, X., Zhang, Z., Mitsui, T., Kamiyama, M., Takeda, M., et al. (2016). Connexin 43 hemichannels contributes to the disassembly of cell junctions through modulation of intracellular oxidative status. *Redox Biol.* 9, 198–209. doi: 10.1016/j.redox.2016.08.008

Cohen-Salmon, M., Maxeiner, S., Kruger, O., Theis, M., Willecke, K., and Petit, C. (2004). Expression of the connexin 43- and connexin 45-encoding genes in the developing and mature mouse inner ear. *Cell Tissue Res.* 316, 15–22. doi: 10.1007/s00441-004-0861-2

Cohen-Salmon, M., Regnault, B., Cayet, N., Caille, D., Demuth, K., Hardelin, J. P., et al. (2007). Connexin 30 deficiency causes instrastrial fluid-blood barrier disruption within the cochlear stria vascularis. *Proc. Natl. Acad. Sci. U. S. A.* 104, 6229–6234. doi: 10.1073/pnas.0605108104

Danesh-Meyer, H. V., and Green, C. R. (2008). Focus on molecules: connexin 43--mind the gap. *Exp. Eye Res.* 87, 494–495. doi: 10.1016/j.exer.2008.01.021

Ezan, P., Andre, P., Cisternino, S., Saubamea, B., Boulay, A. C., Doutremer, S., et al. (2012). Deletion of astroglial connexins weakens the blood-brain barrier. *J. Cereb. Blood Flow Metab.* 32, 1457–1467. doi: 10.1038/jcbfm.2012.45

Figueroa, X. F., and Duling, B. R. (2009). Gap junctions in the control of vascular function. *Antioxid. Redox Signal.* 11, 251–266. doi: 10.1089/ars.2008.2117

Forge, A., Marziano, N. K., Casalotti, S. O., Becker, D. L., and Jagger, D. (2003). The inner ear contains heteromeric channels composed of cx26 and

cx30 and deafness-related mutations in cx26 have a dominant negative effect on cx30. *Cell Commun. Adhes.* 10, 341–346. doi: 10.1080/cac.10.4-6.341.346

Hansen, D. B., Ye, Z. C., Calloe, K., Braunstein, T. H., Hofgaard, J. P., Ransom, B. R., et al. (2014). Activation, permeability, and inhibition of astrocytic and neuronal large pore (hemi)channels. *J. Biol. Chem.* 289, 26058–26073. doi: 10.1074/jbc.M114.582155

Hoang Dinh, E., Ahmad, S., Chang, Q., Tang, W., Stong, B., and Lin, X. (2009). Diverse deafness mechanisms of connexin mutations revealed by studies using in vitro approaches and mouse models. *Brain Res.* 1277, 52–69. doi: 10.1016/j.brainres.2009.02.008

Hollenbach, J., Jung, K., Noelke, J., Gasse, H., Pfarrer, C., Koy, M., et al. (2018). Loss of connexin 43 in murine sertoli cells and its effect on blood-testis barrier formation and dynamics. *PLoS One* 13:e0198100. doi: 10.1371/journal.pone.0198100

Hong, H. M., Yang, J. J., Shieh, J. C., Lin, M. L., and Li, S. Y. (2010). Novel mutations in the connexin 43 (GJA1) and GJA1 pseudogene may contribute to nonsyndromic hearing loss. *Hum. Genet.* 127, 545–551. doi: 10.1007/s00439-010-0791-x

Ivanova, E., Kovacs-Oller, T., and Sagdullaev, B. T. (2017). Vascular pericyte impairment and connexin 43 gap junction deficit contribute to vasomotor decline in diabetic retinopathy. *J. Neurosci.* 37, 7580–7594. doi: 10.1523/JNEUROSCI.0187-17.2017

Jagger, D. J., and Forge, A. (2015). Connexins and gap junctions in the inner ear--it's not just about K^+ recycling. *Cell Tissue Res.* 360, 633–644. doi: 10.1007/s00441-014-2029-z

Jiang, G., Dong, S., Yu, M., Han, X., Zheng, C., Zhu, X., et al. (2017). Influence of gap junction intercellular communication composed of connexin 43 on the antineoplastic effect of adriamycin in breast cancer cells. *Oncol. Lett.* 13, 857–866. doi: 10.3892/ol.2016.5471

Jiao, H., Wang, Z., Liu, Y., Wang, P., and Xue, Y. (2011). Specific role of tight junction proteins claudin-5, occludin, and ZO-1 of the blood-brain barrier in a focal cerebral ischemic insult. *J. Mol. Neurosci.* 44, 130–139. doi: 10.1007/s12031-011-9496-4

Johnson, A. M., Roach, J. P., Hu, A., Stamatovic, S. M., Zochowski, M. R., Keep, R. F., et al. (2018). Connexin 43 gap junctions contribute to brain endothelial barrier hyperpermeability in familial cerebral cavernous malformations type III by modulating tight junction structure. *FASEB J.* 32, 2615–2629. doi: 10.1096/fj.201700699R

Juhn, S. K. (1988). Barrier systems in the inner ear. *Acta Otolaryngol. Suppl.* 458, 79–83. doi: 10.3109/00016488809125107

Juhn, S. K., and Rybak, L. P. (1981). Labyrinthine barriers and cochlear homeostasis. *Acta Otolaryngol.* 91, 529–534. doi: 10.3109/00016488109138538

Kim, A. H., Nahm, E., Sollas, A., Mattiace, L., and Rozental, R. (2013). Connexin 43 and hearing: possible implications for retrocochlear auditory processing. *Laryngoscope* 123, 3185–3193. doi: 10.1002/lary.24249

Laing, J. G., Chou, B. C., and Steinberg, T. H. (2005). ZO-1 alters the plasma membrane localization and function of Cx43 in osteoblastic cells. *J. Cell Sci.* 118, 2167–2176. doi: 10.1242/jcs.02329

Lapenna, A., De Palma, M., and Lewis, C. E. (2018). Perivascular macrophages in health and disease. *Nat. Rev. Immunol.* 18, 689–702. doi: 10.1038/s41577-018-0056-9

Lee, J. R., and White, T. W. (2009). Connexin-26 mutations in deafness and skin disease. *Expert Rev. Mol. Med.* 11:e35. doi: 10.1017/S1462399409001276

Li, M. W., Mruk, D. D., Lee, W. M., and Cheng, C. Y. (2010). Connexin 43 is critical to maintain the homeostasis of the blood-testis barrier via its effects on tight junction reassembly. *Proc. Natl. Acad. Sci. U. S. A.* 107, 17998–18003. doi: 10.1073/pnas.1007047107

Liu, W., Glueckert, R., Linthicum, F. H., Rieger, G., Blumer, M., Bitsche, M., et al. (2014). Possible role of gap junction intercellular channels and connexin 43 in satellite glial cells (SGCs) for preservation of human spiral ganglion neurons: a comparative study with clinical implications. *Cell Tissue Res.* 355, 267–278. doi: 10.1007/s00441-013-1735-2

Liu, X. Z., Xia, X. J., Adams, J., Chen, Z. Y., Welch, K. O., Tekin, M., et al. (2001). Mutations in GJA1 (connexin 43) are associated with non-syndromic autosomal recessive deafness. *Hum. Mol. Genet.* 10, 2945–2951. doi: 10.1093/hmg/10.25.2945

Liu, W. J., and Yang, J. (2015). Preferentially regulated expression of connexin 43 in the developing spiral ganglion neurons and afferent terminals in post-natal rat cochlea. *Eur. J. Histochem.* 59:2464. doi: 10.4081/ejh.2015.2464

Mammano, F. (2019). Inner ear connexin channels: roles in development and maintenance of cochlear function. *Cold Spring Harb. Perspect. Med.* 9:a033233. doi: 10.1101/cshperspect.a033233

Martinez, A. D., Acuna, R., Figueroa, V., Maripillan, J., and Nicholson, B. (2009). Gap-junction channels dysfunction in deafness and hearing loss. *Antioxid. Redox Signal.* 11, 309–322. doi: 10.1089/ars.2008.2138

Nagy, J. I., Dudek, F. E., and Rash, J. E. (2004). Update on connexins and gap junctions in neurons and glia in the mammalian nervous system. *Brain Res. Rev.* 47, 191–215. doi: 10.1016/j.brainresrev.2004.05.005

Nagy, J. I., Li, X., Rempel, J., Stelmack, G., Patel, D., Staines, W. A., et al. (2001). Connexin 26 in adult rodent central nervous system: demonstration at astrocytic gap junctions and colocalization with connexin 30 and connexin 43. *J. Comp. Neurol.* 441, 302–323. doi: 10.1002/cne.1414

Nagy, J. I., and Rash, J. E. (2000). Connexins and gap junctions of astrocytes and oligodendrocytes in the CNS. *Brain Res. Rev.* 32, 29–44. doi: 10.1016/S0165-0173(99)00066-1

Naus, C. C., Bechberger, J. F., and Paul, D. L. (1991). Gap junction gene expression in human seizure disorder. *Exp. Neurol.* 111, 198–203. doi: 10.1016/0014-4886(91)90007-Y

Neng, L., Zhang, F., Kachelmeier, A., and Shi, X. (2013). Endothelial cell, pericyte, and perivascular resident macrophage-type melanocyte interactions regulate cochlear intrastrial fluid-blood barrier permeability. *J. Assoc. Res. Otolaryngol.* 14, 175–185. doi: 10.1007/s10162-012-0365-9

Neng, L., Zhang, J., Yang, J., Zhang, F., Lopez, I. A., Dong, M., et al. (2015). Structural changes in thestrial blood-labyrinth barrier of aged C57BL/6 mice. *Cell Tissue Res.* 361, 685–696. doi: 10.1007/s00441-015-2147-2

Ohlemiller, K. K., Rice, M. E., and Gagnon, P. M. (2008). Strial microvascular pathology and age-associated endocochlear potential decline in NOD congenic mice. *Hear. Res.* 244, 85–97. doi: 10.1016/j.heares.2008.08.001

Patuzzi, R. (2011). Ion flow in stria vascularis and the production and regulation of cochlear endolymph and the endolymphatic potential. *Hear. Res.* 277, 4–19. doi: 10.1016/j.heares.2011.01.010

Plontke, S. K., Biegner, T., Kammerer, B., Delabar, U., and Salt, A. N. (2008). Dexamethasone concentration gradients along scala tympani after application to the round window membrane. *Otol. Neurotol.* 29, 401–406. doi: 10.1097/MAO.0b013e318161aaae

Procacci, P., Magnaghi, V., and Pannese, E. (2008). Perineuronal satellite cells in mouse spinal ganglia express the gap junction protein connexin 43 throughout life with decline in old age. *Brain Res. Bull.* 75, 562–569. doi: 10.1016/j.brainresbull.2007.09.007

Qi, W., Ding, D., Zhu, H., Lu, D., Wang, Y., Ding, J., et al. (2014). Efficient siRNA transfection to the inner ear through the intact round window by a novel proteidic delivery technology in the chinchilla. *Gene Ther.* 21, 10–18. doi: 10.1038/gt.2013.49

Qu, Y., Tang, W., Zhou, B., Ahmad, S., Chang, Q., Li, X., et al. (2012). Early developmental expression of connexin 26 in the cochlea contributes to its dominate functional role in the cochlear gap junctions. *Biochem. Biophys. Res. Commun.* 417, 245–250. doi: 10.1016/j.bbrc.2011.11.093

Shi, X. (2010). Resident macrophages in the cochlear blood-labyrinth barrier and their renewal via migration of bone-marrow-derived cells. *Cell Tissue Res.* 342, 21–30. doi: 10.1007/s00441-010-1040-2

Shi, X. (2011). Physiopathology of the cochlear microcirculation. *Hear. Res.* 282, 10–24. doi: 10.1016/j.heares.2011.08.006

Shi, X. (2016). Pathophysiology of the cochlear intrastrial fluid-blood barrier (review). *Hear. Res.* 338, 52–63. doi: 10.1016/j.heares.2016.01.010

Shi, X., Han, W., Yamamoto, H., Tang, W., Lin, X., Xiu, R., et al. (2008). The cochlear pericytes. *Microcirculation* 15, 515–529. doi: 10.1080/10739680802047445

Steel, K. P., and Barkway, C. (1989). Another role for melanocytes: their importance for normal stria vascularis development in the mammalian inner ear. *Development* 107, 453–463.

Sun, Y., Tang, W., Chang, Q., Wang, Y., Kong, W., and Lin, X. (2009). Connexin 30 null and conditional connexin 26 null mice display distinct pattern and time course of cellular degeneration in the cochlea. *J. Comp. Neurol.* 516, 569–579. doi: 10.1002/cne.22117

Suzuki, T., Takamatsu, T., and Oyamada, M. (2003). Expression of gap junction protein connexin 43 in the adult rat cochlea: comparison with connexin 26. *J. Histochem. Cytochem.* 51, 903–912. doi: 10.1177/002215540305100705

Takeuchi, S., and Ando, M. (1998). Inwardly rectifying K^+ currents in intermediate cells in the cochlea of gerbils: a possible contribution to

the endocochlear potential. *Neurosci. Lett.* 247, 175–178. doi: 10.1016/S0304-3940(98)00318-8

Tasaki, I., and Spyropoulos, C. S. (1959). Stria vascularis as source of endocochlear potential. *J. Neurophysiol.* 22, 149–155. doi: 10.1152/jn.1959.22.2.149

Verselis, V. K. (2019). Connexin hemichannels and cochlear function. *Neurosci. Lett.* 695, 40–45. doi: 10.1016/j.neulet.2017.09.020

Wangemann, P. (2002). K^+ cycling and the endocochlear potential. *Hear. Res.* 165, 1–9. doi: 10.1016/S0378-5955(02)00279-4

Wangemann, P. (2006). Supporting sensory transduction: cochlear fluid homeostasis and the endocochlear potential. *J. Physiol.* 576, 11–21. doi: 10.1113/jphysiol.2006.112888

Wangemann, P., and Schacht, J. (1996). "Homeostasic mechanisms in the cochlea" in *The cochlea*. eds. P. Dallos, A. N. Popper and R. R. Fay (New York: Springer), 130–185.

Wingard, J. C., and Zhao, H. B. (2015). Cellular and deafness mechanisms underlying connexin mutation-induced hearing loss - a common hereditary deafness. *Front. Cell. Neurosci.* 9:202. doi: 10.3389/fncel.2015.00202

Winkler, E. A., Bell, R. D., and Zlokovic, B. V. (2011). Central nervous system pericytes in health and disease. *Nat. Neurosci.* 14, 1398–1405. doi: 10.1038/nn.2946

Xiao, F., Weng, J., Fan, K., and Wang, W. (2011). Detailed regulatory mechanism of the interaction between ZO-1 PDZ2 and connexin 43 revealed by MD simulations. *PLoS One* 6:e21527. doi: 10.1371/journal.pone.0021527

Yang, Y., Dai, M., Wilson, T. M., Omelchenko, I., Klimek, J. E., Wilmarth, P. A., et al. (2011). Na^+/K^+-ATPase alpha1 identified as an abundant protein in the blood-labyrinth barrier that plays an essential role in the barrier integrity. *PLoS One* 6:e16547. doi: 10.1371/journal.pone.0016547

Yang, J. J., Huang, S. H., Chou, K. H., Liao, P. J., Su, C. C., and Li, S. Y. (2007). Identification of mutations in members of the connexin gene family as a cause of nonsyndromic deafness in Taiwan. *Audiol. Neurootol.* 12, 198–208. doi: 10.1159/000099024

Zdebik, A. A., Wangemann, P., and Jentsch, T. J. (2009). Potassium ion movement in the inner ear: insights from genetic disease and mouse models. *Physiology* 24, 307–316. doi: 10.1152/physiol.00018.2009

Zhang, Q., Bai, X., Liu, Y., Wang, K., Shen, B., and Sun, X. (2018). Current concepts and perspectives on connexin 43: a mini review. *Curr. Protein Pept. Sci.* 19, 1049–1057. doi: 10.2174/1389203719666180709103515

Zhang, J., Chen, S., Hou, Z., Cai, J., Dong, M., and Shi, X. (2015). Lipopolysaccharide-induced middle ear inflammation disrupts the cochlear intra-strial fluid-blood barrier through down-regulation of tight junction proteins. *PLoS One* 10:e0122572. doi: 10.1371/journal.pone.0122572

Zhang, W., Dai, M., Fridberger, A., Hassan, A., Degagne, J., Neng, L., et al. (2012). Perivascular-resident macrophage-like melanocytes in the inner ear are essential for the integrity of the intrastrial fluid-blood barrier. *Proc. Natl. Acad. Sci. U. S. A.* 109, 10388–10393. doi: 10.1073/pnas.1205210109

Zhang, F., Dai, M., Neng, L., Zhang, J. H., Zhi, Z., Fridberger, A., et al. (2013). Perivascular macrophage-like melanocyte responsiveness to acoustic trauma-a salient feature of strial barrier associated hearing loss. *FASEB J.* 27, 3730–3740. doi: 10.1096/fj.13-232892

Zhu, Y., Gao, Y., Tao, C., Shao, M., Zhao, S., Huang, W., et al. (2016). Connexin 43 mediates white adipose tissue beiging by facilitating the propagation of sympathetic neuronal signals. *Cell Metab.* 24, 420–433. doi: 10.1016/j.cmet.2016.08.005

Conflict of Interest: The authors declare that the research was conducted in the absence of any commercial or financial relationships that could be construed as a potential conflict of interest.

frontiers in Physiology

REVIEW
published: 25 September 2020
doi: 10.3389/fphys.2020.584135

Vasculo-Neuronal Coupling and Neurovascular Coupling at the Neurovascular Unit: Impact of Hypertension

*Jessica L. Presa[1,2], Flavia Saravia[2], Zsolt Bagi[1] and Jessica A. Filosa[1]**

[1] Department of Physiology, Medical College of Georgia, Augusta University, Augusta, GA, United States, [2] Departamento de Química Biológica, Facultad de Ciencias Exactas y Naturales, Universidad de Buenos Aires and Instituto de Biología y Medicina Experimental, CONICET, Buenos Aires, Argentina

Components of the neurovascular unit (NVU) establish dynamic crosstalk that regulates cerebral blood flow and maintain brain homeostasis. Here, we describe accumulating evidence for cellular elements of the NVU contributing to critical physiological processes such as cerebral autoregulation, neurovascular coupling, and vasculo-neuronal coupling. We discuss how alterations in the cellular mechanisms governing NVU homeostasis can lead to pathological changes in which vascular endothelial and smooth muscle cell, pericyte and astrocyte function may play a key role. Because hypertension is a modifiable risk factor for stroke and accelerated cognitive decline in aging, we focus on hypertension-associated changes on cerebral arteriole function and structure, and the molecular mechanisms through which these may contribute to cognitive decline. We gather recent emerging evidence concerning cognitive loss in hypertension and the link with vascular dementia and Alzheimer's disease. Collectively, we summarize how vascular dysfunction, chronic hypoperfusion, oxidative stress, and inflammatory processes can uncouple communication at the NVU impairing cerebral perfusion and contributing to neurodegeneration.

Keywords: neurovascular, astrocyte, cogntive decline, ischemia, pulsatility

OPEN ACCESS

Edited by:
Xavier Figueroa, Pontificia Universidad Católica de Chile, Chile

Reviewed by:
Zoltan I. Ungvari, The University of Oklahoma Health Sciences Center, United States
Jillian L. Stobart, University of Manitoba, Canada

****Correspondence:***
Jessica A. Filosa
jfilosa@augusta.edu

Specialty section:
This article was submitted to Vascular Physiology, a section of the journal Frontiers in Physiology

Received: *16 July 2020*
Accepted: *04 September 2020*
Published: *25 September 2020*

Citation:
Presa JL, Saravia F, Bagi Z and Filosa JA (2020) Vasculo-Neuronal Coupling and Neurovascular Coupling at the Neurovascular Unit: Impact of Hypertension. Front. Physiol. 11:584135. doi: 10.3389/fphys.2020.584135

THE NEUROVASCULAR UNIT: A GENERAL OVERVIEW

Blood flow in the brain is directed through a vascular network that links interconnected surface (pial) arteries to penetrating (parenchymal) arterioles and a vast network of capillaries, ultimately draining back to the surface via post-capillary venules and veins. Perfusion within the brain is a highly controlled process maintained through the operation of activity-dependent as well as constitutive mechanisms. Importantly, these mechanisms act in concert to ensure brain homeostasis and optimal functioning.

The brain is a complex functional and structural organizational unit. The smallest level of cellular interactions establishing brain perfusion is the neurovascular unit (NVU) (Iadecola, 2017), which comprises, at minimum, neurons, astrocytes, endothelial cells, vascular smooth muscle cells (VSMCs) and/or pericytes. Dynamic communication among these components contributes to the moment to moment regulation of arteriole and capillary blood flow and provides neurons

with energy substrates as well as removal of waste metabolites. In the classic view, neuron-to-vessel communication (including via astrocytes), referred to as neurovascular coupling (NVC) and neurometabolic coupling, links increases in neuronal metabolic activity to increases in local blood flow (functional hyperemia). Importantly, interactions at the NVU are also bidirectional, with ongoing vessel-to-neuronal signaling, or vasculo-neuronal coupling (VNC), playing a role in establishing homeostasis at the NVU. In this review, we discuss dynamic signaling pathways at the NVU and how diseases, such as hypertension, affect them leading to cognitive dysfunction and neurodegeneration.

Endothelial Cells

While the skull protects the brain from the external environment, endothelial cells are the first line of defense against the entrance of blood-borne pathogens, inflammatory-inducing components of the blood and circulating macrophages and are thus important contributors to brain homeostasis. The brain endothelium expresses highly specialized proteins, termed adherens and tight junction proteins, that mediate tight cell-to-cell contacts. These adherens (e.g., cadherins and junctional adhesion molecules) and tight junctions (e.g., occludins and claudins) contribute to formation of the blood–brain barrier (BBB), which maintains the high transendothelial electrical resistance and low paracellular transport properties characteristic of the brain endothelium (Sweeney et al., 2019; De Silva and Faraci, 2020). The basement membrane, comprising a family of proteins called perlecans (Thomsen et al., 2017), surrounds the endothelium and is also involved in homeostasis and maintenance of the BBB as well as communication at the NVU. Proteins of the basement membrane are known targets in disease; when their function is impaired, the integrity of the BBB is disrupted and the passage of molecules is dysregulated (Roberts et al., 2012; Mortensen et al., 2019). Mural cells and astrocytic endfeet surrounding the endothelium further contribute to maintenance of the BBB. In addition, endothelial cells release vasoactive signals, such as nitric oxide (NO), that control vascular resistance and thereby blood flow (Iadecola, 2013). The cellular mechanisms that drive endothelial-mediated changes in vascular tone include mechanical forces (e.g., wall shear stress), signals released by neighboring cells and electrical coupling such as endothelium-vascular smooth muscle cell (VSMC) interactions that drive hyperpolarization of the membrane potential of VSMCs, resulting in dilation (Longden et al., 2017). For example, agonist-induced activation of endothelial cell TRPV4 channels [i.e., epoxyeicosatrienoic acids (EETs)] increase calcium leading to the activation of intermediate (IK) and small (SK) conductance K^+ channels which through myoendothelial junction causes hyperpolarization of VSMCs membrane potential resulting in vasodilation (Sonkusare et al., 2012). In addition, endothelial cells are electrically coupled via gap junctions allowing for the fast conductance of current along the endothelial syncytium, which at the arteriole level can also influence VSMC membrane potential (Figueroa and Duling, 2009; Bagher and Segal, 2011). A critical example of this process, discussed later in the review, is the activation of inwardly rectifying K^+ (Kir2.1) channels in endothelial cells resulting in the upstream propagation of a hyperpolarizing current and dilation of parenchymal arterioles (Longden et al., 2017). For a detailed review of these mechanisms (see Harraz et al., 2020).

Vascular Smooth Muscle Cells

As blood moves from larger arterioles downstream toward capillaries and then venules, its flow is regulated by crosstalk among various cells. Zonation—a gradual phenotypic change along the arteriovenous axis—was recently reported based on single-cell transcriptomics studies (Vanlandewijck et al., 2018). When applied to target disease-mediated changes in gene expression, transcriptomic studies such as this may help identify key drivers of small vessel disease and impaired communication at the NVU. In penetrating arterioles, a single layer of VSMCs wraps around the basal lamina, which in turn covers the entire endothelial cell layer. VSMCs play an essential role in the regulation of vascular tone (Hill-Eubanks et al., 2014) and also contribute to arterial elasticity by secreting extracellular matrix proteins (Wight, 2008).

Pericytes

Pericytes are a pluripotent, perivascular mural cell type that is mainly found covering capillaries. Pericytes are also known to contribute to the maintenance and integrity of the BBB (Sweeney et al., 2019). They have further been proposed to regulate capillary blood flow by virtue of their contractile properties (Hall et al., 2014; Grutzendler and Nedergaard, 2019), a concept that is currently a matter of controversy largely owing to the lack of a consensus of phenotypic definition of SMCs versus pericytes. Functionally, it has been suggested that, during functional hyperemia, pericytes respond to glutamate released signals and dilate capillaries via a prostaglandin E_2-dependent pathway (Hall et al., 2014). In support of a role for impaired neurovascular-mediated signaling, pericyte position and function are altered by disease conditions such as stroke (Hall et al., 2014; Berthiaume et al., 2018a,b), diabetes (Rom et al., 2020) and Alzheimer's disease (AD) (Sagare et al., 2013; Nortley et al., 2019; Montagne et al., 2020), as well as disturbances in the circadian clock system (Nakazato et al., 2017)—all of which are associated with neurodegeneration.

Astrocytes

Astrocytic endfoot processes make contact with the abluminal surface of mural cells, establishing the gliovascular interface (Simard et al., 2003). Astrocytes regulate cerebral blood flow (CBF) and contribute to the maintenance and integrity of the BBB. The multiple functions of astrocytes are reflected in the plethora of ion channels and receptors they express, as well as their active release of numerous vasoactive signals and gliotransmitters known to modulate vascular, microglial, and neuronal function (Araque et al., 2014). However, the nature of communication channels established between astrocytes, blood vessels, and neurons are unclear. The use of fluorescent dyes (Tsien, 1988, 1989) has enabled glioscientists to visualize astrocytic Ca^{2+} events (Cornell-Bell et al., 1990), giving rise to an upsurge in research and knowledge on astrocyte function and intercellular communication. Visualization of astrocyte Ca^{2+} dynamics was later improved with the development of Ca^{2+}

indicators of the GCaMP series, either genetically encoded in transgenic mice or delivered via viruses (Bazargani and Attwell, 2016). The combined use of this approach with various astrocyte promoters such as Aldh1l1, Slc 1a3, GFAP, and GLAST has provided further knowledge on astrocyte heterogeneity in function, brain region specificity and structural dynamics.

Astrocytic Ca^{2+} events can be spontaneous or activity-dependent. As is the case for a number of astrocyte functions, Ca^{2+} events are *compartmentalized* (Bazargani and Attwell, 2016), with large Ca^{2+} events occurring in the soma and smaller events occurring in processes and microdomains. Importantly, these events can have different activity patterns. How these patterns relate to function is currently under investigation, supported by emerging sophisticated quantitative analytical techniques (Wang et al., 2019a). Dynamic Ca^{2+} events take the form of both intracellular- and intercellular-mediated signals, the latter of which can spread in the form of *waves* throughout the astrocytic syncytium via gap junctions (Munoz et al., 2015; Lapato and Tiwari-Woodruff, 2018). Ca^{2+} events may originate within different subcompartments, including the endoplasmic reticulum and mitochondria, and discrete sites, such as inositol trisphosphate (IP_3) receptors. In addition, Ca^{2+} events may be initiated by activation of membrane-bound ion channels, receptors or transporters, such as vanilloid-type transient receptor potential channels (e.g., TRPV4) and Na^+/Ca^{2+} exchangers. Notably, some of these surface proteins are functionally coupled to glutamate and GABA co-transporters (e.g., Glu/Na^+, GABA/Na^+ cotransporters), and thereby play an essential role in regulating ambient glutamate and GABA levels (for a review, see Oheim et al., 2018; Verkhratsky et al., 2019).

Astrocyte-derived vasoactive signals include prostaglandins, epoxyeicosatrienoic acids (EETs), glutamate, K^+, adenosine and ATP, among others (Girouard and Iadecola, 2006; Attwell et al., 2010). The mechanisms by which each of these signaling molecules contribute to the regulation of vascular tone appear to be vessel specific (i.e., arteriole vs. capillary) (Mishra et al., 2016).

While the participation of astrocytic Ca^{2+} events in NVC has been questioned, mainly due to inconsistencies in the temporal relationship between Ca^{2+} events and vascular responses (Nizar et al., 2013; Bonder and McCarthy, 2014), these discrepancies could reflect unintended consequences of specific experimental manipulations, such as targeting a single Ca^{2+} pathway (IP_3 receptor 2-knockout mice), failure to consider alternative Ca^{2+} sources [e.g., TRPV4 channels (Dunn et al., 2013)], anesthesia (Thrane et al., 2012; Tran and Gordon, 2015) and the arousal state of the animal (Tran et al., 2018). Technical limitations, such as the temporal and/or spatial resolution of acquired images, could also account for differences between studies. To this end, GCaMP-Ca^{2+} indicators have shed new light on this issue (Bazargani and Attwell, 2016). Using 3D imaging, Bindocci et al. (2017) discovered that Ca^{2+} events occurred more rapidly in astrocytic endfeet than in the soma. Global Ca^{2+} events associated with mouse movement were multifocal and spread from multiple gliapil toward the core of the cell. Endfoot Ca^{2+} events at the gliovascular interface exhibited asynchronous patterns (Bindocci et al., 2017). Moreover, astrocytic Ca^{2+} transients have been shown to propagate between cell subcompartments, highlighting the diversity of responses (Grosche et al., 1999; Kanemaru et al., 2014). In an awake *in vivo* two-photon mouse model, Tran et al. (2018) evaluated astrocyte Ca^{2+} dynamics in peri-arterioles and peri-capillary astrocytes of the barrel cortex in response to sensory stimulation or volitional behaviors. The authors observed delayed (following dilations) astrocyte Ca^{2+} increases in turn dependent on the mouse's action at the time of the stimulus. Using varied stimulation approaches the authors showed that the neurovascular pathway was linked to endothelial-derived nitric oxide (Tran et al., 2018). Unraveling the functional significance of astrocytic Ca^{2+} activity patterns—and sources (Srinivasan et al., 2015)—under both physiological and non-physiological conditions is thus of critical importance. In addition, further studies designed to link activity patterns with astrocyte population subtype are needed (Sofroniew and Vinters, 2010; Lundgaard et al., 2014).

Astrocytes are also critically involved in removing waste from the brain via the glymphatic system, a process that involves the highly specific endfoot marker and water ion channel, aquaporin 4 (AQP4). The glymphatic system operates through vessel-to-glia crosstalk mediated, at least in part, by arteriole pulsatility and impaired in aged mice (Kress et al., 2014). Although this latter mechanism is not fully established, it has been proposed that these pulsations are the driving force for promoting the convection of ions, solutes and waste products across the brain interstitial space without the need to cross the BBB. There is some evidence that the absence of AQP4 at the gliovascular interface impairs clearance and transport via the glymphatic system (Iliff et al., 2012, 2013).

Microglia

Microglia are the resident immune cells of the brain (Bilbo and Stevens, 2017). These embryonic mesoderm-derived cells constantly surveil the CNS for unfamiliar antigens, pathogens, apoptotic cells, and foreign particles. Their dynamic phagocytic activity and active release of immune signals play critical roles in brain homeostasis and repair processes (Hanisch and Kettenmann, 2007). However, the neuroprotective microglial state (surveillance/execution mode) can be disturbed during pathology, causing these cells to shift toward a reactive phenotype. These reactive microglia respond with exacerbated secretion of proinflammatory mediators (Vinuesa et al., 2019) and altered phagocytotic properties (Baik et al., 2019; Zhang et al., 2020).

Whether microglia directly impact cerebrovascular function is poorly understood. It has been reported that, after a cortical stroke, microglia are recruited toward vessels, where they can phagocytize endothelial cells and thereby contribute to the increased loss of BBB integrity (Jolivel et al., 2015). Using an *in vitro* approach, the authors of this latter study provided evidence that fibrinogen and albumin, plasma components found in the brain parenchyma after stroke, exacerbated the secretion of microglial proinflammatory cytokines and acted as chemoattractants. However, whether phagocytosis of endothelial

cells by microglia, a potential step in vascular repair, is part of a normal physiological process remains unknown.

To investigate this, Halder and Milner (2019) used a mouse model of mild chronic hypoxia that causes vascular leakiness and microglia clustering around vessels. Under these hypoxic conditions, pharmacological depletion of microglia increased BBB leakiness and caused a loss of tight junction proteins. It also led to astrocyte-vessel uncoupling, as evidenced by a decrease in the number of vessels positive for the perivascular astrocyte endfoot marker, AQP4. However, under normoxic conditions, microglia depletion did not impact vascular integrity. Thus, it is likely that coupling of these interactions is dependent on key signals released only in a pathological setting that may be absent under physiological conditions.

As alluded to above, proper operation of homeostatic mechanisms involves dynamic crosstalk among cells of the NVU, many of which have overlapping or complementary functions. These observations call for an integrated approach for addressing the functional status of the NVU and its vulnerability under disease conditions.

CEREBRAL BLOOD FLOW, NEUROVASCULAR COUPLING, AND VASCULO-NEURONAL COUPLING

High energy demands, as occur during information processing and maintenance of homeostatic processes, are sustained by redundant NVU-mediated mechanisms that ensure constitutive perfusion (Zlokovic, 2005). The driving force for CBF is cerebral perfusion pressure (CPP), defined as the difference between mean arterial pressure (MAP) and intracranial pressure (ICP). In the absence of a neuronal stimulus, CBF is relatively constant, but can be affected by changes in cardiac output, vascular resistance and altered intravascular as well as intracranial pressure gradients.

Cerebral Autoregulation

The dynamic mechanisms that regulate basal CBF are largely driven by the fine balance between vasodilatory and vasoconstrictive signaling pathways (Hill-Eubanks et al., 2014) and the integration of reflex autonomic pathways and local control processes, including cerebral autoregulation (Bayliss, 1902; Silverman and Petersen, 2020). The mechanisms underlying cerebral autoregulation include pressure-induced vasoconstriction (myogenic response) (Brayden et al., 2013; Cipolla et al., 2014; Pires et al., 2015) as well as metabolic and humoral signaling (Koller and Toth, 2012). The best-studied of these cellular pathways is the myogenic response, which involves activation of mechanosensitive Ca^{2+}-permeable ion channels and a subsequent increase in Ca^{2+} influx into VSMCs, resulting in elevated intracellular Ca^{2+} and vasoconstriction (Hill et al., 2006; Cipolla, 2009; Li et al., 2014). In cerebral vessels, this process is both pressure and flow/wall shear stress dependent (Koller and Toth, 2012).

Under physiological conditions, these dynamic mechanisms operate within a MAP range of 50 to 160 mmHg and serve to adjust the diameter of arterioles to maintain approximately constant CBF (Silverman and Petersen, 2020). However, the actual systemic arterial pressure range corresponding to this plateau phase varies (Faraco and Iadecola, 2013), with potentially significant differences reported between individuals (Tzeng et al., 2010; Liu et al., 2016; de Jong et al., 2017; Xing et al., 2017; Elting et al., 2020). Moreover, chronic diseases, such as hypertension and cerebral ischemia, can shift this autoregulatory range. Consequently, impairment of autoregulatory mechanisms that buffer blood pressure fluctuations can increase the vulnerability of the microcirculation, and hence the NVU (Iadecola, 2017). Cerebral autoregulation can be assessed by measuring changes in CBF in response to physiological stimuli (e.g., exercise, hypercapnia or orthostatic challenges), a response referred to as cerebrovascular reactivity (Lavi et al., 2006). Cerebrovascular reactivity is reduced in hypertension and large-artery stiffness is increased (Chirinos et al., 2019; Marmarelis et al., 2020; Silverman and Petersen, 2020), both of which contribute to cognitive decline, as we discuss below in more detail in this review article.

Neurovascular Coupling

In contrast to cerebral autoregulation, which constitutively regulates CBF, NVC is a dynamic process characterized by robust vascular responses to vasoactive signals released upon local increases in neuronal activity. NVC mechanisms form the basis of functional hyperemic responses. The rapid redirection of blood flow driven by increases in neuronal activity ensures the targeted, uninterrupted flow of blood that is critical for brain viability and ongoing brain functions. Details of the proposed signals underlying NVC have been extensively reviewed previously (Iadecola, 2017; Hosford and Gourine, 2019).

While the sequence of events underlying communication among the various cells of the NVU is poorly understood, the current view is that capillaries and arterioles are critical for the *initiation* (Mishra et al., 2016; Rungta et al., 2018) and *conduction/integration* (Longden et al., 2017) of NVC responses. Longden et al. (2017) recently established an essential role for capillary endothelial cells in both initiation and conduction of NVC responses, showing that activation of Kir2.1 channels in capillary endothelial cells by extracellular K^+, which is released during each action potential, generates a hyperpolarizing (electrical) signal that back-propagates to cause dilation of upstream penetrating arterioles and pial arteries, thereby inducing an increase in blood flow to the site of signal initiation (Tian et al., 2010; Chen et al., 2011, 2014; Longden et al., 2017; Cai et al., 2018; Rungta et al., 2018). Notably, this hyperpolarizing current travels millimeters before dissipating (Iadecola et al., 1997; Chen et al., 2011). This spatial spread of the vascular signal relative to the initiation point could lead to a mismatch between the site of elevated neural activity and the location of vascular responses, highlighting the potential role of additional mechanisms at different levels of the vascular network in decoding functional hemodynamics (Jukovskaya et al., 2011; O'Herron et al., 2016). Indeed, using two-photon imaging, O'Herron et al. (2016) demonstrated that neuronal activity was more strongly coupled to the responses of nearby parenchymal arterioles than with the responses of upstream pial vessels.

Interestingly, it is conceivable that the propagating dilatory signal not only moves upstream to the surface but also travels from the surface back down into penetrating branches. Though this aspect of vascular signaling has received little attention, low-resolution vascular imaging suggests that it readily occurs (Chen et al., 2011), providing a possible explanation for the residual mismatch between neural activity and nearby vascular responses.

There is also evidence supporting pericytes and VSMCs as first responders (Hall et al., 2014; Mishra et al., 2016). Using brain slices, Mishra et al. (2016) showed that neuronal activity evokes increases in astrocytic Ca^{2+} (via activation of the ionotropic ATP receptor, $P2X_1$) that stimulate the synthesis of prostaglandin E2 (PGE_2) and its release from astrocytic endfeet, resulting in capillary dilation through activation of EP_4 receptors on pericytes. However, in a follow-up study using two-photon *in vivo* imaging, Rungta et al. (2018) assessed changes in intracellular Ca^{2+} in pericytes and VSMCs in relation to distinct capillary and arteriole Ca^{2+} levels induced by olfactory neuronal activation (Rungta et al., 2018). In this study, an odor stimulus was followed by fast, synchronized decreases in Ca^{2+} in arterioles and first-order capillaries (less than ∼50 μm from the arteriole) (Rungta et al., 2018). It was determined that pericytes near the activated synaptic site responded with a delayed drop in Ca^{2+} as opposed to mural cells upstream. Thus, the authors proposed the drop in Ca^{2+} was likely generated from heterocellular electrical coupling between endothelial and mural cells via a retrograde hyperpolarization and transfer of current via myo-endothelial junctions (Iadecola et al., 1997; Chen et al., 2014; Longden et al., 2017; Harraz et al., 2020). Collectively, these studies support capillary endothelial cells as the initiators of the NVC response.

Another mechanism shown to contribute to the initiation of functional hyperemic responses involves changes in the velocity of red blood cells (Wei et al., 2016), a process that is independent of NVU vasoactive signals (Grutzendler and Nedergaard, 2019). Wei et al. (2016) provided evidence that the transient decrease in tissue O_2 tension resulting from neuronal-evoked increases in metabolic activity (Devor et al., 2011) increases red blood cell deformability and velocity in capillaries. The authors proposed that O_2 release-induced displacement of ankyrin from band 3 weakens spectrin-actin cytoskeleton interactions (Stefanovic et al., 2013; Zhou et al., 2019), thereby increasing erythrocytes deformability (Wei et al., 2016), a phenomenon later confirmed using both *ex vivo* (microfluidics) and *in vivo* (two-photon imaging) approaches (Zhou et al., 2019).

Understanding the cellular mechanisms underlying efficient NVC is crucial for the development of therapeutic approaches targeting potential mismatches in metabolic demand and supply as occurs in disease conditions, making this an active area of investigation.

Vasculo-Neuronal Coupling

While NVC mechanisms act to communicate information from neurons to the vasculature, communication in the opposite direction has also been proposed. At the cellular level, this modality of communication is referred to as VNC. This concept, encapsulated in the hemo-neural hypothesis, posits that hemodynamic signals modify glial and neuronal function to maintain cerebral homeostasis and contribute to information processing in the brain (Moore and Cao, 2008; Cao et al., 2009). In support of vascular-to-neuron signaling in the brain, Waki et al. (2006) showed that inhibition of eNOS in the nucleus tractus solitarii (NTS) decreased arterial pressure in the spontaneously hypertensive rat (SHR) model, indicating a role for endothelial-derived NO in the NTS in modulating cardiac baroreceptor reflex gain and arterial pressure. Using acute rat brain slices and a mechanical stimulation paradigm that targets endothelial cells, Kozlov further demonstrated that VSMCs and astrocyte endfeet generate inhibitory, slow, outward currents in mitral cells of the olfactory bulb that are mediated by GABA released from astrocytes (Kozlov et al., 2006). Thesen et al. (2012) provided indirect experimental evidence in favor of the hemo-neuronal hypothesis in humans, demonstrating changes in neuronal activity in response to hypercapnia (5% CO_2). Specifically, they showed that hypercapnia, a prominent inducer of vascular dilation, decreased the magnetoencephalogram response to auditory and visual tasks (Thesen et al., 2012), reducing both evoked and spontaneous spectral power indicative of neuronal activity. These data support a link between resting perfusion status and neuronal activity and highlight the importance of considering this linkage in assessments of activity-dependent changes in blood flow. However, because pH acidification can independently affect blood vessels and neuronal activity, the concept will require further refinement.

Using a brain slice model, our group showed that arteriole constriction is associated with inhibition of neuronal firing, whereas dilation is linked to activation of neuronal firing. A detailed investigation of the constriction-dependent pathway revealed the involvement of TRPV4 channel-mediated, Ca^{2+}-dependent events in astrocytes (Kim et al., 2015, 2016). While the mechanisms are incompletely understood, the constriction-evoked inhibition in neuronal activity was unaffected by blockers of NO, $GABA_A$ receptors or glutamate receptors. On the other hand, the response was significantly blunted by an adenosine A1 receptor blocker, and to some extent by blockade of $GABA_B$ receptors (Kim et al., 2016).

Both arteriole constriction and dilation induce changes in astrocytic Ca^{2+}, independent of neuronal activity (Kim et al., 2015; Rosenegger et al., 2015). One possible mechanism for this is that changes in vessel diameter trigger activation of mechanosensitive ion channels, or receptors, at the NVU. The resulting increase in astrocytic Ca^{2+} could then engage downstream pathways, leading to changes in neuronal activity. While evidence supports mechanosensitivity in astrocytes, how this might influence neurovascular interactions is unclear, as these processes remain largely unexplored. Mechanostimulus-induced changes in astrocytic Ca^{2+} could be attributable to a number of different ion channels, including P2 × 7 (Beckel et al., 2014; Albalawi et al., 2017), TRPV4 (Ryskamp et al., 2011; Dunn et al., 2013; Choi et al., 2015), Piezo1 (Choi et al., 2015; Velasco-Estevez et al., 2020), and pannexin1 (Minelli et al., 2007; Suadicani et al., 2012). Evidence also supports the idea that mechanical stimulation causes the release of adenosine in the brain. Further studies addressing the implications of mechanical

distortion-driven signaling at the NVU are clearly warranted. A good starting point would be the gliovascular interface, where specialized ion channels reside and where arteriole pulsation may play an important role in conveying mechanoregulation-driven communication (Ross et al., 2014; Nguyen and Venton, 2015; Wang and Venton, 2019; Wei et al., 2019).

We proposed VNC as a constitutively active mechanism involved in the modulation of resting neuronal activity that contributes to matching perfusion levels with energy demand. In this view, VNC would serve to safeguard neurons in cases where perfusion was compromised. A further prediction is that, in the healthy brain, VNC is overridden during increases in neuronal activity, such as those evoked during NVC. If VNC is linked to mechanosensitivity at the NVU, its operation could be further affected by intracranial and intravascular pressure gradients, which have recognized relevance in stroke and traumatic brain injury. The potential intersection of such pressure gradients with VNC could also be important in the context of hypertension, vascular stiffness and small vessel disease, an issue that warrants further investigation.

VASCULAR RISK FACTORS AND THE NVU

Hypertension

Genetic, epigenetic, and lifestyle factors contribute to hypertension (Padmanabhan et al., 2015). Also, the prevalence and severity of hypertension increase with age. From age 20–85 years of age, the lifetime risk of hypertension has been estimated at 69.3–86.1% depending on sex and race (Virani et al., 2020). With the world's older population rising, the number of older adults with hypertension is expected to grow by 20% by 2050 (Benetos et al., 2019; Volpe et al., 2019). Yet, many older adults remain untreated or the management of their hypertension challenging to address. In the brain, chronically increased arterial pressure leads to lacunar infarcts, white matter hyperintensities, and cerebral microbleeds (Joutel and Faraci, 2014). Hypertension also results in blood vessel remodeling, increased cerebrovascular resistance, cerebral hypoperfusion and impaired NVC (Girouard and Iadecola, 2006; Calcinaghi et al., 2013; Alosco et al., 2014; Hu et al., 2017), making it a risk factor for small vessel disease (Joutel and Chabriat, 2017) and a leading contributor to stroke. Importantly, untreated mid-life hypertension is a modifiable risk factor for the early development of dementia (Mogi, 2019).

In response to elevated intravascular pressure, arteries undergo various remodeling processes, including hypertrophic remodeling, hypotrophic remodeling, inward remodeling, and arterial stiffening (Baumbach and Ghoneim, 1993; Intengan and Schiffrin, 2001; Pires et al., 2013). The most-studied cerebral vascular beds in hypertension include branches of the internal carotids and vertebral arteries, which perfuse the brain and cerebellum/brainstem, respectively. Hypertension differentially affects these two branches of the circulation, with vertebral artery remodeling preceding that of the common carotids (Dickinson and Thomason, 1959). These anatomical and functional observations support the idea that brain areas that are home to cardiovascular-related control centers may be the first targets of the disease. Thus, hypertension leads to regional variations in CBF (i.e., hypoperfusion) and, consequently, changes in neuronal output function.

Importantly, hypertension also alters the normal function of parenchymal arterioles—the ultimate effector of parenchymal perfusion (Iddings et al., 2015; Pires et al., 2015; Sweet et al., 2015; Diaz et al., 2019). Parenchymal arterioles from SHRs and their stroke-prone SHRSP derivatives exhibit increased tone (Iddings et al., 2015; Pires et al., 2015; Sweet et al., 2015), increased wall thickness and passive distensibility (Sweet et al., 2015), decreased resting lumen diameter, and inward remodeling (Pires et al., 2015). Our group also reported increases in parenchymal arteriole tone in *ex vivo* brain slice preparations from mice infused with Ang II (600 ng/kg/min) for 28 days (Diaz et al., 2019). In addition, DOCA-salt–induced hypertension has been shown to impair endothelium-dependent dilation via dysfunctional cyclooxygenase (COX) and NO signaling (Matin et al., 2016).

It has previously been shown that the reduced cerebral perfusion and pathological parenchymal arteriole remodeling are reversed by endothelial cell-specific knockout of the mineralocorticoid receptor (MR) or MR antagonism in mice (Diaz-Otero et al., 2017). Diaz-Otero and colleagues showed that MR activation impairs TRPV4 channel-mediated dilation of parenchymal arterioles in a mouse model of angiotensin II (Ang II)-induced hypertension. The authors also reported that, in the hypertensive group, MR blockade rescued myogenic tone, reduced microglia density, and improved cognitive function (Diaz-Otero et al., 2018). The authors then evaluated the role of TRPV4 channels in vessel dysfunction using a TRPV4-knockout rat model [WKY-Trpv4(em4Mcwi)], reporting reduced cerebral perfusion with no changes in parenchymal arteriole structure or myogenic tone. However, these rats did show impaired endothelium-dependent dilation and cognitive function in association with gliosis (Diaz-Otero et al., 2019). It has further been shown that relaxation of VSMCs is diminished in mesenteric arteries of SHR and SHRSP models; this effect was attributed to a decrease in the generation of the endothelium-dependent hyperpolarizing factor, a process that likely depends on TRPV4 and SK channel signaling (Seki et al., 2017). TRPV4 channel activity was further evaluated by Tajada et al. (2017) using super-resolution imaging. These authors showed that TRPV4 channel activity was dependent on the protein kinase Cα (PKCα) membrane-anchoring protein AKP150, and further demonstrated that Ang II produced a decay in TRPV4 activation that was negatively correlated with the distance between TRPV4 channels and AKAP.

Yamasaki et al. (2020) showed that angiotensin II type 1 receptors (AT_1Rs) were differentially expressed between pial arteries and parenchymal arterioles of the cerebral microvasculature. These authors reported that, whereas mRNA expression levels of the angiotensin II receptor subtypes AT_1R_a and AT_1R_b were comparable in parenchymal arterioles, expression levels of AT_1R_b were ∼11-fold higher than those of AT_1R_a in pial arteries. These differences in expression suggest

differences in the sensitivity of these vessels to Ang II (Yamasaki et al., 2020). However, how expression of these receptors is altered throughout the different stages of hypertension was not evaluated in this study. An important functional observation was that AT_1R activation in parenchymal arterioles is important for the initiation, but not the maintenance, of the myogenic response. The authors suggested that a G protein-coupled receptor (GPCRs), such as AT_1R, acts as the main intravascular pressure sensor, providing a molecular pathway critical for cerebral autoregulation (Yamasaki et al., 2020).

Hypertension also targets cerebral capillaries. Hypertension impairs endothelial function and BBB integrity (Santisteban and Iadecola, 2018). Both animal models of hypertension (Tarantini et al., 2016) and hypertensive patients (Bosch et al., 2017) show capillary rarefaction. Loss of capillaries is associated with ischemia resulting in inadequate metabolic supply to neurons and glial cells contributing to elevated oxidative stress and inflammation and an overall toxic environment. There's also a synergistic effect of hypertension with both aging and AD on microvascular damage (Toth et al., 2013; Tarantini et al., 2016). Accompanied by a decrease in the number of upstream arterioles (De Silva and Faraci, 2020), hypertension contributes to an overall reduction in cerebral perfusion. Because endothelial dysfunction is a hallmark of hypertension, it would be important to address whether hypertension alters the electrical conduction of endothelial cells and, thus, the ability of capillaries to initiate the propagation of the upstream vasodilation, characteristic of the NVC response (Chen et al., 2014; Longden et al., 2017). A critical factor associated with the retrograde upstream propagation of the hyperpolarizing current is phosphatidylinositol 4,5-bisphosphate (PIP_2). Gq-protein-coupled receptors, targets of numerous NVC mediators, evokes PLC-mediated hydrolysis of PIP_2 into IP_3 and DAG, which in turn modulate ion channels involved in the regulation of vascular tone (Harraz et al., 2018b) including Kir2.1 and TRPV4 ion channels (Harraz et al., 2018a,b; Moshkforoush et al., 2020). Given that ischemia alters oxidative phosphorylation and ATP synthesis, the impact of PIP_2-mediated ion channel regulation on the vasculature is of importance (Harraz et al., 2018b). Future work on this research area will help elucidate the effect of aging, as well as hypertension-induced capillary dysfunction, has on the mechanisms underlying neurovascular uncoupling.

Collectively, these studies support the concept that parenchymal arterioles and capillaries are a target of hypertension, which manifests as increased tone and endothelial dysfunction, and is accompanied with gliosis (Iddings et al., 2015; Pires et al., 2015; Sweet et al., 2015; Diaz et al., 2019).

Hypoperfusion and Oxidative Stress in Hypertension

Reduced CBF is correlated with accelerated cognitive decline and ultimately leads to dementia (Hakim, 2019). Using MRI analyses and clinical history data for 59 patients who suffered a transient ischemic attack, Wang and colleagues reported that 67.8% of such patients presented a history of hypertension. They also observed a strong correlation between hypertension and perfusion abnormalities that was independent of the ischemic attack (Wang et al., 2019b). Hypertension, together with hypoperfusion, can result in significant dysregulation of cerebral vessels, increasing vascular resistance and exacerbating myogenic constriction (Iddings et al., 2015). As part of a consequent, and presumably protective, response mechanism, hypertension shifts the cerebral autoregulation curve to the right (Koller and Toth, 2012), an adaptation that also increases the risk for hypoperfusion when systemic blood pressure decreases (Faraco and Iadecola, 2013; Toth et al., 2017). However, these protective adaptations may be lost in the aged brain. Using an Ang II-infused model of hypertension in mice, Toth et al. (2013) investigated the effects of increased pressure-induced tone in middle cerebral arteries of 3-month-old mice. They found that the mechanism governing increased tone involved upregulation of the vasoconstrictor pathway driven by 20-HETE (20-hydroxy-5,8,11,14-eicosatetraenoic acid) and the canonical transient receptor potential cation channel member, TRPC6. However, in aged mice (24 months), this mechanism was impaired, increasing the vulnerability of the cerebral microcirculation to blood pressure fluctuations (Toth et al., 2013).

Chan et al. (2019) recently provided support for a role for endothelial TRPV4 channels in the regulation of parenchymal arteriole tone and vascular remodeling during hypoperfusion. In these studies, wild-type and TRPV4-knockout (KO) mice were subjected to unilateral common carotid artery occlusion (UCCAo) for 28 days. In wild-type mice, UCCAo caused a decrease in active tone and increased passive inner diameters (Chan et al., 2019). The decreased tone was dependent on TRPV4 channel function but not the outward remodeling. These effects of UCCAo on myogenic tone did not involve NO signaling. The same group showed decreased myogenic tone in control WKY rats subjected to UCCAo, an effect that was not observed in SHRSP model animals (Sweet et al., 2015). Together, these data suggest that ischemia, as well as hypertension, result in the activation of distinct compensatory processes. While ischemia-related signaling is geared toward maintaining vessels open and sustaining CBF, hypertension-induced increases in vascular tone serve to prevent hyperperfusion-induced microvascular damage. In hypertension, remodeling and increased vascular reactivity may lead to hypoperfusion and the onset of cerebral ischemia.

Reactive oxygen species (ROS), which are elevated in hypertension (Montezano et al., 2015), are involved in vascular inflammation, fibrosis and arterial remodeling (Tanaka and Laurindo, 2017), and thus contribute to vascular dysfunction (Lopes et al., 2015). Using a transcriptomic approach, Walas et al. (2019) presented evidence that, prior to the onset of hypertension, cerebral arteries from the posterior circulation of 5-week-old SHRs exhibit elevated expression of genes related to remodeling, oxidative stress, and inflammatory pathways, notably including a 40% increase in genes related to fibrosis (e.g., TGFβ). Among the changes noted during this pre-hypertension period were dysregulation of pro-fibrotic pathways (e.g., upregulation of enolase-1) and inflammatory pathways

(e.g., inhibition of interferons, TLR3 and STAT1) as well as altered mitochondrial function. The authors proposed that these changes support previously reported immune cell infiltration (Waki et al., 2007, 2013; Xu et al., 2012; Marvar et al., 2016). The resulting vessel remodeling alters vascular function, increasing cerebrovascular resistance and decreasing CBF, both of which contribute to increased sympathetic nerve activity via the Cushing mechanism, as recently reviewed (McBryde et al., 2017). The onset of hypertension was thus regarded as a secondary insult that worsened vessel fibrosis and stiffening and also caused endothelial dysfunction. These results obtained using the SHR model suggest that early therapeutic approaches targeting immune system dysfunction may prevent vascular dysfunction associated with hypertension.

Increased oxidative stress and resulting endothelial dysfunction are also associated with decreased CBF and increased BBB permeability (Iadecola, 2013). Moreover, hypertension is correlated with the size and prevalence of microbleeds (Vernooij et al., 2008; Shams et al., 2015)—a marker of vessel damage—and BBB breakdown. Increased ROS levels promote increases in intracellular astrocytic Ca^{2+}, which has been linked to the ability of astrocytes to sense hypoxia (Angelova and Abramov, 2016). In the context of exacerbated ROS levels in disease, this mechanism may contribute to the pathogenesis of neurodegenerative disorders.

In mice, Ang II-dependent hypertension impaired NVC-evoked increases in CBF and endothelial-mediated vasodilation (Capone et al., 2012; Johnson et al., 2013). Ang II-induced hypertension is associated with increased activation of NADPH oxidase and enhanced ROS production (Kazama et al., 2004; Capone et al., 2011). Iulita et al. (2019) provided evidence that in a murine Ang II-dependent model of hypertension (1000 ng/kg/min), the adoptive transfer of Treg cells prevented neurovascular uncoupling and endothelial dysfunction. Neuroprotective effects were linked to IL-10 signaling and abolished in IL-10 deficient mice. Notably, the adoptive transfer of Tregs reduced Ang II-induced systemic inflammation, microgliosis and superoxide radicals (Iulita et al., 2019). Faraco et al. (2016), investigated the contribution of perivascular macrophages (PVMs), resident brain macrophages with the capacity to generate ROS, to hypertension-induced neurovascular and cognitive dysfunction. Low Ang II doses was shown to increase BBB permeability and Ang II access into perivascular spaces. The subsequent PVM activation, via AT1R and the NADPH oxidase subunit NOX2, contributed to ROS production (Faraco et al., 2016). The authors further demonstrated that in BPH/2J mice, PVM depletion improved cognitive impairments, providing an important link between hypertension, PVM/inflammation, and cognitive dysfunction (Faraco et al., 2016). The same group recently demonstrated that Ang II-induced hypertension in mice leads to tight junction remodeling and increased BBB permeability, an effect more pronounced in arterioles than capillaries (Santisteban et al., 2020). The authors proposed a mechanism by which circulating Ang II leads to AT1a receptor activation in endothelial cells and downregulation of *Mfsd2a*. The resulting increased vesicular transport of Ang II into the perivascular space would then lead to AT1R and NOX2 activation in PVM, increasing BBB disruption (Santisteban et al., 2020).

Inflammation, Aberrant Astrocytic Ca^{2+} and Disease

While astrocytes are known for their trophic support, these cells also participate in proinflammatory processes (Pomilio et al., 2016; Verkhratsky and Nedergaard, 2018). Alteration in glial function and morphology (i.e., astrogliosis) is associated with disease states, vasodilator dysfunction of cerebral parenchymal arterioles (Bagi et al., 2018) and cognitive dysfunction (Verkhratsky and Nedergaard, 2018). Hypertension, regarded as a chronic inflammatory state (De Miguel et al., 2015; Rodriguez-Iturbe et al., 2017), impairs one of the first barriers of brain protection, the BBB (Katsi et al., 2020; Santisteban et al., 2020). BBB dysfunction facilitates the infiltration of plasma components to the brain and the production of proinflammatory signals that lead to microglia and astrocyte activation. These inflammatory processes impair the glial trophic support of both the vasculature and neurons (Iadecola, 2013). The extensive coverage of astrocytic processes along the cerebral microcirculation could be regarded as the next in line protective barrier (Sofroniew, 2015). However, how endothelial dysfunction alters the functional properties of astrocytes remains poorly understood. We speculate that the progressive impairment of the cerebral microcirculation, accompanied by the release of inflammatory markers, contributes to a shift in astrocyte phenotype from protective to inflammatory. Consequently, neuroinflammation directed by glial cells may contribute to hypertension-related cognitive impairment.

Efforts have been made to delineate astrocyte functional phenotypes based on the expression of specific markers, as previously reviewed (Miller, 2018). To this point, however, molecular profiling strategies (e.g., single-cell transcriptomics), have not been able to fully determine astrocyte functional status. Despite transcriptomic comparisons between astrocytes positive for GFAP, ALDH1L1, GLT1 or HEPACAM, the co-expression of markers in the majority of astrocytes has limited the ability to identify astrocyte subpopulations (Lovatt et al., 2007; Yang et al., 2011; Zhang et al., 2016).

To date, two major astrocyte phenotypes have been described based on their susceptibility to signals from microglia. A1 astrocytes, analogous to the controversial M1 microglia subtype, develop a proinflammatory phenotype that cannot support synapse formation or phagocytosis. The A1 phenotype is primarily driven by interleukin (IL)-1α, tumor necrosis factor (TNF)-α, and C1q (complement component 1, subcomponent q) (Liddelow et al., 2017). On the other hand, trophic or protective astrocytes, referred to as A2 astrocytes, represent the normally functioning astrocyte subtype. The A2 astrocyte phenotype is also linked to the promotion of neuronal survival following ischemia (Liddelow et al., 2017; Clarke et al., 2018). Importantly, whether astrocytes can reversibly switch from one phenotype to the other is presently unknown.

Given limited knowledge on the factors leading to astrocytes functional transition from supportive to proinflammatory,

alternative approaches, including incorporation of an assessment of Ca^{2+} dynamics, are pivotal for interpreting astrocyte function and population subtype. Increasing evidence pointing to aberrant astrocytic Ca^{2+} as an early indicator of disease state and severity strengthens the importance of decoding astrocyte communication at the NVU for optimal brain function (Shigetomi et al., 2019).

Models of cerebrovascular pathology such as stroke (Morrison and Filosa, 2016; Morrison and Filosa, 2019) and AD, show increases in astrocyte Ca^{2+} events (Delekate et al., 2014). Less understood, however, is the impact of hypertension on astrocyte Ca^{2+} dynamics and function. Ohara and Nabika (2016) identified a point mutation in stromal interaction molecule-1 (Stim1) in the SHRSP model, and further showed that truncated STIM1 impaired Ca^{2+} signaling regulated by store-operated Ca^{2+}-entry in cultured astrocytes. Diaz et al. (2019) showed augmented spontaneous and myogenic-evoked Ca^{2+} events in microdomains of cortical astrocytes from Ang II-induced hypertensive mice, events that were accompanied by increased TRPV4 channel function. Although it is not entirely clear how this contributes to pathogenesis, the authors hypothesized that sustained intracellular Ca^{2+} elevations in astrocytes could trigger or facilitate the transition of these cells to a proinflammatory state. In support of this, exacerbated TRPV4 channel activation has been linked to the release of proinflammatory signals (Krizaj et al., 2014) that may, in turn, initiate astrocyte-microglia interactions (e.g., ATP, DAMPs), establishing a feed-forward response that aggravates neuroinflammation at the NVU.

In AD, astrocytes in the vicinity of amyloid plaques exhibit abnormally elevated Ca^{2+} levels (Shigetomi et al., 2019). Astrocytes in acute brain slices also respond to exposure to Aβ oligomers with an increase in intracellular Ca^{2+} (Tyurikova et al., 2018). Similar findings have been reported in stroke, were astrocytes in proximity to damaged tissue show increased Ca^{2+} (Shigetomi et al., 2019). Notably, suppression of aberrant astrocytic Ca^{2+} signals in the context of stroke reduces cell and tissue damage (Ding et al., 2009), indicating that astrocyte Ca^{2+} overload can lead to pathology. Further studies are needed to uncover mechanistic details of altered astrocytic Ca^{2+} signaling in AD models.

Vascular Stiffness

There are several human studies and observations indicating that hypertension and aging exert synergistic effects on cognitive decline (Csiszar et al., 2013). In fact, hypertension may prompt the early onset of mechanisms underlying accelerated aging. Both hypertension and aging increase vascular stiffness. In healthy elastic arteries (thoracic aorta and common carotid artery), the compliance of these vessels dampens pressure and flow fluctuations, thereby allowing delivery of a steady flow of blood to the more vulnerable microcirculation (Chirinos et al., 2019). Sustained mechanical stress causes arteries to lose their distensibility, leading to increased stiffness (Avolio et al., 2018; Mitchell, 2018). Thus, both age and hypertension result in a reduction in pressure-buffering capacity upstream from the cerebral microcirculation. As a consequence, the amplitude of pulsations transmitted to the carotids is increased (Mitchell et al., 2011). At the microcirculation level, hypertension contributes to small vessel disease (Faraci, 2018). Moreover, hypertension results in increase wall stiffness of larger vessels (i.e., posterior cerebral artery) and increased wall stress and wall thickness of parenchymal arteriole (Diaz-Otero et al., 2016). While few have addressed the importance of understanding the relationship between the macro- and micro-vasculature, these questions are emerging (Climie et al., 2019) and constitute new paradigms toward the development of new therapeutic targets addressing the impact of cardiovascular disease on cognitive function.

Arterial stiffness is a predictor of cardiovascular risk. In clinical practice, the gold standard for measurements of regional arterial stiffness is pulse wave velocity (PWV) (Negoita et al., 2018). The PWV, often measured from the carotid to the femoral artery, is defined as the distance traveled by the pulse wave from the carotid point to the femoral point (ΔL) divided by the time of travel (ΔT) or, $PWV = \Delta L/\Delta T$. In the aging population, increased pulse pressure is also linked to hypertension. To this end, measurements of wave intensity and wave separation analysis (Fok et al., 2014; Su et al., 2017) allow pressures to be separated into the push forward (from the ventricle against the arterial tree) and backward (from arterial tree against the ventricle) components (Fok et al., 2014). Thus, different components of the pressure wave can provide information related to the pressures generated from the ventricle and the arterial tree.

Arteries from hypertensive patients exhibit increased stiffness and a loss of distensibility, which increases their susceptibility to pulse pressure-mediated damage (Lacolley et al., 2018). A previous study evaluated the relationship between small vessel disease and aortic PWV in 167 hypertensive patients without a history of vascular or cerebrovascular disease (Henskens et al., 2008), demonstrating a positive correlation between PWV and white matter hyperintensities and the presence of silent lacunar infarcts. This correlation held even in younger patients (<50 years old) and was independent of vascular risk factors (i.e., MAP and age). Increasing the duration of the momentum of the pulse pressure increased the risk for tissue damage (Henskens et al., 2008).

A study that followed > 3000 patients evaluated the relationship between downstream small vessel damage and cognitive decline. Using forward compression wave intensity (FCWI), which measures the intensity of pulsatile waves traveling via the carotids toward the brain, it was concluded that elevated carotid artery FCWI was correlated with earlier cognitive decline, independently of other cardiovascular factors (Chiesa et al., 2019). In this study, participants were examined for changes in memory, executive function, and fluency over 13 years. Those with a higher FCWI in the carotid artery showed a 50% greater chance of developing cognitive dysfunction, even after adjusting for several factors, including education. In a cross-sectional study that included 668 females and males between 69 and 93 years of age, Mitchell et al. (2011) reported that higher carotid pulse pressure and carotid flow pulse amplitude were correlated with reduced cognitive function, assessed by tests of memory, executive function, and processing speed (Mitchell et al., 2011).

An increase in PWV was shown to contribute to cognitive dysfunction through its negative impacts on white and gray matter volumes and its positive correlation with lacunar infarcts and white matter hyperintensities.

Increased vascular stiffness may result from increases in blood pressure variability (BPV) (Rothwell, 2010; Schillaci et al., 2012), defined as blood pressure fluctuations over time, where time can be measured in seconds to years (short-term, $\leq$ 24 h; mid-term, days/weeks; long-term, years) (Stevens et al., 2016, 2019). BPV is emerging as an independent predictor of cardiovascular risk and dementia (Merkler and Iadecola, 2017; Oishi et al., 2017). While the mechanisms underlying BPV are still unclear, augmented blood pressure fluctuations may be the result of reduced ability to buffer normal changes due to impaired vascular function (e.g., increased vascular stiffness), impaired baroreflex sensitivity and/or sympathetic nerve responses (Schillaci et al., 2012). BPV contributes to cardiovascular complications in hypertension, and antihypertensive agents that control it help prevent the development of cardiovascular events (Rothwell et al., 2010; Parati et al., 2012). A meta-analysis that included data from 27 articles and more than 12,000 individuals determined that greater short-term (24 h) BPV in humans was correlated with subcortical infarct, lacunae, white matter hyperintensities, cerebral microbleeds and/or enlarged perivascular spaces (Tully et al., 2020). Further supporting the adverse effect of increased BPV on neurovascular function, Oishi et al. (2017), provided evidence that BPV, is an independent risk factor in the development of AD and vascular cognitive impairment/dementia.

Multiple cellular and extracellular matrix mechanisms contribute to vascular stiffness, including elastin fragmentation, collagen deposition, advanced glycation endproduct (AGE)-mediated collagen and elastin cross-linking, impaired VSMC function and calcification, endothelial dysfunction, inflammation and oxidative stress, among others (Chirinos et al., 2019). While advances have been made in elucidating the impact of the renin-angiotensin system (RAS), especially Ang II (Forrester et al., 2018), on vascular fibrosis and arterial stiffness, the underlying cellular and molecular mechanisms remain elusive. Ang II in hypertension and arteriosclerosis is linked to inflammation and oxidative stress (Rodriguez-Iturbe et al., 2017). In VSMCs, elevated intracellular Ca^{2+}, increased actin-myosin cross-bridge formation, cytoskeleton rearrangement, ROS, inflammation-related non-coding RNAs, as well as Ca^{2+}-independent mechanisms involving RhoA-Rho kinase, protein kinase C and mitogen-activated protein kinase signaling lead to increased vasoconstriction and arterial remodeling, as recently reviewed by Touyz et al. (2018). Using a mouse model of arterial stiffness induced by administration of $CaCl_2$ into the adventitia of the carotid artery, Sadekova et al. (2018) showed increased microglia and astrocyte reactivity in the hippocampus and frontal cortex. In this case, the observed gliosis was associated with NADPH-generated oxidative stress (Sadekova et al., 2018).

Taken together, while numerous human studies and observations found strong correlations between arterial stiffening and impaired cerebrovascular function in hypertension and cognitive decline, the apparent lack of direct mechanistic links and experimental evidence for well-defined molecular targets prevents therapeutic progress.

VASCULAR CONTRIBUTORS TO COGNITIVE IMPAIRMENT AND DEMENTIA

The prevalence of hypertension, a modifiable risk factor for cardiovascular disease, increases with age. Importantly, in hypertensive patients, aging accelerates cognitive decline (Livingston et al., 2017). Thus, understanding the cellular mechanisms underlying hypertension- and aging-induced cognitive decline is pivotal for the development of therapeutic strategies in the prevention of vascular-related dementia.

The most common form of dementia is AD, a multifactorial neurodegenerative disease (Pomilio et al., 2020). Early presentations of AD include neurovascular dysfunction and microvasculature alterations (Sagare et al., 2013). Iturria-Medina et al. (2016) analyzed 7,700 brain images and dozens of plasma and cerebrospinal fluid biomarkers from the Alzheimer's Disease Neuroimaging Initiative (ADNI), looking for abnormalities related to vascular, amyloid, metabolic, functional, and structural changes. They found that vascular dysfunction was an early pathological event. Importantly, cognitive decline was noticeable from the initial stages of late-onset AD and was associated with vascular alterations.

Mouse models of familial AD exhibit differences depending on the specific mutations and transgenes they carry. However, many present vascular alterations (Iadecola, 2017), including altered cerebral perfusion (Hebert et al., 2013; Guo et al., 2019), impaired NVC (Badhwar et al., 2013; Lu et al., 2019), capillary endothelial degeneration, thickening (Zlokovic, 2005), and loss of pericytes and BBB integrity (Sagare et al., 2013; Montagne et al., 2020), before behavioral changes and deposition of amyloid plaques. As in humans, these observations support the notion that vascular dysfunction is an essential factor in the onset of cognitive decline.

Increased blood pressure in mid-life is positively associated with cognitive decline or AD late in life (Skoog et al., 1996). A recent report of a clinical trial with a 6-year follow-up concluded that controlling blood pressure at a target level less than 140 mmHg decreased the incidence of mild cognitive impairment and lowered the risk of dementia (Sprint Mind Investigators for the Sprint Research Group, Williamson et al., 2019). Given the availability of potentially beneficial therapeutics and the lack of successful interventions for AD (Edwards Iii et al., 2019), antihypertensive drugs have been explored as AD treatments. A retrospective cohort analysis of patients taking antihypertensive RAS-acting medicines, including angiotensin-converting enzyme inhibitors (ACEIs) and Ang II receptor blockers (ARBs), reported that AD incidence was lower in women (both Caucasian and African American) and Caucasian men taking ARBs compared with their counterparts not taking RAS-acting drugs (Barthold et al., 2018). Furthermore, a meta-analysis found that controlling blood pressure with antihypertensive drugs in and of itself may have positive outcomes for cognitive function (Ding et al., 2020).

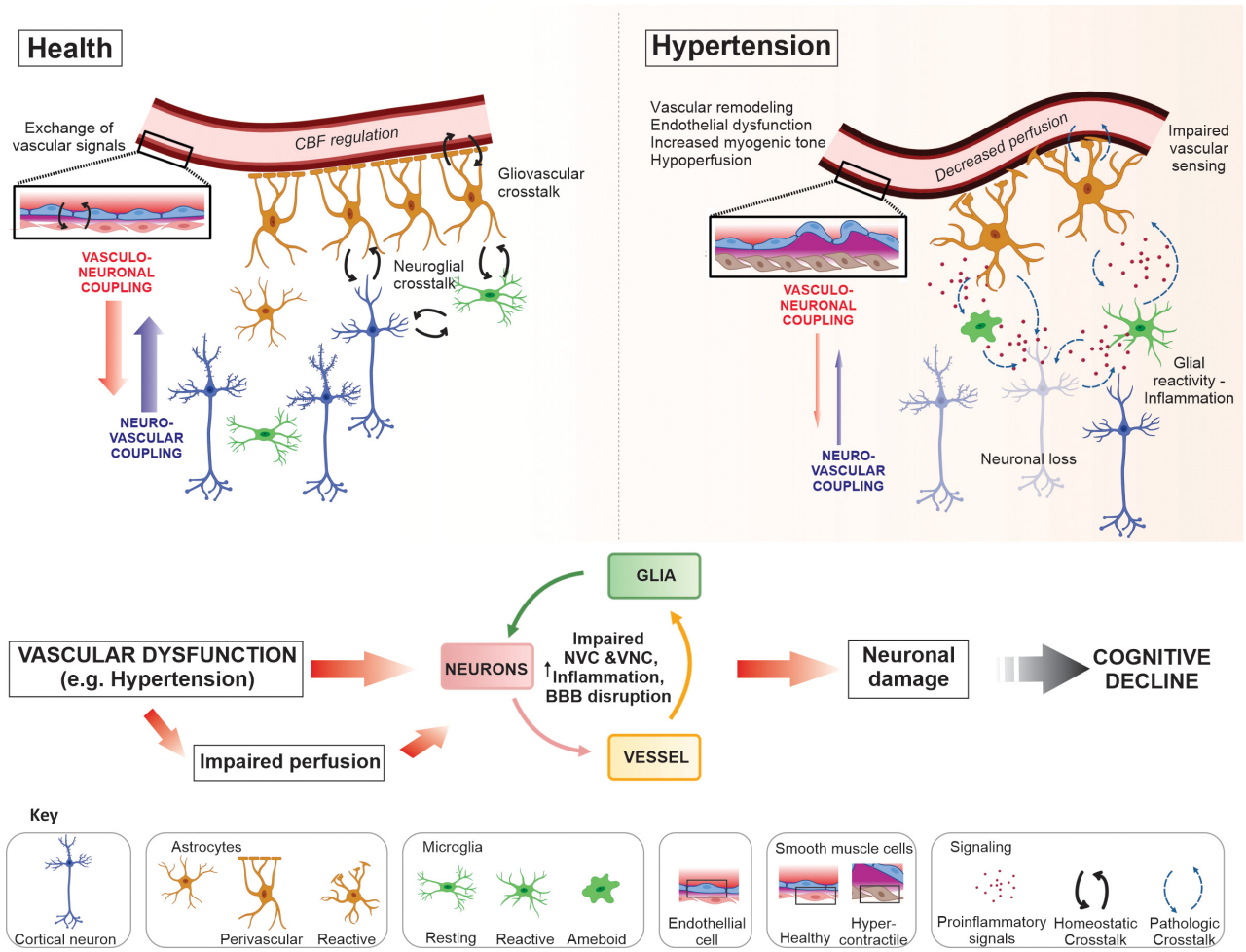

FIGURE 1 | Neurovascular unit crosstalk interactions in health and disease. In the healthy brain dynamic crosstalk interactions at the neurovascular unit (NVU), via multiple signaling modalities, maintain a homeostatic environment optimal for neuronal function. Astrocytes and microglia are target of neuronal signals, i.e., through specific receptors or extracellular vesicles, to which they respond exerting several functions in coordination (for example, neuronal support, synaptic development and formation, phagocytosis and modulation of neuronal activity). The NVU crosstalk also includes the release of vasoactive signals from vascular, glial and neuronal cells. Together, signals from these cells aid in the regulation of cerebral blood flow (CBF), a process requiring both neurovascular (NVC) and vasculo-neuronal coupling (VNC); maintenance of the blood–brain barrier (BBB); immune surveillance; ionic and neurotransmitter homeostasis; metabolic support; and neurotransmission, to name a few. Disease conditions such as hypertension evoked changes at the NVU that progressively impaired communication between cells shifting the normal crosstalk into a pathological state. Vascular dysfunction, including remodeling, endothelial and vascular smooth muscle cell (VSMC) dysfunction, vascular and glial inflammation (i.e., astrogliosis and microgliosis), all contribute to impaired perfusion to the NVU and loss of BBB integrity. The constitutive presence of these deleterious processes diminishes the stability of the NVU and impair neuronal function contributing to neurodegeneration and, ultimately, cognitive decline.

Targeting the RAS using Ang II receptor blockers has proven beneficial for cognition in both human patients and animal models. AD mice (*J20* model) treated with losartan showed improved posterior cerebral artery reactivity and restoration of functional hyperemia, this despite the fact that amyloid deposits in the brain did not decrease, and even showed a tendency to increase. Remarkably, losartan improved outcomes in cognitive tests in AD mice. At the cellular level, losartan decreased the oxidative state/stress and astrogliosis (Royea et al., 2017). These results are in agreement with those of another study in which losartan treatment improved cerebrovascular and cognitive function in older mice (12 months) (Ongali et al., 2014). These observations argue against a link between Ang II receptors and amyloid pathology-related cognitive dysfunction, but favor the idea that improving vascular function with the use of antihypertensive drugs could positively impact cognitive outcomes in AD. In humans, telmisartan treatment was associated with increased resting CBF and improved cognitive function (Kume et al., 2012), supporting the use of antihypertensive treatments to improve vascular function and cerebral perfusion. In a randomized controlled trial, 6-month treatment with telmisartan, an AT_1R blocker, in probable AD patients with essential hypertension decreased proinflammatory cytokines in the CSF and increased $A\beta_{1-42}$, indicative of augmented clearance (Li et al., 2012). An important point to consider, however, is

that not all drugs that block Ang II receptors are helpful in restoring cognitive function (Trigiani et al., 2018) or are effective in long-established AD pathology, as seen in mice (Ongali et al., 2016).

The use of antihypertensive drugs has also been proposed as a strategy for ameliorating amyloid pathology. A recent study in which regulation of the RAS was enhanced through ACE2 in the Tg2676 mice model of AD showed that spatial memory was improved in association with a reduction in soluble and insoluble Aβ in the hippocampus (Evans et al., 2020). Here, however, vascular function was not evaluated. Ang-II–infused hypertensive mice exhibit increased production of amyloid precursor protein (APP) binding proteins (Csiszar et al., 2013). Yet, no changes in the production of APP-processing enzymes that participate in the amyloidogenic process were found.

Further studies are needed to determine the effects of antihypertensive drugs and their mechanisms of action concerning the vascular component of AD. These drugs might be useful in the prevention of AD and dementia by preserving vascular function. However, their potential to mitigate the contribution of amyloid pathology cannot be ruled out. In this latter context, it could be that the driver of amyloid pathology in hypertensive models and patients relates to the deleterious effects of hypoxia/ischemia on vascular function, as these conditions activate the processing of APP (Shiota et al., 2013).

Whether independent or as a result of hypertension, evidence also supports a link between arterial stiffness and AD pathology and related dementias. Notably, arterial stiffness is a contributing factor to pulsatile hemodynamics, cerebral hypoperfusion, and microvascular damage. In older adults, arterial stiffness is positively correlated with an increased incidence of cerebral small vessel disease (Hughes et al., 2015; Chirinos et al., 2019). Rivera-Rivera et al. (2020) showed that cerebrovascular stiffness was increased in middle-aged AD patients. In this work, the authors employed high temporal resolution 4D flow magnetic resonance imaging (MRI) to assess transcranial PWV in 160 participants classified according to cognitive function. They found that transcranial PWV was significantly increased in subjects with myocardial infarct or AD.

Notably, maladapted cerebral hemodynamics could lead to alterations in the structural and functional connectivity of the brain, as exemplified by white matter lesions/hyperintensities, a symptom of small vessel disease and parenchymal artery dysfunction (Bagi et al., 2018). At rest, the brain exhibits slow blood flow fluctuations that are interpreted as providing effective connectivity between regions comprising what is known as the default mode network (Raichle, 2015). Reduced functional connectivity between the hippocampus and other brain regions is found in AD patients (Allen et al., 2007), and has been shown to correlate with behavioral changes (Multani et al., 2019).

As is the case in hypertension and aging, diminished cerebral perfusion, perhaps initiated by morphological alterations of the microvasculature, may play a role in the development of AD through increases in oxidative stress and compromised neurovascular interactions. Decreased oxygen delivery to brain regions, including the hippocampus, leads to neurodegeneration and cognitive decline (de la Torre, 2000; Mehla et al., 2018). Tong et al. (2012) showed therapeutic benefits from simvastatin treatment in a mouse model of AD. Simvastatin lowered O_2^- production and normalized antioxidant superoxide dismutase 2 levels. Importantly, simvastatin restored cerebrovascular function and NVC in both aged (12 months) and adult mice (6 months). Short- and long-term memory was restored in aged adults but not aged AD mice, even without effects on plaque or amyloid β (Aβ) levels.

At the level of the NVU, Aβ has been shown to cause pericyte-induced capillary constriction in both AD patients and an AD mouse model. The underlying mechanism was found to involve the generation of ROS (mainly via NOX4), resulting in the release of the potent vasoconstrictor agent, endothelin-1 (ET-1). ET-1, in turn, acted through ET_A receptors to evoke pericyte constriction. Notably, Aβ-evoked constrictions were prevented by blocking NOX4 or ET_A (Nortley et al., 2019). A recent study showed that secretion of APOE4 by pericytes resulted in activation of cyclophilin A and stimulation of downstream protein matrix metalloproteinase-9. Increased inflammation in pericytes, and possibly endothelial cells, increased BBB leakiness in the hippocampus and parahippocampus brain areas associated with learning and memory.

Aβ peptide aggregation in the wall of cerebral microvessels (cerebral amyloid angiopathy) also impairs vascular function (Kimbrough et al., 2015) and is a risk factor for vascular cognitive impairment. Using a combination of *ex vivo* and *in vivo* imaging approaches in mice, Kimbrough et al. (2015) found that astrocyte endfeet were separated from cerebral vessel segments that showed amyloid deposits and that astrocyte stimulation resulted in poor vascular responses. In contrast, astrocyte-induced vascular responses were intact in vessel segments that lacked amyloid deposits (Kimbrough et al., 2015). Collectively, these observations support a role for astrocytes in the regulation of CBF in AD.

The importance of vascular homeostasis in AD and associated dementias has become an important shift in the quest to identify the factors contributing to cognitive decline (Csiszar et al., 2017). Collectively, the above findings call for controlled clinical trials and advanced animal models to help disentangle mechanisms targeted by antihypertensive and antioxidant treatments in the therapeutic benefits of these drugs in the setting of vascular-related cognitive impairment and dementia.

CONCLUSION

This review highlights key crosstalk dynamics at the NVU, which maintain homeostasis in the brain (**Figure 1**). We discussed key molecular regulators of parenchymal arteriole vascular tone and the pathological changes these arterioles undergo in disease conditions, primarily hypertension. In addition, we describe how other components of the NVU (e.g., glial cells) may contribute to disease progression (**Figure 1**). Clearly, more work is needed to understand the cellular mechanisms underlying loss of function at the NVU and how vascular alterations (i.e., vascular stiffness, remodeling, and

astrocyte-vascular uncoupling) impact homeostatic as well as energy-dependent processes in the brain. While vascular dysfunction is strongly linked to cognitive decline, many factors such as the cellular targets involved in disease-specific insults (i.e., CBF, intravascular pressure, ischemia, inflammation) as well as the consequences these have on cerebral perfusion and neuronal functional remain ill define. Thus, future studies addressing the cellular and molecular players in the loss of physiological crosstalk at the NVU are needed to shed light on early processes, with therapeutic potential, to prevent what in later life manifests as vascular cognitive impairment and dementia.

AUTHOR CONTRIBUTIONS

All authors listed have made a substantial, direct and intellectual contribution to the work, and approved it for publication.

FUNDING

This work was supported by funding from the National Institute of Neurological Disorders and Stroke (NINDS) (1R01NS082521-01) of the NIH to JF.

REFERENCES

Albalawi, F., Lu, W., Beckel, J. M., Lim, J. C., McCaughey, S. A., and Mitchell, C. H. (2017). The P2X7 receptor primes IL-1beta and the NLRP3 inflammasome in astrocytes exposed to mechanical strain. *Front. Cell. Neurosci.* 11:227. doi: 10.3389/fncel.2017.00227

Allen, G., Barnard, H., McColl, R., Hester, A. L., Fields, J. A., Weiner, M. F., et al. (2007). Reduced hippocampal functional connectivity in Alzheimer disease. *Arch. Neurol.* 64, 1482–1487. doi: 10.1001/archneur.64.10.1482

Alosco, M. L., Gunstad, J., Xu, X., Clark, U. S., Labbe, D. R., Riskin-Jones, H. H., et al. (2014). The impact of hypertension on cerebral perfusion and cortical thickness in older adults. *J. Am. Soc. Hypertens.* 8, 561–570. doi: 10.1016/j.jash.2014.04.002

Angelova, P. R., and Abramov, A. Y. (2016). Functional role of mitochondrial reactive oxygen species in physiology. *Free Radic. Biol. Med.* 100, 81–85. doi: 10.1016/j.freeradbiomed.2016.06.005

Araque, A., Carmignoto, G., Haydon, P. G., Oliet, S. H., Robitaille, R., and Volterra, A. (2014). Gliotransmitters travel in time and space. *Neuron* 81, 728–739. doi: 10.1016/j.neuron.2014.02.007

Attwell, D., Buchan, A. M., Charpak, S., Lauritzen, M., Macvicar, B. A., and Newman, E. A. (2010). Glial and neuronal control of brain blood flow. *Nature* 468, 232–243. doi: 10.1038/nature09613

Avolio, A., Kim, M. O., Adji, A., Gangoda, S., Avadhanam, B., Tan, I., et al. (2018). Cerebral haemodynamics: effects of systemic arterial pulsatile function and hypertension. *Curr. Hypertens. Rep.* 20:20.

Badhwar, A., Lerch, J. P., Hamel, E., and Sled, J. G. (2013). Impaired structural correlates of memory in Alzheimer's disease mice. *Neuroimage Clin.* 3, 290–300. doi: 10.1016/j.nicl.2013.08.017

Bagher, P., and Segal, S. S. (2011). Regulation of blood flow in the microcirculation: role of conducted vasodilation. *Acta Physiol (Oxf)* 202, 271–284. doi: 10.1111/j.1748-1716.2010.02244.x

Bagi, Z., Brandner, D. D., Le, P., McNeal, D. W., Gong, X., Dou, H., et al. (2018). Vasodilator dysfunction and oligodendrocyte dysmaturation in aging white matter. *Ann. Neurol.* 83, 142–152. doi: 10.1002/ana.25129

Baik, S. H., Kang, S., Lee, W., Choi, H., Chung, S., Kim, J. I., et al. (2019). A breakdown in metabolic reprogramming causes microglia dysfunction in Alzheimer's disease. *Cell Metab.* 30:e496.

Barthold, D., Joyce, G., Wharton, W., Kehoe, P., and Zissimopoulos, J. (2018). The association of multiple anti-hypertensive medication classes with Alzheimer's disease incidence across sex, race, and ethnicity. *PLoS One* 13:e0206705. doi: 10.1371/journal.pone.0206705

Baumbach, G. L., and Ghoneim, S. (1993). Vascular remodeling in hypertension. *Scanning Microsc.* 7, 137–142.

Bayliss, W. M. (1902). On the local reactions of the arterial wall to changes of internal pressure. *J. Physiol.* 28, 220–231. doi: 10.1113/jphysiol.1902.sp000911

Bazargani, N., and Attwell, D. (2016). Astrocyte calcium signaling: the third wave. *Nat. Neurosci.* 19, 182–189. doi: 10.1038/nn.4201

Beckel, J. M., Argall, A. J., Lim, J. C., Xia, J., Lu, W., Coffey, E. E., et al. (2014). Mechanosensitive release of adenosine 5'-triphosphate through pannexin channels and mechanosensitive upregulation of pannexin channels in optic nerve head astrocytes: a mechanism for purinergic involvement in chronic strain. *Glia* 62, 1486–1501. doi: 10.1002/glia.22695

Benetos, A., Petrovic, M., and Strandberg, T. (2019). Hypertension management in older and frail older patients. *Circ. Res.* 124, 1045–1060. doi: 10.1161/circresaha.118.313236

Berthiaume, A. A., Grant, R. I., McDowell, K. P., Underly, R. G., Hartmann, D. A., Levy, M., et al. (2018a). Dynamic remodeling of pericytes *in vivo* maintains capillary coverage in the adult mouse brain. *Cell Rep.* 22, 8–16. doi: 10.1016/j.celrep.2017.12.016

Berthiaume, A. A., Hartmann, D. A., Majesky, M. W., Bhat, N. R., and Shih, A. Y. (2018b). Pericyte structural remodeling in cerebrovascular health and homeostasis. *Front. Aging Neurosci.* 10:210. doi: 10.3389/fnagi.2018.00210

Bilbo, S., and Stevens, B. (2017). Microglia: the Brain's first responders. *Cerebrum* 2017:cer-14-17.

Bindocci, E., Savtchouk, I., Liaudet, N., Becker, D., Carriero, G., and Volterra, A. (2017). Three-dimensional Ca2+ imaging advances understanding of astrocyte biology. *Science* 356:eaai8185. doi: 10.1126/science.aai8185

Bonder, D. E., and McCarthy, K. D. (2014). Astrocytic Gq-GPCR-Linked IP3R-dependent Ca2+ signaling does not mediate neurovascular coupling in mouse visual cortex *in vivo*. *J. Neurosci.* 34, 13139–13150. doi: 10.1523/jneurosci.2591-14.2014

Bosch, A. J., Harazny, J. M., Kistner, I., Friedrich, S., Wojtkiewicz, J., and Schmieder, R. E. (2017). Retinal capillary rarefaction in patients with untreated mild-moderate hypertension. *BMC Cardiovasc. Disord.* 17:300. doi: 10.1186/s12872-017-0732-x

Brayden, J. E., Li, Y., and Tavares, M. J. (2013). Purinergic receptors regulate myogenic tone in cerebral parenchymal arterioles. *J. Cereb. Blood Flow Metab.* 33, 293–299. doi: 10.1038/jcbfm.2012.169

Cai, C., Fordsmann, J. C., Jensen, S. H., Gesslein, B., Lonstrup, M., Hald, B. O., et al. (2018). Stimulation-induced increases in cerebral blood flow and local capillary vasoconstriction depend on conducted vascular responses. *Proc. Natl. Acad. Sci. U.S.A.* 115, E5796–E5804.

Calcinaghi, N., Wyss, M. T., Jolivet, R., Singh, A., Keller, A. L., Winnik, S., et al. (2013). Multimodal imaging in rats reveals impaired neurovascular coupling in sustained hypertension. *Stroke* 44, 1957–1964. doi: 10.1161/strokeaha.111.000185

Cao, R., Higashikubo, B. T., Cardin, J., Knoblich, U., Ramos, R., Nelson, M. T., et al. (2009). Pinacidil induces vascular dilation and hyperemia *in vivo* and does not impact biophysical properties of neurons and astrocytes *in vitro*. *Cleve. Clin. J. Med.* 76(Suppl. 2), S80–S85.

Capone, C., Faraco, G., Park, L., Cao, X., Davisson, R. L., and Iadecola, C. (2011). The cerebrovascular dysfunction induced by slow pressor doses of angiotensin II precedes the development of hypertension. *Am. J. Physiol. Heart Circ. Physiol.* 300, H397–H407.

Capone, C., Faraco, G., Peterson, J. R., Coleman, C., Anrather, J., Milner, T. A., et al. (2012). Central cardiovascular circuits contribute to the neurovascular dysfunction in angiotensin II hypertension. *J. Neurosci.* 32, 4878–4886. doi: 10.1523/jneurosci.6262-11.2012

Chan, S. L., Nelson, M. T., and Cipolla, M. J. (2019). Transient receptor potential vanilloid-4 channels are involved in diminished myogenic tone in brain parenchymal arterioles in response to chronic hypoperfusion in mice. *Acta Physiol.* 225:e13181. doi: 10.1111/apha.13181

Chen, B. R., Bouchard, M. B., McCaslin, A. F., Burgess, S. A., and Hillman, E. M. (2011). High-speed vascular dynamics of the hemodynamic response. *Neuroimage* 54, 1021–1030. doi: 10.1016/j.neuroimage.2010.09.036

Chen, B. R., Kozberg, M. G., Bouchard, M. B., Shaik, M. A., and Hillman, E. M. (2014). A critical role for the vascular endothelium in functional neurovascular coupling in the brain. *J. Am. Heart Assoc.* 3:e000787.

Chiesa, S. T., Masi, S., Shipley, M. J., Ellins, E. A., Fraser, A. G., Hughes, A. D., et al. (2019). Carotid artery wave intensity in mid- to late-life predicts cognitive decline: the Whitehall II study. *Eur. Heart J.* 40, 2300–2309. doi: 10.1093/eurheartj/ehz189

Chirinos, J. A., Segers, P., Hughes, T., and Townsend, R. (2019). Large-artery stiffness in health and disease: JACC state-of-the-art review. *J. Am. Coll. Cardiol.* 74, 1237–1263. doi: 10.1016/j.jacc.2019.07.012

Choi, H. J., Sun, D., and Jakobs, T. C. (2015). Astrocytes in the optic nerve head express putative mechanosensitive channels. *Mol. Vis.* 21, 749–766.

Cipolla, M. J. (2009). *The Cerebral Circulation*. San Rafael, CA: Morgan & Claypool Life.

Cipolla, M. J., Sweet, J., Chan, S. L., Tavares, M. J., Gokina, N., and Brayden, J. E. (2014). Increased pressure-induced tone in rat parenchymal arterioles vs. middle cerebral arteries: role of ion channels and calcium sensitivity. *J. Appl. Physiol.* 117, 53–59. doi: 10.1152/japplphysiol.00253.2014

Clarke, L. E., Liddelow, S. A., Chakraborty, C., Munch, A. E., Heiman, M., and Barres, B. A. (2018). Normal aging induces A1-like astrocyte reactivity. *Proc. Natl. Acad. Sci. U.S.A.* 115, E1896–E1905.

Climie, R. E., Gallo, A., Picone, D. S., Di Lascio, N., van Sloten, T. T., Guala, A., et al. (2019). Measuring the interaction between the macro- and micro-vasculature. *Front. Cardiovasc. Med.* 6:169. doi: 10.3389/fcvm.2019.00169

Cornell-Bell, A. H., Finkbeiner, S. M., Cooper, M. S., and Smith, S. J. (1990). Glutamate induces calcium waves in cultured astrocytes: long-range glial signaling. *Science* 247, 470–473. doi: 10.1126/science.1967852

Csiszar, A., Tarantini, S., Fulop, G. A., Kiss, T., Valcarcel-Ares, M. N., Galvan, V., et al. (2017). Hypertension impairs neurovascular coupling and promotes microvascular injury: role in exacerbation of Alzheimer's disease. *Geroscience* 39, 359–372. doi: 10.1007/s11357-017-9991-9

Csiszar, A., Tucsek, Z., Toth, P., Sosnowska, D., Gautam, T., Koller, A., et al. (2013). Synergistic effects of hypertension and aging on cognitive function and hippocampal expression of genes involved in beta-amyloid generation and Alzheimer's disease. *Am. J. Physiol. Heart Circ. Physiol.* 305, H1120–H1130.

de Jong, D. L. K., Tarumi, T., Liu, J., Zhang, R., and Claassen, J. (2017). Lack of linear correlation between dynamic and steady-state cerebral autoregulation. *J. Physiol.* 595, 5623–5636. doi: 10.1113/jp274304

de la Torre, J. C. (2000). Critically attained threshold of cerebral hypoperfusion: the CATCH hypothesis of Alzheimer's pathogenesis. *Neurobiol. Aging* 21, 331–342. doi: 10.1016/s0197-4580(00)00111-1

De Miguel, C., Rudemiller, N. P., Abais, J. M., and Mattson, D. L. (2015). Inflammation and hypertension: new understandings and potential therapeutic targets. *Curr. Hypertens. Rep.* 17:507.

De Silva, T. M., and Faraci, F. M. (2020). Contributions of aging to cerebral small vessel disease. *Annu. Rev. Physiol.* 82, 275–295.

Delekate, A., Fuchtemeier, M., Schumacher, T., Ulbrich, C., Foddis, M., and Petzold, G. C. (2014). Metabotropic P2Y1 receptor signalling mediates astrocytic hyperactivity *in vivo* in an Alzheimer's disease mouse model. *Nat. Commun.* 5:5422.

Devor, A., Sakadzic, S., Saisan, P. A., Yaseen, M. A., Roussakis, E., Srinivasan, V. J., et al. (2011). "Overshoot" of O(2) is required to maintain baseline tissue oxygenation at locations distal to blood vessels. *J. Neurosci.* 31, 13676–13681. doi: 10.1523/jneurosci.1968-11.2011

Diaz, J. R., Kim, K. J., Brands, M. W., and Filosa, J. A. (2019). Augmented astrocyte microdomain Ca(2+) dynamics and parenchymal arteriole tone in angiotensin II-infused hypertensive mice. *Glia* 67, 551–565. doi: 10.1002/glia.23564

Diaz-Otero, J. M., Fisher, C., Downs, K., Moss, M. E., Jaffe, I. Z., Jackson, W. F., et al. (2017). Endothelial mineralocorticoid receptor mediates parenchymal arteriole and posterior cerebral artery remodeling during angiotensin II-Induced hypertension. *Hypertension* 70, 1113–1121. doi: 10.1161/hypertensionaha.117.09598

Diaz-Otero, J. M., Garver, H., Fink, G. D., Jackson, W. F., and Dorrance, A. M. (2016). Aging is associated with changes to the biomechanical properties of the posterior cerebral artery and parenchymal arterioles. *Am. J. Physiol. Heart Circ. Physiol.* 310, H365–H375.

Diaz-Otero, J. M., Yen, T. C., Ahmad, A., Laimon-Thomson, E., Abolibdeh, B., Kelly, K., et al. (2019). Transient receptor potential vanilloid 4 channels are important regulators of parenchymal arteriole dilation and cognitive function. *Microcirculation* 26:e12535.

Diaz-Otero, J. M., Yen, T. C., Fisher, C., Bota, D., Jackson, W. F., and Dorrance, A. M. (2018). Mineralocorticoid receptor antagonism improves parenchymal arteriole dilation via a TRPV4-dependent mechanism and prevents cognitive dysfunction in hypertension. *Am. J. Physiol. Heart Circ. Physiol.* 315, H1304–H1315.

Dickinson, C. J., and Thomason, A. D. (1959). Vertebral and internal carotid arteries in relation to hypertension and cerebrovascular disease. *Lancet* 2, 46–48. doi: 10.1016/s0140-6736(59)90494-5

Ding, J., Davis-Plourde, K. L., Sedaghat, S., Tully, P. J., Wang, W., Phillips, C., et al. (2020). Antihypertensive medications and risk for incident dementia and Alzheimer's disease: a meta-analysis of individual participant data from prospective cohort studies. *Lancet Neurol.* 19, 61–70. doi: 10.1016/s1474-4422(19)30393-x

Ding, S., Wang, T., Cui, W., and Haydon, P. G. (2009). Photothrombosis ischemia stimulates a sustained astrocytic Ca2+ signaling *in vivo*. *Glia* 57, 767–776. doi: 10.1002/glia.20804

Dunn, K. M., Hill-Eubanks, D. C., Liedtke, W. B., and Nelson, M. T. (2013). TRPV4 channels stimulate Ca2+-induced Ca2+ release in astrocytic endfeet and amplify neurovascular coupling responses. *Proc. Natl. Acad. Sci. U.S.A.* 110, 6157–6162. doi: 10.1073/pnas.1216514110

Edwards Iii, G. A., Gamez, N., Escobedo, G. Jr., Calderon, O., and Moreno-Gonzalez, I. (2019). Modifiable risk factors for Alzheimer's disease. *Front. Aging Neurosci.* 11:146. doi: 10.3389/fnagi.2019.00146

Elting, J. W., Sanders, M. L., Panerai, R. B., Aries, M., Bor-Seng-Shu, E., Caicedo, A., et al. (2020). Assessment of dynamic cerebral autoregulation in humans: Is reproducibility dependent on blood pressure variability? *PLoS One* 15:e0227651. doi: 10.1371/journal.pone.0227651

Evans, C. E., Miners, J. S., Piva, G., Willis, C. L., Heard, D. M., Kidd, E. J., et al. (2020). ACE2 activation protects against cognitive decline and reduces amyloid pathology in the Tg2576 mouse model of Alzheimer's disease. *Acta Neuropathol.* 139, 485–502. doi: 10.1007/s00401-019-02098-6

Faraci, F. M. (2018). Watching small vessel disease grow. *Circ. Res.* 122, 810–812. doi: 10.1161/circresaha.118.312762

Faraco, G., and Iadecola, C. (2013). Hypertension: a harbinger of stroke and dementia. *Hypertension* 62, 810–817. doi: 10.1161/hypertensionaha.113.01063

Faraco, G., Sugiyama, Y., Lane, D., Garcia-Bonilla, L., Chang, H., Santisteban, M. M., et al. (2016). Perivascular macrophages mediate the neurovascular and cognitive dysfunction associated with hypertension. *J. Clin. Invest.* 126, 4674–4689. doi: 10.1172/jci86950

Figueroa, X. F., and Duling, B. R. (2009). Gap junctions in the control of vascular function. *Antioxid. Redox Signal.* 11, 251–266. doi: 10.1089/ars.2008.2117

Fok, H., Guilcher, A., Brett, S., Jiang, B., Li, Y., Epstein, S., et al. (2014). Dominance of the forward compression wave in determining pulsatile components of blood pressure: similarities between inotropic stimulation and essential hypertension. *Hypertension* 64, 1116–1123. doi: 10.1161/hypertensionaha.114.04050

Forrester, S. J., Booz, G. W., Sigmund, C. D., Coffman, T. M., Kawai, T., Rizzo, V., et al. (2018). Angiotensin II signal transduction: an update on mechanisms of physiology and pathophysiology. *Physiol. Rev.* 98, 1627–1738. doi: 10.1152/physrev.00038.2017

Girouard, H., and Iadecola, C. (2006). Neurovascular coupling in the normal brain and in hypertension, stroke, and Alzheimer disease. *J. Appl. Physiol.* 100, 328–335. doi: 10.1152/japplphysiol.00966.2005

Grosche, J., Matyash, V., Moller, T., Verkhratsky, A., Reichenbach, A., and Kettenmann, H. (1999). Microdomains for neuron-glia interaction: parallel fiber signaling to Bergmann glial cells. *Nat. Neurosci.* 2, 139–143. doi: 10.1038/5692

Grutzendler, J., and Nedergaard, M. (2019). Cellular control of brain capillary blood flow: *in vivo* imaging veritas. *Trends Neurosci.* 42, 528–536. doi: 10.1016/j.tins.2019.05.009

Guo, Y., Li, X., Zhang, M., Chen, N., Wu, S., Lei, J., et al. (2019). Age and brain regionassociated alterations of cerebral blood flow in early Alzheimer's disease assessed in AbetaPPSWE/PS1DeltaE9 transgenic mice using arterial spin labeling. *Mol. Med. Rep.* 19, 3045–3052.

Hakim, A. M. (2019). Small vessel disease. *Front. Neurol.* 10:1020. doi: 10.3389/fneur.2019.01020

Halder, S. K., and Milner, R. (2019). A critical role for microglia in maintaining vascular integrity in the hypoxic spinal cord. *Proc. Natl. Acad. Sci. U.S.A.* 116, 26029–26037. doi: 10.1073/pnas.1912178116

Hall, C. N., Reynell, C., Gesslein, B., Hamilton, N. B., Mishra, A., Sutherland, B. A., et al. (2014). Capillary pericytes regulate cerebral blood flow in health and disease. *Nature* 508, 55–60. doi: 10.1038/nature13165

Hanisch, U. K., and Kettenmann, H. (2007). Microglia: active sensor and versatile effector cells in the normal and pathologic brain. *Nat. Neurosci.* 10, 1387–1394. doi: 10.1038/nn1997

Harraz, O. F., Hill-Eubanks, D., and Nelson, M. T. (2020). PIP2: a critical regulator of vascular ion channels hiding in plain sight. *Proc. Natl. Acad. Sci. U.S.A.* 117, 20378–20389. doi: 10.1073/pnas.2006737117

Harraz, O. F., Longden, T. A., Dabertrand, F., Hill-Eubanks, D., and Nelson, M. T. (2018a). Endothelial GqPCR activity controls capillary electrical signaling and brain blood flow through PIP2 depletion. *Proc. Natl. Acad. Sci. U.S.A.* 115, E3569–E3577.

Harraz, O. F., Longden, T. A., Hill-Eubanks, D., and Nelson, M. T. (2018b). PIP2 depletion promotes TRPV4 channel activity in mouse brain capillary endothelial cells. *eLife* 7:e38689.

Hebert, F., Grand'maison, M., Ho, M. K., Lerch, J. P., Hamel, E., and Bedell, B. J. (2013). Cortical atrophy and hypoperfusion in a transgenic mouse model of Alzheimer's disease. *Neurobiol. Aging* 34, 1644–1652. doi: 10.1016/j.neurobiolaging.2012.11.022

Henskens, L. H., Kroon, A. A., van Oostenbrugge, R. J., Gronenschild, E. H., Fuss-Lejeune, M. M., Hofman, P. A., et al. (2008). Increased aortic pulse wave velocity is associated with silent cerebral small-vessel disease in hypertensive patients. *Hypertension* 52, 1120–1126. doi: 10.1161/hypertensionaha.108.119024

Hill, M. A., Davis, M. J., Meininger, G. A., Potocnik, S. J., and Murphy, T. V. (2006). Arteriolar myogenic signalling mechanisms: implications for local vascular function. *Clin. Hemorheol. Microcirc.* 34, 67–79.

Hill-Eubanks, D. C., Gonzales, A. L., Sonkusare, S. K., and Nelson, M. T. (2014). Vascular TRP channels: performing under pressure and going with the flow. *Physiology* 29, 343–360. doi: 10.1152/physiol.00009.2014

Hosford, P. S., and Gourine, A. V. (2019). What is the key mediator of the neurovascular coupling response? *Neurosci. Biobehav. Rev.* 96, 174–181. doi: 10.1016/j.neubiorev.2018.11.011

Hu, X., De Silva, T. M., Chen, J., and Faraci, F. M. (2017). Cerebral vascular disease and neurovascular injury in ischemic stroke. *Circ. Res.* 120, 449–471. doi: 10.1161/circresaha.116.308427

Hughes, T. M., Craft, S., and Lopez, O. L. (2015). Review of 'the potential role of arterial stiffness in the pathogenesis of Alzheimer's disease'. *Neurodegener. Dis. Manage.* 5, 121–135. doi: 10.2217/nmt.14.53

Iadecola, C. (2013). The pathobiology of vascular dementia. *Neuron* 80, 844–866. doi: 10.1016/j.neuron.2013.10.008

Iadecola, C. (2017). The neurovascular unit coming of age: a journey through neurovascular coupling in health and disease. *Neuron* 96, 17–42. doi: 10.1016/j.neuron.2017.07.030

Iadecola, C., Yang, G., Ebner, T. J., and Chen, G. (1997). Local and propagated vascular responses evoked by focal synaptic activity in cerebellar cortex. *J. Neurophysiol.* 78, 651–659. doi: 10.1152/jn.1997.78.2.651

Iddings, J. A., Kim, K. J., Zhou, Y., Higashimori, H., and Filosa, J. A. (2015). Enhanced parenchymal arteriole tone and astrocyte signaling protect neurovascular coupling mediated parenchymal arteriole vasodilation in the spontaneously hypertensive rat. *J. Cereb. Blood Flow Metab.* 35, 1127–1136. doi: 10.1038/jcbfm.2015.31

Iliff, J. J., Wang, M., Liao, Y., Plogg, B. A., Peng, W., Gundersen, G. A., et al. (2012). A paravascular pathway facilitates CSF flow through the brain parenchyma and the clearance of interstitial solutes, including amyloid beta. *Sci. Transl. Med.* 4:147ra111. doi: 10.1126/scitranslmed.3003748

Iliff, J. J., Wang, M., Zeppenfeld, D. M., Venkataraman, A., Plog, B. A., Liao, Y., et al. (2013). Cerebral arterial pulsation drives paravascular CSF-interstitial fluid exchange in the murine brain. *J. Neurosci.* 33, 18190–18199. doi: 10.1523/jneurosci.1592-13.2013

Intengan, H. D., and Schiffrin, E. L. (2001). Vascular remodeling in hypertension. *Hypertension* 38, 581–587. doi: 10.1161/hy09t1.096249

Iturria-Medina, Y., Sotero, R. C., Toussaint, P. J., Mateos-Perez, J. M., Evans, A. C., Alzheimer's Disease, et al. (2016). Early role of vascular dysregulation on late-onset Alzheimer's disease based on multifactorial data-driven analysis. *Nat. Commun.* 7:11934.

Iulita, M. F., Duchemin, S., Vallerand, D., Barhoumi, T., Alvarez, F., Istomine, R., et al. (2019). CD4(+) regulatory T lymphocytes prevent impaired cerebral blood flow in angiotensin II-induced hypertension. *J. Am. Heart Assoc.* 8, e009372.

Johnson, A. W., Kinzenbaw, D. A., Modrick, M. L., and Faraci, F. M. (2013). Small-molecule inhibitors of signal transducer and activator of transcription 3 protect against angiotensin II-induced vascular dysfunction and hypertension. *Hypertension* 61, 437–442. doi: 10.1161/hypertensionaha.111.00299

Jolivel, V., Bicker, F., Biname, F., Ploen, R., Keller, S., Gollan, R., et al. (2015). Perivascular microglia promote blood vessel disintegration in the ischemic penumbra. *Acta Neuropathol.* 129, 279–295. doi: 10.1007/s00401-014-1372-1

Joutel, A., and Chabriat, H. (2017). Pathogenesis of white matter changes in cerebral small vessel diseases: beyond vessel-intrinsic mechanisms. *Clin. Sci.* 131, 635–651. doi: 10.1042/cs20160380

Joutel, A., and Faraci, F. M. (2014). Cerebral small vessel disease: insights and opportunities from mouse models of collagen IV-related small vessel disease and cerebral autosomal dominant arteriopathy with subcortical infarcts and leukoencephalopathy. *Stroke* 45, 1215–1221. doi: 10.1161/strokeaha.113.002878

Jukovskaya, N., Tiret, P., Lecoq, J., and Charpak, S. (2011). What does local functional hyperemia tell about local neuronal activation? *J. Neurosci.* 31, 1579–1582. doi: 10.1523/jneurosci.3146-10.2011

Kanemaru, K., Sekiya, H., Xu, M., Satoh, K., Kitajima, N., Yoshida, K., et al. (2014). *In vivo* visualization of subtle, transient, and local activity of astrocytes using an ultrasensitive Ca(2+) indicator. *Cell Rep.* 8, 311–318. doi: 10.1016/j.celrep.2014.05.056

Katsi, V., Marketou, M., Maragkoudakis, S., Didagelos, M., Charalambous, G., Parthenakis, F., et al. (2020). Blood-brain barrier dysfunction: the undervalued frontier of hypertension. *J. Hum. Hypertens*. doi: 10.1038/s41371-020-0352-2 [Epub ahead of print].

Kazama, K., Anrather, J., Zhou, P., Girouard, H., Frys, K., Milner, T. A., et al. (2004). Angiotensin II impairs neurovascular coupling in neocortex through NADPH oxidase-derived radicals. *Circ. Res.* 95, 1019–1026. doi: 10.1161/01.res.0000148637.85595.c5

Kim, K. J., Iddings, J. A., Stern, J. E., Blanco, V. M., Croom, D., Kirov, S. A., et al. (2015). Astrocyte contributions to flow/pressure-evoked parenchymal arteriole vasoconstriction. *J. Neurosci.* 35, 8245–8257. doi: 10.1523/jneurosci.4486-14.2015

Kim, K. J., Ramiro Diaz, J., Iddings, J. A., and Filosa, J. A. (2016). Vasculo-neuronal coupling: retrograde vascular communication to brain neurons. *J. Neurosci.* 36, 12624–12639. doi: 10.1523/jneurosci.1300-16.2016

Kimbrough, I. F., Robel, S., Roberson, E. D., and Sontheimer, H. (2015). Vascular amyloidosis impairs the gliovascular unit in a mouse model of Alzheimer's disease. *Brain* 138, 3716–3733. doi: 10.1093/brain/awv327

Koller, A., and Toth, P. (2012). Contribution of flow-dependent vasomotor mechanisms to the autoregulation of cerebral blood flow. *J. Vasc. Res.* 49, 375–389. doi: 10.1159/000338747

Kozlov, A. S., Angulo, M. C., Audinat, E., and Charpak, S. (2006). Target cell-specific modulation of neuronal activity by astrocytes. *Proc. Natl. Acad. Sci. U.S.A.* 103, 10058–10063. doi: 10.1073/pnas.0603741103

Kress, B. T., Iliff, J. J., Xia, M., Wang, M., Wei, H. S., Zeppenfeld, D., et al. (2014). Impairment of paravascular clearance pathways in the aging brain. *Ann. Neurol.* 76, 845–861. doi: 10.1002/ana.24271

Krizaj, D., Ryskamp, D. A., Tian, N., Tezel, G., Mitchell, C. H., Slepak, V. Z., et al. (2014). From mechanosensitivity to inflammatory responses: new players in the pathology of glaucoma. *Curr. Eye Res.* 39, 105–119. doi: 10.3109/02713683.2013.836541

Kume, K., Hanyu, H., Sakurai, H., Takada, Y., Onuma, T., and Iwamoto, T. (2012). Effects of telmisartan on cognition and regional cerebral blood flow in hypertensive patients with Alzheimer's disease. *Geriatr. Gerontol. Int.* 12, 207–214. doi: 10.1111/j.1447-0594.2011.00746.x

Lacolley, P., Regnault, V., and Avolio, A. P. (2018). Smooth muscle cell and arterial aging: basic and clinical aspects. *Cardiovasc. Res.* 114, 513–528. doi: 10.1093/cvr/cvy009

Lapato, A. S., and Tiwari-Woodruff, S. K. (2018). Connexins and pannexins: at the junction of neuro-glial homeostasis & disease. *J. Neurosci. Res.* 96, 31–44. doi: 10.1002/jnr.24088

Lavi, S., Gaitini, D., Milloul, V., and Jacob, G. (2006). Impaired cerebral CO2 vasoreactivity: association with endothelial dysfunction. *Am. J. Physiol. Heart Circ. Physiol.* 291, H1856–H1861.

Li, W., Zhang, J. W., Lu, F., Ma, M. M., Wang, J. Q., Suo, A. Q., et al. (2012). [Effects of telmisartan on the level of Abeta1-42, interleukin-1beta, tumor necrosis factor alpha and cognition in hypertensive patients with Alzheimer's disease]. *Zhonghua Yi Xue Za Zhi* 92, 2743–2746.

Li, Y., Baylie, R. L., Tavares, M. J., and Brayden, J. E. (2014). TRPM4 channels couple purinergic receptor mechanoactivation and myogenic tone development in cerebral parenchymal arterioles. *J. Cereb. Blood Flow Metab.* 34, 1706–1714. doi: 10.1038/jcbfm.2014.139

Liddelow, S. A., Guttenplan, K. A., Clarke, L. E., Bennett, F. C., Bohlen, C. J., Schirmer, L., et al. (2017). Neurotoxic reactive astrocytes are induced by activated microglia. *Nature* 541, 481–487.

Liu, J., Tseng, B. Y., Khan, M. A., Tarumi, T., Hill, C., Mirshams, N., et al. (2016). Individual variability of cerebral autoregulation, posterior cerebral circulation and white matter hyperintensity. *J. Physiol.* 594, 3141–3155. doi: 10.1113/jp271068

Livingston, G., Sommerlad, A., Orgeta, V., Costafreda, S. G., Huntley, J., Ames, D., et al. (2017). Dementia prevention, intervention, and care. *Lancet* 390, 2673–2734.

Longden, T. A., Dabertrand, F., Koide, M., Gonzales, A. L., Tykocki, N. R., Brayden, J. E., et al. (2017). Capillary K+-sensing initiates retrograde hyperpolarization to increase local cerebral blood flow. *Nat. Neurosci.* 20, 717–726. doi: 10.1038/nn.4533

Lopes, R. A., Neves, K. B., Tostes, R. C., Montezano, A. C., and Touyz, R. M. (2015). Downregulation of nuclear factor erythroid 2-related factor and associated antioxidant genes contributes to redox-sensitive vascular dysfunction in hypertension. *Hypertension* 66, 1240–1250. doi: 10.1161/hypertensionaha.115.06163

Lovatt, D., Sonnewald, U., Waagepetersen, H. S., Schousboe, A., He, W., Lin, J. H., et al. (2007). The transcriptome and metabolic gene signature of protoplasmic astrocytes in the adult murine cortex. *J. Neurosci.* 27, 12255–12266. doi: 10.1523/jneurosci.3404-07.2007

Lu, X., Moeini, M., Li, B., Lu, Y., Damseh, R., Pouliot, P., et al. (2019). A pilot study investigating changes in capillary hemodynamics and its modulation by exercise in the APP-PS1 Alzheimer mouse model. *Front. Neurosci.* 13:1261. doi: 10.3389/fnins.2019.01261

Lundgaard, I., Osorio, M. J., Kress, B. T., Sanggaard, S., and Nedergaard, M. (2014). White matter astrocytes in health and disease. *Neuroscience* 276, 161–173. doi: 10.1016/j.neuroscience.2013.10.050

Marmarelis, V. Z., Shin, D. C., Oesterreich, M., and Mueller, M. (2020). Quantification of dynamic cerebral autoregulation and CO2 dynamic vasomotor reactivity impairment in essential hypertension. *J. Appl. Physiol.* 128, 397–409. doi: 10.1152/japplphysiol.00620.2019

Marvar, P. J., Hendy, E. B., Cruise, T. D., Walas, D., DeCicco, D., Vadigepalli, R., et al. (2016). Systemic leukotriene B4 receptor antagonism lowers arterial blood pressure and improves autonomic function in the spontaneously hypertensive rat. *J. Physiol.* 594, 5975–5989. doi: 10.1113/jp272065

Matin, N., Pires, P. W., Garver, H., Jackson, W. F., and Dorrance, A. M. (2016). DOCA-salt hypertension impairs artery function in rat middle cerebral artery and parenchymal arterioles. *Microcirculation* 23, 571–579. doi: 10.1111/micc.12308

McBryde, F. D., Malpas, S. C., and Paton, J. F. (2017). Intracranial mechanisms for preserving brain blood flow in health and disease. *Acta Physiol.* 219, 274–287. doi: 10.1111/apha.12706

Mehla, J., Lacoursiere, S., Stuart, E., McDonald, R. J., and Mohajerani, M. H. (2018). Gradual cerebral hypoperfusion impairs fear conditioning and object recognition learning and memory in mice: potential roles of neurodegeneration and cholinergic dysfunction. *J. Alzheimers Dis.* 61, 283–293. doi: 10.3233/jad-170635

Merkler, A. E., and Iadecola, C. (2017). Rollercoaster blood pressure: An Alzheimer disease risk factor? *Circulation* 136, 526–528. doi: 10.1161/circulationaha.117.029618

Miller, S. J. (2018). Astrocyte heterogeneity in the adult central nervous system. *Front. Cell. Neurosci.* 12:401.

Minelli, A., Castaldo, P., Gobbi, P., Salucci, S., Magi, S., and Amoroso, S. (2007). Cellular and subcellular localization of Na+-Ca2+ exchanger protein isoforms, NCX1, NCX2, and NCX3 in cerebral cortex and hippocampus of adult rat. *Cell Calcium* 41, 221–234. doi: 10.1016/j.ceca.2006.06.004

Mishra, A., Reynolds, J. P., Chen, Y., Gourine, A. V., Rusakov, D. A., and Attwell, D. (2016). Astrocytes mediate neurovascular signaling to capillary pericytes but not to arterioles. *Nat. Neurosci.* 19, 1619–1627. doi: 10.1038/nn.4428

Mitchell, G. F. (2018). Aortic stiffness, pressure and flow pulsatility, and target organ damage. *J. Appl. Physiol.* 125, 1871–1880. doi: 10.1152/japplphysiol.00108.2018

Mitchell, G. F., van Buchem, M. A., Sigurdsson, S., Gotal, J. D., Jonsdottir, M. K., Kjartansson, O., et al. (2011). Arterial stiffness, pressure and flow pulsatility and brain structure and function: the Age, Gene/Environment Susceptibility–Reykjavik study. *Brain* 134, 3398–3407. doi: 10.1093/brain/awr253

Mogi, M. (2019). Could management of blood pressure prevent dementia in the elderly? *Clin. Hypertens.* 25:27.

Montagne, A., Nation, D. A., Sagare, A. P., Barisano, G., Sweeney, M. D., Chakhoyan, A., et al. (2020). APOE4 leads to blood-brain barrier dysfunction predicting cognitive decline. *Nature* 581, 71–76.

Montezano, A. C., Dulak-Lis, M., Tsiropoulou, S., Harvey, A., Briones, A. M., and Touyz, R. M. (2015). Oxidative stress and human hypertension: vascular mechanisms, biomarkers, and novel therapies. *Can. J. Cardiol.* 31, 631–641. doi: 10.1016/j.cjca.2015.02.008

Moore, C. I., and Cao, R. (2008). The hemo-neural hypothesis: on the role of blood flow in information processing. *J. Neurophysiol.* 99, 2035–2047. doi: 10.1152/jn.01366.2006

Morrison, H. W., and Filosa, J. A. (2016). Sex differences in astrocyte and microglia responses immediately following middle cerebral artery occlusion in adult mice. *Neuroscience* 339, 85–99. doi: 10.1016/j.neuroscience.2016.09.047

Morrison, H. W., and Filosa, J. A. (2019). Stroke and the neurovascular unit: glial cells, sex differences, and hypertension. *Am. J. Physiol. Cell Physiol.* 316, C325–C339.

Mortensen, K. N., Sanggaard, S., Mestre, H., Lee, H., Kostrikov, S., Xavier, A. L. R., et al. (2019). Impaired glymphatic transport in spontaneously hypertensive rats. *J. Neurosci.* 39, 6365–6377. doi: 10.1523/jneurosci.1974-18.2019

Moshkforoush, A., Ashenagar, B., Harraz, O. F., Dabertrand, F., Longden, T. A., Nelson, M. T., et al. (2020). The capillary Kir channel as sensor and amplifier of neuronal signals: modeling insights on K(+)-mediated neurovascular communication. *Proc. Natl. Acad. Sci. U.S.A.* 117, 16626–16637. doi: 10.1073/pnas.2000151117

Multani, N., Taghdiri, F., Anor, C. J., Varriano, B., Misquitta, K., Tang-Wai, D. F., et al. (2019). Association between social cognition changes and resting state functional connectivity in frontotemporal dementia, Alzheimer's Disease, Parkinson's disease, and healthy controls. *Front. Neurosci.* 13:1259. doi: 10.3389/fnins.2019.01259

Munoz, M. F., Puebla, M., and Figueroa, X. F. (2015). Control of the neurovascular coupling by nitric oxide-dependent regulation of astrocytic Ca(2+) signaling. *Front. Cell. Neurosci.* 9:59. doi: 10.3389/fncel.2015.00059

Nakazato, R., Kawabe, K., Yamada, D., Ikeno, S., Mieda, M., Shimba, S., et al. (2017). Disruption of bmal1 impairs blood-brain barrier integrity via pericyte dysfunction. *J. Neurosci.* 37, 10052–10062. doi: 10.1523/jneurosci.3639-16.2017

Negoita, M., Hughes, A. D., Parker, K. H., and Khir, A. W. (2018). A method for determining local pulse wave velocity in human ascending aorta from sequential ultrasound measurements of diameter and velocity. *Physiol. Meas.* 39:114009. doi: 10.1088/1361-6579/aae8a0

Nguyen, M. D., and Venton, B. J. (2015). Fast-scan cyclic voltammetry for the characterization of rapid adenosine release. *Comput. Struct. Biotechnol. J.* 13, 47–54. doi: 10.1016/j.csbj.2014.12.006

Nizar, K., Uhlirova, H., Tian, P., Saisan, P. A., Cheng, Q., Reznichenko, L., et al. (2013). *In vivo* stimulus-induced vasodilation occurs without IP3 receptor activation and may precede astrocytic calcium increase. *J. Neurosci.* 33, 8411–8422. doi: 10.1523/jneurosci.3285-12.2013

Nortley, R., Korte, N., Izquierdo, P., Hirunpattarasilp, C., Mishra, A., Jaunmuktane, Z., et al. (2019). Amyloid beta oligomers constrict human capillaries in Alzheimer's disease via signaling to pericytes. *Science* 365:eaav9518. doi: 10.1126/science.aav9518

Ohara, H., and Nabika, T. (2016). A nonsense mutation of Stim1 identified in stroke-prone spontaneously hypertensive rats decreased the store-operated calcium entry in astrocytes. *Biochem. Biophys. Res. Commun.* 476, 406–411. doi: 10.1016/j.bbrc.2016.05.134

Oheim, M., Schmidt, E., and Hirrlinger, J. (2018). Local energy on demand: Are 'spontaneous' astrocytic Ca(2+)-microdomains the regulatory unit for astrocyte-neuron metabolic cooperation? *Brain Res. Bull.* 136, 54–64. doi: 10.1016/j.brainresbull.2017.04.011

O'Herron, P., Chhatbar, P. Y., Levy, M., Shen, Z., Schramm, A. E., Lu, Z., et al. (2016). Neural correlates of single-vessel haemodynamic responses *in vivo*. *Nature* 534, 378–382. doi: 10.1038/nature17965

Oishi, E., Ohara, T., Sakata, S., Fukuhara, M., Hata, J., Yoshida, D., et al. (2017). Day-to-day blood pressure variability and risk of dementia in a general japanese elderly population: the hisayama study. *Circulation* 136, 516–525. doi: 10.1161/circulationaha.116.025667

Ongali, B., Nicolakakis, N., Tong, X. K., Aboulkassim, T., Imboden, H., and Hamel, E. (2016). Enalapril alone or co-administered with losartan rescues cerebrovascular dysfunction, but not mnemonic deficits or amyloidosis in a mouse model of Alzheimer's disease. *J. Alzheimers Dis.* 51, 1183–1195. doi: 10.3233/jad-150868

Ongali, B., Nicolakakis, N., Tong, X. K., Aboulkassim, T., Papadopoulos, P., Rosa-Neto, P., et al. (2014). Angiotensin II type 1 receptor blocker losartan prevents and rescues cerebrovascular, neuropathological and cognitive deficits in an Alzheimer's disease model. *Neurobiol. Dis.* 68, 126–136. doi: 10.1016/j.nbd.2014.04.018

Padmanabhan, S., Caulfield, M., and Dominiczak, A. F. (2015). Genetic and molecular aspects of hypertension. *Circ. Res.* 116, 937–959. doi: 10.1161/circresaha.116.303647

Parati, G., Ochoa, J. E., and Bilo, G. (2012). Blood pressure variability, cardiovascular risk, and risk for renal disease progression. *Curr. Hypertens. Rep.* 14, 421–431. doi: 10.1007/s11906-012-0290-7

Pires, P. W., Dams Ramos, C. M., Matin, N., and Dorrance, A. M. (2013). The effects of hypertension on the cerebral circulation. *Am. J. Physiol. Heart Circ. Physiol.* 304, H1598–H1614. doi: 10.1007/978-1-4612-0303-2_33

Pires, P. W., Jackson, W. F., and Dorrance, A. M. (2015). Regulation of myogenic tone and structure of parenchymal arterioles by hypertension and the mineralocorticoid receptor. *Am. J. Physiol. Heart Circ. Physiol.* 309, H127–H136.

Pomilio, C., Gorojod, R. M., Riudavets, M., Vinuesa, A., Presa, J., Gregosa, A., et al. (2020). Microglial autophagy is impaired by prolonged exposure to beta-amyloid peptides: evidence from experimental models and Alzheimer's disease patients. *Geroscience* 42, 613–632. doi: 10.1007/s11357-020-00161-9

Pomilio, C., Pavia, P., Gorojod, R. M., Vinuesa, A., Alaimo, A., Galvan, V., et al. (2016). Glial alterations from early to late stages in a model of Alzheimer's disease: evidence of autophagy involvement in Abeta internalization. *Hippocampus* 26, 194–210. doi: 10.1002/hipo.22503

Raichle, M. E. (2015). The restless brain: how intrinsic activity organizes brain function. *Philos. Trans. R. Soc. Lond. B Biol. Sci.* 370:20140172. doi: 10.1098/rstb.2014.0172

Rivera-Rivera, L. A., Cody, K. A., Eisenmenger, L., Cary, P., Rowley, H. A., Carlsson, C. M., et al. (2020). Assessment of vascular stiffness in the internal carotid artery proximal to the carotid canal in Alzheimer's disease using pulse wave velocity from low rank reconstructed 4D flow MRI. *J. Cereb. Blood Flow Metab*. doi: 10.1177/0271678X20910302 [Epub ahead of print].

Roberts, J., Kahle, M. P., and Bix, G. J. (2012). Perlecan and the blood-brain barrier: Beneficial proteolysis? *Front. Pharmacol.* 3:155. doi: 10.3389/fphar.2012.00155

Rodriguez-Iturbe, B., Pons, H., and Johnson, R. J. (2017). Role of the immune system in hypertension. *Physiol. Rev.* 97, 1127–1164.

Rom, S., Heldt, N. A., Gajghate, S., Seliga, A., Reichenbach, N. L., and Persidsky, Y. (2020). Hyperglycemia and advanced glycation end products disrupt BBB and promote occludin and claudin-5 protein secretion on extracellular microvesicles. *Sci. Rep.* 10:7274.

Rosenegger, D. G., Tran, C. H., Wamsteeker Cusulin, J. I., and Gordon, G. R. (2015). Tonic local brain blood flow control by astrocytes independent of phasic neurovascular coupling. *J. Neurosci.* 35, 13463–13474. doi: 10.1523/jneurosci.1780-15.2015

Ross, A. E., Nguyen, M. D., Privman, E., and Venton, B. J. (2014). Mechanical stimulation evokes rapid increases in extracellular adenosine concentration in the prefrontal cortex. *J. Neurochem.* 130, 50–60. doi: 10.1111/jnc.12711

Rothwell, P. M. (2010). Limitations of the usual blood-pressure hypothesis and importance of variability, instability, and episodic hypertension. *Lancet* 375, 938–948. doi: 10.1016/s0140-6736(10)60309-1

Rothwell, P. M., Howard, S. C., Dolan, E., O'Brien, E., Dobson, J. E., Dahlof, B., et al. (2010). Effects of beta blockers and calcium-channel blockers on within-individual variability in blood pressure and risk of stroke. *Lancet Neurol.* 9, 469–480. doi: 10.1016/s1474-4422(10)70066-1

Royea, J., Zhang, L., Tong, X. K., and Hamel, E. (2017). Angiotensin IV receptors mediate the cognitive and cerebrovascular benefits of losartan in a mouse model of Alzheimer's disease. *J. Neurosci.* 37, 5562–5573. doi: 10.1523/jneurosci.0329-17.2017

Rungta, R. L., Chaigneau, E., Osmanski, B. F., and Charpak, S. (2018). Vascular Compartmentalization of Functional Hyperemia from the Synapse to the Pia. *Neuron* 99, 362–375.e4.

Ryskamp, D. A., Witkovsky, P., Barabas, P., Huang, W., Koehler, C., Akimov, N. P., et al. (2011). The polymodal ion channel transient receptor potential vanilloid 4 modulates calcium flux, spiking rate, and apoptosis of mouse retinal ganglion cells. *J. Neurosci.* 31, 7089–7101. doi: 10.1523/jneurosci.0359-11.2011

Sadekova, N., Iulita, M. F., Vallerand, D., Muhire, G., Bourmoum, M., Claing, A., et al. (2018). Arterial stiffness induced by carotid calcification leads to cerebral gliosis mediated by oxidative stress. *J. Hypertens.* 36, 286–298. doi: 10.1097/hjh.0000000000001557

Sagare, A. P., Bell, R. D., Zhao, Z., Ma, Q., Winkler, E. A., Ramanathan, A., et al. (2013). Pericyte loss influences Alzheimer-like neurodegeneration in mice. *Nat. Commun.* 4:2932.

Santisteban, M. M., Ahn, S. J., Lane, D., Faraco, G., Garcia-Bonilla, L., Racchumi, G., et al. (2020). Endothelium-macrophage crosstalk mediates blood-brain barrier dysfunction in hypertension. *Hypertension* 76, 795–807. doi: 10.1161/hypertensionaha.120.15581

Santisteban, M. M., and Iadecola, C. (2018). Hypertension, dietary salt and cognitive impairment. *J. Cereb. Blood Flow Metab.* 38, 2112–2128. doi: 10.1177/0271678x18803374

Schillaci, G., Bilo, G., Pucci, G., Laurent, S., Macquin-Mavier, I., Boutouyrie, P., et al. (2012). Relationship between short-term blood pressure variability and large-artery stiffness in human hypertension: findings from 2 large databases. *Hypertension* 60, 369–377. doi: 10.1161/hypertensionaha.112.197491

Seki, T., Goto, K., Kiyohara, K., Kansui, Y., Murakami, N., Haga, Y., et al. (2017). Downregulation of Endothelial Transient Receptor Potential Vanilloid Type 4 Channel and Small-Conductance of Ca2+-Activated K+ Channels Underpins Impaired Endothelium-Dependent Hyperpolarization in Hypertension. *Hypertension* 69, 143–153. doi: 10.1161/hypertensionaha.116.07110

Shams, S., Martola, J., Granberg, T., Li, X., Shams, M., Fereshtehnejad, S. M., et al. (2015). Cerebral microbleeds: different prevalence, topography, and risk factors depending on dementia diagnosis-the Karolinska Imaging Dementia Study. *AJNR Am. J. Neuroradiol.* 36, 661–666. doi: 10.3174/ajnr.a4176

Shigetomi, E., Saito, K., Sano, F., and Koizumi, S. (2019). Aberrant calcium signals in reactive astrocytes: a key process in neurological disorders. *Int. J. Mol. Sci.* 20:996. doi: 10.3390/ijms20040996

Shiota, S., Takekawa, H., Matsumoto, S. E., Takeda, K., Nurwidya, F., Yoshioka, Y., et al. (2013). Chronic intermittent hypoxia/reoxygenation facilitate amyloid-beta generation in mice. *J. Alzheimers Dis.* 37, 325–333. doi: 10.3233/jad-130419

Silverman, A., and Petersen, N. H. (2020). *Physiology, Cerebral Autoregulation*. Treasure Island, FL: StatPearls.

Simard, M., Arcuino, G., Takano, T., Liu, Q. S., and Nedergaard, M. (2003). Signaling at the gliovascular interface. *J. Neurosci.* 23, 9254–9262. doi: 10.1523/jneurosci.23-27-09254.2003

Skoog, I., Lernfelt, B., Landahl, S., Palmertz, B., Andreasson, L. A., Nilsson, L., et al. (1996). 15-year longitudinal study of blood pressure and dementia. *Lancet* 347, 1141–1145. doi: 10.1016/s0140-6736(96)90608-x

Sofroniew, M. V. (2015). Astrocyte barriers to neurotoxic inflammation. *Nat. Rev. Neurosci.* 16, 249–263. doi: 10.1038/nrn3898

Sofroniew, M. V., and Vinters, H. V. (2010). Astrocytes: biology and pathology. *Acta Neuropathol.* 119, 7–35. doi: 10.1007/s00401-009-0619-8

Sonkusare, S. K., Bonev, A. D., Ledoux, J., Liedtke, W., Kotlikoff, M. I., Heppner, T. J., et al. (2012). Elementary Ca2+ signals through endothelial TRPV4 channels regulate vascular function. *Science* 336, 597–601. doi: 10.1126/science.1216283

Sprint Mind Investigators for the Sprint Research Group, Williamson, J. D., Pajewski, N. M., Auchus, A. P., Bryan, R. N., Chelune, G., et al. (2019). Effect of intensive vs standard blood pressure control on probable dementia: a randomized clinical trial. *JAMA* 321, 553–561.

Srinivasan, R., Huang, B. S., Venugopal, S., Johnston, A. D., Chai, H., Zeng, H., et al. (2015). Ca(2+) signaling in astrocytes from Ip3r2(−/−) mice in brain slices and during startle responses *in vivo*. *Nat. Neurosci.* 18, 708–717. doi: 10.1038/nn.4001

Stefanovic, M., Puchulu-Campanella, E., Kodippili, G., and Low, P. S. (2013). Oxygen regulates the band 3-ankyrin bridge in the human erythrocyte membrane. *Biochem. J.* 449, 143–150. doi: 10.1042/bj20120869

Stevens, S. L., McManus, R. J., and Stevens, R. J. (2019). The utility of long-term blood pressure variability for cardiovascular risk prediction in primary care. *J. Hypertens.* 37, 522–529. doi: 10.1097/hjh.0000000000001923

Stevens, S. L., Wood, S., Koshiaris, C., Law, K., Glasziou, P., Stevens, R. J., et al. (2016). Blood pressure variability and cardiovascular disease: systematic review and meta-analysis. *BMJ* 354:i4098. doi: 10.1136/bmj.i4098

Su, J., Manisty, C., Parker, K. H., Simonsen, U., Nielsen-Kudsk, J. E., Mellemkjaer, S., et al. (2017). Wave intensity analysis provides novel insights into pulmonary arterial hypertension and chronic thromboembolic pulmonary hypertension. *J. Am. Heart Assoc.* 6:e006679.

Suadicani, S. O., Iglesias, R., Wang, J., Dahl, G., Spray, D. C., and Scemes, E. (2012). ATP signaling is deficient in cultured Pannexin1-null mouse astrocytes. *Glia* 60, 1106–1116. doi: 10.1002/glia.22338

Sweeney, M. D., Zhao, Z., Montagne, A., Nelson, A. R., and Zlokovic, B. V. (2019). Blood-brain barrier: from physiology to disease and back. *Physiol. Rev.* 99, 21–78. doi: 10.1152/physrev.00050.2017

Sweet, J. G., Chan, S. L., and Cipolla, M. J. (2015). Effect of hypertension and carotid occlusion on brain parenchymal arteriole structure and reactivity. *J. Appl. Physiol.* 119, 817–823. doi: 10.1152/japplphysiol.00467.2015

Tajada, S., Moreno, C. M., O'Dwyer, S., Woods, S., Sato, D., Navedo, M. F., et al. (2017). Distance constraints on activation of TRPV4 channels by AKAP150-bound PKCalpha in arterial myocytes. *J. Gen. Physiol.* 149, 639–659. doi: 10.1085/jgp.201611709

Tanaka, L. Y., and Laurindo, F. R. M. (2017). Vascular remodeling: a redox-modulated mechanism of vessel caliber regulation. *Free Radic. Biol. Med.* 109, 11–21. doi: 10.1016/j.freeradbiomed.2017.01.025

Tarantini, S., Tucsek, Z., Valcarcel-Ares, M. N., Toth, P., Gautam, T., Giles, C. B., et al. (2016). Circulating IGF-1 deficiency exacerbates hypertension-induced microvascular rarefaction in the mouse hippocampus and retrosplenial cortex: implications for cerebromicrovascular and brain aging. *Age* 38, 273–289. doi: 10.1007/s11357-016-9931-0

Thesen, T., Leontiev, O., Song, T., Dehghani, N., Hagler, D. J. Jr., et al. (2012). Depression of cortical activity in humans by mild hypercapnia. *Hum. Brain Mapp.* 33, 715–726. doi: 10.1002/hbm.21242

Thomsen, M. S., Routhe, L. J., and Moos, T. (2017). The vascular basement membrane in the healthy and pathological brain. *J. Cereb. Blood Flow Metab.* 37, 3300–3317. doi: 10.1177/0271678x17722436

Thrane, A. S., Rangroo Thrane, V., Zeppenfeld, D., Lou, N., Xu, Q., Nagelhus, E. A., et al. (2012). General anesthesia selectively disrupts astrocyte calcium signaling in the awake mouse cortex. *Proc. Natl. Acad. Sci. U.S.A.* 109, 18974–18979. doi: 10.1073/pnas.1209448109

Tian, P., Teng, I. C., May, L. D., Kurz, R., Lu, K., Scadeng, M., et al. (2010). Cortical depth-specific microvascular dilation underlies laminar differences in blood oxygenation level-dependent functional MRI signal. *Proc. Natl. Acad. Sci. U.S.A.* 107, 15246–15251. doi: 10.1073/pnas.1006735107

Toth, P., Tarantini, S., Csiszar, A., and Ungvari, Z. (2017). Functional vascular contributions to cognitive impairment and dementia: mechanisms and consequences of cerebral autoregulatory dysfunction, endothelial impairment, and neurovascular uncoupling in aging. *Am. J. Physiol. Heart Circ. Physiol.* 312, H1–H20.

Toth, P., Tucsek, Z., Sosnowska, D., Gautam, T., Mitschelen, M., Tarantini, S., et al. (2013). Age-related autoregulatory dysfunction and cerebromicrovascular injury in mice with angiotensin II-induced hypertension. *J. Cereb. Blood Flow Metab.* 33, 1732–1742. doi: 10.1038/jcbfm.2013.143

Tong, X. K., Lecrux, C., Rosa-Neto, P., and Hamel, E. (2012). Age-dependent rescue by simvastatin of Alzheimer's disease cerebrovascular and memory deficits. *J. Neurosci.* 32, 4705–4715. doi: 10.1523/JNEUROSCI.0169-12.2012

Touyz, R. M., Alves-Lopes, R., Rios, F. J., Camargo, L. L., Anagnostopoulou, A., Arner, A., et al. (2018). Vascular smooth muscle contraction in hypertension. *Cardiovasc. Res.* 114, 529–539.

Tran, C. H., and Gordon, G. R. (2015). Astrocyte and microvascular imaging in awake animals using two-photon microscopy. *Microcirculation* 22, 219–227. doi: 10.1111/micc.12188

Tran, C. H. T., Peringod, G., and Gordon, G. R. (2018). Astrocytes integrate behavioral state and vascular signals during functional hyperemia. *Neuron* 100, 1133–1148.e3.

Trigiani, L. J., Royea, J., Lacalle-Aurioles, M., Tong, X. K., and Hamel, E. (2018). Pleiotropic benefits of the angiotensin receptor blocker candesartan in a mouse model of Alzheimer disease. *Hypertension* 72, 1217–1226. doi: 10.1161/hypertensionaha.118.11775

Tsien, R. Y. (1988). Fluorescence measurement and photochemical manipulation of cytosolic free calcium. *Trends Neurosci.* 11, 419–424. doi: 10.1016/0166-2236(88)90192-0

Tsien, R. Y. (1989). Fluorescence ratio imaging of dynamic intracellular signals. *Acta Physiol. Scand. Suppl.* 582:6.

Tully, P. J., Yano, Y., Launer, L. J., Kario, K., Nagai, M., Mooijaart, S. P., et al. (2020). Association between blood pressure variability and cerebral small-vessel disease: a systematic review and meta-analysis. *J. Am. Heart Assoc.* 9:e013841.

Tyurikova, O., Zheng, K., Rings, A., Drews, A., Klenerman, D., and Rusakov, D. A. (2018). Monitoring Ca(2+) elevations in individual astrocytes upon local release of amyloid beta in acute brain slices. *Brain Res. Bull.* 136, 85–90. doi: 10.1016/j.brainresbull.2016.12.007

Tzeng, Y. C., Lucas, S. J., Atkinson, G., Willie, C. K., and Ainslie, P. N. (2010). Fundamental relationships between arterial baroreflex sensitivity and dynamic cerebral autoregulation in humans. *J. Appl. Physiol.* 108, 1162–1168. doi: 10.1152/japplphysiol.01390.2009

Vanlandewijck, M., He, L., Mae, M. A., Andrae, J., Ando, K., Del Gaudio, F., et al. (2018). A molecular atlas of cell types and zonation in the brain vasculature. *Nature* 554, 475–480. doi: 10.1038/nature25739

Velasco-Estevez, M., Rolle, S. O., Mampay, M., Dev, K. K., and Sheridan, G. K. (2020). Piezo1 regulates calcium oscillations and cytokine release from astrocytes. *Glia* 68, 145–160. doi: 10.1002/glia.23709

Verkhratsky, A., and Nedergaard, M. (2018). Physiology of astroglia. *Physiol. Rev.* 98, 239–389. doi: 10.1152/physrev.00042.2016

Verkhratsky, A., Parpura, V., Vardjan, N., and Zorec, R. (2019). Physiology of astroglia. *Adv. Exp. Med. Biol.* 1175, 45–91.

Vernooij, M. W., van der Lugt, A., Ikram, M. A., Wielopolski, P. A., Niessen, W. J., Hofman, A., et al. (2008). Prevalence and risk factors of cerebral microbleeds: the Rotterdam Scan Study. *Neurology* 70, 1208–1214. doi: 10.1212/01.wnl.0000307750.41970.d9

Vinuesa, A., Bentivegna, M., Calfa, G., Filipello, F., Pomilio, C., Bonaventura, M. M., et al. (2019). Early exposure to a high-fat diet impacts on hippocampal plasticity: implication of microglia-derived exosome-like extracellular vesicles. *Mol. Neurobiol.* 56, 5075–5094. doi: 10.1007/s12035-018-1435-8

Virani, S. S., Alonso, A., Benjamin, E. J., Bittencourt, M. S., Callaway, C. W., Carson, A. P., et al. (2020). Heart disease and stroke statistics-2020 update: a report from the American heart association. *Circulation* 141, e139–e596.

Volpe, M., Battistoni, A., Rubattu, S., and Tocci, G. (2019). Hypertension in the elderly: which are the blood pressure threshold values? *Eur. Heart J.* 21, B105–B106.

Waki, H., Hendy, E. B., Hindmarch, C. C., Gouraud, S., Toward, M., Kasparov, S., et al. (2013). Excessive leukotriene B4 in nucleus tractus solitarii is prohypertensive in spontaneously hypertensive rats. *Hypertension* 61, 194–201. doi: 10.1161/hypertensionaha.112.192252

Waki, H., Liu, B., Miyake, M., Katahira, K., Murphy, D., Kasparov, S., et al. (2007). Junctional adhesion molecule-1 is upregulated in spontaneously hypertensive rats: evidence for a prohypertensive role within the brain stem. *Hypertension* 49, 1321–1327. doi: 10.1161/hypertensionaha.106.085589

Waki, H., Murphy, D., Yao, S. T., Kasparov, S., and Paton, J. F. (2006). Endothelial NO synthase activity in nucleus tractus solitarii contributes to hypertension in

spontaneously hypertensive rats. *Hypertension* 48, 644–650. doi: 10.1161/01.hyp.0000238200.46085.c6

Walas, D., Nowicki-Osuch, K., Alibhai, D., von Linstow, Roloff, E., Coghill, J., et al. (2019). Inflammatory pathways are central to posterior cerebrovascular artery remodelling prior to the onset of congenital hypertension. *J. Cereb. Blood Flow Metab.* 39, 1803–1817. doi: 10.1177/0271678x18769180

Wang, Y., DelRosso, N. V., Vaidyanathan, T. V., Cahill, M. K., Reitman, M. E., Pittolo, S., et al. (2019a). Accurate quantification of astrocyte and neurotransmitter fluorescence dynamics for single-cell and population-level physiology. *Nat. Neurosci.* 22, 1936–1944. doi: 10.1038/s41593-019-0492-2

Wang, Y., Liang, H., Luo, Y., Zhou, Y., Jin, L., Wang, S., et al. (2019b). History of hypertension is associated With MR Hypoperfusion in Chinese inpatients With DWI-negative TIA. *Front. Neurol.* 10:867. doi: 10.3389/fneur.2019.00867

Wang, Y., and Venton, B. J. (2019). Comparison of spontaneous and mechanically-stimulated adenosine release in mice. *Neurochem. Int.* 124, 46–50. doi: 10.1016/j.neuint.2018.12.007

Wei, H. S., Kang, H., Rasheed, I. Y., Zhou, S., Lou, N., Gershteyn, A., et al. (2016). Erythrocytes are oxygen-sensing regulators of the cerebral microcirculation. *Neuron* 91, 851–862. doi: 10.1016/j.neuron.2016.07.016

Wei, L., Mousawi, F., Li, D., Roger, S., Li, J., Yang, X., et al. (2019). Adenosine triphosphate release and P2 receptor signaling in piezo1 channel-dependent mechanoregulation. *Front. Pharmacol.* 10:1304.

Wight, T. N. (2008). Arterial remodeling in vascular disease: a key role for hyaluronan and versican. *Front. Biosci.* 13:4933–4937. doi: 10.2741/3052

Xing, C. Y., Tarumi, T., Meijers, R. L., Turner, M., Repshas, J., Xiong, L., et al. (2017). Arterial pressure, heart rate, and cerebral hemodynamics across the adult life span. *Hypertension* 69, 712–720. doi: 10.1161/hypertensionaha.116.08986

Xu, H., Oliveira-Sales, E. B., McBride, F., Liu, B., Hewinson, J., Toward, M., et al. (2012). Upregulation of junctional adhesion molecule-A is a putative prognostic marker of hypertension. *Cardiovasc. Res.* 96, 552–560. doi: 10.1093/cvr/cvs273

Yamasaki, E., Thakore, P., Krishnan, V., and Earley, S. (2020). Differential expression of angiotensin II type 1 receptor subtypes within the cerebral microvasculature. *Am. J. Physiol. Heart Circ. Physiol.* 318, H461–H469.

Yang, Y., Vidensky, S., Jin, L., Jie, C., Lorenzini, I., Frankl, M., et al. (2011). Molecular comparison of GLT1+ and ALDH1L1+ astrocytes *in vivo* in astroglial reporter mice. *Glia* 59, 200–207. doi: 10.1002/glia.21089

Zhang, L. Y., Pan, J., Mamtilahun, M., Zhu, Y., Wang, L., Venkatesh, A., et al. (2020). Microglia exacerbate white matter injury via complement C3/C3aR pathway after hypoperfusion. *Theranostics* 10, 74–90. doi: 10.7150/thno.35841

Zhang, Y., Sloan, S. A., Clarke, L. E., Caneda, C., Plaza, C. A., Blumenthal, P. D., et al. (2016). Purification and characterization of progenitor and mature human astrocytes reveals transcriptional and functional differences with mouse. *Neuron* 89, 37–53. doi: 10.1016/j.neuron.2015.11.013

Zhou, S., Giannetto, M., DeCourcey, J., Kang, H., Kang, N., Li, Y., et al. (2019). Oxygen tension-mediated erythrocyte membrane interactions regulate cerebral capillary hyperemia. *Sci. Adv.* 5:eaaw4466. doi: 10.1126/sciadv.aaw4466

Zlokovic, B. V. (2005). Neurovascular mechanisms of Alzheimer's neurodegeneration. *Trends Neurosci.* 28, 202–208. doi: 10.1016/j.tins.2005.02.001

Conflict of Interest: The authors declare that the research was conducted in the absence of any commercial or financial relationships that could be construed as a potential conflict of interest.

frontiers in Physiology

MINI REVIEW
published: 29 October 2020
doi: 10.3389/fphys.2020.594097

The Role of Connexin 43 and Pannexin 1 During Acute Inflammation

*Petra Kameritsch[1,2] and Kristin Pogoda[3]**

[1] Institute of Cardiovascular Physiology and Pathophysiology, Biomedical Center, Ludwig-Maximilians-University Munich, Munich, Germany, [2] Walter Brendel Center of Experimental Medicine, University Hospital, Ludwig-Maximilians-University Munich, Munich, Germany, [3] Medical Faculty, Department of Physiology, Augsburg University, Augsburg, Germany

During acute inflammation, the recruitment of leukocytes from the blood stream into the inflamed tissue is a well-described mechanism encompassing the interaction of endothelial cells with leukocytes allowing leukocytes to reach the site of tissue injury or infection where they can fulfill their function such as phagocytosis. This process requires a fine-tuned regulation of a plethora of signaling cascades, which are still incompletely understood. Here, connexin 43 (Cx43) and pannexin 1 (Panx1) are known to be pivotal for the correct communication of endothelial cells with leukocytes. Pharmacological as well as genetic approaches provide evidence that endothelial Cx43-hemichannels and Panx1-channels release signaling molecules including ATP and thereby regulate vessel function and permeability as well as the recruitment of leukocytes during acute inflammation. Furthermore, Cx43 hemichannels and Panx1-channels in leukocytes release signaling molecules and can mediate the activation and function of leukocytes in an autocrine manner. The focus of the present review is to summarize the current knowledge of the role of Cx43 and Panx1 in endothelial cells and leukocytes in the vasculature during acute inflammation and to discuss relevant molecular mechanisms regulating Cx43 and Panx1 function.

Keywords: hemichannel, leukocyte, connexin, gap junction, acute inflammation, endothelial cells, ATP

OPEN ACCESS

Edited by:
Xavier Figueroa, Pontificia Universidad Católica de Chile, Chile

Reviewed by:
Juan C. Saez, Pontificia Universidad Católica de Chile, Chile
Brant Isakson, University of Virginia, United States

****Correspondence:***
Kristin Pogoda
kristin.pogoda@med.uni-augsburg.de

Specialty section:
This article was submitted to Vascular Physiology, a section of the journal Frontiers in Physiology

Received: *12 August 2020*
Accepted: *08 October 2020*
Published: *29 October 2020*

Citation:
Kameritsch P and Pogoda K (2020) The Role of Connexin 43 and Pannexin 1 During Acute Inflammation. Front. Physiol. 11:594097. doi: 10.3389/fphys.2020.594097

INTRODUCTION

During acute inflammation the recruitment of leukocytes from the bloodstream to the site of injury or infection is a highly regulated mechanism to ensure that leukocytes leave the bloodstream specifically at the inflammatory site to eliminate the inflammatory trigger (Nourshargh and Alon, 2014). In a series of different consecutive steps including rolling, adhesion processes, crawling, and transmigration through the microvascular endothelial layer leukocytes are in close contact to the endothelium (Nourshargh and Alon, 2014). For a correct regulation of these events during the recruitment cascade, the interaction and communication between leukocytes and endothelial cells (EC) but also between leukocytes or between EC are of particular importance.

Gap junction channels (GJ) are formed by two hemichannels, composed of six connexin (Cx) proteins, and allow the direct transfer of molecules between adjacent cells in a tissue (Kumar and Gilula, 1996). Cx-hemichannels can act as a transmembrane conduit between the cytoplasm and

the extracellular space to release paracrine or autocrine signaling molecules (Bruzzone et al., 2001; De Vuyst et al., 2007; Willebrords et al., 2016). Under physiological conditions they are normally closed but open with injury and inflammation and can induce cytokine release (Cheng et al., 2014). Pannexins (Panx) form functional membrane channels and are like Cx-hemichannels and GJ permeable to small molecules including ATP, ions or metabolites (Bruzzone et al., 2003; Zhou et al., 2019). Panx mediated ATP-release has been implicated in inflammatory responses of several immune cells (Lohman et al., 2015; Zhou et al., 2019). Cx and Panx are widely expressed in immune cells and are critically involved in immune cell functions and the regulation of inflammatory responses (Oviedo-Orta and Howard Evans, 2004; Glass et al., 2015; Esseltine and Laird, 2016; Aasen et al., 2019). Among them connexin 43 (Cx43) and pannexin 1 (Panx1) are present in all immune cells and the most studied isoforms (Esseltine and Laird, 2016; Valdebenito et al., 2018; Wang and Chen, 2018). In this mini review we will address the role of Cx43-hemichannels, Panx1-channels as well the intercellular communication via GJ in EC and leukocytes during acute inflammation.

IMPACT OF Panx1 AND Cx43 FOR COMMUNICATION OF EC AND DIFFERENT TYPES OF LEUKOCYTES (SEE FIGURE 1)

Intercellular communication between various cells of the immune system has been described for many years (Hulser and Peters, 1972) and in the last decades the expression pattern of Cx as well as the coupling between immune cells or with EC was analyzed. Also the role of endothelial Cx/GJ for the behavior of leukocytes was focus of many studies (Oviedo-Orta and Howard Evans, 2004; Okamoto and Suzuki, 2017). Intercellular coupling between lymphocytes expressing Cx40 and Cx43 (Oviedo-Orta et al., 2000) was involved in the proliferation of T-cell subsets (Zhang et al., 2018) and lymphocyte-macrophage-coupling (Bermudez-Fajardo et al., 2007). Other leukocytes like neutrophils express various Cx, among them Cx43 (Jara et al., 1995) and are able to form functional GJ among themselves (Branes et al., 2002).

Also direct or indirect communication of leukocytes with other cell types like endothelial (Zahler et al., 2003), epithelial (Pepin et al., 2020), or cancer cells (Hofmann et al., 2019) has been detected. Zahler et al. (2003) analyzed neutrophils that were able to exchange a GJ permeable dye with EC and Sarieddine et al. (2009) could demonstrate that adhesion of neutrophils was regulated by gap junctional coupling via Cx43 with endothelial (and epithelial) cells in the lung. Direct communication between lymphocytes is suggested to play a role in T-lymphocyte proliferation contributing to hypertensive inflammatory response (Ni et al., 2017) and GJ between cytotoxic T-lymphocytes and cancer cells allowed the immune system to control cancer cells (Hofmann et al., 2019). Furthermore, Cx43 expression and GJ communication were shown to be transiently induced between monocytes/macrophages at inflammatory sites (Eugenin et al., 2003) and macrophages were shown to communicate via GJ with epithelial cells thereby amplifying the antiviral response (Pepin et al., 2020).

Li et al. (2019) confirmed the role of Cx43 in promoting the adhesion of monocytes to EC. In contrast to others, the authors did not find any adhesive effects of the GJ but could show that enhanced expression of Cx43 in EC led to activation of the PI3K/AKT/NF-κB signaling pathway finally enhancing VCAM-1 and ICAM-1 expression and thereby increasing monocyte–endothelial adhesion. This effect seems to be prominent in EC exposed to high blood pressure leading to an enhanced expression of Cx43 and therefore to an enhanced monocyte-endothelial adhesion. Furthermore, Cx43 expression in monocytes also affects monocyte-endothelial adhesion (Ji et al., 2019) as inhibition of Cx43 expression in monocytes led to a decreased activity of the PI3K/AKT/NF-κB signaling pathway resulting in a decreased monocyte-endothelial adhesion, finally offering new thoughts for understanding atherosclerosis. The release of IL-17 from lymphocytes led to a decrease of Cx43 expression in limbal vascular EC (Qin et al., 2019) indicating an indirect communication of lymphocytes with EC.

Panx can similar to Cx act as hemichannels and were described to be able to form intercellular channels (Bruzzone et al., 2003; Sohl et al., 2005). However, most publications describe their function as hemichannels (Lohman et al., 2015) suggesting an indirect coupling of cells via the release of signaling molecules affecting regulatory processes of effector cells. Panx expression in EC and during inflammation has been reviewed recently (Begandt et al., 2017) and although Panx are known to be important in this context, their regulation in inflammation is unclear (Begandt et al., 2017). However, post-translational modifications of Panx1 (phosphorylation, S-nitrosylation, or caspase cleavage) can affect channel properties (Boyce et al., 2018). As demonstrated in smooth muscle cells a direct Src-dependent phosphorylation at Tyr198 within a Src homology 2 (SH2) domain in the intracellular loop seems to be involved in Panx1-dependent regulation of adrenergic mediated vasoconstriction (Delalio et al., 2019). Moreover, it was shown that spironolactone, an anti-hypertensive drug, inhibits the permeability of Panx1-channels thereby regulating α-adrenergic vasoconstriction (Good et al., 2018).

Under ischemic (Kaneko et al., 2015) or pro-inflammatory (Lohman et al., 2015) conditions, the latter only in venous but not arterial EC, the permeability of endothelial Panx1-channels was increased leading to decreased leukocyte adhesion (Lohman et al., 2015). Furthermore, the opening of Panx1 seems to be involved in ischemia/reperfusion injury-induced inflammation in the brain (Thuringer et al., 2015; Wei et al., 2015) and the lung increasing next to others vascular permeability and neutrophil infiltration (Sharma et al., 2018). Other inflammatory mediators like thrombin or histamine also led to an increased permeability of Panx1 whereas Cx43-hemichannel activity was reduced in this context (Godecke et al., 2012). Next to EC, Panx have also been shown to be expressed in leukocytes (Schenk et al., 2008; Woehrle et al., 2010; Li et al., 2018) and their expression was upregulated due to infection (Li et al., 2018). However, not only the expression

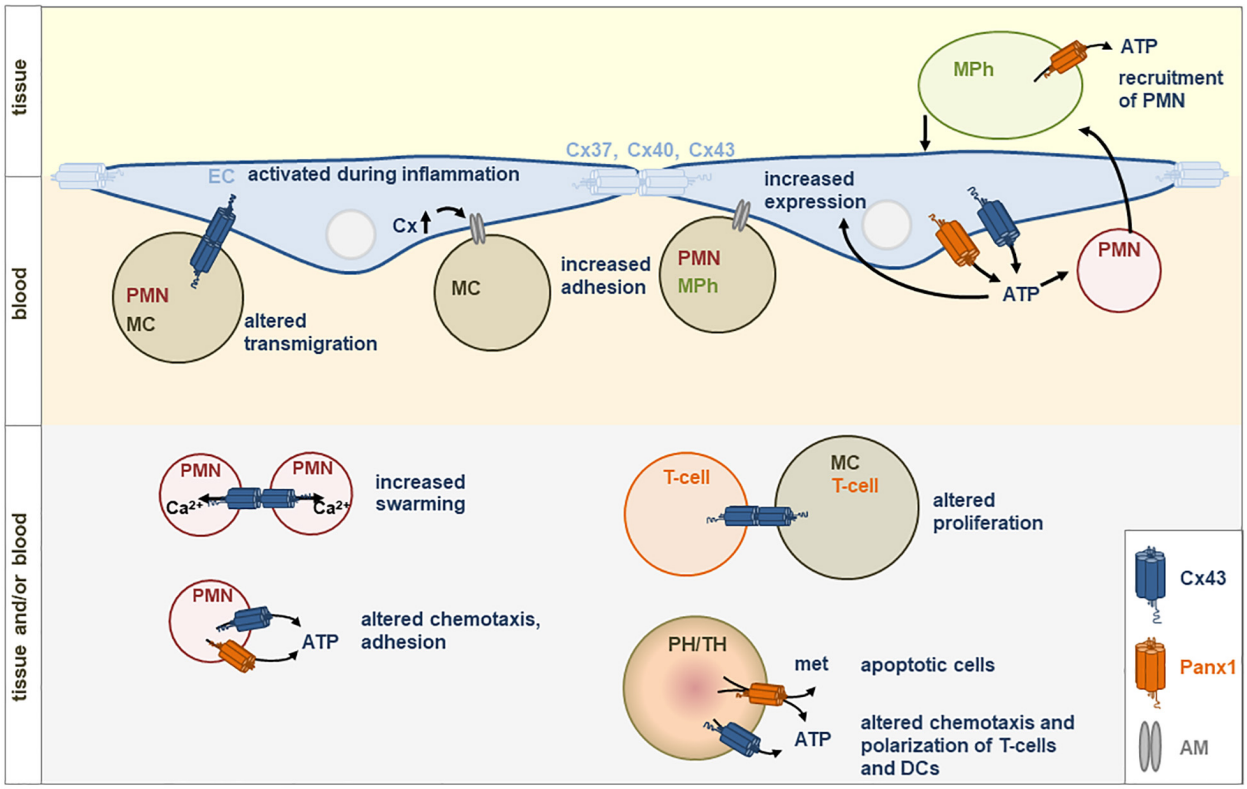

FIGURE 1 | Direct (gap junctions) or indirect (via hemichannels) communication between immune cells (PH, phagocytes; TH, thymocytes; PMN, neutrophils; MC, monocytes; MPh, macrophages) or with endothelial cells (EC) is involved in immune responses. Gap junctions are built by connexins (Cx). Hemichannels can be formed by Cx43 or Panx1. met, metabolites; PIH, pregnancy induced hypertension; AM, adhesion molecules; ATP, Adenosine triphosphate.

was upregulated but also its distribution pattern within the cell changed due to activation of the immune system. In primary T-cells Panx1 was distributed homogenously via the cell surface and translocated rapidly to the immune synapse after stimulation of the cells (Woehrle et al., 2010).

Cx43 IN LEUKOCYTE RECRUITMENT DURING ACUTE INFLAMMATION

Leukocyte recruitment during acute inflammation seems to be highly reliant on endothelial Cx43. TNFα-induced leukocyte adhesion and transmigration *in vivo* were reduced in endothelial Cx43-deficient mice as well as in the presence of GJ blockers in wild-type animals (Veliz et al., 2008). In a model of acute lung injury Cx43 was markedly enhanced in the lung of mice subjected to instillation with LPS and neutrophil recruitment was up-regulated in homozygous $Cx43^{+/+}$ compared to heterozygous $Cx43^{\pm}$ mice (Sarieddine et al., 2009). *In vitro* studies confirmed a reduced adhesion of activated neutrophils to EC or alveolar epithelial cells with blocked Cx43-containing GJ, which are both involved in LPS-induced lung inflammation. In contrast, incubation of GJ-blocked neutrophils with untreated EC did not reduce the number of adherent neutrophils (Sarieddine et al., 2009) indicating that a signal transfer between endothelial or epithelial cells via Cx43-containing GJ significantly contributes to neutrophil recruitment during acute inflammation. In contrast, Cx40 expression is downregulated during acute lung injury and endothelial-specific deletion of Cx40 resulted in increased transmigration of neutrophils after intratracheal instillation of LPS. Downregulation of Cx40 in EC *in vitro*, which was accompanied by a decreased expression and activity of CD73, increased adhesion of neutrophils to the endothelial monolayer suggesting an anti-inflammatory protective role in contrast to Cx43 (Chadjichristos et al., 2010; Scheckenbach et al., 2011). In another study it was shown that treatment of EC with peptidoglycan, a gram-positive bacterial cell wall component, induced ATP-release via Cx43-hemichannel opening which elicited a pro-inflammatory response by induction of interleukin 6 and Toll-like receptor 2 expression (Robertson et al., 2010), both known to be involved in leukocyte recruitment (Jones, 2005; Sabroe et al., 2005).

In neutrophils, Cx43 is primarily involved in ATP-release via hemichannels (Eltzschig et al., 2006). Dependent on the extracellular ATP concentration different functions like chemotaxis or adhesion are affected by different purinergic receptors (Trautmann, 2009; Wang and Chen, 2018). The ATP-release via Cx43-hemichannels from activated neutrophils during acute inflammation may have endothelial barrier protective and anti-inflammatory effects (Eltzschig et al., 2006).

Phosphorylation of Cx43 at Ser368 is associated with reduced opening (Bao et al., 2004) and ATP-release of activated neutrophils is regulated by Ser368 de-phosphorylation via phosphatase A. This phosphorylation-dependent ATP-release decreased endothelial paracellular permeability by modulating endothelial adenosine responses and might serve as a stopping signal for neutrophil chemotaxis (Eltzschig et al., 2006) to halt their migration at the infectious site. Moreover, it has been shown that LPS-induced autocrine ATP signaling inhibited neutrophil chemotaxis and knockout of the ATP receptor (P2X1) in neutrophil-like differentiated HL-60 cells recovered chemotaxis (Wang et al., 2017). LPS-induced ATP-release through Cx43-hemichannels of activated neutrophils induced a calcium ion (Ca^{2+}) influx via P2X1 receptors, a ligand-gated cation channel with high Ca^{2+} permeability, which reduced neutrophil chemotaxis by activating myosin light chain phosphorylation (Wang et al., 2017). Of note, degranulation and phagocytosis were enhanced by autocrine ATP-release. Hence, activated neutrophils release ATP to stop chemotaxis which might therefore facilitate the bactericidal functions of neutrophils (Wang et al., 2017). Moreover, neutrophil Cx43 has been shown to be crucial for coordinated Ca^{2+} fluxes and initiation of the neutrophil swarming (Poplimont et al., 2020). The first step, the initial recruitment of neutrophils to the site of inflammation is induced by damage-associated molecular patterns (DAMPs) from damaged or dead cells and pathogen-associated molecular patterns (PAMPs) released by invading microorganisms, causing the release of chemoattractants by local tissue cells. In contrast, the second step, the highly coordinated neutrophil movement with dense clusters and swarm aggregation at the wound core is mediated by paracrine release of the chemoattractant leukotriene B4 (LTB4), whose synthesis requires a sustained Ca^{2+} flux (Kienle and Lammermann, 2016; Poplimont et al., 2020). Cx43-dependent ATP-release via hemichannels induced calcium signal propagation in clustering neutrophils leading to LTB4 biosynthesis in neutrophils in a zebrafish model (Poplimont et al., 2020). The authors conclude that hemichannel opening of pioneer neutrophils upon contact with death-specific signals such as fMLP mediate Ca^{2+} flux-dependent LTB4-release, activating a secondary Cx43-channel opening leading to sustained intracluster Ca^{2+} fluxes (Poplimont et al., 2020). This study indicates that Cx43-channels play a crucial role for neutrophil swarm generation and chemoattractant production during acute inflammation.

The motility and transendothelial migration of B-cells also depend on Cx43 and are decreased after downregulation, likely regulated channel-independently by Cx43 (Machtaler et al., 2014), indicating that Cx43 can affect the individual steps of leukocyte recruitment via different mechanisms.

Panx1 IN LEUKOCYTE RECRUITMENT DURING ACUTE INFLAMMATION

Panx can be considered as key upstream molecules in inflammasome activation (Pelegrin and Surprenant, 2006) and several studies have shown that ATP-release through Panx1-channels enhances inflammatory responses (Adamson and Leitinger, 2014). The progressive opening of Panx1-channels in response to inflammatory stimuli can be activated by a caspase-dependent cleavage of the C-terminal tail controlling channel permeability (Makarenkova et al., 2018; Chen et al., 2019) associated with NLRP3 inflammasome activation in apoptotic macrophages (Chen et al., 2020). Moreover, Panx1 promotes recognition of bacterial molecules to activate the cryopyrin inflammasome (Kanneganti et al., 2007). The interaction of Panx with $P2X_7$ receptors has been reported to create a large permeable pore at the cell membrane and ATP-mediated activation of the inflammasome promotes the secretion of cytokines (Adamson and Leitinger, 2014). The release of ATP via Panx1-channels is involved in leukocytes recruitment by guiding chemotaxis of neutrophils and macrophages via purinergic receptor signaling activated by extracellular ATP (Adamson and Leitinger, 2014). Studies on neutrophil migration showed that ATP-release via Panx1-channels plays a dual role to trigger signals: excitatory signals by amplifying chemotactic signals and facilitating gradient sensing at the front of polarized neutrophils and inhibitory signals via A_{2A} adenosine receptors involved in blocking chemoattractant receptor signaling at the back of migrating neutrophils, demonstrating the role of Panx1 as fine-tune regulator of chemotactic responses of neutrophils (Chen et al., 2006, 2010; Bao et al., 2013). The ATP-release via Panx1-channels and autocrine stimulation of $P2X_4$ receptors also contributes to T-cell polarization and migration, whereas blocking of $P2X_4$ receptors inhibited T-cell activation and migration *in vitro* (Ledderose et al., 2018). ATP-release via Panx1 is also required for secretion of IL-1β from macrophages induced by $P2X_7$ receptor activation (Pelegrin and Surprenant, 2006). In dendritic cells extracellular ATP stimulated fast cell migration through an autocrine signaling loop initiated by $P2X_7$ receptor activation and amplified by opening of Panx1-channels and supplementary release of ATP (Saez et al., 2017).

The extravasation of leukocytes across the vascular wall to the site of injury is dependent on Panx1-mediated ATP-release from venous endothelium (Lohman et al., 2015). Stimulation of venous EC with TNFα induced expression and activation of Panx1-channels stimulating Ca^{2+}-dependent synthesis of IL-1β (Yang et al., 2020) and ATP-release inducing leukocyte adhesion and emigration *in vitro* and *in vivo* (Lohman et al., 2015). The latter might be partially mediated by increased endothelial expression of the adhesion molecule VCAM-1 (Dosch et al., 2018). Notably, EC derived nitric oxide can inhibit Panx1 activity through S-nitrosylation which reduces ATP-release and Panx1-channel currents in murine EC (Lohman et al., 2012).

Recently, Tam et al. (2020) demonstrated that during metabolic inflammation pro-inflammatory macrophages release chemotactic factors upon exposure to saturated fatty acids, such as palmitate, which was associated with recruitment and infiltration of neutrophils into adipose tissues. Heat inactivation or proteinase K digestion of media released by fatty acid treated macrophages did not alter neutrophil recruitment but was effective to inhibit CXCL-1 induced chemotaxis suggesting that these macrophage derived chemotactic factors are not

proteins (Tam et al., 2020). Moreover, the authors found that palmitate upregulated Panx1-channel expression in macrophages mediating neutrophil attraction by release of nucleotides such as ATP. The thereby following purinergic receptor stimulation and signaling induces neutrophil migration (Tam et al., 2020). These results emphasize the role of Panx1 in neutrophil recruitment and its contribution to inflammatory response during obesity. The impact of Panx1 for leukocyte recruitment during inflammation has also been demonstrated using a pharmacologic blocking of Panx1-channels by trovafloxacin, which decreased ICAM-1 expression and delayed recruitment of monocytes and neutrophils (Giustarini et al., 2019).

Due to the fact that Panx1-channels also regulate host responses to viruses (Orellana et al., 2013; Malik and Eugenin, 2019) the impact of Panx1 in COVID19 patients displaying hyper-inflammation has recently been discussed (Swayne et al., 2020). For the patient recovery especially the early phase of innate immunity seems to be critical and immunosuppression could limit viral entry and disease progression. Therefore, targeting Panx1-channels could improve therapeutic approaches and might reduce SARS-CoV-2 infectivity and vascular inflammatory responses in COVID19 patients (Swayne et al., 2020).

MOLECULES TRANSMITTED VIA Panx1-CHANNELS AND Cx43-CHANNELS

There are many data about the release of ATP via Cx43- or Panx1-channels: neutrophils for example are known to release ATP via Cx43-hemichannels during hypoxia or inflammation (Eltzschig et al., 2008). In inflamed lung EC, the release of ATP was shown to be mediated via Panx1 (Sharma et al., 2018) and in a fish model tPanx1-channels in leukocytes and other cells were responsible for the release of ATP (Li et al., 2018). In smooth muscle cells Panx1 mediated ATP-release is regulated by a direct Src-dependent phosphorylation at Tyr198 (Delalio et al., 2019) and purinergic regulation of migrating T-cells was shown to be stimulated by an ATP-release via Panx1 (Ledderose et al., 2018). For intercellular communication via GJ, it is common knowledge that molecules up to a size of 1.8 kD can be transferred between cells (Neijssen et al., 2005). Typically, ions like K^+ or Ca^{2+} and second messengers like cAMP were shown to diffuse from one cell to the other (Valiunas et al., 2019) but for the communication between either immune cells or between immune and endothelial/epithelial cells less data are available. Zhang et al. speculated that ATP diffuses via GJ between lymphocytes (Zhang et al., 2018). For cytotoxic T-cells that form GJ with cancer cells leading to an enhanced granzyme B activity in cancer cells it was thought that granzyme B or Ca^{2+} may be transferred (Hofmann et al., 2019) and macrophages that communicate via GJ with epithelial cells (Pepin et al., 2020) seem to mediate cGAMP via intercellular channels. Also peptides have been shown to be transferred via GJ between cells causing recognition of nearby bystander cells and activated monocytes by cytotoxic T-cells (Neijssen et al., 2005).

DISCUSSION

The activity of both Cx43-hemichannels and Panx1-channels depends on diverse environmental stimuli and increases under pathophysiological conditions including acute inflammation. Their opening allows the release of signaling molecules from the cytoplasm acting as autocrine or paracrine messengers (Evans et al., 2006) and enables activated EC and leukocytes to fine-tune responses during acute inflammation. Most of the described effects of inflammatory cells are mediated via ATP-release through Cx43-hemichannels or Panx1-channels and purinergic receptor signaling but also the gap junctional transfer of signaling molecules affects the recruitment of leukocytes. Despite the increasing amount of studies on Cx- and Panx-functions in EC and leukocytes still little is known about their interplay and regulation during acute and chronic inflammation and requires further investigations. Moreover, it should be mentioned that pharmacologic inhibition of Cx43-hemichannels at least partly affects Panx1 and GJ and making the discrimination between hemichannels and GJ difficult (Willebrords et al., 2017). However, targeting Panx1- or Cx43-dependent ATP-release and purinergic signaling could represent a promising approach for the therapeutical treatment of acute inflammation.

AUTHOR CONTRIBUTIONS

PK and KP wrote the manuscript. Both authors contributed to the article and approved the submitted version.

REFERENCES

Aasen, T., Leithe, E., Graham, S. V., Kameritsch, P., Mayan, M. D., Mesnil, M., et al. (2019). Connexins in cancer: bridging the gap to the clinic. *Oncogene* 38, 4429–4451. doi: 10.1038/s41388-019-0741-6

Adamson, S. E., and Leitinger, N. (2014). The role of pannexin1 in the induction and resolution of inflammation. *FEBS Lett.* 588, 1416–1422. doi: 10.1016/j.febslet.2014.03.009

Bao, X., Altenberg, G. A., and Reuss, L. (2004). Mechanism of regulation of the gap junction protein connexin 43 by protein kinase C-mediated phosphorylation. *Am. J. Physiol. Cell Physiol.* 286, C647–C654. doi: 10.1152/ajpcell.00295.2003

Bao, Y., Chen, Y., Ledderose, C., Li, L., and Junger, W. G. (2013). Pannexin 1 channels link chemoattractant receptor signaling to local excitation and global inhibition responses at the front and back of polarized neutrophils. *J. Biol. Chem.* 288, 22650–22657. doi: 10.1074/jbc.M113.476283

Begandt, D., Good, M. E., Keller, A. S., Delalio, L. J., Rowley, C., Isakson, B. E., et al. (2017). Pannexin channel and connexin hemichannel expression in vascular function and inflammation. *BMC Cell Biol.* 18:2. doi: 10.1186/s12860-016-0119-3

Bermudez-Fajardo, A., Yliharsila, M., Evans, W. H., Newby, A. C., and Oviedo-Orta, E. (2007). CD4+ T lymphocyte subsets express connexin 43 and establish gap junction channel communication with macrophages in vitro. *J. Leukoc. Biol.* 82, 608–612. doi: 10.1189/jlb.0307134

Boyce, A. K. J., Epp, A. L., Nagarajan, A., and Swayne, L. A. (2018). Transcriptional and post-translational regulation of pannexins. *Biochim. Biophys. Acta Biomembr.* 1860, 72–82. doi: 10.1016/j.bbamem.2017.03.004

Branes, M. C., Contreras, J. E., and Saez, J. C. (2002). Activation of human polymorphonuclear cells induces formation of functional gap junctions and expression of connexins. *Med. Sci. Monit.* 8, BR313–BR323.

Bruzzone, R., Hormuzdi, S. G., Barbe, M. T., Herb, A., and Monyer, H. (2003). Pannexins, a family of gap junction proteins expressed in brain. *Proc. Natl. Acad. Sci. U.S.A.* 100, 13644–13649. doi: 10.1073/pnas.2233464100

Bruzzone, S., Guida, L., Zocchi, E., Franco, L., and De Flora, A. (2001). Connexin 43 hemi channels mediate Ca2+-regulated transmembrane NAD+ fluxes in intact cells. *FASEB J.* 15, 10–12. doi: 10.1096/fj.00-0566fje

Chadjichristos, C. E., Scheckenbach, K. E., Van Veen, T. A., Richani Sarieddine, M. Z., De Wit, C., Yang, Z., et al. (2010). Endothelial-specific deletion of connexin40 promotes atherosclerosis by increasing CD73-dependent leukocyte adhesion. *Circulation* 121, 123–131. doi: 10.1161/CIRCULATIONAHA.109.867176

Chen, K. W., Demarco, B., and Broz, P. (2020). Pannexin-1 promotes NLRP3 activation during apoptosis but is dispensable for canonical or noncanonical inflammasome activation. *Eur. J. Immunol.* 50, 170–177. doi: 10.1002/eji.201948254

Chen, W., Zhu, S., Wang, Y., Li, J., Qiang, X., Zhao, X., et al. (2019). Enhanced macrophage Pannexin 1 expression and hemichannel activation exacerbates lethal experimental sepsis. *Sci. Rep.* 9:160. doi: 10.1038/s41598-018-37232-z

Chen, Y., Corriden, R., Inoue, Y., Yip, L., Hashiguchi, N., Zinkernagel, A., et al. (2006). ATP release guides neutrophil chemotaxis via P2Y2 and A3 receptors. *Science* 314, 1792–1795. doi: 10.1126/science.1132559

Chen, Y., Yao, Y., Sumi, Y., Li, A., To, U. K., Elkhal, A., et al. (2010). Purinergic signaling: a fundamental mechanism in neutrophil activation. *Sci. Signal.* 3:ra45. doi: 10.1126/scisignal.2000549

Cheng, R. D., Ren, J. J., Zhang, Y. Y., and Ye, X. M. (2014). P2X4 receptors expressed on microglial cells in post-ischemic inflammation of brain ischemic injury. *Neurochem. Int.* 67, 9–13. doi: 10.1016/j.neuint.2014.01.011

De Vuyst, E., Decrock, E., De Bock, M., Yamasaki, H., Naus, C. C., Evans, W. H., et al. (2007). Connexin hemichannels and gap junction channels are differentially influenced by lipopolysaccharide and basic fibroblast growth factor. *Mol. Biol. Cell* 18, 34–46. doi: 10.1091/mbc.e06-03-0182

Delalio, L. J., Billaud, M., Ruddiman, C. A., Johnstone, S. R., Butcher, J. T., Wolpe, A. G., et al. (2019). Constitutive SRC-mediated phosphorylation of pannexin 1 at tyrosine 198 occurs at the plasma membrane. *J. Biol. Chem.* 294, 6940–6956. doi: 10.1074/jbc.RA118.006982

Dosch, M., Gerber, J., Jebbawi, F., and Beldi, G. (2018). Mechanisms of ATP release by inflammatory cells. *Int. J. Mol. Sci.* 19:1222. doi: 10.3390/ijms19041222

Eltzschig, H. K., Eckle, T., Mager, A., Kuper, N., Karcher, C., Weissmuller, T., et al. (2006). ATP release from activated neutrophils occurs via connexin 43 and modulates adenosine-dependent endothelial cell function. *Circ. Res.* 99, 1100–1108. doi: 10.1161/01.RES.0000250174.31269.70

Eltzschig, H. K., Macmanus, C. F., and Colgan, S. P. (2008). Neutrophils as sources of extracellular nucleotides: functional consequences at the vascular interface. *Trends Cardiovasc. Med.* 18, 103–107. doi: 10.1016/j.tcm.2008.01.006

Esseltine, J. L., and Laird, D. W. (2016). Next-generation connexin and pannexin cell biology. *Trends Cell. Biol.* 26, 944–955. doi: 10.1016/j.tcb.2016.06.003

Eugenin, E. A., Branes, M. C., Berman, J. W., and Saez, J. C. (2003). TNF-alpha plus IFN-gamma induce connexin43 expression and formation of gap junctions between human monocytes/macrophages that enhance physiological responses. *J. Immunol.* 170, 1320–1328. doi: 10.4049/jimmunol.170.3.1320

Evans, W. H., De Vuyst, E., and Leybaert, L. (2006). The gap junction cellular internet: connexin hemichannels enter the signalling limelight. *Biochem. J.* 397, 1–14. doi: 10.1042/BJ20060175

Giustarini, G., Vrisekoop, N., Kruijssen, L., Wagenaar, L., Van Staveren, S., Van Roest, M., et al. (2019). Trovafloxacin-induced liver injury: lack in regulation of inflammation by inhibition of nucleotide release and neutrophil movement. *Toxicol. Sci.* 167, 385–396. doi: 10.1093/toxsci/kfy244

Glass, A. M., Snyder, E. G., and Taffet, S. M. (2015). Connexins and pannexins in the immune system and lymphatic organs. *Cell Mol. Life Sci.* 72, 2899–2910. doi: 10.1007/s00018-015-1966-3

Godecke, S., Roderigo, C., Rose, C. R., Rauch, B. H., Godecke, A., and Schrader, J. (2012). Thrombin-induced ATP release from human umbilical vein endothelial cells. *Am. J. Physiol. Cell Physiol.* 302, C915–C923. doi: 10.1152/ajpcell.00283.2010

Good, M. E., Chiu, Y. H., Poon, I. K. H., Medina, C. B., Butcher, J. T., Mendu, S. K., et al. (2018). Pannexin 1 channels as an unexpected new target of the anti-hypertensive drug spironolactone. *Circ. Res.* 122, 606–615. doi: 10.1161/CIRCRESAHA.117.312380

Hofmann, F., Navarrete, M., Alvarez, J., Guerrero, I., Gleisner, M. A., Tittarelli, A., et al. (2019). Cx43-Gap junctions accumulate at the cytotoxic immunological synapse enabling Cytotoxic T lymphocyte melanoma cell killing. *Int. J. Mol. Sci.* 20:4509. doi: 10.3390/ijms20184509

Hulser, D. F., and Peters, J. H. (1972). Contact cooperation in stimulated lymphocytes. II. Electrophysiological investigations on intercellular communication. *Exp. Cell Res.* 74, 319–326. doi: 10.1016/0014-4827(72)90383-7

Jara, P. I., Boric, M. P., and Saez, J. C. (1995). Leukocytes express connexin 43 after activation with lipopolysaccharide and appear to form gap junctions with endothelial cells after ischemia-reperfusion. *Proc. Natl. Acad. Sci. U.S.A.* 92, 7011–7015. doi: 10.1073/pnas.92.15.7011

Ji, H., Qiu, R., Gao, X., Zhang, R., Li, X., Hei, Z., et al. (2019). Propofol attenuates monocyte-endothelial adhesion via modulating connexin43 expression in monocytes. *Life Sci.* 232:116624. doi: 10.1016/j.lfs.2019.116624

Jones, S. A. (2005). Directing transition from innate to acquired immunity: defining a role for IL-6. *J. Immunol.* 175, 3463–3468. doi: 10.4049/jimmunol.175.6.3463

Kaneko, Y., Tachikawa, M., Akaogi, R., Fujimoto, K., Ishibashi, M., Uchida, Y., et al. (2015). Contribution of pannexin 1 and connexin 43 hemichannels to extracellular calcium-dependent transport dynamics in human blood-brain barrier endothelial cells. *J. Pharmacol. Exp. Ther.* 353, 192–200. doi: 10.1124/jpet.114.220210

Kanneganti, T. D., Lamkanfi, M., Kim, Y. G., Chen, G., Park, J. H., Franchi, L., et al. (2007). Pannexin-1-mediated recognition of bacterial molecules activates the cryopyrin inflammasome independent of Toll-like receptor signaling. *Immunity* 26, 433–443. doi: 10.1016/j.immuni.2007.03.008

Kienle, K., and Lammermann, T. (2016). Neutrophil swarming: an essential process of the neutrophil tissue response. *Immunol. Rev.* 273, 76–93. doi: 10.1111/imr.12458

Kumar, N. M., and Gilula, N. B. (1996). The gap junction communication channel. *Cell* 84, 381–388. doi: 10.1016/s0092-8674(00)81282-9

Ledderose, C., Liu, K., Kondo, Y., Slubowski, C. J., Dertnig, T., Denicolo, S., et al. (2018). Purinergic P2X4 receptors and mitochondrial ATP production regulate T cell migration. *J. Clin. Invest.* 128, 3583–3594. doi: 10.1172/JCI120972

Li, S., Li, J., Wang, N., Zhang, T., Xu, Y., and Sun, J. (2018). Expression analysis of Pannexin1 channel gene in response to immune challenges and its role in infection-induced ATP release in tilapia (*Oreochromis niloticus*). *Fish Shellfish Immunol.* 81, 470–475. doi: 10.1016/j.fsi.2018.07.050

Li, X., Zhang, Q., Zhang, R., Cheng, N., Guo, N., Liu, Y., et al. (2019). Down-regulation of Cx43 expression on PIH-HUVEC cells attenuates monocyte-endothelial adhesion. *Thromb. Res.* 179, 104–113. doi: 10.1016/j.thromres.2019.05.009

Lohman, A. W., Leskov, I. L., Butcher, J. T., Johnstone, S. R., Stokes, T. A., Begandt, D., et al. (2015). Pannexin 1 channels regulate leukocyte emigration through the venous endothelium during acute inflammation. *Nat. Commun.* 6:7965. doi: 10.1038/ncomms8965

Lohman, A. W., Weaver, J. L., Billaud, M., Sandilos, J. K., Griffiths, R., Straub, A. C., et al. (2012). S-nitrosylation inhibits pannexin 1 channel function. *J. Biol. Chem.* 287, 39602–39612. doi: 10.1074/jbc.M112.397976

Machtaler, S., Choi, K., Dang-Lawson, M., Falk, L., Pournia, F., Naus, C. C., et al. (2014). The role of the gap junction protein connexin43 in B lymphocyte motility and migration. *FEBS Lett.* 588, 1249–1258. doi: 10.1016/j.febslet.2014.01.027

Makarenkova, H. P., Shah, S. B., and Shestopalov, V. I. (2018). The two faces of pannexins: new roles in inflammation and repair. *J. Inflamm. Res.* 11, 273–288. doi: 10.2147/JIR.S128401

Malik, S., and Eugenin, E. A. (2019). Role of connexin and pannexin containing channels in HIV infection and NeuroAIDS. *Neurosci. Lett.* 695, 86–90. doi: 10.1016/j.neulet.2017.09.005

Neijssen, J., Herberts, C., Drijfhout, J. W., Reits, E., Janssen, L., and Neefjes, J. (2005). Cross-presentation by intercellular peptide transfer through gap junctions. *Nature* 434, 83–88. doi: 10.1038/nature03290

Ni, X., Wang, A., Zhang, L., Shan, L. Y., Zhang, H. C., Li, L., et al. (2017). Up-regulation of gap junction in peripheral blood T lymphocytes contributes to

the inflammatory response in essential hypertension. *PLoS ONE* 12:e0184773. doi: 10.1371/journal.pone.0184773

Nourshargh, S., and Alon, R. (2014). Leukocyte migration into inflamed tissues. *Immunity* 41, 694–707. doi: 10.1016/j.immuni.2014.10.008

Okamoto, T., and Suzuki, K. (2017). The role of gap junction-mediated endothelial cell-cell interaction in the crosstalk between inflammation and blood coagulation. *Int. J. Mol. Sci.* 18:2254. doi: 10.3390/ijms18112254

Orellana, J. A., Velasquez, S., Williams, D. W., Saez, J. C., Berman, J. W., and Eugenin, E. A. (2013). Pannexin1 hemichannels are critical for HIV infection of human primary CD4+ T lymphocytes. *J. Leukoc. Biol.* 94, 399–407. doi: 10.1189/jlb.0512249

Oviedo-Orta, E., and Howard Evans, W. (2004). Gap junctions and connexin-mediated communication in the immune system. *Biochim. Biophys. Acta* 1662, 102–112. doi: 10.1016/j.bbamem.2003.10.021

Oviedo-Orta, E., Hoy, T., and Evans, W. H. (2000). Intercellular communication in the immune system: differential expression of connexin40 and 43, and perturbation of gap junction channel functions in peripheral blood and tonsil human lymphocyte subpopulations. *Immunology* 99, 578–590. doi: 10.1046/j.1365-2567.2000.00991.x

Pelegrin, P., and Surprenant, A. (2006). Pannexin-1 mediates large pore formation and interleukin-1beta release by the ATP-gated P2X7 receptor. *EMBO J.* 25, 5071–5082. doi: 10.1038/sj.emboj.7601378

Pepin, G., De Nardo, D., Rootes, C. L., Ullah, T. R., Al-Asmari, S. S., Balka, K. R., et al. (2020). Connexin-dependent transfer of cGAMP to phagocytes modulates antiviral responses. *mBio* 11:e03187-19. doi: 10.1128/mBio.03187-19

Poplimont, H., Georgantzoglou, A., Boulch, M., Walker, H. A., Coombs, C., Papaleonidopoulou, F., et al. (2020). Neutrophil swarming in damaged tissue is orchestrated by connexins and cooperative calcium alarm signals. *Curr. Biol.* 30, 2761–2776.e7. doi: 10.1016/j.cub.2020.05.030

Qin, X. H., Ma, X., Fang, S. F., Zhang, Z. Z., and Lu, J. M. (2019). IL-17 produced by Th17 cells alleviates the severity of fungal keratitis by suppressing CX43 expression in corneal peripheral vascular endothelial cells. *Cell Cycle* 18, 274–287. doi: 10.1080/15384101.2018.1556059

Robertson, J., Lang, S., Lambert, P. A., and Martin, P. E. (2010). Peptidoglycan derived from *Staphylococcus epidermidis* induces Connexin43 hemichannel activity with consequences on the innate immune response in endothelial cells. *Biochem. J.* 432, 133–143. doi: 10.1042/BJ20091753

Sabroe, I., Dower, S. K., and Whyte, M. K. (2005). The role of Toll-like receptors in the regulation of neutrophil migration, activation, and apoptosis. *Clin. Infect. Dis.* 41(Suppl. 7), S421–S426. doi: 10.1086/431992

Saez, P. J., Vargas, P., Shoji, K. F., Harcha, P. A., Lennon-Dumenil, A. M., and Saez, J. C. (2017). ATP promotes the fast migration of dendritic cells through the activity of pannexin 1 channels and P2X7 receptors. *Sci. Signal.* 10:eaah7107. doi: 10.1126/scisignal.aah7107

Sarieddine, M. Z., Scheckenbach, K. E., Foglia, B., Maass, K., Garcia, I., Kwak, B. R., et al. (2009). Connexin43 modulates neutrophil recruitment to the lung. *J. Cell. Mol. Med.* 13, 4560–4570. doi: 10.1111/j.1582-4934.2008.00654.x

Scheckenbach, K. E., Crespin, S., Kwak, B. R., and Chanson, M. (2011). Connexin channel-dependent signaling pathways in inflammation. *J. Vasc. Res.* 48, 91–103. doi: 10.1159/000316942

Schenk, U., Westendorf, A. M., Radaelli, E., Casati, A., Ferro, M., Fumagalli, M., et al. (2008). Purinergic control of T cell activation by ATP released through pannexin-1 hemichannels. *Sci. Signal.* 1:ra6. doi: 10.1126/scisignal.1160583

Sharma, A. K., Charles, E. J., Zhao, Y., Narahari, A. K., Baderdinni, P. K., Good, M. E., et al. (2018). Pannexin-1 channels on endothelial cells mediate vascular inflammation during lung ischemia-reperfusion injury. *Am. J. Physiol. Lung Cell. Mol. Physiol.* 315, L301–L312. doi: 10.1152/ajplung.00004.2018

Sohl, G., Maxeiner, S., and Willecke, K. (2005). Expression and functions of neuronal gap junctions. *Nat. Rev. Neurosci.* 6, 191–200. doi: 10.1038/nrn1627

Swayne, L. A., Johnstone, S. R., Ng, C. S., Sanchez-Arias, J. C., Good, M. E., Penuela, S., et al. (2020). Consideration of Pannexin 1 channels in COVID-19 pathology and treatment. *Am. J. Physiol. Lung Cell. Mol. Physiol.* 319, L121–L125. doi: 10.1152/ajplung.00146.2020

Tam, T. H., Chan, K. L., Boroumand, P., Liu, Z., Brozinick, J. T., Bui, H. H., et al. (2020). Nucleotides released from palmitate-activated murine macrophages attract neutrophils. *J. Biol. Chem.* 295, 4902–4911. doi: 10.1074/jbc.RA119.010868

Thuringer, D., Berthenet, K., Cronier, L., Jego, G., Solary, E., and Garrido, C. (2015). Oncogenic extracellular HSP70 disrupts the gap-junctional coupling between capillary cells. *Oncotarget* 6, 10267–10283. doi: 10.18632/oncotarget.3522

Trautmann, A. (2009). Extracellular ATP in the immune system: more than just a "danger signal". *Sci. Signal.* 2:e6. doi: 10.1126/scisignal.256pe6

Valdebenito, S., Barreto, A., and Eugenin, E. A. (2018). The role of connexin and pannexin containing channels in the innate and acquired immune response. *Biochim. Biophys. Acta Biomembr.* 1860, 154–165. doi: 10.1016/j.bbamem.2017.05.015

Valiunas, V., Brink, P. R., and White, T. W. (2019). Lens connexin channels have differential permeability to the second messenger cAMP. *Invest. Ophthalmol. Vis. Sci.* 60, 3821–3829. doi: 10.1167/iovs.19-27302

Veliz, L. P., Gonzalez, F. G., Duling, B. R., Saez, J. C., and Boric, M. P. (2008). Functional role of gap junctions in cytokine-induced leukocyte adhesion to endothelium in vivo. *Am. J. Physiol. Heart Circ. Physiol.* 295, H1056–H1066. doi: 10.1152/ajpheart.00266.2008

Wang, X., and Chen, D. (2018). Purinergic regulation of neutrophil function. *Front. Immunol.* 9:399. doi: 10.3389/fimmu.2018.00399

Wang, X., Qin, W., Xu, X., Xiong, Y., Zhang, Y., Zhang, H., et al. (2017). Endotoxin-induced autocrine ATP signaling inhibits neutrophil chemotaxis through enhancing myosin light chain phosphorylation. *Proc. Natl. Acad. Sci. U.S.A.* 114, 4483–4488. doi: 10.1073/pnas.1616752114

Wei, R., Wang, J., Xu, Y., Yin, B., He, F., Du, Y., et al. (2015). Probenecid protects against cerebral ischemia/reperfusion injury by inhibiting lysosomal and inflammatory damage in rats. *Neuroscience* 301, 168–177. doi: 10.1016/j.neuroscience.2015.05.070

Willebrords, J., Crespo Yanguas, S., Maes, M., Decrock, E., Wang, N., Leybaert, L., et al. (2016). Connexins and their channels in inflammation. *Crit. Rev. Biochem. Mol. Biol.* 51, 413–439. doi: 10.1080/10409238.2016.1204980

Willebrords, J., Maes, M., Crespo Yanguas, S., and Vinken, M. (2017). Inhibitors of connexin and pannexin channels as potential therapeutics. *Pharmacol. Ther.* 180, 144–160. doi: 10.1016/j.pharmthera.2017.07.001

Woehrle, T., Yip, L., Elkhal, A., Sumi, Y., Chen, Y., Yao, Y., et al. (2010). Pannexin-1 hemichannel-mediated ATP release together with P2X1 and P2X4 receptors regulate T-cell activation at the immune synapse. *Blood* 116, 3475–3484. doi: 10.1182/blood-2010-04-277707

Yang, Y., Delalio, L. J., Best, A. K., Macal, E., Milstein, J., Donnelly, I., et al. (2020). Endothelial Pannexin 1 channels control inflammation by regulating intracellular calcium. *J. Immunol.* 204, 2995–3007. doi: 10.4049/jimmunol.1901089

Zahler, S., Hoffmann, A., Gloe, T., and Pohl, U. (2003). Gap-junctional coupling between neutrophils and endothelial cells: a novel modulator of transendothelial migration. *J. Leukoc. Biol.* 73, 118–126. doi: 10.1189/jlb.0402184

Zhang, H. C., Zhang, Z. S., Zhang, L., Wang, A., Zhu, H., Li, L., et al. (2018). Connexin 43 in splenic lymphocytes is involved in the regulation of CD4+CD25+ T lymphocyte proliferation and cytokine production in hypertensive inflammation. *Int. J. Mol. Med.* 41, 13–24. doi: 10.3892/ijmm.2017.3201

Zhou, K. Q., Green, C. R., Bennet, L., Gunn, A. J., and Davidson, J. O. (2019). The role of connexin and pannexin channels in perinatal brain injury and inflammation. *Front. Physiol.* 10:141. doi: 10.3389/fphys.2019.00141

Conflict of Interest: The authors declare that the research was conducted in the absence of any commercial or financial relationships that could be construed as a potential conflict of interest.

frontiers in Cardiovascular Medicine

ORIGINAL RESEARCH
published: 12 November 2020
doi: 10.3389/fcvm.2020.581362

Identification of Transcriptional Variation in Aortic Remodeling Using a Murine Transverse Aortic Constriction (TAC) Model

Xinlu Zhang[1,2†], Ting Feng[2†], Xin-Xin I. Zeng[3], Hongbin Liang[2], Bo Situ[1], Qiuxia Zhang[2], Fengyun Zhou[2], Yejia Chen[2], Tao Wang[1], Du Cai[1], Xinxin Lin[2], Jiancheng Xiu[2] and Lei Zheng[1]**

[1] Department of Laboratory Medicine, Nanfang Hospital, Southern Medical University, Guangzhou, China, [2] Department of Cardiology, Nanfang Hospital, Southern Medical University, Guangzhou, China, [3] Human Genetics Program, Sanford Burnham Prebys Medical Discovery Institute, La Jolla, CA, United States

OPEN ACCESS

Edited by:
Xavier Figueroa,
Pontificia Universidad Católica de Chile, Chile

Reviewed by:
Jian Wu,
Fudan University, China
Hui-Hua Li,
Dalian Medical University, China

***Correspondence:**
Lei Zheng
nfyyzhenglei@smu.edu.cn
Jiancheng Xiu
xiujc@126.com

[†] These authors have contributed equally to this work

Specialty section:
This article was submitted to Hypertension, a section of the journal Frontiers in Cardiovascular Medicine

Received: 08 July 2020
Accepted: 24 September 2020
Published: 12 November 2020

Citation:
Zhang X, Feng T, Zeng X-XI, Liang H, Situ B, Zhang Q, Zhou F, Chen Y, Wang T, Cai D, Lin X, Xiu J and Zheng L (2020) Identification of Transcriptional Variation in Aortic Remodeling Using a Murine Transverse Aortic Constriction (TAC) Model. Front. Cardiovasc. Med. 7:581362. doi: 10.3389/fcvm.2020.581362

Arterial remodeling is a major pathological consequence of hypertension, which is recognized as the most common chronic non-communicable disease. However, the detailed mechanism of how arterial remodeling is induced by hypertension has not yet been fully elucidated. Evaluating the transcriptional changes in arterial tissue in response to elevated blood pressure at an early stage may provide new insights and identify novel therapeutic candidates in preventing arterial remodeling. Here, we used the ascending aorta of the transverse aortic constriction (TAC) model to induce arterial remodeling in C57BL/6 male mice. Age-matched mice were subjected to sham surgery as controls. The TAC model was only considered successful if the mice conformed to the criteria (RC/LC blood flow velocity with 5–10-fold change) 1 week after the surgery. Two weeks after surgery, the ascending aorta developed severe remodeling in TAC mice as compared to the sham group. High throughput sequencing was then applied to identify differentially expressed (DE) transcripts. In silicon analysis were then performed to systematically network transcriptional changes. A total of 1,019 mRNAs were significantly changed between TAC and the sham group at the transcriptional level. GO (Gene Ontology) and KEGG (Kyoto Encyclopedia of Genes and Genomes) analysis revealed that stress/stimulus/immune-related biological processes played a crucial role during arterial remodeling. Our data provide a comprehensive understanding of global gene expression changes in the TAC model, which suggests that targeting inflammation and vascular smooth cell transformation are potential therapeutic strategies to interfere with the aortic remodeling at an early stage in the development of hypertension.

Keywords: hypertension, arterial remodeling, transverse aortic constriction (TAC), transcriptional changes, bioinformatics analysis

INTRODUCTION

Hypertension is the most prevalent chronic non-infectious disease and one of the most significant risk factors for cardiovascular and cerebrovascular diseases (1, 2). The World Health Organization estimates that more than 1.13 billion people worldwide suffer from high blood pressure. More importantly, due to the aging population, the number of hypertension patients is expected to be

over 1.5 billion by 2025 globally (3). The increasing burden of hypertension not only enhances the morbidity and mortality of cardiovascular and kidney diseases, it also causes increasing economic costs that affect the whole society (4). Although clinical anti-hypertensive drugs, including ACEI, ARB, and β-blockers, have certain functions in inhibiting vascular remodeling while also reducing blood pressure, the clinical benefits of these drugs are not satisfactory (5). Therefore, there is high demand and an urgent need to uncover new therapeutic targets for hypertension therapies.

Arterial remodeling is one of the significant pathological consequences of high blood pressure, which ultimately induces arteriosclerosis and tissue damage in various organs (6, 7). Arterial remodeling is influenced by hemodynamic loading, neuro-hormonal activation, inflammation, immunity, and other potential factors. Among them, hemodynamic changes can activate vascular biochemical signals via sensing mechanical transduction variation, followed by multiple cytological pathological and physiological alterations, such as cell hypertrophy, proliferation, apoptosis, and extracellular matrix (ECM) turnover. The classical phenotypic transformation of arterial remodeling is located in the median vascular smooth muscle cells, which is manifested as hypertrophy, high proliferation, increased migration to the endothelium, and a large amount of ECM deposition (8, 9). The ultimate goal of inhibiting hypertension-induced vascular remodeling is to prevent end-organ damage, whereas inflammation is a key mediator between these two events (10), thus, targeting inflammation is a straightforward strategy to avoid hypertension associated organ damage.

The TAC-induced hypertension model is a well-established system that accurately mimics pathological changes, including thickening of the medial and adventitia of blood vessels as well as inhibition of endothelial cells-vascular smooth muscle cells (EC-VSMC) dependent vasomotor function (11, 12). Although AT1 receptor activation plays an important role in pressure-induced arterial remodeling in the TAC model (13), the sophisticated mechanism of how hypertension induces arterial remodeling remains unclear. Here, we used RNA Sequencing (RNA-seq) to identify DE transcripts during the arterial remodeling development and to validate these transcriptional alternations by analyzing mouse aorta tissues with multiple assays, which can reveal novel biomarkers and therapeutic targets for hypertension-induced arterial remodeling at an early stage of the disease.

MATERIALS AND METHODS

Establishment of Transverse Aortic Constriction (TAC) Model

All animal care and experimental procedures were approved by the Institutional Animal Care and Use Committee of Southern Medical University and performed in accordance with the Guide for the Care and Use of Laboratory Animals published by the United States National Institutes of Health. C57BL/6J male mice (8 weeks old, 20–25 g) were intraperitoneally anesthetized with a mixture of xylazine (5 mg/kg) and ketamine (100 mg/kg), and awareness was monitored by the negative tail pinch reflex. Mice were fixed on a temperature-controlled operating table in the supine position. After an endotracheal tube was inserted, the mice were supported by a mouse mini-ventilator (Alcott biotech, Shanghai, China). The respiration rate was set to 150 breaths/min, tidal volumes to 2 ml/min, and inspiration/expiration ratio to 1:1.3. After depilation with depilatory cream and routine disinfection, the mouse skin was incised next to the sternum to the second rib. By penetrating the second intercostal space with forceps to expose the thymus, and then displace the thymus until the aortic arch appeared clearly. A curved needle was used to assist in pulling the 6-0 suture under the aortic arch. A27G needle was specially processed as a spacer for TAC-ligation and the needle was withdrawn after tight banding. Finally, the chest was closed and the animal was monitored until fully recovered. Sham-operated mice were subjected to the same procedure but without banding. One week after the operation, mice were subject to ultrasound to examine whether the TAC model was successfully established according to previously reported standards (14, 15). Two weeks later, mice were sacrificed by anesthesia overdosing with intra-peritoneal injection of pentobarbital sodium and cervical dislocation, and their ascending aortas were collected for further analysis. For histological examinations, aortas were fixed in 4% formalin, whereas for other analyses the aortas were stored at −80°C until the analysis.

Invasive Measurement of Hemodynamics

Left ventricular (LV) hemodynamics were evaluated before the animals were sacrificed. LV hemodynamics were performed under anesthesia (1.5–2% isofluorane, 2 L/min oxygen flow rate) with mice incubated and ventilated. A 1.0 F catheter (Millar Instruments, Inc., Houston, TX) was inserted into the right carotid artery and advanced to the LV. The parameters of the LV systolic pressure (LVSP), LV end-diastolic pressure (LVEDP), and the maximum and minimum rates of change of the LV pressure (max dp/dt and min dp/dt, respectively) were recorded. The exponential time constant of LV relaxation (τ) was then calculated using Power Lab software (blood pressure module; AD Instruments, Shanghai Trading Co., Shanghai, China).

Echocardiography

Echocardiography was performed in anesthetized (3–5% isoflurane for induction, 1–1.5% for maintenance, with a 0.8 L/min oxygen flow rate) mice at 7 and 14 days after surgery using a VEVO2100 Imaging System (Visual Sonics, ON, Canada) with a 40-MHz probe. After the mice were fixed on a heating plate (37°C), the throat and the chest of mice were depilated, followed by ultrasonic coupling agent treatment. Firstly, the aorta was located in B-Mode, with the presence of the brachiocephalic trunk, the left common carotid artery, and the left subclavian artery as the standard view. After successful positioning and switching to color Doppler Mode, the ligation stenosis was selected as the measurement point, then switched to pulsed-wave Doppler Mode, images were acquired with cine store and frame store for subsequent measurements and calculations. Meanwhile,

the probe was placed at an angle of 45 degrees on each side of the neck to assess blood flow velocities in the right common carotid artery (RCCA) and the left common carotid artery (LCCA), respectively. Subsequently, the long axis and short axis of the heart were acquired in B-Mode, while the measurements were performed under M-Mode for evaluation of cardiac function. All scanning and analysis were performed in a double-blind fashion. Only mice with a right carotid/left carotid (RC/LC) flow ratio within a certain range (5–10) in the TAC group and a sham animal with RC/LC of ∼1 1 week after surgery were included in further analyses (13).

Histomorphometric Study

Two weeks after the procedure, the animals were anesthetized and fixed with 20 ml of 1 × PBS perfusion, followed by 10 ml of 4% paraformaldehyde for 3 min under physiological pressure. The ascending aorta was then excised and further fixed overnight. The tissues were then embedded transversely in paraffin and cut at 4 μm thickness. Cross-sections were stained by hematoxylin and eosin (H&E) (Biosharp, Hefei, China) according to standard protocol. For morphometric analysis, images of H&E stained cross-sections were acquired and recorded with the Olympus BX53® microscope (Center Valley, PA, USA) at 400 × magnifications. The thickness of vascular media was analyzed using ImageJ software (National Institutes of Health, Bethesda, MD). The medial area was defined as the area between the external and internal elastic lamina. The adventitia area was defined as the area between the external elastic lamina and the tunica externa as well as the outermost layer of the vessel. Sections were also stained with Sirius red (Leagene, Beijing, China) to determine the collagen content and with improved Weigert's staining (Leagene, Beijing, China) to detect the expression of elastin. Vascular morphology was determined using an Olympus cell Sens imaging system at 400 × magnification. The expression of elastic fibers was calculated as the area of elastic fibers/area of the media × 100%, and the area of collagen fibers was directly used to show the expression of collagen fibers. We used ImageJ software for all these area measurements, and two sections from one specimen derived from each mouse were selected randomly. Five mice for each group were used in the final analysis.

Immunohistochemistry and Immunofluorescence

Mouse tissues were de-paraffinized, rehydrated, and incubated in 3% hydrogenperoxide for 10 min to block endogenous peroxidase activity. The sections were placed into a pre-boiled citric acid buffer solution for antigen retrieval using routine methods. Next, slides were cooled down and then washed 3 times in 1 × PBS. Sections were then pre-incubated with 5% bovine serum to block non-specific binding for 1 h at room temperature and then incubated with primary antibodies at 4°C overnight. Immunohistochemistry staining was performed with a two-step detection kit (Zhongshan Golden Bridge Biotechnology, Beijing, China) according to the manufacturer's protocol. After three washes with 1 × PBS, the slides were exposed to diaminobenzidine with a DAB IHC Detection Kit (Zhongshan Golden Bridge Biotechnology, Beijing, China) for positive immunostaining and counterstained with Mayer's hematoxylin (Solarbio, Beijing, China). Images were captured with an Olympus BX53® microscope (Center Valley, PA, USA) at 400 × magnifications. We used positive staining to establish proteins of interest, which were evaluated using average optical density (AOD) across the section area. The primary antibodies were α-smooth muscle actin rabbit mAb (α-SMA)(1:700, CST, USA), rabbit anti-collagen I polyclonal antibody(COL-I)(1:500, Bioss, Beijing, China), Angptl1rabbit mAb (1:500, Santa Cruz, USA) and PCNA rabbit mAb (1:8,000, CST, USA), and rabbit anti-TGF-β1 polyclonal antibody (1:500, Bioss, Beijing, China). ImageJ software was used (8–10 randomly chosen sections per sample) for quantification. For immunofluorescence staining, most of the procedures were protected from light. Goat Anti-Rabbit IgG(H+L) Cy3 (1:500, Bioworld, USA) secondary antibodies were added for 1 h at 37°C. Slides were then stained with DAPI (Bestbio, Shanghai, China) according to the manufacturer's instructions. Elastic fibers were monitored with its auto-fluorescence. The images were obtained with a Leica (TCS Sp8) confocal microscopy (Leica, Germany) at 400 × magnification. The primary antibodies used in this study were PCNA rabbit mAb (1:800, CST, USA) and rabbit anti-TGF-β1 polyclonal antibody (1:200, Bioss, Beijing, China).

Western Blotting

Proteins were extracted from the ascending aorta tissues by RIPA buffer (FDbio, Hangzhou, China) which were added with protease inhibitor (Solarbio, Beijing, China) (1:100) and quantified by BCA assay (Thermo Fisher, USA). Protein samples were mixed with a loading buffer and PageRuler™ Prestained Protein Ladder (10–180 kDa) (Thermo Fisher, USA) protein marker and separated by 10% SDS-PAGE, then transferred onto Immobilon-PSQ PVDF Membrane (Millipore, USA). The membranes were incubated at room temperature for 1 h in blocking buffer (5% non-fat powder in Tris-buffered saline and Tween 20 (TBST) buffer). After blocking, the membranes were incubated with primary antibodies overnight at 4°C. The primary antibodies we used were α-SMA rabbit mAb (1:700, CST, USA), rabbit anti-COL-I polyclonal antibody (1:500, Bioss, Beijing, China), Angptl1mouse mAb (1:500, Santa Cruz, USA), PCNA rabbit mAb (1:8,000, CST, USA), rabbit anti-TGF-β1 polyclonal antibody (1:500, Bioss, Beijing, China), GAPDH mouse mAb (1:5,000, Proteintech, USA), and β-Tubulin mouse mAb (1:50,000, Proteintech, USA). After washing 3 times with TBST, they were incubated with goat anti-rabbit IgG-HRP (1:5,000, FDbio, Hangzhou, China) or goat anti-mouse IgG-HRP (1:5,000, FDbio, Hangzhou, China). After another 3 washes with TBST, immunoreactive bands were detected by ECL Substrate (FDbio, Hangzhou, China) and visualized by the chemiluminescence imager GeneGnome XRQ (Syngene, MD). To calculate the relative expression, the intensity of α-SMA, COL-I, and TGF-β1 were normalized to GAPDH, while PCNA were normalized to β-Tubulin using ImageJ.

RNA Sequencing

Total RNA was extracted using the Trizol reagent kit (Invitrogen, Carlsbad, CA, USA) according to the manufacturer's protocol ($n = 4$ per group), 2 weeks after the TAC surgery. RNA quality was assessed on an Agilent 2100 Bioanalyzer (RIN>7) (Agilent Technologies, Palo Alto, CA, USA) and double-checked using RNase free agarose gel electrophoresis. After total RNA was extracted, 1 μg of total RNA was used to prepare the mRNA library. The enriched mRNAs were fragmented into short fragments using a fragmentation buffer and reverse transcribed into cDNA with random primers. Second-strand cDNA were synthesized by DNA polymerase I, RNase H, dNTP (dUTP instead of dTTP). Next, the cDNA fragments were purified with QiaQuick PCR extraction kit(Qiagen, Venlo, The Netherlands), end-repaired, poly(A)-added, and ligated to Illumina sequencing adapters. Then UNG (Uracil-N-Glycosylase) was used to digest the second-strand cDNA. The digested products were size selected by agarose gel electrophoresis, PCR amplified, and sequenced using Illumina HiSeq^{TM} 4000 by Gene De novo Biotechnology Co. (Guangzhou, China). To obtain high-quality clean reads, reads were further filtered by fastp (16) (version 0.18.0). The criteria were as follows: (1) removing reads containing adapters; (2) removing reads containing more than 10% unknown nucleotides (N); (3), and removing low quality reads containing more than 50% of low quality ($Q \leq 20$) bases. The short reads alignment tool Bowtie2 (17) (version 2.2.8) was used for mapping the reads to ribosome RNA (rRNA) database. The rRNA mapped reads were then excluded, and the remaining reads were further assembled for transcriptome analysis. An index of the reference genome (GRCm38.p6) was built, and paired-end clean reads were mapped to the reference genome using HISAT2 (18) (version 2.1.0) with "rna-strandness RF" and other parameters set as a default. Transcript abundance was quantified by StringTie (19, 20) (version 1.3.4), using a reference-based approach. For each transcription region, an FPKM (fragment per kilo base of transcript per million mapped reads) value was calculated to quantify its expression abundance and variations.

Sequencing Data Analyses

All sequencing raw data were deposited at Sequence Read Archive (NCBI SRA database) with the submission ID SRP278673. Differentially expressed transcripts (DEGs) were performed by DESeq2 (21) software between two different groups and by edgeR (22) between two samples. We considered mRNA with a fold change ≥2 and a false discovery rate (FDR) < 0.05 in comparison as significant DEGs. Differentially expressed coding RNAs were then subjected to enrichment analysis of GO functions and KEGG pathways. All DEGs were mapped to GO terms in the Gene Ontology database (http://www.geneontology.org/). GO enrichment analysis provided all GO terms that were significantly enriched in DEGs, comparing them to the genome background and filtering the DEGs that corresponded to biological functions. The calculated *p*-value was analyzed with FDR Correction, using FDR ≤ 0.05 as a threshold. The GO terms that fulfilled this condition were defined as significantly enriched GO terms in DEGs. This analysis was able to uncover the main biological functions of DEGs. Pathway enrichment analysis using the KEGG database (23) identified significantly enriched metabolic or signal transduction pathways in DEGs. The Protein-Protein interaction (PPI) network was outlined using String v10 (24), which indicated genes as nodes and interaction as lines in the network. The network file was visualized using Cytoscape (v3.7.1) (25) software to present a core and hub gene biological interaction.

TABLE 1 | Primers of quantitative real-time PCR.

Primer names	Forward (5′-3′)	Reverse (5′-3′)
Runx2	CCTTCAAGGTTGTAGCCCTC	GGAGTAGTTCTCATCATTCCCG
Agtr2	TCCTGGGATTCACCAACAGC	CTCTCTTGCCTTGGAGCCAA
Itga2	TTCAGAGCAGAGTTTAGACCTG	AACACTTCTGCACTTCGTTTAC
Runx1	CCATCACCGTCTTTACAAATCC	ATCATCTAGTTTCTGCCGATGT
Itga8	CCCGATGGTGACTGGAACAA	TACACGCTCGAAGTTGCTGT
Agt	ATGAACTTGCCACTGGAGGG	GATGCTGTTGTCCACCCAGA
Gapdh	GGTTGTCTCCTGCGACTTCA	TGGTCCAGGGTTTCTTACTCC

qRT-PCR

Isolated RNAs were also subjected to qRT-PCR validation. RNAs were reverse-transcribed to cDNA by using a Prime-Script RT reagent Kit (TaKaRa, Dalian, China). Real-time PCR was performed using Light Cycler 480 II equipment (Roche Diagnostics, Basel, Switzerland). The primers used in this study are listed in **Table 1**. The reliability of primer sets and the quality of qRT-PCR experiments were validated by a single peak melt curve representing a single PCR product. The expression levels of target mRNAs were calculated by using the 2-ΔΔCt method by normalizing the expression vs. that of Gapdh.

Statistical Analysis

The data were analyzed using SPSS, version 20.0 (SPSS, Inc. Chicago, IL). Quantitative data were presented as the mean ± SEM (standard error of the mean). The statistical significance between two experimental groups was analyzed using an unpaired two-sided *t*-test and $P < 0.05$ was considered as statistically significant.

RESULTS

Increased Ascending Aortic Pressure and Remodeling of the Aortic Wall in the TAC Model

Eight-week-old C57BL/6J mice were used to establish the TAC model by ligating between the brachiocephalic trunk and the left common carotid artery (LCCA) (**Figure 1A**). The blood flow velocity of the aortic ligated site (**Supplementary Figure 1A**), right common carotid artery (RCCA) (upper panel of **Figure 1B**), and LCCA (lower panel of **Figure 1B**) were determined by ultrasound 1 week after surgery. The blood flow velocity at the aortic ligation site of the TAC group was ∼2.9 times higher than that of the sham group (**Supplementary Figure 1B**), indicating

increased aortic pressure in the TAC group. TAC with RC/LC of 5–10 and the Sham ∼ 1 (**Figure 1C**) were included in subsequent experiments. Two weeks after the operation, the diameter of the aortic ligament near the proximal end was measured by ultrasound (**Supplementary Figure 1C**), and the TAC group was 0.19 mm wider than the sham group on average (**Supplementary Figure 1D**).

Before sacrificing the mice at 2 weeks, they were subjected to an invasive catheter to detect pressure of left ventricle to reflect the pressure of the proximal end of ascending aorta. The results indicated that Left ventricular systolic pressure (LVSP) in the TAC group was significantly higher than the sham group (**Supplementary Figures 2A,B**). The maximum rate of change of the left ventricular pressure (dp/dt max) (**Supplementary Figure 2C**) and contractility (**Supplementary Figure 2D**) were also increased, suggesting enhanced systolic function of the heart in the TAC group., However, the indicators for diastolic function such as the left ventricular end-diastolic pressure (LVEDP) (**Supplementary Figure 2B**), minimum rate of change of the left ventricular pressure (dp/dt min) (**Supplementary Figure 2C**) and exponential time constant of relaxation (τ) (**Supplementary Figure 2E**) had no significant changes, suggesting no significant change in diastolic function in TAC treated mice.

The ascending aorta in the TAC group was significantly thickened when compared to the sham group 2 weeks after the TAC procedure, no aneurysms and thrombi were detected with microscopic examination. Morphological analysis revealed that the ascending aorta median thickness was significantly increased in the TAC group as much as 80.65% as compared to the sham group (**Figure 1D**). To further illustrate the remodeling of the aorta by TAC, Weigert's staining was performed to determine the elastic fibers of the media in TAC treated mice's ascending aorta (**Figure 1E**), indicating decreased compliance of the media in TAC group. Sirius red staining showed that collagen was dramatically accumulated in the ascending aorta of the surgery group, especially in the adventitia. The adventitia collagen deposition area was about 2.55 times larger than that of the sham group (**Figure 1F**). Of note, these histological changes induced by TAC are similar to those phenotypes observed in the ascending aorta with AngII infusion (26, 27) and in spontaneously hypertensive rats according to our previous study (28).

Transcriptional Changes Identified by RNA-Seq in TAC Models

The RNA-Seq was performed with ascending aortas dissected from TAC or sham control mice, respectively. Using well-established criterion including fold change> 2.0, $P < 0.05$ and FDR < 0.05, a total of 1,019 differentially expressed mRNAs were identified. Among them, 722 mRNAs were up-regulated and 297 were down-regulated in the TAC group (**Figure 2A**). The detailed information of DE mRNAs was listed in Additional file 1. A Volcano map was built with significantly differentially expressed genes (DEGs) between TAC and sham groups (**Figure 2B**), genes involved in immune response or ECM turnover, such as *Scube1, Scube2, C3ar1,C5ar2, Tlr6, Tlr7 and Col11a1,Col1a2, Itga11,* were highlighted. Interestingly, it is reported that Scube1is expressed in both mouse and human endothelial cells and over-expressed in the plasma of essential hypertension patients (29, 30), making it as a potential biomarker for hypertension diagnosis. Hierarchical clustering showed TAC and sham control were well-distinguished by differently expressed mRNA, with all the subjects correctly classified (**Figure 2C**). PCA analysis also revealed distinct expression profile of DEGs between the TAC and sham groups (**Supplementary Figure 3**).

qRT-PCR was performed to validate RNA deep sequencing results. A total of 6 mRNAs (*Runx2, Agtr2, Itga2, Runx1, Itga8, Ag*t) were randomly selected for validation. The qRT-PCR results showed that the expression patterns of these selected mRNAs were perfectly in consistent with the RNA deep sequencing data (**Supplementary Figure 4**).

Functional Enrichment Assay of Transcripts in TAC Models

We then analyzed the molecular functions of differentially expressed mRNAs using GO and KEGG databases. The top GO enrichment terms of the biological process were immune system process and cell surface receptor signaling pathway (**Figure 3A**); the top enrichment terms for cellular component were extracellular region, extracellular matrix, and collagen-containing extracellular matrix (**Supplementary Figure 5A**); the top enrichment terms for molecular function were extracellular matrix structural constituent and protein binding (**Supplementary Figure 5C**). In addition, the inflammatory response, lymphocyte activation, and regulation of response to stimulus, were also up-regulated in the TAC group as revealed by GO enrichment analysis. For those down-regulated transcripts, the most enriched term of the biological process was the oxidation-reduction process (**Figure 3B**); the mitochondrial part and mitochondrion were the most enriched terms for cellular component (**Supplementary Figure 5B**); and the oxido-reductase activity as well as cofactor binding were the top enriched terms for molecular function (**Supplementary Figure 5D**).

To further analyze the DEGs, KEGG pathway enrichment was used to analyze those up-regulated transcripts (**Figure 3C**) or down-regulated transcripts (**Figure 3D**), respectively. Our result suggested that cytokine-cytokine receptor interaction, ECM-receptor interaction, NF-kappa B signaling pathway were highly activated and enriched in TAC group, in contrast, oxidative phosphorylation, cardiac muscle contraction, and vascular smooth muscle contraction were inhibited in the TAC group. Intriguingly, the p53 signaling pathway was also up-regulated in KEGG enrichment analysis. These results collectively indicated that immune response, stress/stimulus-related processes played a vital role in pressure overload induced ascending aorta remodeling.

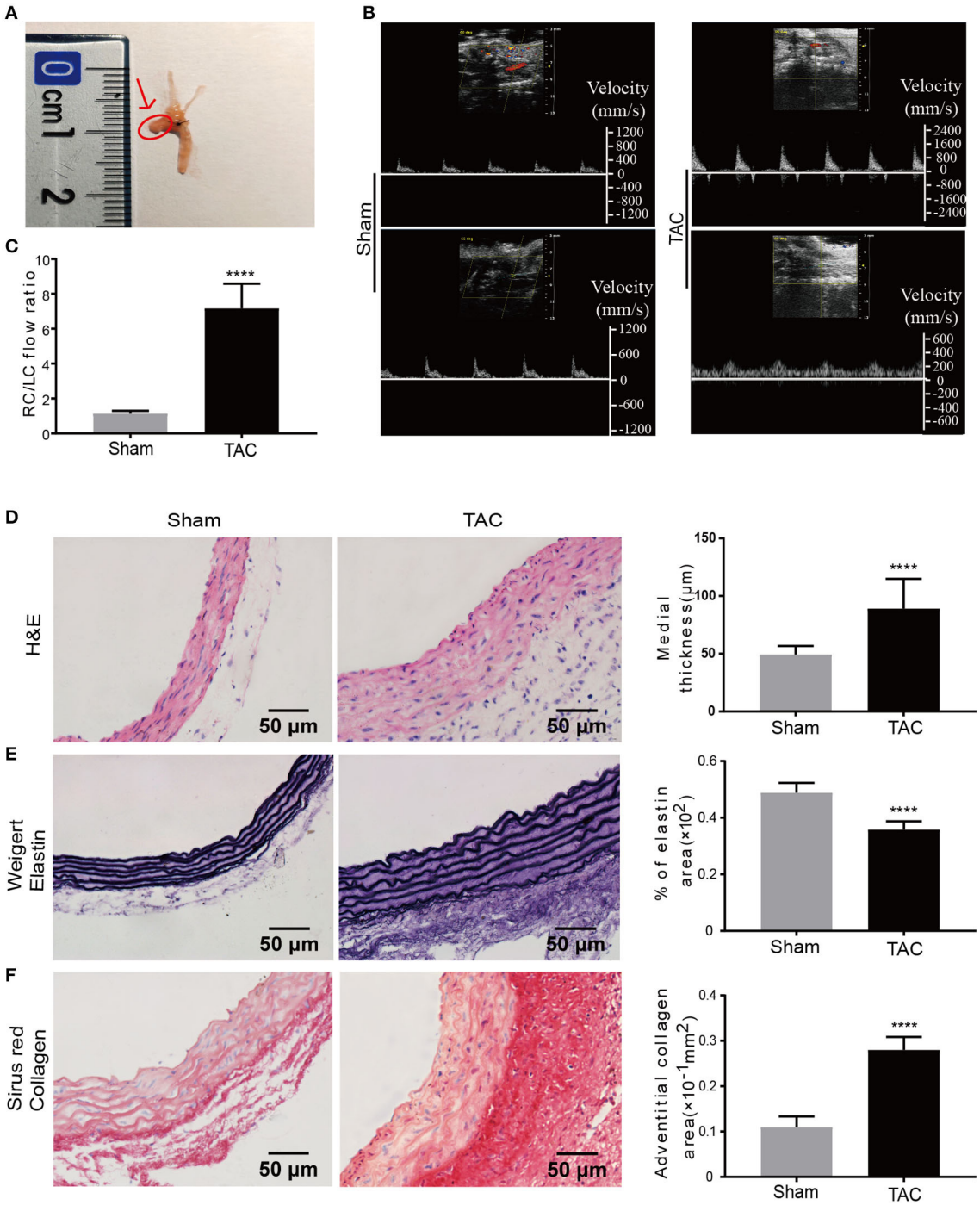

FIGURE 1 | Increased blood pressure and remodeling of the aortic wall in established TAC model. **(A)** TAC was constructed by ligation between the brachiocephalic trunk and LCCA. Tissues used for all analysis are indicated by the arrow and the red circle; **(B)** Blood flow velocity measurement at RCCA and LCCA of the sham or TAC groups, respectively; **(C)** Right carotid /left carotid (RC/LC) flow ratio of TAC and sham group; **(D–F)** Representative images and quantification analysis of hematoxylin and eosin (H&E) staining **(D)**, Weigert's staining **(E)**, and Sirius red staining **(F)**; $n = 6$ per group. Original magnification: ×400. ****$P < 0.0001$.

The Interactions Network of Most Significant DEGs in the TAC Model

The KEGG analysis was further performed in the top 200 up-regulated and top 200 down-regulated DEGs, and the results showed that the major enrichment pathways were ECM-receptor interactions (e.g., *Itga2b, Tnn, Thbs1,* and *Itga11*), complement and coagulation cascades (e.g., *Fgg, C7, A2m,* and *Gpx1*) and vascular smooth muscle contraction (e.g., *Pla2g5, Myh11, Myl6,*

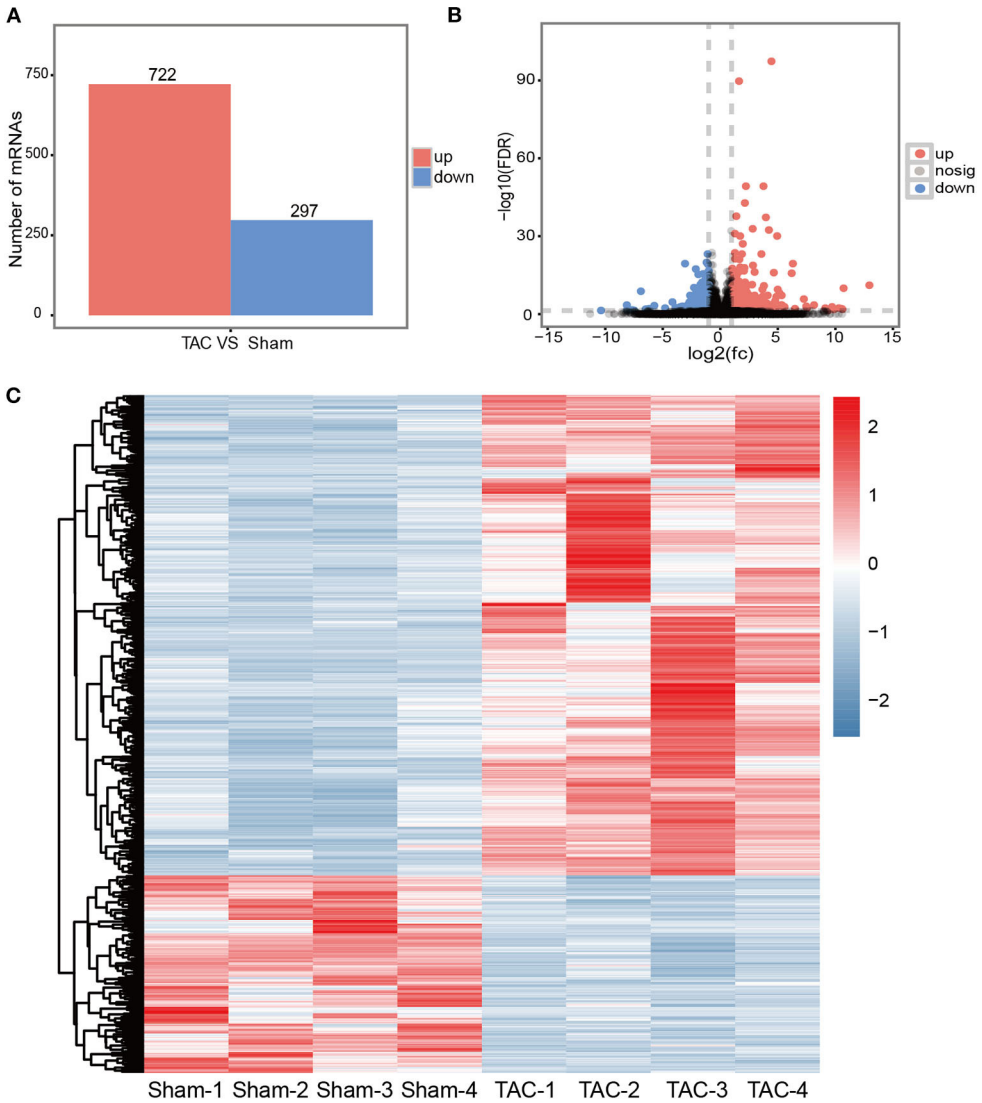

FIGURE 2 | Transcriptional changes in TAC models. **(A)** An overview of DEGs in TAC models; **(B)** Volcano plot illustrating DEGs between the TAC and sham groups. Up-regulated mRNAs are labeled in red, down-regulated in blue, and the rest in gray; **(C)** Hierarchically clustered heat map illustrating DEGs between TAC and sham groups, fold change >2.0, $P < 0.05$ and FDR < 0.05, $n = 4$ per group.

Kcnmb4, and *Mylk4*) (**Figure 4A**). We then used the String database to establish a protein-protein interaction (PPI) network using top 200 up-regulated and top 200 down-regulated DEGs (**Figure 4B**). Accordingly, those up-regulated DEGs such as *Cxcr6, Cxcl3, Tlr3, Thbs1, Col11a1, Angptl1, Mmp12, Itga11, Bmper, Col8a1,* and *Piezo2,* and those down-regulated DEGs like *Alb, Kng2, Itga2b, Cox5b, Cox6a1*, and *Fgg* are promising targets for further investigation (**Figure 4B**).

Validation of DEGs Revealed by RNA-Seq

To validate our findings of those transcriptional changed DEGs, we then analyzed the protein expression level using multiple approaches. First, we determined the cell proliferation and immune response *in situ* by staining with PCNA and TGF-β1. In line with the previous finding, we observed a significantly increased expression of PCNA and TGF-β1 in adventitia in the TAC model (**Supplementary Figure 6**). Intriguingly, α-smooth muscle actin (α-SMA), a surface marker of contractile smooth muscle cells, was significantly decreased in TAC model (**Figures 5A,B**); in contrast, Collagen I (COL-I) (**Figures 5A,C**), a Angptl1 (**Figures 5A,D**) TGF-β1 (**Figures 5A,E**) and PCNA (**Figures 5F,G**) were highly expressed in the ascending aorta where remodeling occurred in TAC model as indicated by immuno-blot analysis. Immunohistochemistry analysis with ascending aorta tissues also showed that down-regulation of α-SMA (**Figure 5H**), but up-regulation of COL-1 (**Figure 5I**), TGF-β1 (**Figure 5L**), Angptl1 (**Figure 5J**) and PCNA (**Figure 5K**) in TAC model as compared to sham surgery treated mice.

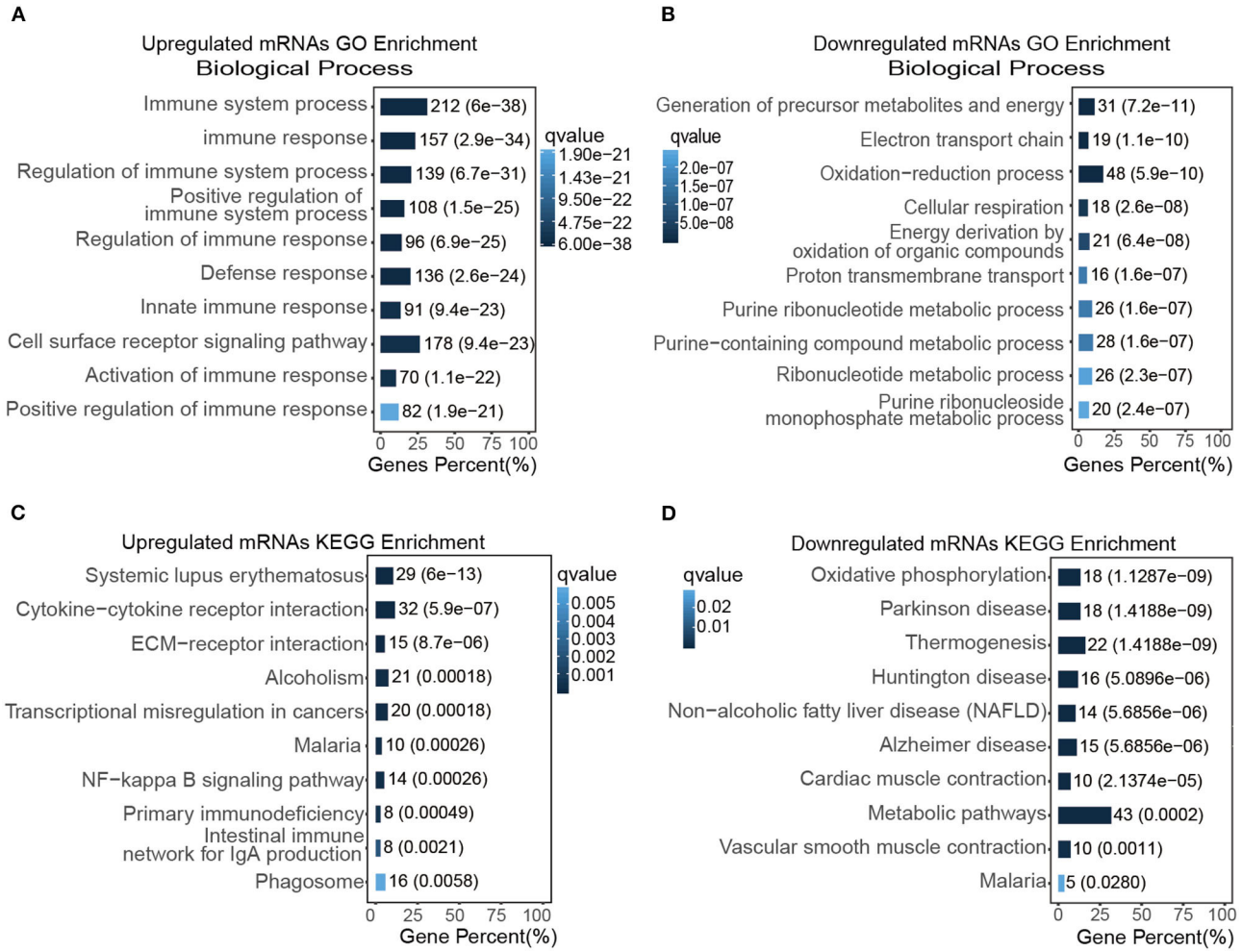

FIGURE 3 | Functional enrichment assay of transcripts in the TAC model. **(A,B)** The top GO enriched biological functions of up **(A)** and down-regulated DEGs **(B)**, respectively; **(C,D)** the top KEGG enrichment items of up **(C)** and down-regulated DEGs **(D)**, respectively.

These results collectively support previous RNA-seq data, which indicates that the immune response and ECM-receptor interaction played a crucial role during high blood pressure induced aortic remodeling.

DISCUSSION

It is widely accepted that the main pathological outcome of hypertension is vascular remodeling. In principle, when hemodynamic changes occur, the shear force decreases, leading to the activation of vascular endothelial cell signaling transduction. This then induces a cascade of downstream responses, such as medial smooth muscle cells and adventitial fibroblasts morphological transformation, infiltration of early inflammatory cells by adventitial cells (31–33). During this process, smooth muscle cells are switched from contractile types to synthetic types, which is the iconic event of vascular remodeling (34–36). However, the underlying molecular mechanism of how hypertension induces vascular remodeling and ultimately organ damage remains unclear. Therefore, the early intervention of this process, by targeting those key regulators or pathways, serves as a promising strategy to delay or prevent hypertension associated with pathological consequences.

Recent studies have shown that the TAC model is an efficient system to recapitulate the infiltration of adventitial macrophages and conversion of adventitial fibroblasts to myofibroblasts, with significant vascular remodeling (37, 38). In response to vascular pressure or injury, vascular adventitia fibroblasts are usually the first sensor to sense hemodynamic changes (39), but how the fibroblasts that are located in the outer membrane transform into myofibroblasts is not fully understood. It is reported that adventitia fibroblasts undergo phenotypic transformation upon sensing vascular injury or blood flow stress and participate in vascular remodeling (38). Activated myofibroblasts not only synthesize large amounts of ECM but also affect the phenotypic transformation, proliferation, apoptosis, and migration of VSMC. When treated with Ang-II, VSMCs proliferate and migrate, and the expression of

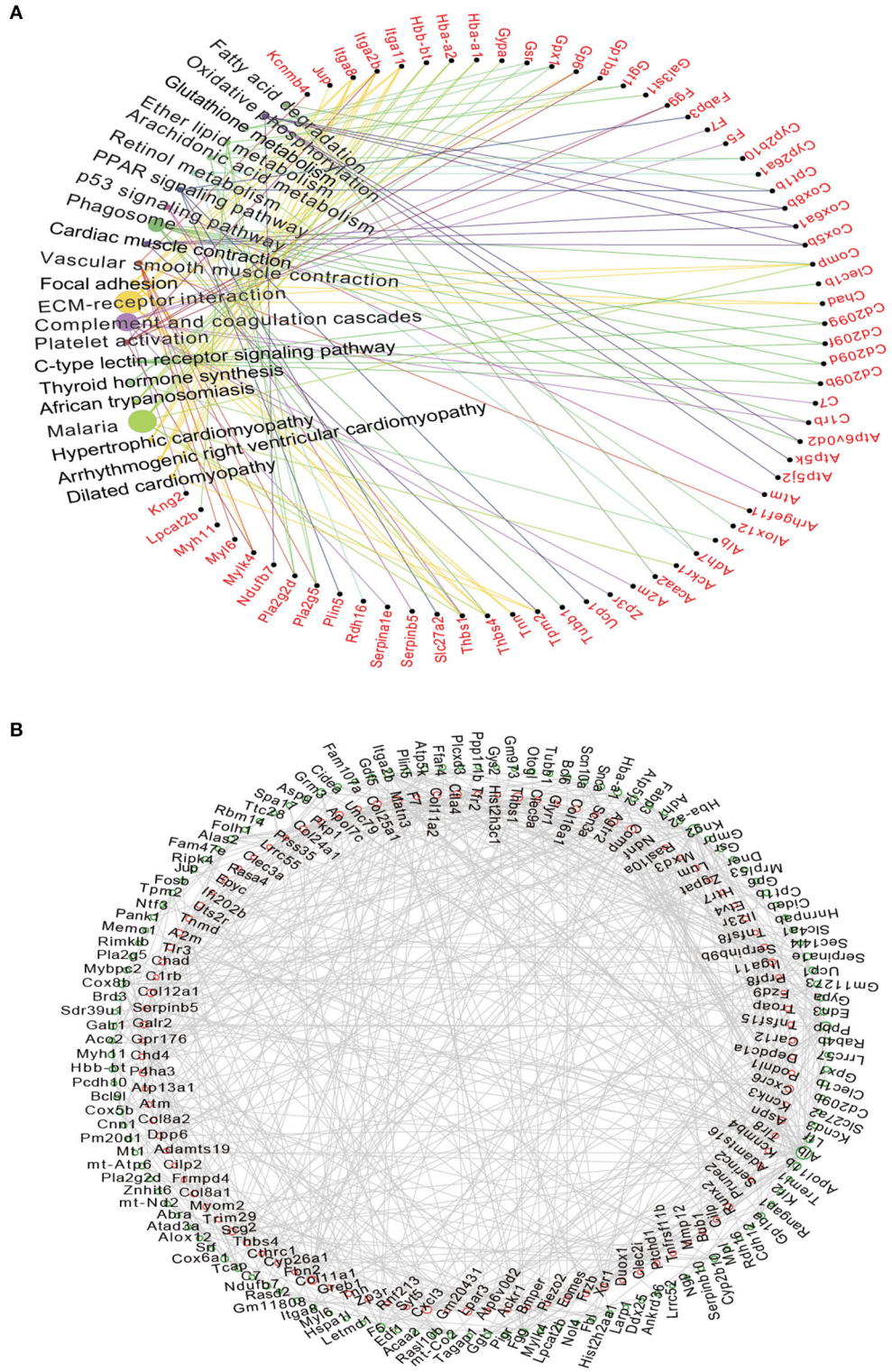

FIGURE 4 | The Network analysis of DEGs and predicted PPI networks in the TAC group. **(A)** KEGG analysis suggested that differentially mRNAs were mainly targeted to the ECM-receptor interaction and Complement and coagulation cascades. Circle size represented degree; **(B)** The network showed the potential relationship between the top 200 differentially up-regulated and down-regulated expressed mRNAs, Up-regulated mRNAs are displayed in the red circle, down-regulated in the green circle.

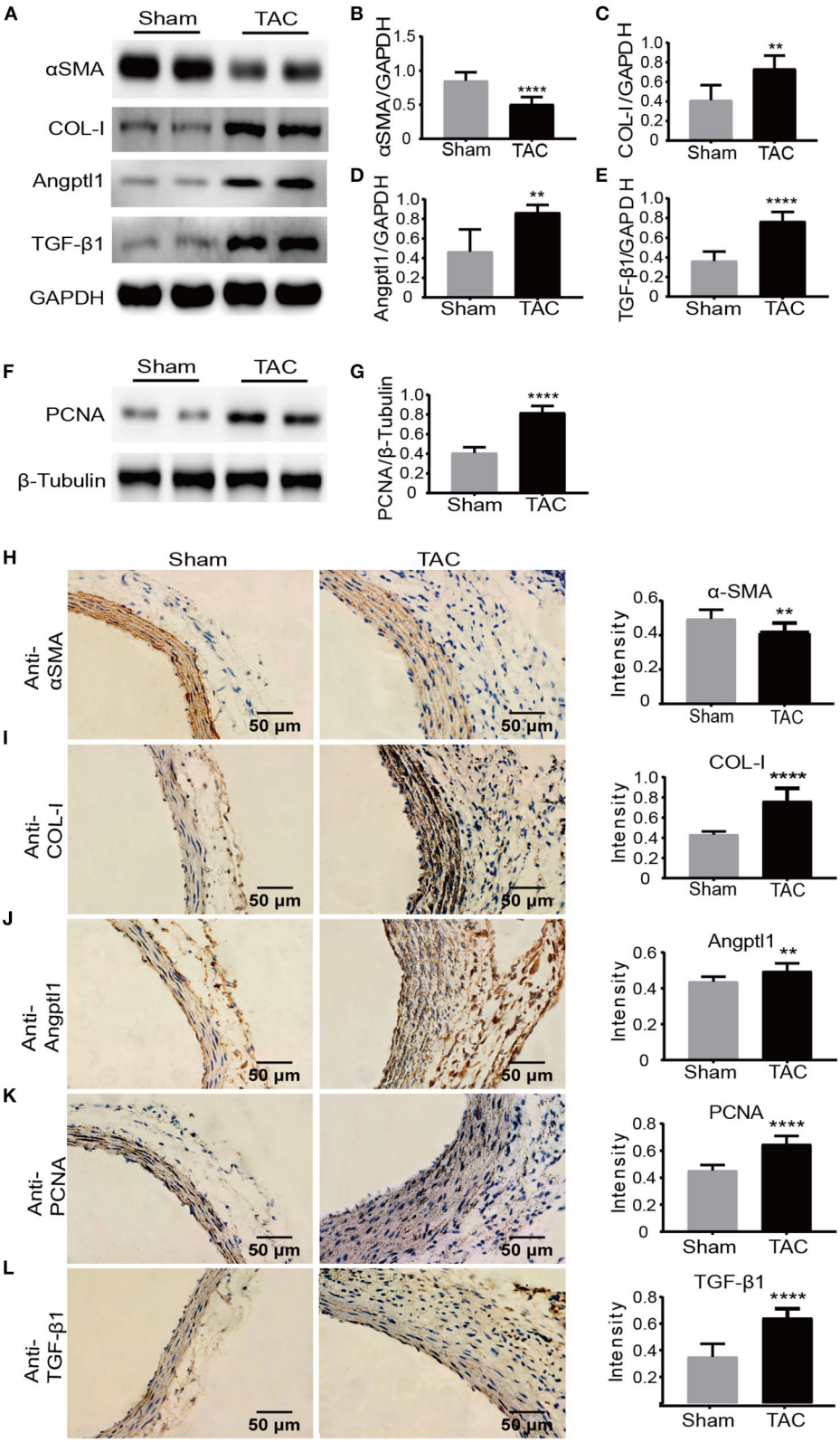

FIGURE 5 | Protein level validation of DEGs revealed by RNA-seq. **(A–G)** Western blot analysis of α-SMA, COL-I, Angptl1, TGF-β1, and PCNA in the TAC and sham groups. GAPDH and β-Tubulin were used as endogenous loading controls. Lysates were prepared from ascending aortas of sham-operated or TAC mice, $n = 5$ per group. The experiments were repeated 3 times independently; **(H–L)** Immunohistochemistry and quantification analysis of α-SMA, COL-I, Angptl1, TGF-β1, and PCNA in ascending aortas derived from TAC or sham controlled mice. $n = 6$ per group. Original magnification: ×400. Scale bars: 50 μm. $^{**}P < 0.01$, $^{****}P < 0.0001$.

α-SMA, a marker for the contractile phenotype of VSMC and myofibroblasts, was decreased (40). A previous study showed that in the TAC model, the expression of α-SMA in the adventitia was increased, but no significant difference was detected in the media 2 weeks after TAC surgery (13). Paradoxically, in our study, the RNA-seq data, protein level analysis as well as *in situ* immunohistochemistry indicated that α-SMA were down-regulated in the ascending aorta in the TAC group as compared to the sham group. It is speculated that the phenotypic transformation of media smooth muscle cells and adventitia fibroblasts might contribute to the different expression patterns of α-SMA in the media and adventitia of remodeling arteries.

In our study, we successfully established a TAC model with morphological and immunohistological validation of vascular tissues, and these tissues were directly subjected to RNA sequencing analysis. Our results showed that upon vascular remodeling, the genes related to extracellular matrix transformation and smooth muscle cell contraction were significantly changed, not surprisingly, inflammation-related genes were also significantly enriched in our analysis, which was consistent with the classical theory that inflammation played an essential role in hypertension-induced vascular remodeling (10) and suggested that anti-inflammation might be a useful strategy to inhibit hypertension associated pathological consequences. Nevertheless, it would be more convincing to use other hypertension or vascular remodeling models to investigate whether our findings were representative. Ultimately, clinical studies with early stage hypertension patients are required to validate these findings.

Among those differentially expressed genes, we observed that many of them were involved in stress/stimulus/immune pathways. For instance, a classical immune response regulator, TGF-β1 was significantly up-regulated at both transcriptional and protein levels. High TGF-β1 expression usually indicated an immune-suppressive micro-environment, which suggested that the tissues of vascular remodeling might lack proper immune surveillance, e.g., increased infiltration of macrophages or regulatory T cells, suggesting that targeting the immune system using small molecular chemicals or mono-antibody might also be useful to treat hypertension-related complications at an early stage. Whether this method could ameliorate vascular remodeling in the TAC model requires further investigation.

The main shortcomings of our study were the age factor and the inadequate time frame. Hypertension is rarely be observed in the young mice we used for the current study and it is also known that mice have an age-related response to cardiac pathologies (41); furthermore, the time frame to perform the TAC study might have been too short to reflect the chronic changes that will occur within the remodeled vessels, thus, a time-dependent study might be necessary to properly mimic clinical phenotype progression. On the other hand, most of the current available classical animal models for the study of hypertension were mainly conducted in aged mice over a longer time-frame. Therefore, it is unfeasible to investigate early pathological events and evaluate whether early interventions would delay or prevent hypertension development. Importantly, the TAC model used for the current study faithfully mimics those early hypertensive pathological changes, e.g., increased blood pressure and aortic remodeling as early as 2 weeks after the ligation surgery. Moreover, a big advantage of this model was that it could be used to quickly estimate if clinically available drugs/drug candidates/herbs/small interfering RNAs could ameliorate such pathological changes, providing a rapid and efficient platform to screen potential therapeutic strategies which can be further validated with other classical hypertension models or clinical trials.

Taken together, we identified a different expressed mRNAs profile, which was associated with the progression of aortic remodeling in the TAC model. These differentially expressed genes might function and interact mutually as a network to mediate hypertension-induced vascular remodeling. Our research suggests that manipulating inflammation and targeting the immune system are potential therapeutic strategies to prevent aortic remodeling induced by blood pressure overload.

DATA AVAILABILITY STATEMENT

All sequencing raw data were submitted and deposited at Sequence Read Archive (NCBI SRA database) with the submission ID PRJNA659049.

ETHICS STATEMENT

The animal study was reviewed and approved by Institutional Animal Care and Use Committee of Southern Medical University.

AUTHOR CONTRIBUTIONS

LZ and JX contributed to the experimental design and manuscript draft. XZ and TF contributed to the experimental design and implementation. X-XZ, BS, QZ, and YC contributed to the data analysis and manuscript draft. HL, FZ, TW, DC, and XL contributed to the experimental implementation and data analysis. All authors reviewed and approved the final manuscript.

FUNDING

This work was supported by the National Natural Science Foundation of China (81800371 and 81974266), Southern Medical University Science Foundation For Youths (PY2017N010), the Major Program of Health Care and Innovation of Guangzhou Project (201704020213), and College Student's Innovative Entrepreneurial Training Plan Program (201912121012).

ACKNOWLEDGMENTS

We thank all the colleagues in our department for their thoughtful discussion and kind suggestions.

SUPPLEMENTARY MATERIAL

The Supplementary Material for this article can be found online at: https://www.frontiersin.org/articles/10.3389/fcvm.2020.581362/full#supplementary-material

REFERENCES

1. Kearney PM, Whelton M, Reynolds K, Muntner P, Whelton PK, He J. Global burden of hypertension: analysis of worldwide data. *Lancet.* (2005) 365:217–23. doi: 10.1016/S0140-6736(05)17741-1
2. Saklayen MG, Deshpande NV. Timeline of history of hypertension treatment. *Front Cardiovasc Med.* (2016) 3:3. doi: 10.3389/fcvm.2016.00003
3. Pierdomenico SD, Di Nicola M, Esposito AL, Di Mascio R, Ballone E, Lapenna D, et al. Prognostic value of different indices of blood pressure variability in hypertensive patients. *Am J Hypertens.* (2009) 22:842–7. doi: 10.1038/ajh.2009.103
4. Mills KT, Bundy JD, Kelly TN, Reed JE, Kearney PM, Reynolds K, et al. Global disparities of hypertension prevalence and control: a systematic analysis of population-based studies from 90 countries. *Circulation.* (2016) 134:441–50. doi: 10.1161/CIRCULATIONAHA.115.018912
5. Viereck J, Kumarswamy R, Foinquinos A, Xiao K, Avramopoulos P, Kunz M, et al. Long noncoding RNA chast promotes cardiac remodeling. *Sci Transl Med.* (2016) 8:326ra22. doi: 10.1126/scitranslmed.aaf1475
6. Laurent S, Boutouyrie P. The structural factor of hypertension: large and small artery alterations. *Circ Res.* (2015) 116:1007–21. doi: 10.1161/CIRCRESAHA.116.303596
7. van Varik BJ, Rennenberg RJMW, Reutelingsperger CP, Kroon AA, de Leeuw PW, Schurgers LJ. Mechanisms of arterial remodeling: lessons from genetic diseases. *Front Genet.* (2012) 3:290. doi: 10.3389/fgene.2012.00290
8. Retailleau K, Duprat F, Arhatte M, Ranade SS, Peyronnet R, Martins JR, et al. Piezo1 in smooth muscle cells is involved in hypertension-dependent arterial remodeling. *Cell Rep.* (2015) 13:1161–71. doi: 10.1016/j.celrep.2015.09.072
9. Yang L, Yang F, Zhao H, Wang M, Zhang Y. Circular RNA circCHFR facilitates the proliferation and migration of vascular smooth muscle via miR-370/FOXO1/Cyclin D1 pathway. *Mol Ther Nucleic Acids.* (2019) 16:434–41. doi: 10.1016/j.omtn.2019.02.028
10. McMaster WG, Kirabo A, Madhur MS, Harrison DG. Inflammation, immunity, and hypertensive end-organ damage. *Circ Res.* (2015) 116:1022–33. doi: 10.1161/CIRCRESAHA.116.303697
11. Chen J, Wu J, Li L, Zou Y, Zhu D, Gao P. Effect of an acute mechanical stimulus on aortic structure in the transverse aortic constriction mouse model. *Clin Exp Pharmacol Physiol.* (2011) 38:570–6. doi: 10.1111/j.1440-1681.2011.05544.x
12. Xu R, Zhang Z, Chen L, Yu H, Guo S, Xu Y, et al. Ascending aortic adventitial remodeling and fibrosis are ameliorated with Apelin-13 in rats after TAC via suppression of the miRNA-122 and LGR4-β-catenin signaling. *Peptides.* (2016) 86:85–94. doi: 10.1016/j.peptides.2016.10.005
13. Kuang S, Geng L, Prakash SK, Cao J, Guo S, Villamizar C, et al. Aortic remodeling after transverse aortic constriction in mice is attenuated with AT1 receptor blockade. *Arterioscler Thromb Vasc Biol.* (2013) 33:2172–9. doi: 10.1161/ATVBAHA.113.301624
14. Eichhorn L, Weisheit CK, Gestrich C, Peukert K, Duerr GD, Ayub MA, et al. A closed-chest model to induce transverse aortic constriction in Mice. *J Visual Exp.* (2018) 134:57397. doi: 10.3791/57397
15. Zaw AM, Williams CM, Law HKW, Chow BKC. Minimally invasive transverse aortic constriction in Mice. *J Visual Exp.* (2017) 121:55293. doi: 10.3791/55293
16. Chen S, Zhou Y, Chen Y, Gu J. fastp: an ultra-fast all-in-one FASTQ preprocessor. *Bioinformatics.* (2018) 34:i884–90. doi: 10.1093/bioinformatics/bty560
17. Langmead B, Salzberg SL. Fast gapped-read alignment with Bowtie 2. *Nat Methods.* (2012) 9:357–9. doi: 10.1038/nmeth.1923
18. Kim D, Langmead B, Salzberg SL. HISAT: a fast spliced aligner with low memory requirements. *Nat Methods.* (2015) 12:357–60. doi: 10.1038/nmeth.3317
19. Pertea M, Pertea GM, Antonescu CM, Chang T, Mendell JT, Salzberg SL. StringTie enables improved reconstruction of a transcriptome from RNA-seq reads. *Nat Biotechnol.* (2015) 33:290–5. doi: 10.1038/nbt.3122
20. Pertea M, Kim D, Pertea GM, Leek JT, Salzberg SL. Transcript-level expression analysis of RNA-seq experiments with HISAT, StringTie and Ballgown. *Nat Protoc.* (2016) 11:1650–67. doi: 10.1038/nprot.2016.095
21. Love MI, Huber W, Anders S. Moderated estimation of fold change and dispersion for RNA-seq data with DESeq2. *Genome Biol.* (2014) 15:550. doi: 10.1186/s13059-014-0550-8
22. Robinson MD, McCarthy DJ, Smyth GK. edgeR: a bioconductor package for differential expression analysis of digital gene expression data. *Bioinformatics.* (2010) 26:139–40. doi: 10.1093/bioinformatics/btp616
23. Kanehisa M, Araki M, Goto S, Hattori M, Hirakawa M, Itoh M, et al. KEGG for linking genomes to life and the environment. *Nucleic Acids Res.* (2008) 36:D480–4. doi: 10.1093/nar/gkm882
24. Szklarczyk D, Franceschini A, Wyder S, Forslund K, Heller D, Huerta-Cepas J, et al. STRING v10: protein-protein interaction networks, integrated over the tree of life. *Nucleic Acids Res.* (2015) 43:D447–52. doi: 10.1093/nar/gku1003
25. Shannon P, Markiel A, Ozier O, Baliga NS, Wang JT, Ramage D, et al. Cytoscape: a software environment for integrated models of biomolecular interaction networks. *Genome Res.* (2003) 13:2498–504. doi: 10.1101/gr.1239303
26. Tieu BC, Lee C, Sun H, Lejeune W, Recinos AR, Ju X, et al. An adventitial IL-6/MCP1 amplification loop accelerates macrophage-mediated vascular inflammation leading to aortic dissection in mice. *J Clin Invest.* (2009) 119:3637–51. doi: 10.1172/JCI38308
27. Daugherty A, Rateri DL, Charo IF, Owens AP, Howatt DA, Cassis LA. Angiotensin II infusion promotes ascending aortic aneurysms: attenuation by CCR2 deficiency in apoE-/- mice. *Clin Sci.* (2010) 118:681–9. doi: 10.1042/CS20090372
28. Zhang X, Wang X, Hu F, Zhou B, Chen H, Zha D, et al. A novel hydrodynamic approach of drag-reducing polymers to improve left ventricular hypertrophy and aortic remodeling in spontaneously hypertensive rats. *Int J Nanomed.* (2016) 11:6743–51. doi: 10.2147/IJN.S119607
29. Tu C, Su Y, Huang Y, Tsai M, Li L, Chen Y, et al. Localization and characterization of a novel secreted protein SCUBE1 in human platelets. *Cardiovasc Res.* (2006) 71:486–95. doi: 10.1016/j.cardiores.2006.04.010
30. Özkan G, Ulusoy S, Menteşe A, Karahan SC, Cansiz M. New marker of platelet activation, SCUBE1, is elevated in hypertensive patients. *Am J Hypertens.* (2013) 26:748–53. doi: 10.1093/ajh/hpt007
31. An SJ, Liu P, Shao TM, Wang ZJ, Lu HG, Jiao Z, et al. Characterization and functions of vascular adventitial fibroblast subpopulations. *Cell Physiol Biochem.* (2015) 35:1137–50. doi: 10.1159/000373939
32. Niu C, Wang X, Zhao M, Cai T, Liu P, Li J, et al. Macrophage foam cell–derived extracellular vesicles promote vascular smooth muscle cell migration and adhesion. *J Am Heart Assoc.* (2016) 5:e004099. doi: 10.1161/JAHA.116.004099
33. Tinajero MG, Gotlieb AI. Recent developments in vascular adventitial pathobiology: the dynamic adventitia as a complex regulator of vascular disease. *Am J Pathol.* (2020) 190:520–34. doi: 10.1016/j.ajpath.2019.10.021
34. Liu M, Gomez D. Smooth muscle cell phenotypic diversity. *Arterioscler Thromb Vasc Biol.* (2019) 39:1715–23. doi: 10.1161/ATVBAHA.119.312131
35. Shi N, Mei X, Chen SY. Smooth muscle cells in vascular remodeling. *Arterioscler Thromb Vasc Biol.* (2019) 39:e247–52. doi: 10.1161/ATVBAHA.119.312581
36. Wang Y, Dong C, Peng G, Huang H, Yu Y, Ji Z, et al. MicroRNA-134-5p regulates media degeneration through inhibiting VSMC phenotypic switch and migration in thoracic aortic dissection. *Mol Ther Nucleic Acids.* (2019) 16:284–94. doi: 10.1016/j.omtn.2019.02.021
37. Lehoux S. Adventures in the adventitia. *Hypertension.* (2016) 67:836–8. doi: 10.1161/HYPERTENSIONAHA.116.06375
38. Sartore S, Chiavegato A, Faggin E, Franch R, Puato M, Ausoni S, et al. Contribution of adventitial fibroblasts to neointima formation and vascular remodeling: from innocent bystander to active participant. *Circ Res.* (2001) 89:1111–21. doi: 10.1161/hh2401.100844
39. Tong Y, Ye C, Ren X, Qiu Y, Zang Y, Xiong X, et al. Exosome-mediated transfer of ACE (Angiotensin-Converting Enzyme) from

adventitial fibroblasts of spontaneously hypertensive rats promotes vascular smooth muscle cell migration. *Hypertension*. (2018) 72:881–8. doi: 10.1161/HYPERTENSIONAHA.118.11375

40. Xu MM, Deng HY, Li HH. MicroRNA-27a regulates angiotensin II-induced vascular smooth muscle cell proliferation and migration by targeting α-smooth muscle-actin in vitro. *Biochem Biophys Res Commun*. (2019) 509:973–7. doi: 10.1016/j.bbrc.2019.01.047
41. Ashton KJ, Willems L, Holmgren K, Ferreira L, Headrick JP. Age-associated shifts in cardiac gene transcription and transcriptional responses to ischemic stress. *Exp Gerontol*. (2006) 41:189–204. doi: 10.1016/j.exger.2005.10.013

Conflict of Interest: The authors declare that the research was conducted in the absence of any commercial or financial relationships that could be construed as a potential conflict of interest.

frontiers in Physiology

REVIEW
published: 13 November 2020
doi: 10.3389/fphys.2020.595526

Role of NO and S-nitrosylation in the Expression of Endothelial Adhesion Proteins That Regulate Leukocyte and Tumor Cell Adhesion

Gaynor Aguilar[1†], Tania Koning[1†], Pamela Ehrenfeld[2,3] and Fabiola A. Sánchez[1,3*]*

[1] Instituto de Inmunología, Facultad de Medicina, Universidad Austral de Chile, Valdivia, Chile, [2] Instituto de Anatomía, Histología y Patología, Facultad de Medicina, Universidad Austral de Chile, Valdivia, Chile, [3] Centro Interdisciplinario de Estudios del Sistema Nervioso, Universidad Austral de Chile, Valdivia, Chile

OPEN ACCESS

Edited by:
Xavier Figueroa, Pontificia Universidad Católica de Chile, Chile

Reviewed by:
Nicola Conran, Campinas State University, Brazil
Carlos Cabañas, Consejo Superior de Investigaciones Científicas (CSIC), Spain

***Correspondence:**
Pamela Ehrenfeld
ingridehrenfeld@uach.cl; pamelaehrenfeld74@gmail.com
Fabiola A. Sánchez
fabiolasanchez@uach.cl

[†] These authors share first authorship

Specialty section:
This article was submitted to Vascular Physiology, a section of the journal Frontiers in Physiology

Received: *16 August 2020*
Accepted: *20 October 2020*
Published: *13 November 2020*

Citation:
Aguilar G, Koning T, Ehrenfeld P and Sánchez FA (2020) Role of NO and S-nitrosylation in the Expression of Endothelial Adhesion Proteins That Regulate Leukocyte and Tumor Cell Adhesion. Front. Physiol. 11:595526. doi: 10.3389/fphys.2020.595526

Leukocyte recruitment is one of the most important cellular responses to tissue damage. Leukocyte extravasation is exquisitely regulated by mechanisms of selective leukocyte-endothelium recognition through adhesion proteins in the endothelial cell surface that recognize specific integrins in the activated leukocytes. A similar mechanism is used by tumor cells during metastasis to extravasate and form a secondary tumor. Nitric oxide (NO) has been classically described as an anti-inflammatory molecule that inhibits leukocyte adhesion. However, the evidence available shows also a positive role of NO in leukocyte adhesion. These apparent discrepancies might be explained by the different NO concentrations reached during the inflammatory response, which are highly modulated by the expression of different nitric oxide synthases, along the inflammatory response and by changes in their subcellular locations.

Keywords: nitric oxide, S-nitrosylation, leukocyte adhesion, tumor cell adhesion, inflammation

LEUKOCYTE ADHESION AND NITRIC OXIDE (NO)

Inflammation involves the interplay of multiple biologic components, among which endothelial cells are key players. Endothelial cells orchestrate leukocyte transmigration to injured tissues by up-regulating adhesion proteins on their surface to bind integrins in leukocytes (Ley et al., 2007; Fan and Ley, 2015; Kreuger and Phillipson, 2016). Initial contact and rolling steps are initiated by endothelial cell leukocyte adhesion molecule-1 (ELAM-1, E-selectin) and P-selectin, which are expressed in the endothelium and bind to L-selectin, PSGL-1, CD44, CD43, and ESL-1 in the leukocyte. During the rolling phase, the interactions between leukocytes and endothelial selectins reduce leukocyte velocity and facilitate their adhesion to endothelium. Selectin proteins have a high degree of association/dissociation with their leukocyte ligands, which allows contact between the endothelial cell and leukocytes and provides enough time and proximity for other adhesion molecules to establish strong bonds between both cells (Sperandio, 2006; Garrido-Urbani et al., 2008; Tvaroška et al., 2020). Firm leukocyte adhesion to endothelial cells is mediated by vascular cell adhesion molecule 1 (VCAM-1) and intercellular adhesion molecule 1 (ICAM-1) that bind to leukocytes integrin's VLA-4, LFA-1, and Mac-1 (Greenwood et al., 2003). Once the leukocytes are attached to the endothelium, they flatten by contacting the endothelium at varying distances,

probably to reduce their exposure to blood flow forces and collisions with circulating blood cells, and subsequently they initiate their trans-endothelial migration (Ley et al., 2007; Leick et al., 2014).

Nitric oxide (NO) is a physiological messenger that regulates many cellular functions, such as vasodilation, angiogenesis, vascular permeability, neurotransmission, cell migration, immune response, cell proliferation and apoptosis (Tuteja et al., 2004; Nagy et al., 2007; Koriyama and Furukawa, 2018; Ehrenfeld et al., 2019; López-Sánchez et al., 2019). NO is produced in the organism by three different nitric oxide synthases: endothelial (eNOS, mainly expressed in endothelium), inducible (iNOS, expressed primarily on the immune system and endothelial cells) and neuronal (nNOS, expressed in the nervous system) (Förstermann and Sessa, 2012). NO produced by these isoforms activates two main signaling pathways: (1) soluble guanylate cyclase – protein kinase G (GC1-PKG) and (2) S-nitrosylation, which is the modification induced by NO in free-thiol cysteines in proteins to form S-nitrosothiols. S-nitrosylation regulates interactions between proteins, phosphorylation and intracellular trafficking (Stamler et al., 1992; Huang et al., 2005; Marín et al., 2012; Guequén et al., 2016).

The first studies addressing the role of NO in leukocyte adhesion used different inhibitors of NO production like L-NG-monomethyl arginine (L-NMMA) or N omega-Nitro-L-arginine methyl ester (L-NAME) to observe the effect on the basal leukocyte adhesion (in the absence of inflammatory stimulation). These experiments showed an increased basal leukocyte adhesion *in vivo* in different animal preparations and endothelial cell cultures *in vitro* (Kubes et al., 1991; Arndt et al., 1993; Ma et al., 1993; Tsao et al., 1994). The opposite approach, to elevate the NO concentration by the use of NO donors, prevented leukocyte adhesion and infiltration depending on NO level (Johnson et al., 1990; Kubes et al., 1991; Kubes and Granger, 1992). Studies using intravital microscopy in knockout (KO) animals for eNOS and nNOS corroborated these results showing increased leukocyte adhesion relative to control animals in the mesentery (Lefer et al., 1999). These observations and those from other laboratories led to the well-established concept that, in healthy endothelium, there is a physiological constitutive level of NO produced by eNOS that confers anti-adhesive and anti-inflammatory properties to the endothelial cell membrane and plays a critical role in preventing leukocyte adhesion (Kubes et al., 1991; Tsao et al., 1994). On the other hand, when the endothelium is stimulated with pro-inflammatory agonist, the effects of NO have not been completely consistent. There is a vast body of evidence showing an inhibitory effect of NO on stimulated leukocyte adhesion (De Caterina et al., 1995; Liu et al., 1998; Baatz and Pleyer, 2001; Lelamali et al., 2001; Lo et al., 2001; Jiang et al., 2005; Shelton et al., 2008); while other reports demonstrate either no effect of inhibition of NO on leukocyte adhesion (Hickey et al., 2001; Shelton et al., 2008) or promotion – mediated by NO – of leukocyte adhesion in response to challenge with cytokines (Bessa et al., 2002; Joussen et al., 2002). These discrepancies may be due to several differences in experimental approaches including timing and duration of the application of agonist/antagonist. We review here how NO regulates leukocyte adhesion by acting on different mechanisms that regulate surface expression of adhesion proteins on the endothelium such as: (a) through transcriptional regulation; (b) through non-transcriptional regulation, including traffic of vesicles to plasma membrane and clustering of adhesion proteins normally expressed in the endothelium. NO can also regulates integrin and protein expression and/or affinity on leukocytes (Kubes et al., 1991; Banick et al., 1997; Mitchell et al., 1998; Thom et al., 2013; Bhopale et al., 2015); however, given the enormous big of data on the topic, this review will focus only in the NO effects on the adhesion protein expression on the endothelium.

Transcriptional Regulation of Adhesion Proteins and NO

The effects of NO on leukocyte adhesion are related to transcriptional regulation of adhesion proteins expression on the endothelium (De Caterina et al., 1995; Khan et al., 1996; Liu et al., 1998; Lefer et al., 1999; Waldow et al., 2006; Buckanovich et al., 2008; Carreau et al., 2011; Stojak et al., 2018). Transcriptional regulation adhesion proteins, as well as numerous proinflammatory genes, is under the control of NF-κB (Springer, 1990; Collins et al., 1995; Ledebur and Parks, 1995; Pierce et al., 1997; Qian and Fulton, 2012), a dimeric protein formed by any of the members of the Rel family (p50, p65 or Rel-A, p52, c-Rel, and RelB) (Thanos and Maniatis, 1995; Marshall and Stamler, 2001). The classic form of NF-κB is the p50–p65 heterodimer that is kept inactive in the cytosol via interaction with the inhibitory protein IKBα (Thanos and Maniatis, 1995; Marshall and Stamler, 2001; Hayden and Ghosh, 2008; Sha and Marshall, 2012). Activation of cytokine receptors promotes the phosphorylation, ubiquitination, and proteasomal degradation of IKBα mediated by the IKKβ subunit of the IKK complex, formed by IKKα, β, and γ, which results in translocation of the p50–p65 heterodimer to the nucleus to bind target DNA sites, and activate gene transcription (Marshall and Stamler, 2001; Hayden and Ghosh, 2008; Sha and Marshall, 2012; **Figure 1**). Activation of the NF-κB pathway leads to *de novo* synthesis of high levels of messenger RNA for E-selectin, P-selectin, ICAM-1, and VCAM-1, which induces an increase in protein expression of these proteins in activated endothelial cells, and enhances the adhesion of leukocytes on the cell surface (Whelan et al., 1991; Iademarco et al., 1992; Van De Stolpe et al., 1994; Pan and McEver, 1995; Xia et al., 2001; Mussbacher et al., 2019).

Early investigations demonstrated that inhibition of NO production activated NF-κB and protein adhesion expression, whereas NO donors had the opposite effect (De Caterina et al., 1995; Khan et al., 1995). These effects were not mediated by the GC1-PKG pathway and appeared to depend strictly on NO concentration, suggesting that S-nitrosylation might be the operating mechanism (De Caterina et al., 1995; Lee et al., 2002; Waldow et al., 2006). Later, it was demonstrated that there is a basal S-nitrosylation of IKKβ that prevents IKBα phosphorylation and degradation, keeping NF-κB inactive (**Figure 2A**; Reynaert et al., 2004). Basal S-nitrosylation of p65 has also been reported in respiratory epithelium (A549 cells) and lung tissue (Kelleher et al., 2007, 2011). Inhibition of NOS activity

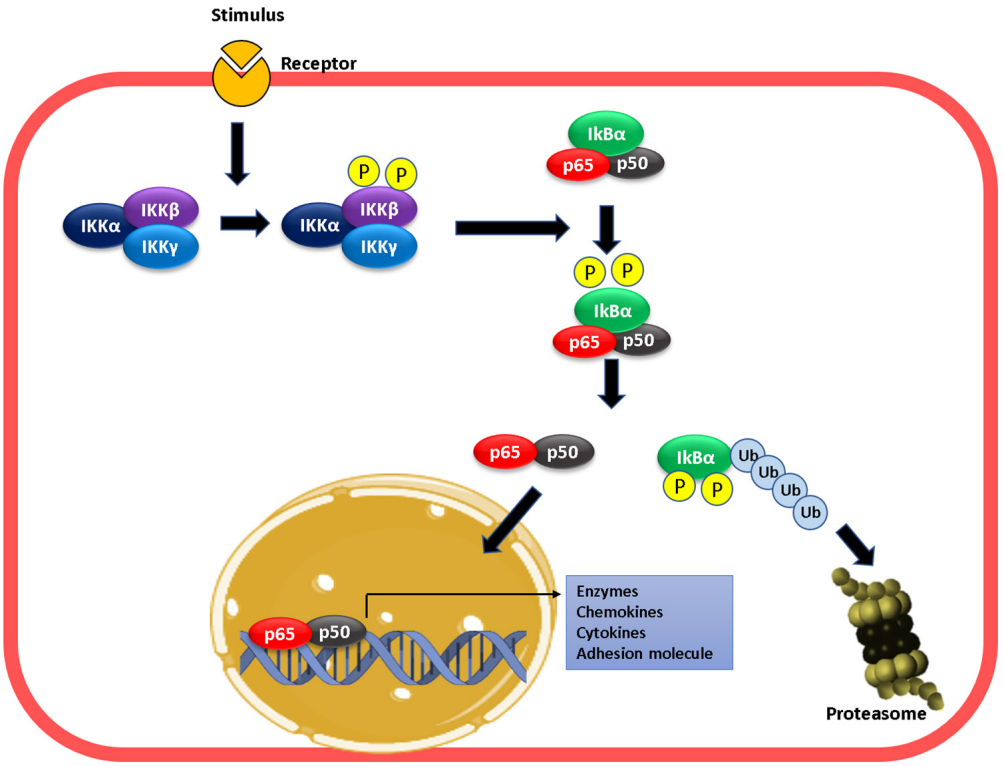

FIGURE 1 | Mechanism of NF-kB activation. Proinflammatory stimulation leads to the phosphorylation of IKKβ leading to phosphorylation of IKBα in NF-κB. This phosphorylation result in the ubiquitination and degradation of IκB-α in the proteasome. At this moment, the dimer p50–p65 enters into the nucleus, binds to the targets gene promoter (κB sites), and activates transcription.

reduced nitrosylation of IKKβ, leading to NF-κB activation in Jurkat T cells (Reynaert et al., 2004). Even though the role of basal S-nitrosylation has not been investigated, studies using cytokine-stimulated cells indicate that S-nitrosylation of p65 blocks the binding of NF-κB to DNA (Kelleher et al., 2007, 2011). Therefore, it is possible that basal S-nitrosylation of p65 contributes to keeping NF-κB inactivated. We postulate that the dynamics of S-nitrosylation cellular levels may be key to activation/inactivation of NF-κB.

After short inflammatory stimulation (10 min–2 h) with TNF-α or LPS, the S-nitrosylation levels of IKKβ and p65 decrease and NF-κB is activated (Reynaert et al., 2004; Kelleher et al., 2011, 2014; **Figure 2B**). At long times of exposure (6h, LPS), p65 is S-nitrosylated again with the consequent NF-κB inactivation (Kelleher et al., 2007, 2011). Studies using iNOS KO mice revealed that the high levels of NO-induced by this enzyme mediated this effect since genetic deletion of iNOS in mice blocks the recovery of S-nitrosylation of p65, and NF-κB activation is maintained along with prolonged inflammation in a model of LPS-induced lung inflammation (Kelleher et al., 2011). In addition, in a colitis model in iNOS KO mice, inflammation and elevated MPO activities persisted at 2 weeks compared to control mice, which improved colitis and decreased MPO activity (Vallance et al., 2004). iNOS also mediates S-nitrosylation of p50, which contributes to inhibiting NF-κB DNA binding (Matthews et al., 1996; DelaTorre et al., 1998; Marshall and Stamler, 2001). Even though it has not been reported, the high levels of NO-induced by iNOS might also re-nitrosylate IKKβ contributing to NF-κB inactivation (**Figure 2C**).

Although the evidence described above strongly points to a physiological role for iNOS in the inactivation of NF-κB, other report demonstrated that higher concentrations of NO – beyond those reached by iNOS expression – are required for NF-κB inactivation by S-nitrosylation of IKKβ and p65 (Qian and Fulton, 2012). It is important, however, to note that the report by Qian and Fulton used endothelial cells transfected with iNOS and not physiological iNOS induction by stimulation with pro-inflammatory cytokines.

In strong contrast to the results described above, other investigations demonstrated that inhibition of NO production did not increase adhesion protein expression induced by cytokines or leukocyte adhesion to endothelial monolayers (De Caterina et al., 1995). Furthermore, some reports have demonstrated that NO promotes protein adhesion expression. In diabetic rats, a high retinal leukocyte adhesion was observed, which correlated with a rise in NO and ICAM-1 levels. Pharmacological inhibition of NOS with L-NAME also reduces leukocyte adhesion (Joussen et al., 2002). In human vascular aortic smooth muscle cells (HASMCs), LPS treatment by 24 h increased ICAM-1 expression. Inhibition of NOS with L-NAME, prior to LPS administration, inhibited this effect, demonstrating that NO is required for enhancing ICAM-1 expression under

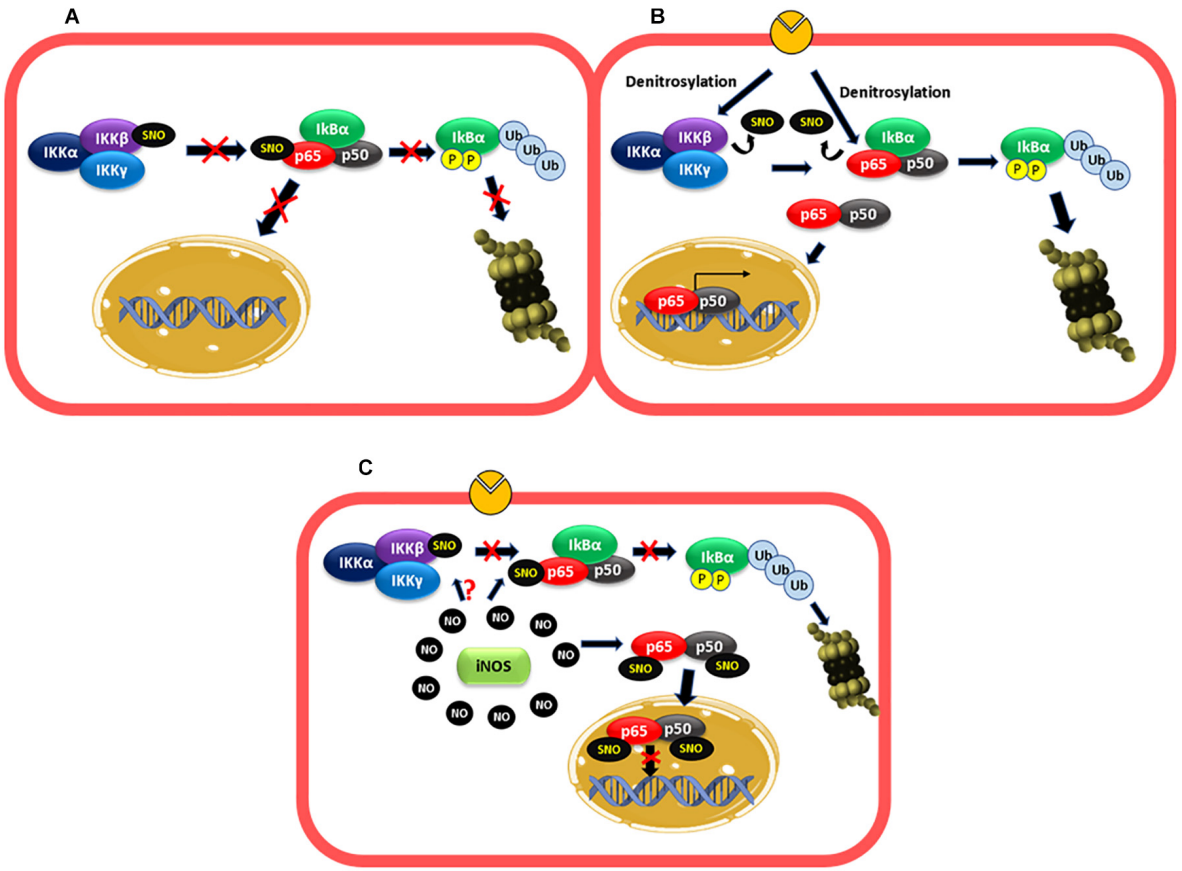

FIGURE 2 | NF-κB is regulated by S-nitrosylation. **(A)** Basal conditions: basal S-nitrosylation of IKKβ and p65 blocks IKBα phosphorylation and degradation proteasomal and the entry of the dimer p50–p65 to the nucleus, keeping NF-κB inactivated. **(B)** Short inflammatory stimulation: under stimulation, there is a decrease in the S-nitrosylation levels of IKKβ and p65 favoring IKBα phosphorylation and proteasomal degradation and the consequent entry of the dimer p50–p65 to the nucleus to increase adhesion protein transcription among others. **(C)** Long stimulation: at long periods of exposure to proinflammatory agents, high levels of NO-produced by iNOS induces S-nitrosylation of p65 and p50, which inhibit the binding of the dimer to the DNA. IKKβ might also be S-nitrosylated contributing to inactivate NF-κB.

this experimental conditions (Heo et al., 2008). In addition, the stimulation of rat microvascular endothelial cells with VEGF, that activates eNOS, increased ICAM-1 expression in 30 min, suggesting that eNOS regulates ICAM-1 transcription (Radisavljevic et al., 2000). The fact that eNOS is involved suggests that low NO concentrations but higher than basal might stimulate adhesion protein transcription. In fact, in HUVECs cells, NO donors increased ICAM-1, VCAM-1, and ELAM-1 expression. This effect was dependent on the NO donor concentrations used, with low concentrations (10 and 50 μM) inducing adhesion protein expression, whereas higher levels (250 and 500 μM) did not cause protein adhesion expression (Sektioglu et al., 2016). Microarray analysis of HUVEC treated with NO donors at low concentration or TNF-α demonstrated that 473 genes were upregulated, including VCAM-1 and E-selectin. The effect of NO donor on protein adhesion expression was dependent on NF-κB activation, because the effect was blocked by the NF-κB inhibitor BAY11-7082. These results coincide with earlier studies demonstrating that low NO concentration improved NF-κB activity induced by TNF-α, whereas higher concentrations inhibited NF-κB activity (Umansky et al., 1998). These low NO doses (but still higher than basal), might be achieved by eNOS activation, as many pro-inflammatory agents induce rapid eNOS activation (Marín et al., 2012; Guequén et al., 2016). The precise mechanism by which exogenous administration of low concentrations of NO activate NF-κB dependent protein adhesion expression in endothelial cells remains to be explored. A possible explanation could be given by the changes in eNOS localization under inflammatory stimulation (**Figure 3**). In non-stimulated cells, basal NO production generated by eNOS (located in the Golgi and caveolae) (Feron and Balligand, 2006; Zhang et al., 2006) maintains an anti-adhesive phenotype through basal S-nitrosylation of IKKβ and p65 (Matsushita et al., 2003; Feron and Balligand, 2006; Zhang et al., 2006). Under short-time stimulated conditions, eNOS is activated and change its localization (Sánchez et al., 2006, 2011; Marín et al., 2012), which might reduce S-nitrosylation of IKKβ and p65 activating NF-κB. Additionally, eNOS-induced NO might activate protein adhesion expression by mechanisms still unknown. At extended times of

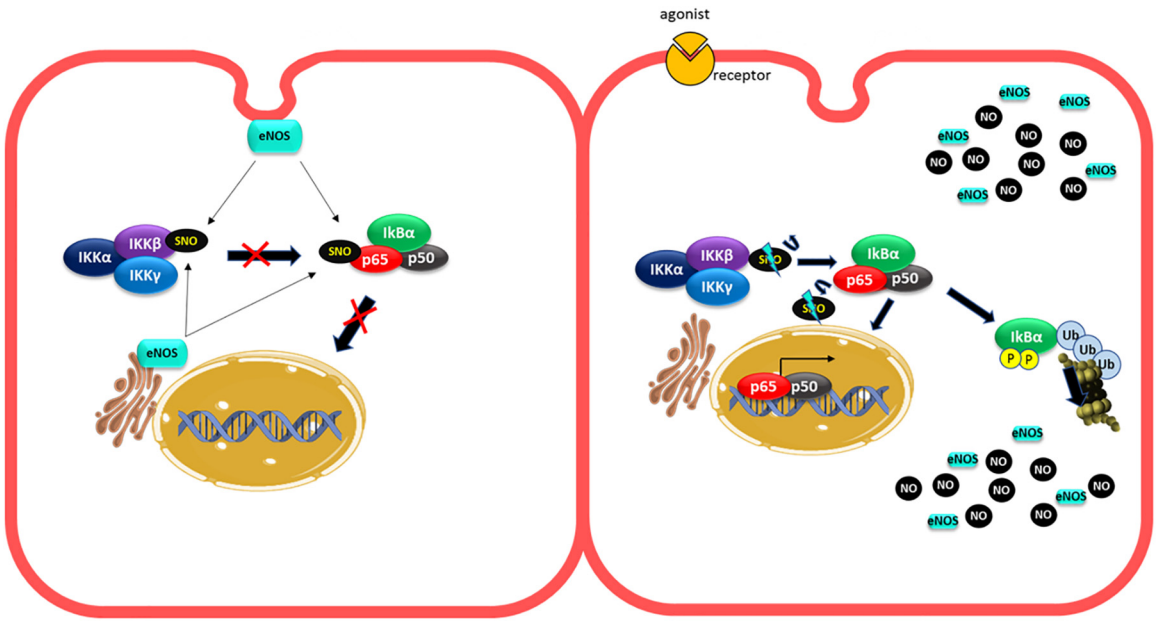

FIGURE 3 | Changes in eNOS localization under short inflammatory stimulation can activate NF-κB. In unstimulated cells, the basal production of NO generated by eNOS (located at the Golgi and caveolae) provides basal S nitrosylation of IKKβ and p65 to maintain an anti-adhesive phenotype **(left pannel)**. Under short-term proinflammatory conditions, eNOS is activated and changes in its location might decrease NO levels around IKKβ and p65, decreasing their S-nitrosylation levels leading to NF-κB activation **(right pannel)**.

inflammatory stimulation, the high levels of NO induced by iNOS activation will inhibit NF-κB by enhancing S-nitrosylation of IKKβ, p65 and additional S-nitrosylation of p50. Thus, low concentrations of NO achieved by eNOS activation and short exposure times to agonists increase adhesion protein expression, whereas higher NO concentrations achieved by iNOS stimulation and longer times of stimulation will inhibit protein adhesion expression (Umansky et al., 1998; Sektioglu et al., 2016).

Non-transcriptional Regulation of Adhesion Proteins and NO

Many pro-inflammatory agents induce a fast leukocyte adhesion observed within minutes of exposure to some pro-inflammatory agents (Dillon et al., 1988; Sugama et al., 1992; Javaid et al., 2003) that cannot be explained by transcriptional regulation. This fast adhesion may be explained by mechanisms such as vesicle traffic and clustering (Javaid et al., 2003; Ley et al., 2007; Lowenstein, 2007; Barreiro et al., 2008; Setiadi and McEver, 2008; Liu et al., 2011).

Vesicle Traffic

Adhesion proteins are stored in vesicles in endothelial cells that are transported to the plasma membrane after inflammatory stimulation. ELAM-1, for instance, is stored in intracellular secretory granules of endothelial cells and is rapidly expressed on the cell surface following degranulation, within minutes of exposure to activating agents such as thrombin, histamine, or phorbol esters (Geng et al., 1990; Larsen et al., 1992). The same is true for P-selectin, which is usually stored in Weibel-Palade bodies (WPB) (Weibel and Palade, 1964; Metcalf et al., 2008). In the case of VCAM-1, evidence indicates that after TNF-α treatment of endothelial cells, vesicular transport from an intracellular pool to the cell surface is increased (MacKesy and Goalstone, 2011).

Clustering

In basal conditions without inflammatory stimulation, low levels of adhesion proteins are present in an inactive state in the endothelial plasma membrane (Barreiro et al., 2002, 2008; Javaid et al., 2003). The lateral association of adhesion proteins, a process known as clustering, also regulates their adhesive capacity (Javaid et al., 2003; Barreiro et al., 2008; Setiadi and McEver, 2008; Liu et al., 2011). Through clustering, cell surface expression of adhesion proteins does not change; instead, they are regrouped and interact with cytoskeletal proteins to increase their avidity for leukocyte integrins (Javaid et al., 2003; Liu et al., 2011). This affinity change process occurs at short times of stimulation (minutes) and allows a fast response under inflammatory stimulation. In the case of ELAM-1, clustering is promoted by association to lipid rafts and caveolae at the plasma membrane (Tilghman and Hoover, 2002a,b; Setiadi and McEver, 2008). P-selectin clustering is mediated by interactions of the cytoplasmic domain of P-selectin with clathrin-coated pits (Setiadi et al., 1998). Clustering of ICAM-1 and VCAM-1 is promoted by association with tetraspanins, which are small transmembrane proteins able to associate laterally with different proteins at the plasma membrane (Barreiro et al., 2008). ICAM-1 clustering is also regulated by protein kinase C zeta (PKCz), that under stimulation with TNF-α, is activated and translocated to

the plasma membrane to phosphorylate ICAM-1 either directly or through Src activation (Javaid et al., 2003; Liu et al., 2011).

NO Role in Vesicle Transport and Clustering

Many reports have demonstrated a NO role in anterograde and retrograde transport (Iwakiri et al., 2006; Lowenstein, 2007; Lee et al., 2009; Marín et al., 2012). N-ethylmaleimide sensible factor (NSF) is an ATPase that modulates vesicular transport (Söllner et al., 1993; Morgan and Burgoyne, 2004) and studies *in vitro* and *in vivo* have shown that there is a basal NSF-S-nitrosylation mediated by eNOS that inhibits the translocation of WPB containing P-selectin to the plasma membrane contributing to the anti-adhesive properties of basal NO production in the endothelium (Matsushita et al., 2003; Lowenstein, 2007). Basal eNOS activity also contributes to the anti-adhesive properties of the endothelium by inhibiting ICAM-1 clustering as it has been demonstrated that eNOS inhibition led to ICAM-1 clustering mediated by Src phosphorylation in endothelial cells *in vitro* and *in vivo* (Xu et al., 2013; Gao et al., 2018). These observations can account for the fast leukocyte adhesion observed when basal NO production is inhibited in the absence of inflammatory stimulation (Kubes et al., 1991; Ma et al., 1993; Gao et al., 2018) but do not explain the fast leukocyte adhesion observed under inflammatory stimulation (Dillon et al., 1988; Sugama et al., 1992; Javaid et al., 2003). Changes in eNOS localization might again explain this effect. In non-stimulated cells, basal NO production generated by eNOS located to the Golgi and caveolae (Feron and Balligand, 2006; Zhang et al., 2006) will maintain an anti-adhesive phenotype in part by basal S-nitrosylation of NSF and also by inhibiting ICAM-1 clustering (Feron and Balligand, 2006; Zhang et al., 2006; Lowenstein, 2007; Mukhopadhyay et al., 2008; Gao et al., 2018; **Figure 4A**). In

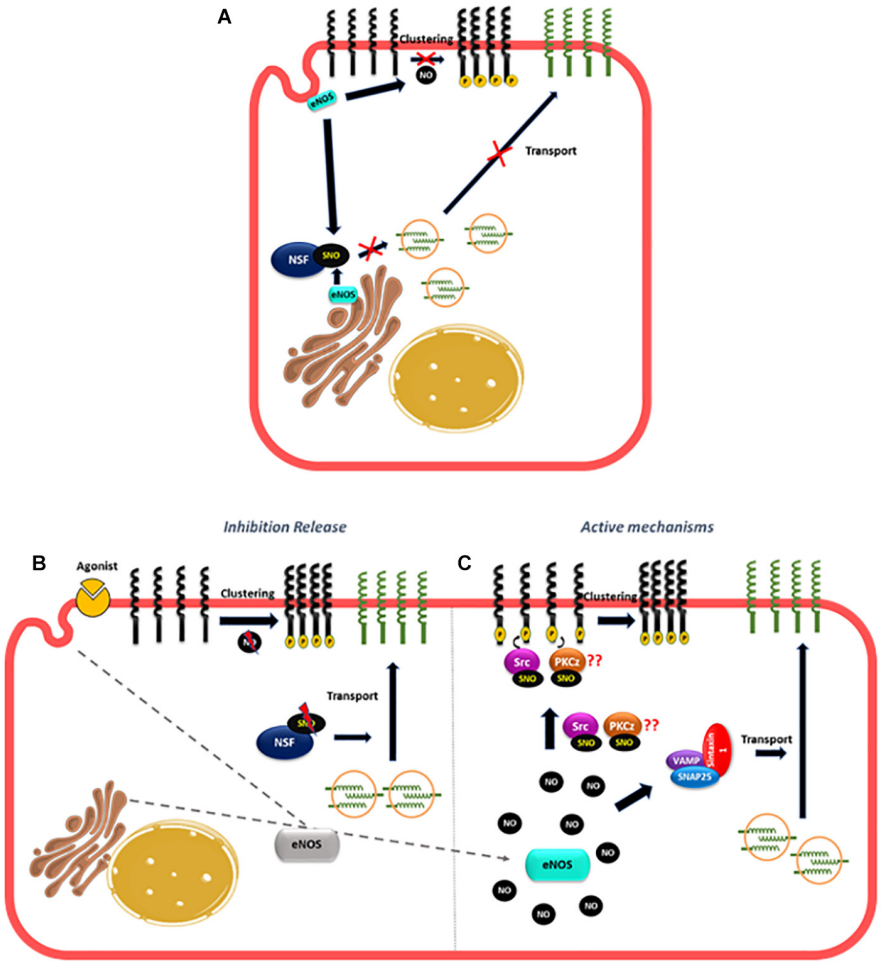

FIGURE 4 | Proposed mechanism of NO role in the fast leukocyte adhesion. **(A)** In unstimulated cells, the basal NO production generated by eNOS located to the Golgi and caveolae maintain an anti-adhesive state in the endothelium by basal NSF-S-nitrosylation that inhibits the translocation of vesicles containing adhesion molecules to the plasma membrane and by blocking the clustering of adhesion molecules like ICAM-1. **(B)** After short inflammatory stimulation, eNOS redistribution, might put NO away from NSF, diminishing NSF-S-nitrosylation to stimulate the transport of vesicles to the plasma membrane. At the same time, the change in eNOS localization might also lower NO levels close to ICAM-1 to promote ICAM-1 clustering. **(C)** At the same time, the movement of eNOS to different subcellular locations will increase NO levels at those locations, which may active the SNAREs complexes (VAMP, SNAP25, and syntaxin) stimulating traffic of vesicles; NO can also induce S-nitrosylation of Src and PKCz to promote ICAM-1 phosphorylation and clustering.

fact, only wild type eNOS (located at Golgi and caveolae) induce NSF-S-nitrosylation and inhibit vesicular transport but not eNOS located at the nucleus (Iwakiri et al., 2006). Furthermore the treatment of endothelial cells with monocrotaline pyrrole (MCPT), a drug that blocks the association of NSF with eNOS at Golgi and prevents eNOS localization in caveolae inhibits NSF-S-nitrosylation (Mukhopadhyay et al., 2008; Lee et al., 2009). After short inflammatory stimulation, eNOS redistribution from caveolae and Golgi to cytosol (Sánchez et al., 2006, 2011; Marín et al., 2012), might reduce S-nitrosylation of NSF, to stimulate the release of WPB bodies (**Figure 4B**). At the same time, the change in eNOS localization might also diminish NO levels close to ICAM-1 in the plasma membrane to stimulate ICAM-1 clustering. On the other hand, the movement of eNOS to different subcellular locations will increase NO levels at those locations, which may actively stimulate traffic of vesicles, stimulating for instance the formation of complexes that promote transport to the cell surface such as VAMP/SNAP-25/syntaxin-1a and/or VAMP-3/syntaxin-2 that have been demonstrated to be stimulated by NO and promote synaptic vesicle exocytosis and release of secretory granules in neurons and platelets, respectively (Meffert et al., 1996; Randriamboavonjy et al., 2004; **Figure 4C**). Interestingly, NSF-S-nitrosylation has also been reported to stimulate protein transport to the cell surface of AMPA receptors and VSVG protein in neurons and epithelial cells, respectively (Huang et al., 2005; Iwakiri et al., 2006) unlike its inhibitory role in endothelial cells. Considering that NSF has 8 cysteines that can be S-nitrosylated (Matsushita et al., 2003), it is possible that different degrees of S-nitrosylation may also play a role in transport to the plasma membrane. Basal S-nitrosylation of NSF will inhibit transport, whereas decrease or elevation in S-nitrosylation might stimulate traffic. Besides traffic, an elevation in NO, might also stimulate ICAM-1 clustering since Src that promote ICAM-1 phosphorylation is activated by S-nitrosylation in another cellular context (Rahman et al., 2010). PKCζ, that also participate in ICAM-1 clustering (Javaid et al., 2003; Matsushita et al., 2003; Liu et al., 2011) might be also activated by NO and S-nitrosylation since N-ethylmaleimide that blocks the thiol groups decreases the activity of PKCζ (Kikkawa et al., 1987) and a PKCζ synthetic peptide containing the activation site is S-nitrosylated *in vitro* (Balendran et al., 2000; Wang et al., 2008).

Thus, the combined effects of releasing the inhibition induced by basal NO on vesicular transport and clustering, plus the active stimulation by NO of pathways that increase vesicular transport and clustering, will induce leukocyte adhesion at short times of simulation.

NO AND TUMOR CELL ADHESION

There is considerable evidence demonstrating a dual role of NO and S-nitrosylation in cancer risk and metastasis (Burke et al., 2017; Rizza and Filomeni, 2018; Ehrenfeld et al., 2019; Hays and Bonavida, 2019; Holotiuk et al., 2019; Somasundaram et al., 2019). The available evidence demonstrates a positive correlation between NO biosynthesis, tumor development and degree of malignancy in a variety of cancers (breast, pancreatic, liver, cervical, ovary, melanoma, nasopharyngeal, stomach, colon, lung, oral, esophagus, glioma, and prostate cancer) (Monteiro et al., 2015; Vanini et al., 2015; Burke et al., 2017; Thomas and Wink, 2017; Somasundaram et al., 2019). On the other hand, in animal studies, inhibition or genetic deletion of eNOS or iNOS can inhibit, have no effect, or even increase primary tumor growth and metastasis depending on the type of cancer (Wang et al., 2001, 2003; Gratton et al., 2003; Heinecke et al., 2014; Granados-Principal et al., 2015; McCrudden et al., 2017; Kij et al., 2018; Romagny et al., 2018; Flaherty et al., 2019). These discrepancies probably reflect the fact that NO effects strongly depend on its concentration, duration of exposure, location and activity of NOS isoforms, tumor type, its microenvironment and sensitivity to NO (Ridnour et al., 2006; López-Sánchez et al., 2019; Somasundaram et al., 2019). In the tumoral microenvironment, tumor cells express iNOS, eNOS, and nNOS, depending on tumor type and stage, endothelial cells express eNOS and iNOS whereas tumor-associated stromal fibroblasts and immune cells express iNOS (Fukumura et al., 2006; Monteiro et al., 2015; López-Sánchez et al., 2019). Therefore, the results can be conflicting depending on the experimental set-up and the cell type being investigated.

Despite remarkable developments in cancer therapeutics, metastasis is still closely associated with high mortality rates in cancer patients. Metastasis occurs when tumor cells separate from the primary tumor, enter the bloodstream (or lymph) and travel to remote organs to form a secondary tumor. One of the final events in metastasis is the extravasation of cancer cells across the endothelial barrier (Talmadge, 2010; Sökeland and Schumacher, 2019). Cytokines and other factors produced by the primary tumor, circulating tumor cells and cells in the metastatic microenvironment promote binding between tumor cells and endothelial cells (Wolf et al., 2012; Reymond et al., 2013; Strilic and Offermanns, 2017). Initial insights into tumor cell extravasation were derived from studies of leukocyte extravasation, resulting in the widely accepted concept that cancer cell and leukocyte extravasation – although different – share many similarities (Strell and Entschladen, 2008; McDowell and Quail, 2019; Sökeland and Schumacher, 2019). Increased cell surface expression of adhesion proteins ELAM-1, ICAM-1, VCAM-1, and P-selectin in the endothelium mediate direct adhesion to CD44, mucin-1 and CD24 in breast tumor cells (Aigner et al., 1998; Rahn et al., 2005; Geng et al., 2012; Shirure et al., 2015). Alternatively, tumor cells can bind to macrophages, neutrophils or platelets in the circulation and these cells mediate the adhesion of tumor cells to the endothelium acting as a bridge among tumor and endothelial cells (Evani et al., 2013; Reymond et al., 2013).

The evidence strongly suggests an stimulatory role of NO in tumor cell adhesion: NOS inhibitors blocked small cell lung carcinoma adhesion to the endothelium treated with pro-inflammatory cytokines (Vidal et al., 1992). NO enhanced fibrosarcoma cell adhesion and invasion through HUVEC monolayers, increasing ICAM-1 and ELAM-1 expression (Yudoh et al., 1997). *In vivo*, NO caused squamous carcinoma cell binding to the hepatic microcirculation (Scher, 2007). Breast circulating

tumor cells MDA-MB-231 adhered to endothelial sites with high NO concentration (Zhang et al., 2016). *Rhus coriaria*, a medicinal plant that in part inhibits NO pathway decreases the adhesion and transmigration of MDA-MB-231 cells to endothelial cells activated with TNF-α (El Hasasna et al., 2016). The mechanisms that increase tumor cell adhesion to endothelium have not been studied in detail but are probably the same already described for leukocyte adhesion involving NF-κB transcriptional regulation, traffic and clustering of adhesion proteins. Additionally, another transcription factor, HIF-1α expressed in endothelial cells, is involved in extravasation of breast cancer cells through the expression of L1CAM adhesion protein that binds to tumor cells, and HIF-1α has been demonstrated to be activated by S-nitrosylation in others cellular contexts (Li et al., 2007; Zhang et al., 2012; Ehrenfeld et al., 2019).

As in leukocyte adhesion to endothelium, NO also shows a negative role in tumor cell adhesion: exogenously applied and endogenously generated NO inhibit melanoma cells adhesion to endothelium activated with lipopolysaccharide (Kong et al., 1996). The NO donor, CAP-NO, inhibited the basal and cytokine-stimulated adhesion of human colorectal cancer cells HT-29 to endothelial cells by inhibiting the expression of adhesion proteins ELAM-1, ICAM-1, and particularly VCAM-1 (Lu et al., 2014). NO donors inhibits the adhesion of MDA-MB231 cells to HUVEC stimulated by IL-1β and the transmigration of breast cancer cells across the lung microvascular endothelium (Kang et al., 2018; Stojak et al., 2018). This effect was mediated by a decrease in ICAM-1 expression. Similar to leukocyte adhesion, the differential effect of NO on tumor cell adhesion might depend on NO concentrations with low concentrations of NO increasing adhesion protein expression and adhesion of tumor cells, whereas higher NO concentrations, inhibiting protein adhesion expression and tumor cell adhesion (Sektioglu et al., 2016).

The effects of NO on adhesion protein expression not only affect tumor cell adhesion at the metastatic site but also infiltration of immune cells in the primary tumor, where it has been demonstrated that NO, produced by iNOS in M1 macrophages, mediates VCAM-1 expression in the endothelium

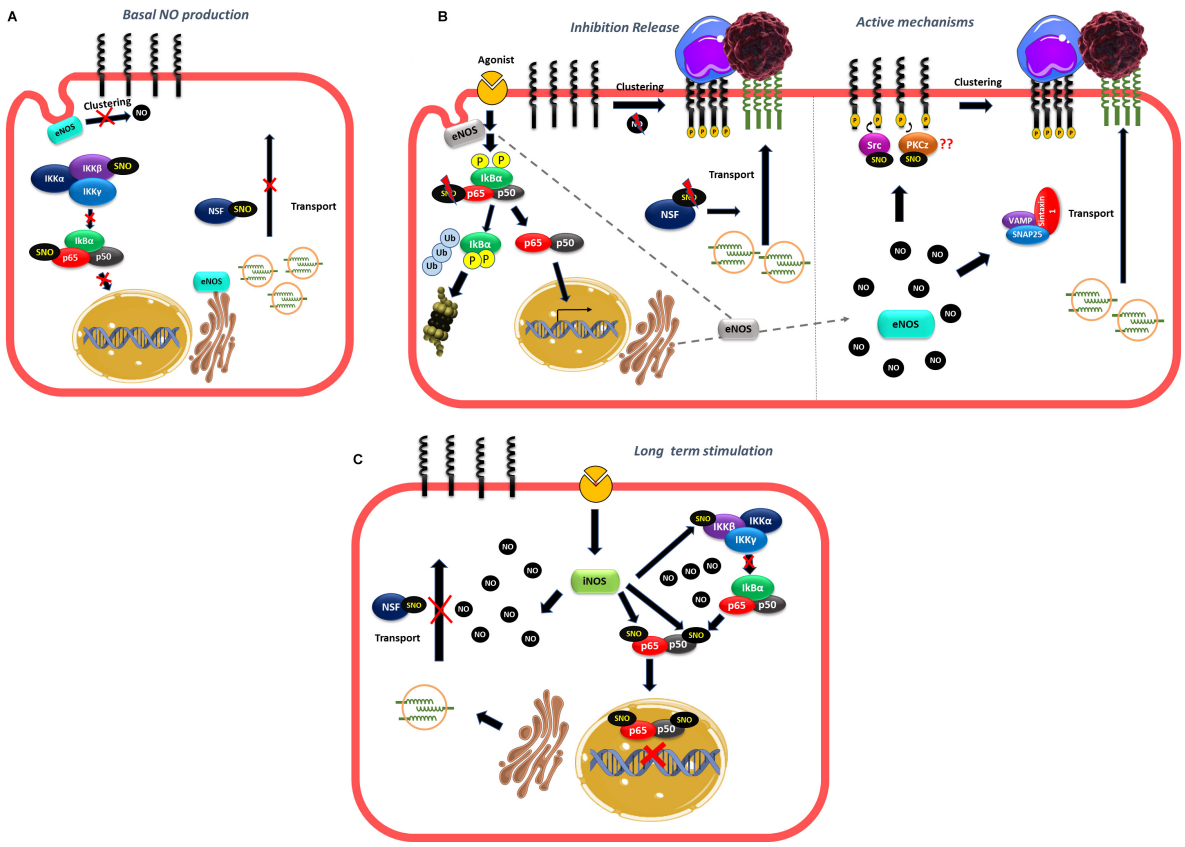

FIGURE 5 | Role of NO in leukocyte and tumor cell adhesion. **(A)** Basal NO production produced by eNOS located to the Golgi and caveolae maintaining an anti-adhesive phenotype by inhibiting NF-κB activation, traffic of vesicles and clustering of adhesion proteins. **(B)** At short times of stimulation movement of eNOS away from Golgi and caveolae release the inhibition caused by NO to stimulate NF-κB activation and transcription of adhesion proteins, traffic of vesicles that contain adhesion proteins and clustering. At the same time, the rise in NO concentration in other subcellular locations may induce active mechanisms of adhesion such as formation of SNAREs complexes that stimulate vesicle traffic to the plasma membrane or to stimulate S-nitrosylation of targets such as Src and PKCz that induce clustering of adhesion proteins stimulating leukocyte and tumor cell adhesion. **(C)** At long times of stimulation, the high NO concentration induced by iNOS activation induce S-nitrosylation of NF-κB and NSF inhibiting the transcription of adhesion proteins and the vesicle transport of adhesion proteins to the plasma membrane.

leading to an improved infiltration of T-lymphocytes specific for the tumor, contributing to decrease tumor growth in a mouse melanoma model (Sektioglu et al., 2016).

After binding to tumor cells, adhesion proteins through their cytosolic tails interact with cytoskeletal proteins inducing changes in the shape of endothelial cells leading to destabilization of the endothelial barrier that facilitates tumor cell transmigration (Müller et al., 2001; Tichet et al., 2015). We have demonstrated that treatment of endothelial cells with conditioned medium from breast cancer cells and cytokines that are elevated in breast cancer patients induces S-nitrosylation of endothelial barrier proteins (p120, VE-cadherin and β-catenin) promoting phosphorylation and perturbation of the interactions among these proteins that leads to their internalization, which destabilizes the endothelial barrier (Marín et al., 2012; Guequén et al., 2016; Zamorano et al., 2019). Thus, better knowledge and understanding of NO biology in cancer is of paramount importance because it regulates not only expression of adhesion proteins that promote metastasis, but also controls the endothelial barrier to promote transmigration of tumor cells and metastasis.

CONCLUSION

The role of NO in leukocyte adhesion to endothelium has been controversial. Whether NO enhances or inhibits leukocyte adhesion depends on local NO concentration. It is reasonable to state that, in non-stimulated cells, NO concentration maintains an anti-adhesive phenotype at the endothelial cell membrane – inasmuch as inhibition of NOS causes increased leukocyte adhesion. This NO produced by eNOS prevents transport of vesicles to the cell surface, clustering of adhesion proteins and transcription of adhesion proteins by keeping NF-κB in an inactive state. However, an increase in eNOS-derived NO concentration to levels slightly above control is compatible with leukocyte adhesion through increasing cell surface transport, clustering of adhesion proteins and transcription of adhesion proteins via NF-κB activation. In addition, high NO concentration – most likely achieved through stimulation of iNOS – inhibits leukocyte adhesion due to S-nitrosylation of p50 and p65 in NF-κB and presumably IKKβ, which blocks entry of NF-κB to the nucleus leading to inhibition of adhesion protein synthesis. Similar to leukocyte-endothelium adhesion, NO also regulates tumor cell adhesion to endothelium probably through the stimulation of the same mechanisms described above as well as opening of the endothelial barrier, all of which enhance tumor cell extravasation and metastasis (**Figure 5**).

AUTHOR CONTRIBUTIONS

GA and TK collaborated in review literature and figures confection. PE collaborated in writing the manuscript and review literature. FS reviewed literature, wrote the manuscript, and reviewed figures. All authors contributed to the article and approved the submitted version.

FUNDING

Fondecyt grant 1201635 and Vicerrectoría de Investigación, Desarrollo y Creación Artística from Universidad Austral de Chile for its continuous support.

REFERENCES

Aigner, S., Ramos, C. L., Hafezi-Moghadam, A., Lawrence, M. B., Friederichs, J., Altevogt, P., et al. (1998). CD24 mediates rolling of breast carcinoma cells on P-selectin. *FASEB J.* 12, 1241–1251. doi: 10.1096/fasebj.12.12.1241

Arndt, H., Russell, J. B., Kurose, I., Kubes, P., and Granger, D. N. (1993). Mediators of leukocyte adhesion in rat mesenteric venules elicited by inhibition of nitric oxide synthesis. *Gastroenterology* 105, 675–680. doi: 10.1016/0016-5085(93)90882-D

Baatz, H., and Pleyer, U. (2001). Modulation of leukocyte-endothelium interaction by nitric oxide synthase inhibitors: effects on leukocyte adhesion in endotoxin-induced uveitis. *Inflamm. Res.* 50, 534–543. doi: 10.1007/PL00000231

Balendran, A., Biondi, R. M., Cheung, P. C. F., Casamayor, A., Deak, M., and Alessi, D. R. (2000). A 3-phosphoinositide-dependent protein kinase-1 (PDK1) docking site is required for the phosphorylation of protein kinase Cζ (PKCζ) and PKC- related kinase 2 by PDK1. *J. Biol. Chem.* 275, 20806–20813. doi: 10.1074/jbc.M000421200

Banick, P. D., Chen, Q., Xu, Y. A., and Thom, S. R. (1997). Nitric oxide inhibits neutrophil B2 integrin function by inhibiting membrane-associated cyclic GMP synthesis. *J. Cell Physiol.* 172, 12–24. doi: 10.1002/(sici)1097-4652(199707)172:1<12::aid-jcp2>3.0.co;2-g

Barreiro, O., Yáñez-Mó, M., Serrador, J. M., Montoya, M. C., Vicente-Manzanares, M., Tejedor, R., et al. (2002). Dynamic interaction of VCAM-1 and ICAM-1 with moesin and ezrin in a novel endothelial docking structure for adherent leukocytes. *J. Cell Biol.* 157, 1233–1245. doi: 10.1083/jcb.200112126

Barreiro, O., Zamai, M., Yáñez-Mó, M., Tejera, E., López-Romero, P., Monk, P. N., et al. (2008). Endothelial adhesion receptors are recruited to adherent leukocytes by inclusion in preformed tetraspanin nanoplatforms. *J. Cell Biol.* 183, 527–542. doi: 10.1083/jcb.200805076

Bessa, X., Elizalde, J. I., Mitjans, F., Piol, V., Miquel, R., Panés, J., et al. (2002). Leukocyte recruitment in colon cancer: role of cell adhesion molecules, nitric oxide, and transforming growth factor β1. *Gastroenterology* 122, 1122–1132. doi: 10.1053/gast.2002.32369

Bhopale, V. M., Yang, M., Yu, K., and Thom, S. R. (2015). Factors associated with nitric oxide-mediated β2 integrin inhibition of neutrophils. *J. Biol. Chem.* 290, 17474–17484. doi: 10.1074/jbc.M115.651620

Buckanovich, R. J., Facciabene, A., Kim, S., Benencia, F., Sasaroli, D., Balint, K., et al. (2008). Endothelin B receptor mediates the endothelial barrier to T cell homing to tumors and disables immune therapy. *Nat. Med.* 14, 28–36. doi: 10.1038/nm1699

Burke, A. J., Garrido, P., Johnson, C., Sullivan, F. J., and Glynn, S. A. (2017). Inflammation and nitrosative stress effects in ovarian and prostate pathology and carcinogenesis. *Antioxidants Redox Signal.* 26, 1078–1090. doi: 10.1089/ars.2017.7004

Carreau, A., Kieda, C., and Grillon, C. (2011). Nitric oxide modulates the expression of endothelial cell adhesion molecules involved in angiogenesis and leukocyte recruitment. *Exp. Cell Res.* 317, 29–41. doi: 10.1016/j.yexcr.2010.08.011

Collins, T., Read, M. A., Neish, A. S., Whitley, M. Z., Thanos, D., and Maniatis, T. (1995). Transcriptional regulation of endothelial cell adhesion molecules: NF-κB and cytokine-inducible enhancers. *FASEB J.* 9, 899–909. doi: 10.1096/fasebj.9.10.7542214

De Caterina, R., Libby, P., Peng, H. B., Thannickal, V. J., Rajavashisth, T. B., Gimbrone, M. A., et al. (1995). Nitric oxide decreases cytokine-induced endothelial activation: nitric oxide selectively reduces endothelial expression of adhesion molecules and proinflammatory cytokines. *J. Clin. Invest.* 96, 60–68. doi: 10.1172/JCI118074

DelaTorre, A., Schroeder, R. A., Bartlett, S. T., Kuo, P. C., Buchman, T. G., Weigel, R. J., et al. (1998). Differential effects of nitric oxide-mediated S-nitrosylation on p50 and c-jun DNA binding. *Surgery* 124, 137–142. doi: 10.1016/S0039-6060(98)70113-8

Dillon, P. K., Fitzpatrick, M. F., Ritter, A. B., and Durán, W. N. (1988). Effect of platelet-activating factor on leukocyte adhesion to microvascular endothelium, time course and dose-response relationships. *Inflammation* 12, 563–573. doi: 10.1007/BF00914318

Ehrenfeld, P., Cordova, F., Duran, W. N., and Sanchez, F. A. (2019). S-nitrosylation and its role in breast cancer angiogenesis and metastasis. *Nitric Oxide Biol. Chem.* 87, 52–59. doi: 10.1016/j.niox.2019.03.002

El Hasasna, H., Saleh, A., Samri, H. A., Athamneh, K., Attoub, S., Arafat, K., et al. (2016). Rhus coriaria suppresses angiogenesis, metastasis and tumor growth of breast cancer through inhibition of STAT3. NFÎ° B and nitric oxide pathways. *Sci. Rep.* 6, 1–15. doi: 10.1038/srep21144

Evani, S. J., Prabhu, R. G., Gnanaruban, V., Finol, E. A., and Ramasubramanian, A. K. (2013). Monocytes mediate metastatic breast tumor cell adhesion to endothelium under flow. *FASEB J.* 27, 3017–3029. doi: 10.1096/fj.12-224824

Fan, Z., and Ley, K. (2015). Leukocyte arrest: biomechanics and molecular mechanisms of β2 integrin activation. *Biorheology* 52, 353–377. doi: 10.3233/BIR-15085

Feron, O., and Balligand, J. L. (2006). Caveolins and the regulation of endothelial nitric oxide synthase in the heart. *Cardiovasc. Res.* 69, 788–797. doi: 10.1016/j.cardiores.2005.12.014

Flaherty, R. L., Intabli, H., Falcinelli, M., Bucca, G., Hesketh, A., Patel, B. A., et al. (2019). Stress hormone-mediated acceleration of breast cancer metastasis is halted by inhibition of nitric oxide synthase. *Cancer Lett.* 459, 59–71. doi: 10.1016/j.canlet.2019.05.027

Förstermann, U., and Sessa, W. C. (2012). Nitric oxide synthases: regulation and function. *Eur. Heart J.* 33, 829–837. doi: 10.1093/eurheartj/ehr304

Fukumura, D., Kashiwagi, S., and Jain, R. K. (2006). The role of nitric oxide in tumour progression. *Nat. Rev. Cancer* 6, 521–534. doi: 10.1038/nrc1910

Gao, F., Lucke-Wold, B. P., Li, X., Logsdon, A. F., Xu, L. C., Xu, S., et al. (2018). Reduction of endothelial nitric oxide increases the adhesiveness of constitutive endothelial membrane ICAM-1 through Src-mediated phosphorylation. *Front. Physiol.* 8:1124. doi: 10.3389/fphys.2017.01124

Garrido-Urbani, S., Bradfield, P. F., Lee, B. P. L., and Imhof, B. A. (2008). Vascular and epithelial junctions: a barrier for leucocyte migration. *Biochem. Soc. Trans.* 36, 203–211. doi: 10.1042/BST0360203

Geng, J. G., Bevilacquat, M. P., Moore, K. L., McIntyre, T. M., Prescott, S. M., Kim, J. M., et al. (1990). Rapid neutrophil adhesion to activated endothelium mediated by GMP-140. *Nature* 343, 757–760. doi: 10.1038/343757a0

Geng, Y., Yeh, K., Takatani, T., and King, M. R. (2012). Three to tango: MUC1 as a ligand for both E-selectin and ICAM-1 in the breast cancer metastatic cascade. *Front. Oncol.* 2:76. doi: 10.3389/fonc.2012.00076

Granados-Principal, S., Liu, Y., Guevara, M. L., Blanco, E., Choi, D. S., Qian, W., et al. (2015). Inhibition of iNOS as a novel effective targeted therapy against triple-negative breast cancer. *Breast Cancer Res.* 17, 1–16. doi: 10.1186/s13058-015-0527-x

Gratton, J. P., Lin, M. I., Yu, J., Weiss, E. D., Jiang, Z. L., Fairchild, T. A., et al. (2003). Selective inhibition of tumor microvascular permeability by cavtratin blocks tumor progression in mice. *Cancer Cell* 4, 31–39. doi: 10.1016/S1535-6108(03)00168-5

Greenwood, J., Amos, C. L., Walters, C. E., Couraud, P.-O., Lyck, R., Engelhardt, B., et al. (2003). Intracellular domain of brain endothelial intercellular adhesion molecule-1 is essential for T lymphocyte-mediated signaling and migration. *J. Immunol.* 171, 2099–2108. doi: 10.4049/jimmunol.171.4.2099

Guequén, A., Carrasco, R., Zamorano, P., Rebolledo, L., Burboa, P., Sarmiento, J., et al. (2016). S-nitrosylation regulates VE-cadherin phosphorylation and internalization in microvascular permeability. *Am. J. Physiol. Heart Circ. Physiol.* 310, H1039–H1044. doi: 10.1152/ajpheart.00063.2016

Hayden, M. S., and Ghosh, S. (2008). Shared Principles in NF-κB Signaling. *Cell* 132, 344–362. doi: 10.1016/j.cell.2008.01.020

Hays, E., and Bonavida, B. (2019). Nitric oxide-mediated enhancement and reversal of resistance of anticancer therapies. *Antioxidants* 8, 1–23. doi: 10.3390/antiox8090407

Heinecke, J. L., Ridnour, L. A., Cheng, R. Y. S., Switzer, C. H., Lizardo, M. M., Khanna, C., et al. (2014). Tumor microenvironment-based feed-forward regulation of NOS2 in breast cancer progression. *Proc. Natl. Acad. Sci. U.S.A.* 111, 6323–6328. doi: 10.1073/pnas.1401799111

Heo, S. K., Yun, H. J., Noh, E. K., Park, W. H., and Park, S. D. (2008). LPS induces inflammatory responses in human aortic vascular smooth muscle cells via Toll-like receptor 4 expression and nitric oxide production. *Immunol. Lett.* 120, 57–64. doi: 10.1016/j.imlet.2008.07.002

Hickey, M. J., Granger, D. N., and Kubes, P. (2001). Inducible nitric oxide synthase (iNOS) and regulation of leucocyte/endothelial cell interactions: studies in iNOS-deficient mice. *Acta Physiol. Scand.* 173, 119–126. doi: 10.1046/j.1365-201X.2001.00892.x

Holotiuk, V. V., Kryzhanivska, A. Y., Churpiy, I. K., Tataryn, B. B., and Ivasiutyn, D. Y. (2019). Role of nitric oxide in pathogenesis of tumor growth and its possible application in cancer treatment. *Exp. Oncol.* 41, 210–215. doi: 10.32471/exp-oncology.2312-8852.vol-41-no-3.13515

Huang, Y., Man, H., Sekine-aizawa, Y., Han, Y., Juluri, K., Luo, H., et al. (2005). S-Nitrosylation of N-Ethylmaleimide Sensitive Factor Mediates Surface Expression of AMPA Receptors. *Neuron* 46, 533–540. doi: 10.1016/j.neuron.2005.03.028

Iademarco, M. F., McQuillan, J. J., Rosen, G. D., and Dean, D. C. (1992). Characterization of the promoter for vascular cell adhesion molecule-1 (VCAM-1). *J. Biol. Chem.* 267, 16323–16329.

Iwakiri, Y., Satoh, A., Chatterjee, S., Toomre, D. K., Chalouni, C. M., Fulton, D., et al. (2006). Nitric oxide synthase generates nitric oxide locally to regulate compartmentalized protein S-nitrosylation and protein trafficking. *Proc. Natl. Acad. Sci. U.S.A.* 103, 19777–19782. doi: 10.1073/pnas.0605907103

Javaid, K., Rahman, A., Anwar, K. N., Frey, R. S., Minshall, R. D., and Malik, A. B. (2003). Tumor necrosis factor-α induces early-onset endothelial adhesivity by protein kinase cζ-dependent activation of intercellular adhesion molecule-1. *Circ. Res.* 92, 1089–1097. doi: 10.1161/01.RES.0000072971.88704.CB

Jiang, M. Z., Tsukahara, H., Hayakawa, K., Todoroki, Y., Tamura, S., Ohshima, Y., et al. (2005). Effects of antioxidants and NO on TNF-α-induced adhesion molecule expression in human pulmonary microvascular endothelial cells. *Respir. Med.* 99, 580–591. doi: 10.1016/j.rmed.2004.10.007

Johnson, G., Tsao, P., and Lefer, A. M. (1990). Synergism between superoxide dismutase and sodium nitrite in cardioprotection following ischemia and reperfusion. *Am. Heart J.* 119, 530–537. doi: 10.1016/S0002-8703(05)80275-3

Joussen, A. M., Poulaki, V., Qin, W., Kirchhof, B., Mitsiades, N., Wiegand, S. J., et al. (2002). Retinal vascular endothelial growth factor induces intercellular adhesion molecule-1 and endothelial nitric oxide synthase expression and initiates early diabetic retinal leukocyte adhesion in vivo. *Am. J. Pathol.* 160, 501–509. doi: 10.1016/S0002-9440(10)64869-9

Kang, F., Zhu, J., Wu, J., Lv, T., Xiang, H., Tian, J., et al. (2018). O 2-3-Aminopropyl diazeniumdiolates suppress the progression of highly metastatic triple-negative breast cancer by inhibition of microvesicle formation via nitric oxide-based epigenetic regulation. *Chem. Sci.* 9, 6893–6898. doi: 10.1039/c8sc00167g

Kelleher, Z. T., Matsumoto, A., Stamler, J. S., and Marshall, H. E. (2007). NOS2 regulation of NF-κB by S-nitrosylation of p65. *J. Biol. Chem.* 282, 30667–30672. doi: 10.1074/jbc.M705929200

Kelleher, Z. T., Potts, E. N., Brahmajothi, M. V., Foster, M. W., Auten, R. L., Michael Foster, W., et al. (2011). NOS2 regulation of LPS-induced airway inflammation via S-nitrosylation of NF-κB p65. *Am. J. Physiol. Lung Cell. Mol. Physiol* 301, L327-L333. doi: 10.1152/ajplung.00463.2010

Kelleher, Z. T., Sha, Y., Foster, M. W., Foster, W. M., Forrester, M. T., and Marshall, H. E. (2014). Thioredoxin-mediated denitrosylation regulates cytokine-induced nuclear factor κB (NF-κB) activation. *J. Biol. Chem.* 289, 3066–3072. doi: 10.1074/jbc.M113.503938

Khan, B. V., Harrison, D. G., Olbrych, M. T., Alexander, R. W., and Medford, R. M. (1996). Nitric oxide regulates vascular cell adhesion molecule 1 gene expression and redox-sensitive transcriptional events in human vascular endothelial cells. *Proc. Natl. Acad. Sci. U.S.A.* 93, 9114–9119. doi: 10.1073/pnas.93.17.9114

Khan, B. V., Parthasarathy, S. S., Alexander, R. W., and Medford, R. M. (1995). Modified low density lipoprotein and its constituents augment cytokine-activated vascular cell adhesion molecule-1 gene expression in human vascular endothelial cells. *J. Clin. Invest.* 95, 1262–1270. doi: 10.1172/JCI117776

Kij, A., Kus, K., Smeda, M., Zakrzewska, A., Proniewski, B., Matyjaszczyk, K., et al. (2018). Differential effects of nitric oxide deficiency on primary tumour growth, pulmonary metastasis and prostacyclin/thromboxane A2 balance in orthotopic and intravenous murine models of 4T1 breast cancer. *J. Physiol. Pharmacol.* 69, 911–919. doi: 10.26402/jpp.2018.6.05

Kikkawa, U., Ogita, K., Ono, Y., Asaoka, Y., Shearman, M. S., Fujii, T., et al. (1987). The common structure and activities of four subspecies of rat brain protein kinase C family. *FEBS Lett.* 223, 212–216. doi: 10.1016/0014-5793(87)80291-0

Kong, L., Dunn, G. D., Keefer, L. K., and Korthuis, R. J. (1996). Nitric oxide reduces tumor cell adhesion to isolated rat postcapillary venules. *Clin. Exp. Metastasis* 14, 335–343. doi: 10.1007/BF00123392

Koriyama, Y., and Furukawa, A. (2018). S-Nitrosylation regulates cell survival and death in the central nervous system. *Neurochem. Res.* 43, 41–49. doi: 10.1007/s11064-017-2303-z

Kreuger, J., and Phillipson, M. (2016). Targeting vascular and leukocyte communication in angiogenesis, inflammation and fibrosis. *Nat. Rev. Drug Discov.* 15, 125–142. doi: 10.1038/nrd.2015.2

Kubes, P., and Granger, D. N. (1992). Nitric oxide modulates microvascular permeability. *Am. J. Physiol. Hear. Circ. Physiol.* 262, H611–H615. doi: 10.1152/ajpheart.1992.262.2.h611

Kubes, P., Suzuki, M., and Granger, D. N. (1991). Nitric oxide: an endogenous modulator of leukocyte adhesion. *Proc. Natl. Acad. Sci. U.S.A.* 88, 4651–4655. doi: 10.1073/pnas.88.11.4651

Larsen, G. R., Sako, D., Ahern, T. J., Shaffer, M., Erban, J., Sajer, S. A., et al. (1992). P-selectin and E-selectin distinct but overlapping leukocyte ligand specificities. *J. Biol. Chemestry* 267, 11104–11110.

Ledebur, H. C., and Parks, T. P. (1995). Transcriptional regulation of the intercellular adhesion molecule-1 gene by inflammatory cytokines in human endothelial cells. *J. Biol. Chem.* 270, 933–943. doi: 10.1074/jbc.270.2.933

Lee, J., Reich, R., Xu, F., and Sehgal, P. B. (2009). Golgi, trafficking, and mitosis dysfunctions in pulmonary arterial endothelial cells exposed to monocrotaline pyrrole and NO scavenging. *Am. J. Physiol. Lung Cell. Mol. Physiol* 297, L715-L728. doi: 10.1152/ajplung.00086.2009

Lee, S. K., Kim, J. H., Yang, W. S., Kim, S. B., Park, S. K., and Park, J. S. (2002). Exogenous nitric oxide inhibits VCAM-1 expression in human peritoneal mesothelial cells: role of cyclic GMP and NF-κB. *Nephron* 90, 447–454. doi: 10.1159/000054733

Lefer, D. J., Jones, S. P., Girod, W. G., Baines, A., Grisham, M. B., Cockrell, A. S., et al. (1999). Leukocyte-endothelial cell interactions in nitric oxide synthase-deficient mice. *Am. J. Physiol. Hear. Circ. Physiol.* 276, 1943–1950. doi: 10.1152/ajpheart.1999.276.6.h1943

Leick, M., Azcutia, V., Newton, G., and Luscinskas, F. W. (2014). Leukocyte recruitment in inflammation: basic concepts and new mechanistic insights based on new models and microscopic imaging technologies. *Cell Tissue Res.* 355, 647–656. doi: 10.1007/s00441-014-1809-9

Lelamali, K., Wang, W., Gengaro, P., Edelstein, C., and Schrier, R. W. (2001). Effects of nitric oxide and peroxynitrite on endotoxin-induced leukocyte adhesion to endothelium. *J. Cell. Physiol.* 188, 337–342. doi: 10.1002/jcp.1128

Ley, K., Laudanna, C., Cybulsky, M. I., and Nourshargh, S. (2007). Getting to the site of inflammation: the leukocyte adhesion cascade updated. *Nat. Rev. Immunol.* 7, 678–689. doi: 10.1038/nri2156

Li, F., Sonveaux, P., Rabbani, Z. N., Liu, S., Yan, B., Huang, Q., et al. (2007). Regulation of HIF-1α Stability through S-Nitrosylation. *Mol. Cell* 26, 63–74. doi: 10.1016/j.molcel.2007.02.024

Liu, G., Vogel, S. M., Gao, X., Javaid, K., Hu, G., Danilov, S. M., et al. (2011). Src phosphorylation of endothelial cell surface intercellular adhesion molecule-1 mediates neutrophil adhesion and contributes to the mechanism of lung inflammation. *Arterioscler. Thromb. Vasc. Biol.* 31, 1342–1350. doi: 10.1161/ATVBAHA.110.222208

Liu, P., Xu, B., Hock, C. E., Nagele, R., Sun, F. F., and Wong, P. Y. K. (1998). No modulates P-selectin and ICAM-1 mRNA expression and hemodynamic alterations in hepatic I/R. *Am. J. Physiol. Hear. Circ. Physiol.* 275, 2191–2198. doi: 10.1152/ajpheart.1998.275.6.h2191

Lo, H. P., Ackland-Berglund, C. E., Pritchard, K. A., Guice, K. S., and Oldham, K. T. (2001). Attenuated expression of inducible nitric oxide synthase in lung microvascular endothelial cells is associated with an increase in ICAM-1 expression. *J. Pediatr. Surg.* 36, 1136–1142. doi: 10.1053/jpsu.2001.25731

López-Sánchez, L. M., Aranda, E., and Rodríguez-Ariza, A. (2019). Nitric oxide and tumor metabolic reprogramming. *Biochem. Pharmacol.* 176:113769. doi: 10.1016/j.bcp.2019.113769

Lowenstein, C. J. (2007). Nitric oxide regulation of protein trafficking in the cardiovascular system. *Cardiovasc. Res.* 75, 240–246. doi: 10.1016/j.cardiores.2007.03.024

Lu, Y., Yu, T., Liang, H., Wang, J., Xie, J., Shao, J., et al. (2014). Nitric oxide inhibits hetero-adhesion of cancer cells to endothelial cells: restraining circulating tumor cells from initiating metastatic cascade. *Sci. Rep.* 4, 1–9. doi: 10.1038/srep04344

Ma, X. I., Weyrich, A. S., Lefer, D. J., and Lefer, A. M. (1993). Diminished basal nitric oxide release after myocardial ischemia and reperfusion promotes neutrophil adherence to coronary endothelium. *Circ. Res.* 72, 403–412. doi: 10.1161/01.res.72.2.403

MacKesy, D. Z., and Goalstone, M. L. (2011). Insulin augments tumor necrosis factor-alpha stimulated expression of vascular cell adhesion molecule-1 in vascular endothelial cells. *J. Inflamm.* 8:34. doi: 10.1186/1476-9255-8-34

Marín, N., Zamorano, P., Carrasco, R., Mujica, P., González, F. G., Quezada, C., et al. (2012). S-Nitrosation of β-catenin and p120 catenin: a novel regulatory mechanism in endothelial hyperpermeability. *Circ. Res.* 111, 553–563. doi: 10.1161/CIRCRESAHA.112.274548

Marshall, H. E., and Stamler, J. S. (2001). Inhibition of NF-κB by S-nitrosylation. *Biochemistry* 40, 1688–1693. doi: 10.1021/bi002239y

Matsushita, K., Morrell, C. N., Cambien, B., Yang, S. X., Yamakuchi, M., Bao, C., et al. (2003). Nitric oxide regulates exocytosis by S-nitrosylation of N-ethylmaleimide-sensitive factor. *Cell* 115, 139–150. doi: 10.1016/S0092-8674(03)00803-1

Matthews, J. R., Botting, C. H., Panico, M., Morris, H. R., and Hay, R. T. (1996). Inhibition of NF-kappaB DNA binding by nitric oxide. *Nucl. Acids Res* 15 24, 2236–2242. doi: 10.1093/nar/24.12.2236

McCrudden, C. M., McBride, J. W., McCaffrey, J., Ali, A. A., Dunne, N. J., Kett, V. L., et al. (2017). Systemic RALA/iNOS nanoparticles: a potent gene therapy for metastatic breast cancer coupled as a biomarker of treatment. *Mol. Ther. Nucleic Acids* 6, 249–258. doi: 10.1016/j.omtn.2016.12.010

McDowell, S. A. C., and Quail, D. F. (2019). Immunological regulation of vascular inflammation during cancer metastasis. *Front. Immunol.* 10:1984. doi: 10.3389/fimmu.2019.01984

Meffert, M. K., Calakos, N. C., Scheller, R. H., and Schulman, H. (1996). Nitric oxide modulates synaptic vesicle docking/fusion reactions. *Neuron* 16, 1229–1236. doi: 10.1016/S0896-6273(00)80149-X

Metcalf, D. J., Nightingale, T. D., Zenner, H. L., Lui-Roberts, W. W., and Cutler, D. F. (2008). Formation and function of Weibel-Palade bodies. *J. Cell Sci.* 121, 19–27. doi: 10.1242/jcs.03494

Mitchell, D. J., Yu, J., and Tyml, K. (1998). Local l-NAME decreases blood flow and increases leukocyte adhesion via CD18. *Am. J. Physiol.* 274, H1264–H1268. doi: 10.1152/ajpheart.1998.274.4.H1264

Monteiro, H., Costa, P., Reis, A., and Stern, A. (2015). Nitric oxide: protein tyrosine phosphorylation and protein S-nitrosylation in cancer. *Biomed. J.* 38, 380–388. doi: 10.4103/2319-4170.158624

Morgan, A., and Burgoyne, R. D. (2004). Membrane traffic: controlling membrane fusion by modifying NSF. *Curr. Biol.* 14, 968–970. doi: 10.1016/j.cub.2004.10.045

Mukhopadhyay, S., Lee, J., and Sehgal, P. B. (2008). Depletion of the ATPase NSF from Golgi membranes with hypo-S-nitrosylation of vasorelevant proteins in endothelial cells exposed to monocrotaline pyrrole. *Am. J. Physiol. Hear. Circ. Physiol.* 295, 1–30. doi: 10.1152/ajpheart.00642.2008

Müller, A., Homey, B., Soto, H., Ge, N., Catron, D., Buchanan, M. E., et al. (2001). Involvement of chemokine receptors in breast cancer metastasis. *Nature* 410, 50–56. doi: 10.1038/35065016

Mussbacher, M., Salzmann, M., Brostjan, C., Hoesel, B., Schoergenhofer, C., Datler, H., et al. (2019). Cell type specific roles of nf-kb linking inflamation and thrombosis. *Front. Immunol.* 10:85. doi: 10.3389/fimmu.2019.00085

Nagy, G., Clark, J. M., Buzás, E. I., Gorman, C. L., and Cope, A. P. (2007). Nitric oxide, chronic inflammation and autoimmunity. *Immunol. Lett.* 111, 1–5. doi: 10.1016/j.imlet.2007.04.013

Pan, J., and McEver, R. P. (1995). Regulation of the human P-selectin promoter by Bcl-3 and specific homodimeric members of the NF-κB/Rel family. *J. Biol. Chem.* 270, 23077–23083. doi: 10.1074/jbc.270.39.23077

Pierce, J. W., Schoenleber, R., Jesmok, G., Best, J., Moore, S. A., Collins, T., et al. (1997). Novel inhibitors of cytokine-induced IκBα phosphorylation and endothelial cell adhesion molecule expression show anti-inflammatory effects in vivo. *J. Biol. Chem.* 272, 21096–21103. doi: 10.1074/jbc.272.34.21096

Qian, J., and Fulton, D. J. R. (2012). Exogenous, but not endogenous nitric oxide inhibits adhesion molecule expression in human endothelial cells. *Front. Physiol.* 3:3. doi: 10.3389/fphys.2012.00003

Radisavljevic, Z., Avraham, H., and Avraham, S. (2000). Vascular endothelial growth factor up-regulates ICAM-1 expression via the phosphatidylinositol 3 OH-kinase/AKT/nitric oxide pathway and modulates migration of brain microvascular endothelial cells. *J. Biol. Chem.* 275, 20770–20774. doi: 10.1074/jbc.M002448200

Rahman, M. A., Senga, T., Ito, S., Hyodo, T., Hasegawa, H., and Hamaguchi, M. (2010). S-nitrosylation at cysteine 498 of c-Src tyrosine kinase regulates nitric oxide-mediated cell invasion. *J. Biol. Chem.* 285, 3806–3814. doi: 10.1074/jbc.M109.059782

Rahn, J. J., Chow, J. W., Horne, G. J., Mah, B. K., Emerman, J. T., Hoffman, P., et al. (2005). MUC1 mediates transendothelial migration in vitro by ligating endothelial cell ICAM-1. *Clin. Exp. Metastasis* 22, 475–483. doi: 10.1007/s10585-005-3098-x

Randriamboavonjy, V., Schrader, J., Busse, R., and Fleming, I. (2004). Insulin induces the release of vasodilator compounds from platelets by a nitric oxide-G Kinase-VAMP-3-dependent pathway. *J. Exp. Med.* 199, 347–356. doi: 10.1084/jem.20030694

Reymond, N., D'Água, B. B., and Ridley, A. J. (2013). Crossing the endothelial barrier during metastasis. *Nat. Rev. Cancer* 13, 858–870. doi: 10.1038/nrc3628

Reynaert, N. L., Ckless, K., Korn, S. H., Vos, N., Guala, A. S., Wouters, E. F. M., et al. (2004). Nitric oxide represses inhibitory κB kinase through S-nitrosylation. *Proc. Natl. Acad. Sci. U.S.A.* 101, 8945–8950. doi: 10.1073/pnas.0400588101

Ridnour, L. A., Thomas, D. D., Donzelli, S., Espey, M. G., Roberts, D. D., Wink, D. A., et al. (2006). The biphasic nature of nitric oxide responses in tumor biology. *Antioxidants Redox Signal.* 8, 1329–1337. doi: 10.1089/ars.2006.8.1329

Rizza, S., and Filomeni, G. (2018). Role, targets and regulation of (de)nitrosylation in malignancy. *Front. Oncol.* 8:334. doi: 10.3389/fonc.2018.00334

Romagny, S., Bouaouiche, S., Lucchi, G., Ducoroy, P., Bertoldo, J. B., Terenzi, H., et al. (2018). S-Nitrosylation of cIAP1 switches cancer cell fate from TNFα/TNFR1-mediated cell survival to cell death. *Cancer Res.* 78, 1948–1957. doi: 10.1158/0008-5472.CAN-17-2078

Sánchez, F. A., Rana, R., González, F. G., Iwahashi, T., Durán, R. G., Fulton, D. J., et al. (2011). Functional significance of cytosolic endothelial nitric-oxide synthase (eNOS): regulation of hyperpermeability. *J. Biol. Chem.* 286, 30409–30414. doi: 10.1074/jbc.M111.234294

Sánchez, F. A., Savalia, N. B., Durán, R. G., Lal, B. K., Boric, M. P., and Durán, W. N. (2006). Functional significance of differential eNOS translocation. *Am. J. Physiol. Hear. Circ. Physiol.* 291, H1058–H1064. doi: 10.1152/ajpheart.00370.2006

Scher, R. L. (2007). Role of nitric oxide in the development of distant metastasis from squamous cell carcinoma. *Laryngoscope* 117, 199–209. doi: 10.1097/MLG.0b013e31802c6e83

Sektioglu, I. M., Carretero, R., Bender, N., Bogdan, C., Garbi, N., Umansky, V., et al. (2016). Macrophage-derived nitric oxide initiates T-cell diapedesis and tumor rejection. *Oncoimmunology* 5:e1204506. doi: 10.1080/2162402X.2016.1204506

Setiadi, H., and McEver, R. P. (2008). Clustering endothelial E-selectin in clathrin-coated pits and lipid rafts enhances leukocyte adhesion under flow. *Blood* 111, 1989–1998. doi: 10.1182/blood-2007-09-113423

Setiadi, H., Sedgewick, G., Erlandsen, S. L., and McEver, R. P. (1998). Interactions of the cytoplasmic domain of P-selectin with clathrin- coated pits enhance leukocyte adhesion under flow. *J. Cell Biol.* 142, 859–871. doi: 10.1083/jcb.142.3.859

Sha, Y., and Marshall, H. E. (2012). S-nitrosylation in the regulation of gene transcription. *Biochim. Biophys. Acta Gen. Subj.* 1820, 701–711. doi: 10.1016/j.bbagen.2011.05.008

Shelton, J. L., Wang, L., Cepinskas, G., Inculet, R., and Mehta, S. (2008). Human neutrophil-pulmonary microvascular endothelial cell interactions in vitro: differential effects of nitric oxide vs. *peroxynitrite*. *Microvasc. Res.* 76, 80–88. doi: 10.1016/j.mvr.2008.06.001

Shirure, V. S., Liu, T., Delgadillo, L. F., Cuckler, C. M., Tees, D. F. J., Benencia, F., et al. (2015). CD44 variant isoforms expressed by breast cancer cells are functional E-selectin ligands under flow conditions. *Am. J. Physiol. Cell Physiol.* 308, C68–C78. doi: 10.1152/ajpcell.00094.2014

Sökeland, G., and Schumacher, U. (2019). The functional role of integrins during intra- and extravasation within the metastatic cascade. *Mol. Cancer* 18:12. doi: 10.1186/s12943-018-0937-3

Söllner, T., Whiteheart, S. W., Brunner, M., Erdjument-Bromage, H., Geromanos, S., Tempst, P., et al. (1993). SNAP receptors implicated in vesicle targeting and fusion. *Nature* 362, 318–324. doi: 10.1038/362318a0

Somasundaram, V., Basudhar, D., Bharadwaj, G., No, J. H., Ridnour, L. A., Cheng, R. Y. S., et al. (2019). Molecular mechanisms of nitric oxide in cancer progression, signal transduction, and metabolism. *Antioxidants Redox Signal.* 30, 1124–1143. doi: 10.1089/ars.2018.7527

Sperandio, M. (2006). Selectins and glycosyltransferases in leukocyte rolling in vivo. *FEBS J.* 273, 4377–4389. doi: 10.1111/j.1742-4658.2006.05437.x

Springer, T. A. (1990). Adhesion receptors of the immune system. *Nature* 346, 425–434. doi: 10.1038/346425a0

Stamler, J. S., Simon, D. I., Osborne, J. A., Mullins, M. E., Jaraki, O., Michel, T., et al. (1992). S-Nitrosylation of proteins with nitric oxide: synthesis and characterization of biologically active compounds. *Proc. Natl. Acad. Sci. U.S.A.* 89, 444–448. doi: 10.1073/pnas.89.1.444

Stojak, M., Kaczara, P., Motterlini, R., and Chlopicki, S. (2018). Modulation of cellular bioenergetics by CO-releasing molecules and NO-donors inhibits the interaction of cancer cells with human lung microvascular endothelial cells. *Pharmacol. Res.* 136, 160–171. doi: 10.1016/j.phrs.2018.09.005

Strell, C., and Entschladen, F. (2008). Extravasation of leukocytes in comparison to tumor cells. *Cell Commun. Signal.* 6:10. doi: 10.1186/1478-811X-6-10

Strilic, B., and Offermanns, S. (2017). Intravascular survival and extravasation of tumor cells. *Cancer Cell* 32, 282–293. doi: 10.1016/j.ccell.2017.07.001

Sugama, Y., Tiruppathi, C., Janakidevi, K., Andersen, T. T., Fenton, J. W., and Malik, A. B. (1992). Thrombin-induced expression of endothelial P-selectin and intercellular adhesion molecule-1: a mechanism for stabilizing neutrophil adhesion. *J. Cell Biol.* 119, 935–944. doi: 10.1083/jcb.119.4.935

Talmadge, J. E. (2010). Models of metastasis in drug discovery. *Methods Mol. Biol.* 602, 215–233. doi: 10.1007/978-1-60761-058-8_13

Thanos, D., and Maniatis, T. (1995). NF-κB: a lesson in family values. *Cell* 80, 529–532. doi: 10.1016/0092-8674(95)90506-5

Thom, S. R., Bhopale, V. M., Milovanova, T. N., Yang, M., Bogush, M., and Buerk, R. G. (2013). Nitric-oxide Synthase-2 linkage to focal adhesion kinase in neutrophils influences enzyme activity and β2 integrin function. *J. Biol. Chem.* 288, 4810–4818. doi: 10.1074/jbc.M112.426353

Thomas, D. D., and Wink, D. A. (2017). NOS2 as an emergent player in progression of cancer. *Antioxidants Redox Signal.* 26, 963–965. doi: 10.1089/ars.2016.6835

Tichet, M., Prodhomme, V., Fenouille, N., Ambrosetti, D., Mallavialle, A., Cerezo, M., et al. (2015). Tumour-derived SPARC drives vascular permeability and extravasation through endothelial VCAM1 signalling to promote metastasis. *Nat. Commun.* 6:6993. doi: 10.1038/ncomms7993

Tilghman, R. W., and Hoover, R. L. (2002a). E-selectin and ICAM-1 are incorporated into detergent-insoluble membrane domains following clustering in endothelial cells. *FEBS Lett.* 525, 83–87. doi: 10.1016/S0014-5793(02)03070-3

Tilghman, R. W., and Hoover, R. L. (2002b). The Src-cortactin pathway is required for clustering of E-selectin and ICAM-1 in endothelial cells. *FASEB J.* 16, 1257–1259. doi: 10.1096/fj.01-0969fje

Tsao, P. S., McEvoy, L. M., Drexler, H., Butcher, E. C., and Cooke, J. P. (1994). Enhanced endothelial adhesiveness in hypercholesterolemia is attenuated by L-arginine. *Circulation* 89, 2176–2182. doi: 10.1161/01.CIR.89.5.2176

Tuteja, N., Chandra, M., Tuteja, R., and Misra, M. K. (2004). Nitric oxide as a unique bioactive signaling messenger in physiology and pathophysiology. *J. Biomed. Biotechnol.* 2004, 227–237. doi: 10.1155/S1110724304402034

Tvaroška, I., Selvaraj, C., and Koèa, J. (2020). Selectins-The two Dr. Jekyll and Mr. Hyde faces of adhesion molecules-A review. *Molecules* 25, 2835. doi: 10.3390/molecules25122835

Umansky, V., Hehner, S. P., Dumont, A., Hofmann, T. G., Schirrmacher, V., Dröge, W., et al. (1998). Co-stimulatory effect of nitric oxide on endothelial NF-κB implies a physiological self-amplifying mechanism. *Eur. J. Immunol.* 28, 2276–2282. doi: 10.1002/(sici)1521-4141(199808)28:08<2276::aid-immu2276>3.0.co;2-h

Vallance, B. A., Dijkstra, G., Qiu, B., Van Der Waaij, L. A., Van Goor, H., Jansen, P. L. M., et al. (2004). Relative contributions of NOS isoforms during experimental colitis: endothelial-derived NOS maintains mucosal integrity. *Am. J. Physiol. Gastrointest. Liver Physiol.* 287, G865–G874. doi: 10.1152/ajpgi.00187.2004

Van De Stolpe, A., Caldenhoven, E., Stade, G., Koenderman, L., Raaijmakers, J. A., and Johnson, J. P. (1994). 12-O-Tetradecanoylphorbol-13-acetatand tumor necrosis factor of intercellular adhesion molecule-1 is a-mediated induction inhibited by dexamethasone. *J. Biol. Chem.* 269, 6185–6192. doi: 10.1016/s0168-8278(96)80237-6

Vanini, F., Kashfi, K., and Nath, N. (2015). The dual role of iNOS in cancer. *Redox Biol.* 6, 334–343. doi: 10.1016/j.redox.2015.08.009

Vidal, M. J., Zocchi, M. R., Poggi, A., Pellegatta, F., and Chierchia, S. L. (1992). Involvement of nitric oxide in tumor cell adhesion to cytokine-activated endothelial cells. *J. Cardiovascul. Pharmacol.* 20(Suppl. 12), S155-S159. doi: 10.1097/00005344-199204002-00044

Waldow, T., Witt, W., Weber, E., and Matschke, K. (2006). Nitric oxide donor-induced persistent inhibition of cell adhesion protein expression and NFκB activation in endothelial cells. *Nitric Oxide Biol. Chem.* 15, 103–113. doi: 10.1016/j.niox.2005.12.005

Wang, B., Xiong, Q., Shi, Q., Tan, D., Le, X., and Xie, K. (2001). Genetic disruption of host nitric oxide synthase II gene impairs melanoma-induced angiogenesis and suppresses pleural effusion. *Int. J. Cancer* 91, 607–611. doi: 10.1002/1097-0215(200002)9999:9999<::aid-ijc1109>3.0.co;2-d

Wang, X., Zalcenstein, A., and Oren, M. (2003). Nitric oxide promotes p53 nuclear retention and sensitizes neuroblastoma cells to apoptosis by ionizing radiation. *Cell Death Differ.* 10, 468–476. doi: 10.1038/sj.cdd.4401181

Wang, Y., Liu, T., Wu, C., and Li, H. (2008). A strategy for direct identification of protein S-nitrosylation sites by quadrupole time-of-flight mass spectrometry. *J. Am. Soc. Mass Spectrom.* 19, 1353–1360. doi: 10.1016/j.jasms.2008.06.001

Weibel, E. R., and Palade, G. E. (1964). NEW CYTOPLASMIC COMPONENTS IN ARTERIAL ENDOTHELIA. *J. Cell Biol.* 23, 101–112. doi: 10.1083/jcb.23.1.101

Whelan, J., Ghersa, P., Van Huijsduijnen, R. H., Gray, J., Chandra, G., Talabot, F., et al. (1991). An NFxB-like factor is essential but not sufficient for cytokine induction of endothelial leukocyte adhesion molecule 1 (ELAM-1) gene transcription. *Nucl. Acids Res.* 19, 2645–2653. doi: 10.1093/nar/19.10.2645

Wolf, M. J., Hoos, A., Bauer, J., Boettcher, S., Knust, M., Weber, A., et al. (2012). Endothelial CCR2 Signaling Induced by Colon Carcinoma Cells Enables Extravasation via the JAK2-Stat5 and p38MAPK Pathway. *Cancer Cell* 22, 91–105. doi: 10.1016/j.ccr.2012.05.023

Xia, Y. F., Liu, L. P., Zhong, C. P., and Geng, J. G. (2001). Nf-κB activation for constitutive expression of VCAM-1 and ICAM-1 on B lymphocytes and plasma cells. *Biochem. Biophys. Res. Commun.* 289, 851–856. doi: 10.1006/bbrc.2001.6067

Xu, S., Zhou, X., Yuan, D., Xu, Y., and He, P. (2013). Caveolin-1 scaffolding domain promotes leukocyte adhesion by reduced basal endothelial nitric oxide-mediated ICAM-1 phosphorylation in rat mesenteric venules. *Am. J. Physiol. Hear. Circ. Physiol* 305, H1484–H1493. doi: 10.1152/ajpheart.00382.2013

Yudoh, K., Matsui, H., and Tsuji, H. (1997). Nitric oxide induced by tumor cells activates tumor cell adhesion to endothelial cells and permeability of the endothelium in vitro. *Clin. Exp. Metastasis* 15, 557–567. doi: 10.1023/A:1018487213157

Zamorano, P., Koning, T., Oyanadel, C., Mardones, G. A., Ehrenfeld, P., Boric, M. P., et al. (2019). Galectin-8 induces endothelial hyperpermeability through the eNOS pathway involving S-nitrosylation-mediated adherens junction disassembly. *Carcinogenesis* 40, 313–323. doi: 10.1093/carcin/bgz002

Zhang, H., Wong, C. C. L., Wei, H., Gilkes, D. M., Korangath, P., Chaturvedi, P., et al. (2012). HIF-1-dependent expression of angiopoietin-like 4 and L1CAM mediates vascular metastasis of hypoxic breast cancer cells to the lungs. *Oncogene* 31, 1757–1770. doi: 10.1038/onc.2011.365

Zhang, L., Zeng, M., and Fu, B. M. (2016). Inhibition of endothelial nitric oxide synthase decreases breast cancer cell MDA-MB-231 adhesion to intact microvessels under physiological flows. *Am. J. Physiol. Hear. Circ. Physiol.* 310, H1735–H1747. doi: 10.1152/ajpheart.00109.2016

Zhang, Q., Church, J. E., Jagnandan, D., Catravas, J. D., Sessa, W. C., and Fulton, D. (2006). Functional relevance of Golgi- and plasma membrane-localized endothelial NO synthase in reconstituted endothelial cells. *Arterioscler. Thromb. Vasc. Biol.* 26, 1015–1021. doi: 10.1161/01.ATV.0000216044.49494.c4

Conflict of Interest: The authors declare that the research was conducted in the absence of any commercial or financial relationships that could be construed as a potential conflict of interest.

frontiers in Cardiovascular Medicine

ORIGINAL RESEARCH
published: 19 November 2020
doi: 10.3389/fcvm.2020.567837

Oxidized Low-Density Lipoprotein Induces WNT5A Signaling Activation in THP-1 Derived Macrophages and a Human Aortic Vascular Smooth Muscle Cell Line

Ian Ackers[1], *Candice Szymanski*[2], *Mitchell J. Silver*[3] *and Ramiro Malgor*[2,4,5]*

[1] Osteopathic Heritage Foundation, Translational Biomedical Sciences Program, Ohio University, Athens, OH, United States, [2] Department of Biomedical Sciences, Ohio University, Athens, OH, United States, [3] Midwest Cardiology Research Foundation, Columbus, OH, United States, [4] The Diabetes Institute, Ohio University, Athens, OH, United States, [5] Molecular and Cellular Biology Graduate Program, Ohio University, Athens, OH, United States

OPEN ACCESS

Edited by:
Xavier Figueroa,
Pontificia Universidad Católica de Chile, Chile

Reviewed by:
Tzong-Shyuan Lee,
National Taiwan University, Taiwan
Jason Johnson,
University of Bristol, United Kingdom

***Correspondence:**
Ramiro Malgor
malgor@ohio.edu

Specialty section:
This article was submitted to Atherosclerosis and Vascular Medicine, a section of the journal Frontiers in Cardiovascular Medicine

Received: 30 May 2020
Accepted: 22 October 2020
Published: 19 November 2020

Citation:
Ackers I, Szymanski C, Silver MJ and Malgor R (2020) Oxidized Low-Density Lipoprotein Induces WNT5A Signaling Activation in THP-1 Derived Macrophages and a Human Aortic Vascular Smooth Muscle Cell Line. Front. Cardiovasc. Med. 7:567837. doi: 10.3389/fcvm.2020.567837

The pathogenesis of atherosclerosis is complex, evolves, and involves many cell types. Macrophages and vascular smooth muscle cells (VSMCs) are critically involved in atherosclerosis development and progression. Several studies have shown that WNT5A protein is abundantly expressed in human atherosclerotic lesions; however, the mechanism and role of WNT signaling pathway activation is not clearly known. Using THP-1 derived macrophages, and human aortic VSMC cells, we evaluated *in vitro* how oxidized low-density lipoprotein (oxLDL) and WNT5A signaling interact in these two cell lines. We used western blot, scratch assay, metabolic proliferation assay, as well as immunostaining to analyze the effect of Wnt signaling activation. The results demonstrated that oxLDL, as well as WNT5A (control), induced Disheveled-2 (DVL2) activation and Kif26b degradation, indicating activation of non-canonical Wnt signaling. We found that oxLDL and WNT5A induced FZD5-ROR2 co-localization at the cellular membrane *in vitro* in THP-1 derived macrophages. Box5 (FZD5 receptor antagonist) inhibited oxLDL-induced DVL2/JNK activation secondary to newly secreted WNT protein from THP-1 derived macrophages. We found that WNT3A (canonical Wnt) and WNT5A showed different roles in this VSMC cell line. These findings indicate that WNT5A is upregulated by oxLDL, promotes foam cell formation, and affects VSMC phenotype and migration in these two cell lines. Also, in these cell lines FZD5 signaling seems to be necessary for lipid accumulation and, through this mechanism, WNT5A could modulate foam cell formation. Thus, our results suggest that WNT5A may contribute to the pathogenesis of vascular disease through modulating macrophage and VSMC behavior.

Keywords: macrophages, vascular smooth muscle cells, foam cells, Wnt signaling, vascular biology

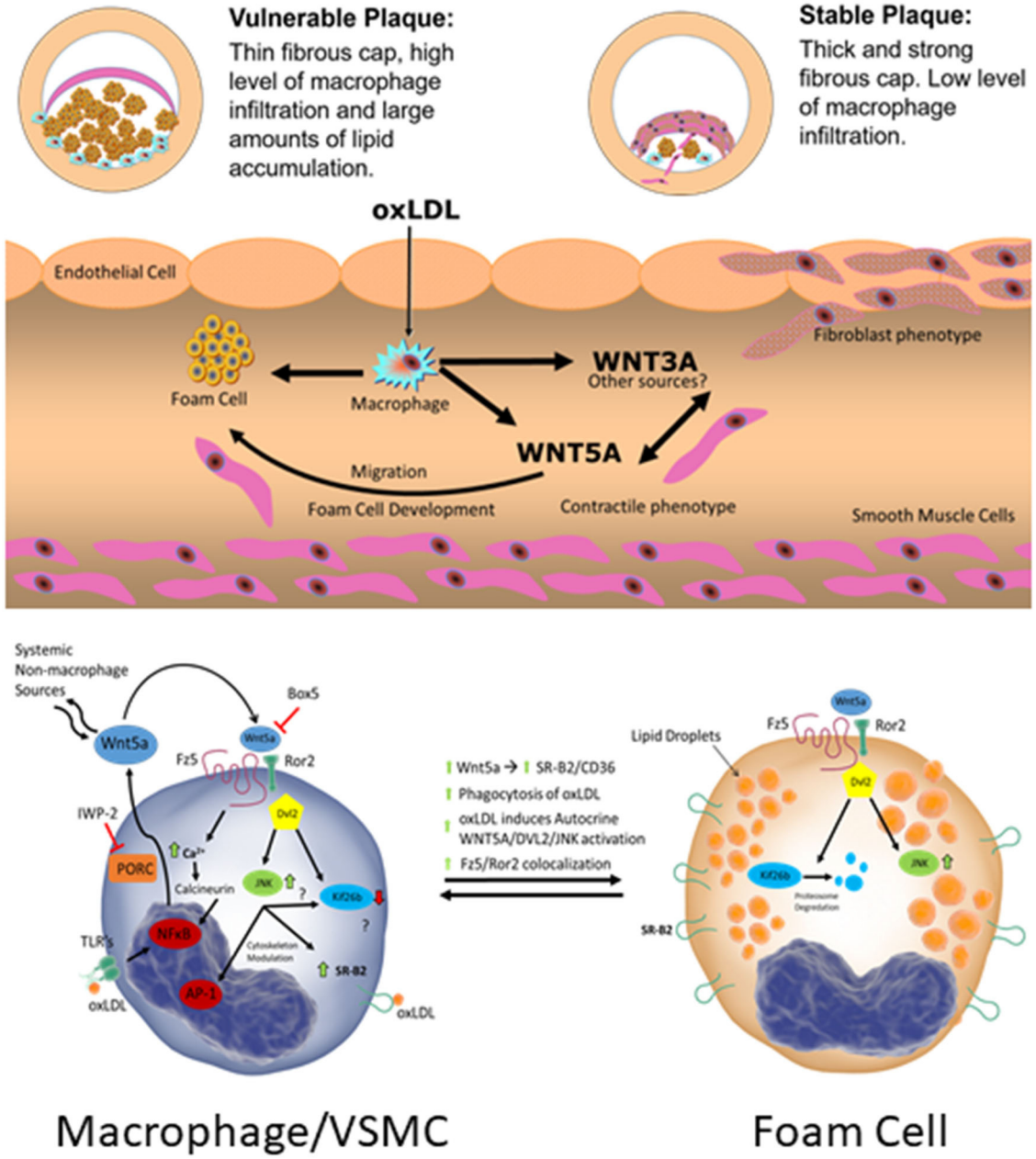

GRAPHICAL ABSTRACT |

INTRODUCTION

Wnt signaling pathway activation has been reported in many cardiovascular diseases and as a consequence, the modulation of Wnt signaling has aroused scientific interest (1–5). Both non-canonical WNT signaling, as well as canonical signaling have been described to be activated in atherosclerosis (6–8). However, the exact mechanism of non-canonical WNT5A signaling in the atherosclerotic plaque remains elusive. The complex pathogenesis of atherosclerosis involves a cascade of biological events including endothelial dysfunction, monocyte transmigration, vascular smooth muscle cell (VSMC) proliferation and migration, as well as foam cell formation, among others (9). Macrophages and VSMC perform crucial roles at different stages in the pathogenesis of atherosclerosis (9, 10). At the beginning, macrophages and VSMC are associated with the development of foam cells, whereas in advanced stages of the disease, macrophages and VSMC are involved in plaque stability and vulnerability (10, 11).

WNTs primarily act as short-range ligands in autocrine and paracrine signaling, leading to the activation of pathways that regulate diverse cellular biological processes including cell proliferation, cell polarity, cell differentiation, and apoptosis (12). WNT signaling is classified into two general pathways: a canonical pathway involving β-catenin and the non-canonical pathway which is β-catenin independent. The latter consists of two sub-groups: the WNT/Ca^{2+} and the Planar Cell Polarity (PCP) pathways (12, 13). Specific WNT/receptor/co-receptor combinations are particularly important in dictating the resulting downstream signaling effects of a given WNT (12). For example, the co-receptor receptor tyrosine kinase-like orphan receptor 2 (ROR2) is critical for activation of the PCP signaling pathway by WNT5A (14, 15). In this pathway, WNT5A binds to the receptor complex consisting of a Frizzled (FZD) receptor (i.e., FZD5) and co-receptor ROR (i.e., ROR2) (16, 17). Unique combinations of the many receptor/co-receptor/ligand binding often correlate to specific downstream effects by a given WNT ligand (12, 18). Downstream of these receptors, reliable readouts for non-canonical signaling activation have been lacking. Three Disheveled (DVL) proteins are integral to the downstream signaling activation of WNT proteins (14, 15). DVL 1, 2, 3 are not specific to a given pathway; however, DVL2 and c-Jun N-terminal kinase (JNK) are important indicators of non-canonical WNT5A/PCP signaling activation (15, 19). Recently, Susman et al. described that Kinesin Family Member 26B (Kif26b) is rapidly degraded in response to non-canonical WNT signaling activation and is a highly specific marker of non-canonical signaling activation (20, 21).

The interaction between oxidized low-density lipoprotein (oxLDL) and macrophages and VSMC is a critical step in the pathogenesis of atherosclerosis, specifically in the formation of foam cells (22, 23). Foam cells are a critical cell type in atherosclerosis development and VSMC's contribute to a large portion (∼50%) of the total foam cell population within the atherosclerotic plaque (23). Activation of macrophages triggers WNT secretion by macrophages and subsequent WNT signaling activation in neighboring cells (24). In this context, our group described increased transcription of WNT5A mRNA in mouse and human macrophages upon exposure to lipopolysaccharide (LPS) and oxLDL (2, 6). Subsequently, we demonstrated that oxLDL increases the expression of CD36 in a FZD5 dependent mechanism (25). CD36 is a key scavenger receptor in macrophages, resulting in lipid uptake and foam cell formation (26). VSMCs also play other important roles in the pathogenesis of atherosclerosis, such as fibrous cap formation. A biological characteristic of VSMCs is their capacity to switch from contractile toward a synthetic phenotype, also referred to as myofibroblast phenotype, involving increased production of extracellular matrix (ECM) and increased proliferation. WNT proteins are implicated in migration and differentiation of VSMCs from the media to the intima which is crucial for fibrous cap formation, an important feature of stable plaques (27–32). These findings demonstrate the importance of macrophages and VSMCs in the atherosclerotic process.

The present study seeks to dissect the effect of oxLDL and WNT5A in THP-1 derived macrophages and a human aortic VSMCs line., Our central hypothesis is that atherogenic stimuli (oxLDL) induce WNT signaling dependent cellular events associated with pathophysiological events in vascular disease.

MATERIALS AND METHODS

In-vitro THP-1 and Derived Macrophages Cell Culture

THP-1 cells (Human Monocytic Leukemia cell line) were purchased (American Type Culture Collection, TIB-202™, Manassas, VA), and were cultured in RPMI-1640 supplemented with 10% FBS (complete RPMI) at 37°C, 5% CO_2 as described previously (6, 33). To induce monocyte-to-macrophage differentiation, THP-1 cells were stimulated with 50 ng/ml Phorbol-12-Myristate-13-Acetate (PMA) for 24 h. After activation and once adherent, the culture medium was removed and replaced with treatment medium (described below). Controls were treated with medium alone plus vehicle where applicable and maintained for the duration of all experiments. At the end of experiments, cell culture medium was collected and centrifuged (900xg) at 4°C for 10 min to remove cell debris. The supernatant was then concentrated 40-fold using Amicon ultra centrifugal filter units (UFC801024, Millipore-Sigma, Burlington, MA). Briefly, supernatant (2 mL) was centrifuged at 7,500xg at 4°C for 10 min (∼50 μL final volume). The supernatant was then stored at −80°C before western blotting.

Treatment medium consisted of basal RPMI-1640 (FBS-free) supplemented with rWNT5A (human recombinant WNT5A, 100 ng/mL, R&D Systems, 645-WN, Minneapolis, MN) or low-density lipoproteins (n-LDL and ox-LDL, Alfa Aesar, J65039 & J65591, both 100 μg/mL) for the indicated duration. FZD5 blocking was performed using commercially available Box5 (#681673, Millipore Sigma, Burlington, MA). Cells were pre-treated with Box5 (100 μM in PBS, 1h) before rWNT5A or lipoprotein treatment as indicated. Inhibition of WNT secretion was performed using a commercially available inhibitor of Porcupine (PORCN), Inhibitor of WNT Production-2 (IWP-2, #681671, Millipore Sigma, Burlington, MA). IWP-1 (5 μM in DMSO) was included for 24 h before LDL treatment. DMSO in equal concentration was used as vehicle control in all experiments using IWP-2. Cells were then analyzed using immunofluorescence, confocal microscopy and western blot, described below.

In-vitro Human Aortic Vascular Smooth Muscle Cell Line Culture

Human aortic vascular smooth muscle cells (VSMCs) were purchased from American Type Culture Collection (T/G HA-VSMC, CRL-1999™, Manassas, VA), and were cultured according to the supplier's instructions at 37°C, 5% CO_2. To make the complete growth medium, the following components (final concentrations) were added to the F-12K base medium (30-2004, ATCC): 0.05 mg/ml ascorbic acid; 0.01 mg/ml

insulin (12585014, Gibco); 0.01 mg/ml transferrin (T8158, Sigma, St. Louis, MO); 10 ng/ml sodium selenite (S5261, Sigma) 20% fetal bovine serum; 10 mM HEPES (7365-45-9, American Bioanalytical, Natick, Massachusetts); 10mM TES (T5691, Sigma).

VSMC in passages 2–6 were used for all experiments. Controls were treated with medium alone plus vehicle where applicable and maintained for the duration of all experiments. Treatment medium consisted of basal medium (F-12K Medium, 30-2004, ATCC) supplemented with 100 ng/mL rWNT5A or rWNT3A (human recombinant WNT5A & WNT3A, 645-WN & 5036-WN respectively, R&D Systems, Minneapolis, MN), 10 ng/mL platelet-derived growth factor-BB (PDGF-BB, GF149, Millipore Sigma, Burlington, MA), or 100 μg/mL low-density lipoproteins (n-LDL and ox-LDL, J65039 & J65591, Alfa Aesar) for the indicated duration. Blocking experiments were performed according to the methods described above.

Migration and Wound Healing Assays

VSMCs were grown in complete growth medium to confluence in 6-well plates and then serum starved (to induce quiescence) for 24 h in serum-free medium (SFM) before treatment. After quiescence/starvation, the cell monolayer was subjected to two parallel scratches on a pre-drawn cross under the plate as a reference point. After the scratch, VSMCs were washed twice with PBS and incubated in 100 ng/mL rWNT5A

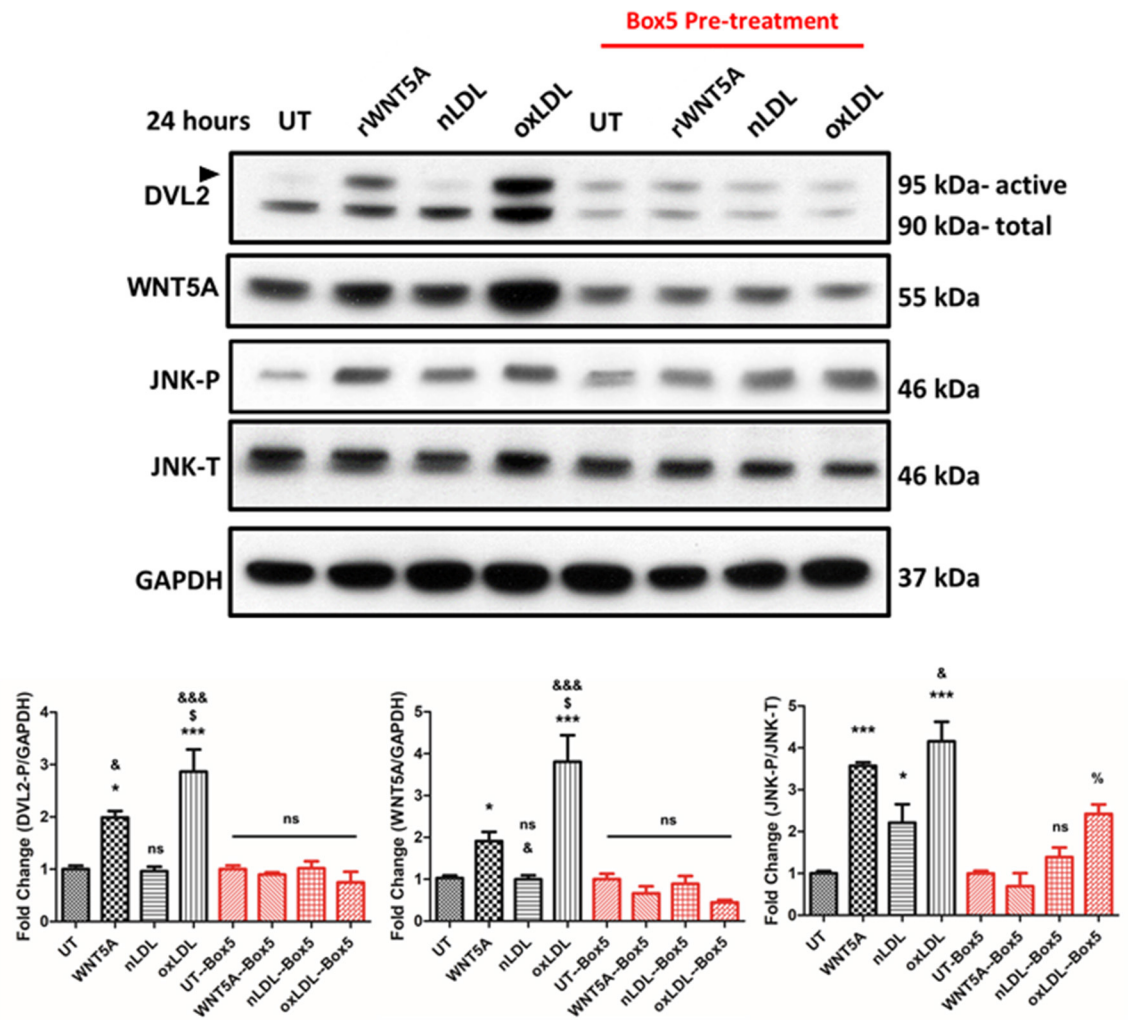

FIGURE 1 | Box5 Blocks rWNT5A and oxLDL-Mediated Non-canonical Wnt Signaling in THP-1-Derived Macrophages. Representative western blots of THP-1-derived macrophages. THP-1-derived macrophages were pre-treated, or not, with Box5 (100 mM) for 1 h or not followed by treatment with rWNT5A (100 ng/mL), nLDL, or oxLDL (both 100 μg/mL) for an additional 24 h. Box5 significantly inhibited rWNT5A-induced and oxLDL-induced DVL2 activation (black arrow). Box5 also inhibited rWNT5A-induced JNK activation but not oxLDL-induced JNK activation, although overall activation was reduced. Experiments were performed in triplicate and western blot band intensities were quantified and are presented as bar graphs (mean ± SEM) of the ratios of DVL2-p/GAPDH, WNT5A/GAPDH, JNK-P/JNK-T expression relative to respective controls (UT or UT-Box5). ns = not significant compared to untreated control (UT or UT-Box5) ($p > 0.05$); * = compared to UT control ($p < 0.05$); *** = compared to UT control ($p < 0.001$); % = compared to Box5 UT control ($p < 0.05$); & = compared to nLDL control ($p < 0.05$); &&& = compared to nLDL control ($p < 0.001$). $ = compared to rWNT5A ($p < 0.05$).

or rWNT3A supplemented treatment medium. To quantify migration, wells were photographed, including reference points, immediately following wounding and every 6 h for 24 h after wounding to measure the wound area migrated by the VSMCs. Phase-contrast images were acquired on a Nikon Eclipse TS100 microscope. Images were processed using analyzed with ImagePro Plus 7 software (Rockville, MD, USA) as follows: the Lopass large spectral filter (width 5, height 4, passes 3) was applied followed by automatic contrast enhancement (Brightness= 76, Contrast= 67, Gamma= 1.0) and finally threshold into binary output for wound area as a percent of total area. Colored vertical lines (red, blue, black) are estimated wound borders for clarity and do not indicate analyzed border data. Five independent experiments were performed.

Proliferation Assay

VSMCs were grown in complete growth medium to ∼60% confluence and then incubated for 24 h in SFM to induce quiescence. After 24 h, cells were then incubated with treatment medium supplemented with 100 ng/mL rWNT5A, 100 ng/mL rWNT3A or 10 ng/mL PDGF-BB and replenished every 24 h. At the end of the experiments, cell proliferation was assayed using CellTiter 96® AQueous One Solution Cell Proliferation Assay (MTS [(3-(4,5-dimethylthiazol-2-yl)-5-(3-carboxymethoxyphenyl)-2-(4-sulfophenyl)-2H-tetrazolium, salt) assay] (Promega, Madison, WI, USA) according to the manufacturer's instructions. Five independent experiments with each treatment group were performed in triplicate.

Lipid Accumulation

Neutral lipid droplets were analyzed using Invitrogen's HCS LipidTOX™ Phospholipidosis and Steatosis Detection Kit for image-based high-content screening assays (Invitrogen, H34476, ThermoFisher Scientific, Waltham, Massachusetts). Staining was prepared following the protocol of the manufacturer. Briefly, VSMCs were fixed in formalin and incubated with HCS LipidTOX™ Red Neutral Lipid Stain. Plates were then sealed without washing and imaged. Images were captured on a Nikon Microphot-SA fluorescence microscope or Nikon Eclipse Confocal Microscope A1 Ti-E (images were recorded at 512 × 512 or 2,048 × 2,048 pixels with a pixel dwell of 3.1) using Nikon NIS-Elements software (Nikon Melville, NY). At least ten high-power fields per biological replicate were collected. Three independent experiments were performed.

Immunofluorescence and Confocal Microscopy

THP-1 cells were cultured on glass coverslips in 12-well plates. At the endpoint of all experiments, cells were washed twice with PBS, then fixed in ice-cold methanol for 10 min and subsequently washed three times with ice-cold PBS. The cells were then blocked with 1% BSA in PBST (PBS + 0.1% Tween 20) for 30 min. Cells were then incubated overnight at 4°C in antibodies

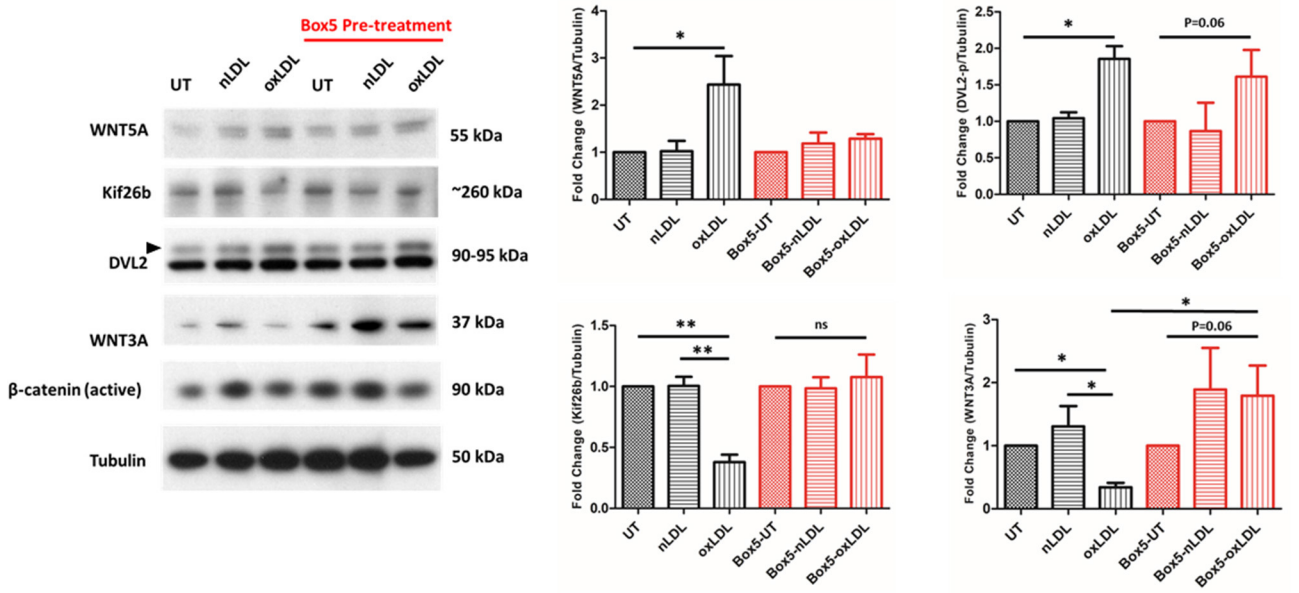

FIGURE 2 | Box5 Blocks rWNT5A and oxLDL Mediated Non-canonical Wnt Signaling in Human Vascular Smooth Muscle Cell Line. Representative western blots evaluating the expression of WNT signaling components in response to oxLDL. In response to oxLDL, there was a significant increase in WNT5A and DVL2 (black arrow) expression ($p < 0.05$, $p < 0.01$; respectively). There was also a significant decrease in Kif26b expression ($p < 0.01$), indicative of activation of non-canonical WNT signaling in oxLDL-treated VSMCs. There was a significant decrease in WNT3A expression ($p < 0.01$), in the oxLDL treated group. An overall increasing trend in WNT3A and active β-catenin expression in the Box5 pre-treated groups was found. All protein experiments were performed in triplicate and western blot band intensities were quantified and are presented as bar graphs (mean ± SEM) of the ratio of control normalized (protein of interest)/tubulin protein. ns = not significant to untreated control (UT or UT-Box5); * = compared between groups ($p < 0.05$); **= compared between groups ($p < 0.01$).

against FZD5 and ROR2 (described in the Immunochemistry section) diluted in 1% BSA-PBST. On separate coverslips, species-matched IgG at the same concentration was used as an isotype control for the primary antibodies. After overnight incubation, the primary antibodies were carefully aspirated, and the cells were washed three times with PBS for 5 min each wash. The cells were then incubated with species-matched secondary antibody (1/1,500, A11008, A11005, Invitrogen) diluted in 1% BSA-PBS at room temperature for 1.5 h. The secondary antibody solution was then decanted and cells washed three times with PBS, 5 min each, in the dark. Coverslips were counterstained with DAPI and mounted on glass slides. Images were captured on a Nikon Eclipse Confocal Microscope A1 Ti-E (images were recorded at 512 × 512 and 2,048 × 2,048 pixels with a pixel dwell of 3.1) using Nikon NIS-Elements software. Experiments were performed in triplicate with at least 10 images per biological replicated captured at 20x, 60x, and 100x. For each experiment and biological replicate, over 100 cells were evaluated.

Western Blot

Experiments were performed on THP-1 derived macrophages and VSMCs as described above (25). Total proteins were extracted using Cell Lysis Buffer (Cell Signaling Technology, Danvers, MA) and Complete EDTA-Free Protease and Phosphatase Inhibitors (Roche, Basel, Switzerland). Protein concentrations from the cell lysates were determined using the bicinchoninic acid assay (BCA) kit (Pierce, Rockford, IL). Equal protein (30 μg) was loaded on 4–12% Bis-Tris gels (Invitrogen, #NP0322BOX) and transferred to polyvinylidene fluoride (PVDF) membranes (ThermoFisher Scientific, 88518), blocked in 5% milk, and probed overnight with specific primary antibodies diluted in 5% BSA in 0.1% TBS-Tween. Primary antibodies included rabbit anti-human PDGF-receptor beta (1/40,000, ab32570, Abcam, Cambridge, UK), rabbit anti-human β-catenin (1/40,000, ab32572, Abcam), rabbit anti-human non-phospho (Active) β-catenin (Ser33/37/Thr41) (1/40,000, #8814 Cell Signaling Technology, Danvers, MA), rabbit anti-human Collagen I (1/40,000, ab138492, Abcam), mouse anti-human Smoothelin (1/40,000, ab8969, Abcam), rabbit anti-human Calponin (1/40,000, ab46794, Abcam), rabbit anti-human CD36 (1/40,000, ab133625, Abcam), rabbit anti-human alpha smooth muscle actin (1/400,000, ab124964, Abcam), rabbit anti-human Disheveled 2 (DVL2) (1/20,000, 3216s, Cell Signaling Technology), Rabbit anti-human CD36 (1/40,000, ab133625 Abcam), Rabbit anti-human Phospho-SAPK/JNK (Thr183/Tyr185) (1:10,000, 9251, Cell Signaling Technology), Rabbit anti-human JNK (1:40,000, 9258, Cell Signaling Technology), mouse anti-human WNT5A (1:180,000, MAB15432, Abnova, Taipei City, Taiwan), rabbit anti-human Kif26b (1:20,000, generously provided by Dr. Henry Ho) (20), mouse anti-human WNT3A (1:40,000, ab81614 Abcam) with mouse anti-human alpha-tubulin (1/100,000, #3873, Cell Signaling Technology) or rabbit anti-human GAPDH (1/80,000, #3683, Cell Signaling Technology) as loading control. JNK proteins (phosphorylated and total) were evaluated on separate membranes and probed on the same day. After overnight incubation at 4°C, membranes were washed and exposed to appropriate HRP conjugated secondary for 1 h (7074s or 7076s, Cell Signaling Technology). Enhanced chemiluminescence reagent (GE Healthcare, Chicago, IL) was used to detect antibody binding and visualized upon exposure to autoradiographic film. All experiments were performed in at least triplicate unless otherwise indicated.

Statistical Analysis

GraphPad Prism5 software was used to generate graphs and for statistical analysis. For MTS proliferation data, one-way analysis of variance (ANOVA) was used to determine differences between groups followed by Tukey *post-hoc* analyses. Lipid accumulation analysis is described above. Migration analysis was performed using a two-way analysis of variance (ANOVA) to determine differences between groups at each time-point followed by Tukey's post-test to compare means. For densitometric analysis of western blots, one-way ANOVA was used to compare means of groups normalized by loading controls. For all analyses, $p <$

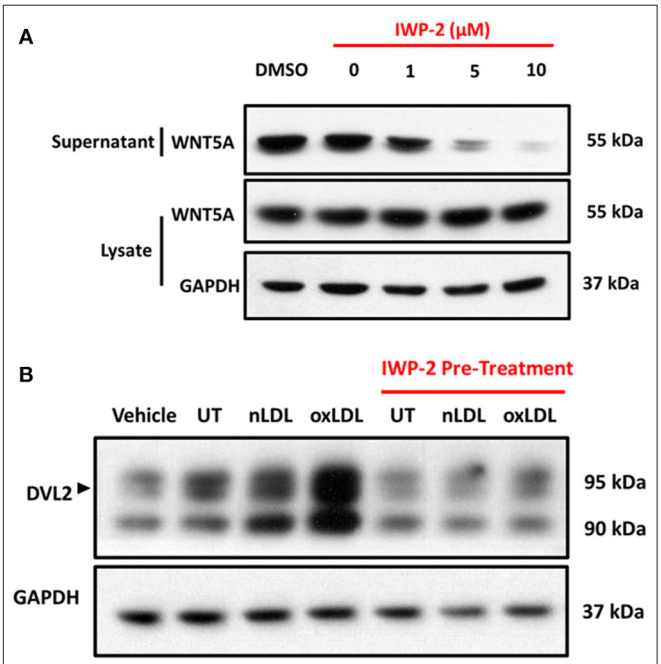

FIGURE 3 | oxLDL-Induced DVL2 Activation is Dependent on WNT Secretion. **(A)** Representative western blots of THP-1-derived macrophages pre-treated with IWP-2 for 24 h at indicated concentrations. Preparation of THP-1 culture medium for western blot was described in the material and methods. In addition to protein estimation by bicinchoninic acid assay (BCA assay), Coomassie staining was used to confirm equal gel loading. IWP-2 demonstrated a concentration-dependent inhibition of WNT5A secretion into the cell culture supernatant, with no appreciable change in the intracellular content detected in whole-cell lysates. **(B)** Representative western blots of THP-1-derived macrophages pre-treated with vehicle (DMSO) or IWP-2 (5 μM) for 24 h and then treated with nLDL, or oxLDL (both 100 μg/mL) for an additional 24 h. IWP-2 inhibited oxLDL-induced DVL2 activation (black arrow), as evidenced by the reduction in intensity and electrophoretic mobility shift from ~90 to ~95 kDa. All experiments were performed in triplicate.

0.05 was considered statistically significant. All experiments were repeated in triplicate unless otherwise indicated.

RESULTS

oxLDL Regulates WNT5A Expression and Signaling Activation in THP-1 Derived Macrophages and Human Aortic Vascular Smooth Muscle Cells

As an approach to investigate the role of oxLDL on WNT signaling in macrophages, THP-1 derived macrophages were used. Results suggest that oxLDL induces WNT5A expression and DVL2 activation in THP-1 derived macrophages (**Figure 1**). To investigate the mechanism, we inhibited at the receptor level (FZD5) and inhibited endogenous WNT secretion.

First, FZD5 signaling was inhibited using the FZD5specific inhibitor Box5. Box5 has been described to be a competitive inhibitor of WNT5A through binding FZD5 receptor (34, 35). The results in **Figure 1** show that Box5 pre-treatment inhibited rWNT5A induced DVL2 activation andoxLDL-induced DVL2 activation in THP-1 derived macrophages (**Figure 1**). Further downstream in the WNT signaling pathway, rWNT5A and oxLDL increased activation of JNK, suggesting non-canonical WNT/PCP pathway activation. In the VSMCs line studied, oxLDL also significantly increased WNT5A expression and DVL2 activation (**Figure 2**, both $p < 0.05$), bul also Box5 pre-treatment inhibited WNT5A signaling activation. Interestingly, oxLDL significantly decreased WNT3A expression in VSMCs and a reduction in active β-catenin relative to UT control (**Figure 2**, $p < 0.01$). Kif26b was significantly decreased in response to oxLDL compared to UT and nLDL (both, $p < 0.01$), confirming an upregulation of non-canonical WNT signaling.

Second, endogenous WNT secretion was inhibited to investigate if oxLDL-induced DVL2 activation was specific to the WNT signaling pathway, or an independent effect of oxLDL. To accomplish this, we used the inhibitor of Wnt Production 2 (IWP-2). In THP-1 derived macrophages there was reduced WNT5A detection in the cell culture supernatant after treatment with increasing concentration of IWP-2, with no changes in WNT5A expression in the whole-cell lysate (**Figure 3A**). We then evaluated the intracellular activation of DVL2 in cells pre-treated for 24 h with IWP-2 (5 μM DMSO) and then treated with nLDL or oxLDL. Compared to control cells, there was a clear decrease in DVL2 activation in response to oxLDL in

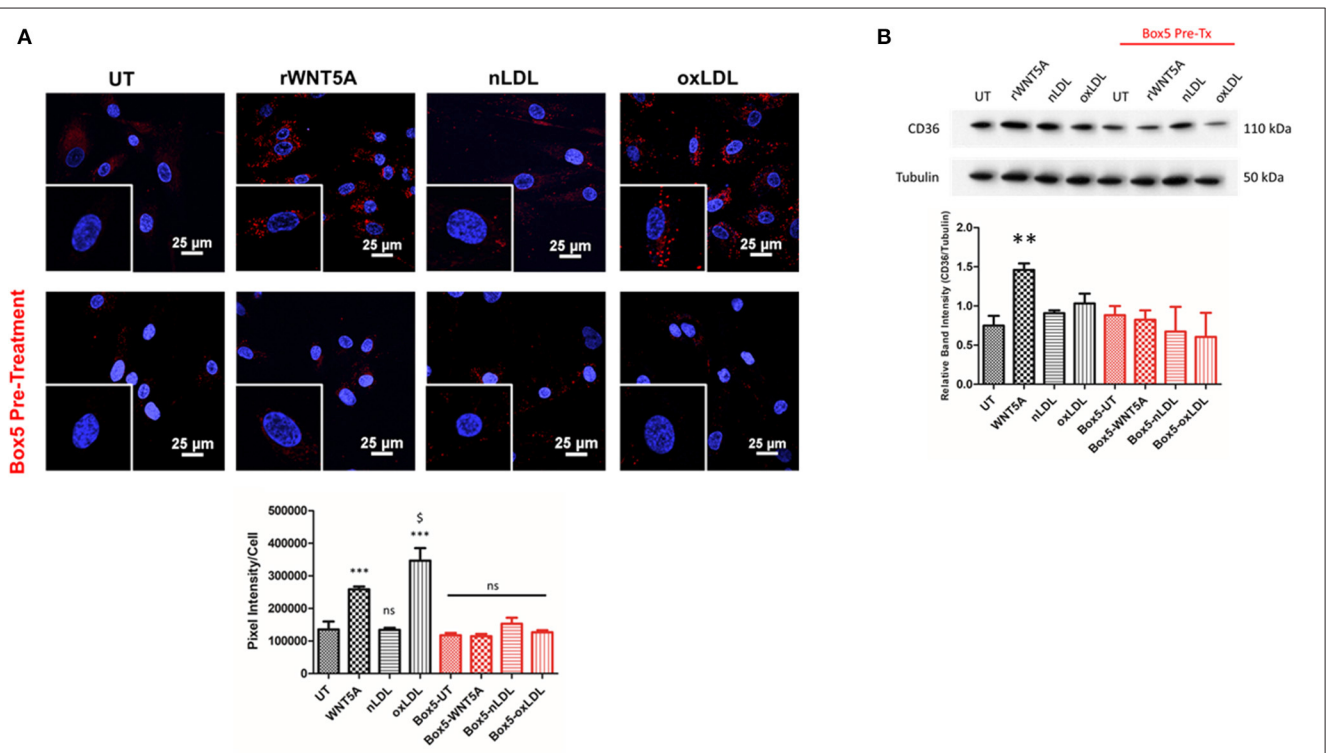

FIGURE 4 | WNT Proteins Regulate Lipid Accumulation in THP-1 Macrophages and VSMCs. **(A)** LipidTOX™ staining was used to evaluate the accumulation of neutral lipids within VSMCs. Representative 60x confocal images are shown. Equally zoomed insets are shown in the bottom left-hand corner of each image. The untreated (UT) controls were held for the duration of all *in vitro* experiments. Compared to UT and nLDL groups, cells treated with rWNT5A (100 ng/ml) and oxLDL (100 μg/mL) have increased red staining in the cytoplasm, indicating an increase in lipid within the cell. Box5 pre-treatment completely blocked lipid accumulation in response to rWNT5A and oxLDL. Quantification of lipid accumulation in each treatment group is representative of two independent experiments. **(B)** Western blots evaluating the expression of CD36 in VSMCs are shown. In response to rWNT5A (100 ng/mL), expression of CD36 in VSMCs was significantly increased (**, $p <$ 0.01), which was blocked by pre-treatment with Box5. *** = compared to UT control ($p < 0.001$); $ = compared to rWNT5A ($p < 0.05$).

the IWP-2 group (**Figure 3B**). **Supplementary Figure 1** shows that WNT5A activated DVL2 over time, as evidenced by the electrophoretic mobility shift from ∼90 to 95 kDa. Together, these results demonstrate that oxLDL-induced DVL2 activation requires intact WNT secretion.

WNT5A Regulates THP-1 Derived Macrophages and VSMC-Derived Foam Cell Formation

To confirm that oxLDL results in lipid accumulation and foam cell development, THP-1 derived macrophages were treated with 100 μg/mL nLDL or oxLDL and stained with LipidTox Red and Oil Red O. Results demonstrated significant lipid accumulation in macrophages treated with oxLDL (**Supplementary Figure 1**). LipidTox staining of VSMCs treated with rWNT5A or oxLDL also resulted in a strong increase in lipid droplet accumulation within the cytoplasm (**Figure 4A**). When VSMCs were pre-treated with Box5, the lipid accumulation in response to WNT5A and oxLDL was significantly blocked (**Figure 4A**, $p < 0.001$). Further, VSMCs increase the expression of CD36 increased in VSMCs in response to rWNT5A (**Figure 4B**, $p < 0.01$). Importantly, this increase was also blocked by Box5, suggesting a FZD5-specific mechanism for lipid accumulation.

The role of canonical signaling in foam cell formation is unknown. Our results demonstrated that WNT3A decreased

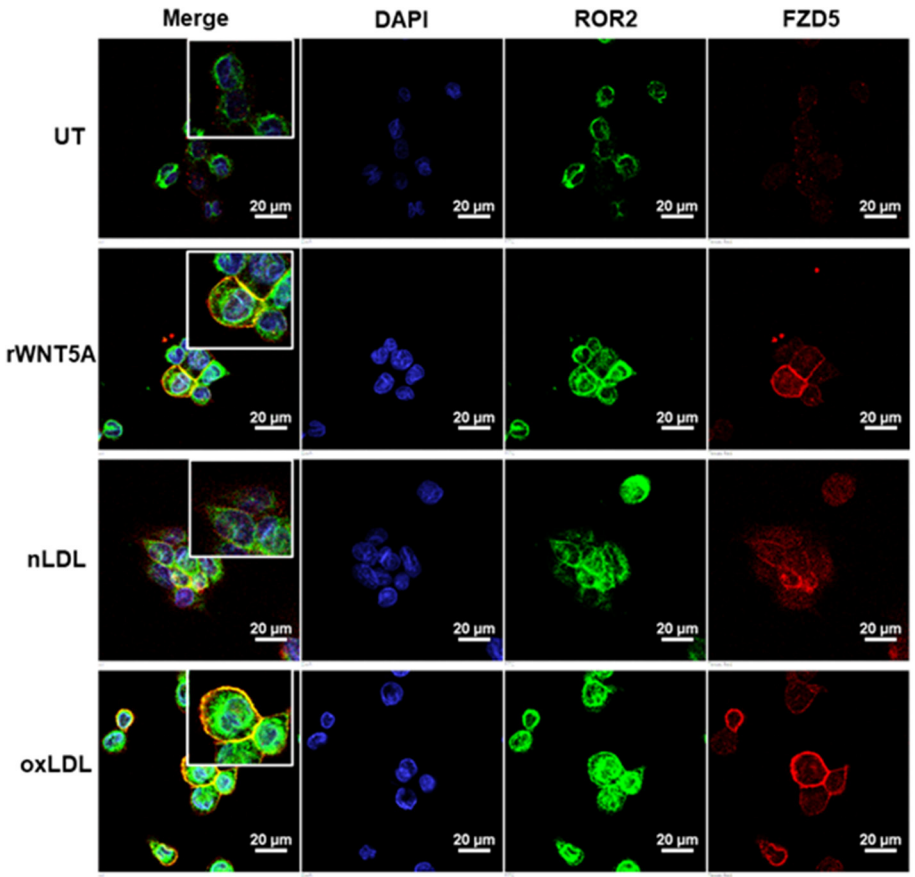

	Pearson's Coefficient:	Overlap Coefficient:
UT	0.548	0.586
rWNT5A	0.78	0.795
nLDL	0.742	0.756
oxLDL	0.875	0.885

FIGURE 5 | WNT5A Receptors, FZD5 and ROR2, are Co-localized *in vitro* in Response to oxLDL and WNT5A. Representative confocal immunofluorescence (IF) images of THP-1-derived macrophages. Cells were differentiated with PMA for 24 h and then treated with rWNT5A (100 ng/mL), (nLDL) or oxLDL (both 100 μg/mL) for an additional 24 h. Cells were then fixed, dual-stained with FZD5 (Red) and ROR2 (Green), and counterstained with 4′,6-diamidino-2-phenylindole (DAPI). Compared to untreated cells (UT), rWNT5A increased the co-localization of the FZD5 and ROR2 receptors at the plasma membrane (Pearson's Correlation: UT = 0.548, rWNT5A = 0.78). Further, oxLDL-treated cells showed an even greater increase in co-localization of the FZD5 and ROR2 receptors compared to all groups (Pearson's Correlation: oxLDL = 0.875). Immunofluorescent images are at 60x with equally zoomed insets for clarity (scale bar= 20 μm). Experiments were performed in duplicate and repeated three independent times. Representative negative control and isotype control images are included in the data supplement (**Supplementary Figure 2**).

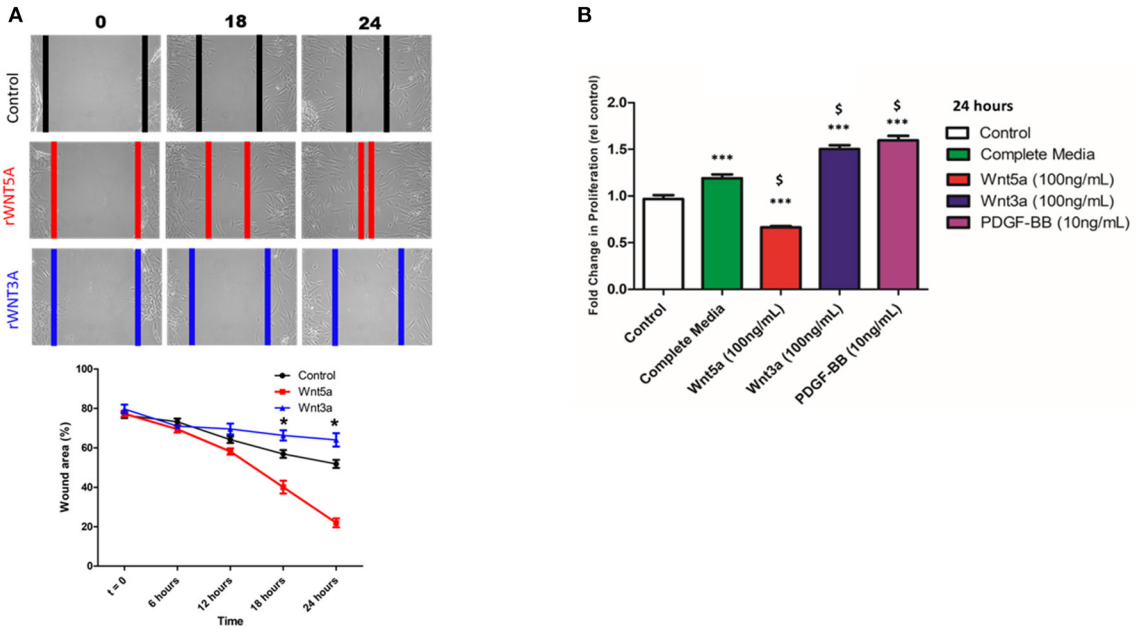

FIGURE 6 | WNT Proteins Differentially Regulate VSMC Migration and Proliferation. **(A)** Representative phase-contrast microscopy images of migrating VSMCs in response to rWNT5A or rWNT3A. Cells were grown to confluence and subjected to wound-healing scratch assay. After the scratch, VSMC were washed 2x with PBS and incubated in rWNT5A or rWNT3A supplemented medium (both 100 ng/mL). VSMCs were then imaged every 6 h. Colored vertical lines are the estimated wound borders for clarity. Quantification was performed on phase-contrast images. rWNT5A promoted migration in comparison to untreated control (UT), as evidenced by a significant decrease in % wound area (*$p < 0.01$, $n = 5$ experiments). Additionally, rWNT3A inhibited migration compared to UT (*$p < 0.01$, $n = 5$ experiments). **(B)** Results of MTS proliferation assays in VSMCs. Cells were seeded at ∼60% confluence then incubated for 24 h in basal medium to induce quiescence. After 24 h, cells were then incubated with the indicated treatment medium. Date were normalized to a standard curve to determine cell number and represented as fold change. rWNT5A inhibited cell proliferation relative to control and complete medium, whereas rWNT3A induced VSMC proliferation almost to the same degree as the positive control (PDGF-BB). Data are representative of five independent experiments with each group performed in triplicate, $ $p < 0.05$ relative to complete medium; ***$p < 0.001$; ns = not significant relative to control for each time point.

lipid droplets in macrophages (**Supplementary Figure 3**). There was an increase in lipid accumulation in the WNT5A-treated group, confirming our previous report (**Supplementary Figure 3**). In the same experiment, macrophages were treated with WNT5A/WNT3A concurrently (both 100 ng/mL) to evaluate if there would be any opposing effects. WNT5A/WNT3A co-treatment demonstrated a similar level of lipid accumulation as untreated (UT) cells, which suggested opposing effects of WNT5A/WNT3A in regulating lipid droplet accumulation.

rWNT5A and oxLDL Promote FZD5 and ROR2 Co-localization *in-vitro* in THP-1 Derived Macrophages

Receptor availability and localization are important for ligand-mediated signaling cascades. We next investigated the mechanism of WNT5A and oxLDL in the co-localization of FZD5 and ROR2 receptors *in-vitro*. **Figure 5** demonstrates the expression of these receptors in THP-1derived macrophages in response to rWNT5A (100 ng/mL), nLDL (100 μg/mL), and oxLDL (100 μg/mL) for 24 h. Results in **Figure 5** show a strong increase in expression of FZD5 and ROR2 in response to rWNT5A, nLDL, and oxLDL. Importantly, there was strong co-localization of these receptors at the cellular membrane in response to WNT5A and oxLDL (**Figure 5**, Pearson's Coefficients of $r = 0.78$ and $r = 0.875$, respectively). Isotype and negative controls are available in the data supplement (**Supplementary Figure 2**). These results provide evidence to suggest that in response to oxLDL non-canonical WNT5A signaling was activated.

WNT5A and WNT3A Differentially Regulate VSMC Migration and Proliferation

A wound healing/scratch assay was used to evaluate the migration *in vitro* of human VSMC cell line in response to rWNT5A or rWNT3A. **Figure 6A** showed representative phase-contrast microscopy images of migrating VSMCs in response to rWNT5A or rWNT3A with approximated migrating border (red, blue, black) for clarity. Quantification of migration demonstrated that, in response to rWNT5A (100 ng/mL), VSMCs migrated significantly more compared to control cells (18 and 24 h, $p < 0.01$) (**Figure 6A**). Further, in response to rWNT3A (100 ng/mL), VSMC migration was reduced relative to control (18 and 24 h, $p < 0.01$) (**Figure 6A**). These results suggested contrasting roles for WNT5A and WNT3A responses in VSMC migratory capacity.

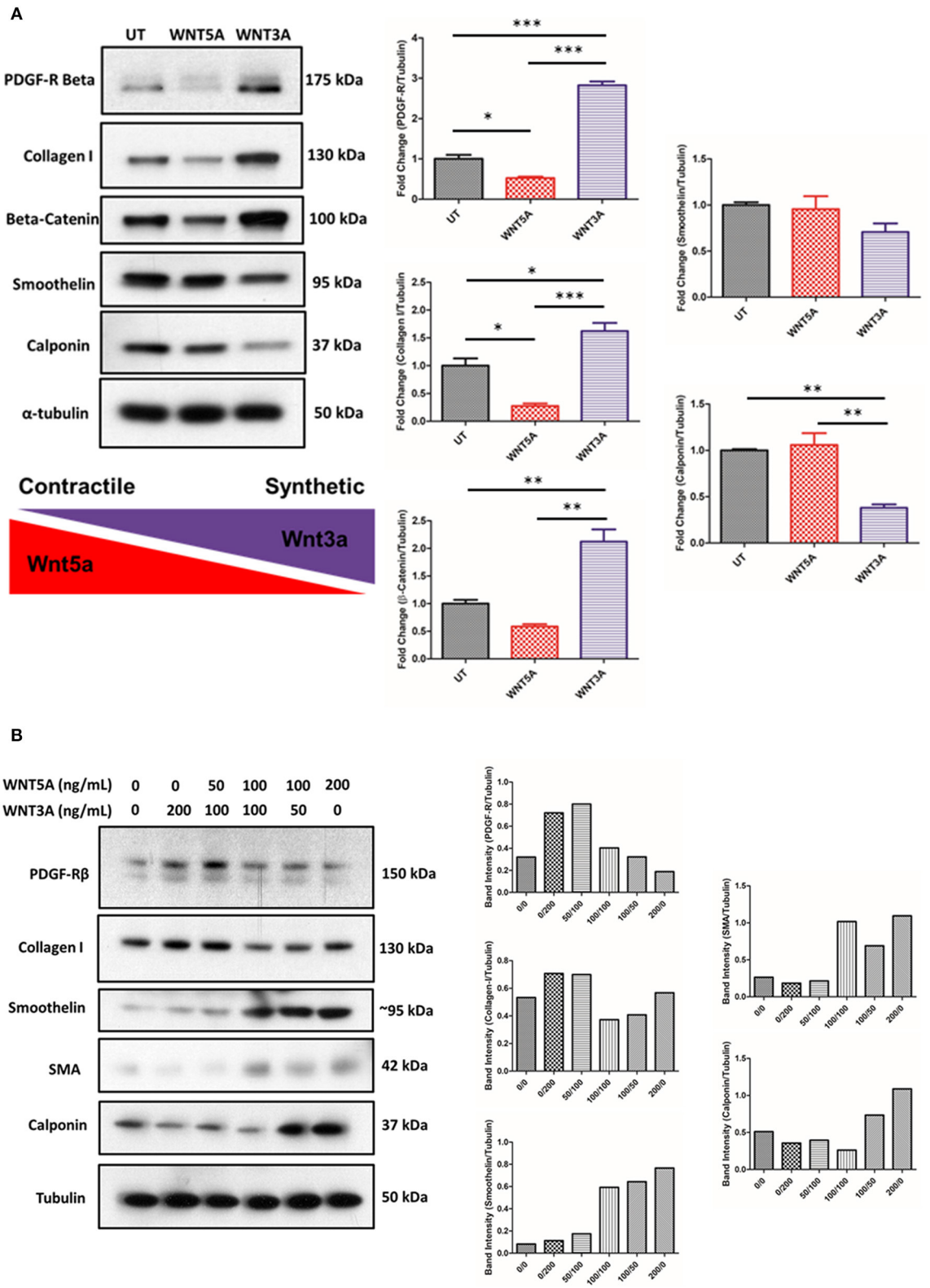

FIGURE 7 | rWNT5A and rWNT3A Regulate VSMC Phenotypic Switching. Representative western blots evaluating the expression of markers of synthetic or contractile VSMCs. VSMCs were incubated in rWNT5A or rWNT3A supplemented medium (both 100 ng/mL) for 24 h. **(A)** rWNT3A increased expression of PDGF-receptor-beta, collagen I, and β-catenin. rWNT3A decreased markers of contractile phenotypic differentiation (calponin, smoothelin). rWNT5A did not

(Continued)

FIGURE 7 | significantly reduce contractile markers. rWNT5A decreased PDGF-receptor-beta and markers of synthetic phenotypic differentiation (collagen I). rWNT5A also decreased β-catenin expression. Experiments were performed in triplicate. **(B)** Representative western blots evaluating expression markers of synthetic or contractile VSMCs. VSMCs were incubated in rWNT5A or rWNT3A in combination at the indicated concentrations (0, 50, 100, 200 ng/mL for each WNT) for 24 h. Taken together, these results suggest that under different concentrations of rWNT5A and rWNT3A, VSMCs up-regulate or down-regulate expression of the assayed phenotypic markers. Data are representative of one experiment performed in duplicate. Western blot band intensities were quantified and are presented as bar graphs (mean ± SEM) as band intensity or ratio of control normalized (protein of interest)/Tubulin. * = $p < 0.05$; ** = $p < 0.01$; *** = $p < 0.001$ significant difference between groups.

Proliferation of VSMCs in response to rWNT5A and rWNT3A was evaluated using MTS [(3-(4,5-dimethylthiazol-2-yl)-5-(3-carboxymethoxyphenyl)-2-(4-sulfophenyl)-2H-tetrazolium, salt] assay. rWNT5A inhibited cell proliferation relative to control and complete medium, whereas rWNT3A induced VSMC proliferation to a similar magnitude as a positive control (PDGF-BB) (**Figure 6B**). These results suggested distinct functions of WNT5A and WNT3A in VSMC proliferation.

WNT5A and WNT3A Perform Contrasting Functions in Determining Phenotypic Markers in the Human VSMC Line Studied

VSMCs were incubated in medium supplemented with 100 ng/mL rWNT5A or rWNT3A for 24 h. Protein lysates were then isolated and assayed by western blot. Results demonstrated that rWNT3A significantly increased the expression of platelet-derived growth factor receptor beta (PDGF-R-β) and β-catenin (**Figure 7A**, $p < 0.001$and $p < 0.01$, respectively). **Figure 7A** also demonstrated that rWNT3A decreased markers of contractile phenotypic differentiation (calponin, $p = 0.01$ and smoothelin, $p =$ ns). Concomitantly, rWNT3A increased expression of the synthetic marker, collagen I ($p < 0.05$). Conversely, rWNT5A decreased ($p < 0.05$) collagen I expression ($p < 0.05$). Furthermore, rWNT5A decreased detection of β-catenin, which was significantly different from WNT3A ($p < 0.01$), and rWNT3A significantly increased β-catenin expression relative to control ($p < 0.01$), confirming significant signaling crosstalk of these two WNT proteins (**Figure 7A**). We next wanted to evaluate if these WNT proteins, given their apparent opposing effects, directly competed to regulate VSMC phenotypic markers.

To determine if WNT signaling pathways interacted, we first chose to test if archetypal WNTs, WNT5A, and WNT3A, interact to determine VSMC phenotypic markers. VSMCs were incubated for 24 h with varying concentrations of recombinant WNT5A/3A proteins. Intriguingly, we found a clear WNT concentration-dependent gradient of the VSMC phenotypic markers investigated (**Figure 7B**). In summary, under higher relative concentrations of WNT5A, VSMC's may be directed toward a more contractile/quiescent phenotype, whereas with higher relative concentrations of WNT3A, VSMCs may be induced toward a synthetic, proliferative phenotype.

DISCUSSION

The interaction between oxLDL, macrophages, and VSMC are critical in the pathogenesis of atherosclerosis, specifically during atheroma formation. In a previous study, our group demonstrated that human peripheral blood macrophages increase transcription of WNT5A mRNA upon exposure to oxLDL (6). More recently, we have reported that WNT5A increases expression of CD36, resulting in oxLDL/lipid uptake within macrophages (25). The results presented in this study expand on this previous work. Our data suggest that WNT5A signaling activation through the FZD5 receptor is a potencial mechanism involved in foam cell formation in THP-1 derived macrophages and human aortic VSMC cell line used in this study. Our results cannot rule out the effects of blocking alternative FZD5 ligands; however, WNT5A, via FZD5 binding, remains an attractive target for therapeutic intervention.

WNT signaling is a complex system of multiple pathways, and the understanding of non-canonical WNT signaling is less well-described. In this study, we investigated the involvement of non-canonical WNT signaling pathways using Kif26b as a specific marker of non-canonical WNT signaling activation (20). Kif26b is specifically targeted by ubiquitination and degradation in a non-canonical WNT signaling-specific manner. Using this approach, we confirmed activation of non-canonical WNT5A signaling activation in VSMCs upon treatment with oxLDL. oxLDL also promotes WNT5A protein expression and secretion in THP-1 macrophages. Thus, non-canonical WNT signaling likely plays a role in arterial wall vascular biology.

WNT signaling activation is dependent on the receptor and cell context; here, we studied two receptors involved in non-canonical WNT signaling, FZD5 and ROR2 (36). Our results showed a high degree of FZD5 and ROR2 co-localization in foam cells *in vitro*. FZD5/ROR2 co-localization was inducible in response to oxLDL and WNT5A; interestingly, this effect was more pronounced with oxLDL treatment. Additionally, our results demonstrated for the first time that oxLDL-induced activation of WNT5A/DVL2 signaling was dependent on WNT5A secretion, suggesting an autocrine, positive-feedback loop (oxLDL/WNT5A/DVL2) where WNT5A signaling was activated in response to oxLDL. Dissecting further down in the WNT signaling pathway, our results showed that oxLDL-induced JNK-p46 activation was only partially blocked by Box5, indicating that oxLDL was likely inducing JNK activation via a secondary pathway independent of FZD5. This result is in line with results reported by Kim et al. where they demonstrated WNT5A induces JNK and NF-κB activation in THP-1 cells (37).

Although evidence has implicated non-canonical WNT signaling as pro-atherogenic (4, 6, 25), numerous reports demonstrated a critical role of the canonical WNT signaling pathway in cardiovascular disease (38–40). Other studies support the concept of an intricate balance of canonical vs. non-canonical WNT signaling pathways and their importance in vascular

biology (41, 42). VSMC phenotypic switching was described as an important initiating factor and key pathophysiological change in proliferative vascular diseases (43, 44). VSMCs have a high capacity to differentiate/de-differentiate from a contractile to a synthetic phenotype, as evidenced by changes in protein markers in response to physical or molecular stimuli from the microenvironment. VSMC phenotypic differentiation involves proliferation, migration, and extracellular matrix (ECM) deposition. The current study showed the effect of WNT signaling on VSMC phenotypic markers. Interestingly, our results showan increase in collagen I protein in response to rWNT3A; this result is in line with previous reports that demonstrated increases collagen I RNA in mouse VSMCs line CRL-2797 in response to WNT3A (5). Further, our data demonstrated that archetypal canonical and non-canonical WNT proteins (WNT3A and WNT5A, respectively) induced proliferation (WNT3A) or migration (WNT5A). Co-treatment experiments demonstrated that the effects of WNT5A and WNT3A can be reversed in a concentration-dependent manner. The phenotypic switching of VSMCs has been associated to fibrous cap thickness, which dictated plaque vulnerability (8, 31, 32). Previous reports in the literature also regard VSMCs as important contributors to the total foam cell population (23). In line with this, our results also show that WNT5A may promote differentiation of thehuman VSMCs line used in the study into foam cells. All of these results suggest that WNT signaling plays a role in vascular smooth muscle cell biology. A limitation of our study is that our *in vitro* models used immortalized cell lines, these studies need to be extended using different models to comprehensively evaluate these novel mechanisms in humans.

In summary, this study implicated WNT5A signaling in THP-1 derived macrophages, human aortic VSMCs, and foam cells with the following lines of evidence. First, oxLDL promoted FZD5 and ROR2 co-localization in THP-1 derived macrophages, providing crucial novel information regarding WNT/FZD5 receptor/co-receptor combinations in foam cells. Further, oxLDL-induced DVL2 activation was dependent on WNT secretion, demonstrating for the first time a mechanism whereby WNT5A signaling was activated in response to oxLDL. Results also suggested that a balance of canonical/non-canonical WNT signaling activation may regulate switching the VSMCs phenotype. Taken together, these results suggest that WNT signaling overall may be an important player in thepathophysiology of vascular disease, making modulation of WNT signaling a potential therapeutic tool to improve cardiovascular disease outcomes.

DATA AVAILABILITY STATEMENT

The raw data supporting the conclusions of this article will be made available by the authors, without undue reservation.

AUTHOR CONTRIBUTIONS

IA, CS, and RM designed the study and prepared the manuscript, with input from all authors. IA and CS performed experiments and data analyses. MS and RM guided the interpretation of the results. All authors contributed to the article and approved the submitted version.

FUNDING

The authors would like to thank the National Institutes of Health and the National Heart, Lung, and Blood Institute (NHLBI-R15HL133885) awarded to RM for helping to fund portions of this work. Other portions of this work would not have been possible without the Kopchick MCB/TBS Research Fellowship awarded to IA. Stipend and fellowship support to IA generously provided by the Osteopathic Heritage Foundations' Dual Degree Program at Ohio University Heritage College of Osteopathic Medicine, Athens, OH.

ACKNOWLEDGMENTS

The authors would like to thank Dr. Karl Willert, Dr. Karen Coschigano, and Dr. Leslie Consitt for helpful critiques, suggestions, and expertise in preparation of this manuscript. Additionally, the Kif26b antibody was generously gifted by Dr. Henry Ho (20). The authors are thankful for Ohio University's Histology Core Facility and Microscopy Core Facility.

SUPPLEMENTARY MATERIAL

The Supplementary Material for this article can be found online at: https://www.frontiersin.org/articles/10.3389/fcvm.2020.567837/full#supplementary-material

Supplementary Figure 1 | Foam Cell Development and WNT5A Signaling. Representative Oil Red O-stained images of THP-1-derived macrophages. Cells were differentiated with PMA for 24 h and then treated with control cholesterol (nLDL) or oxidized cholesterol (oxLDL) (both 100 μg/mL) for an additional 24 h. Cells were then imaged by light microscopy. The same treatment experiment was performed using a different detection system. Invitrogen's HCS LipidTOX Phospholipidosis and Steatosis Detection Kit for image-based high content screening assays [ThermoFisher Scientific (Invitrogen, H34476), Waltham, MA, USA] were used previously in our lab. Staining was prepared following the manufacturer's protocol. Western blotting was used to evaluate the activation of WNT5A signaling pathway activation in response to rWNT5A. Macrophages were differentiated as described in the Materials and Methods section. Compared to untreated (UT), macrophages treated with rWNT5A (100 ng/ml) had significant DVL2 activation (black arrow), evidenced by the electrophoretic mobility shift of the band from ∼90 to ∼95 kDa which has been previously described (15). DVL2 activation can be appreciated in 30 min of rWNT5norA treatment and sustained to 6 h. JNK was also activated over the same time frame. Experiments were performed in triplicate and western blot band intensities were quantified and are presented as bar graphs (mean ± SEM) of the ratio of JNK-P/JNK-T and DVL2/GAPDH expression relative to control. Quantification of band pixel intensity was determined by ImageJ software from three independent experiments. ns = $p > 0.05$, $^{*}p < 0.05$, $^{**}p < 0.01$, $^{***}p < 0.001$.

Supplementary Figure 2 | Co-localization in Macrophage Culture. Representative confocal fluorescent images of THP-1-derived macrophages. Cells were treated as described in the Materials and Methods section. On separate coverslips, species-matched IgG at the same concentration was used as isotype control and no primary antibody was used as negative control; cells were counterstained with 4′,6-diamidino-2-phenylindole (DAPI) and images are at 600x (scale bar = 50 μm).

Supplementary Figure 3 | Lipid Accumulation in response to WNT proteins in THP-1. Representative confocal fluorescent images of THP-1- derived macrophages. LipidTOX^{TM} staining was used to evaluate the accumulation of neutral lipids within differentiated macrophages. The untreated (UT) controls were held for the duration of the *in vitro* experiments. Cells were treated with rWNT5A (100 ng/ml), rWNT3A (100 ng/ml), or in combination (both 100 ng/ml) as described in the Materials and Methods section. Cells were counterstained with 4′,6-diamidino-2-phenylindole (DAPI) and images are at 600X (scale bar = 50 μm). Quantification of lipid accumulation was represented as pixel intensity per cell as a measure of lipid droplet density and intensity. Data are representative of n = 2 experiments and are presented as bar graphs (mean ± SEM).

REFERENCES

1. Foulquier S, Daskalopoulos EP, Lluri G, Hermans KCM, Deb A, Blankesteijn WM. WNT signaling in cardiac and vascular disease. *Pharmacol Rev.* (2018) 70:68–141. doi: 10.1124/pr.117.013896
2. Christman MA, Goetz DJ, Dickerson E, McCall KD, Lewis CJ, Benencia F, et al. Wnt5a is expressed in murine and human atherosclerotic lesions. *Am J Physiol Heart Circ Physiol.* (2008) 294:H2864–70. doi: 10.1152/ajpheart.00982.2007
3. Malgor R, Bhatt PM, Connolly BA, Jacoby DL, Feldmann KJ, Silver MJ, et al. Wnt5a, TLR2 and TLR4 are elevated in advanced human atherosclerotic lesions. *Inflamm Res.* (2014) 63:277–85. doi: 10.1007/s00011-013-0697-x
4. Yang L, Chu Y, Wang Y, Zhao X, Xu W, Zhang P, et al. siRNA-mediated silencing of Wnt5a regulates inflammatory responses in atherosclerosis through the MAPK/NF-κB pathways. *Int J Mol Med.* (2014) 34:1147–52. doi: 10.3892/ijmm.2014.1860
5. Carthy JM, Luo Z, McManus BM. WNT3A induces a contractile and secretory phenotype in cultured vascular smooth muscle cells that is associated with increased gap junction communication. *Lab Invest.* (2012) 92:246–55. doi: 10.1038/labinvest.2011.164
6. Bhatt PM, Lewis CJ, House DL, Keller CM, Kohn LD, Silver MJ, et al. Increased Wnt5a mRNA expression in advanced atherosclerotic lesions, and oxidized LDL treated human monocyte-derived macrophages. *Open Circ Vasc J.* (2012) 5:1–7. doi: 10.2174/1877382601205010001
7. Wang X, Xiao Y, Mou Y, Zhao Y, Blankesteijn WM, Hall JL. A role for the β-catenin/T-cell factor signaling cascade in vascular remodeling. *Circ Res.* (2002) 90:340–7. doi: 10.1161/hh0302.104466
8. Mill C, Tsaousi A, Woodward E, Johnson J, George S. Increased expression of Wnt5A in unstable atherosclerotic plaques is associated with increased MMP expression and may contribute to instability. *Atherosclerosis.* (2010) 213:e12. doi: 10.1016/j.atherosclerosis.2010.08.022
9. Hansson GK, Libby P. The immune response in atherosclerosis: a double-edged sword. *Nat Rev Immunol.* (2006) 6:508–19. doi: 10.1038/nri1882
10. Naghavi M, Libby P, Falk E, Casscells SW, Litovsky S, Rumberger J, et al. From vulnerable plaque to vulnerable patient A call for new definitions and risk assessment strategies: part I. *Circulation.* (2003) 108:1664–72. doi: 10.1161/01.CIR.0000087480.94275.97
11. Moore KJ, Tabas I. Macrophages in the pathogenesis of atherosclerosis. *Cell.* (2011) 145:341–55. doi: 10.1016/j.cell.2011.04.005
12. Gordon MD, Nusse R. Wnt signaling: multiple pathways, multiple receptors, and multiple transcription factors. *J Biol Chem.* (2006) 281:22429–33. doi: 10.1074/jbc.R600015200
13. van Amerongen R, Nusse R. Towards an integrated view of Wnt signaling in development. *Development.* (2009) 136:3205–14. doi: 10.1242/dev.033910
14. Ho H-YH, Susman MW, Bikoff JB, Ryu YK, Jonas AM, Hu L, et al. Wnt5a-Ror-Dishevelled signaling constitutes a core developmental pathway that controls tissue morphogenesis. *Proc Natl Acad Sci.* (2012) 109:4044–51. doi: 10.1073/pnas.1200421109
15. Nishita M, Itsukushima S, Nomachi A, Endo M, Wang Z, Inaba D, et al. Ror2/frizzled complex mediates Wnt5a-Induced AP-1 activation by regulating dishevelled polymerization. *Mol Cell Biol.* (2010) 30:3610–9. doi: 10.1128/MCB.00177-10
16. Kurayoshi M, Yamamoto H, Izumi S, Kikuchi A. Post-translational palmitoylation and glycosylation of Wnt-5a are necessary for its signalling. *Biochem J.* (2007) 402(Pt 3):515–23. doi: 10.1042/BJ20061476
17. Sato A, Yamamoto H, Sakane H, Koyama H, Kikuchi A. Wnt5a regulates distinct signalling pathways by binding to Frizzled2. *EMBO J.* (2010) 29:41–54. doi: 10.1038/emboj.2009.322
18. Ring L, Neth P, Weber C, Steffens S, Faussner A. β-Catenin-dependent pathway activation by both promiscuous "canonical" WNT3a–, and specific "noncanonical" WNT4– and WNT5a–FZD receptor combinations with strong differences in LRP5 and LRP6 dependency. *Cell Signal.* (2014) 26:260–7. doi: 10.1016/j.cellsig.2013.11.021
19. Endo M, Nishita M, Minami Y. Analysis of Wnt/planar cell polarity pathway in cultured cells. In: *Planar Cell Polarity*. New York, NY: Springer (2012). p. 201–14. Available from: https://link.springer.com/protocol/10.1007/978-1-61779-510-7_16 doi: 10.1007/978-1-61779-510-7_16 (accessed February 1, 2018).
20. Susman MW, Karuna EP, Kunz RC, Gujral TS, Cantú AV, Choi SS, et al. Kinesin superfamily protein Kif26b links Wnt5a-Ror signaling to the control of cell and tissue behaviors in vertebrates. *Elife.* (2017) 6:e26509. doi: 10.7554/eLife.26509
21. Karuna EP, Choi SS, Scales MK, Hum J, Cohen M, Fierro FA, et al. Identification of a WNT5A-responsive degradation domain in the kinesin superfamily protein KIF26B. *Genes.* (2018) 9:196. doi: 10.3390/genes9040196
22. Rios FJO, Koga MM, Ferracini M, Jancar S. Co-Stimulation of PAFR and CD36 is required for oxLDL-induced human macrophages activation. *PLoS ONE.* (2012) 7:e36632. doi: 10.1371/journal.pone.0036632
23. Allahverdian S, Chehroudi AC, McManus BM, Abraham T, Francis GA. Contribution of intimal smooth muscle cells to cholesterol accumulation and macrophage-like cells in human atherosclerosis. *Circulation.* (2014) 129:1551–9. doi: 10.1161/CIRCULATIONAHA.113.005015
24. Schaale K, Neumann J, Schneider D, Ehlers S, Reiling N. Wnt signaling in macrophages: augmenting and inhibiting mycobacteria-induced inflammatory responses. *Eur J Cell Biol.* (2011) 90:553–9. doi: 10.1016/j.ejcb.2010.11.004
25. Ackers I, Szymanski C, Duckett KJ, Consitt LA, Silver MJ, Malgor R. Blocking Wnt5a signaling decreases CD36 expression and foam cell formation in atherosclerosis. *Cardiovasc Pathol.* (2018) 34:1–8. doi: 10.1016/j.carpath.2018.01.008
26. Yu M, Jiang M, Chen Y, Zhang S, Zhang W, Yang X, et al. Inhibition of macrophage CD36 expression and cellular oxidized low density lipoprotein (oxLDL) accumulation by Tamoxifen A Peroxisome Proliferator-Activated Receptor (PPAR)γ-dependent mechanism. *J Biol Chem.* (2016) 291:16977–89. doi: 10.1074/jbc.M116.740092
27. Owens GK, Kumar MS, Wamhoff BR. Molecular regulation of vascular smooth muscle cell differentiation in development and disease. *Physiol Rev.* (2004) 84:767–801. doi: 10.1152/physrev.00041.2003
28. Hao H, Gabbiani G, Bochaton-Piallat M-L. Arterial smooth muscle cell heterogeneity: implications for atherosclerosis and restenosis development. *Arterioscler Thromb Vasc Biol.* (2003) 23:1510–20. doi: 10.1161/01.ATV.0000090130.85752.ED
29. Gerthoffer WT. Mechanisms of vascular smooth muscle cell migration. *Circ Res.* (2007) 100:607–21. doi: 10.1161/01.RES.0000258492.96097.47
30. Brown BA, Connolly GM, Mill CEJ, Williams H, Angelini GD, Johnson JL, et al. Aging differentially modulates the Wnt pro-survival signalling pathways in vascular smooth muscle cells. *Aging Cell.* (2018) 18:e12844. doi: 10.1111/acel.12844
31. Tsaousi A, Williams H, Lyon CA, Taylor V, Swain A, Johnson JL, et al. Wnt4/β-catenin signaling induces VSMC proliferation and is associated with intimal thickeningnovelty and significance. *Circ Res.* (2011) 108:427–36. doi: 10.1161/CIRCRESAHA.110.233999
32. Lyon C, Mill C, Tsaousi A, Williams H, George S. Regulation of VSMC behavior by the cadherin-catenin complex. *Front Biosci.* (2011) 16:644–57. doi: 10.2741/3711
33. Fuhrman B, Partoush A, Volkova N, Aviram M. Ox-LDL induces monocyte-to-macrophage differentiation *in vivo*: possible role for the macrophage colony stimulating factor receptor (M-CSF-R).

Atherosclerosis. (2008) 196:598–607. doi: 10.1016/j.atherosclerosis.2007.06.026
34. Jenei V, Sherwood V, Howlin J, Linnskog R, Säfholm A, Axelsson L, et al. A t-butyloxycarbonyl-modified Wnt5a-derived hexapeptide functions as a potent antagonist of Wnt5a-dependent melanoma cell invasion. *Proc Natl Acad Sci USA.* (2009) 106:19473–8. doi: 10.1073/pnas.0909409106
35. Säfholm A, Leandersson K, Dejmek J, Nielsen CK, Villoutreix BO, Andersson T. A formylated hexapeptide ligand mimics the ability of Wnt-5a to impair migration of human breast epithelial cells. *J Biol Chem.* (2006) 281:2740–9. doi: 10.1074/jbc.M508386200
36. Mikels AJ, Nusse R. Purified Wnt5a protein activates or inhibits β-catenin–TCF signaling depending on receptor context. *PLOS Biol.* (2006) 4:e115. doi: 10.1371/journal.pbio.0040115
37. Kim J, Chang W, Jung Y, Song K, Lee I. Wnt5a activates THP-1 monocytic cells via a β-catenin-independent pathway involving JNK and NF-κB activation. *Cytokine.* (2012) 60:242–8. doi: 10.1016/j.cyto.2012.06.013
38. Cheng W-L, Yang Y, Zhang X-J, Guo J, Gong J, Gong F-H, et al. Dickkopf-3 ablation attenuates the development of atherosclerosis in ApoE-deficient mice. *J Am Heart Assoc.* (2017) 6:e004690. doi: 10.1161/JAHA.116.004690
39. Mani A, Radhakrishnan J, Wang H, Mani A, Mani M-A, Nelson-Williams C, et al. LRP6 mutation in a family with early coronary disease and metabolic risk factors. *Science.* (2007) 315:1278–82. doi: 10.1126/science.1136370
40. Sarzani R, Salvi F, Bordicchia M, Guerra F, Battistoni I, Pagliariccio G, et al. Carotid artery atherosclerosis in hypertensive patients with a functional LDL receptor-related protein 6 gene variant. *Nutr Metab Cardiovasc Dis.* (2011) 21:150–6. doi: 10.1016/j.numecd.2009.08.004
41. Kim K-I, Park KU, Chun EJ, Choi SI, Cho Y-S, Youn T-J, et al. A novel biomarker of coronary atherosclerosis: serum DKK1 concentration correlates with coronary artery calcification and atherosclerotic plaques. *J Korean Med Sci.* (2011) 26:1178. doi: 10.3346/jkms.2011.26.9.1178
42. Albanese I, Yu B, Al-Kindi H, Barratt B, Ott L, Al-Refai M, et al. Role of noncanonical Wnt signaling pathway in human aortic valve calcification highlights. *Arterioscler Thromb Vasc Biol.* (2017) 37:543–52. doi: 10.1161/ATVBAHA.116.308394
43. Zhu S-B, Zhu J, Zhou Z-Z, Xi E-P, Wang R-P, Zhang Y. TGF-β1 induces human aortic vascular smooth muscle cell phenotype switch through PI3K/AKT/ID2 signaling. *Am J Transl Res*. (2015) 7:2764–74.
44. Jiang D, Yang Y, Li D. Lipopolysaccharide induced vascular smooth muscle cells proliferation: a new potential therapeutic target for proliferative vascular diseases. *Cell Prolif.* (2017) 50:e12332. doi: 10.1111/cpr.12332

Conflict of Interest: The authors declare that the research was conducted in the absence of any commercial or financial relationships that could be construed as a potential conflict of interest.

frontiers in Physiology

ORIGINAL RESEARCH
published: 08 December 2020
doi: 10.3389/fphys.2020.565240

Identification of Pathways and Key Genes in Venous Remodeling After Arteriovenous Fistula by Bioinformatics Analysis

Kong Jie[1†], Wang Feng[2†], Zhao Boxiang[1†], Gong Maofeng[1], Zhang Jianbin[3], Lu Zhaoxuan[1], Zhou Yangyi[1], Chen Liang[1], Su Haobo[1], Lou Wensheng[1], Chen Guoping[1], Gu Jianping[1], He Xu[1]* and Wen Jianyan[3]**

[1] Department of Interventional Radiology, Nanjing First Hospital, Nanjing Medical University, Nanjing, China, [2] Graduate School of Peking Union Medical College, Beijing, China, [3] Department of Cardiovascular Surgery, China-Japan Friendship Hospital, Beijing, China

OPEN ACCESS

Edited by:
Xavier Figueroa,
Pontificia Universidad Católica de Chile, Chile

Reviewed by:
Shuo Wang,
Capital Medical University, China
Andrea Remuzzi,
University of Bergamo, Italy

***Correspondence:**
Gu Jianping
cjr.gujianping@vip.163.com
He Xu
hexunj@163.com
Wen Jianyan
jianyanwen@sina.com

[†]These authors share first authorship

Specialty section:
This article was submitted to Vascular Physiology, a section of the journal Frontiers in Physiology

Received: 24 May 2020
Accepted: 30 October 2020
Published: 08 December 2020

Citation:
Jie K, Feng W, Boxiang Z, Maofeng G, Jianbin Z, Zhaoxuan L, Yangyi Z, Liang C, Haobo S, Wensheng L, Guoping C, Jianping G, Xu H and Jianyan W (2020) Identification of Pathways and Key Genes in Venous Remodeling After Arteriovenous Fistula by Bioinformatics Analysis. Front. Physiol. 11:565240. doi: 10.3389/fphys.2020.565240

The arteriovenous fistula (AVF) is the first choice for vascular access for hemodialysis of renal failure patients. Venous remodeling after exposure to high fistula flow is important for AVF to mature but the mechanism underlying remodeling is still unknown. The objective of this study is to identify the molecular mechanisms that contribute to venous remodeling after AVF. To screen and identify the differentially expressed genes (DEGs) that may involve venous remodeling after AVF, we used bioinformatics to download the public microarray data (GSE39488) from the Gene Expression Omnibus (GEO) and screen for DEGs. We then performed gene ontology (GO) function analysis, Kyoto Encyclopedia of Genes and Genomes (KEGG) pathway analysis, and gene set enrichment analysis (GSEA) for the functional annotation of DEGs. The protein-protein interaction (PPI) network was constructed and the hub genes were carried out. Finally, we harvested 12 normal vein samples and 12 AVF vein samples which were used to confirm the expressions of the hub genes by immunohistochemistry. A total of 45 DEGs were detected, including 32 upregulated and 13 downregulated DEGs. The biological process (BP) of the GO analysis were enriched in the extrinsic apoptotic signaling pathway, cGMP-mediated pathway signaling, and molting cycle. The KEGG pathway analysis showed that the upregulated DEGs were enriched in glycosaminoglycan biosynthesis and purine metabolism, while the downregulated DEGs were mainly enriched in pathways of glycosaminoglycan biosynthesis, antifolate resistance, and ABC transporters. The GSEA analysis result showed that the top three involved pathways were oxidative phosphorylation, TNFA signaling via NF-KB, and the inflammatory response. The PPI was constructed and the hub genes found through the method of DMNC showed that INHBA and NR4A2 might play an important role in venous remodeling after AVF. The integrated optical density (DOI) examined by immunohistochemistry staining showed that the expression of both INHBA and NR4A2 increased in AVF compared to the control group. Our research contributes to the understanding of the molecular mechanism of venous remodeling after exposure to high fistula flow, which may be useful in treating AVF failure.

Keywords: hub gene, protein interaction maps, gene ontology, arteriovenous fistula, venous remodeling

INTRODUCTION

Incidences of chronic kidney disease (CKD) and end-stage renal disease (ESRD) are rising due to the aging population and the increasing prevalence of diabetes (Vachharajani et al., 2014). Hemodialysis (HD) is the treatment of choice for ESDR patients, and over 1.5 million people worldwide receive regular HD (Grassmann et al., 2005). Well-functioning vascular access is crucial for hemodialysis (HD) patients and the ideal permanent vascular access for HD is through the native arteriovenous fistula (AVF) (Roy-Chaudhury et al., 2001; Grassmann et al., 2005; Vascular Access Work Group, 2006; Sadaghianloo et al., 2015). The AVF connects high blood pressures arterial blood flow directly into the vein, exposing the vein to disturbed flow patterns, resulting in a thickened vein wall. The outflow vein is dilated and its wall is thickened due to increased blood flow after the construction of autogenous AV access (Dixon, 2006). Although the outflow vein commonly matures for HD 3 to 4 months after creation, almost 60% of AVFs fail to mature sufficiently. Our poor understanding of the molecular mechanism of venous remodeling after the construction of AVF limits our ability to predict or prevent the non-maturation of AVF (Dixon, 2006; Dember et al., 2014).

The prevention of AVF non-maturation may benefit from compressive molecular profiling studies that reveal dysregulated genes and pathways underlying AVF non-maturation. Many researchers have tried to study the molecular mechanism involved in AVF failure. For example, Martinez reported that pro-inflammatory genes, such as CSF3R, FPR1, S100A8, S100A9, and VNN2, were upregulated in the pre-access veins just before AVF failed (Martinez et al., 2019). But this study did not report the changed genes before and after the construction of AVF (Martinez et al., 2019). Xie et al. (2019) reported that LMO7 could suppress the vascular fibrotic responses through the TGF-β pathway. The cellular events causing arterialization of the vein may serve as potential targets for the prevention of AVF non-maturation. However, the exact underlying mechanism of AVF non-maturation has not yet been completely understood. It is also crucial to identify novel molecular biomarkers for individualized therapy and early diagnosis. Chip technology has the capacity to detect all the genes within a sample to screen for differentially expressed genes (DEGs), so it could improve the understanding of AVF non-maturation.

We downloaded the array data of GSE39488 from the Gene Expression Omnibus (GEO)[1] to study the differentially expressed genes (DEGs) between AVF samples and control samples. R was used to identify DEGS, and conduct the enrichment analyses, including gene ontology (GO) analysis, Kyoto Encyclopedia of Genes and Genomes (KEGG) pathway enrichment analysis, and gene set enrichment analysis (GSEA) (Martinez et al., 2019). Furthermore, the protein-protein interaction (PPI) of DEGs was constructed; hub genes with a high degree of DNMC were identified by the software Cytoscape with plug-in cytoHubba. Our results may aid in the design of subsequent experimental studies of AVF, and contribute to the understanding of the molecular mechanisms associated with the development of AVF failure.

MATERIALS AND METHODS

Microarray Data

The gene expression profile of GSE39488 was downloaded from the Gene Expression Omnibus database (GEO) (see footnote). That dataset is based on the GPL10332 platform (Agilent-026652 Whole Human Genome Microarray 4 × 44K v2). The GSE39488 dataset contained 10 samples, including 4 control samples and 6 AVF samples.

Intra-Group Data Repeatability Test

Repeatability between the two groups was evaluated by the Pearson's correlation test. All statistical computing and graphics were performed using the R software. A heat map of correlation was drawn to visualize the correlations between all samples in the dataset using the pheatmap package of R. Principal component analysis (PCA) was performed to visualize the gene expression to assess sample relationships and variability.

Identification of DEGs

Bioconductor project[2] was used for the analysis and comprehension of high-throughput genomic data while the significantly differentially expressed genes (DEGs) between AVF samples and control samples were identified by the Bioconductor package limma. A *t*-test in the limma package was used to calculate the *p*-values of DEGs. The adjusted *p*-value cutoff was set at 0.05 and the $|\log FC| > 0.5$ was the filter criteria. A set of 45 DEGs were found from 22,683 genes, including 32 upregulated and 13 downregulated genes. A heatmap of DEGs was generated in R with the R package "pheatmap."

Functional Annotation for DEGs Using GO, KEGG, and GSEA Analysis

The clusterProfiler package is a tool used to implement methods when analyzing and visualizing the functional profiles of genomic coordinates and was used to perform GO, KEGG, and GSEA analysis (Yu et al., 2012). Gene ontology (GO) analysis is a useful method which includes three key biological aspects: BP (biological process), MF (molecular function), and CC (cellular component). KEGG is a commonly used bioinformatics database[3] which analyzes gene functions and enriched genes with their pathways (Altermann and Klaenhammer, 2005). The GO and KEGG enrichment analyses were performed for DEGs by the clusterProfiler package with the *p*-value cutoff and the *q*-value cutoff set to 0.01 and 0.05, respectively (Yu et al., 2012). Gene set enrichment analysis (GSEA) is a computational method to find the statistically significant difference between biological samples in a previously defined set of genes and was also performed using the clusterProfiler package.

[1] http://www.ncbi.nlm.nih.gov/geo/

[2] http://www.bioconductor.org/

[3] https://www.kegg.jp/

Construction and Analysis of the PPI Network and Identification of Hub Genes

The online Search Tool for the Retrieval of Interacting Genes (STRING) database[4] was used to predict the PPI (protein-protein interaction) network from the imported DEGs (Szklarczyk et al., 2015). Cytoscape[5] (Smoot et al., 2011) was used to visualize the PPI network. The plug-in cytoHubba was used to identify the hub genes through the score of DNMC. The top 10 genes with a high degree of DNMC were selected as hub genes.

Immunocytochemistry

This study was approved by both the Medical Ethics Committee of the Nanjing First Hospital, China (KY20190823-22) and the Medical Ethics Committee of the China-Japan Friendship Hospital of Beijing, China (2019-25-1) and received informed consent from all of the patients. A 1-cm segment of the venous end distal to the anastomosis was collected as the AVF sample during the operation of the repair of the AVF. The normal veins were pieces of the great saphenous vein collected from patients who underwent coronary artery bypass grafting. The Declaration of Helsinki was strictly followed. Both the normal vein and the AVF vein samples were collected during the operation and were dehydrated and embedded in paraffin. After that, the samples were sectioned into 5 μm thick pieces, and were dewaxed, rehydrated, and stained with hematoxylin and eosin sequentially until transparent. Afterward, the sections were deparaffinated, blocked, and incubated with the primary antibody Anti-Inhibin beta A antibody (INHBA, abcam) or Anti-Nurr1 antibody (NR4A2, abcam) at 4°C overnight. The expression of both INHBA and NR4A2 were calculated as the integrated optical density (DOI) of the area which was stained yellow-brown by the Image-Pro Plus 6.0 (IPP 6.0, Media Cybernetics, United States). The DOI of both groups were present as mean and standard deviation (SD) and the independent *t*-test was performed by R software version 3.6.2 to analyze the difference between the two groups. $P < 0.05$ was considered as statistically significant.

RESULTS

Validation of the Dataset

To further validate the dataset, we used a Pearson's correlation test between different samples and applied the principal component analysis (PCA) to test the potential associations between the AVF samples and control samples. Based on the Pearson's correlation test, the heatmap of correlation in the GSE39488 dataset showed there were strong correlations among the control samples and the AVF samples (**Figure 1A**). The PCA of the GSE39488 showed that the intra-group data repeatability was acceptable. The distances between the AVF samples was close to the distance between control samples in both PC1 and PC2 (**Figure 1B**).

[4]https://string-db.org/

[5]http://cytoscape.org/

Identification of DEGs

A total of 45 DEGs were found based on the criteria of an adjusted *p*-value of less than 0.05 and a | logFC| value of more than 0.5, with 32 upregulated and 13 downregulated genes. Both the heatmap (**Figure 2A**) and Volcano plots (**Figure 2B**) were used to illustrate the DEGs.

Functional and Pathway Enrichment Analysis

The R package clusterProfiler was used to perform the biological functions and pathways analyses including GO, KEGG, and GSEA. Both the upregulated and the downregulated DEGs were enriched by GO categories, respectively, but no GO term was enriched by the downregulated DEGs, this may be because there were only 13 downregulated DEGs. The results of the biological process (BP) GO category showed that the upregulated DEGs were enriched in the extrinsic apoptotic signaling pathway, cGMP-mediated pathway signaling, and molting cycle (**Figure 3A**) while there was no GO term enriched in both the cellular component (CC) and molecular function (MF) categories. The results of the KEGG pathways analysis showed that the upregulated DEGs were mainly enriched in the pathways of glycosaminoglycan biosynthesis and purine metabolism (**Figure 3B**) while the downregulated DEGs were mainly enriched in the pathways of glycosaminoglycan biosynthesis, antifolate resistance, and ABC transporters (**Figure 3C**). The results of gene set enrichment analysis (GSEA) showed that the top three pathways/gene sets were significantly downregulated between the AVF and control samples including in oxidative phosphorylation, TNFA signaling via NF-κB, and the inflammatory response (**Figure 4A**). We found four DEGs belonging to the NF-κB pathway, those were NR4A2, INHBA, EGR2, and OLR1 (**Figure 4B**).

Construction of the Protein-Protein Interaction (PPI) Network and the Selection of Hub Genes

The interactive relationships among DEGs were analyzed by the STRING database (see foot note) (Search Tool for the Retrieval of Interacting Genes) to construct the PPI network (Szklarczyk et al., 2015). The result of the PPI network is presented by the Cytoscape software in **Figure 5A**. The plug-in cytoHubba of the Cytoscape software was used to find hub genes by the method of DMNC (**Figure 5B**) and the top ten hub genes were INHBA, NR4A2, TNFRSF12A, MFGE8, CYR61, KRT17, OLR1, DPP4, KRT14, and ABCG2.

Demographic Data of the Patients and the Expression of Both INHBA and NR4A2

Patient clinical characteristics including age, gender, hypertension, diabetes mellitus, hyperlipidemia, smoking, and BMI were collected and compared between groups. The one-stage AVF s was performed in our center so we did not require the removement of venous segments. As a result,

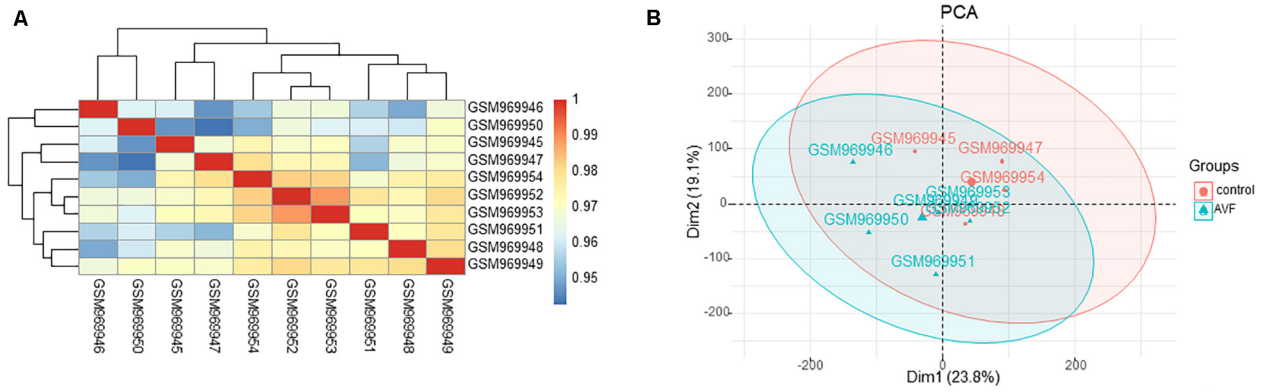

FIGURE 1 | Intra-sample data repeatability test for GSE39488 by the Pearson's correlation analysis and PCA. **(A)** All samples from the GSE39488 dataset were analyzed through Pearson's correlation analysis. The correlation coefficient were reflected by the colors. **(B)** All samples from the GSE39488 dataset were analyzed using PCA. The PC1 and PC2 are represented on the *X*-axis and *Y*-axis, respectively. PCA, principal component analysis; PC1, principal component 1; PC2, principal component 2.

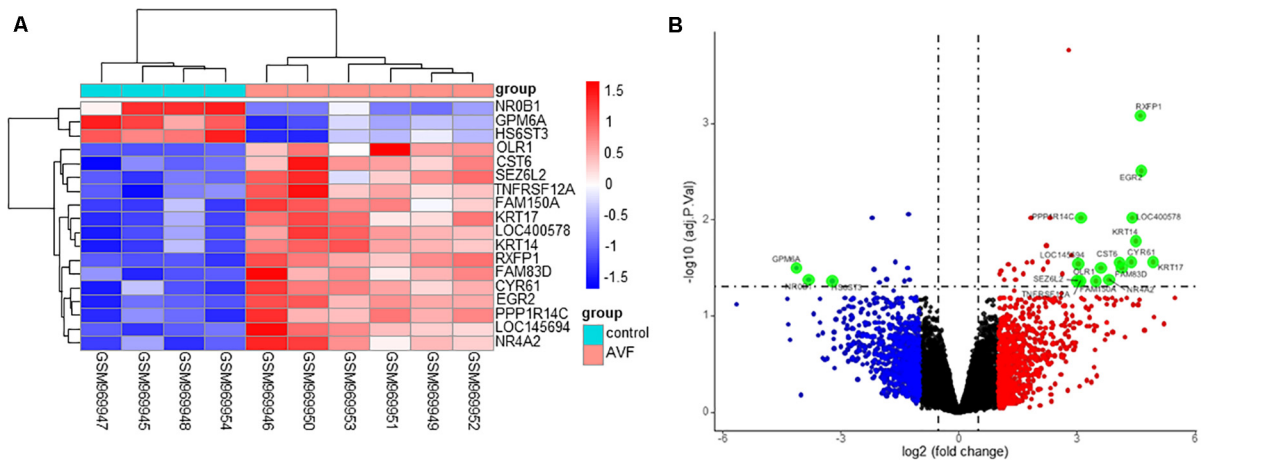

FIGURE 2 | Identification of DEGs between control samples and AVF samples. **(A)** A heatmap showing the DEGs between two groups. **(B)** A Volcano plot showing the DEGs between two groups after analysis of the GSE39488 dataset with the R software. The *X*-axis represents the | logFC| and the *Y*-axis represents the *p*-value (log-scaled). FC, fold change.

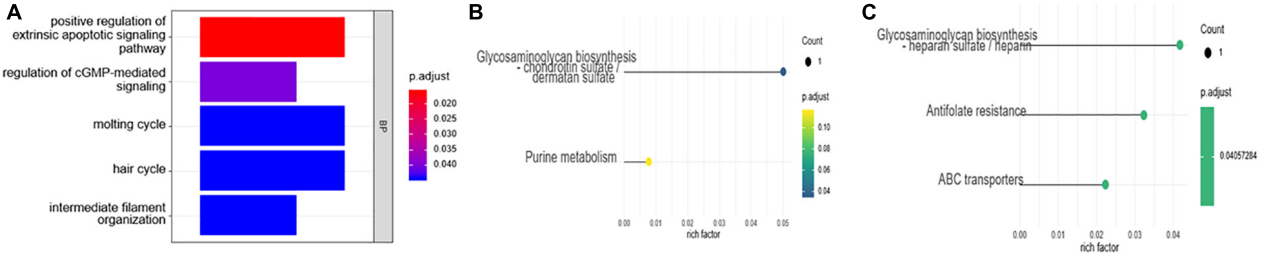

FIGURE 3 | The enrichment analysis of the DEGs using the GO and KEGG analyses. **(A)** The biological process (BP) of the GO analysis. **(B)** The results of the KEGG pathways analysis of the upregulated DEGs. **(C)** The results of the KEGG pathways analysis of the downregulated DEGs.

the normal veins were collected for the control group. The results presented in **Table 1** show that all of the clinical characteristics were not statistically different between the two groups. Immunohistochemistry was used to assess the expression of both INHBA and NR4A2 (**Figure 6**). The integrated optical density (DOI), calculated by the IPP 6.0, was used to examine the expression of the protein. INHBA was significantly higher in the AVF group (9897.19 ± 2034.88, n = 12) compared to

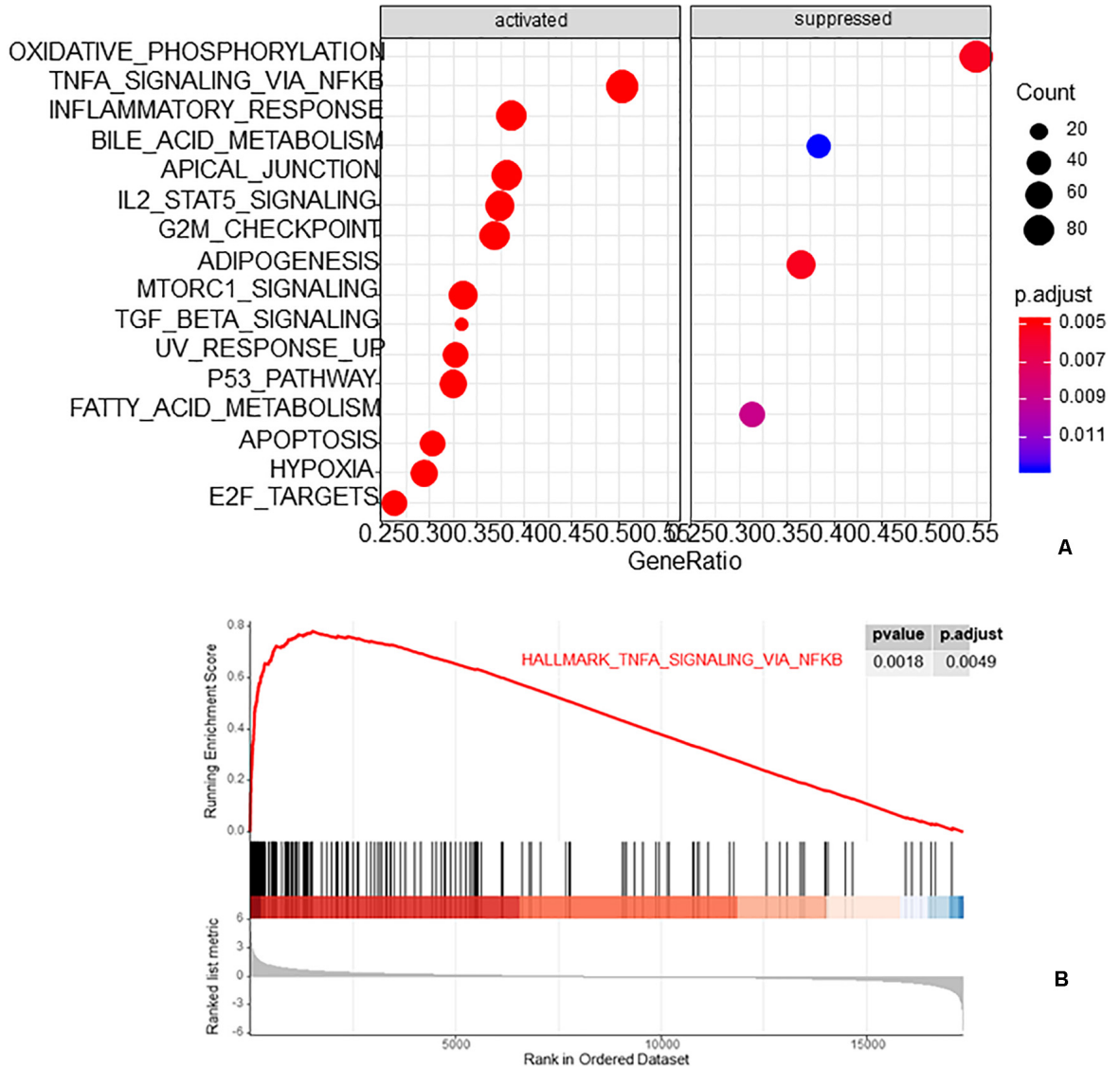

FIGURE 4 | The results of gene set enrichment analysis (GSEA). **(A)** The top three pathways/gene sets enriched by GSEA. **(B)** The NF-κB pathway was enriched by GSEA.

the normal group (7641.65 ± 1818.00, n = 12), and the p-value was 0.009. NR4A2 was significantly higher in the AVF group (9513.74 ± 1925.76, n = 12) compared to the normal group (7641.65 ± 1818.00, n = 12), and the p-value was 0.023.

DISCUSSION

It is widely accepted that AVF represents the first choice for vascular access for hemodialysis (Jindal et al., 2006; Vascular Access Work Group, 2006). However, the rate of non-maturation of AVF has increased because an increasing number of elderly and frail patients are received AVF for hemodialysis (Al-Jaishi et al., 2014). Many researchers have reported a highly complex genomic landscape after the construction of AVF (Martinez et al., 2019). The molecular mechanisms that distinguish between normal veins and veins exposed to high blood flow after the construction of AVF are poorly understood, but are of major importance for combatting AVF non-maturation.

In this study, a total of 45 DEGs (32 upregulated and 13 downregulated) were recognized by comparing normal vein samples and AVF vein samples. GO biological analysis results showed that these DEGs were mainly associated with the extrinsic apoptotic signaling pathway, cGMP-mediated pathway signaling, and the molting cycle. The KEGG pathways analysis of the upregulated DEGs included glycosaminoglycan biosynthesis and purine metabolism while the downregulated DEGs included glycosaminoglycan biosynthesis, antifolate resistance, and ABC transporters. The GSEA analysis represented the top three pathways/gene sets in which the AVF samples were significantly

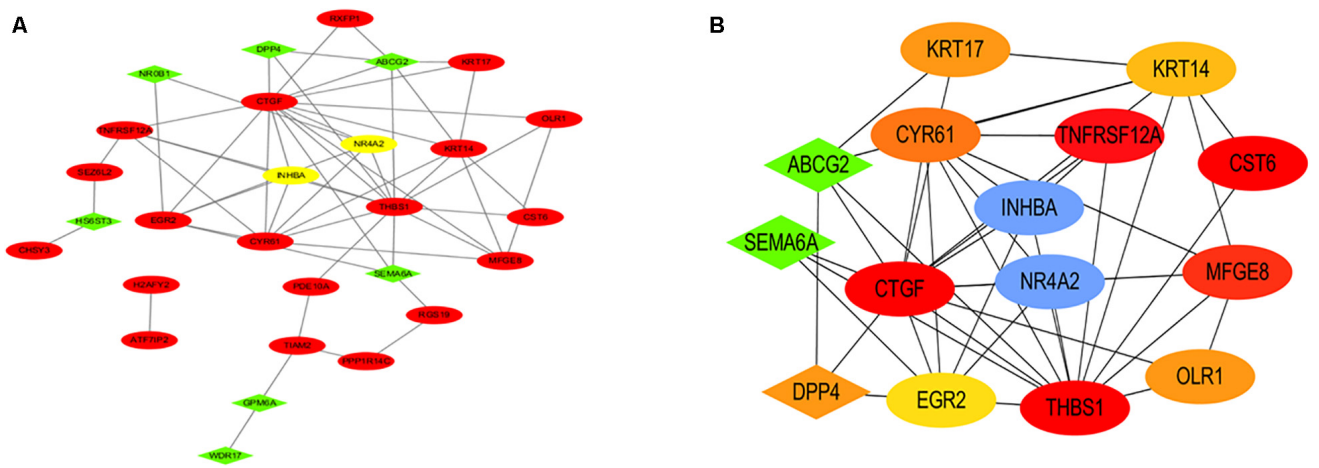

FIGURE 5 | PPI network and hub genes. **(A)** The PPI network analyzed by the STRING database is presented. **(B)** The hub genes included INHBA, NR4A2, TNFRSF12A, MFGE8, CYR61, KRT17, OLR1, DPP4, KRT14, and ABCG2.

involved in oxidative phosphorylation, TNFA signaling via NF-κB, and the inflammatory response. Many studies have reported that vein remodeling after AVF was associated with inflammatory and NF-κB pathways, this is consistent with our study (Khavanin Zadeh et al., 2015; Brahmbhatt and Misra, 2016; Viecelli et al., 2018; Chen B. et al., 2019; Martinez et al., 2019). Brahmbhatt reported that many factors, such as uremia and hypoxia, can upregulate the inflammatory response, and eventually lead to intimal hyperplasia and secondary thrombosis of AVF (Brahmbhatt and Misra, 2016). Khavanin Zadeh reported that AVF failure has a significantly higher CRP positive rate (Khavanin Zadeh et al., 2015).

Subsequently, key genes were identified by the construction of a PPI network, and the hub genes were discovered through the DMNC method. The top ten hub genes were INHBA, NR4A2, TNFRSF12A, MFGE8, CYR61, KRT17, OLR1, DPP4, KRT14, and ABCG2. The first two genes, INHBA and NR4A2, are involved in the NF-κB signaling pathway, which is consistent with the result of GSEA. INHBA (inhibin subunit beta A) is a gene that could encode a type of the TGF-beta (transforming growth factor-beta) superfamily of proteins (Fagerberg et al., 2014). Castier, Y reported that the induction of NF-κB by shear stress contributes to matrix metalloproteinases induction and affects the vascular remodeling of vascular enlargement after AVF (Castier et al., 2009). In the study of Fukasawa, M, a balloon catheter containing an NF-κB decoy oligodeoxynucleotide could sustain for a longer period of time compared to the control group (Fukasawa et al., 2019). NR4A2 (nuclear receptor subfamily 4 group A member 2) could encode one of the steroid-thyroid hormone-retinoid receptor superfamily, which may act as a transcription factor (Fagerberg et al., 2014). TNFA signaling via NF-κB was enriched by the GSEA analysis. Among these top 10 hub genes, INHBA and NR4A2 were related to the TNFA signaling pathway. So we focused on INHBA and NR4A2. Both INHBA and NR4A2 have been reported to be involved in the NF-κB pathway in many studies. Wamsley et al. (2015) reported that NF-κB activity is needed to upregulate INHBA which could maintain mesenchymal phenotypes. The research from Chen J. et al. (2019) identified NR4A transcription factors as having an important role in the lesser effect of T cells against solid tumors. Popichak KA reported that NR4A2 could suppress the inflammatory response of NF-κB. We confirmed that the expression of both INHBA and NR4A2 were increased in the AVF samples by immunohistochemistry. Both INHBA and NR4A2 may be potential therapeutic targets for the prevention of AVF. We will try to suppress these genes *in vivo* and *in vitro* in future to confirm their role in AVF.

There are several limitations in this study. Firstly, the control samples are not from uremic patients because it is difficult to obtain normal vein samples from uremic patients according to the Declaration of Helsinki. In our center, we used one-stage

TABLE 1 | Demographic data of patients.

	Normal (*n* = 12)	AVF (*n* = 12)	*P*-value
Age			
Mean (SD)	59.8 (9.17)	58.4 (10.1)	0.738
Gender			
Female	4 (33.3%)	6 (50.0%)	0.679
Hypertension			
Yes	10 (83.3%)	6 (50.0%)	0.194
Diabetes mellitus			
Yes	10 (83.3%)	8 (66.7%)	0.637
Hyperlipidemia			
Yes	6 (50.0%)	8 (66.7%)	0.679
Smoke			
Yes	2 (16.7%)	2 (16.7%)	1
BMI			
Mean (SD)	22.3 (1.44)	23.5 (2.75)	0.21

AVF, arteriovenous fistula; BMI, body mass index.

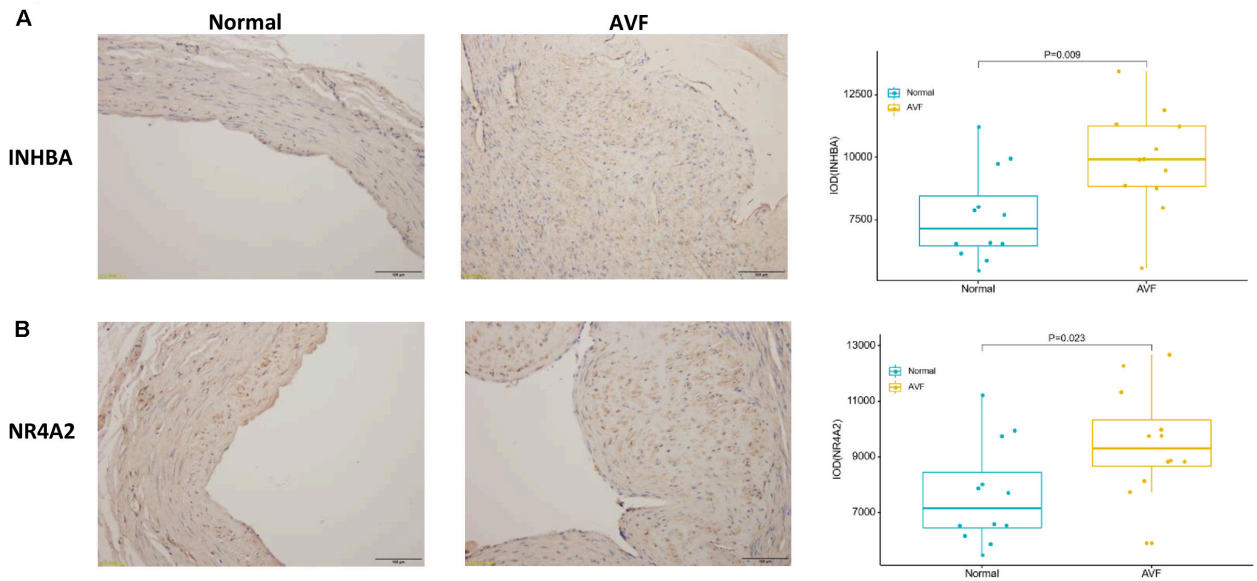

FIGURE 6 | The result of immunohistochemistry staining showed that the expression of INHBA and NR4A2 were increased in AVF. **(A)** A typical representative photomicrograph of immunohistochemistry staining for INHBA. A box plot was used to show that the expression of INHBA significantly increased in AVF. **(B)** A typical representative photomicrograph of immunohistochemistry staining for NR4A2. A box plot was used to show that the expression of NR4A2 significantly increased in AVF.

AVFs so we did not require the removal of the venous segments. As a result, we did not collect venous samples from uremic patients. We will try to collect normal vein samples from uremic patients for the further study. Secondly, each sample was collected at a different time after AVF surgery. The collection time depended on the patency time of the AVF. We will enlarge the sample size so that we can collect AVF samples at the same time in a future study. Thirdly, we did not isolate the endothelial cells from the smooth muscle cells and then analyze them separately. We will try to analyze different cell types in the future study.

CONCLUSION

This study identified a total of 45 DEGs. GO, KEGG, and GSEA enrichment analyses were performed and the NF-κB pathway was suggested to be involved in vein remodeling. The hub genes were identified, including INHBA and NR4A2. Both of these two genes have been reported to be associated with the NF-κB pathway in many studies. Altogether, our study indicates that vein remodeling may be regulated by INHBA and NR4A2 through the NF-κB pathway. Therefore, the detailed investigation of the molecular mechanism and clinical application of these genes are needed in the future.

DATA AVAILABILITY STATEMENT

The datasets presented in this study can be found in online repositories. The names of the repository/repositories and accession number(s) can be found in the article/supplementary material.

ETHICS STATEMENT

This study was approved by the Medical Ethics Committee of the Nanjing First Hospital, China (KY20190823-22) and the Medical Ethics Committee of the China-Japan Friendship Hospital of Beijing, China (2019-25-1) and received written informed consent from all of the parents.

AUTHOR CONTRIBUTIONS

GJ, WJ, and HX designed, guided, and funded the study. KJ and ZB conducted most of the experimental work. GM helped with the software calculation. LZ and ZY assisted with drawing pictures. CL helped with the revised picture. KJ, SH, LW, and CG performed the data analysis. WF performed the immunocytochemistry. KJ and GM conducted the data interpretation. KJ and ZB performed the drafting of the manuscript. GJ and HX did the critical revision of the manuscript and final approval for publication. All authors contributed to the article and approved the submitted version.

FUNDING

This work was supported by grants from the National Natural Science Foundation of China (No. 81871463).

REFERENCES

Al-Jaishi, A. A., Oliver, M. J., Thomas, S. M., Lok, C. E., Zhang, J. C., Garg, A. X., et al. (2014). Patency rates of the arteriovenous fistula for hemodialysis: a systematic review and meta-analysis. *Am. J. Kidney Dis.* 63, 464–478. doi: 10.1053/j.ajkd.2013.08.023

Altermann, E., and Klaenhammer, T. R. (2005). PathwayVoyager: pathway mapping using the kyoto encyclopedia of genes and genomes (KEGG) database. *BMC Genomics* 6:60.

Brahmbhatt, A., and Misra, S. (2016). The biology of hemodialysis vascular access failure. *Semin. Intervent. Radiol.* 33, 15–20.

Castier, Y., Ramkhelawon, B., Riou, S., Tedgui, A., and Lehoux, S. (2009). Role of NF-kappaB in flow-induced vascular remodeling. *Antioxid. Redox Signal.* 11, 1641–1649. doi: 10.1089/ars.2008.2393

Chen, B., Wang, P., Brem, A., Dworkin, L., Liu, Z., Gong, R., et al. (2019). Mineralocorticoid receptor: a hidden culprit for hemodialysis vascular access dysfunction. *EBioMedicine.* 39, 621–627. doi: 10.1016/j.ebiom.2018.11.054

Chen, J., López-Moyado, I. F., Seo, H., Lio, C. J., Hempleman, L. J., Sekiya, T., et al. (2019). NR4A transcription factors limit CAR T cell function in solid tumours. *Nature* 567, 530–534. doi: 10.1038/s41586-019-0985-x

Dember, L. M., Imrey, P. B., Beck, G. J., Cheung, A. K., Himmelfarb, J., Huber, T. S., et al. (2014). Objectives and design of the hemodialysis fistula maturation study. *Am. J. Kidney Dis.* 63, 104–112. doi: 10.1053/j.ajkd.2013.06.024

Dixon, B. S. (2006). Why don't fistulas mature? *Kidney Intl.* 70, 1413–1422. doi: 10.1038/sj.ki.5001747

Fagerberg, L., Hallström, B. M., Oksvold, P., Kampf, C., Djureinovic, D., Odeberg, J., et al. (2014). Analysis of the human tissue-specific expression by genome-wide integration of transcriptomics and antibody-based proteomics. *Mol. Cell Proteomics* 13, 397–406. doi: 10.1074/mcp.m113.035600

Fukasawa, M., Isobe, M., Nanto, S., Nakamura, M., Haruguchi, H., Miyake, T., et al. (2019). NF-κB decoy oligodeoxynucleotide-coated balloon catheter for arteriovenous fistula in hemodialysis. *Kidney Intl. Rep.* 4, 126–138. doi: 10.1016/j.ekir.2018.09.016

Grassmann, A., Gioberge, S., Moeller, S., and Brown, G. (2005). ESRD patients in 2004: global overview of patient numbers, treatment modalities and associated trends. *Nephrol. Dial. Transplant.* 20, 2587–2593. doi: 10.1093/ndt/gfi159

Jindal, K., Chan, C. T., Deziel, C., Hirsch, D., Soroka, S. D., Tonelli, M., et al. (2006). Hemodialysis clinical practice guidelines for the Canadian Society of Nephrology. *J. Am. Soc. Nephrol.* 17(3 Suppl. 1), S1–S27.

Khavanin Zadeh, M., Mohammadipour, S., and Omrani, Z. (2015). Correlation between CRP and early failure of arteriovenous fistula (AVF). *Med. J. Islam Repub. Iran* 29:219.

Martinez, L., Tabbara, M., Duque, J. C., Selman, G., Falcon, N. S., Paez, A., et al. (2019). Transcriptomics of human arteriovenous fistula failure: genes associated with nonmaturation. *Am. J. Kidney Dis.* 74, 73–81. doi: 10.1053/j.ajkd.2018.12.035

Roy-Chaudhury, P., Kelly, B. S., Miller, M. A., Reaves, A., Armstrong, J., and Nanayakkara, N. (2001). Venous neointimal hyperplasia in polytetrafluoroethylene dialysis grafts. *Kidney Intl.* 59, 2325–2334. doi: 10.1046/j.1523-1755.2001.0590062325.x

Sadaghianloo, N., Jean-Baptiste, E., Rajhi, K., François, E., Declemy, S., Dardik, A., et al. (2015). Increased reintervention in radial-cephalic arteriovenous fistulas with anastomotic angles of less than 30 degrees. *J. Vasc. Surg.* 62, 1583–1589. doi: 10.1016/j.jvs.2015.07.074

Smoot, M. E., Ono, K., Ruscheinski, J., Wang, P. L., and Ideker, T. (2011). Cytoscape 2.8: new features for data integration and network visualization. *Bioinformatics* 27, 431–432. doi: 10.1093/bioinformatics/btq675

Szklarczyk, D., Franceschini, A., Wyder, S., Forslund, K., Heller, D., Huerta-Cepas, J., et al. (2015). STRING v10: protein-protein interaction networks, integrated over the tree of life. *Nucleic Acids Res.* 43, D447–D452.

Vachharajani, T. J., Moist, L. M., Glickman, M. H., Vazquez, M. A., Polkinghorne, K. R., Lok, C. E., et al. (2014). Elderly patients with CKD–dilemmas in dialysis therapy and vascular access. *Nat. Rev. Nephrol.* 10, 116–122. doi: 10.1038/nrneph.2013.256

Vascular Access Work Group (2006). Clinical practice guidelines for vascular access. *Am. J. Kidney Dis.* 48(Suppl. 1), S248–S273.

Viecelli, A. K., Mori, T. A., Roy-Chaudhury, P., Polkinghorne, K. R., Hawley, C. M., Johnson, D. W., et al. (2018). The pathogenesis of hemodialysis vascular access failure and systemic therapies for its prevention: optimism unfulfilled. *Semin. Dial.* 31, 244–257. doi: 10.1111/sdi.12658

Wamsley, J. J., Kumar, M., Allison, D. F., Clift, S. H., Holzknecht, C. M., Szymura, S. J., et al. (2015). Activin upregulation by NF-κB is required to maintain mesenchymal features of cancer stem-like cells in non-small cell lung cancer. *Cancer Res.* 75, 426–435. doi: 10.1158/0008-5472.can-13-2702

Xie, Y., Ostriker, A. C., Jin, Y., Hu, H., Sizer, A. J., Peng, G., et al. (2019). LMO7 Is a negative feedback regulator of transforming growth factor β signaling and fibrosis. *Circulation* 139, 679–693. doi: 10.1161/circulationaha.118.034615

Yu, G., Wang, L. G., Han, Y., and He, Q. Y. (2012). ClusterProfiler: an R Package for Comparing Biological Themes Among Gene Clusters: an R package for comparing biological themes among gene clusters. *OMICS* 16, 284–287. doi: 10.1089/omi.2011.0118

Conflict of Interest: The authors declare that the research was conducted in the absence of any commercial or financial relationships that could be construed as a potential conflict of interest.

frontiers in Physiology

REVIEW
published: 23 December 2020
doi: 10.3389/fphys.2020.602930

Endothelium-Derived Hyperpolarizing Factor and Myoendothelial Coupling: The *in vivo* Perspective

Kjestine Schmidt[1,2] *and Cor de Wit*[1,2]*

[1]*Institut für Physiologie, Universität zu Lübeck, Lübeck, Germany,* [2]*Deutsches Zentrum für Herz-Kreislauf-Forschung (DZHK) e.V. (German Center for Cardiovascular Research), Partner Site Hamburg/Kiel/Lübeck, Lübeck, Germany*

The endothelium controls vascular tone adopting blood flow to tissue needs. It releases chemical mediators [e.g., nitric oxide (NO), prostaglandins (PG)] and exerts appreciable dilation through smooth muscle hyperpolarization, thus termed endothelium-dependent hyperpolarization (EDH). Initially, EDH was attributed to release of a factor, but later it was suggested that smooth muscle hyperpolarization might be derived from radial spread of an initial endothelial hyperpolarization through heterocellular channels coupling these vascular cells. The channels are indeed present and formed by connexins that enrich in gap junctions (GJ). *In vitro* data suggest that myoendothelial coupling underlies EDH-type dilations as evidenced by blocking experiments as well as simultaneous, merely identical membrane potential changes in endothelial and smooth muscle cells (SMCs), which is indicative of coupling through ohmic resistors. However, connexin-deficient animals do not display any attenuation of EDH-type dilations *in vivo*, and endothelial and SMCs exhibit distinct and barely superimposable membrane potential changes exerted by different means *in vivo*. Even if studied in the exact same artery EDH-type dilation exhibits distinct features *in vitro* and *in vivo*: in isometrically mounted vessels, it is rather weak and depends on myoendothelial coupling through connexin40 (Cx40), whereas *in vivo* as well as *in vitro* under isobaric conditions it is powerful and independent of myoendothelial coupling through Cx40. It is concluded that EDH-type dilations are distinct and a significant dependence on myoendothelial coupling *in vitro* does not reflect the situation under physiologic conditions *in vivo*. Myoendothelial coupling may act as a backup mechanism that is uncovered in the absence of the powerful EDH-type response and possibly reflects a situation in a pathophysiologic environment.

Keywords: connexins, gap junctions, endothelium-dependent hyperpolarization, myoendothelial coupling, microcirculation

OPEN ACCESS

Edited by:
Zsolt Bagi,
Augusta University, United States

Reviewed by:
Daniel Henrion,
INSERM U1083 Physiopathologie Mitochondriale et Cardiovasculaire, France
Donald Welsh,
University of Calgary, Canada

***Correspondence:**
Cor de Wit
dewit@uni-luebeck.de

Specialty section:
This article was submitted to Vascular Physiology, a section of the journal Frontiers in Physiology

Received: *04 September 2020*
Accepted: *30 November 2020*
Published: *23 December 2020*

Citation:
Schmidt K and de Wit C (2020) Endothelium-Derived Hyperpolarizing Factor and Myoendothelial Coupling: The in vivo Perspective. Front. Physiol. 11:602930. doi: 10.3389/fphys.2020.602930

INTRODUCTION

The endothelium contributes importantly to the regulation of vascular tone and thereby controls organ perfusion. Endothelial cells (ECs) communicate in different languages (or signaling pathways) to smooth muscle cells (SMCs), one of which is the release of chemical substances or mediators that diffuse through the narrow intercellular space before reaching membrane

or intracellular proteins as receptors. The outstanding molecules acting as chemical mediators in this pathway of intercellular communication are PG [cyclooxygenase (COX) products] and the gaseous transmitter nitric oxide (NO) which is produced by endothelial NO-synthase and easily diffuses through plasma membranes to reach its target, the intracellularly localized soluble guanylyl cyclase (sGC; Qian and Fulton, 2013; Luo et al., 2016; Nava and Llorens, 2019). Apart from these molecules, other chemical entities have been suggested to be released from ECs and relax smooth muscle, among them K^+ ions, lipophilic compounds (e.g., epoxyeicosanoids, EETs), proteins (C-type natriuretic peptide), radicals [hydrogen peroxide (H_2O_2)], and other gaseous molecules [CO, hydrogen sulfide (H_2S); **Figure 1**; Feletou and Vanhoutte, 2009; Garland et al., 2011; Feletou et al., 2012; Ellinsworth et al., 2014, 2016; Feletou, 2016; Freed and Gutterman, 2017; Garland and Dora, 2017].

However, this is a "sticky" business as it is difficult to imagine that several of these compounds are easily and quickly transferable. The smooth muscle relaxes by the opening of K^+-channels, which induce relaxation likely through closure of voltage-gated Ca^{2+}-channels representing a rather speedy signaling pathway. Since the dilaton is depending on the presence of ECs and characterized by smooth muscle hyperpolarization, this obscure mediator has been termed endothelium-derived hyperpolarizing factor (EDHF) assuming that also this mechanism communicates in the same language, i.e., release of a mediator as for the classical autacoids, NO, and PG. However, this view was challenged and a direct electrotonic way of communication was suggested. Charge is transferred from ECs to smooth muscle through intercellular channels [myoendothelial gap junctions (GJs), MEGJs] driven by an initial endothelial hyperpolarization that spreads radially into the vessel wall (**Figure 1**; de Wit and Griffith, 2010; Freed and Gutterman, 2017; Garland and Dora, 2017).

We describe in this short review the structural requirements and illuminate the experimental evidence obtained *in vivo* that argues against or in favor of the hypothesis that EDHF indeed is an EDH-type dilation rather than being a freely diffusible molecule. Other important functions of myoendothelial coupling, including the transfer of calcium or intracellular messengers, such as inositol-1,4,5-triphosphate (IP3) that modulate vascular responses (Looft-Wilson et al., 2017; Biwer et al., 2018;

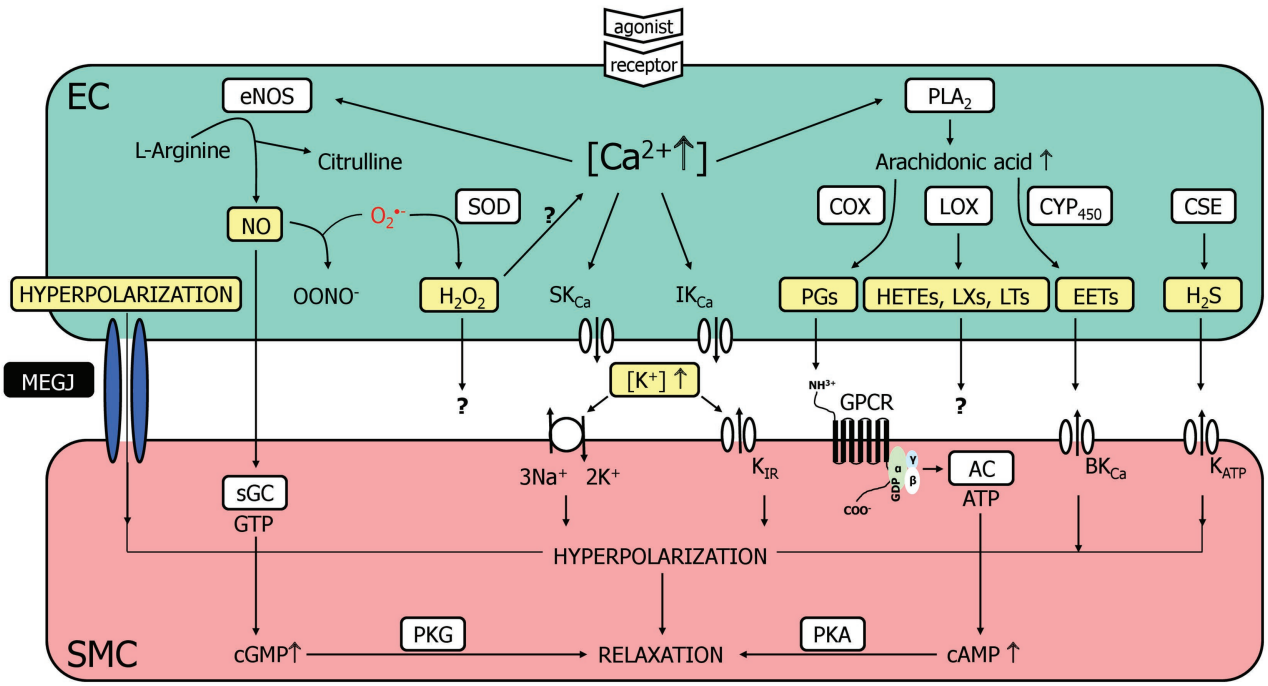

FIGURE 1 | A multitude of endothelial molecules and mechanisms (depicted in yellow boxes) relax vascular smooth muscle. The well-accepted chemical mediators such as nitric oxide (NO) and prostaglandins (PG) are shown, and a variety of substances that have been suggested to underly the endothelium-dependent hyperpolarization (EDH)-type dilation. Importantly, a completely distinct pathway, namely radial electrotonic spread of endothelial hyperpolarizations through myoendothelial coupling was also proposed to initiate the EDH-type dilation. However, the evidence was mostly acquired *in vitro*, whereas data obtained *in vivo* argue against this hypothesis. This justifies reconsideration of other molecules as outlined. For further details, see text. AC, adenylyl cyclase; cAMP, cyclic adenosine monophosphate; cGMP, cyclic guanosine monophosphate; COX, cyclooxygenase; CSE, cystathionine-lyase; CYP450, cytochrome P450 epoxygenase; EC, endothelial cell; eNOS, endothelial nitric oxide synthase; EETs, epoxyeicosatrienoic acids; GPCR, G-protein coupled receptor; HETEs, hydroxyeicosatrienoic acids; H_2O_2, hydrogen peroxide; H_2S, hydrogen sulfide; K_{Ca}, Ca^{2+}-activated K^+-channel with small (SK_{Ca}), intermediate (IK_{Ca}) or big conductance (BK_{Ca}); K_{ATP}, ATP-sensitive K^+-channels; K_{IR}, inwardly rectifying K^+-channel; LOX, lipoxygenase; LTs, leukotrienes; LXs, lipoxines; MEGJ, myoendothelial gap junctions; NO, nitric oxide; $OONO^-$, peroxynitrite anion; O_2^-, superoxide anion; PGs, prostaglandins; PKA, protein kinase A; PKG, protein kinase G; PLA_2, phospholipase A_2; sGC, soluble guanylyl cyclase; SMC, smooth muscle cell; SOD; superoxide dismutase.

Wei et al., 2018; Wilson et al., 2019) are reviewed in detail elsewhere (Billaud et al., 2014; Straub et al., 2014; Pogoda and Kameritsch, 2019; Pohl, 2020) and are not addressed in detail in this manuscript. This aspect is mainly examined *in vitro* and due to the lack of experimental data, it is currently unknown if such a signaling pathway is of importance *in vivo*.

GAP JUNCTIONS AND THE MOLECULAR BRICKS (CONNEXINS)

Gap junctions are composed of connexin proteins and six of these molecules assemble to form a hexameric hemichannel. Two of them from adjacent cells dock together and interlink the cytoplasms of these cells through a channel that is tightly sealed against the extracellular environment. The intercellular channels either connect equal (homocellular) or different cell types (heterocellular, e.g., myoendothelial coupling) and allow transfer of small molecules (< 1 kDa) and ions. The latter equals current flow along an electrochemical potential difference and, ultimately, permits the transfer of membrane potential changes between interconnected cells. Hundreds of such channels are located at GJ where adjoining plasma membranes are only 2 nm apart (Saez et al., 2003; Nielsen et al., 2012; Grosely and Sorgen, 2013). GJ can be visualized by electron microscopy and appears as an electron-dense pentalaminar area that can be easily identified between adjacent ECs because of their abundance and the large size of the plaques. They are found to a lesser extent between SMCs, which is possibly due to the smaller plaque size and the limited number of GJ (Sandow et al., 2012). Alternatively, the presence of GJ may be implicated from the demonstration of connexin protein expression by immunostaining. A tremendous amount of publications detected connexins in vascular cells (ECs and SMCs) but this imaging technique does not allow to distinguish homocellular GJ from heterocellular GJ (de Wit, 2004; Figueroa et al., 2004). Moreover, connexin staining is indicated in many cases but the demonstration of a proper functional localization, i.e., inside the plasma membrane, is lacking.

The family of connexin genes is comprised of ~20 members (in humans 21, in mice 20), and the proteins are named according to their theoretical molecular mass; for example, connexin40 (Cx40) has a predicted molecular mass of about 40 kDa (Sohl and Willecke, 2004). In the cardiovascular system, Cx40, Cx37, Cx43, and Cx45 are expressed (Haefliger et al., 2004; Morel, 2014). Their expression pattern is not specific for ECS or SMCs, but a subtype preponderance was found: Cx40 and Cx37 prevail in the endothelium throughout the vascular tree and reportedly Cx43 is also expressed specifically in larger vessels (Gustafsson et al., 2003; Sandow et al., 2003; Rummery and Hill, 2004; de Wit et al., 2006; Haddock et al., 2006; Hakim et al., 2008; Sorensen and Holstein-Rathlou, 2012; Pohl, 2020). Cx43 and Cx45 are the dominant subtypes expressed in SMCs (Hill et al., 2002; Wolfle et al., 2007; Schmidt et al., 2012), but Cx37 was also reported for smooth muscle (Sandow et al., 2003; Alonso et al., 2010a), whereas Cx40 is only found in a very few instances in these cells. Interestingly, Cx40 and Cx37 are also found abundantly in renin producing cells and serve important functions in renin secretion (Wagner and Kurtz, 2013).

Having the expression pattern in mind, MEGJ may be composed of Cx40, Cx37, and Cx43 provided from the endothelial side and Cx43, Cx45, and Cx37 from smooth muscle (Sandow et al., 2009, 2012). This important information is experimentally difficult to obtain in vessels, however, in an *in vitro* co-culture system, myoendothelial junctions were composed of Cx40 and Cx43 provided by both cell types. This occured despite the expression of Cx37 in endothelial and SMCs in this artificial system but this connexin was excluded from these junctions (Isakson and Duling, 2005). Experimental data from intact vessels are scarce: in rat basilar artery using serial section and immunoelectron microscopy, Haddock et al. (2006) demonstrated myoendothelial junctions in which Cx40 and Cx37 were located, others confirmed the presence of Cx37 and Cx40 in different vessels (Mather et al., 2005; Isakson et al., 2008), and also Cx43 was identified at MEGJ (Straub et al., 2010; Pogoda et al., 2014).

Recently, Cx37 was shown to be enriched specifically at sites where endothelial and SMCs come into contact (the internal elastic lamina) in murine small skeletal muscle arteries. Functionally, the authors observed in a culture system, a modulation of Cx37 permeability by NO specifically for this connexin (compared to Cx40 and Cx43) and conclude from these findings that NO exerts a specific modulatory effect on myoendothelial junctions due to the fact that Cx37 is the main Cx at this strategic location, and NO preferentially affects its function (Pogoda et al., 2014). The inhibitory effect of NO on Ca^{2+} permeability of MEGJ was elicited through enhanced phosphorylation of Cx37 at position 332 (Y332) by inhibition of the protein tyrosine phosphatase SHP-2. This effect prevented in isolated vessels the Ca^{2+} drainage from the endothelium into the smooth muscle and enhanced thereby Ca^{2+} levels in ECs promoting vasodilation induced by vasoactive agonists (Pogoda et al., 2017). Taken together, these data are somewhat contradictory (Cx37) and can be only regarded as an initial step on the bumpy road with many experimental obstacles to uncover the subtypes of Cx being localized at the MEGJ.

EXPERIMENTAL OBSERVATIONS SUGGESTING ELECTRICAL MYOENDOTHELIAL COUPLING *in vitro*

Direct injection of electrical current into ECs in isolated arterioles evoked endothelial hyperpolarizations that were conducted electrotonically (i.e., passively) to subjacent SMCs and, conversely, action potentials originating in the arterial media were rapidly conducted to the endothelium (Emerson and Segal, 2000, 2001; Yamamoto et al., 2001). The signal amplitude was reduced in either direction by about 15%, without change in form, suggesting that myoendothelial junctions behave as ohmic resistors that mediate the heterocellular spread of membrane potential changes without rectification (Yamamoto et al., 2001). Circumferential and subsequent longitudinal spread of hyperpolarization was

also demonstrated in conduit vessels (strips of rabbit iliac and porcine coronary artery), from which the endothelium had been partly removed, following hyperpolarization of the residual endothelium (Griffith et al., 2002; Selemidis and Cocks, 2007). A direct heterocellular communication invoking larger molecules was visualized using dyes that diffused from initially loaded ECs into SMCs in the media *via* GJs (Griffith et al., 2002; Kansui et al., 2008; Saliez et al., 2008; Billaud et al., 2009).

If such molecules are able to diffuse through GJ it opens the possibility that non-electrotonic mechanisms contribute to vascular tone regulation, e.g., diffusion of IP_3 and/or Ca^{2+} ions in either direction (Isakson et al., 2007; Isakson, 2008). For example, the transfer of Ca^{2+} from activated smooth muscle to endothelium has been implicated in a feedback mechanism that evokes an endothelial dilation, thereby counterbalancing the constriction initiated in the smooth muscle by e.g., phenylephrine (Dora et al., 1997; Yashiro and Duling, 2000; Kerr et al., 2012; Biwer et al., 2018; Wei et al., 2018; Wilson et al., 2019). This feedback is tightly controlled (Straub et al., 2012; Biwer et al., 2018) and, interestingly, the artificial modulation of heterocellular contact in larger arteries may alter their vascular function (Shu et al., 2019). The hypothesis that myoendothelial junctions serve as conduits for charge transfer and represent mechanistically the EDH-type dilation instead of an EDHF that traverses the extracellular space has been reviewed excellently in more detail elsewhere (Griffith, 2004; Figueroa and Duling, 2009; de Wit and Griffith, 2010; Garland et al., 2011; Ellinsworth et al., 2014; Freed and Gutterman, 2017; Garland and Dora, 2017).

Proof of concept additionally requires blockage of the gap junctional pathway and the abrogation of EDH-type responses. However, GJs are difficult to block efficiently and comcomitantly avoid nonspecific effects. Application of short interfering peptides (so-called connexin-mimetic peptides) is a useful strategy that provides even certain specificity for different connexin subtypes depending on the amino acid sequences of the peptide. In fact, numerous studies have shown that they are able to suppress EDHF-type smooth muscle hyperpolarizations and dilations *in vitro* (Griffith, 2004; de Wit and Griffith, 2010). In some vessels, connexin-mimetic peptides targeted against Cx37 and/or Cx40 attenuated endothelium-dependent smooth muscle hyperpolarization (Chaytor et al., 2005), whereas in other arteries, peptide combinations to target Cx37, Cx40, and Cx43 collectively were required to block of EDH-type responses (Chaytor et al., 2001; Matchkov et al., 2006).

Aiming at the protein structure with a blocking antibody provides a distinct, very specific approach to verify the functional necessity of connexins. Mather et al. (2005) loaded ECs with antibodies targeted against the cytoplasmic tail of Cx40 and observed an abrogation of EDH-type responses in rat mesenteric small arteries. This occurred without affecting increases in endothelial calcium and, importantly, antibodies directed against Cx37 and Cx43 were inactive suggesting that Cx40 is a key player in the response (Mather et al., 2005). The endothelium opposes myogenic constrictions through NO release (de Wit et al., 1998) and EDH-type dilations possibly through Ca^{2+} transfer from smooth muscle to endothelium as outlined above. The latter opposing mechanism was abrogated in mice carrying a mutant Cx40 protein, which also impaired chemical coupling (Chaston et al., 2013).

Taken together, there is compelling evidence that myoendothelial coupling through connexins provides a functional pathway that allows electrotonic spread of membrane potential changes (and signaling molecules). Blockade of this pathway attenuates or even abrogates EDH-type dilations *in vitro*. Specifically, Cx40 (and Cx37) seem to be invoked and appear to be a required brick of the intercellular signaling pathway.

MYOENDOTHELIAL COUPLING AS THE EDH-MECHANISM *in vivo*: THE EVIDENCE IS LACKING

Collecting evidence *in vivo* is more cumbersome; however, an efficient strategy is the use of mice deficient for connexins. We published the first study on vascular connexin function by using Cx40-deficient mice in which we demonstrated a crucial role for Cx40 to conduct endothelium-dependent dilations longitudinally along the vessel wall, thereby coordinating vascular cellular behavior (de Wit et al., 2000; Wolfle et al., 2007) that was shortly later confirmed by Figueroa et al. (2003). However, Cx40 is not required for radial electrotonic signal transmission because acetylcholine-induced EDH-type dilations were nearly preserved in skeletal muscle arterioles studied by intravital microscopy in anaesthestized Cx40-deficent mice. Later, we re-examined these responses in more detail and demonstrated a very minor (if any) attenuation of EDH-type dilations upon acetylcholine (Milkau et al., 2010).

In awake Cx40-deficient mice, intraarterial acetylcholine reduced blood pressure to the same absolute level as in wildtype controls, despite their initially elevated arterial pressure (de Wit et al., 2003). This hypotensive response can be attributed to the EDHF phenomenon because it is unaffected by NO-synthase inhibition and is preserved in mice with targeted disruption of the NO-cyclic guanosine monophosphate (cGMP) pathway (Koeppen et al., 2004). Furthermore, resistance changes in the renal circulation in response to acetylcholine were comparable in wildtype and Cx40-deficient mice (Just et al., 2009).

Collectively, these results argue against the hypothesis that Cx40 is universally required for EDH-type signaling *in vivo*. These differences may relate indeed due to *in vivo* vs. *in vitro* vascular behavior or caused by different vessel sizes. Arteries studied *in vitro* are usually larger (> 100 μm) than arterioles accessible for intravital microscopy examined *in vivo* (20–50 μm). The latter arterioles are those that provide the vascular resistance, and their behavior is revealed by pressure drop or resistance measurements in intact organs or animals.

To exclude effects related to vessel size differences, we performed measurements on a small murine artery (gracilis artery) that exhibits a diameter (~130 μm) allowing *in vitro* as well as *in vivo* examination because the artery is located at a spot that is accessible for intravital microscopy. This small artery exhibits *in vitro* an acetylcholine-induced

dilation that is mediated to a considerable part by an EDH-type mechanism (~60%, the remaining portion is mediated by NO and PG). Thus, the EDH-type dilation is larger than in a conducting artery (femoral artery), which relies mostly on NO but it is smaller than in arterioles. Arteriolar responses in the microcirculation *in vivo* are nearly exclusively mediated by EDH-type dilation (Si et al., 2006; Brahler et al., 2009; Wolfle et al., 2009).

In any case, acetylcholine-induced dilations were attenuated in gracilis arteries harvested from Cx40-deficient mice compared to wildtype mice if studied isometrically *in vitro* using wire myography. Blockade of NO-synthase and COX nearly abrogated the dilation in Cx40-deficient arteries but uncovered EDH-type dilations in wildtype mice. This demonstrates that EDH-type dilations require Cx40 in this setting and suggest that myoendothelial coupling requiring Cx40 supports this pathway (**Figure 2**, left; Boettcher and de Wit, 2011). However, if the exact same vessel was examined at isobaric conditions (pressure myograph), the dilation upon acetylcholine was firstly not attenuated by NO-synthase and COX inhibition in wildtype and secondly fully preserved in Cx40-deficient vessels. This demonstrates that EDH-type dilations, firstly, are more powerful at these experimental conditions (isobaric study) and, secondly, are fully preserved in the absence of Cx40 and, thus, most likely independent of myoendothelial coupling. The exact same results were found if this vessel was studied in the anesthetized mouse *in vivo* (**Figure 2**, left panel; Boettcher and de Wit, 2011).

In line with this, an attenuation of the EDH-type dilation in Cx40-deficient vessels was also observed in renal arteries (interlobar vessels) that were studied isometrically *in vitro* using wire myography. In addition to myoendothelial coupling, endothelial K^+ release contributed to the EDH-type dilation in these vessels since a blockade of inwardly rectifying K^+-channel (K_{IR}) and the sodium pump reduced the responses in both, wildtype and Cx40-deficient mice (Brasen et al., 2018). Although the responses were not studied *in vivo* in this study, acetylcholine infusion decreased vascular resistance in the renal circulation measured *in vivo* to a comparable degree in wildtype and Cx40-deficient mice (Just et al., 2009) indicating again intact EDH-type dilations in Cx40-deficient mice *in vivo*.

DISTINCT VASCULAR RESPONSES ARE NOT RELATED TO CONCOMITANT HYPERTENSION

Since mice globally deficient for Cx40 are hypertensive due to an abrogated feedback of pressure on renin release (Wagner et al., 2007, 2010; Schweda et al., 2009), hypertension might be a causative factor in impairing the EDH-type dilation through modifying myoendothelial junctions by an alteration of connexin expression (Figueroa et al., 2006; Meens et al., 2013). Therefore, we examined arteries from mice with EC-specific deletion of Cx40, which are normotensive (Wagner et al., 2010; Jobs et al., 2012). However, arteries exhibited similar characteristics: The acetylcholine-induced

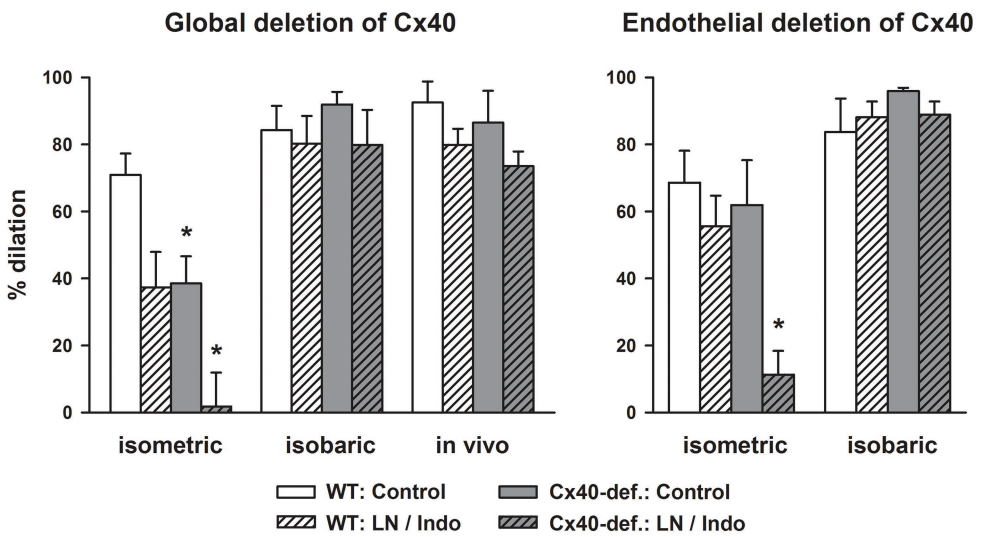

FIGURE 2 | EDH-type dilations are abrogated in gracilis arteries in the absence of connexin40 (Cx40) only if studied *in vitro* in an isometric setting. Acetylcholine (3 μM) induced dilations in gracilis artery studied *in vitro* either in a wire- (isometric) or a pressure-myograph (isobaric) or *in vivo* in anesthetized mice. Cx40 was either deleted globally (left) or in an endothelial-specific manner (right) and compared to respective wildtype mice. Under isometric conditions, blockade of NO-synthase and COX reduced the response in wildtype and abrogated it in Cx40-deficient mice demonstrating a dependence of EDH-type dilations on Cx40 and supposedly on myoendothelial coupling in this setting. In marked contrast, EDH-type dilations were completely preserved in Cx40-deficient mice under isobaric conditions and *in vivo*. Thus, under these conditions, EDH-type dilations are independent of the presence of Cx40. Interestingly, EDH was more powerful under these experimental conditions and induced near full dilation in all genotypes. * indicates $p < 0.05$ vs. wildtype; LN/Indo, L-nitro-arginine (300 μM) and indometacin (3 μM) to block NO-synthase and COX; Cx40-def, Cx40-deficient mice either global or endothelial-cell specific deletion using Cre recombinase driven by TIE2 in mice carrying homozygously a Cx40 floxed gene. The full data set is published (Boettcher and de Wit, 2011).

dilation in isometrically mounted vessels was abrogated after the blockade of NO synthase and COX in the absence of endothelial Cx40 but not in wildtype vessels. This confirmed an EDH-type dilation in wildtype vessels that is not found in the absence of endothelial Cx40 and indicates that this part of the acetylcholine-response is dependent on myoendothelial coupling in this setting.

In marked contrast, a fully intact EDH-type dilation upon acetylcholine was found in vessels from endothelial-specific Cx40-deficient mice if mounted isobarically (**Figure 2**, right; Boettcher and de Wit, 2011). As before, the EDH-type dilation in the isobaric setting was more powerful in both genotypes, and an attenuation of the response after NO synthase and COX inhibition was neither observed in wildtype vessels nor in vessels deficient for endothelial Cx40 (**Figure 2**, right). This suggests that this EDH-type dilation, which was only observed in the isobaric setting or *in vivo*, is independent of Cx40. Furthermore, this powerful response is even capable to replace the dilatory function of other endothelial mediators (mainly NO). Importantly, EC-specific Cx40-deficient mice are not hypertensive (Wagner et al., 2010; Jobs et al., 2012) excluding that hypertension modulates connexin expression and that such an alteration had caused the defects observed in globally Cx40-deficient mice.

The divergent results observed in isobaric or isometric vessel study are striking. A key experimental difference is the change in wall tension during constriction and dilation. In isometric conditions, wall tension decreases during dilations and rises during constriction whereas the opposite is true for isobaric (and *in vivo*) conditions. These different experimental setups have also shown to modulate the sensitivity of rat mesenteric arteries for vasoconstrictors (Buus et al., 1994). This may be related to changes in membrane potential because a small initial depolarization did offset the differences in agonist sensitivity (Dunn et al., 1994). Modulatory effects of experimental conditions were also demonstrated on EDH-type dilations: Lowering the extracellular Ca^{2+} concentration shifted the type of endothelial K_{Ca} channel initiating the EDH response from $K_{Ca}2.3$ to $K_{Ca}3.1$. This also affected the link to the vessel relaxation, which shifted from myoendothelial coupling to the activation of the Na^+/K^+ ATPase, thus defining distinct EDHF pathways depending on experimental conditions (Dora et al., 2008).

Since ECs express both connexins, Cx40 and Cx37, in abundant amounts, the question arises why Cx37 is not able to replace the function of Cx40. Contrary to an anticipated compensatory upregulation in Cx40-deficient vessels, Cx37 expression is actually downregulated in the aortic endothelium (Simon and McWhorter, 2003), and Cx37 cannot be detected by immunostaining in arterioles (de Wit, 2010; Jobs et al., 2012). Recent work identified spare Cx37 expression in skeletal muscle arterioles and, in addition, demonstrated the presence of myoendothelial junctions in Cx40-deficient mice (Howitt et al., 2013). Interestingly, Cx40 and Cx37 are located tightly together suggesting physical interaction (Alonso et al., 2010b). Thus, Cx40 seems to be required to locate Cx37 appropriately in the endothelial plasma membrane, and a potentially remaining Cx37 expression is functionally insufficient. Conversely, deficiency of Cx37 did not result in noticeable defects of vascular regulation (Figueroa and Duling, 2008) or renin secretion (Wagner et al., 2009) suggesting that the role of Cx37 can be replaced by Cx40.

EDH-TYPE DILATIONS ELICITED BY OTHER AGONISTS ARE LIKEWISE INDEPENDENT OF CX40 *in vivo*

Acetylcholine activates muscarinic G-protein coupled receptors (GPCRs) that initiate a Ca^{2+}-dependent signaling pathway ultimately leading to endothelial hyperpolarization by means of the activation of endothelial Ca^{2+}-dependent K^+-channels ($K_{Ca}3.1$, $K_{Ca}2.3$; Brahler et al., 2009). This last element in the cascade can be activated pharmacologically by compounds, such as SKA-31 (Sankaranarayanan et al., 2009). In fact, SKA-31 exhibits a higher sensitivity toward $K_{Ca}3.1$ and produces arteriolar dilation *in vivo* specifically *via* activation of this endothelial ion channel and the ensuing endothelial hyperpolarization supposedly occurs without increases of endothelial Ca^{2+}. This even more "pure" EDH-type dilation is likewise unimpeded in Cx40-deficient arterioles examined in the microcirculation *in vivo* (Radtke et al., 2013). Similarly, the arterial pressure decreases upon systemic application of SKA-31 were not attenuated in either global or endothelial-specific Cx40-deficient mice (Radtke et al., 2013). This verifies that endothelial hyperpolarization through activation of $K_{Ca}3.1$ initiates an EDH-type dilation which is independent of Cx40 *in vivo* and thus likely independent of myoendothelial junctions.

Taken together, a strong powerful EDH-type dilation exists *in vivo* that acts independent of Cx40. We suggest that we need to reconsider the "sticky" business, which may not be so sticky at all in search for this mediator (**Figure 1**). Importantly, this powerful mechanism is lost *in vitro* in certain experimental settings (isometric setup). At such conditions, myoendothelial coupling may take over and provide a remaining, less powerful EDH-type dilation that is, in fact, dependent on Cx40.

LACK OF EVIDENCE FOR CHARGE TRANSMISSION BY MYOENDOTHELIAL COUPLING *in vivo*

Having provided evidence that lack of Cx40 (and Cx37) leaves EDH-type dilations fully intact *in vivo* it remains to be considered if myoendothelial coupling exists *in vivo* at all. It may well be that heterocellular coupling is turned off during physiologic vascular control and is only activated during special (pathophysiologic?) conditions. In contrast to the findings with isolated arteries and arterioles described above, a number of studies have failed to demonstrate tight electric myoendothelial coupling in arterioles *in vivo* (de Wit et al., 2008). For example, electrophysiological measurements *in vivo* demonstrated differences in the resting membrane potential of endothelial and SMCs in the order of 10 mV in murine skeletal muscle arterioles (Siegl et al., 2005). Additionally, acetylcholine-induced hyperpolarization of SMCs was selectively blocked by a specific K^+-channel blocker

without modifying endothelial hyperpolarization (Siegl et al., 2005). Conversely, adenosine dilated arterioles by activating smooth muscle K_{ATP} channels but did not hyperpolarize the endothelium (de Wit, 2010); whereas in isolated conduit arteries, K_{ATP} mediated hyperpolarization is transmitted to the endothelium *via* MEGJ (Murai et al., 1999). Also in hamster arterioles *in vivo*, smooth muscle depolarizations did not affect the membrane potential of ECs: hyperpolarizations initiated by acetylcholine differed in amplitude and form between endothelial and SMCs (Welsh and Segal, 1998). Again, endothelial and smooth muscle hyperpolarization exhibited differential sensitivity to inhibitors (Welsh and Segal, 2000). Finally, selective destruction of endothelial or SMCs along the conduction pathway suggests that hyperpolarization is not freely transferred between the two cell types (Budel et al., 2003).

These experimental findings do not provide evidence for functional myoendothelial coupling that aligns the membrane potential of endothelial and SMCs *in vivo*. The data rather suggest that the membrane potential of these distinct cell populations is regulated independently reflecting their specific functions. Interestingly, connexins at the myoendothelial junctions are subject to functional regulation (Straub et al., 2010; Westcott and Segal, 2013), which may provide an explanation for the discrepant *in vivo* findings. Although significant charge transfer through MEGJ was not convincingly demonstrated *in vivo*, significant contributions of myoendothelial coupling to vascular function may well be of importance, for example the transfer of intracellular messengers (Looft-Wilson et al., 2017; Biwer et al., 2018; Wei et al., 2018; Wilson et al., 2019; Pohl, 2020).

CONCLUSION

Many *in vitro* studies demonstrate an important role for myoendothelial coupling by transferring charge from endothelial to SMCs to elicit EDH-type dilations. However, *in vivo* a distinct, more powerful mechanism is responsible for such dilations that easily overcome the lack of myoendothelial coupling. The evidence for efficient charge transfer through myoendothelial coupling *in vivo* is scarce. This is not related to a lack of data, in fact, many laboratories have attempted to tackle this important question, but failed to find solid evidence documenting myoendothelial coupling. In fact, these efforts have accumulated strong indications for the opposite, i.e., endothelial and SMCs "do their own thing" with respect to membrane potential. However, under certain experimental conditions, myoendothelial coupling supports EDH-type dilation, but this EDH-type response is rather weak compared to the EDH-mechanism acting *in vivo*.

AUTHOR CONTRIBUTIONS

All authors listed have made a substantial, direct and intellectual contribution to the work, and approved it for publication.

REFERENCES

Alonso, F., Boittin, F. X., Beny, J. L., and Haefliger, J. A. (2010b). Loss of connexin40 is associated with decreased endothelium-dependent relaxations and eNOS levels in the mouse aorta. *Am. J. Physiol. Heart Circ. Physiol.* 299, H1365–H1373. doi: 10.1152/ajpheart.00029.2010

Alonso, F., Krattinger, N., Mazzolai, L., Simon, A., Waeber, G., Meda, P., et al. (2010a). An angiotensin II- and NF-kappaB-dependent mechanism increases connexin 43 in murine arteries targeted by renin-dependent hypertension. *Cardiovasc. Res.* 87, 166–176. doi: 10.1093/cvr/cvq031

Billaud, M., Lohman, A. W., Johnstone, S. R., Biwer, L. A., Mutchler, S., and Isakson, B. E. (2014). Regulation of cellular communication by signaling microdomains in the blood vessel wall. *Pharmacol. Rev.* 66, 513–569. doi: 10.1124/pr.112.007351

Billaud, M., Marthan, R., Savineau, J. P., and Guibert, C. (2009). Vascular smooth muscle modulates endothelial control of vasoreactivity via reactive oxygen species production through myoendothelial communications. *PLoS One* 4:e6432. doi: 10.1371/journal.pone.0006432

Biwer, L. A., Good, M. E., Hong, K., Patel, R. K., Agrawal, N., Looft-Wilson, R., et al. (2018). Non-endoplasmic reticulum-based calr (calreticulin) can coordinate heterocellular calcium signaling and vascular function. *Arterioscler. Thromb. Vasc. Biol.* 38, 120–130. doi: 10.1161/ATVBAHA.117.309886

Boettcher, M., and de Wit, C. (2011). Distinct endothelium-derived hyperpolarizing factors emerge in vitro and in vivo and are mediated in part via connexin 40-dependent myoendothelial coupling. *Hypertension* 57, 802–808. doi: 10.1161/HYPERTENSIONAHA.110.165894

Brahler, S., Kaistha, A., Schmidt, V. J., Wolfle, S. E., Busch, C., Kaistha, B. P., et al. (2009). Genetic deficit of SK3 and IK1 channels disrupts the endothelium-derived hyperpolarizing factor vasodilator pathway and causes hypertension. *Circulation* 119, 2323–2332. doi: 10.1161/CIRCULATIONAHA.108.846634

Brasen, J. C., de Wit, C., and Sorensen, C. M. (2018). Myoendothelial coupling through Cx40 contributes to EDH-induced vasodilation in murine renal arteries: evidence from experiments and modelling. *Acta Physiol.* 222:e12906. doi: 10.1111/apha.12906

Budel, S., Bartlett, I. S., and Segal, S. S. (2003). Homocellular conduction along endothelium and smooth muscle of arterioles in hamster cheek pouch: unmasking an NO wave. *Circ. Res.* 93, 61–68. doi: 10.1161/01.RES.0000080318.81205.FD

Buus, N. H., VanBavel, E., and Mulvany, M. J. (1994). Differences in sensitivity of rat mesenteric small arteries to agonists when studied as ring preparations or as cannulated preparations. *Br. J. Pharmacol.* 112, 579–587. doi: 10.1111/j.1476-5381.1994.tb13114.x

Chaston, D. J., Baillie, B. K., Grayson, T. H., Courjaret, R. J., Heisler, J. M., Lau, K. A., et al. (2013). Polymorphism in endothelial connexin40 enhances sensitivity to intraluminal pressure and increases arterial stiffness. *Arterioscler. Thromb. Vasc. Biol.* 33, 962–970. doi: 10.1161/ATVBAHA.112.300957

Chaytor, A. T., Bakker, L. M., Edwards, D. H., and Griffith, T. M. (2005). Connexin-mimetic peptides dissociate electrotonic EDHF-type signalling via myoendothelial and smooth muscle gap junctions in the rabbit iliac artery. *Br. J. Pharmacol.* 144, 108–114. doi: 10.1038/sj.bjp.0706046

Chaytor, A. T., Martin, P. E., Edwards, D. H., and Griffith, T. M. (2001). Gap junctional communication underpins EDHF-type relaxations evoked by ACh in the rat hepatic artery. *Am. J. Physiol. Heart Circ. Physiol.* 280, H2441–H2450. doi: 10.1152/ajpheart.2001.280.6.H2441

de Wit, C. (2004). Connexins pave the way for vascular communication. *News Physiol. Sci.* 19, 148–153. doi: 10.1152/nips.01520.2004

de Wit, C. (2010). Different pathways with distinct properties conduct dilations in the microcirculation in vivo. *Cardiovasc. Res.* 85, 604–613. doi: 10.1093/cvr/cvp340

de Wit, C., Boettcher, M., and Schmidt, V. J. (2008). Signaling across myoendothelial gap junctions—fact or fiction? *Cell Commun. Adhes.* 15, 231–245. doi: 10.1080/15419060802440260

de Wit, C., and Griffith, T. M. (2010). Connexins and gap junctions in the EDHF phenomenon and conducted vasomotor responses. *Pflugers Arch.* 459, 897–914. doi: 10.1007/s00424-010-0830-4

de Wit, C., Jahrbeck, B., Schafer, C., Bolz, S. S., and Pohl, U. (1998). Nitric oxide opposes myogenic pressure responses predominantly in large arterioles in vivo. *Hypertension* 31, 787–794. doi: 10.1161/01.HYP.31.3.787

de Wit, C., Roos, F., Bolz, S. S., Kirchhoff, S., Kruger, O., Willecke, K., et al. (2000). Impaired conduction of vasodilation along arterioles in connexin40 deficient mice. *Circ. Res.* 86, 649–655. doi: 10.1161/01.RES.86.6.649

de Wit, C., Roos, F., Bolz, S. S., and Pohl, U. (2003). Lack of vascular connexin 40 is associated with hypertension and irregular arteriolar vasomotion. *Physiol. Genomics* 13, 169–177. doi: 10.1152/physiolgenomics.00169.2002

de Wit, C., Wolfle, S. E., and Hopfl, B. (2006). Connexin-dependent communication within the vascular wall: contribution to the control of arteriolar diameter. *Adv. Cardiol.* 42, 268–283. doi: 10.1159/000092575

Dora, K. A., Doyle, M. P., and Duling, B. R. (1997). Elevation of intracellular calcium in smooth muscle causes endothelial cell generation of NO in arterioles. *Proc. Natl. Acad. Sci. U. S. A.* 94, 6529–6534. doi: 10.1073/pnas.94.12.6529

Dora, K. A., Gallagher, N. T., McNeish, A., and Garland, C. J. (2008). Modulation of endothelial cell KCa3.1 channels during endothelium-derived hyperpolarizing factor signaling in mesenteric resistance arteries. *Circ. Res.* 102, 1247–1255. doi: 10.1161/CIRCRESAHA.108.172379

Dunn, W. R., Wellman, G. C., and Bevan, J. A. (1994). Enhanced resistance artery sensitivity to agonists under isobaric compared with isometric conditions. *Am. J. Phys.* 266, H147–H155. doi: 10.1152/ajpheart.1994.266.1.H147

Ellinsworth, D. C., Earley, S., Murphy, T. V., and Sandow, S. L. (2014). Endothelial control of vasodilation: integration of myoendothelial microdomain signalling and modulation by epoxyeicosatrienoic acids. *Pflugers Arch.* 466, 389–405. doi: 10.1007/s00424-013-1303-3

Ellinsworth, D. C., Sandow, S. L., Shukla, N., Liu, Y., Jeremy, J. Y., and Gutterman, D. D. (2016). Endothelium-derived hyperpolarization and coronary vasodilation: diverse and integrated roles of epoxyeicosatrienoic acids, hydrogen peroxide, and gap junctions. *Microcirculation* 23, 15–32. doi: 10.1111/micc.12255

Emerson, G. G., and Segal, S. S. (2000). Electrical coupling between endothelial cells and smooth muscle cells in hamster feed arteries—role in vasomotor control. *Circ. Res.* 87, 474–479. doi: 10.1161/01.RES.87.6.474

Emerson, G. G., and Segal, S. S. (2001). Electrical activation of endothelium evokes vasodilation and hyperpolarization along hamster feed arteries. *Am. J. Physiol. Heart Circ. Physiol.* 280, H160–H167. doi: 10.1152/ajpheart.2001.280.1.H160

Feletou, M. (2016). Endothelium-dependent hyperpolarization and endothelial dysfunction. *J. Cardiovasc. Pharmacol.* 67, 373–387. doi: 10.1097/FJC.0000000000000346

Feletou, M., Kohler, R., and Vanhoutte, P. M. (2012). Nitric oxide: orchestrator of endothelium-dependent responses. *Ann. Med.* 44, 694–716. doi: 10.3109/07853890.2011.585658

Feletou, M., and Vanhoutte, P. M. (2009). EDHF: an update. *Clin. Sci.* 117, 139–155. doi: 10.1042/CS20090096

Figueroa, X. F., and Duling, B. R. (2008). Dissection of two Cx37-independent conducted vasodilator mechanisms by deletion of Cx40: electrotonic versus regenerative conduction. *Am. J. Physiol. Heart Circ. Physiol.* 295, H2001–H2007. doi: 10.1152/ajpheart.00063.2008

Figueroa, X. F., and Duling, B. R. (2009). Gap junctions in the control of vascular function. *Antioxid. Redox Signal.* 11, 251–266. doi: 10.1089/ars.2008.2117

Figueroa, X. F., Isakson, B. E., and Duling, B. R. (2004). Connexins: gaps in our knowledge of vascular function. *Physiology* 19, 277–284. doi: 10.1152/physiol.00008.2004

Figueroa, X. F., Isakson, B. E., and Duling, B. R. (2006). Vascular gap junctions in hypertension. *Hypertension* 48, 804–811. doi: 10.1161/01.HYP.0000242483.03361.da

Figueroa, X. F., Paul, D. L., Simon, A. M., Goodenough, D. A., Day, K. H., Damon, D. N., et al. (2003). Central role of connexin40 in the propagation of electrically activated vasodilation in mouse cremasteric arterioles in vivo. *Circ. Res.* 92, 793–800. doi: 10.1161/01.RES.0000065918.90271.9A

Freed, J. K., and Gutterman, D. D. (2017). Communication is key: mechanisms of intercellular signaling in vasodilation. *J. Cardiovasc. Pharmacol.* 69, 264–272. doi: 10.1097/FJC.0000000000000463

Garland, C. J., and Dora, K. A. (2017). EDH: endothelium-dependent hyperpolarization and microvascular signalling. *Acta Physiol.* 219, 152–161. doi: 10.1111/apha.12649

Garland, C. J., Hiley, C. R., and Dora, K. A. (2011). EDHF: spreading the influence of the endothelium. *Br. J. Pharmacol.* 164, 839–852. doi: 10.1111/j.1476-5381.2010.01148.x

Griffith, T. M. (2004). Endothelium-dependent smooth muscle hyperpolarization: do gap junctions provide a unifying hypothesis? *Br. J. Pharmacol.* 141, 881–903. doi: 10.1038/sj.bjp.0705698

Griffith, T. M., Chaytor, A. T., Taylor, H. J., Giddings, B. D., and Edwards, D. H. (2002). cAMP facilitates EDHF-type relaxations in conduit arteries by enhancing electrotonic conduction via gap junctions. *Proc. Natl. Acad. Sci. U.S.A.* 99, 6392–6397. doi: 10.1073/pnas.092089799

Grosely, R., and Sorgen, P. L. (2013). A history of gap junction structure: hexagonal arrays to atomic resolution. *Cell Commun. Adhes.* 20, 11–20. doi: 10.3109/15419061.2013.775256

Gustafsson, F., Mikkelsen, H. B., Arensbak, B., Thuneberg, L., Neve, S., Jensen, L. J., et al. (2003). Expression of connexin 37, 40 and 43 in rat mesenteric arterioles and resistance arteries. *Histochem. Cell Biol.* 119, 139–148. doi: 10.1007/s00418-002-0493-0

Haddock, R. E., Grayson, T. H., Brackenbury, T. D., Meaney, K. R., Neylon, C. B., Sandow, S. L., et al. (2006). Endothelial coordination of cerebral vasomotion via myoendothelial gap junctions containing connexins 37 and 40. *Am. J. Physiol. Heart Circ. Physiol.* 291, H2047–H2056. doi: 10.1152/ajpheart.00484.2006

Haefliger, J. A., Nicod, P., and Meda, P. (2004). Contribution of connexins to the function of the vascular wall. *Cardiovasc. Res.* 62, 345–356. doi: 10.1016/j.cardiores.2003.11.015

Hakim, C. H., Jackson, W. F., and Segal, S. S. (2008). Connexin isoform expression in smooth muscle cells and endothelial cells of hamster cheek pouch arterioles and retractor feed arteries. *Microcirculation* 15, 503–514. doi: 10.1080/10739680801982808

Hill, C. E., Rummery, N., Hickey, H., and Sandow, S. L. (2002). Heterogeneity in the distribution of vascular gap junctions and connexins: implications for function. *Clin. Exp. Pharmacol. Physiol.* 29, 620–625. doi: 10.1046/j.1440-1681.2002.03699.x

Howitt, L., Chaston, D. J., Sandow, S. L., Matthaei, K. I., Edwards, F. R., and Hill, C. E. (2013). Spreading vasodilatation in the murine microcirculation: attenuation by oxidative stress-induced change in electromechanical coupling. *J. Physiol.* 591, 2157–2173. doi: 10.1113/jphysiol.2013.250928

Isakson, B. E. (2008). Localized expression of an ins(1,4,5)P3 receptor at the myoendothelial junction selectively regulates heterocellular Ca^{2+} communication. *J. Cell Sci.* 121, 3664–3673. doi: 10.1242/jcs.037481

Isakson, B. E., Best, A. K., and Duling, B. R. (2008). Incidence of protein on actin bridges between endothelium and smooth muscle in arterioles demonstrates heterogeneous connexin expression and phosphorylation. *Am. J. Physiol. Heart Circ. Physiol.* 294, H2898–H2904. doi: 10.1152/ajpheart.91488.2007

Isakson, B. E., and Duling, B. R. (2005). Heterocellular contact at the myoendothelial junction influences gap junction organization. *Circ. Res.* 97, 44–51. doi: 10.1161/01.RES.0000173461.36221.2e

Isakson, B. E., Ramos, S. I., and Duling, B. R. (2007). Ca^{2+} and inositol 1,4,5-trisphosphate-mediated signaling across the myoendothelial junction. *Circ. Res.* 100, 246–254. doi: 10.1161/01.RES.0000257744.23795.93

Jobs, A., Schmidt, K., Schmidt, V. J., Lubkemeier, I., van Veen, T. A. B., Kurtz, A., et al. (2012). Defective Cx40 maintains Cx37 expression but intact Cx40 is crucial for conducted dilations irrespective of hypertension. *Hypertension* 60, 1422–1429. doi: 10.1161/HYPERTENSIONAHA.112.201194

Just, A., Kurtz, L., de Wit, C., Wagner, C., Kurtz, A., and Arendshorst, W. J. (2009). Connexin 40 mediates the tubuloglomerular feedback contribution to renal blood flow autoregulation. *J. Am. Soc. Nephrol.* 20, 1577–1585. doi: 10.1681/ASN.2008090943

Kansui, Y., Garland, C. J., and Dora, K. A. (2008). Enhanced spontaneous Ca^{2+} events in endothelial cells reflect signalling through myoendothelial gap junctions in pressurized mesenteric arteries. *Cell Calcium* 44, 135–146. doi: 10.1016/j.ceca.2007.11.012

Kerr, P. M., Tam, R., Ondrusova, K., Mittal, R., Narang, D., Tran, C. H. T., et al. (2012). Endothelial feedback and the myoendothelial projection. *Microcirculation* 19, 416–422. doi: 10.1111/j.1549-8719.2012.00187.x

Koeppen, M., Feil, R., Siegl, D., Feil, S., Hofmann, F., Pohl, U., et al. (2004). cGMP-dependent protein kinase mediates NO- but not acetylcholine-induced dilations in resistance vessels in vivo. *Hypertension* 44, 952–955. doi: 10.1161/01.HYP.0000147661.80059.ca

Looft-Wilson, R. C., Goodell, C. R., Mutch, C. A., Mutchler, S. M., Miller, K. L., and Guraya, M. (2017). Increased myoendothelial feedback is associated with increased connexin37 and IK1 channel expression in mesenteric arteries of diet-induced hyperhomocysteinemic mice. *Microcirculation* 24:e12398. doi: 10.1111/micc.12398

Luo, W., Liu, B., and Zhou, Y. (2016). The endothelial cyclooxygenase pathway: insights from mouse arteries. *Eur. J. Pharmacol.* 780, 148–158. doi: 10.1016/j.ejphar.2016.03.043

Matchkov, V. V., Rahman, A., Bakker, L. M., Griffith, T. M., Nilsson, H., and Aalkjaer, C. (2006). Analysis of effects of connexin-mimetic peptides in rat mesenteric small arteries. *Am. J. Physiol. Heart Circ. Physiol.* 291, H357–H367. doi: 10.1152/ajpheart.00681.2005

Mather, S., Dora, K. A., Sandow, S. L., Winter, P., and Garland, C. J. (2005). Rapid endothelial cell-selective loading of connexin 40 antibody blocks endothelium-derived hyperpolarizing factor dilation in rat small mesenteric arteries. *Circ. Res.* 97, 399–407. doi: 10.1161/01.RES.0000178008.46759.d0

Meens, M. J., Pfenniger, A., Kwak, B. R., and Delmar, M. (2013). Regulation of cardiovascular connexins by mechanical forces and junctions. *Cardiovasc. Res.* 99, 304–314. doi: 10.1093/cvr/cvt095

Milkau, M., Kohler, R., and de Wit, C. (2010). Crucial importance of the endothelial K^+ channel SK3 and connexin40 in arteriolar dilations during skeletal muscle contraction. *FASEB J.* 24, 3572–3579. doi: 10.1096/fj.10-158956

Morel, S. (2014). Multiple roles of connexins in atherosclerosis- and restenosis-induced vascular remodelling. *J. Vasc. Res.* 51, 149–161. doi: 10.1159/000362122

Murai, T., Muraki, K., Imaizumi, Y., and Watanabe, M. (1999). Levcromakalim causes indirect endothelial hyperpolarization via a myo-endothelial pathway. *Br. J. Pharmacol.* 128, 1491–1496. doi: 10.1038/sj.bjp.0702956

Nava, E., and Llorens, S. (2019). The local regulation of vascular function: from an inside-outside to an outside-inside model. *Front. Physiol.* 10:729. doi: 10.3389/fphys.2019.00729

Nielsen, M. S., Axelsen, L. N., Sorgen, P. L., Verma, V., Delmar, M., and Holstein-Rathlou, N. H. (2012). Gap junctions. *Compr. Physiol.* 2, 1981–2035. doi: 10.1002/cphy.c110051

Pogoda, K., Fuller, M., Pohl, U., and Kameritsch, P. (2014). NO, via its target Cx37, modulates calcium signal propagation selectively at myoendothelial gap junctions. *Cell Commun. Signal.* 12:33. doi: 10.1186/1478-811X-12-33

Pogoda, K., and Kameritsch, P. (2019). Molecular regulation of myoendothelial gap junctions. *Curr. Opin. Pharmacol.* 45, 16–22. doi: 10.1016/j.coph.2019.03.006

Pogoda, K., Mannell, H., Blodow, S., Schneider, H., Schubert, K. M., Qiu, J., et al. (2017). NO augments endothelial reactivity by reducing myoendothelial calcium signal spreading: a novel role for Cx37 (Connexin 37) and the protein tyrosine phosphatase SHP-2. *Arterioscler. Thromb. Vasc. Biol.* 37, 2280–2290. doi: 10.1161/ATVBAHA.117.309913

Pohl, U. (2020). Connexins: key players in the control of vascular plasticity and function. *Physiol. Rev.* 100, 525–572. doi: 10.1152/physrev.00010.2019

Qian, J., and Fulton, D. (2013). Post-translational regulation of endothelial nitric oxide synthase in vascular endothelium. *Front. Physiol.* 4:347. doi: 10.3389/fphys.2013.00347

Radtke, J., Schmidt, K., Wulff, H., Kohler, R., and de Wit, C. (2013). Activation of KCa3.1 by SKA-31 induces arteriolar dilation and lowers blood pressure in normo- and hypertensive connexin40-deficient mice. *Br. J. Pharmacol.* 170, 293–303. doi: 10.1111/bph.12267

Rummery, N. M., and Hill, C. E. (2004). Vascular gap junctions and implications for hypertension. *Clin. Exp. Pharmacol. Physiol.* 31, 659–667. doi: 10.1111/j.1440-1681.2004.04071.x

Saez, J. C., Berthoud, V. M., Branes, M. C., Martinez, A. D., and Beyer, E. C. (2003). Plasma membrane channels formed by connexins: their regulation and functions. *Physiol. Rev.* 83, 1359–1400. doi: 10.1152/physrev.00007.2003

Saliez, J., Bouzin, C., Rath, G., Ghisdal, P., Desjardins, F., Rezzani, R., et al. (2008). Role of caveolar compartmentation in endothelium-derived hyperpolarizing factor-mediated relaxation: Ca^{2+} signals and gap junction function are regulated by caveolin in endothelial cells. *Circulation* 117, 1065–1074. doi: 10.1161/CIRCULATIONAHA.107.731679

Sandow, S. L., Gzik, D. J., and Lee, R. M. K. W. (2009). Arterial internal elastic lamina holes: relationship to function? *J. Anat.* 214, 258–266. doi: 10.1111/j.1469-7580.2008.01020.x

Sandow, S. L., Looft-Wilson, R., Doran, B., Grayson, T. H., Segal, S. S., and Hill, C. E. (2003). Expression of homocellular and heterocellular gap junctions in hamster arterioles and feed arteries. *Cardiovasc. Res.* 60, 643–653. doi: 10.1016/j.cardiores.2003.09.017

Sandow, S. L., Senadheera, S., Bertrand, P. P., Murphy, T. V., and Tare, M. (2012). Myoendothelial contacts, gap junctions, and microdomains: anatomical links to function? *Microcirculation* 19, 403–415. doi: 10.1111/j.1549-8719.2011.00146.x

Sankaranarayanan, A., Raman, G., Busch, C., Schultz, T., Zimin, P. I., Hoyer, J., et al. (2009). Naphtho[1,2-d]thiazol-2-ylamine (SKA-31), a new activator of KCa2 and KCa3.1 potassium channels, potentiates the endothelium-derived hyperpolarizing factor response and lowers blood pressure. *Mol. Pharmacol.* 75, 281–295. doi: 10.1124/mol.108.051425

Schmidt, V. J., Jobs, A., von Maltzahn, J., Worsdorfer, P., Willecke, K., and de Wit, C. (2012). Connexin45 is expressed in vascular smooth muscle but its function remains elusive. *PLoS One* 7:e42287. doi: 10.1371/journal.pone.0042287

Schweda, F., Kurtz, L., de Wit, C., Janssen-Bienhold, U., Kurtz, A., and Wagner, C. (2009). Substitution of connexin40 with connexin45 prevents hyperreninemia and attenuates hypertension. *Kidney Int.* 75, 482–489. doi: 10.1038/ki.2008.637

Selemidis, S., and Cocks, T. (2007). Smooth muscle mediates circumferential conduction of hyperpolarization and relaxation to focal endothelial cell activation in large coronary arteries. *Naunyn Schmiedebergs Arch. Pharmacol.* 375, 85–94. doi: 10.1007/s00210-007-0149-7

Shu, X., Ruddiman, C. A., Keller, T. C. S., Keller, A. S., Yang, Y., Good, M. E., et al. (2019). Heterocellular contact can dictate arterial function. *Circ. Res.* 124, 1473–1481. doi: 10.1161/CIRCRESAHA.118.313926

Si, H., Heyken, W. T., Wolfle, S. E., Tysiac, M., Schubert, R., Grgic, I., et al. (2006). Impaired endothelium-derived hyperpolarizing factor-mediated dilations and increased blood pressure in mice deficient of the intermediate-conductance Ca^{2+} activated K^+ channel. *Circ. Res.* 99, 537–544. doi: 10.1161/01.RES.0000238377.08219.0c

Siegl, D., Koeppen, M., Wolfle, S. E., Pohl, U., and de Wit, C. (2005). Myoendothelial coupling is not prominent in arterioles within the mouse cremaster microcirculation in vivo. *Circ. Res.* 97, 781–788. doi: 10.1161/01.RES.0000186193.22438.6c

Simon, A. M., and McWhorter, A. R. (2003). Decreased intercellular dye-transfer and downregulation of non-ablated connexins in aortic endothelium deficient in connexin37 or connexin40. *J. Cell Sci.* 116, 2223–2236. doi: 10.1242/jcs.00429

Sohl, G., and Willecke, K. (2004). Gap junctions and the connexin protein family. *Cardiovasc. Res.* 62, 228–232. doi: 10.1016/j.cardiores.2003.11.013

Sorensen, C. M., and Holstein-Rathlou, N. H. (2012). Cell-cell communication in the kidney microcirculation. *Microcirculation* 19, 451–460. doi: 10.1111/j.1549-8719.2011.00149.x

Straub, A. C., Johnstone, S. R., Heberlein, K. R., Rizzo, M. J., Best, A. K., Boitano, S., et al. (2010). Site-specific connexin phosphorylation is associated with reduced heterocellular communication between smooth muscle and endothelium. *J. Vasc. Res.* 47, 277–286. doi: 10.1159/000265562

Straub, A. C., Lohman, A. W., Billaud, M., Johnstone, S. R., Dwyer, S. T., Lee, M. Y., et al. (2012). Endothelial cell expression of haemoglobin alpha regulates nitric oxide signalling. *Nature* 491, 473–477. doi: 10.1038/nature11626

Straub, A. C., Zeigler, A. C., and Isakson, B. E. (2014). The myoendothelial junction: connections that deliver the message. *Physiology* 29, 242–249. doi: 10.1152/physiol.00042.2013

Wagner, C., de Wit, C., Kurtz, L., Grunberger, C., Kurtz, A., and Schweda, F. (2007). Connexin40 is essential for the pressure control of renin synthesis and secretion. *Circ. Res.* 100, 556–563. doi: 10.1161/01.RES.0000258856.19922.45

Wagner, C., Jobs, A., Schweda, F., Kurtz, L., Kurt, B., Lopez, M. L. S., et al. (2010). Selective deletion of connexin 40 in renin-producing cells impairs renal baroreceptor function and is associated with arterial hypertension. *Kidney Int.* 78, 762–768. doi: 10.1038/ki.2010.257

Wagner, C., and Kurtz, A. (2013). Distribution and functional relevance of connexins in renin-producing cells. *Pflugers Arch.* 465, 71–77. doi: 10.1007/s00424-012-1134-7

Wagner, C., Kurtz, L., Schweda, F., Simon, A. M., and Kurtz, A. (2009). Connexin 37 is dispensable for the control of the renin system and for positioning of renin-producing cells in the kidney. *Pflugers Arch.* 459, 151–158. doi: 10.1007/s00424-009-0707-6

Wei, R., Lunn, S. E., Tam, R., Gust, S. L., Classen, B., Kerr, P. M., et al. (2018). Vasoconstrictor stimulus determines the functional contribution of

myoendothelial feedback to mesenteric arterial tone. *J. Physiol.* 596, 1181–1197. doi: 10.1113/JP274797

Welsh, D. G., and Segal, S. S. (1998). Endothelial and smooth muscle cell conduction in arterioles controlling blood flow. *Am. J. Phys.* 274, H178–H186. doi: 10.1152/ajpheart.1998.274.1.H178

Welsh, D. G., and Segal, S. S. (2000). Role of EDHF in conduction of vasodilation along hamster cheek pouch arterioles in vivo. *Am. J. Physiol. Heart Circ. Physiol.* 278, H1832–H1839. doi: 10.1152/ajpheart.2000.278.6.H1832

Westcott, E. B., and Segal, S. S. (2013). Perivascular innervation: a multiplicity of roles in vasomotor control and myoendothelial signaling. *Microcirculation* 20, 217–238. doi: 10.1111/micc.12035

Wilson, C., Zhang, X., Buckley, C., Heathcote, H. R., Lee, M. D., and McCarron, J. G. (2019). Increased vascular contractility in hypertension results from impaired endothelial calcium signaling. *Hypertension* 74, 1200–1214. doi: 10.1161/HYPERTENSIONAHA.119.13791

Wolfle, S. E., Schmidt, V. J., Hoepfl, B., Gebert, A., Alcolea, S., Gros, D., et al. (2007). Connexin45 cannot replace the function of connexin40 in conducting endothelium-dependent dilations along arterioles. *Circ. Res.* 101, 1292–1299. doi: 10.1161/CIRCRESAHA.107.163279

Wolfle, S. E., Schmidt, V. J., Hoyer, J., Kohler, R., and de Wit, C. (2009). Prominent role of KCa3.1 in endothelium-derived hyperpolarizing factor-type dilations and conducted responses in the microcirculation in vivo. *Cardiovasc. Res.* 82, 476–483. doi: 10.1093/cvr/cvp060

Yamamoto, Y., Klemm, M. F., Edwards, F. R., and Suzuki, H. (2001). Intercellular electrical communication among smooth muscle and endothelial cells in Guinea-pig mesenteric arterioles. *J. Physiol.* 535, 181–195. doi: 10.1111/j.1469-7793.2001.00181.x

Yashiro, Y., and Duling, B. R. (2000). Integrated Ca^{2+} signaling between smooth muscle and endothelium of resistance vessels. *Circ. Res.* 87, 1048–1054. doi: 10.1161/01.RES.87.11.1048

Conflict of Interest: The authors declare that the research was conducted in the absence of any commercial or financial relationships that could be construed as a potential conflict of interest.

Advantages of publishing in Frontiers

OPEN ACCESS
Articles are free to read for greatest visibility and readership

FAST PUBLICATION
Around 90 days from submission to decision

HIGH QUALITY PEER-REVIEW
Rigorous, collaborative, and constructive peer-review

TRANSPARENT PEER-REVIEW
Editors and reviewers acknowledged by name on published articles

Frontiers
Avenue du Tribunal-Fédéral 34
1005 Lausanne | Switzerland

Visit us: www.frontiersin.org
Contact us: frontiersin.org/about/contact

REPRODUCIBILITY OF RESEARCH
Support open data and methods to enhance research reproducibility

DIGITAL PUBLISHING
Articles designed for optimal readership across devices

FOLLOW US
@frontiersin

IMPACT METRICS
Advanced article metrics track visibility across digital media

EXTENSIVE PROMOTION
Marketing and promotion of impactful research

LOOP RESEARCH NETWORK
Our network increases your article's readership